

THIS WEEK

EDITORIALS

SLEEP Science of slumber needs seriously snoozy volunteers **p.408**

WORLD VIEW Europe should make up its mind on new crop breeding **p.409**



MIGRATION Snails—to-go as snacks reveal old Irish arrival **p.410**

A culture of consent

More than 50 years after the WI-38 cell line was derived from a fetus, science and society has still to get to grips with the ethical issues of using human tissue in research.

Tissue is removed from a woman in hospital. A scientist grows the tissue into a cell line. The cell line becomes one of the most important medical tools worldwide. Millions of lives are saved and millions of dollars made. The woman who made the breakthrough possible and her family are largely forgotten. Sound familiar?

That story describes the development of the famous HeLa cell line, grown from cancer tissue taken from a poor black woman without her consent, and brilliantly recorded by Rebecca Skloot in her best-seller *The Immortal Life of Henrietta Lacks* (Crown, 2010). But it also neatly summarizes a separate tale that has echoes of the HeLa case and raises many of the same ethical questions of consent and obligation. Until now, that story has failed to reach the broad audience it deserves.

The cell line in this case is called WI-38, in which the initials represent the Wistar Institute of Anatomy and Biology in Philadelphia, Pennsylvania, where the early work was done. WI-38 has arguably had an even bigger impact on science and medicine than the HeLa line. Whereas HeLa cells are cancerous, WI-38 cells are healthy and normal. They have been widely used for the production of virus vaccines given to many people worldwide — against rubella, for instance — and in research as a prototypical normal human cell.

As the News Feature on page 422 reports, the WI-38 cells came from a legally aborted fetus. More than half a century ago, a Swedish woman had her pregnancy terminated and the WI-38 cells were grown from tissue samples taken from the lungs of the fetus. That makes some people uncomfortable, but fetal tissue remains a useful and common tool in medicine today. In addition to its use in vaccine production, it has been used to make drugs against rheumatoid arthritis and cystic fibrosis. Therapies using cells derived from fetuses are being developed to treat haemophilia and to help patients on chemotherapy fight off infection.

A QUESTION OF OWNERSHIP

Last September, Leonard Hayflick, the scientist who derived the cell line, outlined the circumstances in a letter to *Science* (L. Hayflick *Science* **337**, 1292; 2012). That letter was a direct response to the questions about the ownership of discarded tissue — and consent for using it — raised by Skloot's book.

Before her death, Henrietta Lacks was not asked for consent regarding the use of her cervical cancer cells. That was accepted practice in 1951, when the HeLa line was derived, as it was 11 years later when the Swedish woman had the legal abortion in 1962 that gave rise to WI-38.

Whether the woman was asked for or gave her consent to the use of the cells at the time of the abortion is not known, and whether she received any compensation seems highly unlikely. The gynaecologist who performed the abortion is dead, as is Sven Gard, the eminent Swedish virologist who arranged the transfer of the fetal lungs to Hayflick in the United States. Hayflick does not know. The woman involved has made it clear she does not want to talk about it and wants to be left alone.

The WI-38 story and Skloot's book both highlight how scientists,

companies and public health have all benefited from tissues with a troubled past — tissues that will stay in widespread use for decades because they are composed of self-replicating cells. Stanley Plotkin, inventor of the rubella vaccine, is quoted in the News Feature as saying that “retrospective ethics is easy but presumptuous”. It is a point worth bearing in mind as scientists, physicians and the public try to navigate these issues.

The World Medical Association's Declaration of Helsinki, which laid out ethical recommendations for research involving human subjects,

“Whether human subjects are protected in research is a live question.”

was not published until 1964. The Karolinska Institute in Stockholm implemented a research-ethics committee in the mid-1960s. And the US government did not publish basic regulations for the protection of human research subjects until 1974.

Still, whether human subjects are being adequately protected in research is a live question. This was shown, for instance, by the controversy in March over whether the parents of premature infants were adequately informed when giving consent for a trial of oxygen therapy (see also A. J. Ammann *Nature* **498**, 7; 2013).

Nor is it clear that scientists completely understand how technological progress is changing the debate about privacy. For instance, despite the publicity around Skloot's book, researchers this year published the HeLa genome (J. J. M. Landry *et al.* *Genes Genomes Genet.* <http://doi.org/k22>; 2013) without informing or asking the permission of Henrietta Lacks' surviving family. (The researchers later removed the sequence from databases after realizing that they had intruded on the family's privacy.)

In July 2011, the US Office for Human Research Protections provisionally proposed the first major revamp of the rules to govern human subjects in research in two decades. Among its suggestions is requiring written consent for the use of leftover tissues from surgeries and other procedures — even those that have been stripped of identifiers. The change is a necessary one, and crucial for public trust and accountability. Alas, nearly two years later, this change and others have not progressed even to the point of being issued as a firm proposal.

Another reason to press for a rule revision that goes the extra mile to involve tissue donors more is evident in Wisconsin. For the second time since 2011, a bill has been introduced to ban research with “any material derived from any cell or tissue of an unborn child”.

Nature opposes the bill, introduced by André Jacque, a Republican member of the Wisconsin State Assembly. Yet it does raise an important issue. Written consents from donors of fetal tissue will not sway those who are opposed to abortion, but would certainly help the case for research. However strong the life-saving benefits seem to scientists and the medical profession, that case can always be — and should be — bolstered in the eyes of the public. On the use of tissue samples such as from the fetus from Sweden and from Henrietta Lacks, and the question of compensation, some would argue that mistakes may have been made. Some would disagree. All can agree there are lessons to learn. ■

Family first

Better sequencing techniques are enabling some scientists to take personal genomics literally.

When Bea Rienhoff was born nearly 10 years ago, her father Hugh and her doctors immediately noticed some worrying signs. Her long fingers and toes curled inwards. Her eyes were spaced just a bit wider than normal, and she was floppy — not like the clenched little bundles of energy her two brothers were at birth. In the joy of the moment, Rienhoff put these nagging concerns aside. But as Bea grew and failed to put on much muscle, he became increasingly worried that she might have a genetic syndrome, one that might lead to dangerous complications with her heart.

Like any parent of a child with a mysterious undiagnosed disease, Rienhoff wanted answers and was willing to do nearly anything to get them. Bea was fortunate: her dad had trained in clinical genetics in the 1980s under Victor McKusick, widely considered the father of the field. And Rienhoff's subsequent work in biotechnology and venture capital filled his address book with the names of movers and shakers in the burgeoning field of genomics.

Rienhoff and Bea appeared on the cover of *Nature* in 2007 as his personal anguish and professional abilities combined in unlikely fashion (see *Nature* 449, 773–776; 2007). He had purchased used laboratory equipment, set it up in his basement and prepared several of Bea's genes for sequencing. That failed to provide an answer. So he reached out to colleagues at Illumina, a genome-sequencing company in San Diego, California, who took the search to the next level by sequencing RNA and DNA from him, Bea, her siblings and her mother.

That work seems to have borne fruit, and Rienhoff is back in the pages of *Nature* this week (see page 418). He and his volunteer collaborators are confident that they have found the mutation responsible for Bea's condition. Bea is still skinny, but otherwise healthy.

Rienhoff's journey into such personal genomics made some people uncomfortable, especially in the early days. Back then, genomics had never been used successfully to unpick the genetic causes of a new disease in a single patient. Usually one or more families with multiple affected members were needed. More worrisome, perhaps, was

Rienhoff's closeness to his study subject. Although a passion for one's work is a feature of good science, people often draw the line when the subject is a family member.

Today, whole- and partial-genome sequencing has been used several times to discover the gene or genes responsible for a new disease. And many high-profile success stories have involved family members of those close to the action.

For instance, when colleagues of geneticist Lynn Jorde at the University of Utah in Salt Lake City were looking for a rare disease on which to test whole-genome sequencing, he suggested asking his two adult stepchildren, Heather and Logan Madsen. They had been diagnosed with Miller syndrome, which affects development of the face

“What Hugh Rienhoff has done is beyond the reach of most parents for now.”

and limbs, among other features. In 2009, Heather, Logan and their mother and father became the first family in the world to have their entire genomes sequenced. Researchers identified a causative mutation for the disorder as a result (see *Nature* 478, 22–24; 2011).

James Lupski, a geneticist at Baylor College of Medicine in Houston, Texas, has a rare

form of the nerve disorder Charcot–Marie–Tooth disease. He and his collaborators sequenced his entire genome and compared it with that of his brother, together with partial sequences from other family members, to identify new mutations associated with the disease (see *Nature* <http://doi.org/cwc5wv>; 2010).

And Retta Beery and her husband Joe, chief information officer at sequencing company Life Technologies in Carlsbad, California, convinced a team at Baylor College of Medicine to sequence their teenage twins Alexis and Noah to refine their diagnosis of dystonia, a muscle-tone disorder that affects movement. Physicians found that the twins had an extra mutation that complicated their disease, and which pointed to better treatment options (see *Nature* <http://doi.org/cj66mr>; 2011).

For Rienhoff, starting such a quest today would probably have been easier. Many paediatric hospitals are gearing up to offer whole- or partial-genome sequencing to families such as his. Still, Rienhoff suspects that might not be enough. It took him years to find the gene responsible in his daughter's case, and his work benefited greatly from his connections in the community and the attendant publicity. Hugh, like his daughter, is special, and what he has done is probably beyond the reach of most parents for now. That won't be the case for long. ■

How do you sleep?

Modern sleep patterns cause ill health, so it is time to work out how much rest we really need.

Sleep, as Shakespeare noted in *Macbeth*, is the chief nourisher in life's feast. But some go hungrier than others, and their ranks are increasing. Some 70 million people in the United States alone are thought to suffer from insomnia or another pathology of sleep.

Sleep is universal, but there is decent evidence that we are doing it wrong. That we need eight hours of sleep a night to function is a myth; that we need our shut-eye in one continued bout is unlikely. Before artificial lights, people went to bed earlier. And it was once more common to have two night-time sleeps, separated by a productive period of wakefulness.

Scientists cannot say for sure how much sleep we need, or when we should take it. As chronobiologist Till Roenneberg points out in a Comment on page 427, part of the reason is that most studies of sleep are done in laboratories. He proposes a radical solution: a

US\$30-million global human sleep project that would start with online logs of the sleep habits of millions of volunteers and finish with DNA tests to work out where those habits come from.

“The practice of going to sleep and waking at unnatural times could be the most prevalent high-risk behaviour in modern society,” says Roenneberg. Many workers at present, he says, could suffer from a form of social jet lag, forced to shuffle sleep patterns between the conflicting time zones of working and work-free days. That could cause poor health — both physical and mental. The solution would be a profound change: restructure work and school schedules to better suit the biological clocks of the majority of the population, once we work out what they are.

The modern world fragments time. We work on call and watch 24-hour news. Television is on-demand and breakfast usually available all day. We sleep when we can, if we can. Sleep has become another demand on us, and one that we like to allot to a specific window of our daily diary. That is a difficult habit to break for scientists as much as anybody, given their often long hours and frequent travel.

People in many countries get as much as two hours less sleep a night than their ancestors did a century or so ago. That must have a consequence. Lack of sleep may not make our hungry lives longer, it just feels that way. ■

➔ NATURE.COM
To comment online,
click on Editorials at:
go.nature.com/xhungv



Europe should rethink its stance on GM crops

*Second-generation crop genetic-modification techniques avoid some of the issues that previously provoked hostility, argues **Brian Heap**.*

Countries in the European Union (EU) are losing ground in the international race to grow more food on increasingly scarce land. This has serious and urgent implications for the EU science base and the environment, as well as for domestic food security, employment and economic growth. It is down to the slow and expensive way that the continent regulates genetically modified (GM) organisms.

Historical attitudes and actions of the EU have constrained the use of GM crops — both at home and in developing countries. The region must now base its regulations in this area on sound science, as it has promised to do. An early test of this commitment will be the EU's approach to the next generation of crop genetic-improvement technologies. These techniques allow scientists to generate plant varieties with desired traits more precisely, rapidly and efficiently than with conventional breeding.

A key feature of many of these techniques, which include some that induce epigenetic modifications (that is, modifications that do not cause changes to the DNA sequence itself), is that they leave the resultant crop free of genes foreign to the species. Indeed, the changes induced by modern genetic modification often cannot be distinguished from those produced by conventional breeding or natural genetic variation. This raises issues for regulators. Put simply, are these plants GM crops?

The difference is more than semantic. A GM classification raises regulatory hurdles and associated costs, which could put the commercial use of these techniques beyond the reach of smaller companies and public-sector researchers. The techniques have the potential to improve crop resistance to disease and to increase yields and nutritional content, but classification as GM would restrict their application to high-value crops, as happened with the first wave of GM crops. It would be perverse if the costs of regulation yet again lock up the promise of agricultural innovation within a few large companies.

As a report published this week by the European Academies Science Advisory Council (EASAC) in Halle, Germany, of which I am president, points out, expert groups have already concluded that many of these new breeding techniques do not constitute 'genetic modification' in the way that the term is usually used. As such, the plants that they produce should not be regulated as GM organisms. Work on these techniques is well advanced, in particular in the United States and Europe. The EU has not yet decided how to classify — and so regulate — plants produced by them, and this is hampering progress there.

The world faces major problems in food security alongside pressures from population growth, climate change and economic and

social instability. The biosciences can play a big part in the sustainable intensification of agriculture, improving efficiency in production and avoiding further loss of biodiversity. As observed in the recent *Nature* special issue on genetic modification (nature.com/gmcrops), the world is changing and many developing countries are now actively engaged in research on advanced technologies in pursuit of their own priorities.

Researchers and plant breeders across Europe urgently need to know the legal status of these novel breeding techniques. Recent safety assessments by expert advisory groups of the European Food Safety Authority in Parma, Italy, have already judged that hazards are similar for conventionally bred plants and those produced by cisgenesis (in

which only genes from the same species or a normally interbreeding relative are introduced), and that targeted mutagenesis (in which only specific nucleotides in a gene are changed) is also likely to minimize unintended effects associated with the disruption of genes or regulatory elements in the modified genome.

Confirmation by the EU that targeted techniques that leave no foreign DNA behind do not fall under the scope of GM legislation would give considerable support to agricultural innovation in Europe. Without this support, there is the risk that scientists and companies in this field will move elsewhere, accelerating the negative impact on the science base and on Europe's competitiveness.

The implications go further. An EU regulatory position not based on sound science could create damaging knock-on effects for developing countries, who may depend on the EU for export

markets or look to it for leadership in managing bioscience innovation. There is an ever-greater requirement for consistent, harmonized, evidence-based policy worldwide to enable synchronous technology development and trade.

At the same time as addressing the proportionate management of these new techniques, the EU must recalibrate its broader approach to GM crop regulation. It must make it transparent, predictable and fit for purpose by taking account of the extensive evidence of safe use of these crops around the world.

In common with other innovation sectors, the objective must be to regulate the product and not the technology that produces it. By making better use of all crop-improvement techniques and so reducing dependence on food and animal-feed imports, the EU can help improve land use elsewhere, and allow more of the agriculture in developing countries to be used for local needs. ■

Brian Heap is president of EASAC.
e-mail: brian.heap@easac.eu

THE
OBJECTIVE
MUST BE TO
REGULATE THE
PRODUCT
AND NOT THE
TECHNOLOGY
THAT PRODUCES IT.

➔ **NATURE.COM**
Discuss this article
online at:
go.nature.com/xpe5bt

RESEARCH HIGHLIGHTS

Selections from the
scientific literature

EVOLUTION

Red Queen forces extinctions

Mammalian extinctions seem to be driven more by a failure to keep up with evolutionary pace than by random swings in diversity.

Tiago Quental at the University of Sao Paulo in Brazil and Charles Marshall at the University of California, Berkeley, analysed 19 mammalian clades — groups of species descended from a common ancestor — that had well-preserved fossil records and had either become extinct or declined in diversity within the past 66 million years.

Diversity loss was due to new lineages arising at lower rates and extinctions occurring at higher rates. The authors say clades' decline can be explained by the Red Queen hypothesis: that species must continue to evolve to keep pace with a deteriorating environment.

Science <http://dx.doi.org/10.1126/science.1239431> (2013)

PLANT SCIENCES

Vegetables' daily rhythm

Harvested vegetables are capable of the same daily cycles as the plants they come from.

Janet Braam at Rice University in Houston, Texas, and her colleagues set the

biological clock of shop-bought cabbages (*Brassica oleracea*) by exposing them to daily light-dark cycles. The researchers found that the cabbage tissue accumulated chemical defences against herbivores during the light cycle. Intact *Arabidopsis* plants

use the same cycle to guard against pests. When the daily rhythm of the cabbages was synced with that of the plant-munching larvae of the moth *Trichoplusia ni* (pictured), the vegetables were nibbled less than those whose rhythm was out of sync.

The protective cycling was reproduced in other harvested



ECOLOGY

Escargot on the go

Ancient humans' taste for snails could explain an unusual pattern of present-day distribution for one snail species.

Adele Grindon and Angus Davison at the University of Nottingham, UK, sequenced a mitochondrial gene in 111 European populations of the land snail *Cepaea nemoralis* (pictured). Of the seven lineages that they identified, one was found just in Ireland and in a region of the Eastern Pyrenees in southwest Europe.

The oldest *C. nemoralis* fossils in Ireland date to about 8,000 years ago — around the time of the first human habitation of the island. The authors suggest that ancient humans might have carried the snails — a popular food — with them as they moved between the Mediterranean and the Atlantic, following Europe's Garonne river.

If examples of other species are found in Ireland and the Iberian peninsula, but not between, this could confirm the migratory route.

PLoS ONE 8, e65792 (2013)

crops, including blueberries, sweet potatoes and carrots, suggesting that it could be a way to protect fruit and vegetables from pests. The researchers speculate that daily rhythms in harvested produce might also affect its nutrient value.

Curr. Biol. <http://dx.doi.org/10.1016/j.cub.2013.05.034> (2013)

ARCHAEOLOGY

Shells show rise of *Homo sapiens*

The size of ancient limpet shells suggests that human populations began swelling around 50,000 years ago, long after key cultural innovations appear in the archaeological record.

Teresa Steele at the University of California, Davis, and Richard Klein at Stanford University, California, measured the size of limpet shells from archaeological sites in South Africa, inferring that smaller shells are linked to increased harvesting and therefore larger human settlements. Shells from the Middle Stone Age, 200,000 to 50,000 years ago, were consistently bigger than shells from Late Stone Age sites, suggesting that there was an increase in population growth in this later era.

Humans living on the coast of South Africa began creating symbolic artefacts, such as shell beads, around 100,000 years ago, when populations are thought to have been smaller. The researchers say their findings challenge the theory that such cultural behaviour was catalysed by high population densities that helped new innovations to spread.

Proc. Natl Acad. Sci. USA <http://dx.doi.org/10.1073/pnas.1304750110> (2013)

LAUREN HOLDEN

D. GOODSPED ET AL.

ATMOSPHERIC SCIENCE

Aerosols suppress hurricanes

Aerosol particles from human activities could have lowered the number of tropical storms over the Atlantic Ocean during the twentieth century.

Natural aerosols such as dust particles are thought to influence hurricane activity, but the effects of anthropogenic aerosols are unclear. A team led by Nick Dunstone at the Met Office Hadley Centre in Exeter, UK, modelled the frequency of North Atlantic tropical storms with simulations that either incorporated or excluded changes in man-made aerosols. The model suggests that as levels of anthropogenic aerosols increased in the earlier part of the century, tropical storm activity dropped; aerosol declines at the end of the century increased storms.

The authors attribute this to the effect of aerosols on clouds. By brightening clouds and causing them to stick around for longer, aerosols cool surface temperatures and shift circulation patterns in a way that suppresses hurricanes.

Nature Geosci. <http://dx.doi.org/10.1038/ngeo1854> (2013)

MATERIALS SCIENCE

Droplets move to softer substrates

Liquid droplets dripped onto a silicone gel will move from thin, stiff regions to thick, springy ones.

This intriguing behaviour, reported by Eric Dufresne at Yale University in New Haven, Connecticut, and his colleagues, occurs because

of the physics of surface tension. A droplet tends to spread out over a thick, deformable surface, but rears up into a spherical shape at thinner, stiffer places. A similar phenomenon occurs in biology, but in reverse: cells tend to move to stiffer parts of a substrate, a process called durotaxis. The biological movement is thought to involve the cell actively sensing its environment and using actin–myosin fibres to control locomotion. The liquid durotaxis can be used to generate patterns of droplets (pictured) without chemical or thermal gradients and might be useful in microfluidics, the authors speculate.

Proc. Natl Acad. Sci. USA
<http://dx.doi.org/10.1073/pnas.1307122110> (2013)

APPLIED PHYSICS

Metamaterial wall amplifies sound

Sound waves can squeeze through holes smaller than their wavelength in a specially fabricated wall.

Metamaterials are artificial materials precisely engineered from metals or plastics to have structures that manipulate sound or light waves. Such materials have already been used to direct light waves through seemingly impassible openings. To accomplish such 'extraordinary transmission' with sound, Sam Lee at Yonsei University in Seoul, South Korea, and his colleagues stretched pieces of plastic film across tiny perforations in a thin metal plate. Incoming sound

waves of a selected frequency resonated with the film, causing air to flow as if it were massless and funnel as much as 97% of the sound through the holes. The sound was intensified within the holes by a factor of up to 5,700, and thus could be used in sensitive detectors, the researchers suggest.

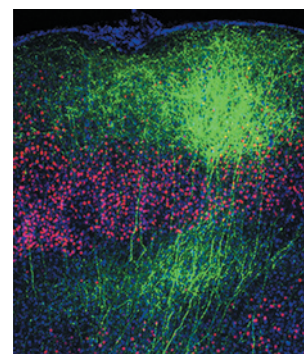
Phys. Rev. Lett. 110, 244302 (2013)

NEUROSCIENCE

Enzyme duo elicit nerve branching

A pair of enzymes control where synapses form in neurons by guiding the transport of energy-producing organelles called mitochondria.

A team led by Franck Polleux at the Scripps Research Institute in La Jolla, California, identified two enzymes that are required for axons (the long message-transmitting stalks of neurons) to branch and form synapses with other neurons. When these enzymes were overexpressed in neurons, mitochondria moving down the axon, along microtubules, were immobilized at the



point where axons would form synapses. Higher levels of these enzymes boosted axon branching (pictured), whereas lower levels reduced it.

The researchers suggest that the two enzymes work together to tell mitochondria where to stop and thus where synapses will form. Mitochondrial transport could factor in the development of a wide range of disorders, including autism, through its effects on synapse formation, the authors say.

Cell <http://dx.doi.org/10.1016/j.cell.2013.05.021> (2013)

➔ **NATURE.COM**

For the latest research published by Nature visit:

www.nature.com/latestresearch

COMMUNITY CHOICE

The most viewed papers in science

GENETIC ENGINEERING

Comprehensive fly library

★ **HIGHLY READ**
on dev.biologists.org in May

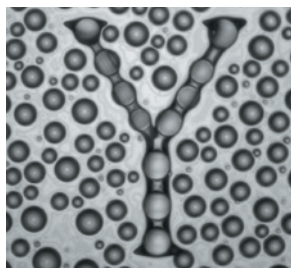
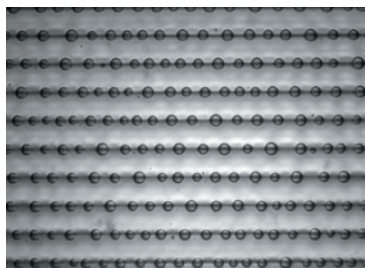
A method that can systematically generate fruitflies to overexpress particular genes will help researchers to explore gene function in the model organism.

Konrad Basler at the University of Zurich, Switzerland, and his colleagues developed a scalable method to overexpress genes at known sites in the genome of the fruitfly *Drosophila*. They coupled a system that allows controlled gene expression with one that allows site-specific integration of a newly introduced gene. The researchers used the technology to establish a library of 1,149 fly strains. The approach could be used to efficiently explore effects of overexpression in a comprehensive set of fly genes and to complement experiments with knockout flies, in which particular genes are disabled or deleted, the authors say.

Development 140, 2434–2442 (2013)

JULIEN COURCHET

ROBERT STYLE



SEVEN DAYS

The news in brief

POLICY

NASA funding plan

Republicans in the US House of Representatives have drafted legislation that would cancel a proposed NASA asteroid-capture mission championed by President Barack Obama. On 19 June, Steven Palazzo (Republican, Mississippi) said that the mission “appears to be a costly and complex distraction”. The House plan, intended to guide NASA budgeting for the next two years, would replenish the space agency’s beleaguered planetary-science division, but would trim funding for climate-change research. The Democratic-controlled Senate is expected to offer its own plan for NASA soon.

Living hybrids

A Japanese science advisory board has recommended relaxing national rules on making human–animal hybrid embryos, to allow *in vivo* experiments. The move came on 18 June, after scientists led by Hiromitsu Nakauchi at the University of Tokyo sought permission to inject human stem cells into pig embryos that lack pancreas-forming cells, to try to grow human organs in pigs. Nakauchi, who plans to open a lab at Stanford University in California in the next few months, says

JOURNALISM AWARDS

Nature podcast editor and reporter Kerri Smith last week won the Association of British Science Writers’ best-feature award for ‘The Ground Breaker’ (*Nature* **489**, 22–25; 2012). Geoff Brumfiel won an award for one of his Fukushima stories (*Nature* **485**, 423–424; 2012); Declan Butler and Leigh Phillips were runners up.



EDGAR SU/REUTERS/CORBIS

Indonesian fires choke nearby countries

A thick haze engulfed areas of Singapore (pictured) and Malaysia last week as forest fires raged on the neighbouring Indonesian island of Sumatra. On 23 June, Malaysia declared a state of emergency in the districts of Muar and Ledang in Johor state. On 20 June, the Singaporean environmental ministry reported a Pollutant Standards Index reading of 371; levels above 300

are deemed hazardous to health. Singaporean officials met representatives of Indonesia last week to urge the country to step up its efforts to stop the fires. Singapore also offered its assistance, including a cloud-seeding aircraft and high-resolution satellite images. Some Indonesian reports suggest that the fires were caused by companies illegally clearing forests.

that he may conduct some experiments outside Japan if the government is slow to adopt the recommendations.

Hepatitis C testing

A panel of health experts assembled by the US government has upgraded its support for hepatitis C screening in all individuals born between 1945 and 1965. The new endorsement, announced on 24 June, increases the likelihood that insurers will cover screening costs and that physicians will perform the tests. US health experts estimate that screening this high-risk population could identify more than 800,000 new cases of the infection, which causes liver disease and cancer. See go.nature.com/akirvr for more.

RESEARCH

Gender imbalance

Female evolutionary biologists may enjoy a smaller level of professional exposure compared with their male colleagues, in part because they give fewer conference talks, according to analysis published on 20 June (J. Schroeder *et al.* *J. Evol. Biol.* <http://doi.org/m2w>; 2013). At the 2011 Congress of the European Society for Evolutionary Biology, women accounted for 23% of the invitations to speak — similar to their representation among senior scientists and those who publish in high-profile journals. However, only 15% of actual conference speakers were women. Female scientists were about twice as

likely as men to turn down the speaking invitations. See *Nature* **495**, 22–24 (2013).

Impact-factor list

The latest journal impact-factor rankings were released on 19 June by Thomson Reuters, an information firm based in New York. A record 66 publications were banned from this year’s report for excessively citing their own articles or those of particular journals. In May, a group of researchers, scientific organizations and publishers criticized the use of impact factors to judge publications and individual scientists, issuing a pledge to “reduce emphasis on the journal impact factor as a promotional tool”. See go.nature.com/ufgbrn for more.

PEOPLE

Nobel physicist dies

Theoretical physicist Kenneth Wilson died on 15 June aged 77, reported Cornell University in Ithaca, New York, last week. While at Cornell, Wilson won the 1982 Nobel Prize in Physics for his theories describing the behaviour of matter at critical points in phase transitions, such as the shift between a liquid and a gas. As an advocate of science education, he also helped to establish the Physics Education Research Group at Ohio State University in Columbus, where he worked from 1988 until retiring in 2008.

Guilty plea

A former scientist at the Los Alamos National Laboratory (LANL) in New Mexico, and his wife, pleaded guilty to federal charges involving the release of classified nuclear-weapons data, the US Department of Justice said on 21 June. Physicist Pedro Leonardo Mascheroni, who worked at LANL from 1979 to 1988, admitted that he shared restricted data in 2008 and 2009 with a person he believed was a Venezuelan government official. His wife, Roxby Mascheroni, who did technical writing and editing at LANL, admitted to conspiring to convey the information.

**The right stuff**

NASA announced its selections for a new class of candidate astronauts last week, the first since 2009. With four men and four women chosen, the group set an agency record for the highest percentage of female candidates. Among those picked is Jessica Meir (pictured), assistant professor of anaesthesia at Massachusetts General Hospital in Boston. The candidates will begin training in August at NASA's Johnson Space Center in Houston, Texas.

Fermilab head

On 20 June, the Fermi National Accelerator Laboratory (Fermilab) in Batavia, Illinois, announced physicist Nigel Lockyer as its next director. Lockyer currently leads TRIUMF, Canada's national laboratory for particle and nuclear physics in Vancouver. He says that he will focus

on getting international collaboration on a large, deep detector for Fermilab's planned Long-Baseline Neutrino Experiment, and on gathering support to build the International Linear Collider to study the Higgs boson. He is due to take up his post on 3 September. See go.nature.com/jp3iku for more.

EVENTS

Magnet on the move

On 22 June, a 15-metre-wide electromagnet began a 5,000-kilometre trip by truck and boat from Brookhaven National Laboratory in Upton, New York, to the Fermi National Accelerator Laboratory in Batavia, Illinois. Heavy rain and wind had postponed the original departure date of 16 June. The magnet is destined for use in the Muon g-2 experiment, which will study how short-lived particles called muons behave in magnetic fields.

BUSINESS

Cheap drugs faster

US pharmaceutical companies will now find it harder to pay the makers of generic drugs to delay releasing cheaper versions of brand-name compounds. In a 5:3 decision, the US Supreme Court sided last week with the Federal Trade Commission

COMING UP

30 JUNE–3 JULY

Kuala Lumpur hosts the 7th International AIDS Society Conference on HIV Pathogenesis, Treatment and Prevention. Highlights include cure strategies and prenatal care. go.nature.com/3zcisw

1–2 JULY

The Basel Declaration Society holds a meeting on transparency in animal research in London, where topics include how to communicate the need for studies on higher mammals. go.nature.com/n7qwsx

in determining that such 'pay-to-delay' practices can violate antitrust regulations. Two days later, the European Commission fined drug company Lundbeck, headquartered in Copenhagen, and several generics makers for delaying release of the generic form of the antidepressant drug citalopram.

AstraZeneca site

The Cambridge Biomedical Campus in the United Kingdom will host a new £330-million (US\$509-million) research and development centre and corporate headquarters for drug giant AstraZeneca, currently based in London. The company announced its selected site on 18 June, and says that it expects to have 2,000 staff at the purpose-built facility by 2016. In March, the company said that it would consolidate various teams at the new hub, including those involved in research on small molecules and biological products, with several hundred jobs being shed in the process.

NATURE.COM

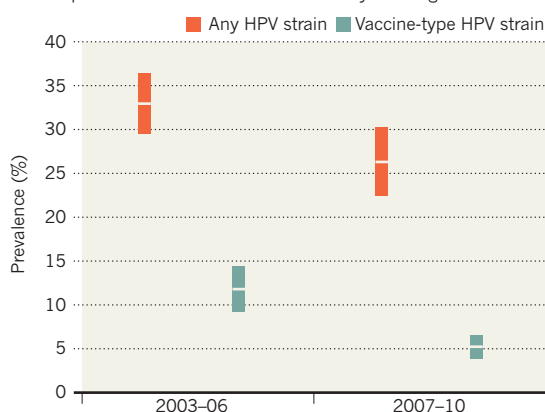
For daily news updates see:
www.nature.com/news

TREND WATCH

The prevalence of certain strains of human papillomavirus (HPV) among US girls aged 14–19 has more than halved since the introduction of a vaccine, says a study (L. E. Markowitz *et al.* *J. Infect. Dis.* <http://doi.org/m2v>; 2013). The US Centers for Disease Control and Prevention in Atlanta, Georgia, added vaccination against four types of HPV to the routine schedule for girls in 2006. Researchers report that the average prevalence of those strains fell from 11.5% in 2003–06 to 5.1% in 2007–10.

US MAKES HEADWAY AGAINST HPV

A US vaccine targeting strains of human papillomavirus (HPV) has cut prevalence of those strains in 14–19-year-old girls.



NEWS IN FOCUS

ENERGY Lithium batteries can pack more punch with sulphur **p.416**

GENETICS A novel mutation is the key to a daughter's diagnosis **p.418**

PHYSICS Theorists find certainty in Heisenberg's uncertainty principle **p.419**



MEDICAL RESEARCH The controversial history of cell line WI-38 **p.422**

LES STONE/REUTERS/CORBIS



Shale-gas extraction has transformed the US energy landscape, but its environmental effects are unclear.

ENERGY

Gas drilling taints groundwater

Chemical analysis links methane in drinking wells to shale-gas extraction.

BY JEFF TOLLEFSON

As shale-gas operations expand across the United States, industry officials and environmentalists are at loggerheads over whether or not shale-gas extraction can contaminate groundwater. Now researchers have traced low levels of methane and other contaminants to a source of shale gas: the sprawling Marcellus Formation, which lies beneath much of New York state, Pennsylvania, West Virginia and Ohio (see 'On tap').

The study, led by researchers at Duke

University in Durham, North Carolina, expands on an earlier analysis of drinking water in northeastern Pennsylvania, where energy companies have used hydraulic fracturing (fracking) to crack the Marcellus Formation and release gas. In that work, the researchers found that contamination rates increased with proximity to wells (S. G. Osborn *et al. Proc. Natl Acad. Sci. USA* **108**, 8172–8176; 2011). Their latest analysis, published on 24 June, goes a step further, by tying the chemical fingerprint of the groundwater contaminants to the

gas being siphoned out of the ground some 2,000–3,000 metres below (R. B. Jackson *et al. Proc. Natl Acad. Sci. USA* <http://doi.org/m3j>; 2013).

"The problems we've seen are probably more common than people realize," says Rob Jackson, director of Duke's Center on Global Change and lead author of the paper. Jackson stresses that the contamination is probably due to poor well construction, rather than hydraulic fracturing itself. But he says that the results are another "wake-up call" for the industry to improve its drilling operations.

The study is the latest salvo in an ongoing debate about the environmental impacts of shale-gas extraction, which has transformed the US energy landscape and is now moving abroad. Such operations are also causing concerns about air pollution and methane emission, which could offset some of the climatic benefits of replacing coal with natural gas. But fears about the potential impact on groundwater resources have taken centre stage in a number of high-profile disputes between scientists, regulators and industry.

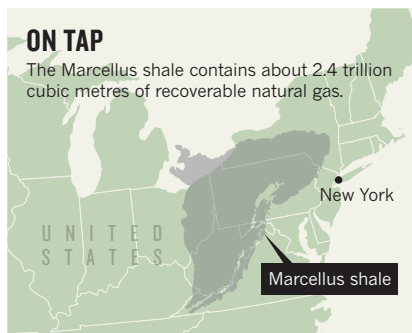
Last week, for example, the US Environmental Protection Agency (EPA) cancelled its probe of groundwater contamination in Pavillion, Wyoming, more than two years after issuing a controversial draft report pinpointing fracking as the cause. The decision leaves the investigation in the hands of state officials, who had criticized the EPA's assessment. And in Dimock, Pennsylvania, which lies in the area covered by the Duke research, allegations of groundwater contamination led state regulators to halt some drilling operations temporarily in 2009 and to fine the primary operator, Cabot Oil and Gas Corporation of Houston, Texas, which settled a lawsuit out of court but did not admit fault.

The Duke team's data provide further evidence that shale development could harm groundwater quality in some areas. Trace amounts of methane are often found in drinking water, and the levels identified by Jackson's team do not necessarily represent a health threat. But in extreme cases, methane contamination can be dangerous: homeowners can sometimes ignite the gas in water coming out of their taps.

Jackson's team found methane in 115 of the 141 shallow drinking-water wells that it sampled. To trace its source, the team examined carbon-isotope ratios of the methane molecules — these ratios differ depending ►

ON TAP

The Marcellus shale contains about 2.4 trillion cubic metres of recoverable natural gas.



► on whether the gas was produced by microorganisms in relatively shallow water or by heat and pressure deep in the Earth. The team also looked at the relative concentrations of ethane, propane and helium — other common by-products of gas extraction that are rare in shallow groundwater sources.

The results suggest that homeowners living up to 1 kilometre from shale-gas wells probably have groundwater contaminated by gas from the Marcellus Formation. But the team did not find evidence that chemicals used in fracking migrated from depth to contaminate aquifers. Jackson says that the methane is probably from leaks in the well casing itself, which would allow direct contamination. The data also suggest that some gas migrated up from geological layers between the Marcellus Formation and the groundwater table.

The data “raise important issues”, says Mark Zoback, a geophysicist at Stanford University in California, who served on a high-level panel that in 2011 recommended improving industry practices to minimize environmental impacts. “There’s a real need in the future to have this kind of sampling before, during and after shale-gas development.”

Officials from Cabot, which operates most of the wells in this area, declined to comment on the study. Steve Everley, a spokesman for Energy In Depth, a research and advocacy arm of the Independent Petroleum Association of America, based in Washington DC, says the Duke study is inconclusive. He notes that recent baseline testing by the US Geological Survey found non-microbial methane in two groundwater wells in northeastern Pennsylvania even before drilling.

Jackson says that his results do not necessarily mean that all drilling operations will have problems. Other research by his team, now in the press in *Applied Geochemistry*, found no evidence of contamination in a shale formation in Arkansas. More importantly, he says, the results suggest that the problem is relatively simple to fix.

“This is about well integrity,” he says. “The industry knows how to do this, and they work hard to maintain well integrity.” ■

ELECTROCHEMISTRY

Sulphur back in vogue for batteries

Lithium–sulphur batteries benefit from new materials.

BY RICHARD VAN NOORDEN

A type of battery first proposed in the 1960s is attracting a fresh surge of interest as scientists and engineers look for ways to extend the range of electric vehicles. The veteran system is the lithium–sulphur battery, now back in fashion as the limitations of expensive, low-capacity lithium-ion batteries become ever more apparent. Over the past two years, what was a trickle of publications has gathered into a wave (see ‘The lithium–sulphur charge’) as scientists wear down once-major stumbling blocks, and the area attracts more funding.

Chemists say that there is substance to the buzz. Although researchers are wary of overstating the case, “we believe that lithium–sulphur is the way to go”, says Ilias Belharouak, a materials scientist who works on batteries at Argonne National Laboratory in Illinois. “There’s promise from many different labs — and some approaches really are working,” adds Linda Nazar, a chemist who studies lithium–sulphur batteries at the University of Waterloo in Ontario, Canada.

Lithium-ion batteries, as their name suggests, shuttle lithium ions from one electrode to another, while forcing electrons around an outside circuit. Improving the energy-density of that system means finding a material that can hold more lithium. Decades ago, sulphur was tipped as a promising candidate¹. It is cheap, abundant and can bond to large numbers of lithium ions. In theory, a battery with a metal lithium anode and a sulphur-based

cathode can hold as much as five times the energy density of today’s batteries, in which lithium ions are held (but not chemically bonded) within the pores of both the carbon and the metal-oxide-based electrodes (see ‘How batteries stack up’). That translates into a greater range for vehicles.

So far, no one has managed to commercialize a lithium–sulphur battery that works well for more than a few dozen charging cycles. The problems are numerous: sulphur does not conduct ions well, so it is hard to get the lithium to move through the sulphur to exploit the whole cathode. And when the lithium ions do start bonding to sulphur atoms, they form soluble compounds — polysulphides — that dissolve in the electrolyte (the liquid through which the ions shuttle). As a result, the sulphur electrode gradually crumbles and the battery loses capacity as it is recharged. Moreover, the lithium metal electrode itself is reactive, although some companies, such as PolyPlus in Berkeley, California, have invented materials to protect it.

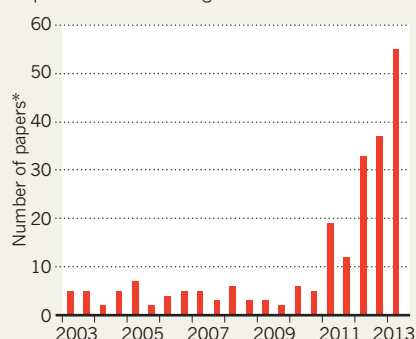
Some of these obstacles are now giving way. In 2009, Nazar’s lab showed how to connect the lithium and sulphur atoms more closely by holding the sulphur within a dense network of carbon fibres a few nanometres apart². Coating those same structures with water-loving polymers helped to trap the polysulphide products. Since then, hundreds of papers have reported related ways of structuring the electrode to function more efficiently.

In January, Yi Cui of Stanford University in California, and his team reported that sulphur nuggets held in titanium dioxide shells — like yolks protected in porous eggshells — maintained 70% storage capacity after 1,000 charging cycles³. And earlier this month, Chengdu Liang’s group at the Oak Ridge National Laboratory in Tennessee, reported a new sulphur-based solid that conducts lithium ions⁴. A liquid electrolyte is no longer needed, Liang says, preventing the problem of soluble polysulphides altogether, and perhaps creating a safer system.

Jay Akhave, who works for the battery firm Altairnano in Reno, Nevada, says that Liang’s find is a “key breakthrough”, although other researchers disagree. Steven Visco, chief executive of PolyPlus, argues that Liang’s new compound — in which long sulphur chains hang off a phosphorus–sulphur molecule — will not survive hundreds of charging cycles.

THE LITHIUM–SULPHUR CHARGE

The number of research papers on lithium–sulphur batteries is rising fast.



*Web of Science, mentioning ‘lithium sulfur’ or ‘lithium sulphur’ in title

SOURCES: J. POWER SOURCES, IM ENERGY, LUX RES.

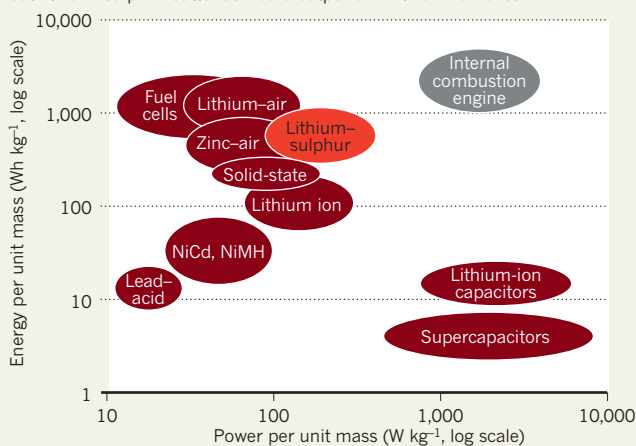
Industrial lithium–sulphur firms are also bullish. At PolyPlus, Visco says that the firm's protective lithium material is advancing batteries that cycle lithium ions through sea water — although not for many cycles. Other companies working hard include Sion Power in Tucson, Arizona (now partly owned by German chemical firm BASF), and Oxis Energy, at the Culham Science Centre in Abingdon, UK.

Last year, these three firms separately announced a total of US\$90 million in new investment, of which some \$15 million came from US federal grants. Another funding boost will come from a new US Department of Energy hub — the Joint Center for Energy Storage, based at Argonne — which aims to make batteries five times more powerful and 80% cheaper within five years. It has \$120 million to give out in research grants, but is not specifically focused on lithium–sulphur.

First sales of prototype batteries are likely to be to military and defence markets, for use in such applications as military drones,

HOW BATTERIES STACK UP

No battery can beat the energy density and power of petrol (gasoline) — but lithium–sulphur batteries would outperform lithium-ion ones.



where the high energy densities and relative safety are more important than the thousands of charge cycles a commercial electric car requires. Researchers do not expect to see a commercial lithium–sulphur battery before the end of the decade. Clever nanostructuring that works in the lab may be too expensive as an industrial proposition. And

the field suffers from hype — with academic discoveries often blurring key details, such as battery currents, to highlight one or two impressive numbers. “We need a concerted effort to make sure cells are standardized, so that we are comparing the same things when reporting data,” says Nazar.

Nonetheless, sulphur is edging ahead of other futuristic battery designs, such as the high-energy-density lithium–air battery — in which lithium ions bind to oxygen sucked in from the atmosphere. There, the ions are hard to recover for recharging and tend to be poisoned by other atmospheric gases.

In that field, says Nazar, scientists are still finding out about the problems. ■

1. Yamin, H., Gorenstein, A., Penciner, J., Sternberg, Y. & Peled, E. *J. Electrochem. Soc.* **135**, 1045–1048 (1988).
2. Ji, X., Lee, K. T. & Nazar, L. F. *Nature Mater.* **8**, 500–506 (2009).
3. Seh, Z. W. *et al.* *Nature Commun.* **4**, 1331 (2013).
4. Lin, Z., Liu, Z., Fu, W., Dudney, N. J. & Liang, C. *Angew. Chem. Int. Edn* <http://dx.doi.org/10.1002/anie.201300680> (2013).

INFECTIOUS DISEASE

Bid to cure HIV ramps up

Clinical trial will aim to replicate virus-expunging therapy that worked in US infant.

BY ERIKA CHECK HAYDEN

HIV-positive mothers who take antiretroviral therapies while pregnant can be prevented from transmitting the virus to their babies 99% of the time — a resounding success story in the decades-long fight against the virus. But what about infants whose mothers do not receive the drugs? Energized by the case of the ‘Mississippi baby’ — who seemed to be cured of HIV after aggressive treatment was begun within hours of birth — researchers are hoping to show that these infants, too, can get off to a healthy start.

At a symposium on HIV cure research on 29 June at the International AIDS Society's biennial meeting in Kuala Lumpur, Malaysia, investigators will describe how they are racing to design a clinical trial to test whether the early treatment works, and why. They hope to treat the first babies by the end of this year.

The trial, sponsored by the International Maternal Pediatric Adolescent AIDS Clinical Trials (IMPACT) Group, marks a change for the field: so far, most research worldwide has

focused on adults. In 2012, the US National Institute of Allergy and Infectious Diseases in Bethesda, Maryland, spent US\$18 million on HIV cure research in adults and adolescents, and just \$45,000 on children. Yet 3.3 million children worldwide have HIV.

“Children have been an afterthought,” says Jeffrey Safritz, director of clinical and basic research for the Elizabeth Glaser Pediatric AIDS Foundation, who is based in Los Angeles, California. “But the immune system of the child might be more easily manipulated to allow a cure.”

This was highlighted in March, when virologist Deborah Persaud of the Johns Hopkins Children's Center in Baltimore, Maryland, announced that a baby in Mississippi who received treatment for HIV within 31 hours of birth stopped medication at 18 months without the virus rebounding (see *Nature* <http://doi.org/m2d>; 2013). Researchers knew that early treatment could help infants to control HIV, but were surprised that they could essentially wipe it out from an infant's body using existing drugs.

Early HIV treatment is helpful for patients



A baby in Lesotho is given anti-HIV drugs at birth.

of any age. It stops the virus from replicating before it can infect central memory T cells, the main immune-cell reservoir where HIV ‘hides’ from drugs. But researchers think that babies are better targets for HIV cures than adults because of their immature immune systems, which respond more mildly when provoked. Because the cells involved in this ‘inflammatory response’ are the same ones that are ▶

GIDEON MENDEL/CORBIS FOR UNICEF

► most susceptible to HIV, this could mean that infants are less prone to the infection spreading. Moreover, babies are born without central memory T cells, so they are likely to have a smaller reservoir of infected cells, says Mike McCune, an immunologist at the University of California, San Francisco.

The IMPAACT study, to be conducted across some of the group's 71 sites worldwide, will screen and treat hundreds of babies to find 20–30 infants who have acquired HIV from untreated mothers or from those whose HIV was not well controlled during pregnancy. Because diagnosing HIV takes up to 7 days, all screened babies will automatically receive a similar treatment to the Mississippi baby: a cocktail of three drugs within 48 hours of birth. Physicians will add a fourth drug if babies then test positive for HIV. Around the age of three, the 20–30 children will be tested to see whether their immune systems make antibodies to HIV or if it can be detected in their blood. Those testing negative on both counts would then be taken off the drugs to see whether they can remain HIV-free.

The practical and ethical challenges of the trial are significant. Babies of untreated HIV-positive women have only a 15–30% chance of infection at birth, so the trial will need to recruit many babies to try to cure the few who are infected. Those who do not contract HIV will be treated anyway, perhaps exposing them to drug side effects. These are usually mild, but can deplete certain blood cells.

But children born to untreated HIV-positive women are already given up to three drugs after birth as a precaution. The potential for finding a cure far outweighs the risks of adding another drug, or of stopping treatment to test whether the cure has worked, says Yvonne Bryson, a physician at the Mattel Children's Hospital at the University of California, Los Angeles, and co-chair of the trial. "There's much more benefit to be gained than risk," she says.

Physicians are already considering changing the way they treat children infected by the virus. Bryson says that families of HIV-positive teenagers who were treated soon after birth and kept on medication are now asking that the teens be taken off the drugs.

Ultimately, the 34 million people worldwide who live with HIV could also benefit, researchers say. If it turns out that infants are more amenable to cures because they have a less active inflammatory response, that might encourage physicians to prescribe treatments that are less likely to trigger inflammation in adults, McCune says.

Bryson, who has worked on HIV since the first case was detected, thinks that the end could be in sight. "I saw patient zero," Bryson says. "I've always been so excited to think that I would see the day that we would arrive at a cure, and I think we're here." ■



LEAH FASTEN

Hugh Rienhoff prepared his daughter's DNA for sequencing at home using second-hand equipment.

PERSONAL GENOMICS

Father's genetic quest pays off

Mutation provides clue to daughter's undefined syndrome.

BY BRENDAN MAHER

Hugh Rienhoff says that his nine-year-old daughter, Bea, is "a fire cracker," "a tomboy" and "a very sassy, impudent girl". But in a forthcoming research paper, he uses rather different terms, describing her hypertelorism (wide spacing between the eyes) and bifid uvula (a cleft in the tissue that hangs from the back of the palate). Both are probably features of a genetic syndrome that Rienhoff has obsessed over since soon after Bea's birth in 2003. Unable to put on much muscle mass, Bea wears braces on her skinny legs to steady her on her curled feet. She is otherwise healthy, but Rienhoff has long worried that his daughter's condition might come with serious heart problems.

Rienhoff, a biotech entrepreneur in San Carlos, California, who had trained as a clinical geneticist in the 1980s, went from doctor to doctor looking for a diagnosis. He bought lab equipment so that he could study his daughter's DNA himself — and in the process, he became a symbol for the do-it-yourself biology movement, and a trailblazer in using DNA technologies to diagnose a rare disease (see *Nature* 449, 773–776; 2007).

"Talk about personal genomics," says Gary Schroth, a research and development director at the genome-sequencing company

Illumina in San Diego, California, who has helped Rienhoff in his search for clues. "It doesn't get any more personal than trying to figure out what's wrong with your own kid."

Now nearly a decade into his quest, Rienhoff has arrived at an answer. Through the partial-genome sequencing of his entire family, he and a group of collaborators have found a mutation in the gene that encodes transforming growth factor- β 3 (TGF- β 3). Genes in the TGF- β pathway control embryogenesis, cell differentiation and cell death, and mutations in several related genes have been associated with Marfan syndrome and Loeys-Dietz syndrome, both of which have symptomatic overlap with Bea's condition. The mutation, which has not been connected to any disease before, seems to be responsible for Bea's clinical features, according to a paper to be published in the *American Journal of Medical Genetics*.

Hal Dietz, a clinician at Johns Hopkins University School of Medicine in Baltimore, Maryland, where Rienhoff trained as a geneticist, isn't surprised that the genetic culprit is in this pathway. "The overwhelming early hypothesis was that this was related," says Dietz, who co-discovered Loeys-Dietz syndrome in 2005.

➔ **NATURE.COM**
For more on Hugh Rienhoff's genetic search, see:
go.nature.com/qvvtks

Rienhoff had long been tapping experts such as Dietz for assistance. In 2005, an examination at Johns Hopkins revealed Bea's bifid uvula. This feature, combined with others, suggested Loeys-Dietz syndrome, which is caused by mutations in TGF- β receptors. But physicians found none of the known mutations after sequencing these genes individually. This was a relief: Loeys-Dietz is associated with devastating cardiovascular complications and an average life span of 26 years.

In 2008, Jay Flatley, chief executive of Illumina, offered Rienhoff the chance to sequence Bea's transcriptome — all of the RNA expressed by a sample of her cells — along with those of her parents and her two brothers. After drilling into the data, Rienhoff and his collaborators found that Bea had inherited from each parent a defective-looking copy of *CPNE1*, a poorly studied gene that seems to encode a membrane protein. It looked like the answer.

But questions remained. The gene did not have obvious connections to Bea's features, and publicly available genome data suggests that the *CPNE1* mutations are present in about 1 in 1,000 people — an indication that there should be many more people like Bea.

Unsatisfied, Rienhoff went back to Illumina in 2009 to ask for more help. He proposed exome sequencing, which captures the whole protein-encoding portion of the genome, and is in some ways more comprehensive than transcriptome sequencing. At the time, Illumina was developing its exome-sequencing technology, and the company again took on the Rienhoff family as a test group.

The analysis pulled up a mutation in one copy of the gene that encodes TGF- β 3 — just in Bea. In cell culture and experiments in frog eggs, the faulty gene seems to produce a non-functional protein that reduces TGF- β signalling. This mechanism would differ from what many suspect is going on in Marfan and Loeys-Dietz syndromes, in which mutations paradoxically amp up TGF- β signalling. A collaborator of Rienhoff is now engineering a mouse that shares Bea's gene variant, which could help to clarify whether the mutation revs up signalling or suppresses it.

The latest study does not define a new 'Rienhoff syndrome'. For that, Rienhoff and his collaborators would need to find other patients who share Bea's features and genetic markers. Rienhoff says that he would be relieved if he found an older person with similar symptoms who seems as vivacious as his daughter, who recently earned an orange belt in karate; it would tell him that cardiovascular complications are not pre-ordained. "If I saw a single case, I might say, 'Hallelujah,'" he says. ■

PHYSICS

Proof mooted for quantum uncertainty

Study confirms principle's limits on measurement accuracy.

BY RON COWEN

Encapsulating the strangeness of quantum mechanics is a single mathematical expression. According to every undergraduate physics textbook, the uncertainty principle states that it is impossible to simultaneously know the exact position and momentum of a subatomic particle — the more precisely one knows the particle's position at a given moment, the less precisely one can know the value of its momentum.

But the original version of the principle, put forward by physicist Werner Heisenberg in 1927, couches quantum indeterminism in a different way — as a fundamental limit to how well a detector can measure quantum properties. Heisenberg offered no direct proof for this version of his principle, and expressed his ideas "only informally and intuitively", says physicist Jos Uffink of the University of Minnesota in Minneapolis.

Now researchers say that they have a formal proof. "Our work shows that you can't measure something with an accuracy any better than the fundamental quantum uncertainty," says Paul Busch, a theoretical physicist at the University of York, UK, who with his colleagues posted the proof on 6 June on the arXiv preprint server¹. Not only does the work place this measurement aspect of the uncertainty principle on solid ground — something that researchers had started to question — but it also suggests that quantum-encrypted messages can be transmitted securely.

In their theoretical work, Busch and his colleagues imagined making simultaneous measurements of a particle's position and momentum in an arbitrary quantum state. They compared the errors in such measurements to two special cases — in which either

the position or the momentum of the particle is well known. They found that the combined errors in measurements of the position or momentum in these two cases obeyed Heisenberg's principle and was always smaller than for cases in which the two properties were measured simultaneously. This step allowed them to prove Heisenberg's original conjecture.

Busch and his co-authors' work "is worth being remembered and maybe even taught through textbooks as the proper version of the Heisenberg error-disturbance relation", says mathematician Hans Maassen of Radboud University in Nijmegen, the Netherlands. However, the proof has reignited a decade-long debate.

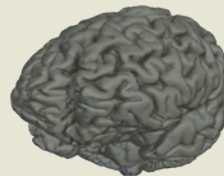
POLARIZED DEBATE

In 2003, physicist Masanao Ozawa, now at Nagoya University in Japan, proposed that the measurement-disturbance version of the Heisenberg uncertainty principle could be violated. Ozawa's theory was published in 2004 (ref. 2) and was corroborated last year, when Aephraim Steinberg and Lee Rozema at the University of Toronto, Canada, and their colleagues reported the results of an experiment in which they measured the polarization of a single photon along two perpendicular directions³.

Just like position and momentum, quantum theory predicts that the polarization along two different axes cannot simultaneously be known with certainty (see *Nature* <http://doi.org/m27>; 2012). The team adopted a strategy in which the polarization is initially probed using a series of 'weak' measurements — detections that barely disturb the system but must be repeated several times to record the same information that a single 'strong' measurement can detect. They found that, on average, the ►



**MORE
ONLINE**



VIDEO

Whole human brain is mapped in 3D go.nature.com/oslb4s

NEWS

- Online games offer trove of brain data go.nature.com/ujowtc
- Violence against women at epidemic proportions go.nature.com/xtgmoh
- Blocking boozy memories reduces risk of relapse go.nature.com/wppqan

► polarization measurements disturbed the system by only about half as much as Heisenberg's original formulation of the uncertainty principle dictates.

Ozawa says that Busch and his collaborators use the worst-case scenario, averaged over many quantum states, to define the disturbance caused by a measuring device. That may not reflect the actual conditions under which a particular quantum system in a particular quantum state is being examined. As a result, Ozawa says, the authors are overestimating measurement errors. But Busch and his colleagues argue that the definition of instrument error Ozawa uses is not universally valid, and therefore does not call into question Heisenberg's principle.

CRYPTIC CLUES

The debate may sound esoteric, but quantifying by how much a measuring device can disturb the properties of a quantum system is crucial to the burgeoning field of quantum cryptography and computing. In principle, a quantum computer would be more secure than an ordinary computer because anyone trying to peer at the information would disturb it, leaving a telltale trace.

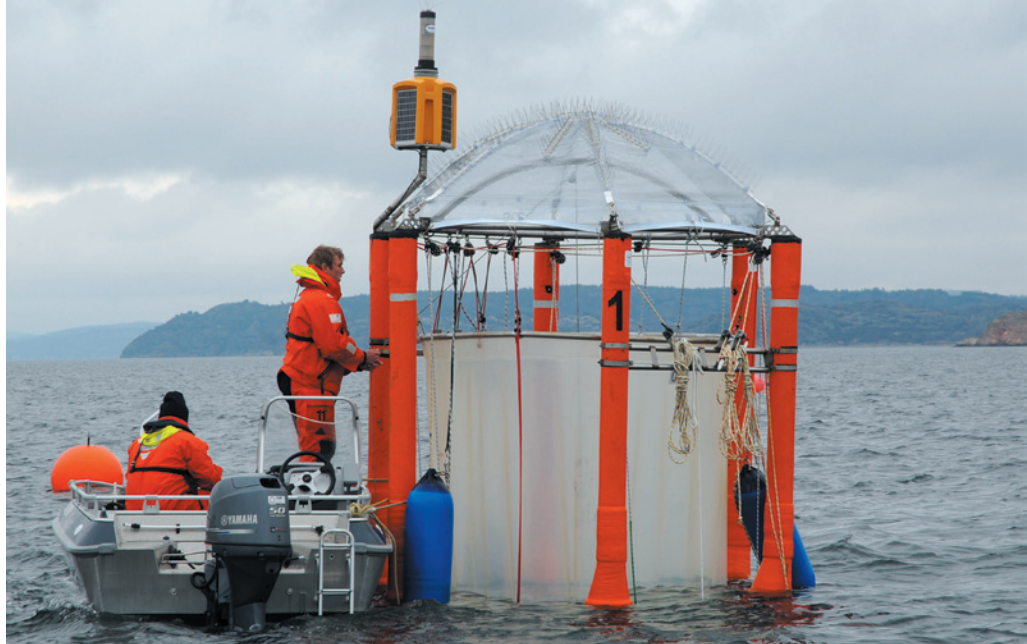
If Ozawa's 2004 work holds up, it would mean that a thief might be able to steal quantum data without anyone knowing, as the furtive measurements might barely disturb the system at all.

But what Busch and his collaborators have proved, says Uffink, is that if an eavesdropper has no control over the state of the quantum system in question — as will typically be the case for a data thief — then the eavesdropper will necessarily disturb the system in the way that the original version of the uncertainty principle predicts. "This is an important result that we did not have before," Uffink says.

Neither Uffink nor quantum theorist Howard Wiseman at Griffith University in Brisbane, Australia, are willing to say that Ozawa's approach is wrong, however. Indeed, it is possible that both results are correct, Wiseman notes.

He suspects that a strange quantum concept known as negative probability — negative dips in the probability distribution of a particle's location or momentum — could be at the heart of the issue. These dips may mean that a measuring device disturbs the system less than the uncertainty principle seems to allow. "The fact these two different definitions give you a different answer is telling you something about the weirdness of quantum mechanics," says Wiseman. ■

1. Busch, P., Lahti, P. & Werner, R. F. Preprint available at <http://arxiv.org/abs/1306.1565> (2013).
2. Ozawa, M. *Ann. Phys.* **311**, 350–416 (2004).
3. Rozema, L. A. *et al. Phys. Rev. Lett.* **109**, 100404 (2012).



Researchers suspend 20-metre-tall sacs in a Swedish fjord to enclose entire ecosystems for study.

MARINE ECOLOGY

Floating tubes test sea-life sensitivity

Ocean labs probe effects of ocean acidification on ecosystems.

BY HRISTIO BOYTCHEV

Global warming is not the only worrying consequence of rising carbon emissions. As levels of carbon dioxide increase in the atmosphere, more of the gas dissolves into the oceans, making the water more acidic. Marine scientists fear that the conditions will disrupt ecosystems by, for example, inhibiting some organisms' ability to build shells. Yet the effects are unclear: in small-scale laboratory tests, certain species have proved surprisingly resilient, and some even flourish.

Marine biologist Ulf Riebesell says that these results tell only part of the story: scientists need to scale up and examine whole ecosystems. Lab studies of isolated species ignore variables such as competition, predation and disease, he says. Even minor effects of acidification on the fitness of individual species — especially small photosynthetic organisms such as phytoplankton — can upset food chains, eventually harming larger species. "If you only focus on the lab results, you are being misled," he says.

Riebesell and his colleagues at GEOMAR Helmholtz Centre for Ocean Research in Kiel, Germany, have developed innovative experimental environments — 20-metre-tall sacs suspended in the ocean, which enclose entire ecosystems and allow the effects of elevated CO₂ to be measured. The first results, published this year, suggest that some plankton thrive in acidic environments and can wreak havoc on food

chains¹. Another experiment will end in July, and preliminary evidence suggests that conches and sea urchins are vulnerable to acidification.

The project is inspired by analogues on land, in which swathes of forest are bathed in extra CO₂ to study the effects on plant life (see *Nature* **496**, 405–406; 2013). For the sea, Riebesell and his colleagues constructed 'mesocosms' — floating cylinders of thin plastic that function like giant test tubes². When first put into the water, the sacs are left open at the top and bottom, allowing hundreds of small species to enter. After several days, they are closed and acidified water is pumped in (see 'Sea lab'). Over weeks or months, researchers measure how the ecosystems inside fare in comparison with those in untreated sacs.

Realizing this simple idea has been challenging. The scientists began in 2006 with a prototype, free-floating in the Baltic Sea, that floated too well: currents carried it along much faster than expected, and the scientists had to chase it in a research ship. After only two days they reached Swedish waters, for which they had no research permits. When they tried to recover the mesocosm, it broke.

The team conducted its first successful experiment in 2010, using a lighter design that was moored in place in the Norwegian Arctic archipelago of Svalbard. The researchers found that, compared with the

MAIKE NICOLA/GEOMAR

➔ **NATURE.COM**
For more on ocean acidification, see:
go.nature.com/ihz4qy

controls, the acidic mesocosms produced less dimethyl sulphide³ — a gas that helps to form clouds, which reflect sunlight and can counter-act climate warming. Riebesell is not sure what causes the change; he thinks that the plankton in the mesocosm might be making less of the gas, or the acidic water could be affecting its stability.

Picophytoplankton, the smallest photosynthetic organisms, turned out to grow better in the acidic mesocosms¹. But at the same time, diatoms — larger algae that are among the most important producers of ocean biomass — suffered. The change could mean that more nutrients are cycled among the picophytoplankton rather than reaching larger animals such as fish. Indeed, preliminary results from the latest experimental run indicate that larvae of sea urchins and Strombidae conches are barely surviving in the acidic mesocosms. However, the scientists think that food quality may not be the main reason for their demise; pathogens and

problems making shells could also have a role.

Adina Paytan, an oceanographer at the University of California, Santa Cruz, says that Riebesell's work "fills an important niche between lab work and field studies" and has "advanced the field considerably". She takes a different systems approach to acidification, studying 'natural mesocosms': underwater springs off Mexico that enrich zones in CO₂.

Riebesell says that these regions are a good lab for studying immobile seagrasses, but not organisms that can move freely. Paytan notes that there are problems with Riebesell's mesocosms: for example, the plastic walls filter out some ultraviolet light, removing a natural stressor for photosynthetic organisms. And the tubes are impermeable, so nutrients in the water become exhausted, and experiments last only a few months. Nevertheless, Paytan says, "we still learn a great lot from these experiments".

This year's run, in the Swedish Gullmar Fjord, uses five control mesocosms and five in which acidity is boosted to levels associated with the atmospheric CO₂ concentrations predicted for the year 2100. The experiment will end next month after a 6-month run — the longest yet — during which the researchers have monitored a natural plankton bloom.

Riebesell and his team seem comfortable with using their mesocosms as a hybrid between a controlled laboratory environment and a natural one. They have introduced fish eggs into the ecosystems for the first time, and Matias Scheinin, a marine biologist at GEOMAR, is using the sacs to explore natural selection. By tracking the abundance of individual strains of diatoms — which can undergo hundreds of generations in a few months — he hopes to identify those that flourish in acidic environments. He will screen them for the genes responsible, to investigate rates and mechanisms of adaptation.

Oceans have gone through major acidification events during climate change in the ancient past. By accelerating evolution, Scheinin wants to get a glimpse of their future. "I have some hope that evolution can help marine life deal with acidification," he says. "It's not the first time it has had to go through it." ■ [SEE COMMENT P.429](#)

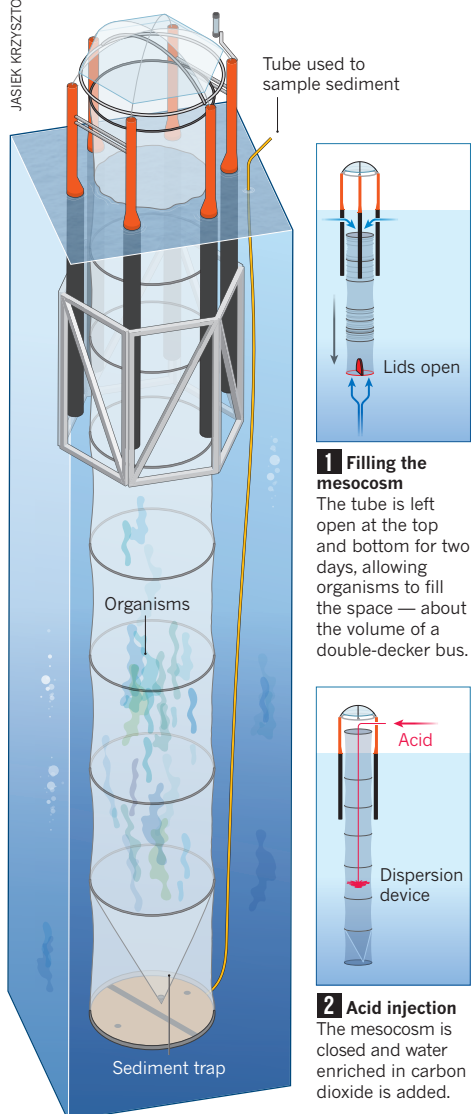
1. Brussaard, C. P. D. *et al. Biogeosciences* **10**, 719–731 (2013).
2. Riebesell, U. *et al. Biogeosciences* **10**, 1835–1847 (2013).
3. Archer, S. D. *et al. Biogeosciences* **10**, 1893–1908 (2013).

CORRECTION

The News story 'Space rovers in record race' (*Nature* **498**, 284–285; 2013) wrongly stated that the Russian scientists used laser mapping from the Lunar Reconnaissance Orbiter to make a three-dimensional representation of the Moon's topography. In fact, they used processed images from the orbiter's narrow-angle camera.

SEA LAB

Scientists are testing the ecosystem-wide effects of ocean acidification in 55-cubic-metre plastic mesocosms.

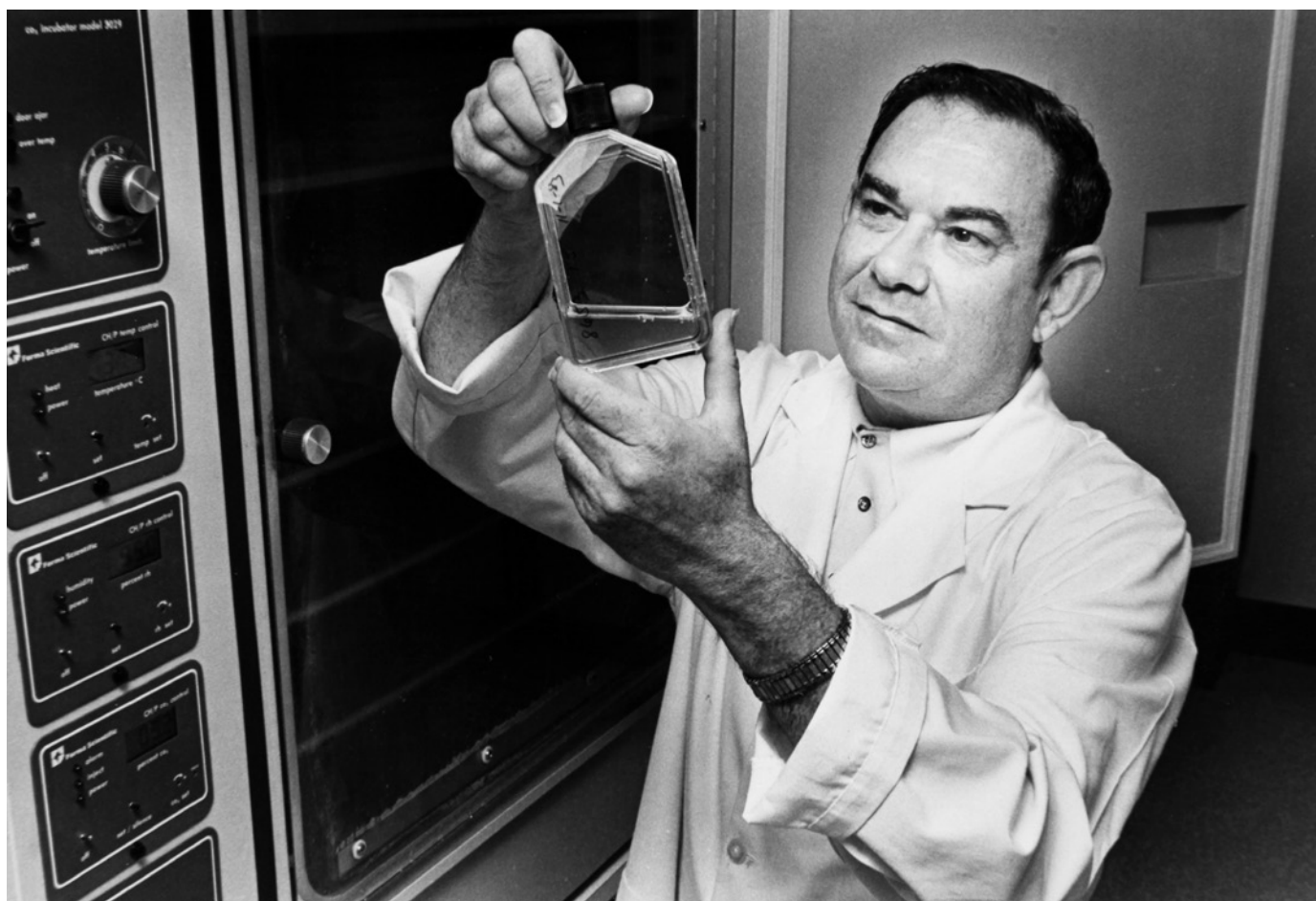


1 Filling the mesocosm

The tube is left open at the top and bottom for two days, allowing organisms to fill the space — about the volume of a double-decker bus.

2 Acid injection

The mesocosm is closed and water enriched in carbon dioxide is added.



COURTESY OF LEONARD HAYFLICK

Leonard Hayflick, pictured in 1982, inspects WI-38 cells that he derived from aborted fetal lungs. The cells have been used to produce vaccines in use worldwide.

Cell division

In 1962, Leonard Hayflick created a cell strain from an aborted fetus. More than 50 years later, WI-38 remains a crucial, but controversial, source of cells.

BY MEREDITH WADMAN

The woman was four months pregnant, but she didn't want another child. In 1962, at a hospital in Sweden, she had a legal abortion.

The fetus — female, 20 centimetres long and wrapped in a sterile green cloth — was delivered to the Karolinska Institute in northwest Stockholm. There, the lungs were dissected, packed on ice and dispatched to the airport, where they were loaded onto a transatlantic flight. A few days later, Leonard Hayflick, an ambitious young microbiologist at the Wistar Institute for Anatomy and Biology in Philadelphia, Pennsylvania, unpacked that box.

Working with a pair of surgical scalpels, Hayflick minced the lungs — each about the size of an adult fingertip — then placed them in a flask with a mix of enzymes that fragmented them into individual cells. These he transferred into several flat-sided glass bottles, to which he added a nutrient broth. He laid the bottles on their sides in a 37 °C incubation room. The cells began to divide.

So began WI-38, a strain of cells that has arguably helped to save more lives than any other created by researchers. Many of the experimental cell lines available at that time, such as the famous HeLa line, had been grown from cancers or were otherwise genetically abnormal. WI-38 cells became the first 'normal' human cells available in virtually unlimited quantities to scientists and to industry and, as a result, have become the most extensively described and studied normal human cells available to this day.

Vaccines made using WI-38 cells have immunized hundreds of millions of people against rubella, rabies, adenovirus, polio, measles, chickenpox and shingles. In the 1960s and 1970s, the cells helped epidemiologists to

NATURE.COM
Listen to a podcast
about the WI-38
story at:
go.nature.com/nkoyah

identify viral culprits in disease outbreaks. Their normality has made them valuable control cells for comparison with diseased ones. And at the Wistar Institute, as in labs and universities around the world, they remain a leading tool for probing the secrets of cellular ageing and cancer.

"Here's a clump of cells that has had an enormous impact on human health," says Paul Offit, chief of the division of infectious diseases at the Children's Hospital of Philadelphia. "These cells from one fetus have no doubt saved the lives of millions of people."

Few people, however, know the troubled history of the cells — one that may offer lessons for modern researchers seeking to work with human tissues. Six years after deriving his famous strain, Hayflick made off with stocks of the cells and later started to charge for shipping them, prompting an epic legal battle with the US National Institutes of Health (NIH) in Bethesda, Maryland, about who owned the cells. That struggle nearly destroyed Hayflick's career and raised questions about whether and how scientists should profit from their inventions.

What's more, the WI-38 strain has helped to generate billions of dollars for companies that produce vaccines based on the cells, yet it seems that the parents of the fetus have earned nothing. That recalls the earlier development of the HeLa cell line, named after the woman whose tumour gave rise to the cells and chronicled in Rebecca Skloot's book *The Immortal Life of Henrietta Lacks* (Crown, 2010). As with HeLa, the WI-38 case highlights questions about if, and how, tissue donors should be compensated that are still urgently debated today. Last month, for example, some scientists in the United States found themselves barred from using new stem-cell lines derived from human embryos because women had been paid for the eggs used to make them (see *Nature* <http://doi.org/mv2>; 2013).

The story of WI-38, unlike that of HeLa, also has its own controversial twist because it was derived from an aborted fetus. For 40 years, anti-abortion activists have protested against the use of WI-38 and vaccines developed from it. "It's still a live issue," says Alta Charo, a professor of law and bioethics at the University of Wisconsin Law School in Madison. "We still have people who refuse to take these vaccines because of their origins in fetal tissue."

SEEKING CELLS

When Hayflick opened up that icy package from Sweden in 1962, he was working at the vanguard of virus research in the United States. At the time, the Wistar Institute was led by Hilary Koprowski, a polio-vaccine pioneer who hired Hayflick to run the centre's cell-culture laboratory and supply cells to researchers. But Hayflick also began investigating whether some human cancers might be caused by viruses. To do so, he needed a resource that did not yet exist: verifiably normal human cells that could be reliably grown in the lab. Fetal cells, he thought, were an ideal candidate, because they were less likely to have been exposed to viruses than adult cells.

Although abortions were technically illegal in Pennsylvania at the time, they were still performed when doctors said they were medically necessary. Hayflick says he was able to obtain fetuses straight from the operating room of the University of Pennsylvania Hospital across the street from Wistar. Unless the tissue was put to some use, he reasoned, "it was definitely going to end up in an incinerator". The University of Pennsylvania says that it is unable to find records to confirm the source of fetal tissues used by Hayflick.

Hayflick developed 25 different fetal-cell strains, numbered WI-1 to WI-25. But several months into the project, he began to notice something strange. Scientific orthodoxy held that cells in culture, properly treated, would replicate forever. But his oldest cell strains were beginning to replicate more slowly. Eventually, they stopped dividing altogether.

In 1961, Hayflick and his colleague Paul Moorhead published a paper¹ that would become one of the most cited publications in biology. Entitled 'The serial cultivation of human diploid cell strains', it showed that normal fetal cells stop replicating after about 50 population doublings. The paper launched a new field: the study of cellular ageing. And the wall that the cells hit — which was later found to arrive much earlier for adult cells, which have already divided many times² — became known as 'the Hayflick limit'.

Crucially, Hayflick and Moorhead also showed that the fetal cells remained viable after months in the freezer and that, once thawed, they would 'remember' how many replications they had been through and would pick up where they left off. "It's apparent," the authors wrote, "that by freezing cells at each subcultivation, or every few sub-

"These cells from one fetus have no doubt saved the lives of millions of people."

cultivations, one could have cells available at any given time and in almost limitless numbers." What's more, the pair's cells turned out to be easy to infect with a broad range of human viruses, suggesting that they would be perfect vehicles in which to grow viruses for vaccines.

Hayflick decided to derive a fetal cell strain that he hoped would become both a ubiquitous laboratory resource and a substrate for industrial-scale vaccine manufacturing. He had support: in February 1962, the National Cancer Institute awarded Wistar, with Hayflick as co-principal investigator, a contract "to produce, characterize, store and study human diploid cell strains and to distribute such cell strains to all qualified investigators".

SUCCESSFUL STRAIN

By this time, Hayflick had turned to a different source for his fetal tissues: Sven Gard, chairman of the department of virology at the Karolinska Institute in Sweden, where abortion was legal. In June 1962, Hayflick received the set of lungs that would give rise to WI-38. He cultured the cells for weeks, splitting them when they covered the bottom of a bottle, so that two bottles became four, four became eight and so on. By the time the original cell population had doubled nine times, there were hundreds of bottles.

On 31 July, in a marathon session for which he recruited a small army of technicians, Hayflick dispensed the cells into more than 800 tiny glass ampoules, sealing each one with a quick pass through the flame of a Bunsen burner. Later, he transferred the precious ampoules to a liquid-nitrogen freezer in the Wistar's basement.

A year later, Hayflick received information from Sweden assuring him that the mother of the fetus and her family were free of cancer and hereditary diseases, something vaccine manufacturers would want to know. Although there is some indication that the mother consented to use of the tissue, *Nature* does not know for sure that she did. Swedish law at the time did not require such consent and, says Niels Lynøe, professor of medical ethics at the Karolinska Institute, "research ethical awareness in Sweden as well as in the US was rather low", before the Helsinki declaration, a statement of human research ethics adopted by the World Medical Association in 1964. In Sweden, "research material like tissues from aborted fetuses were available and used for research without consent or the knowledge of patients for a long time", both before and after consent rules were tightened later in the 1960s, says Solveig Jülich, a historian of medicine at Stockholm University.

Armed with the ampoules, Hayflick now launched WI-38 on its

march around the globe. During his frequent flights abroad, he often toted a small liquid-nitrogen freezer bearing WI-38 ampoules. In this way, he hand-delivered the cells to colleagues in London, Moscow, Leningrad and Belgrade. He also mailed out hundreds of 'starter' cultures grown from the ampoules. Scientists were hungry for the cells in part because they were a cheap, plentiful model for studying the fundamental biology of normal human cells — and soon papers began to appear, probing everything from the cells' respiration³ to their constituent fatty molecules⁴.

WI-38 found a greater use in virology, where the ease of infecting the cells with a panoply of human viruses quickly made the strain an important virus-identification tool. In 1967, the cells became a workhorse in a World Health Organization survey of viruses causing lower respiratory tract infections in hospitalized children on four continents.

Hayflick also supplied WI-38 liberally to aspiring vaccine-makers. One was Stanley Plotkin, a Wistar scientist and a physician who had seen at first hand the effects of the huge rubella epidemic that swept the United Kingdom and the United States in the early 1960s. Rubella can be devastating to fetuses whose mothers are infected: those that are not killed *in utero* are frequently born blind, deaf, mentally disabled or with some combination of these conditions.

Working at the Wistar, Plotkin grew rubella in WI-38 at 30°C, cooler than body temperature, creating a weakened strain that still fired up the immune system enough to protect against future infections. Trials showed that his vaccine induced better immunity against rubella than competitors⁵. Plotkin's vaccine was licensed in Europe in 1970 and in the United States in 1979. A version made by the pharmaceutical company Merck, based in New Jersey, is today the only rubella vaccine available in the United States, and GlaxoSmithKline uses Plotkin's weakened virus in a rubella vaccine that it markets in Europe and Australia.

The rubella vaccine was only one of many made using WI-38. In the 1960s, a WI-38-based measles vaccine was licensed in the former Soviet Union and Koprowski developed a rabies vaccine using the cells. In the early 1970s, the pharmaceutical company Wyeth (now part of Pfizer) launched an oral adenovirus vaccine developed using WI-38 and Pfizer, based in New York, used WI-38 to make a vaccine against polio. Today, the cells are also used by Merck to make vaccines against chickenpox and the painful nerve infection shingles.

SENSE OF EXCLUSION

Despite his groundbreaking paper and the growing prominence of WI-38, Hayflick felt like a second-class citizen at the Wistar Institute. He was never promoted to a full member, and he believed that Koprowski, much as he publicly bragged about WI-38, saw him as more of a technician than a scientist. (Koprowski died last April.)

Hayflick's simmering sense of exclusion boiled over when one day, Hayflick says, he learned that Koprowski had offered a guaranteed supply of WI-38 to the British drug-maker Burroughs Wellcome (one of the companies that merged into GlaxoSmithKline), along with

Hayflick's cell-culture technology for producing live polio vaccine⁶, all in exchange for royalties to the institute. Hayflick says that he was shocked that Koprowski intended the institute to profit from WI-38 and believes that it had kept him in the dark.

Hayflick found a new job as a professor of medical microbiology at Stanford University in California, to start in July 1968. In January that year, he met to discuss the fate of the 370-odd remaining WI-38 ampoules with Koprowski and representatives from the NIH and the American Type Culture Collection (ATCC), then in Rockville, Maryland, a non-profit organization that distributes cell cultures. The participants agreed that Hayflick could take ten ampoules of WI-38 with him to Stanford, and that ten would stay at the Wistar. The rest would remain the property of the NIH's cancer institute and were to be transferred to the ATCC, which would handle distribution from that point on.

Hayflick was troubled by the plan, which he says he felt under pressure to sign. And he felt a sense of injustice. Companies, and the Wistar, he now believed, were profiting from cells he had created and handed to them freely. "To then have [them] descend on what I had

struggled so hard to give value to, and try to take it for their own benefit," he says. "I think that an average person would be capable of understanding why I was — to put it mildly — concerned." The Wistar Institute says that it acted ethically in conducting research that led to the development of WI-38 and that it received royalties from licensed vaccines grown in WI-38 cells but not from licensing the cells.

At some point after that January meeting, Hayflick made a quiet trip to the Wistar basement and packed all the WI-38 ampoules into a portable, 30-litre liquid-nitrogen tank. In June 1968, he strapped the container into the back seat of his green

Buick LeSabre next to two of his children, and motored to California. "I just absconded with the cells," Hayflick says with a wry smile.

Once in Stanford, Hayflick began charging for many of the WI-38 cultures that he was sending out to hundreds of scientists who were still asking for them. His fee was US\$15 — the same amount charged by the ATCC for cell shipments — and he banked the money in an account he called 'Cell Culture Fund'. By May 1975, he had accrued more than \$66,000.

Hayflick was determined, he says, to keep the funds in a separate account until some independent legal authority could determine who owned the cells. The issue didn't come up until the spring of 1975, when he was interviewed at the NIH as a candidate to direct its new National Institute on Aging. The NIH decided to turn to its Division of Management Survey and Review, an office that investigated allegations of mismanagement of NIH funds. It sent three accountants to Hayflick's Stanford lab, where they spent days going over records and assessing his inventory of WI-38.

Their report became public in March 1976, when the NIH provided it under the Freedom of Information Act (FOIA) to several journalists. Accounts of its contents soon appeared in *Science* and on the front page of *The New York Times*. "Within 24 hours my career was in the sewer," Hayflick says. The report said that Hayflick had sold "the property of the United States Government" and banked the money; that the WI-38 ampoules had been poorly accounted for; and that some ampoules were contaminated with bacteria. Hayflick strongly



Hilary Koprowski, director of the Wistar Institute, is inoculated by Stanley Plotkin with rabies vaccine developed using WI-38, in 1971.

WISTAR INST.

disagrees with the report. He says that no legal decision gives the government title to WI-38; that he sequestered the funds received for preparing and shipping WI-38 in an account until ownership could be established; and that no evidence has ever been provided for the assertion of mismanagement. Hayflick explains that, contrary to common practice in 1962, he had not laced the cells with antibiotics at the outset because vaccine manufacturers feared allergic reactions to the drugs.

Shortly before the *Science* article⁷ was published, Hayflick sued the NIH. He argued that the agency had violated the 1974 Privacy Act by making his name and the allegations against him available under the FOIA without including his rebuttal. He also sued for title to WI-38 and its proceeds. By then, Hayflick was also facing a criminal investigation: Stanford University had alerted local prosecutors that the case could be one of criminal theft of government property. (The prosecutors subsequently found no grounds for criminal investigation and dropped the case.) Meanwhile, some vaccine manufacturers, fearing that there would not be enough stock of WI-38 to meet future needs, switched much of their work to an alternative fetal cell strain, MRC-5.

Hayflick resigned from Stanford in February 1976 and was soon in an unemployment line collecting \$104 a week. Not only was he jobless, he was without the cells that he described to *Science* that spring as “like my children”. The NIH had taken them from his lab while he was at a conference the previous year.

CHANGING TIMES

Some months later, Hayflick landed a job across the San Francisco Bay at the Children’s Hospital, Oakland, and sought to revive his research on ageing. In 1977, peer reviewers approved his application for a three-year NIH grant and, after a lengthy fight with the NIH to get both the funding and some WI-38 cells, in January 1981 he received six of the original ampoules of cells.

One month earlier, the Bayh–Dole Act had become law, giving institutions the right to claim title to inventions made using government funds, as long as they gave the inventors a piece of the royalties. Hayflick’s invention predated the law, but the new mindset that Bayh–Dole represented made it harder for the government to justify the continued legal fight over WI-38, which by then had stretched on for nearly five years. In summer 1981, the Department of Justice wrote to Hayflick’s lawyers, offering to settle the lawsuit out of court, and Hayflick assented. With both sides agreeing that the issues were in reasonable dispute, and neither side admitting liability, the settlement allowed Hayflick title to the six original WI-38 ampoules now in his possession, and to their progeny. The government would retain title to the 19 original ampoules in its hands. As for the proceeds from his sales of WI-38, which, with interest, had grown to around \$90,000, Hayflick would keep it. He spent it all, he says, and more, to pay his lawyers; he has never profited financially from WI-38, he says.

Scientists, meanwhile, were continuing to benefit academically

from the cells. By the mid-1980s, thanks to revolutionary new tools in molecular biology, WI-38 was helping them explore everything from gene expression in human leukaemias⁸ to the effects of the just-cloned tumour necrosis factor⁹, an important immune regulatory protein.

“We still have people who refuse to take these vaccines because of their origins in fetal tissue.”

The cells have played “a very critical role in studying cellular senescence,” adds Rugang Zhang, who works in this field at the Wistar Institute. That’s because they so reliably stop replicating after about 50 divisions and because scientists have, over time, built up a wealth of knowledge about the reasons why. In the 1990s, for instance, WI-38 was used to discover the most widely used marker of cellular senescence¹⁰. More recently, Zhang’s team used the cells to discover a pathway by which the complex of DNA and proteins known as chromatin controls cell proliferation¹¹.

But the controversies surrounding the cells have rumbled on. Back in July 1973, Hayflick received a call at home from a senior medical officer at NASA. Skylab 3 had taken off several hours earlier from the Kennedy Space Center in Florida, bound for the Space Station. The NASA physician was contending with anti-abortion demonstrators who were protesting about the presence aboard of WI-38 cells, which were going to be used to detect the effects of zero-gravity on cell growth and structure. Once Hayflick explained that the abortion from which the cells were derived had occurred legally in Sweden, the physician said that he would defuse the situation — but concerns among anti-abortionists about WI-38 have lasted to this day.

“Other vaccines are produced in a completely morally non-objectionable way. So why aren’t we doing this with all vaccines?” says Debi Vinnedge, the executive director of Children of God for Life, a group based in Largo, Florida, that opposes the use of WI-38 in vaccine-making. In 2003, Vinnedge wrote to the Vatican asking for an official position on whether Catholics could ethically receive vaccines made using cells from aborted fetuses. She waited two years for an answer. The letter, when it came, concluded that where no alternative exists, it is “lawful” for parents to have their children immunized with vaccines made using WI-38 and MRC-5, to avoid serious risk to their own offspring and to the population as a whole.

Still, the Vatican wrote, faithful Catholics should “employ every lawful means in order to make life difficult for the pharmaceutical industries” that use such cells. Merck, a major producer of Plotkin’s rubella vaccine, has been a perennial target of abortion opponents, who have pressed the issue at Merck’s US shareholder meetings. (Merck said in a statement to *Nature* that “it would be exceedingly difficult, if at all possible, to develop and test an alternative”, and emphasized the vaccine’s long record of safety and effectiveness.) The irony of the protest is not lost on Plotkin. “I am fond of saying that rubella vaccine has prevented thousands more abortions than have ever been prevented by Catholic religionists,” he says.

Profits from Merck’s rubella vaccine represent a big slice of the billions of dollars that have been made from products that have involved the use of WI-38. Among the other companies that have made money from WI-38 are Barr Laboratories (now part of Teva Pharmaceuticals, based in Petach Tikva, Israel), which today makes the adenovirus vaccine given to all US military recruits, and Sigma Aldrich in St Louis,

LEONARD HAYFLICK



Some original glass ampoules of WI-38 cells, created in 1962.



RAMIN RAHIMIAN/GETTY IMAGES

Leonard Hayflick today at his house in Sea Ranch, California. “We all owe a moral debt to the tissue donors,” he says.

Missouri, which charges \$424 in the United States for a vial of the cells.

Legal experts say it is unlikely that the parents of the fetus, or their heirs, would have any legal grounds to demand compensation for tissue collected over 50 years ago. At the time that WI-38 was derived, use of tissue without consent was routine in the United States, as it was in Sweden. Under current rules, researchers supported by US government grants are free to make use of surgically removed tissue — including aborted tissue — that has been stripped of its identifiers, without consent. However, some states have stricter rules.

But, says Charo, “if we continue to debate it entirely in legal terms, it feels like we’re missing the emotional centre of the story”. It could be argued, she says, “that if somebody else is making a fortune off of this, they ought to share the wealth. It’s not a legal judgment. It’s a judgement about morality.”

The scientists and academic institutions that have worked with WI-38 and that commented for this story say that they do not see their work on the cells as unethical, in part because of the standards that existed at the time the cell strain was created. It is unfair, say some, to examine past acts by today’s more stringent ethical expectations. “At the time [the fetus] was obtained there was no issue in using discarded material,” says Plotkin. “Retrospective ethics is easy but presumptuous.” Most companies in this story declined to comment; GlaxoSmith-Kline says that it is committed to upholding high ethical standards.

Regarding the situation today, Scott Kominers, a research scholar at the Becker Friedman Institute at the University of Chicago, Illinois, argues that offering donors a share in future profits from their tissues could encourage them to donate and fuel medical progress¹². “We think that if you offer some sort of value-based compensation you’d be likely to boost tissue supply,” he says. But Steven Joffe, a paediatric oncologist who directs the ethics programme at Harvard’s translational medicine centre in Boston, Massachusetts, is concerned that compensating donors may paradoxically decrease their willingness to donate tissues, by taking altruism out of the equation. What’s more, he says, the one-to-one relationship of WI-38, or of HeLa, to a donor, is rare. Far more often, modern medical products — such as therapeutic proteins extracted from donated blood — come from many samples combined. In these cases, he says, “trying to account for all these multiple holders of rights

to income streams would just bring science to a standstill”.

If nothing else, the WI-38 story highlights the benefits of discussing the issues of compensation and consent with tissue donors at the outset. In the case of WI-38, suggests Charo, returning to the donor now, even with an offer of compensation, “may also be a way of reopening an experience that may for her have been painful. You have to be careful.”

Hayflick argues that there are at least four stakeholders with title to WI-38 or any human cell culture: the tissue donors, the scientists whose work gave it value, the scientists’ institution and the body that funded the work. “Like me,” he adds, “hundreds of other scientists had their careers advanced using WI-38 and other human cell cultures so we all owe a moral debt to the tissue donors.”

Now 85 and regarded as a grand old man of ageing research, Hayflick hung onto his ampoules of WI-38 for decades, keeping them for many years in the garage of his home in California. But in 2007, weary of monthly treks to collect fresh liquid nitrogen, he donated them to the Coriell Institute in Camden, New Jersey, which, he says, he trusts to bank them safely.

In the end, he says, letting the cells go was no more traumatic than launching his own five biological offspring into the world: “It was about time that my ‘children’ — now adults — should leave home.” ■

Meredith Wadman is Nature’s biomedical reporter in Washington DC. [SEE EDITORIAL P.407.](#)

1. Hayflick, L. & Moorhead, P. S. *Exp. Cell Res.* **25**, 585–621 (1961).
2. Hayflick, L. *Exp. Cell Res.* **37**, 614–636 (1965).
3. Cristofalo, V. J. & Kritchevsky, D. J. *Cell Physiol.* **67**, 125–132 (1966).
4. Kritchevsky, D. & Howard, B. V. *Ann. Med. Exp. Biol. Fenn.* **44**, 343–347 (1966).
5. Freestone, D. S., Reynolds, G. M., McKinnon, J. A. & Prydie, J. *Br. J. Prev. Soc. Med.* **29**, 258–261 (1975).
6. Hayflick, L., Plotkin, S. A., Norton, T. W. & Koprowski, H. *Am. J. Hyg.* **75**, 240–258 (1962).
7. Wade, N. *Science* **192**, 125–127 (1976).
8. Calabretta, B. et al. *Proc. Natl Acad. Sci. USA* **82**, 4463–4467 (1985).
9. Sugarman, B. J. et al. *Science* **230**, 943–945 (1985).
10. Dimri, G. P. et al. *Proc. Natl Acad. Sci. USA* **92**, 9363–9367 (1995).
11. Zhang, R. et al. *Dev. Cell* **8**, 19–30 (2005).
12. Kominers, S. D. & Becker, G. S. *Science* **337**, 1292–1293 (2012).

COMMENT

ECOLOGY Bigger studies needed to understand impact of acidifying oceans **p.429**

HISTORY The man behind the bull's-eye lens, secret of the modern lighthouse **p.430**

FICTION Ex-director of Royal Institution turns novelist **p.432**



OBITUARY Joe Farman, discoverer of the ozone hole, remembered **p.435**

ILLUSTRATION BY PETE ELLIS/DRAWGOOD.COM



The human sleep project

To establish the true role of sleep, researchers must gather real-world data from thousands, even millions, of people, says **Till Roenneberg**.

Sleep is essential for health, performance and wellbeing. Yet in many countries, people are getting one to two hours less of it each night than their ancestors did 50–100 years ago. Even when people have the opportunity to sleep, many cannot. Sleep pathologies are approaching epidemic levels, affecting an estimated 70 million people in the United States alone (see go.nature.com/6dgqhg). And in some countries, direct and indirect costs of sleep-related problems are thought to approach 1% of gross domestic product¹. Despite these alarming numbers, sleep research ranks only 91st in the 235 categories on this year's funding

list of the US National Institutes of Health — below, for instance, studies of tobacco (see go.nature.com/ces1rf).

Researchers have made great advances in understanding which neurotransmitters and brain regions are involved in sleep², and how the timings of sleep and wakefulness are controlled by an internal (circadian) clock³, among other things. Yet we still do not have answers to the most basic questions. It is not really understood, for instance, what sleep is for, how much is optimal, how sleep quality can be measured and predicted, or the role of genetic and environmental factors in determining ideal sleeping patterns.

One reason for this lack of understanding is that most of what is known about sleep comes from laboratory studies. Subjects in these studies tend to be mice or hamsters that are kept in artificial light–dark cycles, or people who have been instructed to sleep at certain times in beds that are not their own, with electrodes fastened to their heads. Assessments of sleep are also often based on subjective responses to questions about how 'well' people feel after they have slept, or whether they think they experienced a good night's sleep. To learn about sleep in the real world, and to establish how to manage sleep to improve productivity, health and ►

► quality of life, we need a multidisciplinary 'human sleep project'.

An attempt to probe sleep *in situ* has been made by my research group at the Ludwig Maximilian University of Munich in Germany. Since 2000, our group has been building a database on daily sleep behaviour called the Munich Chronotype Questionnaire (MCTQ). We have publicized our project in newspapers, on the radio and on television, requesting people to fill out an online questionnaire. Participants are asked to provide the times at which they go to bed, prepare for sleep, fall asleep, wake up and get up⁴. In exchange, they receive a document revealing how their sleeping behaviour compares with the rest of the population. Importantly, people give this information for both working and non-working days. Our database now includes entries from more than 150,000 individuals from all over the world.

Using these data, we have assessed how the amount of sleep that people get, and when they get it, changes with factors such as age, season, location and even daylight saving time⁴. Our results suggest that although people sleep for the same amount of time on work-free days as they did ten years ago, on work days, they sleep for about 38 minutes less than they used to⁴. We also discovered that throughout their school and working lives, people seem to oscillate between undersleeping on work days and oversleeping on work-free days (see 'Losing sleep'), with 80% of people needing an alarm clock to wake up on work days⁴. These findings indicate that much of the working population experiences what we call 'social jet lag': people switch between different 'time zones' every week, one dictated by their work schedules, the other by their biological clock.

BEDTIME STORY

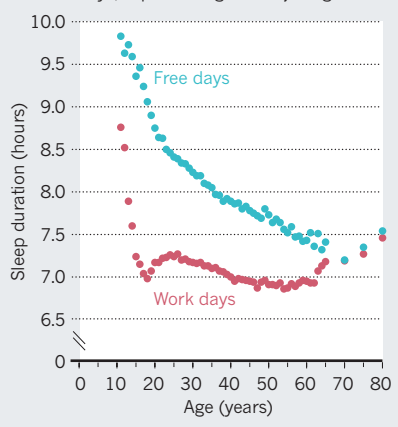
The practice of going to sleep and waking up at 'unnatural' times could be the most prevalent high-risk behaviour in modern society. With every hour of social jet lag (the difference between the social and the biological time zone), the chances of being overweight or obese increase by 33% (ref. 4). This substantiates an association between sleep duration and metabolic problems that was found five years ago⁵. My colleagues and I have also associated social jet lag with smoking, with increased consumption of alcohol or caffeine⁴, and with signs of depression such as appetite loss and feelings of sadness⁶.

I believe that what has emerged from the MCTQ database is only the tip of the iceberg. Thanks to the Internet and personal monitoring devices, it should be possible to obtain systematic and quantitative information about the sleeping patterns of thousands, even millions, of people.

To transform our understanding of sleep, a broad data-collection strategy is required.

LOSING SLEEP

Answers to a questionnaire indicate that many people oversleep on free days and undersleep on work days, experiencing 'social jet lag'.



This would involve inviting millions of people to fill out online questionnaires, tens of thousands to keep online sleep diaries and several thousand to submit real-time data from recording devices. A subset of these people would then be asked to supply their DNA. (Once the sleep phenotype is better understood, researchers would be in a good position to probe its genetics.)

A key goal of a human sleep project would be to identify simple, effective indicators that sidestep the need for cumbersome electrodes, or for blood or saliva samples, which are used to obtain conventional markers of circadian rhythms, such as the hormone melatonin. Many sleep-tracking devices are now available or are in development, such as wristwatch-like gadgets that measure movement and light. Other devices use information detected by mobile phones, or communicate with mobile phones, which can upload data to the Internet. These can monitor skin temperature and skin conductance (a measure of perspiration, indicative of stress levels), respiration rate, blood-oxygen levels, electrical activity in the heart, and even blood pressure. Such parameters could potentially enable researchers to establish individuals' circadian timing, and when and how well they sleep.

Computer scientists with expertise in biomedical, Internet and mobile-phone technologies will be crucial for designing and building tracking devices, and for developing standard operating procedures for the generation, uploading and storage of data. Ultimately, the analysis of data collected in such a project could give rise to fresh hypotheses that lead to new experiments in the laboratory. These in turn may help researchers to improve *in situ* recording methods.

Data should be collected from various time zones and geographical locations, and at different times of year. It is also important that participants represent diverse populations, and should include people living in different

states of modernization (people living without electricity and people living in large cities), as well as, for instance, shift-workers, people who are blind, people with metabolic syndromes, and so on.

Together with colleagues from the chronobiology laboratory at the university hospital in Porto Alegre, Brazil, we have begun to measure sleep, activity, light exposure and other variables in an Afro-Brazilian community, the Quilombos. This group of people is culturally and genetically homogeneous. But the diversity of the lifestyles of individual populations, which are scattered throughout Brazil, offers an opportunity to investigate the changes to human sleep over the past 150 years of industrialization: some live on farms with no electricity; others live and work in modern cities.

A human sleep project would need around US\$30 million of funding from governments and national and international granting agencies. Biotechnology companies may also want to invest in return for using the project's results to guide the mass production of simple sleep-tracking devices. Such devices will be valuable to sleep researchers, to physicians who want to diagnose and treat sleep problems, and perhaps even to pilots or business executives who want to optimize their sleep patterns while travelling, as well as to people who simply want to sleep better.

The project could also lead people to adopt more individualized schedules, which some fear would disrupt the synchronization of societies. But if work schedules were adapted to suit the biological clocks of most of the population, the benefits to society would outweigh a relatively small disruption. The MCTQ indicates that in 44% of the population assessed, the circadian timing of people differs by only 30 minutes, and that in 77% of the population, the timing falls within a three-hour range.

I am convinced that a human sleep project, and the changes in behaviour it would bring, could be one of the most cost-effective ways to improve health, performance and quality of life for millions for people. A preparatory meeting will take place this August in Munich, in conjunction with the congress of the European Biological Rhythms Society. ■

Till Roenneberg is professor of chronobiology at the Ludwig Maximilian University in Munich, Germany.
e-mail: till.roenneberg@med.uni-muenchen.de

- Hillman, D. R., Murphy, A. S., Antic, R. & Pezzullo, L. *Sleep* **29**, 299–305 (2006).
- Saper, C. B., Fuller, P. M., Pedersen, N. P., Lu, J. & Scammell, T. E. *Neuron* **68**, 1023–1042 (2010).
- Wyatt, J. K., Ritz-De Cecco, A., Czeisler, C. A. & Dijk, D.-J. *Am. J. Physiol.* **277**, R1152–R1163 (1999).
- Roenneberg, T., Allebrandt, K. V., Mew, M. & Vetter, C. *Curr. Biol.* **22**, 939–943 (2012).
- Van Cauter, E., Spiegel, K., Tasali, E. & Leproult, R. *Sleep Med.* **9**, S23–S28 (2008).
- Levandovski, R. *et al. Chronobiol. Int.* **28**, 771–778 (2011).

SOURCE: REF 4

Get ready for ocean acidification

Sam Dupont and Hans Pörtner call for experiments of greater complexity that can probe how plummeting pH will affect marine ecosystems as the climate warms.

Oceans are becoming more acidic as they draw rising levels of carbon dioxide from the atmosphere. Since 1850, the acidity of the surface ocean has increased by almost 30%, and could double or triple further by 2100 as the growing human population leads to higher CO₂ emissions. Ocean acidification will cause marine ecosystems to undergo major changes that scientists are only beginning to understand.

Past work has tended to focus on the immediate responses of single marine species to acidification, but researchers now know that some species are more resilient to rising acidity than others. The challenge is to understand how whole ecosystems react to a range of climate-related stressors, including temperature.

We believe that the ocean-acidification field must move away from testing only individual species in simple experimental conditions and instead perform more complex and extended experiments (see page 420). These would involve all life stages of target species and their food webs, would embrace environmental complexity and last for months to years. The aim should be to derive a set of unifying principles to help identify which sensitive species and ecosystems to protect in the face of rising ocean acidity.

SURPRISING RESILIENCE?

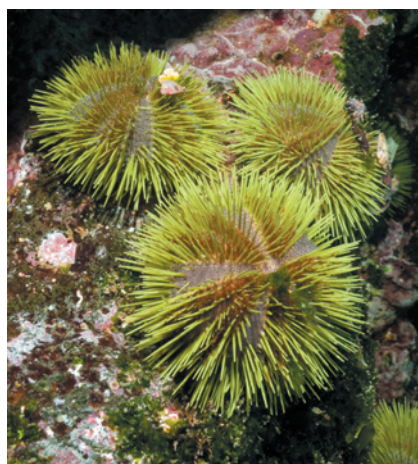
We have known for decades that ocean acidification threatens calcifying organisms such as corals, clams, mussels and brittlestars — some to the point of possible extinction within decades. It came as a surprise in the past few years that some calcifier species are resilient to acidification, such as the mussels that thrive in Kiel fjord in Germany despite a seasonal flow of CO₂-rich waters¹.

Other organisms can be both vulnerable and resilient at different times in their life cycles, such as some phytoplankton, fish and sea urchins. Initially, female green sea urchins (*Strongylocentrotus droebachiensis*) that are exposed to acidification produce around one-fifth the number of eggs produced by urchins in current ocean pH conditions. But after 16 months, adults acclimatize and reproduce as normal. Juvenile urchins, however, remain sensitive to acidification and show up to a nine-fold increase in mortality².

The impacts of acidification on sensitive species cascade across ecosystems. Copepods, a major food source for fish, are resilient but would be affected if their

phytoplankton food source declined. In mussels, more abundant food may counter-balance the increased energy costs of resisting the impacts of ocean acidification¹.

Increasing atmospheric CO₂ will also



It takes up to 16 months for green sea urchins to acclimatize to acidified conditions.

cause average global temperatures to rise. Temperature is a key driver for biological change. Organisms specialize within certain temperature ranges and are sensitive to extremes. Ocean acidification modulates responses to temperature, and vice versa. Whereas mild warming on the cold side of a species' typical thermal range may be beneficial, exposure to higher temperatures enhances the sensitivity of some species, including Arctic spider crabs (*Hyas araneus*), to acidification³. The combined effects of local variability in acidity, temperature and human-made eutrophication or pollution may be more detrimental than for each factor alone.

To understand what future oceans might look like, marine scientists need to assess how whole ecosystems respond to rising acidity over time frames that are long enough to track generations of organisms to see which ones die or adapt. Because acidification develops in tandem with human-driven environmental changes, experiments must become more sophisticated and realistic. No single experiment can capture the complexity, so a variety of approaches will be needed.

Single-species investigations will remain valuable. Mesocosms — parts of ecosystems that are brought under controlled,

experimental conditions — can unravel the role of some ecological interactions. Combined chemical and biological monitoring and modelling can reveal natural variability in ecosystem responses. Investigations of species within temperature and acidity gradients can help to assess which organisms will adapt.

ECOSYSTEM EFFECTS

Although researcher numbers, funding and methodologies will always be limiting, we think that the field is being held back by a much bigger problem — a lack of knowledge of the overarching principles for how ocean acidification affects species and ecosystems. These will be crucial for addressing issues including shifts in biogeochemical processes, such as nitrogen fixation, and the interactions between animals, plants and bacteria.

Elaborating these unifying principles will require an interdisciplinary approach that structures research within and between multinational and national projects on ocean acidification. The Ocean Acidification International Coordination Centre, announced in June 2012, is a welcome first step.

Ocean acidification is already affecting marine ecosystems and their services to humankind. In light of the millennia it will take to reverse changes in ocean chemistry, we believe that research should be oriented towards finding solutions, rather than to simply documenting the disaster. Ultimately, only the reduction of atmospheric CO₂ levels will alleviate the challenges of ocean acidification. Meanwhile, researchers can improve understanding of the biological impacts of ocean acidification and identify the organisms and ecosystems that are most at risk. We can also buy some time through reducing human pressures such as overfishing, eutrophication and pollution. ■

Sam Dupont is a marine biologist at the University of Gothenburg, Kristineberg, Sweden. **Hans Pörtner** is professor of ecophysiology at the Alfred Wegener Institute, Bremerhaven, Germany.
e-mail: sam.dupont@bioenv.gu.se

1. Thomsen, J. et al. *Biogeosciences* **7**, 3879–3891 (2010).
2. Dupont, S., Dorey, N., Stumpp, M., Melzner, F. & Thorndyke, M. *Mar. Biol.* <http://dx.doi.org/10.1007/s00227-012-1921-x> (2012).
3. Pörtner, H. O. & Farrell, A. P. *Science* **322**, 690–692 (2008).



A Fresnel lens inside Cape Blanco Lighthouse in Oregon.

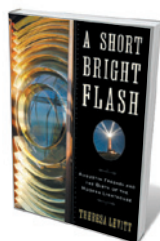
HISTORY

Beam me home

Joanne Baker enjoys a biography of the doughty French inventor of the bull's-eye lens, the secret of the modern lighthouse.

At a remote lighthouse on the English coast, I toured the tower and saw a starfish of beams reaching 20 kilometres across the sea from its revolving glass crown. I imagined the light sucking vast amounts of power from the electric grid, until I saw the bulb: a 20-watt halogen candle smaller than my thumb. It is not in the bulb, but in the glass encasing it, that the power lies.

Nineteenth-century French physicist Augustin Fresnel worked the physical magic of this lens. The light is focused into beams by concentric rings of prisms, each an inch thick and stacked in metre-high panes set into a brass frame. As the apparatus turns on a bed of oil, the beam sweeps across the waves. In *A Short Bright Flash*, historian



**A Short Bright Flash:
Augustin Fresnel and
the Birth of the Modern
Lighthouse**

THERESA LEVITT
W. W. Norton: 2013

Theresa Levitt recounts how these lenses came to keep ships safe near the shore and how they spread around the world.

Much trade was conducted by sea in the early nineteenth century and hundreds of vessels ran aground in Europe each year, most at night. Newspapers were filled with stories of shipwrecks and lost crews. France had 20 lighthouses by 1800; Britain,

a handful more. These relied on the dim lighting of oil lamps reflected by mirrors, a technology little changed since the first lighthouses of the ancient world — the third-century BC Colossus of Rhodes and Pharos of Alexandria.

Fresnel spent years trying to understand the diffraction of light, first in his spare time while building roads across France for Napoleon, then while jostling with scientific luminaries in Paris. Influenced by physicist and astronomer François Arago — famous for studies on light and magnetism, and helping to discover the planet Neptune — Fresnel came up with controversial extensions to the wave theory of light. In 1819, Arago invited Fresnel to work at the Lighthouse Commission in France, created in 1811 by Napoleon

to spread 'beacons of light' around his empire. Fresnel saw that lenses would do a better job than mirrors.

The problem was how to capture enough light and focus it. A lens close to a lamp would intercept most of its glare, but forming a beam necessitates bending the rays through a large angle and would require a bulbous lens, which would absorb more of the light. To capture the same amount of light, a thinner lens farther away would have to be larger than could be manufactured at the time. At a demonstration to the commission in 1821, Fresnel placed his bull's-eye lens alongside other reflectors high on the Paris Observatory. The public and commissioners across the city saw that Fresnel's was by far the brightest.

Fresnel built a lens for the country's most prestigious lighthouse at Cordouan, the 'Versailles of the sea' at the mouth of the Gironde estuary near Bordeaux. Installed in July 1823, its beams could be seen by tall ships up to 33 nautical miles (61 kilometres) away. In 1825, Fresnel revealed a map for 51 lighthouses around the French coast of different sizes and illumination patterns. Two years later he was dead from tuberculosis, and it was left to his brother Leonor to complete the scheme in 1854.

Hundreds of lighthouses with Fresnel lenses had been built by then, from Africa to Brazil. The United States was an exception. Stephen Pleasonton, accountant of the US Lighthouse Establishment, notably refused to sanction the purchase of the lenses, citing cost. US lights burned sperm whale oil at the time and Pleasonton insisted that more efficient lamps were the way to economize.

But with westward expansion and the advent of railways and the telegraph, science and technology rose in the country's esteem. In 1852, Congress passed a bill to create the US Lighthouse Board after several congressmen were stuck in fog on a boat to New York and saw how bad existing lighthouses were. Fresnel lenses were then systematically introduced. Levitt describes how the disabling of lighthouses played a central part in both the American Civil War and the Second World War.

The invention of radar meant that few lighthouses were built and many were decommissioned after the Second World War. Yet working towers retain their Fresnel lenses, which also appear in everything from traffic lights to overhead projectors. Levitt's detailed history is worth ploughing through to see how important scientists and engineers have been in saving sailors' lives. The French saying '*Faire rayonner la France*' ('Make France radiant') sums it up. Fresnel indeed lit up his country and the world. ■

Joanne Baker is senior comment editor at Nature.

Books in brief



The Shadow King: The Bizarre Afterlife of King Tut's Mummy

Jo Marchant DA CAPO PRESS (2013)

The nimbus of romance around Tutankhamun can hide the academic feuds fought over the boy-king's 3,300-year-old mummy. Jo Marchant lifts the golden mask to delve into findings on the enigmatic Egyptian and his relatives. Her rip-roaring story unwraps the science layer by layer, in tandem with the momentous discoveries and the emergence of theories on the ruler's health and parentage. From anatomist Douglas Derry's 1925 autopsy to the X-rays, scans and DNA testing that followed, Marchant lays bare the physical Tut who left behind the crumbling bones.



The Human Spark: The Science of Human Development

Jerome Kagan BASIC BOOKS (2013)

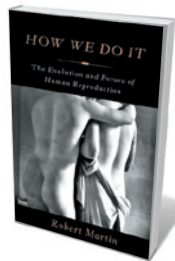
As developmental psychologist Jerome Kagan points out, physics (starting with Galileo) is 400 years old; the scientific study of children is 150. This complex field remains in some ways as plastic as the human brain. In his masterful survey, Kagan filters findings in the field. He examines cultural influences, cognition in the first three years of life, morality, the influence of social groupings such as class, and the explosion of mental illness in the young. An authoritative study of the dance of genes and environment in each child as they grow in universally human, and profoundly individual, ways.



The Lost World of Fossil Lake: Snapshots from Deep Time

Lance Grande UNIVERSITY OF CHICAGO PRESS (2013)

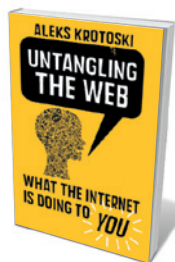
Fossil, Wyoming, is a ghost town twice over. Its human population drifted away decades ago. But its most famous denizens disappeared in the Eocene epoch tens of millions of years ago: crocodiles, dragonflies, alligators, horses the size of dogs and 23 species of fish. In this lush, in-depth guide to the area's fossilized fauna, palaeontologist Lance Grande, curator at Chicago's wonderful Field Museum, offers an in-depth portrait of an aquatic community that thrived in a subtropical wonderland of jungles and volcanoes. Beautifully illustrated in colour, including a field guide and atlas.



How We Do It: The Evolution and Future of Human Reproduction

Robert Martin BASIC BOOKS (2013)

Sex, parenting and fertility — human reproduction is one of the most hotly debated areas of human behaviour. Biological anthropologist Robert Martin wields decades of research to get at the evolutionary facts and inform people's reproductive decisions. He explains why it takes hundreds of millions of sperm to fertilize one egg; the low-down on procreation and conception; and key aspects of caregiving, including a natural history of suckling. Fascinating detours abound — such as the successful, and sensitive, toilet training of six-month-old babies by Kenya's Digo people.



Untangling the Web: What the Internet is Doing to You

Aleks Krotoski FABER AND FABER (2013)

Social psychologist Aleks Krotoski is a geek's geek and authority on the World Wide Web — the social experiment that now involves 2 billion people. Is it working wonders or wreaking havoc? Krotoski joins a host of others in attempting to pick over the claims regarding the pros (such as social empowerment) and cons (such as the growth of cults) of the web. Her verdict is mixed: she avers, for example, that the loss of privacy from digital exposure is real, but that the jury is still out on evidence for Internet addiction. **Barbara Kiser**

SCIENCE FICTION

Broken brains and runaway technology

Jennifer Rohn enters the dystopian world of Susan Greenfield's first novel.

In her debut novel *2121*, the outspoken neuroscientist Susan Greenfield wants us to be very afraid about the effect of computers and the Internet on our way of life, and even on the structures of our brains. Greenfield, the former director of the Royal Institution of Great Britain, has delivered this cautionary message extensively in other media, notably in her non-fiction book *Tomorrow's People: How 21st-Century Technology Is Changing the Way We Think and Feel* (Allen Lane, 2003).

2121 projects what Greenfield thinks might happen in a hundred years or so if our digital obsessions persist unchecked. In the novel, humanity is split into two groups so distinct that they are nearly different species. The majority, known as the Others, have embraced genetics-perfecting techniques such as mutation correction and *in vitro* fertilization with approved donors, and have surrendered completely to technology they no longer understand. They possess no self-consciousness, engage in minimal personal contact and live entirely for pleasure, using

drugs and implants that make life one long video game. Their truncated attention spans mean that they can scarcely remember how to communicate.

The other group, a splinter population known as the N-Ps (for 'Neo-Platonic' or 'Neo-Puritan'), has set up an independent society in an isolated area on the other side of a mountain. The lives of these people centre on earnest work, intellectual enrichment and physical exercise. Most technologies are

"Fiction is a valuable way to engage people with science, but interesting ideas are not enough."

banned, along with anything spontaneous or emotional — "What's an exciting feeling?" one N-P child enquires of his father, who replies, "It's when you feel so funny inside that you cannot concentrate on learning things." As with Spock, the half-human Vulcan character in *Star Trek*, true emotions still occur, but the N-Ps are trained to suppress them.

At the beginning of the story, N-P neuroscientist Fred is dispatched by his government employers to the world of the Others to assess whether they pose a threat. The Others are largely oblivious to real-life stimuli, so Fred is able to study them as if they are goldfish in a bowl. The experiment begins to break down when Fred becomes seduced by the Others' lifestyle and behaviour, and loses his scientific objectivity. In parallel, his main experimental subject has learned so many N-P



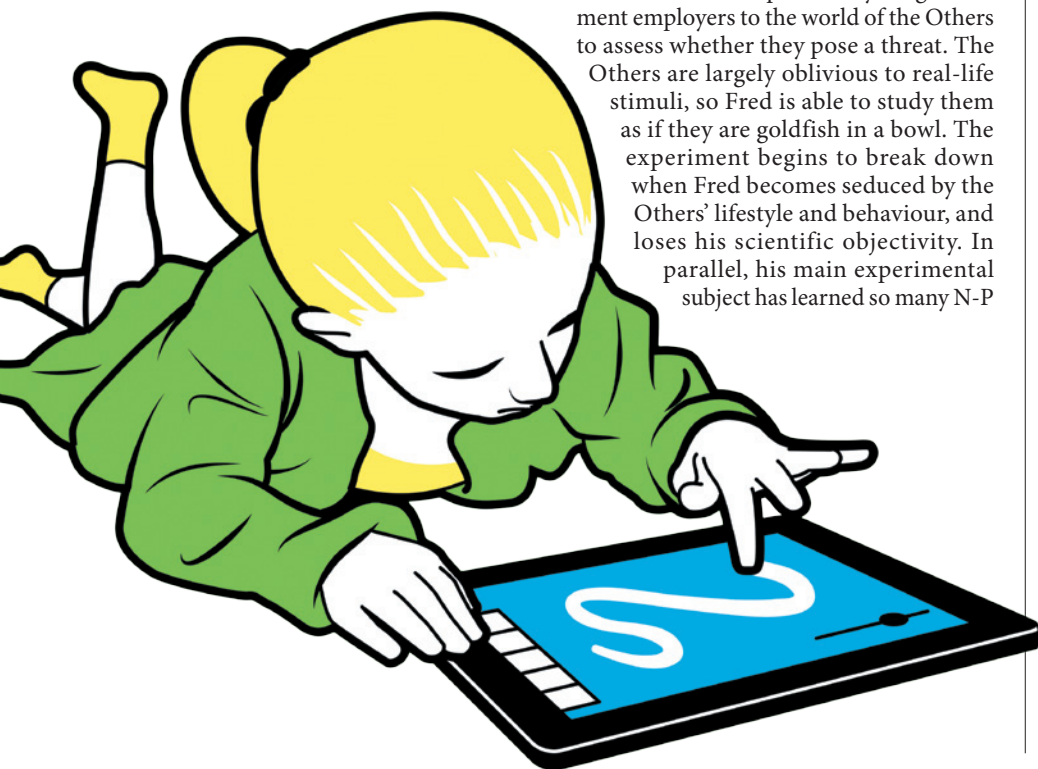
2121
SUSAN GREENFIELD
Head of Zeus: 2013.

characteristics from Fred that she starts to break free from the experiment, as well as from the Others' mental prison, with potentially world-changing consequences.

2121 conveys many of Greenfield's pet ideas, and her portrayal of a civilization on the slide to nowhere is evocative and sometimes alarming. But as a work of fiction it disappoints. The pace never picks up in a story woven together from the supposed audio diaries of several characters — multiple first-person narratives that confine the action to their limited points of view. The dialogue in these diaries is freighted with vast amounts of exposition and scientific facts, interrupted by long, introspective passages. Moreover, the dual civilizations are so one-note that they fail to live and breathe. In fact, Greenfield confesses in her Afterword that the Others and the N-Ps are caricatures. Fiction is a valuable way to engage people with science, but interesting ideas are not enough: a lively story and believable characters are essential.

The book will not enlighten those eager for proof of Greenfield's oft-voiced claims about the perils of ubiquitous technology. But the novel does make you think. Anyone who has watched people stroking their smartphones rather than talking to one another, or who feels alarmed by Google's web- and video-enabled spectacles, will probably experience some unease over the descriptions of the Others' oblivion. Still, we lack solid evidence that the "all-too-inevitable outcomes of the twenty-first century lifestyle" may be a loss of brain health, consciousness and identity, as Greenfield states in the Afterword. *2121* remains — for now — firmly lodged in the realm of speculative fiction. ■

Jennifer Rohn is a cell biologist at University College London and the editor of *LabLit.com*. Her latest novel is *The Honest Look*.
e-mail: jenny@lablit.com



MCKIBILLO/GETTY

ARIANE KOEK



Bill Fontana listens in to CERN's power supply.

Q&A: Bill Fontana Sound chaser

Audio sculptor Bill Fontana creates recordings of particle generators as artist-in-residence at CERN, Europe's particle-physics laboratory near Geneva, Switzerland. Ahead of his opening lecture, Fontana talks about probing the links between the speeds of sound and light, and chasing vibrations in gases, liquids and solids.

NICK HIGGINS



What did you do when you first visited CERN last winter?

I made audio recordings of the machines they use to generate subatomic particles. Probably the most interesting was

at 'the source', a device the size of a wine bottle where the protons begin their journey around the 27-kilometre-long ring of the Large Hadron Collider. The magnets that propel the protons when they leave the bottle produce rhythmic pulses every 1.2 seconds. The recordings were made with accelerometers mounted on the machines to pick up the sounds inside them, like a stethoscope picks up a heartbeat. The devices have a clock-like quality to them, similar in my mind to the giant mechanism inside London's Big Ben clock tower.

What will you do on your return this month?

I'll be building up recordings for my sound sculpture, which has a working title of *Acoustic Time Travel*. In a sense, I am mimicking the protocol of a scientific experiment. I plan to design a series of short sound bursts to test the sonic properties of various materials. The Large Hadron Collider will be turned off

for repairs, so I'll be able to explore its underground tunnels that stretch for miles and miles. I will play back some of my recordings there, using accelerometers mounted on the machinery to explore how these sounds travel through the space.

What do the physicists think of your work?

I have played my recordings for several scientists at CERN. They work with these machines every day, so they tend to disregard the sounds they make. To hear the sounds played back in all their intensity caused surprise, and maybe a little wonder.

How did you begin recording sound?

I started out as a composer in the 1960s, but then recognized that the acts of listening and recording can be equal in mental intensity to writing music. In the 1970s, I had a chance to record the effect of a total solar eclipse on the birds and animals of an Australian rainforest. At first, no creature knew what time it was, so they all started calling at the same time. Then the moment of the eclipse arrived, and the sounds cut to silence. I was fascinated that such a moment might not occur again for hundreds of years. It is something

NATURE.COM
Listen to a recording by Bill Fontana at CERN:
go.nature.com/jnc1jv

I think about often when recording: this moment, that we're alive and listening, is

never going to happen again. When I place live microphones in an environment, I want to convince people that the moment they are experiencing is unique and real, and that everything around them is alive with hidden dimensions of sound.

How do you work as a sound sculptor?

For 30 years, I have been making sound installations that transform our perceptions of public space. I put microphones and speakers in museums and monuments around the world. I am interested in letting people 'hear as far as they can see' by transmitting faraway sounds to them electromagnetically at the speed of light — from bell towers throughout Venice or traffic around the Arc de Triomphe in Paris — before the sounds arrive through the air. This allows me to investigate the relationship between the speeds of sound and light.

How do you draw on technology?

Measurement technology is essential to my work. I have used acoustic microphones that pick up sounds from the air, underwater sensors known as hydrophones and accelerometers that measure the vibration of solid materials. I plan to use seismic networks to explore the energy of ocean waves that spread underground after they reach the shore. I couldn't do my work without technology, but it is a means to an end.

What will you present at your 4 July lecture?

The lecture falls on the first anniversary of the announcement of the discovery of the Higgs boson. CERN director-general Rolf-Dieter Heuer will introduce myself and young cosmologist Subodh Patil, my inspirational partner, in the Globe of Science and Innovation. I will play some of the recordings of machinery and talk about my plans for the summer. Subodh will explain how the cosmic microwave background can be thought of as the echo of the Big Bang and what acoustic vibrations in the early Universe's plasma can reveal about its physics. We will give another lecture at the end of my residency about the discoveries we have made, after my work has been heard at the Ars Electronica Festival in Linz, Austria.

What would you like to do next?

There is a rare compound, tungstate, that looks like a crystal and is extremely heavy for its size. If you send a beam of photons into it, it slows the light down. At CERN, they use this material to see particle collisions in slow motion. I am told that if you could get a sound wave into tungstate, you might be able to speed it up to almost the speed of light. My fantasy is that, if I could get a large enough piece and then pass a vibration through it over a long distance, I could achieve a very long Doppler shift. ■

INTERVIEW BY JASCHA HOFFMAN

Correspondence

Society should decide on UK badger cull

As epidemiologists, we agree with the chief scientist of the UK Department for Environment, Food and Rural Affairs that badger culling is an “evidence-based” policy for controlling bovine tuberculosis (TB) in Britain (*Nature* <http://doi.org/mxd>; 2013). We disagree with other, less positive interpretations of that evidence (*Nature* **490**, 317–318; 2012).

The evidence comes from a large-scale, long-term, government project — the Randomised Badger Culling Trial (RBCT). This roughly halved the incidence of TB in cattle herds in the culling area following 4–7 annual badger culls (H. E. Jenkins *et al.* *PLoS ONE* **5**, e9090; 2010). The reductions in disease were not immediately evident owing to the long incubation period of bovine TB. There were also transient increases in incidence outside the cull areas, attributed to increased badger movements.

The mixed reaction to the RBCT results might reflect the way the data were collated and interpreted. Widely quoted summary statistics from the RBCT include data collected at the start (before any effect was likely) and long after culling had ceased. In our view, this approach is appropriate for testing for statistical significance but is not the best way to quantify effectiveness for a trial.

These analyses were never intended to account for the nonlinear impact of sustained reductions in transmission. For bovine TB in England, where various control measures are already in place, basic epidemiological principles predict that even a small reduction in transmission rate could have large benefits.

All this has confused the debate, and risks compromising the interpretation of future trials of alternative control options, such as badger vaccination.

Planned pilot studies will

establish whether badger control is practicable, humane and safe. It is for society to decide whether badgers should be culled at all.

Mark Woolhouse *University of Edinburgh, UK.*

mark.woolhouse@ed.ac.uk

James Wood *University of Cambridge, UK.*

InterAcademy Panel to inform policy

The InterAcademy Panel (IAP) of the Global Network of Science Academies, co-chaired by two of us (V.t.M. and M.H.), draws on the best international science and is free of vested political and commercial interests. It is in a strong position to identify and inform emerging policy issues.

Many science academies already advise governments on national policy-making and some contribute at a regional level, including the European Academies Science Advisory Council. Bringing together regional networks within the IAP encourages sharing of good practice and generates resources for tackling global issues such as sustainable development.

The IAP is working with the scientific community through its science-education programme and helped to create the Global Young Academy to support the development of early-career scientists. It recently issued a statement on population as part of its aim to address the world's strategic priorities (see go.nature.com/whxzi4).

The immediate challenges for the IAP are to build critical mass, to develop sustained links with policy-makers rather than waiting for a policy crisis, and to ensure accountability with the wider scientific community.

Volker ter Meulen, Mohamed Hassan *IAP, Trieste, Italy.*

volker.termeulen@mail.uni-wuerzburg.de

Robin Fears *German National Academy of Sciences Leopoldina, Halle, Germany.*

Nuclear plans add to pressure on Caatinga

Brazil's government is planning to build a nuclear power plant on the São Francisco River in the semi-arid Caatinga region, which is experiencing a long and severe drought (see R. L. M. Novaes *et al.* *Nature* **498**, 170; 2013). Now is not the time to put the area's most important water resource under even more pressure.

The river is already heavily used as a water supply and for power generation, irrigation, aquaculture, transport and tourism. The Caatinga region is home to traditional communities whose main livelihoods are fisheries and agriculture. The power plant would displace these communities, resulting in the loss of physical assets and undermining their cultural identity. Water from the reactor cooling system could raise the river's temperature, threatening the survival and balance of ecological networks.

As with the Belo Monte dam, the government is again pushing ahead with a major infrastructure project with seemingly little thought for the social, cultural or environmental consequences.

Erika dos Santos Nunes *State University of Bahia, Salvador, Brazil.*

erika.santosnunes@hotmail.com

**On behalf of 4 co-signatories. See go.nature.com/tenkss for full list.*

Relaxed laws imperil Australian wildlife

Policy and legislative changes by Australia's state governments are eroding the vital protection of the country's unique biodiversity.

Reserves are being opened up to ecologically disruptive activities, such as grazing by domestic livestock, logging, mining, recreational hunting and fishing, and commercial development. Protected habitats on private and leasehold land are imperilled too. Queensland

and Victoria, for example, are relaxing hard-won laws that limit vegetation clearance on private land, further accelerating the loss of regional biodiversity.

Collectively, these actions increase the pressure on biodiversity conservation in protected areas, many of which are already showing biodiversity loss (for example, the Kakadu National Park in northern Australia). Ecological connectivity is being lost, which will hamper the dispersal of species and their ability to respond to climate-change effects.

Species extinctions are primed to increase. Too many of the country's unique fauna and flora have been wiped out over the past two centuries (see, for example, C. Johnson *Australia's Mammal Extinctions*; Cambridge Univ. Press, 2006), including the Christmas Island pipistrelle bat (*Pipistrellus murrayi*) in 2009.

There could be no worse time to weaken reserve protection and relax laws designed to reduce habitat loss.

Euan G. Ritchie *Deakin University, Burwood, Victoria, Australia.*

e.ritchie@deakin.edu.au

**On behalf of 21 co-signatories. See go.nature.com/xhhtgb for full list.*

American football is clear on uncertainty

Nic Fleming suggests that soccer fans at this month's Confederations Cup in Brazil should recognize that electronic-eye verdicts on goal-line accuracy are not always definitive (*Nature* **497**, 537; 2013). By contrast, American football fans are already well aware of the limitations of replays.

In American football, a call is overturned only if there is indisputable visual evidence from the video review that the on-field call was incorrect. If the replay results are ambiguous, the field call stands.

Eric Altschuler *New Jersey Medical School, Newark, USA.*
altschel@umdnj.edu

Joe Farman

(1930–2013)

Discoverer of the ozone hole.

Joe Farman led a team of scientists to make one of the most important geophysical discoveries of the twentieth century. In 1985, the group from the British Antarctic Survey discovered a hole in the ozone layer — the atmospheric shield that absorbs ultraviolet rays. Their seminal article in *Nature* helped to convince scientists, the public, politicians and even the chemical industry that synthetic chemicals had driven a 40% decline in ozone levels over Antarctica in less than a decade.

Farman, who died in Cambridge, UK, on 11 May, was born in Norfolk in 1930. As a student at King Edward VI's Grammar School in Norwich, he won a scholarship to Corpus Christi College at the University of Cambridge, where he studied natural sciences. After graduating in 1953, he worked on guided missiles for three years at de Havilland Propellers, a British company. He then joined the Falkland Islands Dependencies Survey, which later became the British Antarctic Survey, the national Antarctic research operation.

Farman worked for the survey, first in Edinburgh and then in Cambridge, until 1990. Initially, he was responsible for providing a range of basic geophysical measurements, including ozone and radiation levels, for the International Geophysical Year that lasted from July 1957 to December 1958. This project aimed, among other goals, to open up the Antarctic continent for scientific research.

In the early 1980s, Farman and his group recorded anomalously low levels of ozone in the stratosphere above Halley Bay in Antarctica. The fact that atmospheric ozone could be depleted by halogen species, such as fluorine and chlorine, had been postulated a decade earlier by atmospheric chemists F. Sherwood Rowland and Mario Molina. But according to their theory, the biggest losses should have occurred some 40 kilometres above Earth's surface. Farman and his colleagues had revealed a rapid depletion of ozone levels in an unexpected place and at an unexpected time of year — spring-time temperatures above Antarctica are so low that any photochemical reactions were predicted to be exceptionally slow. Furthermore, satellite data from NASA apparently showed no such decline in ozone.

Farman's first reaction was to check and recheck the Dobson instruments — the devices used to calculate the thickness of the ozone layer by measuring the amount of ultraviolet radiation penetrating the

atmosphere. But along with his colleagues Brian Gardiner and Jonathan Shanklin, he could find no error. Meteorological data from Halley Bay also ruled out the possibility that some unforeseen weather phenomenon was to blame.

To solve the puzzle, Farman had to turn to chemistry. The group's paper (J. C. Farman *et al.* *Nature* **315**, 207–210; 1985) bravely identified the breakdown products of chlorofluorocarbons (CFCs) as the cause of the ozone loss.



Their strong statement was more remarkable in the light of Farman's innate caution.

As well as driving a sea change in attitudes towards the ozone problem, the group's discovery helped to bring about the Montreal Protocol, a 1987 international treaty to protect the ozone layer and to phase out CFCs and other ozone-depleting gases. Kofi Annan, former Secretary General of the United Nations, has described the protocol as “perhaps the single most successful international agreement to date”.

When Farman reached retirement age in 1990, he started working as a volunteer consultant for the European Ozone Research Coordinating Unit, which was relocated from the Cambridge offices of the British Antarctic Survey to the University of Cambridge's chemistry department in 1995. While the two of us (J.P. and N.H.) each took a turn at heading the unit, Farman, although unpaid, came in nearly every day.

Farman's scientific life was characterized by a painstaking attention to detail. He believed in the primacy of data and the need

for decades-long records in geophysics. For him, theory came a distant second to measurements, and computer models were distinctly suspect. We often saw him colouring in meteorological or satellite ozone maps, which allowed him to think about what the data were showing in a way that producing a computer plot would not have done. And of course, he delighted in finding occasional errors in computer-generated plots from NASA or the UK Met Office.

Joe was rigorous, critical of everything and dogged. And he absolutely hated being wrong. When writing reports, such as the series of Stratospheric Ozone Review Group reports for the UK Department of the Environment in the late 1980s and early 1990s, Joe wanted to test every statement to destruction. He was both a frustrating colleague and a joy to work with.

Joe did not naturally seek the limelight, so it was remarkable that after the publication of the ozone-hole paper, he entered the policy arena so keenly and effectively. He did so at a time when the United Kingdom, with the personal backing of then Prime Minister Margaret Thatcher, was taking a leading role in the international negotiations that in 1990 resulted in the London Amendment to the Montreal Protocol. This amendment has been successful in bringing significant reductions in CFC emissions.

Whether Joe talked to industry representatives or to journalists, it was always important to him to educate them about the science. In fact, it was his scientific integrity that gave him such credibility as a public advocate in the development of the Montreal Protocol.

Joe was a wonderful friend and colleague — generous with advice and ideas about science, but also about wine, English rugby, gardening, cross-country skiing and the conducting of Hector Berlioz's music, all delivered with his surreal good humour (he loved *The Goon Show*). He was awarded several prizes and honorary degrees, and took great pleasure, in particular, in the fellowship and then honorary fellowship conferred on him by his old college at Cambridge. He is survived by Paula, his wife of 42 years.

John Pyle and Neil Harris are at the Department of Chemistry, University of Cambridge, UK. J.P. is also at the National Centre for Atmospheric Science, UK.
e-mails: john.pyle@atm.ch.cam.ac.uk;
neil.harris@ozone-sec.ch.cam.ac.uk

Spooky action gets collective

Thousands of atoms in a gas can share a single Rydberg excitation. Quantum entanglement between such an excitation and a single photon has now been realized deterministically. [SEE LETTER P.466](#)

MATTHIAS WEIDEMÜLLER

Entanglement is a ubiquitous phenomenon in quantum physics. Owing to the intimate correlations imposed by entanglement, a measurement on one of the constituents of an entangled system forces another constituent to acquire a specific, previously undetermined state. It does not even matter how far apart the constituents are; this astonishing effect still holds. That is why Einstein called the effect ‘spooky action at a distance’. Entanglement between pairs of particles, such as single photons and atoms, has been achieved experimentally in several ways. On page 466 of this issue, Li *et al.*¹ demonstrate a method to entangle light and a collective excitation of an ensemble of roughly 1,000 atoms, in a fully deterministic way*.

The authors used an array of micrometre-sized atomic clouds, each representing an independent ensemble, and laser fields that bring the atoms from their ground state to highly excited electronic states called Rydberg states. The atoms are cooled to temperatures close to absolute zero, thus freezing all atomic motion, and are confined by light forces. The van der Waals interaction between two Rydberg atoms in an ensemble strongly depends on the degree of electronic excitation and can vastly exceed the interaction between atoms in the ground state². This interaction causes a shift in the energy levels of the atoms that prevents all but one atom in the ensemble from being in the Rydberg state — a phenomenon known as Rydberg blockade³. Therefore, the entire atomic cloud contains only one Rydberg excitation.

Because any of the atoms can be excited in the first place, quantum mechanics demands the peculiar effect that the single excitation is shared among all atoms simultaneously. This collective excitation, or spin wave, can be visualized by imagining a full football stadium. Spectators sitting on their seats represent atoms in their ground state, whereas spectators standing with hands raised denote atoms in the excited (Rydberg) state. A spin wave then corresponds to a coherent excitation of the spectators, naturally resulting in a ‘Mexican wave’

*This article and the paper under discussion¹ were published online on 19 June 2013.

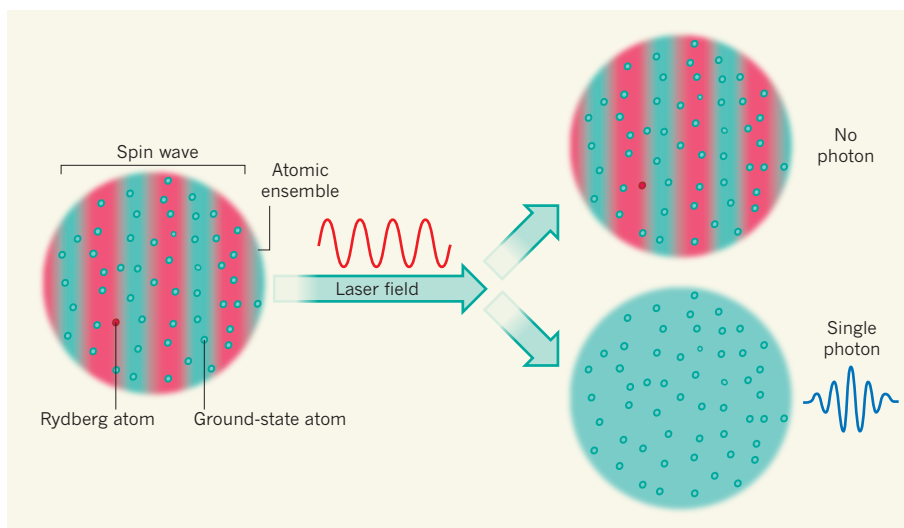


Figure 1 | Entangling an atomic collective excitation with a photon. Li *et al.*¹ have created a Rydberg excitation (spin) wave in an ultracold ensemble of roughly 1,000 atoms. The ensemble contains one atom in a highly excited, Rydberg state; all other atoms are in the ground state. By illuminating this single-excitation spin wave, which is shared by all of the atoms, with a laser field, the authors transformed it into an entangled state that involves the spin wave and no photon, or all atoms in the ground state and exactly one photon.

passing through the stadium. However, with Rydberg blockade, the spin wave, although it is spread over the entire atomic cloud, contains only one excitation shared collectively by all atoms — a true one-(wo)man Mexican wave. Such a single-excitation spin wave has a great advantage: it does not matter how many atoms actually participate in it, there is always exactly one delocalized excitation in the ensemble. Therefore, each of the ensembles in the array of atomic clouds, despite vast fluctuations in the numbers of atoms, represents essentially the same quantum-mechanical state. The robustness of this state preparation lies in the magic of the Rydberg blockade.

As the study's authors and others have previously shown^{4,5}, a single Rydberg spin wave can effectively be transformed into a light field comprising just a single photon. However, in those experiments the spin wave decayed rapidly. Li *et al.* have now used a special optical trap that confines the atoms and at the same time ensures a long lifetime for each of the single spin waves in the array. By using an extra laser field, the authors transformed the spin wave into a veritable entangled state between

matter and light (Fig. 1). The entangled state involves a quantum-mechanical superposition of either the Rydberg spin wave and no photon, or all atoms in the ground state and exactly one photon in the light field. In the classical world, a Mexican wave does not necessarily stimulate the home team to score a goal, which in this analogy corresponds to the presence of a photon. In the quantum world, however, entanglement creates a perfect correlation: the entangled state corresponds to the stadium being in a superposition of Mexican wave and no goal yet, or to a goal being scored and no Mexican wave.

Using state-of-the-art protocols to determine the full quantum state of a system, Li *et al.* verify with high fidelity that their system was prepared in the desired entangled quantum state. In particular, the authors mapped the atomic state on to a light field, which could then be investigated using tomographic methods that are well established in quantum information science. The presence of quantum entanglement was unambiguously confirmed in these measurements. In future experiments, the structure and dynamics of

single or multiple spin waves might be studied by detecting the excited atoms directly, perhaps even with high spatial resolution^{6,7}.

Li and colleagues' experiment is by no means the first demonstration of deterministic atom–light entanglement. A prominent example, involving single Rydberg atoms in a microwave cavity, is the Nobel-prizewinning work by Serge Haroche and co-workers⁸. Alternative approaches to deterministic entanglement involve single atoms in optical cavities, which allow spontaneous photon emission from the atom to be transformed into a fully coherent exchange of excitation between the atom and

the cavity's quantized light field^{9,10}. The novel entanglement of an ensemble of atoms with a photon demonstrated so impressively by Li *et al.* opens new avenues to making robust quantum networks for exchanging quantum information between matter and light, and could potentially be used to create large-scale quantum networks involving vast arrays of atomic ensembles. ■

Matthias Weidemüller is at the Physics Institute and the Heidelberg Center for Quantum Dynamics, University of Heidelberg, 69120 Heidelberg, Germany.

e-mail: weidemueller@uni-heidelberg.de

1. Li, L., Dudin, Y. O. & Kuzmich, A. *Nature* **498**, 466–469 (2013).
2. Saffman, M., Walker, T. G. & Mølmer, K. *Rev. Mod. Phys.* **82**, 2313–2363 (2010).
3. Comparat, D. & Pillet, P. J. *Opt. Soc. Am. B* **27**, A208–A232 (2010).
4. Dudin, Y. O. & Kuzmich, A. *Science* **336**, 887–889 (2012).
5. Peyronel, T. *et al.* *Nature* **488**, 57–60 (2012).
6. Hofmann, C. S. *et al.* *Phys. Rev. Lett.* **110**, 203601 (2013).
7. Schaub, P. *et al.* *Nature* **491**, 87–91 (2012).
8. Raimond, J. M., Brune, M. & Haroche, S. *Rev. Mod. Phys.* **73**, 565–582 (2001).
9. Ritter, S. *et al.* *Nature* **484**, 195–200 (2012).
10. Stute, A. *et al.* *Nature* **485**, 482–485 (2012).

REGENERATIVE BIOLOGY

Heartbroken embryos heal

An area of injured heart in zebrafish embryos repairs itself using cells from neighbouring areas. The regenerating cells seem to originate from an intermediate progenitor–cell population. SEE LETTER P.497

KENNETH R. CHIEN

More than a century ago, the pre-eminent geneticist Thomas Hunt Morgan noted¹ that “regeneration takes place not only in adult organisms but also in embryos, and larvae of many animals”. In this issue, Zhang *et al.*² (page 497) take a notable step towards understanding the mechanism underlying such spontaneous repair in the hearts of vertebrate embryos. Their data have important implications across the fields of evolutionary, developmental and regenerative biology, and potentially offer insight into pathways that lead to congenital heart disease in children*.

The authors destroyed, in a spatially and temporally controlled way, muscle cells in a specific region of the heart ventricle of zebrafish (*Danio rerio*) embryos. They then used state-of-the-art genetically triggered cell-lineage tracing to track spontaneous regeneration in the injured ventricular chamber.

Consistent with earlier studies^{3–5}, the researchers report that regeneration occurs, in part, through proliferation of residual ventricular muscle cells that have survived the destruction process. Surprisingly, however, atrial muscle cells also made a major and essential contribution to regeneration. These cells normally reside in the atrium chamber of the heart. But after injury to the ventricle, they migrated to the neighbouring ventricular chamber, proliferated and

subsequently differentiated into ventricular muscle cells (Fig. 1).

Zhang *et al.* conclude that, during this migratory transition, atrial cells revert to an atrial-progenitor-like state, similar to that of early precursors in the second heart field (one of the two fields from which most of the vertebrate heart develops) that give rise to many of the atrial structures during cardiogenesis^{6,7}. The cells then develop features of ventricular muscle cells. The precise cellular signals that govern this remarkable switch in fate from one cardiac-muscle cell type to another remain unknown, but the authors implicate the Notch signalling pathway in this process.

Despite having known for decades that heart regeneration occurs in lower vertebrates, researchers have only recently made notable progress towards understanding the mechanism involved. It is generally accepted that initial dedifferentiation is a crucial step in regeneration. In the adult zebrafish heart, this seems to involve basic muscle units losing their structure and primitive cardiac cells acquiring features of differentiated cells; these cells might represent a naturally occurring heart progenitor from an earlier embryonic state^{4,5}. In many ways, Zhang and co-workers' data from embryos fit into this model. However, they more clearly define this intermediate state as one that leans towards a naturally occurring progenitor-cell-like state.

The authors' findings imply that some of the cells migrating into the ventricular region after injury originate from the outflow tract — the largest region that contains progenitor cells of the second heart field^{6,7}. Similarly, during cardiogenesis, many atrial cells originate from progenitors in the second heart field^{6–8}. Could this field carry cells of an intermediate state, those between an atrial progenitor cell and a fully differentiated atrial cell? And can cells in this field switch fates in response to specific paracrine signals, which mediate communication between nearby cells?

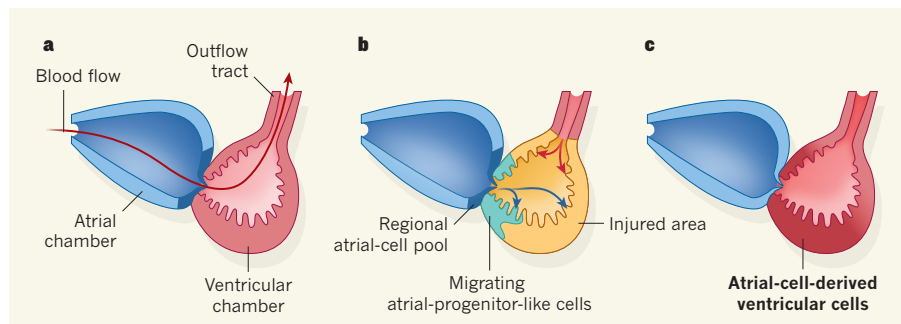


Figure 1 | Spontaneous repair and regeneration of the heart. **a**, The heart of the embryonic zebrafish is composed of an atrial and a ventricular chamber, in which blood passes sequentially through the outflow tract to the rest of the body. **b**, Zhang *et al.*² partly destroyed the ventricular muscle by genetic manipulation. This led to dedifferentiation of a regional pool of atrial cells at the border with the ventricular chamber and their conversion to atrial-progenitor-like cells, which expanded in number and migrated to the injured ventricular chamber. Moreover, native ventricular muscle cells increased in number, and cells of the outflow tract migrated to the injured zone. **c**, The migrated cells eventually became ventricular muscle cells and repaired the damaged area.

*This article and the paper under discussion² were published online on 19 June 2013.

Zhang and colleagues' experimental set-up should ultimately help to answer these questions, and might even uncover potential paracrine cues for embryonic atrial-cell dedifferentiation, for atrial-progenitor-cell expansion and migration, and for atrial-ventricular reprogramming. Researchers have directed such reprogramming using specific cardiac transcription factors, albeit relatively inefficiently^{9–11}. If adult atrial cells could be converted into atrial progenitors using naturally occurring paracrine signals, it may obviate the need for potential gene therapy to induce expression of transcription factors as part of the treatment of cardiac disorders.

From an evolutionary perspective, there is a major selective advantage in the ability of the vertebrate embryonic heart to spontaneously regenerate. But is this ability shared by other vertebrate species, including mammals? The neonatal mouse heart muscle can undergo several rounds of replication¹², and a small proportion of the cells that cover the surface of its ventricular muscle can spontaneously regenerate until a few days after birth, before this ability is lost¹³. Moreover, the mouse embryonic heart can completely replace defective heart muscle *in utero*¹⁴, suggesting that mammals have a program of spontaneous embryonic-heart repair that cannot be detected by simple morphological evaluation.

The adult human heart seems to have negligible ability to regenerate spontaneously after losing heart muscle to coronary artery disease and associated myocardial infarction — modern problems that are unlikely to have undergone significant evolutionary pressure. In light of Zhang and colleagues' data, it would be interesting to infer the likelihood of embryonic-heart repair from studying cardiogenesis in non-human primates, the heart structure of which is inherently more complex than that of zebrafish, developing over months rather than a few days.

Should the results of the present study be replicated in mammalian systems, it may eventually be possible to manipulate this natural process to treat heart disorders. Transplantation of differentiated cardiac-muscle cells into models of an injured mammalian adult heart have had mixed results¹⁵. An alternative solution might be to present atrial cells with appropriate cues to convert them into atrial-like progenitors. Indeed, one way forward could be to manipulate both progenitor cells from natural cardiogenesis⁶ and human pluripotent-stem-cell systems with paracrine signals that drive specific progenitor cells towards repairing the heart^{8,16}.

Zhang and co-authors' data may also be relevant to the most common organ malformation in children — congenital heart disease. The researchers identify a host of progenitor-cell markers that are associated with the process of embryonic-heart repair, many of which influence cell-fate decisions. Mutations in these and

other developmental regulatory genes¹⁷, as well as naturally occurring sequence variations in other specific genes¹⁸, create the risk of, and in certain cases cause, congenital heart disease, possibly through interruption of key steps in the formation, renewal and differentiation of heart progenitor cells.

This prompts an intriguing question: does congenital heart disease reflect just a defect in the initial steps of cardiogenesis or also impairment of spontaneous embryonic-heart repair by a small subset of heart progenitor cells? To directly address this question, developing large-mammal models of congenital heart disease would be crucial. Given that *in utero* interventional therapy already exists for serious fetal heart disorders, one could foresee a translational move towards delivering progenitor cells or paracrine signals, which might enable regenerative cardiovascular therapies to be carried out in children. ■

Kenneth R. Chien is in the Department of Cell and Molecular Biology and Medicine,

Karolinska Institutet, 17177 Stockholm, Sweden, and at Harvard University, Cambridge, Massachusetts, USA.
e-mail: kenneth.chien@ki.se

1. Morgan, T. H. in *Regeneration* (Macmillan, 1901).
2. Zhang, R. *et al. Nature* **498**, 497–501 (2013).
3. Poss, K. D., Wilson, L. G. & Keating, M. T. *Science* **298**, 2188–2190 (2002).
4. Kikuchi, K. & Poss, K. D. *Annu. Rev. Cell. Dev. Biol.* **28**, 719–741 (2012).
5. Jopling, C. *et al. Nature* **464**, 606–609 (2010).
6. Laugwitz, K. L. *et al. Nature* **433**, 647–653 (2005).
7. Moretti, A. *et al. Cell* **127**, 1151–1165 (2006).
8. Bu, L. *et al. Nature* **460**, 113–117 (2009).
9. Song, K. *et al. Nature* **485**, 599–604 (2012).
10. Qian, L. *et al. Nature* **485**, 593–598 (2012).
11. Inagawa, K. *et al. Circ. Res.* **111**, 1147–1156 (2012).
12. Fernandez, E., Siddiquee, Z. & Shohet, R. V. *Dev. Dyn.* **221**, 302–310 (2001).
13. Mahmoud, A. I. *et al. Nature* **497**, 249–253 (2013).
14. Drenckhahn, J. D. *et al. Dev. Cell* **4**, 521–533 (2008).
15. Yang, L. *et al. Nature* **453**, 524–528 (2008).
16. Mummery, C. L., Davis, R. P. & Krieger, J. E. *Sci. Transl. Med.* **2**, 27 (2010).
17. Zaidi, S. *et al. Nature* **498**, 220–223 (2013).
18. Stevens, K. N. *et al. PLoS ONE* **5**, e10855 (2010).

APPLIED PHYSICS

Cloaking of heat

For time immemorial, clothes have been used for thermal insulation. Cloaking devices have now been demonstrated that insulate from heat while maintaining its flow, thus hiding objects from heat sensors.

ULF LEONHARDT

Over the past decade, invisibility has turned from fiction into science¹. Yet invisibility cloaking is still a long way from being a practical technology. Ideas from the science of invisibility² have, however, inspired other applications of cloaking that are more practical and equally exciting, such as the cloaking of sound³, vibrations⁴, water waves⁵ or perhaps even seismic waves⁶. Writing in *Physical Review Letters*, Schittny *et al.*⁷ demonstrate a fundamentally different type of cloaking: that of heat.

Light, sound and earthquakes have one feature in common: they are waves. The oscillations of these waves spread like ripples in a pond. Light, for example, is an electromagnetic wave, in which magnetic oscillations induce an electric field that, in turn, produces a magnetic field, and so forth. Heat, however, is not a wave. It does not oscillate; it simply flows from hot to cold by diffusion, much like a piece of sugar dissolves in a cup of coffee. The sugar diffuses from high to low concentration until the coffee is equally sweet everywhere.

So how can the flow of heat be controlled? The rate of heat diffusion, called thermal conductivity, varies a great deal from material to

material. Metals, for example, are good heat conductors, whereas plastics and ceramics are poor by comparison — the spoon in a cup of hot coffee feels hot, whereas the cup is merely warm. Empty space is the poorest heat conductor; it has zero thermal conductivity because heat can flow only in materials.

If space does not conduct heat, then how can the heat of the Sun reach Earth? Rather than heat, the Sun sends out thermal radiation, which consists of electromagnetic waves in the infrared band of the spectrum. Only after absorption does thermal radiation turn into heat. Infrared radiation is different from heat in many ways — for example, it can be reflected, such as in solar collectors, and it can be cloaked.

Cloaking exploits some of the ideas from the physics of space, in particular those of Einstein's theory of general relativity. This theory states that the laws of physics are the same in all reference frames. Light propagates with the same speed and along straight lines in all straight coordinate frames. However, this behaviour is different in curved coordinates. Seen from the perspective of a curved frame, a straight line will no longer look straight. So, in curved frames, light rays are curved. The same bending of light occurs in optical materials.

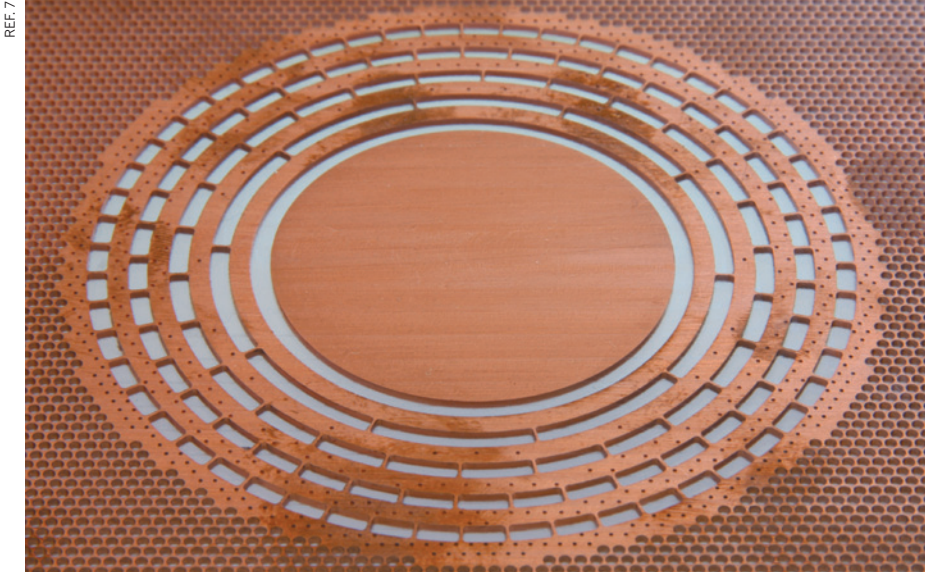


Figure 1 | A thermal cloaking device. Schittny and colleagues' thermal cloak⁷ consists of copper rings and bridges interlaid with plastic. The copper disk in the centre of the device is the object to be concealed from heat sensors placed outside the device. The disk is about 5 centimetres across.

Cloaking uses this feature of general relativity. A cloaking device transforms the space occupied by the object to be made invisible; hence, the object disappears. This transformation is performed with a material that has optical properties that can be calculated from Einstein's theory.

Electromagnetic waves are the most natural candidates for cloaking, at least in theory, because they propagate through empty space and their behaviour is therefore closest to the principles of general relativity. It is astonishing that other waves such as sound or even seismic waves follow suit, as these can propagate only in materials. That Schittny *et al.* have demonstrated heat-cloaking is even more astounding, because heat is neither a wave nor flows in empty space. Most surprising of all is that the cloaking of heat is relatively easy in practice.

For cloaking, the large differences in the heat conductivities of different materials is an advantage. The heat-cloaking device developed by Schittny and colleagues consists of copper rings interlaid with plastic, with a few copper bridges between them (Fig. 1). A second, more refined device, made recently⁸, uses five different materials. In Schittny and co-workers' device, the copper conducts the heat around the object to be cloaked, while the plastic insulates. The precise ratio between copper and plastic, and the required number of bridges, are obtained from an adaptation^{9,10} of Einstein's theory, and are designed such that the device transforms space. The transformation of space ensures that heat flows, as it would through a uniform piece of material, around the object — as if the object were not there. A heat detector would not sense anything unusual.

One may wonder why this is new. For time immemorial, people have put on clothes,

including cloaks, as insulation from the cold and the heat. As well as providing insulation, clothes change the flow of heat around them. Therefore, heat sensors can still detect the people. Similarly, a woman may use a veil to hide her face, but it does not hide her presence. An invisibility cloak would make her disappear, just as a thermal cloak conceals an object from heat detection.

Whether these tricks with heat can be developed from hot topic to practical application is

not clear. The authors^{7,8} speculate that miniaturized devices may help to cool computer chips, from which the extraction of heat is a major challenge. In any case, the realization of astrophysical ideas in laboratory experiments is exciting, particularly as the experiments are related to another of Einstein's favourite fields: thermodynamics. Einstein received his Nobel prize for his theory of diffusion, not for relativity. Perhaps he would have received another prize for general relativity had he lived longer. Thermal cloaking combines the two subjects. Einstein himself might have been pleased by how these ideas are developing. ■

Ulf Leonhardt is in the Centre for Optical and Electromagnetic Research, South China Normal University, Guangzhou, China, and at the Weizmann Institute of Science, 76100 Rehovot, Israel.
e-mail: ulf.leonhardt@weizmann.ac.il

1. Service, R. F. & Cho, A. *Science* **330**, 1622 (2010).
2. Leonhardt, U. & Philbin, T. G. *Geometry and Light: The Science of Invisibility* (Dover, 2010).
3. Zhang, S., Xia, C. & Fang, N. *Phys. Rev. Lett.* **106**, 024301 (2011).
4. Stenger, N., Wilhelm, M. & Wegener, M. *Phys. Rev. Lett.* **108**, 014301 (2012).
5. Farhat, M. *et al. Phys. Rev. Lett.* **101**, 134501 (2008).
6. Brûlé, S. *et al.* Preprint at <http://arxiv.org/abs/1301.7642> (2013).
7. Schittny, R. *et al. Phys. Rev. Lett.* **110**, 195901 (2013).
8. Ma, Y. G. *et al.* Preprint at <http://arxiv.org/abs/1305.2871> (2013).
9. Guenneau, S., Amra, C. & Veynante, D. *Opt. Express* **20**, 8207 (2012).
10. Smerlak, M. *New. J. Phys.* **14**, 023019 (2012).

NEUROSCIENCE

Stem cells in multiple time zones

In fruitfly larvae, neural stem cells generate different cell types at different times. It emerges that these temporal progressions are controlled by multiple cascades of gene transcription factors. SEE ARTICLES P.449 & P.456

STEFAN THOR

During development of the central nervous system, neural stem cells are given 'GPS coordinates' — positional information that instructs them on what types of neuronal and glial cell to make and where. There is increasing evidence^{1–3} that these cells also require 'clock input': temporal information that allows them to generate different cell types at different times, with a fixed birth order. Such temporal progressions have been observed even in cultures of single neural stem cells^{4–6}. In two papers in this issue, Bayraktar

and Doe⁷ (page 449) and Li *et al.*⁸ (page 456) identify regulatory molecular cascades that ensure proper temporal progression of neural stem cells in the fruitfly *Drosophila melanogaster*^{*}.

The *Drosophila* central nervous system (CNS) is built in two phases: an embryonic phase, which establishes most of the basic wiring and function; and a larval phase, which expands on the framework of the embryonic CNS and builds the much larger and more complex adult CNS. During both phases, neural

^{*}This article and the papers under discussion^{7,8} were published online on 19 June 2013.

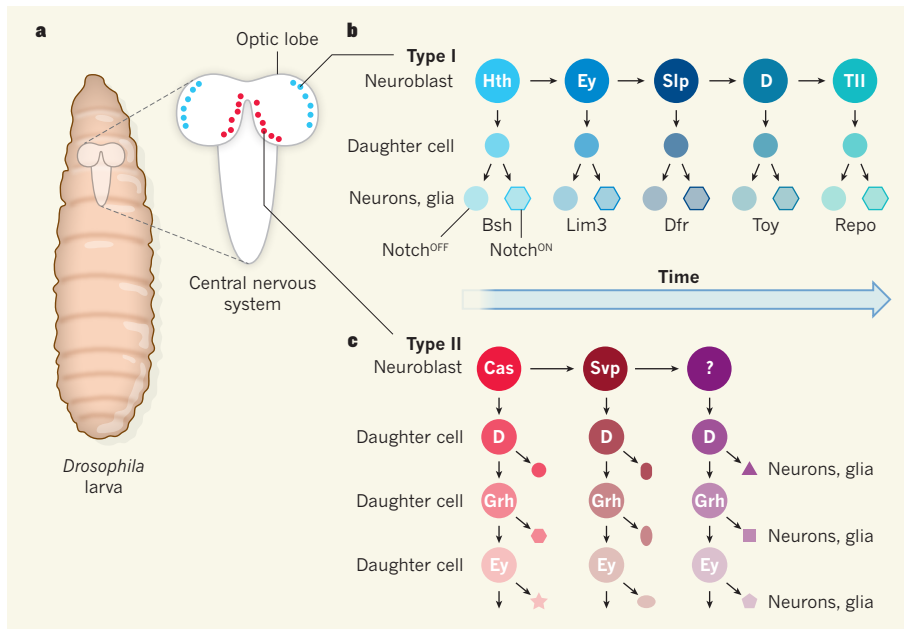


Figure 1 | Time-dependent evolution of neural lineage trees. **a**, Neuroblasts in the central nervous system of *Drosophila melanogaster* larvae are divided into type I (which have daughter cells that divide once) and type II (which have daughter cells that divide several times). **b**, Li *et al.*⁸ reveal that the temporal progression of type I neuroblasts is controlled by the expression of a cascade of regulatory transcription factors (Hth–Ey–Slp–D–Tll), which results in generation of different types of neuronal and glial cell that express specific transcription factors: Bsh, Lim3, Dfr, Toy or Repo. Asymmetric Notch signalling in sibling neurons and glia contributes to this diversification process. **c**, Bayraktar and Doe⁷ report that in type II lineages, separate cascades occur in two main branches: one in the neuroblast itself (Cas–Svp) and one in each daughter branch (Cas–D–Grh–Ey). This allows for the generation of even greater diversity in cell types originating from a single neuroblast.

stem cells — also known in insects as neuroblasts — divide asymmetrically, renewing themselves while also forming daughter cells that have more limited potential for renewal. In many cases, the daughter cells will divide only once, and such lineages are referred to as type I.

Seminal studies of the CNS of *Drosophila* embryos^{9–13} have provided a framework for temporal research. They showed that the expression of transcription factors in neuroblasts progresses in a temporal cascade of Hb–Kr–Pdm–Cas–Grh. Moreover, each factor regulates the adjacent ones, ensuring precise progression of the cascade. Each factor also controls the neuroblasts' specification competence, as is evident from different types of neuronal and glial cell being generated in each temporal window. However, such a cascade has not been identified during later stages of *Drosophila* CNS development, and similarly elaborate cascades have not been reported in other animals.

Li *et al.* identify genes and pathways that control the temporal progression of type I neuroblasts in the optic lobes of fly larvae. These neuroblasts generate cell-rich lineages containing a striking complexity of neuronal types that mediate processing of visual input from the eye (Fig. 1a,b). By surveying a large number of regulatory genes, the authors find that optic-lobe neuroblasts sequentially express a different series of transcription

factors (Hth–Ey–Slp–D–Tll) from embryonic neuroblasts. The researchers further investigate regulatory interplay between these transcription factors, showing that whereas Hth is not necessary for the cascade's progression, Ey, Slp and D are. Moreover, mutating or overactivating these factors affects the type of cell generated, as is evident from the expression of Bsh, Lim3, Dfr, Ap, Toy and Repo — transcription factors that are differentially expressed in downstream cells of different fates.

However, this regulatory cascade only partly explains how the great diversity of neuronal cell types is established in optic-lobe lineages. Li *et al.* therefore investigated the role of the Notch signalling pathway, which acts asymmetrically during the development of embryonic neural lineages, thus ensuring differing fates for 'sibling' neurons^{14,15}. The authors find that, indeed, Notch signalling is crucial for establishing asymmetric cell fate in sibling neurons in optic-lobe lineages as well. So a temporal cascade combined with asymmetric Notch signalling in sibling neurons seems to generate the high degree of neuronal diversity observed in optic-lobe lineages.

Bayraktar and Doe establish an entirely new concept in temporal coding. In addition to the type I lineages, in which daughter cells usually divide once, a second subclass of larval neuroblasts designated type II has been identified^{16–18}. Intriguingly, type II neuroblasts generate daughter cells that divide multiple

times. This means that, compared with embryonic lineages, which typically contain 10–15 cells, type II lineages are relatively large, containing as many as 500 cells, and display tremendous cell-type diversity.

Controlling cell-type diversity in such large and multi-branching lineages presents an additional challenge for the control of temporal events. Bayraktar and Doe provide evidence for an exciting evolutionary solution to this problem — multiple temporal cascades along different branches of a lineage tree.

The authors show that type II neuroblasts also undergo a time-dependent change in cell-specification competence, which is evident from the generation of different cell types over time and the sequential expression of regulatory transcription factors. In addition, these neuroblasts' daughter cells independently progress through a programmed transcription-factor cascade. Mutating or overactivating the daughter-cell temporal genes affects the fates of neurons and glia. Strikingly, although each daughter cell undergoes the same temporal progression, the types of neuron generated differ over time owing to the ongoing temporal progression in the neuroblast itself (Fig. 1c). Basically, as the neuroblast changes over time, the same cascades in the daughter cells have different informational values. These are exciting findings and provide an alternative concept for thinking about temporal progression during the development of large neural lineages.

A question relevant to both studies is how the temporal genes connect to genes regulating terminal differentiation — how do the temporal genes actually dictate unique neural-cell fates? Another important issue pertains to a more complete and detailed mapping of type I and II lineage trees: the current studies did map the temporal expression of key regulatory genes and the resulting temporal generation of distinct cell types, but the precise, single-cell resolution of these large lineage trees awaits further investigation. This poses a challenge because of the complexity and size of these larval lineages (for example, each type II lineage has almost as many cells as one *Caenorhabditis elegans* worm). Nonetheless, full resolution of these lineage trees is necessary, because further surprises are likely to be in store.

Studies in mammals have identified temporal progressions in neural stem cells' specification competence both *in vivo* and *in vitro*^{2,5,6}. However, there has been limited success in identifying bona fide temporal gene cascades in which regulatory factors are expressed in a sequential manner, regulate each other and regulate cell-specification competence. The two latest studies suggest that regulatory genes with other known functions may be involved in temporal cascades in mammalian neural progenitors, similarly to Hth, Ey and Tll, which are all better known for other roles in *Drosophila* development. Thus, broad, temporally

focused surveys of regulatory-gene expression may help to identify temporal cascades in the mammalian nervous system. ■

Stefan Thor is in the Department of Clinical and Experimental Medicine, Linköping University, Linköping 58185, Sweden.
e-mail: stefan.thor@liu.se

1. Jacob, J., Maurange, C. & Gould, A. P. *Development* **135**, 3481–3489 (2008).
2. Okano, H. & Temple, S. *Curr. Opin. Neurobiol.* **19**,

- 112–119 (2009).
3. Pearson, B. J. & Doe, C. Q. *Annu. Rev. Cell Dev. Biol.* **20**, 619–647 (2004).
4. Brody, T. & Odenwald, W. F. *Dev. Biol.* **226**, 34–44 (2000).
5. Gaspard, N. et al. *Nature* **455**, 351–357 (2008).
6. Shen, Q. et al. *Nature Neurosci.* **9**, 743–751 (2006).
7. Bayraktar, O. A. & Doe, C. Q. *Nature* **498**, 449–455 (2013).
8. Li, X. et al. *Nature* **498**, 456–462 (2013).
9. Baumgardt, M., Karlsson, D., Terriente, J., Díaz-Benjumea, F. J. & Thor, S. *Cell* **139**, 969–982 (2009).
10. Isshiki, T., Pearson, B., Holbrook, S. & Doe, C. Q. *Cell*

- 106**, 511–521 (2001).
11. Kambadur, R. et al. *Genes Dev.* **12**, 246–260 (1998).
12. Maurange, C., Cheng, L. & Gould, A. P. *Cell* **133**, 891–902 (2008).
13. Novotny, T., Eiselt, R. & Urban, J. *Development* **129**, 1027–1036 (2002).
14. Guo, M., Jan, L. Y. & Jan, Y. N. *Neuron* **17**, 27–41 (1996).
15. Spana, E. P. & Doe, C. Q. *Neuron* **17**, 21–26 (1996).
16. Bello, B. C., Izergera, N., Caussinus, E. & Reichert, H. *Neural Dev.* **3**, 5 (2008).
17. Boone, J. Q. & Doe, C. Q. *Dev. Neurobiol.* **68**, 1185–1195 (2008).
18. Bowman, S. K. et al. *Dev. Cell* **14**, 535–546 (2008).

ELECTRONICS

The road to carbon nanotube transistors

Purifying and positioning carbon nanotubes are challenges for the synthesis of electronic devices based on these nanomaterials. Recent advances in such areas reveal trends that are beating an exciting path towards transistor technology.

AARON D. FRANKLIN

For nearly five decades, scientists and engineers have managed to drive revolutionary technology by shrinking silicon transistors, the building blocks for all computing. Now transistors are approaching fundamental roadblocks that mean the devices cannot still be fashioned from silicon if they are to become any smaller. Researchers are therefore looking for materials to replace silicon. The road to producing transistors from single-walled carbon nanotubes (CNTs) — one of the most promising options — has been hedged about by the difficulties of purifying and controllably positioning these tiny molecular cylinders, which have a diameter of about 1 nanometre. Writing in *Nature Nanotechnology*, Jin et al.¹ report a method for obtaining arrays of highly purified semiconducting CNTs. This result, when considered with other advances in purifying and placing CNTs, suggests a promising future for CNT-driven electronics.

The motivation for pursuing a computing technology based on CNT transistors includes their ability to operate at low voltages² (saving chip power) and their exceptional performance in devices in which the length of the current-carrying CNT channel is less than 10 nanometres³. Because CNTs can be metallic or semiconducting, isolation of purely semiconducting nanotubes has been of great concern. For high-performance logic applications, which would require billions of transistors integrated on a chip, the impurity concentration of metallic CNTs would need to be less than 0.0001%. With statistical analyses indicating that 33% of all CNTs are metallic, this is a daunting target.

Jin and colleagues have managed to achieve the selective removal of metallic CNTs from an array of such nanotubes on a chip without damaging the semiconducting nanotubes. Starting with a parallel array of long CNTs, the authors coat the substrate supporting these nanotubes with a special organic thin film (a resist) that is sensitive to thermal

fluctuations. Therefore, when a nanotube conducts an electric current, heat is dissipated (a process known as Joule heating), locally breaking down the resist to create a small trench that exposes the nanotube. This useful thermophysical behaviour led the researchers to dub the 25-nm-thick resist material a ‘thermocapillary resist’. When an electric field is applied to a portion of the CNTs, the semiconducting nanotubes are electrically switched off (blocking current flow), leaving only the metallic CNTs to carry electrons. Thus, only the metallic CNTs are exposed in resist trenches and they can be removed using an oxygen plasma.

The advantages of this approach include high selectivity for metallic CNTs, a lack of specificity for nanotube diameter and removal of the entire length of unwanted CNTs — previous methods have failed in one or more of these categories. The use of electromagnetically induced Joule heating may eliminate the

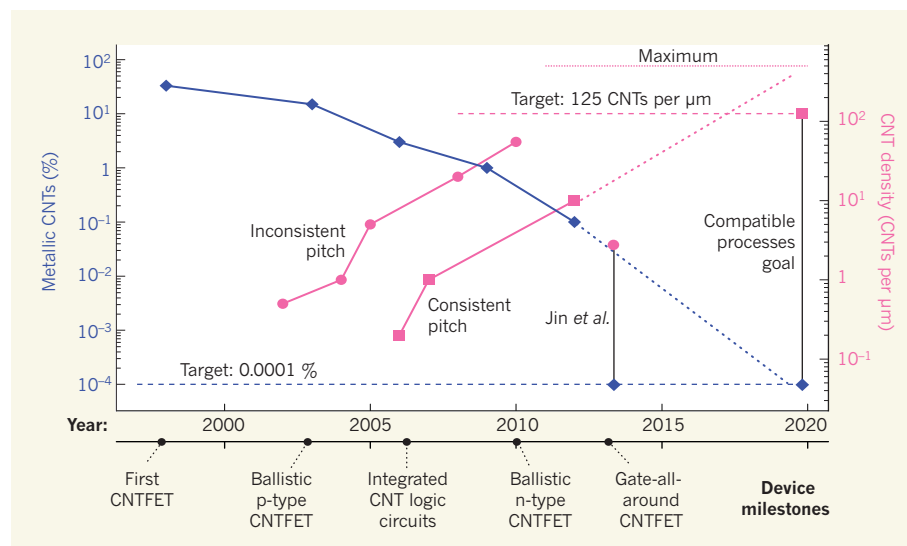


Figure 1 | Targets for carbon nanotube (CNT) transistors. The graph shows the progress in CNT transistor technology since the first demonstration of a CNT field-effect transistor (CNTFET) in 1998. The purity of semiconducting CNT material is plotted in terms of percentage of metallic CNT impurity. The placement of CNTs at a certain density is shown for both consistent and inconsistent pitch (distance) between CNTs, with the target of 125 CNTs per micrometre specified, along with the maximum of 500 CNTs per μm obtained when the CNTs are packed together without a gap between them. Trends in both purification and placement over the past decade suggest the ability to meet their targets before 2020, provided the scientific effort continues (dotted-line trajectories). Jin et al. introduce¹ a superb purification technique that is combined with a modest density of CNTs at an inconsistent pitch. Final approaches for achieving both less than 0.0001% of metallic CNTs and a CNT density of more than 125 CNTs per μm with consistent pitch must be compatible.

need for metal electrodes to create current flow in the metallic CNTs.

This impressive advance is best considered in light of the ultimate targets for CNT transistors. From an industry perspective, CNTs are among the most viable options for a transistor technology involving minimum device-feature sizes of less than 7 nm, which is slated for production by the early 2020s. There have been many breakthroughs in the isolation of semiconducting nanotubes dispersed in a solution⁴, leading to promising progress that is on track to yield the target purity of 0.0001% by 2020 (Fig. 1). However, a challenge with all solution-based processes is that they must be compatible with a strategy for positioning the CNTs. The thermocapillary-resist approach of Jin *et al.* is encouraging because it works on CNTs that are already positioned in aligned arrays — although improvements are needed to thin the resist and shrink the resulting trench widths (at present, about 250 nm) to be compatible with a higher CNT density. The authors' technique is a superb approach for applications that do not require very high CNT placement density, such as thin-film transistors, which drive displays, and could potentially lead to high-performance CNT transistor technology.

In a technological application, each transistor will require several parallel CNT channels to drive the required current. Therefore, the CNTs must be placed at a small pitch (distance between CNTs) to maximize the current per transistor width. CNTs grown on quartz substrates are excellent for yielding⁵ parallel nanotubes at a density of up to 55 CNTs per micrometre. However, they do not provide consistent pitch, which is essential for achieving a high density of integrated devices in which the number of CNT channels per device is constant.

In the mid-2000s, it was shown that CNTs could be coated with certain molecules to tune their attraction to different surfaces⁶. This attribute has been exploited⁷ most recently to boost the density of nanotubes placed at a controlled pitch to 10 CNTs per μm . As was the case for the trend in increasing purity of semiconducting CNTs, progress in increasing nanotube density with a regular pitch indicates that the baseline target of 125 CNTs per μm should be attainable before 2020 (Fig. 1).

We have known for years that a silicon-based device will not be able to provide the necessary performance at the dimensions desired for 2020 technologies⁸. Although the postulated trajectories shown in Figure 1 indicate that CNTs can be ready by this time, without substantial effort by the scientific community these trends will undoubtedly flatten. Neither of the required targets is fundamentally impossible, yet neither is possible without sustained, even increased, global scientific effort to yield more discoveries like those of Jin and colleagues. Some 10 years of data suggest that,

with enough effort, this News & Views article could be viewed on an electronic device driven by CNT transistors before the end of the next decade. In short, the road is before us — will we take it? ■

Aaron D. Franklin is at the IBM T. J. Watson Research Center, Yorktown Heights, New York 10598, USA.
e-mail: aaronf@us.ibm.com

CELL SIGNALLING

Nutrient sensing lost in cancer

Cells can sense and respond to fluctuations in nutrient availability. Mutations that disrupt such lines of nutrient communication with the cellular growth machinery seem to contribute to the uncontrolled growth of cancer cells.

SUCHITHRA MENON & BRENDAN D. MANNING

Various signals, including those stemming from nutrients such as carbohydrates and amino acids, tightly coordinate cell growth. These signals can be altered in disease states, such as obesity and cancer. Reporting in *Science*, Bar-Peled *et al.*¹ identify a protein complex called GATOR that is crucial for linking nutrient sensing by the cell to the control of cell growth. They also find that this complex is disrupted in some cancers, hinting at a mechanism by which cancer cells disconnect their growth from normal growth-control signals.

Cells monitor nutrient levels through both

systemic and local lines of communication. The systemic signals reflect the nutrient status of the whole organism and come in the form of secreted factors, such as the hormone insulin, which can travel to all parts of the body. Local signals come from nutrients within cells, because cells closely monitor their own levels of glucose, amino acids and other nutrients or their metabolic products.

One component of the cellular nutrient-detection system is the protein complex mTORC1, which senses both systemic and local nutrient signals. Under nutrient-rich conditions, mTORC1 is activated to promote the conversion of nutrients into cellular building blocks — proteins, lipids and nucleic

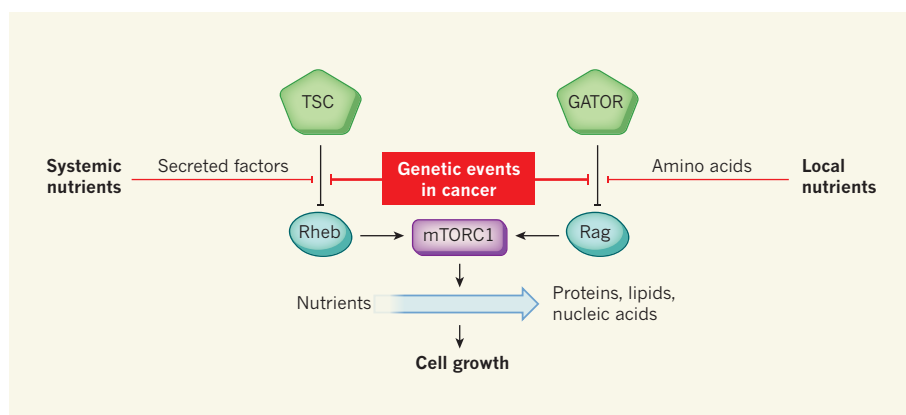


Figure 1 | Nutrient sensing and mTORC1. The protein complex mTORC1 senses systemic and local levels of nutrients through two parallel regulatory circuits that control Rheb and Rag proteins. Secreted factors such as insulin relay systemic nutrient status to cells, initiating pathways that relieve the inhibition of Rheb by the protein complex TSC. Bar-Peled *et al.*¹ report that the GATOR protein complex inhibits Rag proteins to signal local (intracellular) shortage of amino acids. In the presence of nutrients, Rheb and Rag proteins act together to induce mTORC1 activation, which results in the conversion of nutrients into proteins, lipids and nucleic acids — macromolecules that are required for cellular growth. In cancer cells, genetic changes can disrupt these two regulatory circuits and activate mTORC1 independently of nutrient availability.

acids^{2,3}. When nutrients are scarce, however, this complex is inactivated, allowing individual cells — and the whole organism — to economize on nutrients by halting cell growth.

Much progress has been made in our understanding of how mTORC1 senses growth signals (Fig. 1). This complex responds to systemic nutrient signals through a biochemical pathway that is initiated at the cell surface by secreted factors. The pathway communicates with a regulatory circuit that involves the protein complex TSC and its target Rheb — an essential activator of mTORC1 (refs 2, 3). In the absence of secreted growth factors, TSC inhibits the ability of Rheb to stimulate mTORC1 activity. As for local nutrients, cells mainly sense intracellular amino-acid levels through a second set of essential mTORC1 activators called Rag proteins^{2,3}. Both Rheb and Rag signals are essential, providing a mechanism by which mTORC1 can integrate systemic and local nutrient signals. Consequently, mTORC1 is activated, and so promotes cell growth, only under conditions that are favourable to both the cell and the whole organism.

Bar-Peled *et al.* identify GATOR as a crucial regulator of Rag proteins. They show that this protein complex is required for mTORC1 inhibition in response to amino-acid shortage in the cell — an evolutionarily conserved mechanism for sensing amino acids that is also present in yeast and fly cells^{1,4,5}. Just as the TSC complex inhibits Rheb, GATOR seems to inhibit the ability of Rag proteins to activate mTORC1 under conditions of nutrient deprivation (Fig. 1).

Because mTORC1 is a major promoter of cell growth, it is not surprising that it is abnormally activated in most human cancers across nearly all cell lineages⁶. Some of the most frequent genetic changes in cancer lead to persistent activation of this complex, at least in part by permanently activating pathways that inhibit the TSC complex. Furthermore, components of the TSC complex are mutated in some cancers and in the cancer-like syndromes tuberous sclerosis complex and lymphangioleiomyomatosis, which are driven by uncontrolled mTORC1 activity. These genetic changes disconnect mTORC1 signaling from systemic nutrient control by growth factors. Loss of TSC-complex-mediated regulation facilitates cell-autonomous growth in a tumour, rendering it largely independent of organismal nutrient status.

The present study suggests that defects in local nutrient sensing can also contribute to mTORC1 activation and tumour-cell growth. The authors show that on disruption of protein components of GATOR, mTORC1 can no longer sense local amino-acid levels, remaining active irrespective of the cellular availability of these nutrients. Moreover, the genes encoding NPRL2, NPRL3 and DEPDC5 (the core components of GATOR that are involved in Rag inhibition) are tumour suppressors, and

their mutation or deletion occur in a variety of human cancers, albeit at low frequency^{1,7}. From the cancer-cell perspective, what could be the advantage to tumour development of disrupting local nutrient signals?

Generally, homeostatic pathways that monitor nutrient fluctuations in the cell, and alter cellular physiology accordingly, promote cell survival. Such adaptive responses would seem to be equally, or even more, important in the immediate environment of a growing tumour, where insufficient or immature vasculature might lead to variable delivery of nutrients to the tumour cells. Loss of other nutrient-sensing pathways (including the LKB1–AMPK pathway) that act as tumour suppressors sensitizes tumour cells to nutrient starvation or to drugs that mimic aspects of starvation^{8,9}. Therefore, a vulnerability to nutrient deprivation is likely to counterbalance the advantage of a sustained increase in mTORC1 activity after GATOR loss. An explanation for selective loss of this and other nutrient-sensing pathways in tumours could be that removal of these brakes on cell growth provides a growth advantage under suboptimal — but not growth-limiting — nutrient levels that would normally inhibit mTORC1.

Bar-Peled and colleagues' findings could have implications for cancer treatment. They find that, compared with some other cancer cells, GATOR-mutant cells are more sensitive to the mTORC1 inhibitor rapamycin. In addition to targeted therapeutics such as rapamycin, exploiting specific vulnerabilities arising from disruption of inherent adaptive responses to nutrient availability might provide alternative strategies for selectively killing cancer cells. Indeed, cancer cells that lack these adaptive responses might be particularly susceptible to nutrient mimetics, such as amino-acid or glucose analogues; drugs that cause general metabolic stress in cells, including the anti-diabetes drug metformin; or compounds that target the specific metabolic dependencies of tumour cells. These are all active areas of investigation in the field of cancer metabolism. ■

Suchithra Menon and Brendan D. Manning
are in the Department of Genetics and Complex Diseases, Harvard School of Public Health, Boston, Massachusetts 02115, USA.
e-mail: bmanning@hsph.harvard.edu

1. Bar-Peled, L. *et al.* *Science* **340**, 1100–1106 (2013).
2. Laplante, M. & Sabatini, D. M. *Cell* **149**, 274–293 (2012).
3. Dibble, C. C. & Manning, B. D. *Nature Cell Biol.* **15**, 555–564 (2013).
4. Neklesa, T. K. & Davis, R. W. *PLoS Genet.* **5**, e1000515 (2009).
5. Panchaud, N., Péli-Gulli, M. P. & De Virgilio, C. *Sci. Signal.* **6**, ra42 (2013).
6. Menon, S. & Manning, B. D. *Oncogene* **27**, S43–S51 (2008).
7. Li, J. *et al.* *Cancer Res.* **64**, 6438 (2004).
8. Leprivier, G. *et al.* *Cell* **153**, 1064–1079 (2013).
9. Shackelford, D. B. *et al.* *Cancer Cell* **23**, 143–158 (2013).



50 Years Ago

Nowadays, most scientists who reach a fair degree of seniority in their profession are called on at some time ... to plan a new laboratory. On the first occasion, they usually tackle this with enthusiasm, pride and little else, other than their own prejudices or knowledge of the deficiencies of the laboratories they have themselves worked in.

From *Nature* 29 June 1963

100 Years Ago

A shameful outrage has just been perpetrated at the Gatty Marine Laboratory of St. Andrews ... The laboratory has always been freely open to scientific workers of both sexes ... and might therefore have been expected to be immune from attack; yet it has been fired, apparently by militant suffragettes ... It appears that on Saturday, June 21, the incendiaries effected an entry by smashing one of the windows ... The print of a small shoe, and suffragette literature stuck between the wall and a rain-pipe, were the only traces left. Fortunately the fire was seen by a fisherman, who gave the alarm.

ALSO:

Yorkshire Education Committee has decided to include in the vacation ... a laboratory course of experimental science ... This course is intended for science teachers in secondary schools, and especially for those who teach the subject to girls and desire to acquaint themselves with methods of correlating it with domestic subjects. It will relate chiefly to the subject of combustion ... provide examples of the teaching of science in relationship to the phenomena and appliances of daily life and especially of domestic life; and give a connected account of the modern science of combustion and the chemistry of flame.

From *Nature* 26 June 1913

ANIMAL BEHAVIOUR

Brain food

Anyone studying for an exam knows that learning and memory cost energy. If energy is limited, cognitive functions can be impaired or traded off. Writing in *Biology Letters*, Jaumann *et al.* used honeybees (*Apis mellifera*) to assess whether changes in resource allocation at the group level might relieve such effects in group-living animals (S. Jaumann, R. Scudelari & D. Naug *Biol. Lett.* <http://dx.doi.org/10.1098/rsbl.2013.0149>; 2013).

They find that learning imposes an energetic cost on individual honeybees from a colony, and that — just as in solitary animals — learning and retention suffer during starvation or following an immunological challenge.

A worldwide trend of colony collapse resulting from bee disappearance is worrying scientists. The authors suggest that diseases, pesticide exposure or habitat changes may impose energetic stresses, particularly on foraging bees, that impair their ability to find their way home. **Marian Turner**



VISUALS UNLIMITED/NATUREPL.COM

EPIDEMIOLOGY

Resistance mapping in malaria

Whole-genome sequencing of human malaria parasites has revealed genomic regions that are associated with resistance to artemisinin-based drugs. The findings may help to explain the origin and spread of this worrying trend.

A. TAYLOR BRIGHT &
ELIZABETH A. WINZELER

Although malaria still causes more than one million deaths annually, the number of reported cases of the disease has been decreasing in recent years^{1,2}. This decrease may be partly attributable to improved surveillance and control of mosquitoes, the malaria parasite's vector. But many experts feel that it is mainly a result of the availability and effectiveness of medicines called artemisinin-based combination therapies. Because this is the only class of anti-malarial therapy that can effectively eliminate multi-drug-resistant malaria infections, the discovery of artemisinin resistance in parasites in western Cambodia³ has been viewed as a potential disaster by the international malaria community, and has sparked intensive effort to identify the genes conferring the resistance. Writing in *Nature Genetics*, Miotto *et al.*⁴ use whole-genome sequencing to investigate 825 samples of *Plasmodium falciparum*

— a common human malaria parasite — from southeast Asia and West Africa in an attempt to reveal the molecular basis and origin of artemisinin resistance.

There is currently no licensed malaria vaccine, so drugs remain the best way to control the infection. Artemisinin-based combination therapies (ACTs) are medicines in which one of the active ingredients is a derivative of artemisinin, a natural product originally isolated from the traditional Chinese medicinal herb sweet wormwood⁵. Although ACTs are very effective at treating malaria, their mechanism of action is not well understood, and resistance mechanisms seem to be different from those for other antimalarials. Resistance is also difficult to quantitate: no sensitive laboratory-based assays are available, and resistance is typically defined by how long it takes for malaria parasites to be cleared from a patient's body after treatment with artemisinin alone, a process in which patient immunity plays a part.

Furthermore, western Cambodia is the same region from which resistance to drugs based

on chloroquine and sulfadoxine-pyrimethamine emerged and spread to the rest of the world in previous decades, leading to millions of extra deaths as these front-line antimalarials were rendered useless^{6–8}. Fears of a repeat of this disaster if artemisinin-resistant parasites become widespread prompted the World Health Organization and other members of the Roll Back Malaria Partnership to launch the Global Plan for Artemisinin Resistance Containment (GPARC) in 2011 (go.nature.com/jgcpzc).

One of the main goals of GPARC is to identify the molecular basis of resistance to artemisinin, but this initiative has been confounded by the fact that this characteristic cannot be reliably assayed or reproduced in the laboratory. Instead, investigators have relied on genetic epidemiology — looking for signatures in parasite genomes that can shed light on the genetic basis of resistance. In these studies, parasite DNA is collected from infected people both in areas in which artemisinin resistance is common and in areas where it is not. By taking advantage of natural parasite sexual crosses that occur in the mosquito, together with conventional genotyping techniques or, most recently, whole-genome sequencing, genomic regions associated with resistant parasite populations can be mapped (Fig. 1). Genes present in these candidate regions are then prioritized for functional studies to validate what role, if any, they have in parasite resistance.

Using such techniques, Miotto *et al.* find evidence of three genetically distinct resistant parasite populations in a quite small geographic area, suggesting that resistance may have arisen independently at least three times.

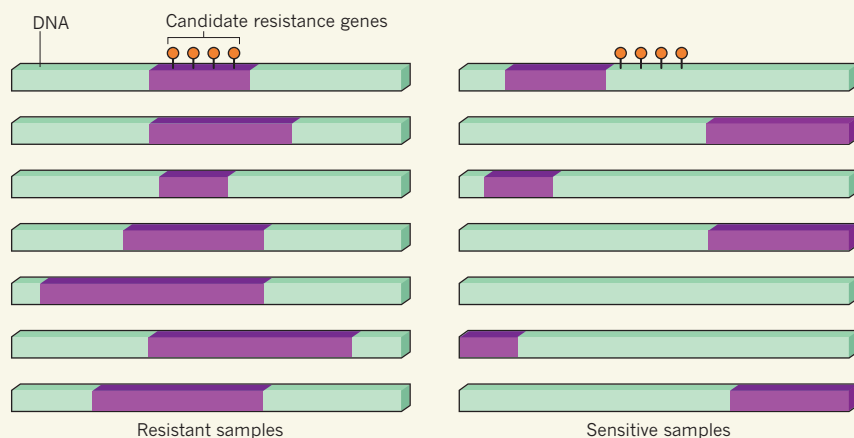


Figure 1 | Pièce de résistance. Miotto *et al.*⁴ found long blocks of sequence, called haplotypes, that contain sequence variants common to many parasite DNA samples from patients showing signs of resistance to artemisinin treatment. An example haplotype is shown in purple. Although parts of this haplotype are also found in parasite DNA samples from drug-sensitive patients, they do not consistently map to a shared chromosomal location. Thus, genes lying in a chromosomal region at which the haplotype is shared across drug-resistant samples are candidate resistance genes that should be prioritized for functional assessment.

In addition, they identify genomic regions that have characteristics indicative of selection pressure; these sites may be associated with artemisinin resistance. One such area is located on chromosome 13 and has also been identified in previous studies^{9,10}. Genes in this region, along with others identified as highly associated with resistance in various other analyses, should serve as starting points for follow-up functional studies. All of Miotto and colleagues' raw sequencing data are publicly available, which will be an invaluable resource for the research community.

Without follow-on functional studies that reveal the exact identity of genetic variants that confer resistance, one cannot be sure that resistance has indeed arisen on several independent occasions, or even that the region on chromosome 13 is truly important. The authors call for further population studies, but unless a clearer signature emerges, such as a copy-number variant (a duplication or amplification of a genomic region), further population studies and sequencing may not provide better resolution, especially if the parasites in a region are closely related to one another. To show definitively that resistance is conferred by a specific genetic variant, the candidate variant would need to be moved into an artemisinin-sensitive parasite clone (through genetic crosses, allelic exchange or genetic engineering) and the resultant parasites tested for resistance or tolerance. Currently, these techniques are too cumbersome in *P. falciparum* to allow assessment of the dozens of candidate variants discovered in this latest study. Nevertheless, new techniques, such as zinc-finger-nuclease technology^{11,12}, could ease the task of investigating candidate variants. Additionally, development of an *in vitro*

assay that would allow artemisinin tolerance and/or resistance to be assessed more readily and sensitively in the field and the laboratory would speed up such efforts.

Miotto and colleagues' work represents a substantial contribution not just to the search for the molecular basis of artemisinin resistance, but also to the larger question of worldwide genetic diversity in *P. falciparum*. Furthermore, the study highlights the great

strides made towards combating malaria in recent years at the international public-health level, to a large extent as a result of increased funding from groups such as Roll Back Malaria and the Bill & Melinda Gates Foundation. The fact that a multi-centre, international study analysing hundreds of parasite samples from around the world could even be attempted, let alone completed, shows how far the malaria research community has come, and how successful the major funders have been at promoting cutting-edge research. But it also highlights the need for more funding to investigate the basic biology of the parasite, so that the hypotheses proffered by population genomics data can be properly tested. ■

A. Taylor Bright and Elizabeth A. Winzeler are in the School of Medicine, University of California, San Diego, La Jolla, California 92093, USA.

e-mail: ewinzeler@ucsd.edu

1. Murray, C. J. L. *et al.* *Lancet* **379**, 413–431 (2012).
2. *World Malaria Report 2012* (World Health Organization, 2012).
3. Noedl, H. *et al.* *N. Engl. J. Med.* **359**, 2619–2620 (2008).
4. Miotto, O. *et al.* *Nature Genet.* **45**, 648–655 (2013).
5. Eastman, R. T. & Fidock, D. A. *Nature Rev. Microbiol.* **7**, 864–874 (2009).
6. Roper, C. *et al.* *Science* **305**, 1124 (2004).
7. Payne, D. *Parasitol. Today* **3**, 241–246 (1987).
8. Mita, T. *et al.* *J. Infect. Dis.* **204**, 1980–1988 (2011).
9. Cheeseman, I. H. *et al.* *Science* **336**, 79–82 (2012).
10. Takala-Harrison, S. *et al.* *Proc. Natl Acad. Sci. USA* **110**, 240–245 (2013).
11. Durai, S. *et al.* *Nucleic Acids Res.* **33**, 5978–5990 (2005).
12. Straimer, J. *et al.* *Nature Meth.* **9**, 993–998 (2012).

PHOTONICS

An ultra-small silicon laser

A micrometre-sized laser has been demonstrated in silicon, the most ubiquitous material of the electronics industry. The device operates at microwatt power levels and could open routes to compact photonic integrated circuits. SEE LETTER P.470

ROEL BAETS

Ever since physicist Christian Doppler described the Doppler effect in 1842, we have known that light scattered by a moving object undergoes a frequency shift. Much later, researchers, including Venkata Raman, discovered the influence of mechanical vibrations in matter on light propagation. But the interaction between light and matter also works the other way around: light can exert forces on particles and set them in motion. These concepts have now been ingeniously combined in what is probably

the smallest laser ever made in silicon. On page 470 of this issue, Takahashi *et al.*¹ report a micrometre-sized Raman silicon laser that operates at microwatt power levels.

In essence, the authors describe an ultra-compact laser on a silicon chip made using mainstream electronic-industry technologies. The laser is 'pumped' by another laser and has a cavity — in which the light generated circulates and is amplified — that is less than 10 µm across. The power of the pump is in the microwatt range, and the laser can produce continuous-wave radiation. As in any laser, the optical oscillation is caused by a combination

of optical amplification and cavity feedback. In most lasers, optical amplification is due to stimulated emission involving the electronic energy levels of the material filling the cavity. If the filling material is crystalline silicon, this approach is not suitable owing to the indirect energy-band structure of the electrons in the crystal lattice. This means that the material's interacting electron wavefunctions have a different momentum, in turn making the emission and amplification of light highly inefficient.

However, the optical amplification in the silicon laser of Takahashi and colleagues results from a different process. The covalently bound atoms in a silicon crystal form a mass-spring system, which behaves like a harmonic oscillator. This system has a natural mechanical (resonance) frequency of about 15.6 terahertz. At room temperature, the thermal energy in the crystal lattice is bundled at this frequency. When a laser pump beam with frequency ν hits the shaking silicon atoms, a small fraction of the beam is scattered in two new frequencies, $\nu \pm 15.6$ THz, an effect called spontaneous Raman scattering that is reminiscent of the Doppler effect.

In their study, Takahashi *et al.* used a beam of frequency 210 THz, which corresponds to a wavelength of 1,428 nanometres. The $\nu - 15.6$ -THz frequency — equivalent to a wavelength of 1,543 nm, which is an important wavelength in optical-fibre communications — is dominant over the upper frequency for quantum-mechanical reasons, and is called the Raman-Stokes frequency. The coexistence of the pump frequency and the Stokes frequency leads to the electric-field intensity of the combined light beam beating at 15.6 THz. The beating in turn exerts a time-periodic force on the silicon atoms and drives them into a more intense vibration, leading to more efficient scattering of the pump beam into the Stokes beam. This two-way mechanism implies optical amplification of the Stokes beam, fed by the pump beam, and is known as stimulated Raman scattering. Hence, this type of laser is called a Raman laser (Fig. 1).

The authors are not the first to report a Raman silicon laser. In 2004, researchers demonstrated² a Raman silicon laser that produces pulsed radiation, and, shortly after, Intel reported a continuous-wave version of this laser³. In spite of the excitement associated with these first silicon lasers, their practical relevance remained limited. The devices were large (centimetre-scale) for an on-chip laser, and the required pump power was high (several tens of milliwatts).

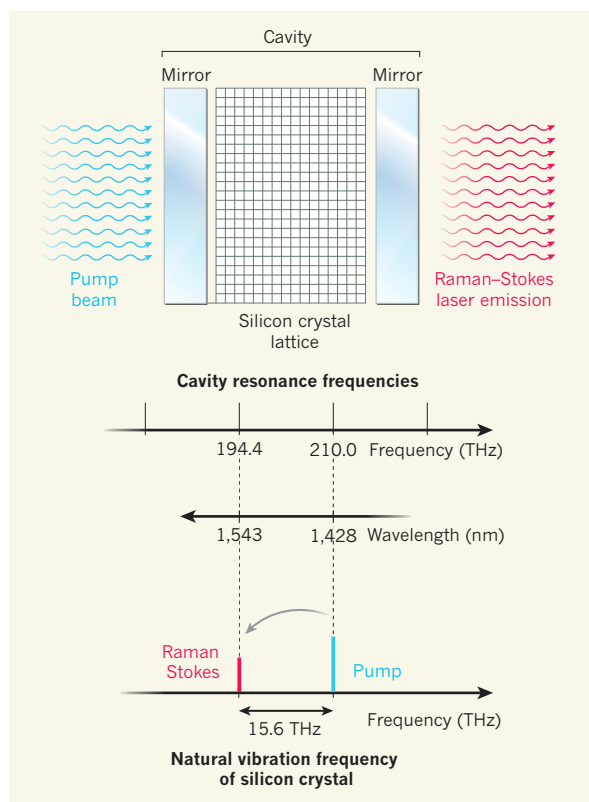


Figure 1 | Raman laser. The basic elements of Takahashi and colleagues' ultra-small silicon Raman laser¹ are shown schematically (top panel). An optical microcavity, here simplified to a simple cavity with two mirrors, rather than the photonic-crystal cavity used by the authors, encloses crystalline silicon. The device is pumped by an external laser beam with a frequency that coincides with one of the cavity's resonance frequencies (bottom panel). The pump light excites the silicon crystal into its natural vibration frequency of 15.6 THz. This causes the pump photons to be scattered to a lower optical frequency, called the Raman-Stokes frequency, which builds up in amplitude. If the cavity is designed such that the Raman-Stokes frequency also coincides with a cavity's resonance frequencies, a laser oscillation arises that has the Raman-Stokes frequency.

Takahashi *et al.* have now changed the ball game by using a photonic-crystal laser cavity. A photonic crystal is nothing but an arrangement of air holes (typically 100 nm in diameter), like an orderly Swiss cheese, in a material with high refractive index — silicon in this case. Each hole is an extremely strong scatterer of light. By adjusting the position and size of each hole — and doing so with nanometre precision — it is possible to engineer the overall scattering in such a way as to keep light waves imprisoned in a cavity and reduce the escape routes to an amazing minimum, at least for a discrete set of optical frequencies that can resonate in the cavity.

Photonic-crystal cavities in silicon are not new, and have been reported by many groups, not least by Takahashi and colleagues in earlier studies⁴. But the challenge for the micrometre-sized silicon Raman laser was literally double: the resonant optical frequencies of the cavity needed to coincide precisely with the frequencies of both the pump beam and of the Raman-Stokes light (Fig. 1). It took an

ingenious cavity design that accounted for the complete vectorial nature of the electromagnetic cavity fields, as well as the detailed physics of the interaction of these fields through Raman scattering, to make it all work.

Will this new laser become relevant for practical applications, unlike its much larger and power-hungry predecessors? In terms of size, power consumption and power-conversion efficiency, the answer may be yes. The main handicap of using a Raman laser as a light source for optical interconnections in electronic systems is that it is an optically pumped device. A normal semiconductor laser such as that used in telecommunications and data communication is electrically powered and electrically modulated. A Raman laser is based on the scattering of high-energy photons to lower-energy photons and therefore can only be optically powered.

To introduce optical powering into electronic systems would require major re-engineering, but it is not fundamentally impossible. The key question is whether it can be done with sufficiently low power losses and at suitably low cost. However, the modulation of the laser should in any case be driven by electrical signals, simply because the signals are produced by electronic circuitry. This can be achieved by incorporating an electrically controlled loss mechanism into the microlaser, as has already been demonstrated⁵ for centimetre-sized silicon Raman lasers. The most obvious way to do so is to build an electronic device known as a *p-n* diode

into the silicon cavity and inject charge carriers into the diode, which leads to absorption of light. Hence, the laser can be switched on and off. The next step would therefore be to make an optically pumped photonic-crystal Raman laser in silicon and to modulate it at gigabit-per-second rates, which are those needed in current data communication, by modulating the electric current through the device. ■

Roel Baets is with the Photonics Research Group in the Department of Information Technology, Ghent University-IMEC, B9000 Ghent, Belgium.
e-mail: roel.baets@intec.ugent.be

1. Takahashi, Y. *et al.* *Nature* **498**, 470–474 (2013).
2. Boyraz, O. & Jalali, B. *Opt. Express* **12**, 5269–5273 (2004).
3. Rong, H. *et al.* *Nature* **433**, 725–728 (2005).
4. Takahashi, Y. *et al.* *Opt. Express* **17**, 18093–18102 (2009).
5. Boyraz, O. & Jalali, B. *Opt. Express* **13**, 796–800 (2005).

Combinatorial temporal patterning in progenitors expands neural diversity

Omer Ali Bayraktar^{1,2} & Chris Q. Doe^{1,2,3}

Human outer subventricular zone (OSVZ) neural progenitors and *Drosophila* type II neuroblasts both generate intermediate neural progenitors (INPs) that populate the adult cerebral cortex or central complex, respectively. It is unknown whether INPs simply expand or also diversify neural cell types. Here we show that *Drosophila* INPs sequentially generate distinct neural subtypes, that INPs sequentially express Dichaete, Grainy head and Eyeless transcription factors, and that these transcription factors are required for the production of distinct neural subtypes. Moreover, parental type II neuroblasts also sequentially express transcription factors and generate different neuronal/glial progeny over time, providing a second temporal identity axis. We conclude that neuroblast and INP temporal patterning axes act together to generate increased neural diversity within the adult central complex; OSVZ progenitors may use similar mechanisms to increase neural diversity in the human brain.

Proper brain development requires the production of a vast array of neurons and glia from a relatively small pool of stem/progenitor cells. Spatial patterning mechanisms generate progenitor diversity along the anterior–posterior and dorso–ventral axes, but the temporal patterning cues used by individual progenitors to make different neural cell types over time remain poorly characterized^{1,2}. *Drosophila* neural progenitors (known as neuroblasts) are a model system to study temporal patterning. Most embryonic and larval neuroblasts undergo a ‘type I’ cell lineage to bud off a series of smaller ganglion mother cells (GMCs) that each make a pair of neurons or glia^{3–8} (Fig. 1a), and transcription factors that specify temporal identity have been characterized in both embryonic neuroblasts^{3–9} and larval neuroblasts^{10,11}.

We and others have recently discovered six ‘type II’ neuroblasts in the dorsomedial larval brain lobe (DM1–DM6) and two with more lateral positions^{12–14} (Fig. 1a). Type II neuroblasts undergo self-renewing asymmetric cell divisions to generate a series of smaller INPs; then each INP also undergoes self-renewing divisions to generate a series of ~six GMCs, which typically each produce two neurons or glia^{12–14} (Fig. 1a). Thus, both neuroblasts and INPs generate a series of progeny over time. For clarity, we state that type II neuroblasts transition from early to late over time, and INPs transition from young to old over time (Fig. 1a). Type II neuroblasts give rise to large clones of neurons and glia that populate the *Drosophila* adult brain central complex (CCX)^{15–17}. Thus, type II neuroblasts share features with human OSVZ progenitors: both progenitors generate INPs, and both are used to increase the number of neurons in a particular brain region^{18,19}. Although there are at least 60 morphologically distinct neurons in the fly adult CCX²⁰, we know virtually nothing about how parental neuroblasts or INPs generate neural diversity.

INPs sequentially express three transcription factors

We asked whether single INPs sequentially express a series of transcription factors, which would be indicative of temporal patterning. We used the previously characterized *R9D11-gal4* line driving the *UAS-GFP* construct to mark all INPs and their progeny from the DM1–DM6 neuroblast lineages¹⁵ (Fig. 1b). INPs can be identified as small Deadpan (Dpn)⁺ green fluorescent protein (GFP)⁺ cells that

are adjacent to the Dpn⁺ GFP[−] type II neuroblast (Fig. 1b); they are distinct from Dpn[−] GMCs and neurons. Importantly, the age of an INP can be determined by its distance from the parental type II neuroblast: newly born young INPs are close to the parental neuroblast, whereas older INPs are displaced further away^{13,15,21} (Fig. 1b). The ability to identify progressively older INPs allowed us to screen for transcription factors that were only present in young, middle or old INPs.

We screened a collection of 60 antibodies to neural transcription factors (Supplementary Table 1), and found three that were sequentially expressed in INPs. In late larvae at 96 h and 120 h after larval hatching (ALH), young INPs near the parental neuroblast contained the SOX-family transcription factor Dichaete (D)^{22,23}; D was not detected in old INPs further from the parental neuroblast (DM3 shown in Fig. 1c, d; similar expression was observed in other dorsomedial lineages; Supplementary Fig. 1). By contrast, the Pax6 transcription factor Eyeless (Ey)²⁴ was detected in old INPs but not young D⁺ INPs; there were very few double-negative or double-positive INPs (Fig. 1c, d). Similarly, the *R12E09-gal4* line containing a 2.7-kilobase (kb) *D* enhancer fragment²⁵ was expressed in young INPs, whereas the *OK107-gal4* enhancer trap at the *ey* locus²⁶ was expressed in old INPs (detailed expression patterns are shown in Supplementary Fig. 2; henceforth called *R12E09^D* and *OK107^{Ey}*). The D-to-Ey series was detected in all type II lineages examined and at all larval stages (DM1–DM6 at 24–120 h ALH; Fig. 1f, Supplementary Tables 2 and 3 and Supplementary Fig. 1). Thus, all INPs—from different type II neuroblasts and from early or late neuroblasts—sequentially express D and Ey (Fig. 1h, i).

In addition, we found that ‘middle-aged’ INPs contained the CP2-family DNA-binding factor Grainy head (Grh)²⁷. Grh was assigned to middle-aged INPs because its expression overlapped both D and Ey at their expression border (Fig. 1e). Thus, INPs transition through four molecular states (Fig. 1h, g); it is likely that several GMCs are born during each of these windows, but for simplicity only one GMC per window is shown in our summaries. The D-to-Grh-to-Ey series was observed in INPs born from multiple type II neuroblasts (DM2–DM6; DM1 does not have detectable Grh) and in INPs born at all larval stages (Fig. 1g, Supplementary Tables 4 and 5 and Supplementary Fig. 1).

¹Howard Hughes Medical Institute, University of Oregon, Eugene, Oregon 97403, USA. ²Institute of Molecular Biology, University of Oregon, Eugene, Oregon 97403, USA. ³Institute of Neuroscience, University of Oregon, Eugene, Oregon 97403, USA.

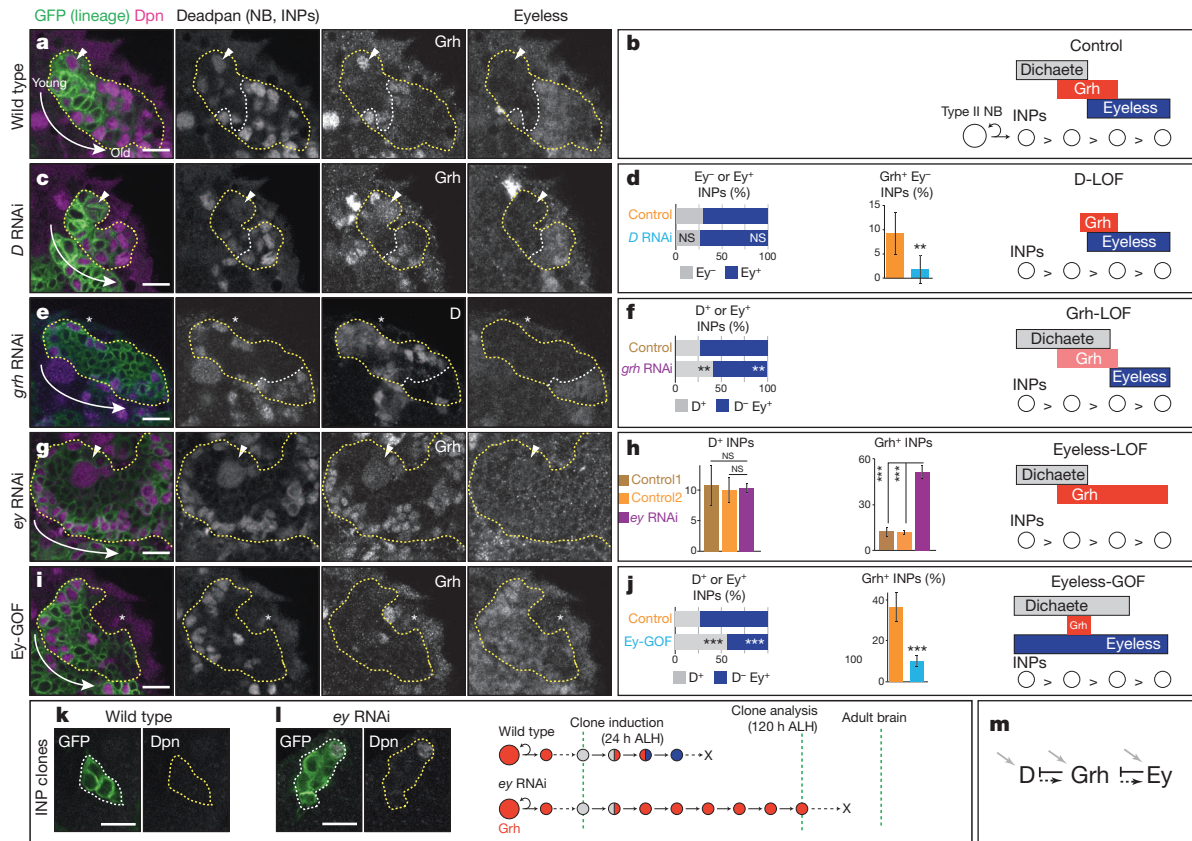


Figure 2 | Cross-regulation between INP temporal transcription factors. **a, c, e, g, i,** INP temporal transcription factor expression in DM2 lineage at 120 h ALH. INPs were marked with GFP (yellow outline) driven by: *wor-gal4 ase-gal80* (**a, c**), *R9D11-gal4* (**e, i**), or *R12E09^D-gal4* (**g**). See Methods for full genotypes. White line denotes the Ey border. Parental type II neuroblasts are marked by an arrowhead, or an asterisk when out of focal plane. **a, b,** Wild-type expression of Grh and Ey in INPs. **c, d,** *D* RNAi delays Grh expression in INPs, such that no Grh⁺ Ey⁻ INPs are observed. For Ey, see Supplementary Fig. 4a, b. Quantification of Ey⁺ and Grh⁺ Ey⁻ INP number is in **d** ($n = 6$). LOF,

loss-of-function. **e, i**, *grh* RNAi extends D expression and delays Ey expression in INPs ($n \geq 5$). **g, h**, *ey* RNAi extends Grh expression in INPs ($n \geq 4$). GOF, gain-of-function. **i, j**, Ey misexpression reduces Grh expression in INPs ($n \geq 5$). **k, l**, *ey* RNAi extends the INP cell lineage. **k**, Wild-type MARCM clones induced early in single INPs never contain an INP at the end of larval life. **l**, *ey* RNAi MARCM clones maintain a single INP at the end of larval life ($n \geq 10$ clones). **m**, Summary. Black arrows, positive regulation; black T-bars, negative regulation; grey arrows, external positive regulation. Scale bars, 10 μ m. All data represent mean \pm s.d. NS, not significant. ** $P < 0.01$; *** $P < 0.001$.

INP markers (Dpn⁺ Ase⁺ nuclear Pros⁻) and retained the ability to generate nuclear Pros⁺ Elav⁺ neurons (Supplementary Fig. 8). We conclude that *ey* RNAi extends individual INP cell lineages beyond that of wild-type INPs.

INPs generate different neurons and glia over time

Next, we asked next whether distinct neuronal or glial subtypes were generated during each transcription factor expression window. To determine the cell types produced by young D^+ INPs or old Ey^+ INPs, we used permanent lineage tracing (see Fig. 3a). Cells labelled by $R12E09^D$ but not $OK107^{ey}$ are generated by young INPs, whereas cells labelled by $OK107^{ey}$ are generated by old INPs (Fig. 3b, e and Supplementary Fig. 3). We screened our collection of 60 transcription factor antibodies and found two that labelled subsets of young INP progeny, and two that labelled subsets of old INP progeny. The transcription factors D and Brain-specific homeobox (Bsh)³¹ labelled sparse, non-overlapping subsets of young INP progeny (Fig. 3c, d), but not old INP progeny (Fig. 3f, g, j and Supplementary Fig. 9). Thus, young INPs generate Bsh⁺ neurons, D⁺ neurons, and many neurons that express neither gene. By contrast, the glial transcription factor Reverse polarity (Repo)^{16,32,33} and the neuronal transcription factor Twin of eyeless (Toy)³⁴ labelled sparse, non-overlapping subsets of old INP progeny, but not young INP progeny (Fig. 3h–j and Supplementary Fig. 9). Additional mechanisms must restrict each marker (D, Bsh, Repo and Toy) to small subsets of young or old INP progeny; for example, each population could arise from just early or late born INPs

within a type II neuroblast lineage (see below). We conclude that INPs sequentially express the D, Grh and Ey transcription factors, and they generate distinct neuronal and glial cell types during successive transcription factor expression windows (Fig. 3k). To our knowledge, these data provide the first evidence in any organism that INPs undergo temporal patterning.

INP factors specify temporally distinct neural subtypes

We wanted to determine whether D, Grh and Ey act as temporal identity factors that specify the identity of INP progeny born during their window of expression. First, we investigate the role of Ey in the specification of late born INP progeny. INP-specific *ey* RNAi resulted in the complete loss of the late born Toy^+ neurons and Repo^+ neuropil glia, but did not alter the number of early born D^+ and Bsh^+ neurons (Fig. 4a–i). Removal of Toy^+ neurons (using *toy* RNAi) does not alter the number of Repo^+ glia, and conversely removal of Repo^+ glia (using *gcm* RNAi) does not alter the number of Toy^+ neurons (Supplementary Fig. 10); thus Ey is independently required for the formation of both classes of late INP progeny. Conversely, permanent misexpression of Ey in early INPs increased late born Toy^+ neurons and decreased early born Bsh^+ neurons (Fig. 4j–n), consistent with Ey specifying late INP temporal identity. Unexpectedly, ectopic Ey reduced the number of late born Repo^+ glia (Fig. 4n and Supplementary Fig. 11). We conclude that Ey is an INP temporal identity factor that promotes the independent specification of late born Toy^+ neurons and Repo^+ glia (Fig. 4o).

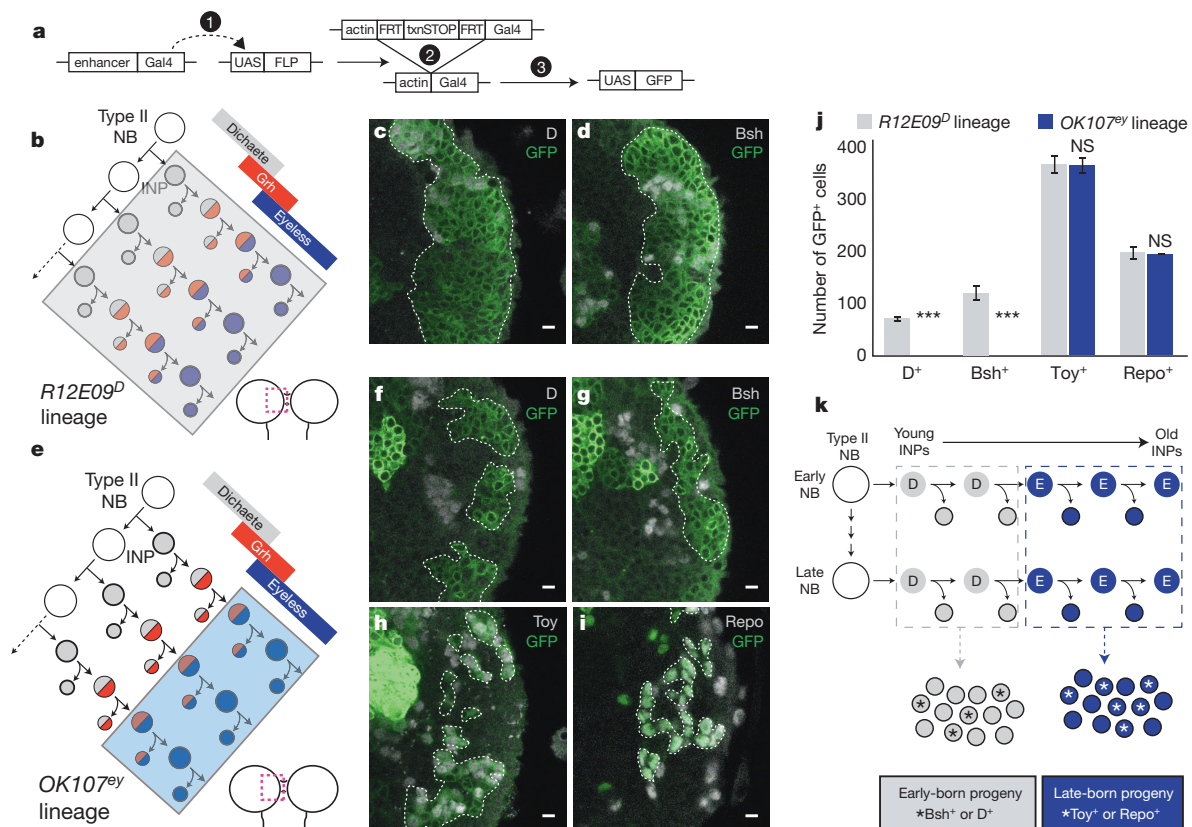


Figure 3 | INPs sequentially generate distinct temporal identities.

a, Genetics of permanent lineage tracing. **b–d**, Permanent lineage tracing of all INP progeny using *R12E09D-gal4*. Summary of GFP expression (**b**) and expression of D and Bsh in the GFP⁺ INP progeny (**c**, **d**). Dashed line surrounds GFP⁺ cells. **e–i**, Permanent lineage tracing of old INP progeny using the late INP *OK107^{ey}-gal4* line. Summary of GFP expression (**e**); D⁺ and

We next tested whether D and Grh specify early and mid INP temporal identity. INP-specific *D* RNAi led to a small but significant reduction in the number of early born Bsh⁺ neurons (Supplementary Fig. 11), whereas INP-specific *grh* RNAi severely reduced the number of early born Bsh⁺ neurons (Supplementary Fig. 11) without impairing INP proliferation (Supplementary Fig. 5) or late INP progeny (Supplementary Fig. 11). This is consistent with the Bsh⁺ neurons deriving from the D⁺ Grh⁺ expression window. Interestingly, misexpression of D or Grh did not increase Bsh⁺ neuron numbers (Supplementary Fig. 11); perhaps D/Grh co-misexpression is required to generate Bsh⁺ neurons. We conclude that both D and Grh are required, but not sufficient, for the production of Bsh⁺ early INP progeny.

Late born INP progeny are required for CCX morphology

The function of early or late born INP progeny in adult brain development is unknown. Here we determine the role of late born INP neurons and glia in the development and function of the adult central complex (CCX), an evolutionarily conserved insect brain structure containing many type II neuroblast progeny^{15–17}. The CCX consists of four interconnected compartments at the protocerebrum midline: the ellipsoid body, the fan-shaped body, the bilaterally paired noduli, and the protocerebral bridge; each of these compartments is formed by a highly diverse set of neurons^{20,35}. First, we used permanent lineage tracing (*OK107^{ey} >> act-gal4 UAS-cd8:GFP*) to map the contribution of late born Ey⁺ INP progeny to the adult CCX. We detected cell bodies in the dorsoposterior region of the CCX (data not shown), and their axonal projections extensively innervated the entire ellipsoid body, fan-shaped body, and protocerebral bridge, with much weaker labelling of the paired noduli (Fig. 5a–d). We conclude that old INPs contribute neurons

Bsh⁺ neurons are excluded from late INP progeny (**f**, **g**), whereas Toy⁺ neurons and Repo⁺ glia are among the late born INP progeny (**h**, **i**); dashed line surrounds GFP⁺ cells. **j**, **k**, Quantification (**j**) and summary (**k**). GFP⁺ INP progeny in DM1–6 lineages were counted; *n* ≥ 3 brain lobes for each marker. Region of dorsomedial brain imaged at 120 h ALH (boxed in cartoon). Scale bars, 5 μm. All data represent mean ± s.d. ****P* < 0.001.

primarily to the ellipsoid body, fan-shaped body and protocerebral bridge regions of the CCX. Second, we used INP-specific *ey* RNAi to delete the late born Toy⁺ neurons and Repo⁺ glia (see Fig. 4). Loss of late born INP progeny generated major neuroanatomical defects throughout the adult CCX: the ellipsoid body and paired noduli were no longer discernible, the fan-shaped body was enlarged, and the protocerebral bridge was fragmented (Fig. 5f–l; quantified in 5o; summarized in 5p). Subsets of this phenotype were observed after removal of Toy⁺ neurons or Repo⁺ glia (Fig. 5m–o and Supplementary Fig. 12), showing that they contribute to distinct aspects of the CCX. Previous studies have described similar or weaker morphological CCX defects in *ey* hypomorphs³⁶, *toy* mutants³⁴, and after broad glia ablation during larval stages³⁷. In addition, we found that *ey* RNAi adults have relatively normal locomotion, but have a significant deficit in negative geotaxis (Fig. 5q and Supplementary Video 1). We conclude that Ey is a temporal identity factor that specifies late born neuron and glial identity, and that these late born neural cell types are essential for assembly of the adult central complex.

Combinatorial temporal patterning increases diversity

We have found that Bsh⁺ neurons and Repo⁺ glia are sparse within the total population of young and old INP progeny, respectively, indicating that other mechanisms must help to restrict the formation of these neural subtypes. One mechanism could be temporal patterning within type II neuroblast lineages.

To determine whether type II neuroblasts change their transcriptional profiles over time, we assayed known temporal transcription factors^{3,5,10,11,38} for expression in type II neuroblasts at five time points in their lineage (24, 48, 72, 96 and 120 h ALH). We observed no type II

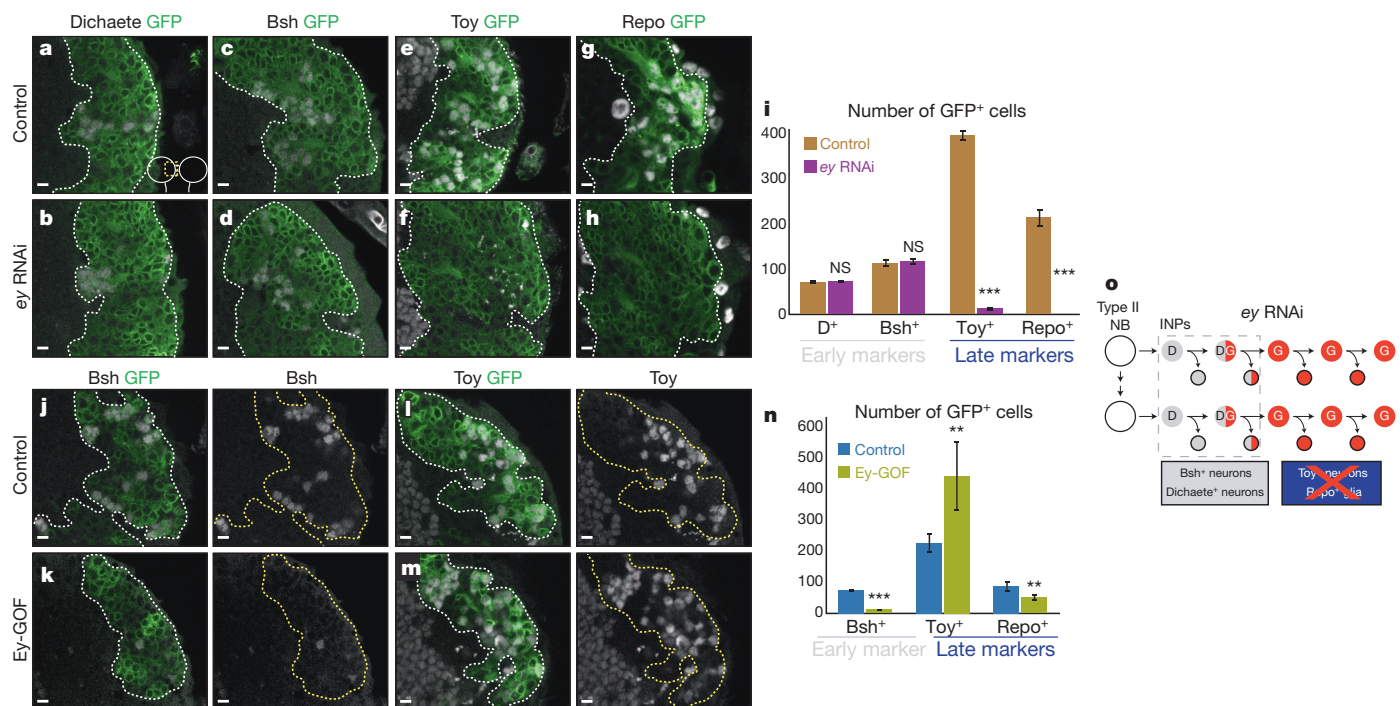


Figure 4 | Eyeless is a temporal identity factor for late born INP progeny. a–i, *ey* RNAi in INP lineages does not affect early born INP progeny (a–d), but eliminates late born *Toy*⁺ neurons (e, f) and *Repo*⁺ neuropil glia (g, h). Quantification ($n \geq 4$ brain lobes) in i. j–n, *Ey* misexpression in INP lineages leads to loss of early born *Bsh*⁺ neurons (j, k), and increases the

number of late born *Toy*⁺ neurons (l, m). Quantification ($n \geq 5$) in n. o, Summary. Region of dorsomedial brain imaged at 120 h ALH (boxed in cartoon). G denotes Grh. Scale bars, 5 μ m. All data represent mean \pm s.d. ** $P < 0.01$; *** $P < 0.001$.

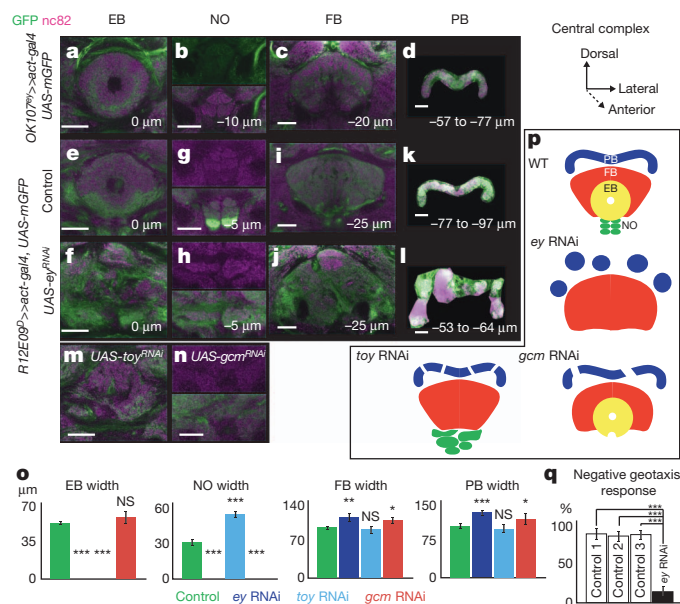


Figure 5 | Eyeless is required for adult brain central complex morphology and behaviour. a–d, Permanent lineage tracing of old INPs and their progeny (*OK107^{ey} >> act-gal4*) extensively labels the adult central complex. EB, ellipsoid body; FB, fan-shaped body; NO, noduli; PB, protocerebral bridge. e–n, *ey* RNAi (f–l), *toy* RNAi (m), or *gcm* RNAi (n) in INP lineages produce distinct defects in CCX morphology. Adult brains, frontal view. The z-coordinates of single confocal sections are shown relative to ellipsoid body position. The protocerebral bridge was cropped out of the brain and displayed as a projection of indicated z-coordinates in d, k and l. Scale bars, 20 μ m. o, Quantification of the width of CCX compartments ($n \geq 5$). p, Summary of CCX morphology after loss of late born INP progeny. q, *ey* RNAi flies have deficits in negative geotaxis. See Methods for controls. All data represent mean \pm s.d. * $P < 0.05$; ** $P < 0.01$; *** $P < 0.001$.

neuroblast expression for Hunchback, Kruppel, Pdm1/2 and Broad, and Grh was expressed in all type II neuroblasts at all time points. However, we identified three transcription factors with temporal expression in type II neuroblasts. D and Castor (Cas) were specifically detected in early type II neuroblasts: 3–4 neuroblasts at 24 h ALH, 0–1 neuroblast at 48 h ALH, and none later (Fig. 6a, b). Although we never detected D simultaneously in all type II neuroblasts at 24 h, permanent lineage tracing with *R12E09^D* labels all type II neuroblasts (Supplementary Fig. 3), indicating that all transiently express D. The third transcription factor, Seven up (Svp), showed a pulse of expression in a subset of type II neuroblasts at 48 h ALH, but was typically absent from younger or older type II neuroblasts (Fig. 6a, b). D, Cas and Svp are all detected in the anterior-most type II neuroblasts (probably corresponding to DM1–DM3), and thus at least these type II neuroblasts must sequentially express D or Cas, and Svp. We conclude that type II neuroblasts can change gene expression over time.

Next, we wanted to determine whether type II neuroblasts produce different INPs over time. We generated permanently labelled clones within the type II neuroblast lineages at progressively later time points (see Methods and Fig. 6c, d). If type II neuroblasts change over time to make different INPs, early and late neuroblast clones should contain different neural subtypes. We assayed clones for *Repo*⁺ glia and *Bsh*⁺ neurons, choosing these markers because *Repo*⁺ neuropil glia have been proposed to be born early in type II neuroblast lineages¹⁷ and *Bsh*⁺ neurons were positioned far from the *Repo*⁺ glia consistent with a different birth-order. *Bsh*⁺ neuron numbers began to decline only in clones induced at the latest time point (Fig. 6e, g, i), showing that they are generated late in the type II neuroblast lineage (Fig. 6j, grey). By contrast, *Repo*⁺ glia were detected in clones induced early but not late (Fig. 6f, h, i), proving that they are specifically generated by early type II neuroblasts (Fig. 6j, blue). This allows us to assign *Repo*⁺ glia to an ‘early neuroblast, old INP’ portion of the lineage, and *Bsh*⁺ neurons to a ‘late neuroblast, young INP’ portion of the lineage (Fig. 6j). We conclude that type II neuroblasts undergo temporal patterning, and

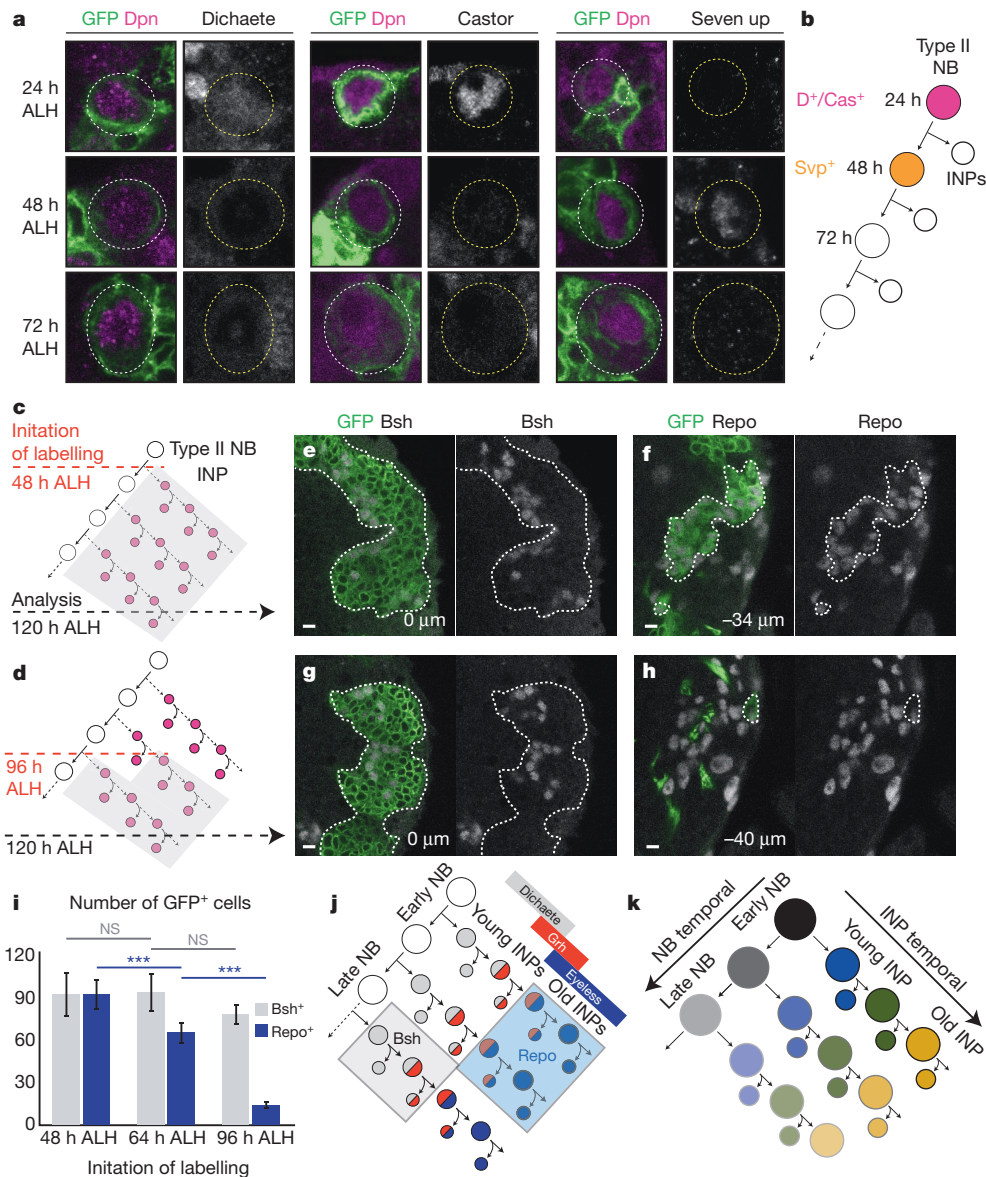


Figure 6 | INP temporal patterning acts combinatorially with neuroblast temporal patterning to increase neural diversity. **a, b**, Expression of D, Castor (Cas), and Seven up (Svp) in the anterior-most type II neuroblasts. Type II neuroblasts are identified with *pointed-gal4* UAS-GFP (GFP; green) and Dpn (magenta). **c, d**, Schematics of INP permanent lineage tracing with *R12E09D-gal4* induced at early (**c**) or late (**d**) larval stages; all time points analysed at 120 h ALH. Grey shading, labelled INP and progeny. **e, f**, Bsh⁺ neurons and Repo⁺ glia are both marked by permanent labelling early in type

II neuroblast lineages. Focal planes: Bsh, near neuroblast; Repo, further from the neuroblast (−34 μm). **g, h**, Bsh⁺ neurons, but not Repo⁺ glia, are marked by permanent labelling late in type II neuroblast lineages. Focal planes: Bsh, near neuroblast; Repo, further from the neuroblast (−40 μm). Scale bars, 5 μm. **i**, Quantification. *n* = 5 for each time point. All data represent mean ± s.d. NS, not significant. ****P* < 0.001. **j**, Distinct neural progeny are born from early versus late type II neuroblast lineages. **k**, Neuroblast and INP temporal patterning act together to generate neural diversity.

propose that neuroblast temporal patterning acts together with INP temporal patterning to increase neural diversity in the adult brain (Fig. 6k).

Discussion

We have shown that INPs sequentially express three transcription factors (D, Grh and then Ey), and that different neural subtypes are generated from successive transcription factor windows. It is likely that multiple GMCs are born from each of the four known INP gene expression windows; GMCs born from a particular gene expression window may have the same identity, or may be further distinguished by ‘subtemporal genes’ as in embryonic type I neuroblast lineages⁹. We also show that each temporal factor is required for the production of a distinct temporal neural subtype. Loss of D or Grh leads to the loss of Bsh⁺ neurons; loss of Ey leads to loss of Toy⁺ neurons and Repo⁺

glia, although the fate of the missing cells is unknown. An unexpected finding was that Ey limits the lifespan of INPs. Mechanisms that prevent INP de-differentiation have been characterized—loss of the translational repressor Brain tumour (Brat) or the transcription factor Earmuff (Erm) causes INPs to de-differentiate into tumorigenic type II neuroblasts^{14,21}—but factors that terminate normal INP proliferation have never before been identified.

The D-to-Grh-to-Ey INP temporal identity factors are all used in other contexts during *Drosophila* development. Many embryonic neuroblasts sequentially express D and Grh³. Ey is expressed in mushroom body neuroblasts³⁹, and is required for development of the adult brain mushroom body⁴⁰. Interestingly, mammalian orthologues of D and Ey (SOX2 and PAX6, respectively) are expressed in neural progenitors⁴¹, including OSVZ progenitors¹⁹, but have not been tested for a role in temporal patterning.

We have shown that there are two axes of temporal patterning within type II neuroblast lineages: both neuroblasts and INPs change over time to make different neurons and glia, thereby expanding neural diversity. It will be important to investigate whether INPs generated by OSVZ neural stem cells undergo similar temporal patterning (perhaps using SOX2 and PAX6), and whether combinatorial temporal patterning contributes to the neuronal complexity of the human neocortex.

METHODS SUMMARY

Larvae were staged to 120 h ALH based on age and morphology unless otherwise indicated; adult females were 3–5 days old. Immunohistochemistry was performed essentially as described¹⁵ and imaged using Zeiss700/710 microscopes. INPs and GMC/neuronal progeny were distinguished by Dpn staining. *R12E09^D* >> *act-gal4* and the ubiquitously expressed temperature-sensitive Gal80 were used for inducible lineage tracing. Standard methods were used to assess geotaxis behaviour⁴². Data represent mean \pm s.d. Two-tailed Student's *t*-tests were used. **P* < 0.05; ***P* < 0.01; ****P* < 0.001.

Full Methods and any associated references are available in the online version of the paper.

Received 19 October 2012; accepted 1 May 2013.

Published online 19 June; corrected online 26 June 2013 (see full-text HTML version for details).

1. Tanabe, Y. & Jessell, T. M. Diversity and pattern in the developing spinal cord. *Science* **274**, 1115–1123 (1996).
2. Krumlauf, R. *et al.* Hox homeobox genes and regionalisation of the nervous system. *J. Neurobiol.* **24**, 1328–1340 (1993).
3. Maurange, C., Cheng, L. & Gould, A. P. Temporal transcription factors and their targets schedule the end of neural proliferation in *Drosophila*. *Cell* **133**, 891–902 (2008).
4. Brody, T. & Odenwald, W. F. Programmed transformations in neuroblast gene expression during *Drosophila* CNS lineage development. *Dev. Biol.* **226**, 34–44 (2000).
5. Isshiki, T., Pearson, B., Holbrook, S. & Doe, C. Q. *Drosophila* neuroblasts sequentially express transcription factors which specify the temporal identity of their neuronal progeny. *Cell* **106**, 511–521 (2001).
6. Tran, K. D. & Doe, C. Q. Pdm and Castor close successive temporal identity windows in the NB3–1 lineage. *Development* **135**, 3491–3499 (2008).
7. Grosskortenhaus, R., Robinson, K. J. & Doe, C. Q. Pdm and Castor specify late-born motor neuron identity in the NB7–1 lineage. *Genes Dev.* **20**, 2618–2627 (2006).
8. Grosskortenhaus, R., Pearson, B. J., Marusich, A. & Doe, C. Q. Regulation of temporal identity transitions in *Drosophila* neuroblasts. *Dev. Cell* **8**, 193–202 (2005).
9. Baumgardt, M., Karlsson, D., Terriente, J., Diaz-Benjumea, F. J. & Thor, S. Neuronal subtype specification within a lineage by opposing temporal feed-forward loops. *Cell* **139**, 969–982 (2009).
10. Zhu, S. *et al.* Gradients of the *Drosophila* Chinmo BTB-zinc finger protein govern neuronal temporal identity. *Cell* **127**, 409–422 (2006).
11. Kao, C. F., Yu, H. H., He, Y., Kao, J. C. & Lee, T. Hierarchical deployment of factors regulating temporal fate in a diverse neuronal lineage of the *Drosophila* central brain. *Neuron* **73**, 677–684 (2012).
12. Bello, B. C., Izergina, N., Caussinus, E. & Reichert, H. Amplification of neural stem cell proliferation by intermediate progenitor cells in *Drosophila* brain development. *Neural Dev.* **3**, 5 (2008).
13. Boone, J. Q. & Doe, C. Q. Identification of *Drosophila* type II neuroblast lineages containing transit amplifying ganglion mother cells. *Dev. Neurobiol.* **68**, 1185–1195 (2008).
14. Bowman, S. K. *et al.* The tumor suppressors Brat and Numb regulate transit-amplifying neuroblast lineages in *Drosophila*. *Dev. Cell* **14**, 535–546 (2008).
15. Bayraktar, O. A., Boone, J. Q., Drummond, M. L. & Doe, C. Q. *Drosophila* type II neuroblast lineages keep Prospero levels low to generate large clones that contribute to the adult brain central complex. *Neural Dev.* **5**, 26 (2010).
16. Viktorin, G., Riebli, N., Popkova, A., Giangrande, A. & Reichert, H. Multipotent neural stem cells generate glial cells of the central complex through transit amplifying intermediate progenitors in *Drosophila* brain development. *Dev. Biol.* **356**, 553–565 (2011).
17. Izergina, N., Balmer, J., Bello, B. & Reichert, H. Postembryonic development of transit amplifying neuroblast lineages in the *Drosophila* brain. *Neural Dev.* **4**, 44 (2009).
18. Fietz, S. A. *et al.* OSVZ progenitors of human and ferret neocortex are epithelial-like and expand by integrin signaling. *Nature Neurosci.* **13**, 690–699 (2010).
19. Hansen, D. V., Lui, J. H., Parker, P. R. & Kriegstein, A. R. Neurogenic radial glia in the outer subventricular zone of human neocortex. *Nature* **464**, 554–561 (2010).
20. Young, J. M. & Armstrong, J. D. Structure of the adult central complex in *Drosophila*: organization of distinct neuronal subsets. *J. Comp. Neurol.* **518**, 1500–1524 (2010).
21. Weng, M., Golden, K. L. & Lee, C. Y. dFezf/Earmuff maintains the restricted developmental potential of intermediate neural progenitors in *Drosophila*. *Dev. Cell* **18**, 126–135 (2010).
22. Russell, S. R., Sanchez-Soriano, N., Wright, C. R. & Ashburner, M. The *Dichaete* gene of *Drosophila melanogaster* encodes a SOX-domain protein required for embryonic segmentation. *Development* **122**, 3669–3676 (1996).
23. Nambu, P. A. & Nambu, J. R. The *Drosophila* fish-hook gene encodes a HMG domain protein essential for segmentation and CNS development. *Development* **122**, 3467–3475 (1996).
24. Halder, G., Callaerts, P. & Gehring, W. J. Induction of ectopic eyes by targeted expression of the *eyeless* gene in *Drosophila*. *Science* **267**, 1788–1792 (1995).
25. Pfeiffer, B. D. *et al.* Tools for neuroanatomy and neurogenetics in *Drosophila*. *Proc. Natl Acad. Sci. USA* **105**, 9715–9720 (2008).
26. Connolly, J. B. *et al.* Associative learning disrupted by impaired G_s signaling in *Drosophila* mushroom bodies. *Science* **274**, 2104–2107 (1996).
27. Uy, A. E., Thompson, C. R. & Bray, S. J. The *Drosophila* tissue-specific factor Grainyhead contains novel DNA-binding and dimerization domains which are conserved in the human protein CP2. *Mol. Cell. Biol.* **14**, 4020–4031 (1994).
28. Almeida, M. S. & Bray, S. J. Regulation of post-embryonic neuroblasts by *Drosophila* Grainyhead. *Mech. Dev.* **122**, 1282–1293 (2005).
29. Neumüller, R. A. *et al.* Genome-wide analysis of self-renewal in *Drosophila* neural stem cells by transgenic RNAi. *Cell Stem Cell* **8**, 580–593 (2011).
30. Lee, T. & Luo, L. Mosaic analysis with a repressible cell marker for studies of gene function in neuronal morphogenesis. *Neuron* **22**, 451–461 (1999).
31. Jones, B. & McGinnis, W. A new *Drosophila* homeobox gene, *bsh*, is expressed in a subset of brain cells during embryogenesis. *Development* **117**, 793–806 (1993).
32. Campbell, G. *et al.* RK2, a glial-specific homeodomain protein required for embryonic nerve cord condensation and viability in *Drosophila*. *Development* **120**, 2957–2966 (1994).
33. Xiong, W. C., Okano, H., Patel, N. H., Blendy, J. A. & Montell, C. *repo* encodes a glial-specific homeo domain protein required in the *Drosophila* nervous system. *Genes Dev.* **8**, 981–994 (1994).
34. Furukubo-Tokunaga, K., Adachi, Y., Kuru, M. & Walldorf, U. Brain patterning defects caused by mutations of the *twin of eyeless* gene in *Drosophila melanogaster*. *Fly (Austin)* **3**, 263–269 (2009).
35. Hanesch, U., Fischbach, K. F. & Heisenberg, M. Neuronal architecture of the central complex in *Drosophila melanogaster*. *Cell Tissue Res.* **257**, 343–366 (1989).
36. Callaerts, P. *et al.* *Drosophila* Pax-6/eyeless is essential for normal adult brain structure and function. *J. Neurobiol.* **46**, 73–88 (2001).
37. Spindler, S. R., Ortiz, I., Fung, S., Takashima, S. & Hartenstein, V. *Drosophila* cortex and neuropile glia influence secondary axon tract growth, pathfinding, and fasciculation in the developing larval brain. *Dev. Biol.* **334**, 355–368 (2009).
38. Chai, P. C., Liu, Z., Chia, W. & Cai, Y. Hedgehog signaling acts with the temporal cascade to promote neuroblast cell cycle exit. *PLoS Biol.* **11**, e1001494 (2013).
39. Noveen, A., Daniel, A. & Hartenstein, V. Early development of the *Drosophila* mushroom body: the roles of *eyeless* and *dachshund*. *Development* **127**, 3475–3488 (2000).
40. Kuru, M. *et al.* Genetic control of development of the mushroom bodies, the associative learning centers in the *Drosophila* brain, by the *eyeless*, *twin of eyeless*, and *Dachshund* genes. *Proc. Natl Acad. Sci. USA* **97**, 2140–2144 (2000).
41. Doe, C. Q. Neural stem cells: Balancing self-renewal with differentiation. *Development* **135**, 1575–1587 (2008).
42. Ali, Y. O., Escala, W., Ruan, K. & Zhai, R. G. Assaying locomotor, learning, and memory deficits in *Drosophila* models of neurodegeneration. *J. Vis. Exp.* **49**, e2504 (2011).

Supplementary Information is available in the online version of the paper.

Acknowledgements We thank L. Manning and K. Hirono for larval brain stains and imaging; S.-L. Lai, J. Eisen, T. Herman and B. Bowerman for comments on the manuscript; T. Carney and M. Miller for discussions; and the fly community for reagents. This work was supported by National Institutes of Health (NIH) grants T32HD216345 and T32GM007413 (to O.A.B.), NIH R01HD27056 (to C.Q.D.) and the Howard Hughes Medical Institute (to C.Q.D.).

Author Contributions O.A.B. performed the experiments; O.A.B. and C.Q.D. conceived of the project and wrote the manuscript.

Author Information Reprints and permissions information is available at www.nature.com/reprints. The authors declare no competing financial interests. Readers are welcome to comment on the online version of the paper. Correspondence and requests for materials should be addressed to C.Q.D. (cdoe@uoregon.edu).

METHODS

Fly stocks. The chromosomes and insertion sites of transgenes (if known) are shown next to genotypes. Unless indicated, lines were obtained from Bloomington stock centre (FlyBase IDs shown).

Enhancer Gal4 lines and reporters: *R9D11-gal4* (III, *attP2*) (ref. 25). *R9D11-gal4* (II, *attP40*) (ref. 43). *R12E09^D-gal4* (III, *attP2*) (ref. 25). *OK107⁹-gal4* (IV) (ref. 26). *R9D11-CD4-tdTom* (III, *attP2*) (ref. 44). *10XUAS-IVS-mCD8::GFP* (III, *su(Hw)attP2*) (ref. 9) (referred to as UAS-GFP). *Pointed-gal4¹⁴⁻⁹⁴* (III) (ref. 45).

Mutant stocks: *D⁸⁷,FRT2A/Tm3,Sb* (ref. 23). *grh³⁷⁰/CyO,actGFP* (ref. 46).

Transgenic RNAi: *UAS-D^{RNAi}* (II; VDRC, 107194). Lines from the TRiP collection (III, *attP2*): *UAS-grh^{RNAi}* (FBst0028820). *UAS-ey^{RNAi}* (FBst0032486). *UAS-toy^{RNAi}* (FBst0029346). *UAS-gcm^{RNAi}* (FBst0031518). TRiP RNAi controls: *y v*; *attP2* and *y sc v*; *UAS-mCherry^{RNAi}*. Other controls: *y w*, *w¹¹⁸*, or *UAS-His2A::mRFP*.

Lineage tracing transgenes: *UAS-FLP* (I; FBst0008208 and III; FBst0008209). *actin-FRT-stop-FRT-gal4* (I; FBst0004779 and III; FBst0004780). *tub-gal80^{ts}* (II; FBst0007108).

Other: *UAS-D* (II) (FBst0008861). *UAS-grh* (II) (ref. 9). *UAS-ey* (II) (FBst0006294).

Recombinant chromosomes generated in this study: *R9D11-gal4*, *UAS-GFP* (III). *R12E09^D-gal4*, *UAS-GFP* (III). *UAS-FLP*, *actin-FRT-stop-FRT-gal4* (both I and III).

Fly genetics. Permanent lineage tracing, which involves the flippase (FLP)-mediated removal of a transcriptional stop cassette between the constitutive *actin* promoter and the *gal4* open reading frame, is summarized in Fig. 3a. For lineage tracing of young or old INP progeny (Figs 3 and 5), the *R12E09^D* or *OK107⁹* Gal4 lines were either crossed to *UAS-FLP*, *actin-FRT-stop-FRT-gal4*; *UAS-GFP* (I;III) for labelling with membrane localized GFP or to *UAS-FLP*, *ubi-FRT-stop-FRT-nGFP* (II) for labelling with nuclear GFP (G-TRACE)⁴⁷.

For driving expression of UAS-RNAi or misexpression transgenes, the following lines were used: *UAS-dcr2*; *wor-gal4*, *ase-gal80*; *UAS-mCD8::GFP* (ref. 29). *R9D11-gal4*; *R9D11-gal4*, *UAS-GFP* (II, III). *R12E09^D >> act-gal4* [*UAS-FLP*, *actin-FRT-stop-FRT-gal4*; *R12E09^D-gal4*, *UAS-GFP/Tm6B* (I;III)]. *R9D11 >> act-gal4* [*UAS-FLP*, *actin-FRT-stop-FRT-gal4*; *R9D11-gal4*, *UAS-GFP* (I;III)]. Below are the genotypes used in RNAi and misexpression experiments

D RNAi was driven by *wor-gal4 ase-gal80 UAS-dcr2* in *D⁸⁷/+*; control was *w¹¹¹⁸*. *grh* RNAi was driven by *R9D11-gal4*, *R9D11-gal4* in *grh³⁷⁰/+*; control was *attP2* (empty transgene docking site). *ey* RNAi was driven by *R12E09^D >> act-gal4*; controls were (1) *attP2* and (2) *UAS-mCherry^{RNAi}*. *Ey-GOF* was driven by *R9D11-gal4 >> act-gal4*; control was *yw* or *UAS-His2A::mRFP* (for quantification of INP progeny). *toy* and *gcm* RNAi were driven by *R12E09^D >> act-gal4*.

For inducible lineage tracing (Fig. 6), *R12E09^D >> act-gal4* was combined with the ubiquitously expressed *tub-gal80^{ts}* so that temperature shifts were used to turn on labelling by *R12E09^D* at different points in the type II neuroblast lineages. *R12E09^D-gal4*, *UAS-GFP* flies were crossed to *tub-gal80^{ts}*; *UAS-FLP*, *actin-FRT-stop-FRT-gal4* (II;III). The newly hatched 0–6 h ALH larvae were reared at restrictive temperature at 18 °C for 72, 96 or 144 h (which correspond to 48, 64 and 96 h of development at 23 °C, respectively), then shifted to permissive temperature at 30 °C to induce labelling.

To generate wild-type or *D⁸⁷* type II NB MARCM clones, *hsFLP*; *tub-gal4*, *UAS-mCD8::GFP/CyO*; *tub-gal80*, *FRT2A/TM6C,Sb* flies were crossed to *FRT2A* or *D⁸⁷,FRT2A/Tm3,Sb* flies respectively. To induce clones, 24 h ALH larvae were heat-shocked at 37 °C for 30 min, and reared to 120 h ALH. To generate wild-type or *ey* RNAi INP MARCM clones, *hsFLP*; *FRT40A*, *tub-gal80/CyO,actGFP*; *tub-gal4*, *UAS-mCD8::GFP/TM6B* flies were crossed to *FRT40A* or *FRT40A*; *UAS-ey^{RNAi}* flies respectively. To induce clones, 24 h ALH larvae were heat-shocked at 37 °C for 1 h, and reared to 120 h ALH. INP clones were identified in the dorso-medial brain as multicellular clones (*n* > 3 cells) without a neuroblast.

Unless indicated otherwise, larvae were staged to 120 h ALH based on age and morphology (late wandering larvae near pupariation) for dissections. For other time points, newly hatched 0–4 h ALH larvae were picked and reared accordingly. Adult females were aged to 3–5 days for dissections.

Immunohistochemistry. Primary antibodies were rat anti-Dpn (1:50, C.Q.D. laboratory), guinea pig anti-Dpn (1:2,000, J. Skeath), chicken anti-GFP (1:2,000, Aves Laboratories), guinea pig anti-D (1:500, J. Nambu), rabbit anti-D (1:500, J. Nambu), rabbit anti-Ey (1:3,500, U. Walldorf), rat anti-Grh (1:1,000, S. Thor), guinea-pig anti-Bsh (1:250, M. Sato), guinea-pig anti-Toy (1:500, U. Walldorf), mouse anti-Repo (1:4, DSHB), mouse anti-nc82 (1:100, DSHB), rabbit anti-DsRed (1:500, Clontech Laboratories), rabbit anti-Ase (1:2,000, C.-Y. Lee), mouse anti-Pros (MR1A, 1:1,000, C.Q.D. laboratory), rat anti-Elav (1:50, DSHB), rabbit anti-Cas (1:1,000, W. Odenwald), rat anti-Svp (1:500, T. Isshiki). Additional primary antibodies are listed in Supplementary Table 1. Secondary antibodies were from Molecular Probes or Jackson ImmunoResearch.

Dissection and immunostaining were performed as described previously¹⁵ with few modifications. Larval brains were fixed in 4% formaldehyde in PBST (1× PBS with 0.3% Triton X-100) for 25 min, rinsed, and blocked in PBST with 5% normal goat and donkey serum mix (Vector Laboratories) for 30 min. Adult brains were fixed in 4% formaldehyde in PBT (1× PBS with 1% Triton X-100), rinsed, and blocked in PBT plus 5% serum. Adult brains were incubated in primary antibodies for 2 days at 4 °C, then in secondary antibodies for 2 days at 4 °C. Brains were stored in Vectashield (Vector Laboratories). For EdU incorporation, dissected larval brains were incubated in S2 medium (Sigma) containing 100 μg ml⁻¹ EdU (Molecular Probes) at 25 °C for 2 h. After completing standard fixation and antibody staining procedures, EdU was detected by following manufacturers protocols (Molecular Probes).

Imaging. Brains were mounted in Vectashield (Vector Laboratories). Images were captured with a Zeiss LSM700 or LSM710 confocal microscope with a z-resolution of 1.0 μm, and processed in the open source software FIJI (<http://fiji.sc>) and Adobe Photoshop CS5. Figures were made in Adobe Illustrator CS5. Three-dimensional brain reconstructions were generated using Imaris software (Bitplane).

Quantification of INPs and progeny. INPs were labelled with cell-type specific Gal4-driven *UAS-mCD8::GFP* and distinguished from their GMC/neuronal progeny by Dpn staining. For the quantification of Grh expression in middle-aged INPs, newly mature INPs that show weak levels of Grh (inherited from immature INPs) were excluded. For the quantification of temporal identities, INP progeny were marked with permanent lineage tracing. GFP⁺ INP progeny in DM1–6 lineages were counted. GFP⁺ Repo⁺ glia in the lateral brain were also counted, see Supplementary Fig. 10. For better labelling of glia, nuclear localized GFP (nGFP) was used.

Negative geotaxis assays were performed as described previously⁴². Ten adults of each genotype (three-day-old virgin females) were placed in a vial at room temperature. Flies were allowed to acclimate for 1 min, and then gently tapped to the bottom of the vial. The number of flies that climbed above the vertical distance of 8 cm by 10 s after the tap was recorded as a percentage of total flies. Ten trials were conducted for each genotype, with a 1-min rest period between each trial. The results of ten trials were averaged and plotted as the negative geotaxis response. *ey* RNAi genotype was *R12E09^D >> act-gal4 UAS-ey^{RNAi}*. Controls were (1) *R12E09^D >> act-gal4 attP2*, (2) *R12E09^D >> act-gal4 UAS-mCherry^{RNAi}*, and (3) *no gal4 >> act-gal4 UAS-ey^{RNAi}*.

Statistics. Data represent mean ± s.d. Two-tailed Student's *t*-tests were used to assess statistical significance. **P* < 0.05; ***P* < 0.01; ****P* < 0.001.

43. Pfeiffer, B. D. *et al.* Refinement of tools for targeted gene expression in *Drosophila*. *Genetics* **186**, 735–755 (2010).
44. Han, C., Jan, L. Y. & Jan, Y. N. Enhancer-driven membrane markers for analysis of nonautonomous mechanisms reveal neuron–glia interactions in *Drosophila*. *Proc. Natl Acad. Sci. USA* **108**, 9673–9678 (2011).
45. Zhu, S., Barshow, S., Wildonger, J., Jan, L. Y. & Jan, Y. N. Ets transcription factor Pointed promotes the generation of intermediate neural progenitors in *Drosophila* larval brains. *Proc. Natl Acad. Sci. USA* **108**, 20615–21620 (2011).
46. Uv, A. E., Harrison, E. J. & Bray, S. J. Tissue-specific splicing and functions of the *Drosophila* transcription factor Grainyhead. *Mol. Cell. Biol.* **17**, 6727–6735 (1997).
47. Evans, C. J. *et al.* G-TRACE: rapid Gal4-based cell lineage analysis in *Drosophila*. *Nature Methods* **6**, 603–605 (2009).

Temporal patterning of *Drosophila* medulla neuroblasts controls neural fates

Xin Li^{1*}, Ted Erclik^{1*}, Claire Bertet¹, Zhenqing Chen¹, Roumen Voutev², Srinidhi Venkatesh¹, Javier Morante^{1†}, Arzu Celik^{1†} & Claude Desplan¹

In the *Drosophila* optic lobes, the medulla processes visual information coming from inner photoreceptors R7 and R8 and from lamina neurons. It contains approximately 40,000 neurons belonging to more than 70 different types. Here we describe how precise temporal patterning of neural progenitors generates these different neural types. Five transcription factors—Homothorax, Eyeless, Sloppy paired, Dichaete and Tailless—are sequentially expressed in a temporal cascade in each of the medulla neuroblasts as they age. Loss of Eyeless, Sloppy paired or Dichaete blocks further progression of the temporal sequence. We provide evidence that this temporal sequence in neuroblasts, together with Notch-dependent binary fate choice, controls the diversification of the neuronal progeny. Although a temporal sequence of transcription factors had been identified in *Drosophila* embryonic neuroblasts, our work illustrates the generality of this strategy, with different sequences of transcription factors being used in different contexts.

Generation of neuronal diversity requires both spatial and temporal patterning of neural progenitors. Vertebrate neural progenitors transit through different competence states as they age, and thus generate a conserved order of different neural types^{1–4}. Similarly, *Drosophila* neuroblasts generate differently fated progeny in a defined order^{5–10}. A molecular mechanism of temporal specification has been identified in the *Drosophila* embryonic nerve cord, where neuroblasts sequentially express several transcription factors as they age: Hunchback (Hb), Krüppel (Kr), Pdm1/Pdm2 (Pdm), Castor (Cas) and Grainy head (Grh)^{7,11–13}. This temporal cascade is necessary and sufficient for the specification of neuronal identities in multiple lineages of the nerve cord^{17–9,11,14–17}. An intriguing question is whether the same temporal gene cascade patterns neural progenitors in other systems. In *Drosophila* antennal lobe neuroblasts, Kr defines 1 out of 40 fates of projection neurons¹⁸. In vertebrates, IKAROS (also known as IKZF1), a mouse orthologue of Hb, is both necessary and sufficient for the early competence state of retinal progenitors¹⁹. However, a cascade of transcription factors analogous to that of *Drosophila* nerve cord neuroblasts has not been reported elsewhere. Thus, it is still not clear whether this powerful mechanism is widely used in other systems. Here we address this question in the *Drosophila* medulla.

The medulla, containing ~40,000 neurons belonging to more than 70 cell types, is the largest neuropil in the visual-processing centre (optic lobe)^{20,21}. It is derived from a larval crescent-shaped neuroepithelium termed the outer proliferation centre (OPC). The single-layered neuroepithelial cells of the OPC proliferate by dividing symmetrically. They are sequentially converted into medulla neuroblasts in a wave of neurogenesis that initiates at the medial edge of the neuroepithelium crescent and progresses laterally^{22–27} (Fig. 1a, c). Each neuroblast then divides asymmetrically multiple times to self-renew and to generate ganglion mother cells (GMCs), which in turn divide once to produce medulla neurons^{22,28,29}. The neuronal progeny of each neuroblast form a chain, with newly generated neurons occupying the most superficial layer close to neuroblasts and GMCs, and the first-born neurons occupying the deepest layer close to the medulla neuropil^{30,31}.

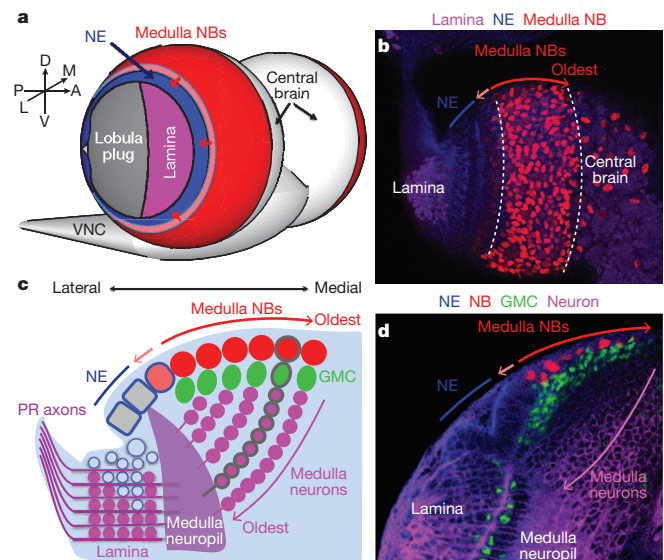


Figure 1 | The developing medulla. **a**, Model of a larval brain showing that the neuroepithelium (blue) gives rise to the lamina on the lateral (L) side and to the medulla on the medial (M) side. A wave of neurogenesis (light red) converts neuroepithelium (NE) cells (blue) into neuroblasts (NBs) (red). A, anterior; D, dorsal; P, posterior; V, ventral; VNC, ventral nerve cord. **b**, Surface view showing neuroepithelium (phalloidin, blue), medulla neuroblasts (Dpn, red), and lamina neurons (Elav, purple). **c**, Cross-sectional model showing neuroblasts (red), GMCs (green) and neurons (purple). A single neuroblast clone is shown by grey thick outlines. PR, photoreceptor. **d**, Cross-sectional view showing the neuroepithelium (DE-cadherin, blue), medulla neuroblasts (Dpn, red), medulla GMCs (Pros, green), medulla and lamina neurons (*elav-gal4* > *UAS-CD8::GFP*, purple). In all panels, the small red arrow depicts the wave of neurogenesis.

¹Department of Biology, New York University, 100 Washington Square East, New York, New York 10003, USA. ²Department of Biochemistry and Molecular Biophysics, Columbia University Medical Center, 701 West 168th Street, New York, New York 10032, USA. [†]Present addresses: Instituto de Neurociencias, CSIC, Universidad Miguel Hernández, Avenida Santiago Ramón y Cajal s/n, 03550 San Juan de Alicante, Spain (J.M.); Bogazici University, Department of Molecular Biology and Genetics, Kuzey Park Binasi 316, 34342 Bebek, Istanbul, Turkey (A.C.).

*These authors contributed equally to this work.

(Fig. 1c, d). Pioneering studies have identified several transcription factors specifying different subsets of medulla neuron types^{21,30,31}. However, it was not clear how their expression in neurons is controlled to generate neuronal diversity.

We found that five transcription factors, Homothorax (Hth), Eyeless (Ey), Sloppy paired 1 and 2 (Slp), Dichaete (D) and Tailless (Tll), are sequentially expressed in medulla neuroblasts as they age. Ey, Slp and D are each required for turning on the next transcription factor in the dividing neuroblasts. Slp and D are also required for turning off the preceding transcription factor. These transcription factors control the expression of downstream transcription factors that mark the identities of the neuronal progeny. Notch-dependent asymmetric division of a novel temporal cascade of transcription factors distinct from the Hb-Kr-Pdm-Cas-Grh sequence suggests that transcription-factor-dependent temporal switching of neural progenitors is a common theme in neuronal specification, with different transcription factor sequences being recruited in different contexts.

A temporal gene cascade in medulla neuroblasts

In the developing medulla, the wave of conversion of neuroepithelium into neuroblasts makes it possible to visualize neuroblasts at different temporal stages in one snapshot, with newly generated neuroblasts on the lateral edge and the oldest neuroblasts on the medial edge of the expanding crescent shaped neuroblast region (Fig. 1a, b). We conducted an antibody screen for transcription factors expressed in the developing medulla and identified five transcription factors, Hth, Ey, Slp1, D and Tll, that are expressed in five consecutive stripes in neuroblasts of increasing ages, with Hth expressed in newly differentiated neuroblasts, and Tll in the oldest neuroblasts (Fig. 2a, b). This suggests that these transcription factors are sequentially expressed in medulla neuroblasts as they age. Neighbouring transcription factor stripes show partial overlap in neuroblasts with the exception of the D and Tll stripes, which abut each other. We and others had previously reported that Hth³¹ and Ey³⁰ were expressed in medulla neuroblasts, but they had not been implicated in controlling neuroblast temporal identities. Hth and Tll also show expression in the neuroepithelium.

To address whether each neuroblast sequentially expresses the five transcription factors, we examined their expression in the neuroblast progeny (Fig. 1c, d). Hth, Ey and Slp1 are expressed in three different layers of neurons that correlate with birth order, that is, Hth in the first-born neurons of each lineage in the deepest layers; Ey or Slp1 in correspondingly more superficial layers, closer to the neuroblasts. This suggests that they are born sequentially in each lineage (Fig. 2c, d, j). D is expressed in two distinct populations of neurons. The more superficial population inherit D from D⁺ neuroblasts (Fig. 2e, above dashed line). D⁺ neurons in deeper layers (corresponding to the Hth and Ey layers) turn on D expression independently and will be discussed later (Fig. 2e, below dashed line). We generated single neuroblast clones and examined the expression of the transcription factors in the neuroblast and its progeny. Single neuroblast clones in which the neuroblast is at the Ey⁺ stage include Ey⁺ GMCs/neurons as well as Hth⁺ neurons (Fig. 2f). This indicates that Ey⁺ neuroblasts have transited through the Hth⁺ stage and generated Hth⁺ neurons. Clones in which the neuroblast is at the D⁺ stage contain Slp1⁺ GMCs and Ey⁺ neurons (Fig. 2g), suggesting that D⁺ neuroblasts have already transited through the Slp1⁺ and Ey⁺ stages. This supports the model that each medulla neuroblast sequentially expresses Hth, Ey, Slp1 and D as it ages, and sequentially produces neurons that inherit and maintain expression of the transcription factor.

slp1 and *slp2* are two homologous genes arranged in tandem and function redundantly in embryonic and eye development^{32,33}. Slp2 is expressed in the same set of medulla neuroblasts as Slp1 (Supplementary Fig. 1a). We will refer to Slp1 and Slp2 collectively as Slp.

Tll is expressed in the oldest medulla neuroblasts. The oldest Tll⁺ neuroblasts show nuclear localization of Prospero (Pros) (Fig. 2h),

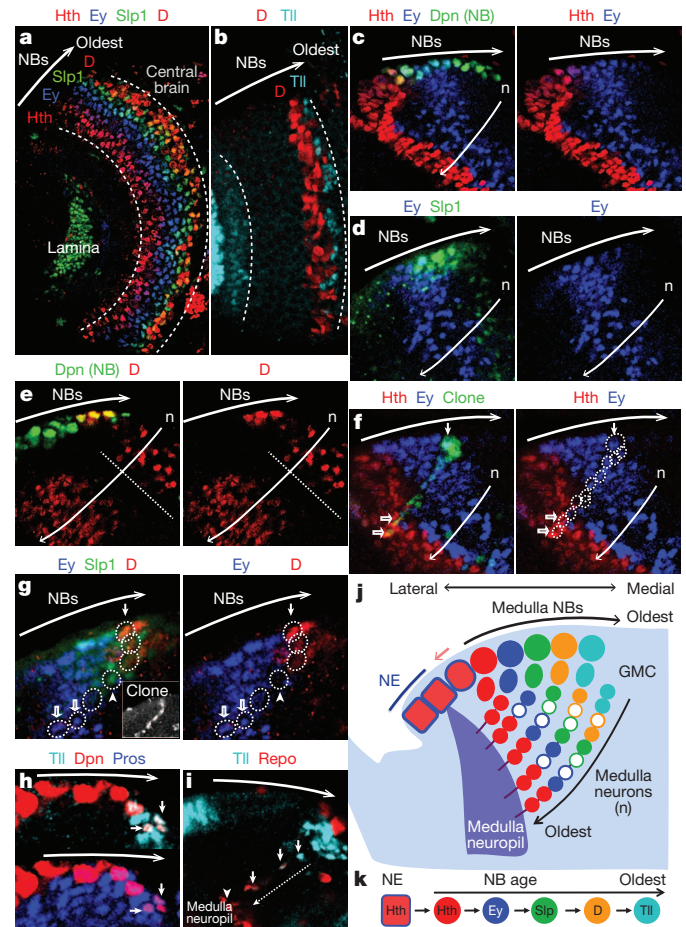


Figure 2 | A temporal sequence of transcription factors in medulla neuroblasts. **a, b**, Surface views showing that neuroblasts sequentially express: Hth (red), Ey (blue), Slp1 (green) and D (red) (**a**), and D (red) and Tll (cyan) (**b**). **c–i**, Cross-sectional views showing the expression of the five transcription factors in neuroblasts and their progeny. **c**, Hth (red), Ey (blue) and Dpn (green). **d**, Ey (blue) and Slp1 (green). **e**, D (red). The dashed line separates the two populations of D⁺ neurons (see text). **n**, neurons. **f**, In a neuroblast clone (β-Gal; green in left, dashed circles in right), the neuroblast is Ey⁺ (blue, small arrow), whereas its progeny are Ey⁺ or Hth⁺ (red, open arrows). **g**, In a neuroblast clone (β-Gal; white in inset), the neuroblast is D⁺ (red, small arrow). It has generated Slp1⁺ (green) GMCs (arrowhead), and Ey⁺ (blue) neurons (open arrows). **h**, The oldest neuroblasts (small arrows) express Tll (cyan in top), Dpn (red) and nuclear Pros (blue in bottom). **i**, Tll⁺ neuroblast progeny (small arrows) lose Tll (cyan), and turn on Repo (red) while migrating (along the dashed arrow) to become medulla neuropil glia (arrowhead). **j**, Schematic model. For simplicity, the overlap between transcription factors is not shown; only one neuroblast/GMC is shown for each stage. D expression in the deeper neuron population is not shown. Empty cells indicate that a subset of neurons born during the Ey, Slp or D windows do not maintain the neuroblast transcription factor. **k**, Model showing that each neuroblast sequentially expresses five transcription factors.

suggesting that they undergo Pros-dependent cell-cycle exit at the end of their life, as in larval nerve cord and central brain neuroblasts³⁴. Tll⁺ neuroblasts and their progeny express *glial cells missing* (*gcm*) (Supplementary Fig. 1b), and the progeny gradually turn off Tll and turn on Repo, a glial-specific marker. These cells migrate towards deeper neuronal layers and take their final position as glial cells around the medulla neuropil (Fig. 2i). Thus, Tll⁺ neuroblasts correspond to previously identified glioblasts between the optic lobe and central brain that express *gcm* and generate medulla neuropil glia^{35,36}. Clones in which the neuroblast is at the Tll⁺ stage contain Hth⁺ neurons and Ey⁺ neurons, among others (Supplementary Fig. 1c), confirming that Tll⁺ neuroblasts represent the final temporal stage of medulla neuroblasts

rather than a separate population of glioblasts. Therefore, these data clearly show that medulla neuroblasts sequentially express five transcription factors as they age. The four earlier temporal stages generate neurons that inherit and maintain the temporal transcription factor present at their birth, although a subset of neurons born during the Ey, Slp or D neuroblast stages lose expression of the neuroblast transcription factor (Fig. 2j). At the final temporal stage, neuroblasts switch to glioblasts and then exit the cell cycle (Fig. 2j, k).

Cross-regulation among temporal transcription factors

We examined whether cross-regulation among transcription factors of the neuroblast temporal sequence contributes to the transition from one transcription factor to the next. Loss of *hth* or its cofactor, *extradenticle* (*exd*), does not affect the expression of Ey and subsequent progression of the neuroblast temporal sequence (data not shown).

We generated *ey*-null mutant clones using a bacterial artificial chromosome (BAC) rescue construct recombined on a chromosome containing a Flip recombinase target (FRT) site in an *ey*^{5.71} null background. We also examined *ey*^{5.71} homozygous mutant larvae. In both cases, Slp expression is lost in neuroblasts, along with neuronal progeny produced by Slp⁺ neuroblasts, marked by the transcription factor Twin of eyeless (Toy, see below) (Fig. 3a and Supplementary Fig. 2a). However, neuroblast division is not affected (Supplementary Fig. 2b), and Hth remains expressed in only the youngest neuroblasts and first-born neurons (Fig. 3b and data not shown). Targeted *ey* RNA interference (RNAi) using a *Vsx*-Gal4 driver that is expressed in the central region of the neuroepithelium and neuroblasts (T. Erclik *et al.*, manuscript submitted) gives the same phenotype (data not shown). This suggests that Ey is required to turn on the next transcription factor, Slp, but is not required to repress Hth (Fig. 3c).

In clones of a deficiency mutation, *slp*^{S37A}, that deletes both *slp1* and *slp2* (ref. 33), neuroblasts normally transit from Hth⁺ to Ey⁺, but older neuroblasts maintain the expression of Ey and do not progress to express D or Tll (Fig. 3d, e and Supplementary Fig. 2f), suggesting that Slp is required to repress *ey* and activate *D*.

Similarly, in *D* mutant clones, neuroblasts are also blocked at the Slp⁺ stage, and do not turn on Tll (Fig. 3f, g), indicating that *D* is required to repress *slp* and activate *tll*. Finally, in *tll* mutant clones, *D* expression is not expanded into oldest neuroblasts, suggesting that *tll* is not required for neuroblasts to turn off *D* (Supplementary Fig. 2j). Thus, in the medulla neuroblast temporal sequence, *ey*, *slp* and *D* are each required for turning on the next transcription factor. *slp* and *D* are also required for turning off the preceding transcription factor (Fig. 3h).

We also examined gain-of-function phenotypes of each gene. However, misexpression of Hth, Ey, Slp1 or Slp2, or D in all neuroblasts or in large neuroblast clones is not sufficient to activate the next transcription factor or repress the previous transcription factor in neuroblasts (Supplementary Fig. 2e, g–i and data not shown). Only misexpressing *tll* in all neuroblasts is sufficient to repress *D* expression (Supplementary Fig. 2k).

In summary, cross-regulation among transcription factors is required for at least some of the transitions. We did not observe cross-regulation between *hth* and *ey*. Because *ey* is already expressed at low levels in the neuroepithelium and in Hth⁺ neuroblasts, an as yet unidentified factor might gradually upregulate *ey* and repress *hth* to achieve the first transition. As *tll* is sufficient but not required to repress *D* expression, additional factors must act redundantly with Tll to repress *D*.

Notch-dependent binary fate choice

The temporal sequence of neuroblasts described above could specify at least four neuron types plus glia (in fact more than ten neuron types plus glia considering that neuroblasts divide several times at each stage with overlaps between neighbouring temporal transcription factors; see Discussion). As this is not sufficient to generate the 70 medulla neuron types, we asked whether another process increases

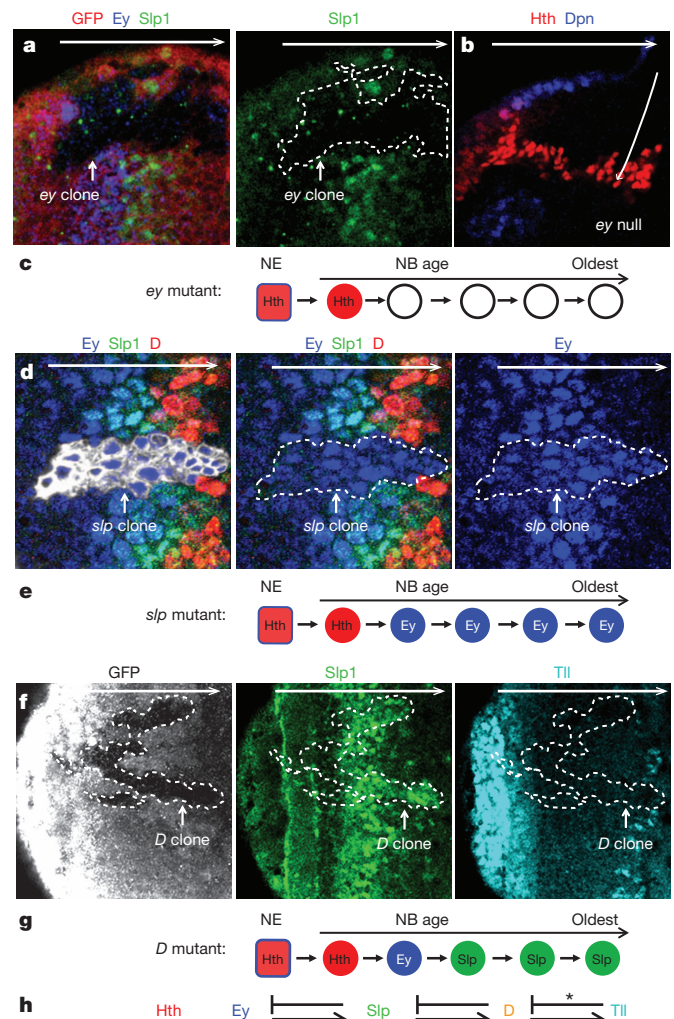


Figure 3 | Cross-regulations between transcription factors in the gene cascade. **a**, Surface view: in an *ey*^{5.71} mutant clone marked by a lack of green fluorescent protein (GFP; red) and Ey (blue), Slp1 (green) is lost in neuroblasts. **b**, Cross-sectional view: in *ey*^{5.71} mutants, Hth (red) is only in the youngest neuroblasts (Dpn marking all neuroblasts, blue). **c**, Summary model. **d**, Surface view: in *slp* mutant MARCM clones (GFP, white in left, dashed line in middle and right), neuroblasts continue to express Ey (blue) and do not turn on D (red). **e**, Summary model. **f**, Surface view: in *D* mutant clones marked by lack of GFP (white in left, dashed line in middle and right), neuroblasts continue to express Slp1 (green) and do not turn on Tll (cyan). **g**, Summary model. **h**, Model summarizing cross-regulations between the five transcription factors. Asterisk denotes sufficient but not required.

diversity in the progeny neurons born from a neuroblast at a specific temporal stage. Apterous (Ap) is known to mark about half of the 70 medulla neuron types²¹. In the larval medulla, Ap is expressed in a salt-and-pepper manner in subsets of neurons born from all temporal stages³⁰ (Fig. 4a, b). In the progeny from Hth⁺ neuroblasts, all neurons seem to maintain Hth, with a subset also expressing Ap (Fig. 4a). However, only half of the neurons born from neuroblasts at other transcription factor stages maintain expression of the neuroblast transcription factor. For instance, in the progeny of Ey⁺ neuroblasts, Ey⁺ neurons are intermingled with about an equal number of Ey⁻ neurons that instead express Ap (Fig. 4a). Neuroblast clones contain intermingled Ey⁺ and Ap⁺ neurons (Fig. 4d). This is also true for the progeny of Slp⁺ neuroblasts: Slp1⁺ neurons are intermingled with Slp1⁻ Ap⁺ neurons (Supplementary Fig. 3a). In the progeny of D⁺ neuroblasts, D and Ap are co-expressed in the same neurons, and they are intermingled with neurons that express neither D nor Ap (Fig. 4b, above dashed line). As mentioned earlier, neurons in deeper neuronal

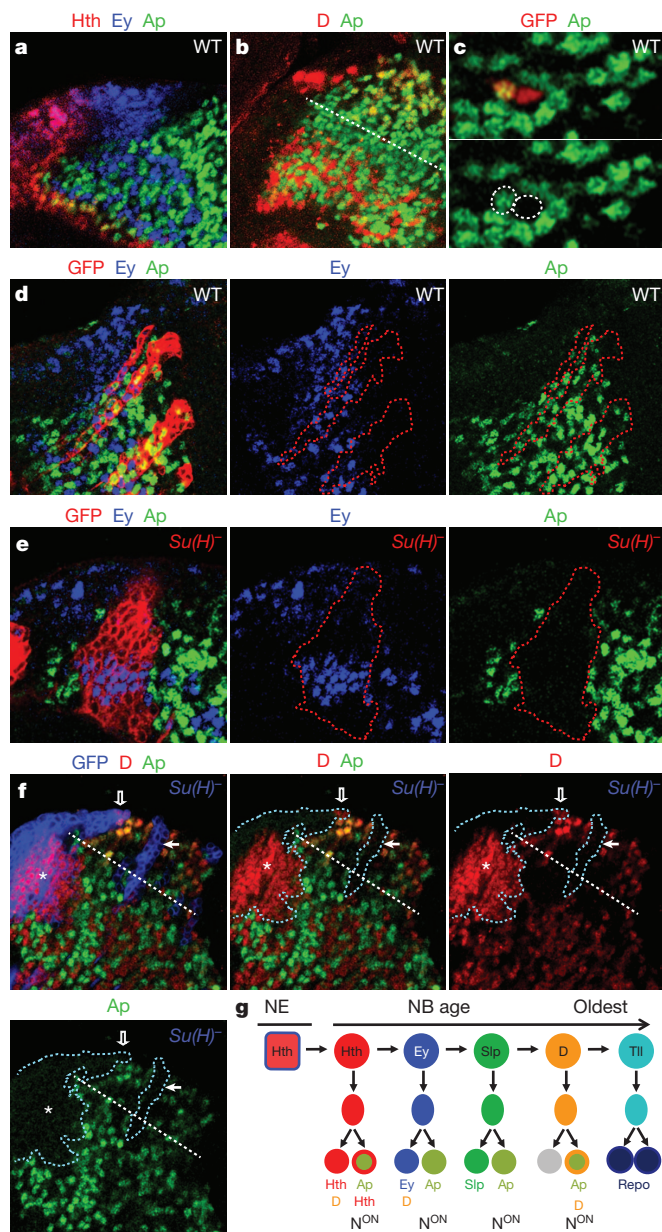


Figure 4 | Notch-dependent asymmetric division of medulla GMCs. All panels are cross-sectional views with Ap (green) and Ey (blue). **a**, A subset of Hth⁺ neurons (red) are Ap⁺, whereas Ey⁺ neurons are intermingled with Ap⁺ neurons. **b**, D⁺ neurons above the dashed line co-express Ap; D expression below the dashed line is in Ap⁻ neurons. **c**, Two daughters of a GMC are labelled by GFP (red). One is Ap⁺, the other is Ap⁻. **d**, Wild-type *tub-gal4* MARCM clones marked by GFP (red) contain both Ap⁺ and Ey⁺ neurons. **e**, **f**, *Su(H)* mutant MARCM clones (GFP, red in **e**, blue in **f**). **e**, Ap is lost and Ey expanded. **f**, D (red) in neuroblasts is not affected (open arrow) but D and Ap are lost in D⁺ neuroblast progeny (above the dashed line, white arrow); the deeper layer of D expression in Ap⁻ neurons (below the dashed line, asterisk) is expanded. **g**, A simplified schematic model.

layers (corresponding to the Ey⁺ and Hth⁺ neuron layers, Fig. 4b, below dashed line) also express D independently, and these neurons are Ap⁻. The expression of Ap is stable from larval to adult stages³⁰ (Supplementary Fig. 3c, d).

The intermingling of Ap⁺ and Ap⁻ neurons raised the possibility that asymmetric division of GMCs gives rise to one Ap⁺ and one Ap⁻ neuron. We generated two-cell clones to visualize the two daughters of a GMC. In every case ($n = 11$), one neuron is Ap⁺ and the other is Ap⁻ (Fig. 4c and Supplementary Fig. 3b), suggesting that asymmetric

division of GMCs diversifies medulla neuron fates by controlling Ap expression.

Asymmetric division of GMCs in *Drosophila* involves Notch (N)-dependent binary fate choice^{37–39}. In the developing medulla, the N pathway is involved in the transition from neuroepithelium to neuroblast, and loss of Su(H), the transcriptional effector of N signalling, leads to faster progression of neurogenesis and neuroblast formation²⁴. However, *Su(H)* mutant neuroblasts still follow the same transcription factor sequence and generate GMCs and neuronal progeny (Supplementary Fig. 3e, f and Fig. 4f, open arrow), allowing us to analyse the effect of loss of N function on GMC progeny diversification. Notably, neurons completely lose Ap expression in the *Su(H)* mutant clones. All mutant neurons born during the Hth⁺ stage still express Hth, but not Ap, suggesting that the N^{ON} daughters of Hth⁺ GMCs are the neurons expressing both Ap and Hth (Supplementary Fig. 3h). In contrast to wild-type clones (Fig. 4d), all *Su(H)* mutant neurons born during the Ey⁺ neuroblast stage express Ey and none express Ap (Fig. 4e). Similarly, all mutant neurons born during the Slp⁺ neuroblast stage express Slp1 but lose Ap (Supplementary Fig. 3g and data not shown). These data suggest that, for Ey⁺ or Slp⁺ GMCs, the N^{OFF} daughter maintains the neuroblast transcription factor expression, whereas the N^{ON} daughter loses this expression but expresses Ap. In the wild-type progeny born during the D⁺ neuroblast stage, Ap⁺ neurons co-express D. Both D and Ap are lost in *Su(H)* mutant clones in the D⁺ neuroblast progeny (Fig. 4f, arrow), confirming that D is transmitted to the Ap⁺ N^{ON} daughter of D⁺ GMCs. By contrast, the D⁺ Ap⁻ neurons in the deeper layers (corresponding to the N^{OFF} progeny born during the Ey⁺ and Hth⁺ neuroblast stages, see above) are expanded in *Su(H)* mutant clones at the expense of Ap⁺ neurons (Fig. 4f, asterisk). Therefore, the deeper layer of D expression is turned on independently in the N^{OFF} daughters of Hth⁺ and Ey⁺ GMCs.

Finally, in wild type, we observe a considerable amount of apoptotic cells dispersed among neurons, suggesting that one daughter of certain GMCs undergoes apoptosis in some of the lineages (Supplementary Fig. 3i). Together these data suggest that Notch-dependent asymmetric division of GMCs further diversifies neuronal identities generated by the temporal sequence of transcription factors (Fig. 4g).

Temporal transcription factors control neural fates

How does the neuroblast transcription factor temporal sequence, together with the Notch-dependent binary fate choice, control neuronal identities in the medulla? We used transcription factor markers specifically expressed in subsets of medulla neurons, but not in neuroblasts, including Brain-specific homeobox (Bsh) and Drifter (Dfr)³¹, as well as other transcription factors identified in our antibody screen, for example, Lim3 and Toy. Bsh is required and sufficient for the Mi1 cell fate⁴⁰, and Dfr is required for the morphogenesis of nine types of medulla neurons, including Mi10, Tm3, TmY3, Tm27 and Tm27Y (ref. 31). We first investigated at which neuroblast temporal stage these neurons were born by examining co-expression with the inherited neuroblast transcription factors. We then examined whether the neuroblast transcription factors regulate expression of these markers and neuron fates. The results for each neuroblast stage are described below.

Hth⁺ neuroblast stage

Bsh is expressed in a subset of Hth⁺ neurons³¹ that also express Ap (Fig. 5a), suggesting that Bsh is in the N^{ON} daughter of Hth⁺ GMCs. Indeed, Bsh expression is lost in both *Su(H)* and *hth* mutant clones (Fig. 5b, c). Thus, both Notch activity and Hth are required for specifying the Mi1 fate, consistent with the previous report that Hth is required for the Mi1 fate³¹. Ectopic expression of Hth in older neuroblasts is also sufficient to generate ectopic Bsh⁺ neurons, although the phenotype becomes less pronounced in later parts of the lineage (Fig. 5d). These data suggest that Hth is necessary and sufficient to specify early born neurons, but the competence to do so in response to sustained expression of Hth decreases over time. This is similar to

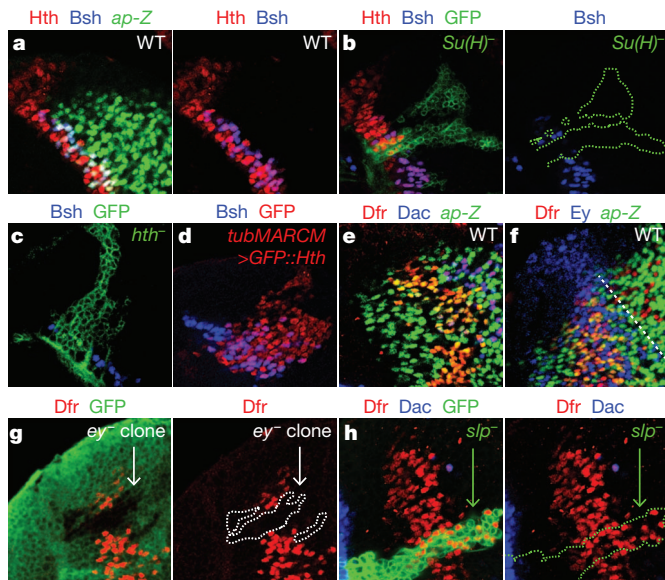


Figure 5 | Hth and Ey are required for neuronal diversity. All images are cross-sectional views of larval medulla. **a**, In wild type, Bsh (blue) is in neurons expressing both *ap-Z* (*ap-Z*; green), an enhancer trap that perfectly mimics Ap expression, and Hth (red). **b**, Bsh (blue), but not Hth (red), is lost in *Su(H)* mutant clones (GFP, green). **c**, Bsh (blue) is lost in *hth*^{P2} mutant clones (GFP, green). **d**, Bsh (blue) is ectopically expressed when UAS-GFP::Hth is driven by *tub-gal4* in a MARCM clone (GFP, red). **e**, In wild type, Dfr (red) is expressed in two-three rows of Ap⁺ (green) neurons. There are also Dfr⁺ Dac⁺ (blue) Ap⁺ neurons in a more superficial layer. **f**, The Ap⁺ Dfr⁺ neurons (below the dashed line) are intermingled with Ey⁺ (blue) neurons. **g**, Dfr expression (red) is lost in *ey*^{5.71} mutant clones marked by lack of GFP (green in left, dashed line in right). **h**, Dfr⁺ (red) neurons are expanded in *slp* mutant clones (GFP, green). In this region there are very few Dfr⁺ Dac⁺ (blue) neurons. The expanded Dfr⁺ neurons do not express Dac.

embryonic CNS neuroblasts, where ectopic Hb is only able to specify early born neurons during a specific time window^{8,41}.

Ey⁺ neuroblast stage

Lim3 is expressed in all Ap⁺ progeny of both Hth⁺ and Ey⁺ neuroblasts (Supplementary Fig. 4a and Fig. 6i). Toy and Dfr are expressed in subsets of neurons born from Ey⁺ neuroblasts, as indicated by their expression in the Ey⁺ neuron progeny layer. The most superficial row of Ey⁺ Ap⁺ neurons express Toy (and Lim3), suggesting that they are the N^{OFF} progeny of the last-born Ey⁺ GMCs (Supplementary Fig. 4c). Dfr is co-expressed with Ap in two or three rows of neurons that are intermingled with Ey⁺ neurons (Fig. 5e, f), suggesting that they are the N^{ON} progeny from Ey⁺ GMCs (Fig. 6i). In addition to these Ap⁺ Dfr⁺ neurons, Dfr is also expressed in some later-born neurons that are Ap⁺ but express another transcription factor: Dachshund (Dac), in specific sub-regions of the medulla crescent³¹ (Fig. 5e).

We tested whether Ey in neuroblasts regulates Dfr expression in neurons. As expected, Dfr-expressing neurons are lost in *ey*-null mutant clones (Fig. 5g), suggesting that they require Ey activity in neuroblasts, even though Ey is not maintained in Ap⁺ Dfr⁺ neurons. Furthermore, in *slp* mutant clones in which neuroblasts remain blocked in the Ey⁺ state, the Ap⁺ Dfr⁺ neuron population is expanded into later-born neurons (Fig. 5h), suggesting that the transition from Ey⁺ to Slp⁺ in neuroblasts is required for shutting off the production of Ap⁺ Dfr⁺ neurons. In addition, Ap⁺ Dfr⁺ neurons are lost in *Su(H)* mutant clones (Supplementary Fig. 4b). Thus, Ey expression in neuroblasts and the Notch pathway together control the generation of Ap⁺ Dfr⁺ neurons.

Slp⁺ and D⁺ neuroblast stages

In addition to its expression with Ey in the N^{OFF} progeny of the last-born Ey⁺ GMCs, Toy is also expressed in Ap⁺ (N^{ON}) neurons in more

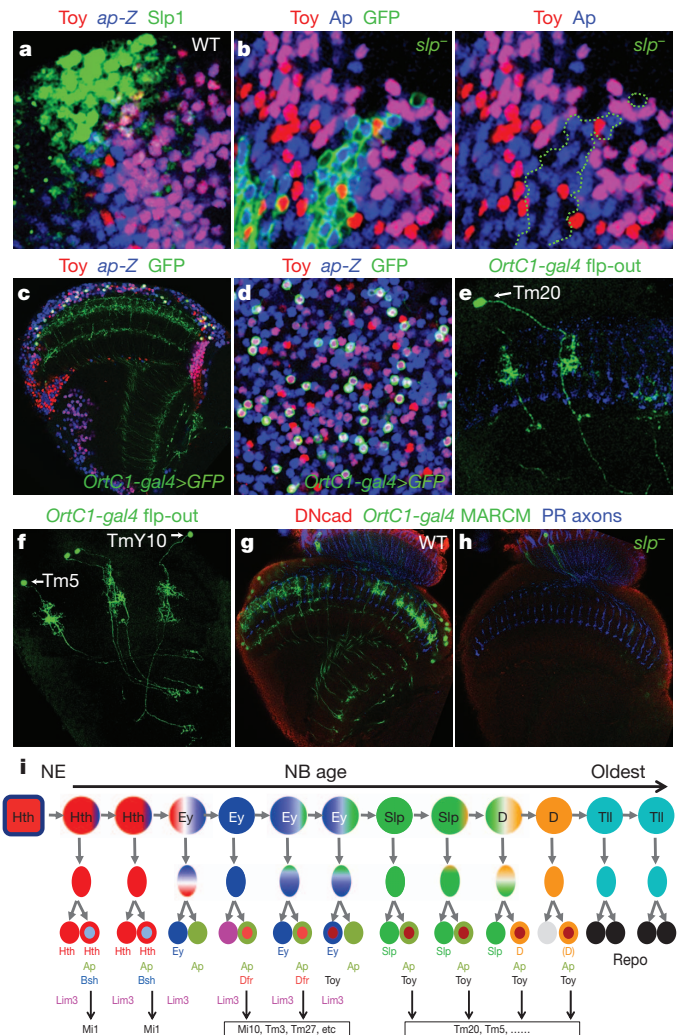


Figure 6 | Slp is required for neuronal diversity. **a**, **b**, Cross-sectional views of larval medulla, with Toy in red and Ap (or *ap-LacZ*) in blue. **a**, In wild type, Toy⁺ neurons in the deeper layer are Ap⁺. The superficial Toy⁺ neurons are Ap⁺ and are intermingled with Slp⁺ neurons (green). **b**, In *slp* mutant clones (GFP, green in left, dashed outline in right), Toy⁺ Ap⁺ neurons disappear. **c**, **d**, Adult medulla with *Ortc1-gal4* > UAS-CD8::GFP (green), *ap-lacZ* (blue) and Toy (red). **c**, Horizontal view. **d**, View through the medulla cortex. **e**, **f**, Flip-out clones in adults (*Ortc1-gal4*, *hsFLP*, UAS-FRT-STOP-FRT-CD8::GFP). Arrows point to neuron cell bodies. **e**, Tm20. Photoreceptor axons in blue. **f**, Tm5 and TmY10. **g**, **h**, *Ortc1-gal4* MARCM clones in adults. **g**, Wild type. DnCad, DN-cadherin. **h**, *slp* mutant. **i**, Simplified model showing neuronal transcription factor markers expressed in progeny of neuroblasts of different stages. The lineage is approximate and does not take into account regional differences. The brackets for 'D' indicate that D is not maintained in all N^{ON} progeny of D⁺ neuroblasts.

superficial layers generated by Slp⁺ and D⁺ neuroblasts (Supplementary Fig. 4c, d and Fig. 6a, i). Consistently, in *Su(H)* mutant clones, we see an expansion of Toy⁺ Ey⁺ neurons in the Ey progeny layer, followed by loss of Toy in the Slp and D progeny layer (Supplementary Fig. 4e).

We tested whether Slp is required for the neuroblasts to switch from generating Toy⁺ Ap⁺ neurons, progeny of Ey⁺ neuroblasts, to generating Toy⁺ Ap⁺ neurons. Indeed, in *slp* mutant clones, the Toy⁺ Ap⁺ neurons largely disappear, whereas Toy⁺ Ap⁺ neurons expand (Fig. 6b).

We examined Ap and Toy expression in specific adult neurons. *Ortc1-gal4* primarily labels Tm20 and Tm5 (C.-H. Lee, personal communication) plus a few TmY10 neurons, and these neurons express both Ap and Toy (Fig. 6c–f). To examine whether Slp is required for the specification of these neuron types, we generated

wild-type or *slp* mutant clones using the mosaic analysis with a repressible cell marker (MARCM) technique by heat-shocking for 1 h at early larval stage and analysed the number of *OrtC1-gal4*-marked neurons in the adult medulla. In wild-type clones, *OrtC1-gal4* marks ~ 100 neurons (95.1 ± 19.3 (mean \pm s.d.), $n = 8$) per medulla (Fig. 6g and Supplementary Fig. 4f, h). By contrast, very few neurons (9.7 ± 11.2 , $n = 17$) are marked by *OrtC1-gal4* in *slp* mutant clones (Fig. 6h and Supplementary Fig. 4g, i). *Slp* is unlikely to directly regulate the *Ort* promoter because *Slp* expression is not maintained in Ap^+ Toy^+ neurons. Furthermore, the expression level of *OrtC1-gal4* in lamina L3 neurons (C.-H. Lee, personal communication) is not affected by *slp* mutation (Fig. 6h). These data suggest that loss of *Slp* expression in neuroblasts strongly affects the generation of Tm20 and Tm5 neurons.

In summary, our data show that the sequential expression of transcription factors in medulla neuroblasts controls the birth-order-dependent expression of different neuronal transcription factor markers, and thus the sequential generation of different neuron types (Fig. 6i).

Discussion

Although a temporal transcription factor sequence that patterns *Drosophila* nerve cord neuroblasts was reported more than a decade ago^{7,12}, it was not clear whether the same or a similar transcription factor sequence patterns neural progenitors in other contexts³. Our identification of a novel temporal transcription factor sequence patterning the *Drosophila* medulla suggests that temporal patterning of neural progenitors is a common theme for generating neuronal diversity, and that different transcription factor sequences might be recruited in different contexts.

There are both similarities and differences between the two neuroblast temporal sequences. In the Hb-Kr-Pdm-Cas-Grh sequence, ectopically expressing one gene is sufficient to activate the next gene, and repress the previous gene, but these cross-regulations are not necessary for the transitions, with the exception of *Castor*^{7,11,12,15}. In the Hth-Ey-Slp-D-Tll sequence, removal of *Ey*, *Slp* or *D* does disrupt cross-regulations necessary for temporal transitions (except the Hth-Ey transition). However, in most cases these cross-regulations are not sufficient to ensure temporal transitions, suggesting that additional timing mechanisms or factors are required.

For simplicity, we represented the medulla neuroblasts as transiting through five transcription factor stages, whereas in fact the number of stages is clearly larger than five (Fig. 6i). First, neuroblasts divide more than once while expressing a given temporal transcription factor, and each GMC can have different sub-temporal identities. Furthermore, there is considerable overlap between subsequent temporal neuroblast transcription factors: neuroblasts expressing two transcription factors are likely to generate different neuron types from neuroblasts expressing either one alone.

Although we are still investigating the complete lineage of medulla neuroblasts, we show here how a novel temporal sequence of transcription factors is required to generate sequentially the diverse neurons that compose the medulla. The requirement for transcription factor sequences in the medulla and in embryonic neuroblasts suggests that this is a general mechanism for the generation of neuronal diversity. Interestingly, the mammalian orthologue of *Slp1*, *FOXG1*, acts in cortical progenitors to suppress early born cortical cell fates⁴². Thus, transcription-factor-dependent temporal patterning of neural progenitors might be a common theme in both vertebrate and invertebrate systems.

METHODS SUMMARY

We screened ~ 200 antibodies against transcription factors from various sources including: the polyclonal antibody collection against *Drosophila* segmentation proteins⁴³; various gifts from the *Drosophila* community; Developmental Studies Hybridoma Bank; and a collection of antibodies generated by the modENCODE project that were provided by N. Nègre and K. White. Wild-type or mutant

MARCM clones were generated by 37 °C heat-shocks at early larvae stages. Wandering third instar larvae or adults were analysed. For the generation of *ey* mutant clones, we used a BAC containing the *ey* genomic region inserted on chromosome 3L, recombined with *FRT80B* and *Ubi-GFP*, and crossed into an *ey*^{J5.71} mutant background. This line was crossed with *hs-Flp*; *FRT80B*, *ey*^{J5.71}/*In(4)ci*^D and the progeny was heat-shocked for 1 h at 37 °C 3 days before dissection of wandering third instar larvae. Single neuroblast clones were generated using *AC225-gal4*, which is expressed in the neuroepithelium-to-neuroblast transition zone, driving *UAS-FLP* combined with *act-FRT-STOP-FRT-nulacZ* and *tub-gal80^{ts}* to provide temporal control. Two-cell clones were generated using two methods: twin-spot MARCM¹⁰, or *pros-gal4* (expressed in GMCs) driving *UAS-FLP* with *ubi-FRT-STOP-FRT-nuGFP* and *tub-gal80^{ts}*.

Full Methods and any associated references are available in the online version of the paper.

Received 6 October 2012; accepted 24 May 2013.

Published online 19 June 2013.

1. Livesey, F. J. & Cepko, C. L. Vertebrate neural cell-fate determination: lessons from the retina. *Nature Rev. Neurosci.* **2**, 109–118 (2001).
2. Molyneaux, B. J., Arlotta, P., Menezes, J. R. & Macklis, J. D. Neuronal subtype specification in the cerebral cortex. *Nature Rev. Neurosci.* **8**, 427–437 (2007).
3. Jacob, J., Mairange, C. & Gould, A. P. Temporal control of neuronal diversity: common regulatory principles in insects and vertebrates? *Development* **135**, 3481–3489 (2008).
4. Okano, H. & Temple, S. Cell types to order: temporal specification of CNS stem cells. *Curr. Opin. Neurobiol.* **19**, 112–119 (2009).
5. Lee, T., Lee, A. & Luo, L. Development of the *Drosophila* mushroom bodies: sequential generation of three distinct types of neurons from a neuroblast. *Development* **126**, 4065–4076 (1999).
6. Akiyama-Oda, Y., Hosoya, T. & Hotta, Y. Asymmetric cell division of thoracic neuroblast 6–4 to bifurcate glial and neuronal lineage in *Drosophila*. *Development* **126**, 1967–1974 (1999).
7. Isshiki, T., Pearson, B., Holbrook, S. & Doe, C. Q. *Drosophila* neuroblasts sequentially express transcription factors which specify the temporal identity of their neuronal progeny. *Cell* **106**, 511–521 (2001).
8. Pearson, B. J. & Doe, C. Q. Regulation of neuroblast competence in *Drosophila*. *Nature* **425**, 624–628 (2003).
9. Baumgardt, M., Karlsson, D., Terriente, J., Diaz-Benjumea, F. J. & Thor, S. Neuronal subtype specification within a lineage by opposing temporal feed-forward loops. *Cell* **139**, 969–982 (2009).
10. Yu, H. H., Chen, C. H., Shi, L., Huang, Y. & Lee, T. Twin-spot MARCM to reveal the developmental origin and identity of neurons. *Nature Neurosci.* **12**, 947–953 (2009).
11. Kambadur, R. et al. Regulation of POU genes by *castor* and *hunchback* establishes layered compartments in the *Drosophila* CNS. *Genes Dev.* **12**, 246–260 (1998).
12. Brody, T. & Odenwald, W. F. Programmed transformations in neuroblast gene expression during *Drosophila* CNS lineage development. *Dev. Biol.* **226**, 34–44 (2000).
13. Grosskortenhaus, R., Pearson, B. J., Marusich, A. & Doe, C. Q. Regulation of temporal identity transitions in *Drosophila* neuroblasts. *Dev. Cell* **8**, 193–202 (2005).
14. Novotny, T., Eiselt, R. & Urban, J. Hunchback is required for the specification of the early sublineage of neuroblast 7–3 in the *Drosophila* central nervous system. *Development* **129**, 1027–1036 (2002).
15. Grosskortenhaus, R., Robinson, K. J. & Doe, C. Q. Pdm and *Castor* specify late-born motor neuron identity in the neuroblast 7–1 lineage. *Genes Dev.* **20**, 2618–2627 (2006).
16. Cleary, M. D. & Doe, C. Q. Regulation of neuroblast competence: multiple temporal identity factors specify distinct neuronal fates within a single early competence window. *Genes Dev.* **20**, 429–434 (2006).
17. Tran, K. D. & Doe, C. Q. Pdm and *Castor* close successive temporal identity windows in the neuroblast 3–1 lineage. *Development* **135**, 3491–3499 (2008).
18. Kao, C. F., Yu, H. H., He, Y., Kao, J. C. & Lee, T. Hierarchical deployment of factors regulating temporal fate in a diverse neuronal lineage of the *Drosophila* central brain. *Neuron* **73**, 677–684 (2012).
19. Elliott, J., Jolicœur, C., Ramamurthy, V. & Cayouette, M. Ikaros confers early temporal competence to mouse retinal progenitor cells. *Neuron* **60**, 26–39 (2008).
20. Fischbach, K. F. & Dittich, A. P. M. The optic lobe of *Drosophila melanogaster*. I. A Golgi analysis of wild-type structure. *Cell Tissue Res.* **258**, 441–475 (1989).
21. Morante, J. & Desplan, C. The color-vision circuit in the medulla of *Drosophila*. *Curr. Biol.* **18**, 553–565 (2008).
22. Egger, B., Boone, J. Q., Stevens, N. R., Brand, A. H. & Doe, C. Q. Regulation of spindle orientation and neural stem cell fate in the *Drosophila* optic lobe. *Neural Dev.* **2**, 1 (2007).
23. Yasugi, T., Umetsu, D., Murakami, S., Sato, M. & Tabata, T. *Drosophila* optic lobe neuroblasts triggered by a wave of proneural gene expression that is negatively regulated by JAK/STAT. *Development* **135**, 1471–1480 (2008).
24. Yasugi, T., Sugie, A., Umetsu, D. & Tabata, T. Coordinated sequential action of EGFR and Notch signaling pathways regulates proneural wave progression in the *Drosophila* optic lobe. *Development* **137**, 3193–3203 (2010).

25. Reddy, B. V., Rauskolb, C. & Irvine, K. D. Influence of Fat-Hippo and Notch signaling on the proliferation and differentiation of *Drosophila* optic neuroepithelia. *Development* **137**, 2397–2408 (2010).
26. Egger, B., Gold, K. S. & Brand, A. H. Notch regulates the switch from symmetric to asymmetric neural stem cell division in the *Drosophila* optic lobe. *Development* **137**, 2981–2987 (2010).
27. Ngo, K. T. *et al.* Concomitant requirement for Notch and Jak/Stat signaling during neuro-epithelial differentiation in the *Drosophila* optic lobe. *Dev. Biol.* **346**, 284–295 (2010).
28. Nassif, C., Noveen, A. & Hartenstein, V. Early development of the *Drosophila* brain: III. The pattern of neuropile founder tracts during the larval period. *J. Comp. Neurol.* **455**, 417–434 (2003).
29. Ceron, J., Gonzalez, C. & Tejedor, F. J. Patterns of cell division and expression of asymmetric cell fate determinants in postembryonic neuroblast lineages of *Drosophila*. *Dev. Biol.* **230**, 125–138 (2001).
30. Morante, J., Erclik, T. & Desplan, C. Cell migration in *Drosophila* optic lobe neurons is controlled by *eyeless/Pax6*. *Development* **138**, 687–693 (2011).
31. Hasegawa, E. *et al.* Concentric zones, cell migration and neuronal circuits in the *Drosophila* visual center. *Development* **138**, 983–993 (2011).
32. Grossniklaus, U., Pearson, R. K. & Gehring, W. J. The *Drosophila* sloppy paired locus encodes two proteins involved in segmentation that show homology to mammalian transcription factors. *Genes Dev.* **6**, 1030–1051 (1992).
33. Sato, A. & Tomlinson, A. Dorsal–ventral midline signaling in the developing *Drosophila* eye. *Development* **134**, 659–667 (2007).
34. Maurange, C., Cheng, L. & Gould, A. P. Temporal transcription factors and their targets schedule the end of neural proliferation in *Drosophila*. *Cell* **133**, 891–902 (2008).
35. Soustelle, L. & Giangrande, A. Novel *gcm*-dependent lineages in the postembryonic nervous system of *Drosophila melanogaster*. *Dev. Dyn.* **236**, 2101–2108 (2007).
36. Colonques, J., Ceron, J. & Tejedor, F. J. Segregation of postembryonic neuronal and glial lineages inferred from a mosaic analysis of the *Drosophila* larval brain. *Mech. Dev.* **124**, 327–340 (2007).
37. Skeath, J. B. & Doe, C. Q. Sanpodo and Notch act in opposition to Numb to distinguish sibling neuron fates in the *Drosophila* CNS. *Development* **125**, 1857–1865 (1998).
38. Truman, J. W., Moats, W., Altman, J., Marin, E. C. & Williams, D. W. Role of Notch signaling in establishing the hemilineages of secondary neurons in *Drosophila melanogaster*. *Development* **137**, 53–61 (2010).
39. Lin, S. *et al.* Lineage-specific effects of Notch/Numb signaling in post-embryonic development of the *Drosophila* brain. *Development* **137**, 43–51 (2010).
40. Hasegawa, E., Kaido, M., Takayama, R. & Sato, M. Brain-specific-homeobox is required for the specification of neuronal types in the *Drosophila* optic lobe. *Dev. Biol.* **1**, 90–99 (2013).
41. Kohwi, M., Lupton, J. R., Lai, S. L., Miller, M. R. & Doe, C. Q. Developmentally regulated subnuclear genome reorganization restricts neural progenitor competence in *Drosophila*. *Cell* **152**, 97–108 (2013).
42. Hanashima, C., Li, S. C., Shen, L., Lai, E. & Fishell, G. *Foxg1* suppresses early cortical cell fate. *Science* **303**, 56–59 (2004).
43. Kosman, D., Small, S. & Reinitz, J. Rapid preparation of a panel of polyclonal antibodies to *Drosophila* segmentation proteins. *Dev. Genes Evol.* **208**, 290–294 (1998).

Supplementary Information is available in the online version of the paper.

Acknowledgements We thank the fly community and the modENCODE team for gifts of antibodies and fly stocks. K. White, N. Negre, D. Vasiliauskas and R. Johnston contributed to screening the modENCODE antibodies. Special thanks to C.-H. Lee for sharing unpublished information and the *OrtC1-gal4* line. We thank R. Mann for suggestions and reagents; and Desplan laboratory members for discussion and support, especially R. Johnston, D. Vasiliauskas and N. Neriec for critically reading the manuscript. This work was supported by National Institutes of Health (NIH) grant R01 Ey017916 to C.D.; The Robert Leet and Clara Guthrie Patterson Trust Postdoctoral Fellowship to X.L.; The Canadian Institutes of Health Research (CIHR) to T.E.; fellowships from EMBO (ALTF 680-2009) and HFSP (LT000077/2010-L) to C.B.; NIH grant GM058575 and a Career Development fellowship from the Leukemia and Lymphoma Society to R.V.

Author Contributions C.D. planned the project and analysed the data together with X.L. and T.E.; T.E., X.L. and C.B. performed the antibody screen; X.L. conducted experiments with Hth, Ey, Slp and Tll neuroblasts as well as Ap and the Notch pathway; T.E. analysed the D neuroblasts; Z.C. generated the *OrtC1-gal4* flip-out and MARCM clones; R.V. generated the *eyBAC* rescue construct and stocks; S.V. examined Slp2 expression; A.C. identified the *AC225-gal4* line and J.M. defined its expression in the transition from neuroepithelium to neuroblast. The manuscript was written by X.L. and C.D., and all authors commented on it.

Author Information Reprints and permissions information is available at www.nature.com/reprints. The authors declare no competing financial interests. Readers are welcome to comment on the online version of the paper. Correspondence and requests for materials should be addressed to C.D. (cd38@nyu.edu).

METHODS

Antibodies and immunostaining. We screened ~200 antibodies against transcription factors from various sources including: the polyclonal antibody collection against *Drosophila* segmentation proteins⁴³; gifts from the fly community; Developmental Studies Hybridoma Bank (DSHB); and a collection of antibodies generated by the modENCODE⁴⁴ project that were provided by N. Negre and K. White. The positive ones among them, and other antibodies used in this work, include rabbit anti Slp1 (1:200) and guinea pig anti Tll (1:200) (segmentation antibodies); rabbit anti-D (1:100) (modENCODE); rabbit anti-Hth (1:500) (from R. Mann), rat anti-Slp1 (1:200) and rat anti-Slp2 (1:200) (from K. Cadigan), guinea-pig anti-D (1:50) (from J. R. Nambu), rabbit anti-DPN (1:500) (from Y.-N. Jan), guinea-pig anti-Dpn (1:1,000), guinea-pig anti-Lim3 (1:250) (from J. Skeath), rat anti-Ap (1:200) (from J. Thomas), guinea-pig anti-Bsh and rat anti-Dfr (from M. Sato), guinea-pig anti-Toy (1:500) (from U. Walldorf); mouse anti-Ey (1:10) (from P. Callaerts and DSHB), mouse anti-Pros (1:10), mouse anti-Repo (1:50), 24B10 (1:20), rat anti DE-cadherin (1:20), rat anti DN-cadherin (1:50) and mouse anti-Dac (1:20) (all from DSHB); sheep anti-GFP (1:500, AbD Serotec), and chick anti- β -gal (1:200, Gallus Immunotech). Secondary antibodies are from Jackson or Invitrogen.

Immunostaining was done as described⁴⁵ with a few modifications. Larval brains or adult brains were dissected in 1× PBS, and fixed in 4% formaldehyde for 30 min (larval) or 45 min (adult) on ice. Brains were incubated in primary antibody solution overnight at 4 °C, washed three times and incubated in secondary antibody solution overnight at 4 °C, washed three times and mounted in Slowfade. Images are acquired using a Leica SP5 confocal. Figures are assembled using Photoshop and Illustrator.

Genetics and fly strains. Canton S is used as wild-type controls. To generate *hth* mutant MARCM clones, flies of *y,w,hsFLP,UAS-CD8::GFP*; ; *tub-gal4, FRT82B, tub-gal80/TM6B* were crossed with *FRT82B, hth^{P2}/TM6B* or *FRT82B, hth¹⁰⁰⁻¹/TM6B* flies (gifts from R. Mann). To generate *exd* mutant MARCM clones, flies of *FRT19A, tub-gal80, hsFLP; UAS-LacZ/CyO*; *tub-gal4/TM6B* were crossed with *FRT19A, exd¹/FM7C* flies (gift from R. Mann). The null mutant of *ey*: *yw; ey^{5.71}/In(4)ciD* was obtained from Bloomington. To generate *slp* mutant MARCM clones, flies of *y,w,hsFLP,UAS-CD8::GFP; FRT40A, tub-gal80; tub-gal4/TM6B* were crossed with *FRT40A, slp^{S37A}/SM6-TM6B* flies (gift from A. Tomlinson). To generate *D* mutant clones, *y,w,hsFLP*; ; *FRT2A, ubi-GFP* was crossed with *FRT2A, D⁸⁷* mutant flies (gift from J. Nambu). To generate *tll* mutant clones, *w; FRT82B, tll¹⁴⁹/TM3* (from M. Kurusu) was crossed with *y,w,hsFLP,UAS-CD8::GFP*; ; *tub-gal4, FRT82B, tub-gal80/TM6B* flies. To generate wild-type or *Su(H)* mutant MARCM clones, flies of *y,w,hsFLP,UAS-CD8::GFP; FRT40A, tub-gal80; tub-gal4/TM6B* were crossed with *FRT40A* or *FRT40A, Su(H)⁴⁴⁷/CyO* flies (gift from F. Schweisguth). For these mutant clones, the progeny were heat-shocked at 37 °C at early larvae stage, and dissected at wandering third instar stage or white pupae stage.

For targeted *ey* RNAi, *Vsx-Gal4* was used to drive two *UAS-ey-RNAi* transgenes (*UAS-ey-RNAi-JF02501* from Bloomington, and *UAS-ey-RNAi-kk107100* from VDRC stock centre) together with *UAS-Dcr-2*.

We used *1407a-gal4* (an insertion into the *inscuteable* locus)⁴⁶, combined with *tub-gal80^{ts}* to drive *UAS-GFP::Hth*, *UAS-Ey* (from Bloomington), *UAS-Slp1* (from A. Tomlinson and G. Struhl), *UAS-D* (from J. Nambu) or *UAS-Tll* (from M. Kurusu) in all neuroblasts, and the progeny were shifted from 18 °C to 29 °C 4 days before dissection of the wandering third instar larvae. For gain of function of *Slp2*, *UAS-Slp2* (from M. Leptin) was crossed with *y,w,hsFLP; UASLacZ; act>y+>gal4*, and the progeny were heat-shocked for 8 min at 37 °C 3 days before dissection of the wandering third instar larvae. For gain-of-function of *Slp1*, flies of *y,w; UAS-Slp1; FRT82B* (from A. Tomlinson and G. Struhl) was

crossed with *y,w,hsFLP,UAS-CD8::GFP*; ; *tub-gal4, FRT82B, tub-gal80 /TM6B* flies, and the progeny were heat-shocked for 1 h at 37 °C 3 days before dissection of the wandering third instar larvae.

To generate *OrtC1-Gal4* wild-type or *slp* mutant MARCM clones, virgin females of *y,w,hsFLP,UAS-CD8::GFP; FRT40A, tub-gal80/CyO*; *OrtC1-gal4, UAS-CD8::GFP/Tm2* (gift from C.-H. Lee) were crossed with *FRT40A/CyO* or *FRT40A, slp^{S37A}/CyO* males. The progeny were heat-shocked at 37 °C at early larval stage for 1 h, and the adult male progeny with the correct genotype were dissected and stained. To generate *OrtC1-Gal4* flip-out clones, *y,w; OrtC1-gal4/CyO; OrtC1-gal4/TM3* (gift from C.-H. Lee) were crossed with *UAS-FRT-STOP-FRT-CD8::GFP*, and the progeny were heat-shocked at late pupal stage, and dissected in the adult stage.

Other strains used include '*ap^{md544}-gal4*', '*ap^{rk568}-lacZ*' (ref. 47), '*yw; act-FRT-STOP-FRT-lacZ*', *UAS-FLP*, and '*UAS-Red-Stinger, UAS-FLP, ubi-FRT-STOP-FRT-NuGFP*' (G-TRACE)⁴⁸.

Generation of *ey* mutant clones by BAC rescue. A BAC that contains the *ey* genomic region (CH321-01A12, BacPac Resources) was inserted by PhiC31 transgenesis on chromosome 3L in attP site *PBac{y+ -attP-3B}VK00031*. The resulting transgenic flies were tested for rescue of the *ey* null allele *ey^{15.71}*. Subsequently, this *ey* BAC insertion was recombined with *FRT80B (P{neoFRT}80B)* and *Ubi-GFP (P{Ubi-GFP(S65T)nl3}3L)*. This chromosome arm was used to generate the strain *y,w,hsFLP; FRT80B, eyBAC, Ubi-GFP/TM6B,Tb; ey^{15.71}* that served as a wild-type copy of *ey* on the third chromosome. To generate mitotic clones this strain was crossed to flies with genotype *hsFLP; FRT80B; ey^{15.71}/In(4)ciD^{c1}, ciD^{c1} pan^{ciD} sv^{pa-pol}*, and the progeny were heat shocked for 1 h at 37 °C 3 days before dissection of the wandering third instar larvae. Clones in larvae that lacked both GFP fluorescence and staining with an anti-Ey antibody were further analysed.

Generation of single-neuroblast clones. Larvae of the genotype *AC225-gal4* (which is expressed in the neuroepithelium-to-neuroblast transition), *tub-gal80^{ts}*, *UAS-FLP* and *act-FRT-STOP-FRT-nuLacZ* were grown at 18 °C, and shifted to 29 °C for 15 min to inactivate *tub-gal80^{ts}* only in scattered newly generated neuroblasts, and after another 3–6 days at 18 °C, the wandering third instar larvae were dissected and stained.

Generation of two-cell clones. Two methods were used. One is twin-spot MARCM¹⁰ (see Supplementary Fig. 3). The flies of *elav-gal4; FRT40A,UAS-CD8::GFP,UAS-rCD2-miRNA/CyO,y+* were crossed with *hsFLP; FRT40A, UAS-rCD2RFP,UAS-GFP-miRNA/CyO,y+* (gifts from T. Lee), and the progeny larvae were heat-shocked at 37 °C for 8 min, and dissected 2 days later as wandering third instar larvae; The other method that was used for Fig. 4c was to treat the larvae with the genotype of *pros-gal4* (that is expressed in GMCs), *tub-gal80^{ts}*, *UAS-FLP* and *ubi-FRT-STOP-FRT-nuGFP* at 29 °C for 1 h to inactivate *tub-gal80^{ts}* only in scattered GMCs, and to perform the staining 2 days later on wandering third instar larvae. Only scattered GMCs flip out the STOP cassette, and transmit the GFP to the two daughters.

44. Roy, S. et al. Identification of functional elements and regulatory circuits by *Drosophila* modENCODE. *Science* **330**, 1787–1797 (2010).
45. Morante, J. & Desplan, C. Dissection and staining of *Drosophila* optic lobes at different stages of development. *Cold Spring Harb. Protoc.* **2011**, 653–656 (2011).
46. Luo, L., Liao, Y. J., Jan, L. Y. & Jan, Y. N. Distinct morphogenetic functions of similar small GTPases: *Drosophila* Drac1 is involved in axonal outgrowth and myoblast fusion. *Genes Dev.* **8**, 1787–1802 (1994).
47. Cohen, B., McGuffin, M. E., Pfeifle, C., Segal, D. & Cohen, S. M. *apterous*, a gene required for imaginal disc development in *Drosophila* encodes a member of the LIM family of developmental regulatory proteins. *Genes Dev.* **6**, 715–729 (1992).
48. Evans, C. J. et al. G-TRACE: rapid Gal4-based cell lineage analysis in *Drosophila*. *Nature Methods* **6**, 603–605 (2009).

Multi-periodic pulsations of a stripped red-giant star in an eclipsing binary system

Pierre F. L. Maxted¹, Aldo M. Serenelli², Andrea Miglio³, Thomas R. Marsh⁴, Ulrich Heber⁵, Vikram S. Dhillon⁶, Stuart Littlefair⁶, Chris Copperwheat⁷, Barry Smalley¹, Elmé Breedt⁴ & Veronika Schaffenroth^{5,8}

Low-mass white-dwarf stars are the remnants of disrupted red-giant stars in binary millisecond pulsars¹ and other exotic binary star systems^{2–4}. Some low-mass white dwarfs cool rapidly, whereas others stay bright for millions of years because of stable fusion in thick surface hydrogen layers⁵. This dichotomy is not well understood, so the potential use of low-mass white dwarfs as independent clocks with which to test the spin-down ages of pulsars^{6,7} or as probes of the extreme environments in which low-mass white dwarfs form^{8–10} cannot fully be exploited. Here we report precise mass and radius measurements for the precursor to a low-mass white dwarf. We find that only models in which this disrupted red-giant star has a thick hydrogen envelope can match the strong constraints provided by our data. Very cool low-mass white dwarfs must therefore have lost their thick hydrogen envelopes by irradiation from pulsar companions^{11,12} or by episodes of unstable hydrogen fusion (shell flashes). We also find that this low-mass white-dwarf precursor is a type of pulsating star not hitherto seen. The observed pulsation frequencies are sensitive to internal processes that determine whether this star will undergo shell flashes.

Most white dwarfs have no internal energy sources and the mass of hydrogen on their surfaces is small (less than 10^{-4} solar masses) so their ‘cooling age’ can be accurately estimated from their current luminosity. The predicted mass range for which shell flashes at the base of the hydrogen envelope occur in low-mass white dwarfs depends on the assumed composition and whether diffusion is included in the model^{13–15}, so it is generally possible to find a scenario for a particular binary millisecond pulsar in which the white-dwarf cooling age is consistent with the pulsar’s spin-down age (inferred from the derivative of its spin period, assuming that angular momentum is

lost by magnetic dipole radiation). However, recent observations have shown that the white-dwarf companion to the pulsar PSR J0751+1807 is much too cool to have a thick hydrogen envelope, yet the white dwarf is not massive enough to have undergone shell flashes and there is no evidence for strong irradiation by the pulsar¹⁶. The standard assumptions used to derive pulsar spin-down ages have also been called into question^{17,18}. A better understanding of the initial hydrogen layer mass and its evolution in low-mass white dwarfs is needed so that we can make an independent test of the spin-down ages for pulsars.

Before becoming low-mass white dwarfs, stripped red-giant stars evolve at nearly constant luminosity towards higher effective temperatures. 1SWASP J024743.37–251549.2 (called J0247–25 herein) was recently discovered to be a binary system in which a star in this rarely observed evolutionary phase (J0247–25B) is totally eclipsed by its companion star (J0247–25A)¹⁹. We have obtained new spectroscopic and photometric observations (Fig. 1) and used these to derive precise astrophysical parameters for both stars (Table 1).

The mass, radius and luminosity of J0247–25A are well matched by models of stars with a metal abundance in the range $Z = 0.004$ – 0.019 , but not for models outside this range (Fig. 2). We have calculated models for the formation of J0247–25B by mass transfer onto the companion star (Fig. 2). We assumed that the mass loss rate is slower than the thermal timescale of the star, so that mass transfer ceases when the equilibrium radius of the star is smaller than the Roche lobe. This is the assumption usually made in the absence of a detailed understanding of the mass loss process^{5,10,15,20}. Diffusion of elements by gravitational settling, chemical diffusion and thermal diffusion are included in our models. We also calculated models without diffusion to investigate the effects of processes such as rotation that may counteract diffusion. The mass of J0247–25B is near the lower limit for the occurrence of shell flashes—these will occur if its metal abundance is high enough ($Z \approx 0.01$) and diffusion can increase the hydrogen abundance in the regions where shell flashes can be initiated.

There is a direct relationship between orbital period, mass and composition that arises from the assumption that the mass-losing star is in equilibrium when mass transfer ceases²⁰. We find a good match to the observed orbital period of J0247–25 for models with a similar range of metal abundance to that of J0247–25A, but not for models outside this composition range (Supplementary Table 5). This result is not strongly affected by the assumptions made about the evolution of the binary system during the mass transfer episode.

All the models that provide a good match to the observed properties of J0247–25B have thick hydrogen envelopes (about 0.005 solar masses). We did produce models for J0247–25B with thin hydrogen envelopes but found that for any reasonable estimate of the composition these models never have properties like J0247–25B. Given the strong observational constraints on the mass, radius, luminosity, age, orbital period and composition for J0247–25 and the pulsation

Table 1 | Properties of J0247–25

Parameter	J0247–25A	J0247–25B
Mass (solar masses)	1.356 ± 0.007	0.186 ± 0.002
Radius (solar radii)	1.697 ± 0.011	0.368 ± 0.005
Effective temperature (K)	$7,730 \pm 200$	$11,380 \pm 400$
log[Luminosity (solar luminosities)]	0.97 ± 0.05	0.31 ± 0.06
log[Surface gravity (cm s^{-2})]	4.111 ± 0.006	4.576 ± 0.011
$v_{\text{rot}} \sin i$ (km s^{-1})	95 ± 5	30 ± 3
Inclination (degrees)		87.3 ± 0.9
Orbital period (days)		0.6678295 ± 0.0000004
Time of mid-eclipse (TDB)		$2,454,454.1066 \pm 0.0002$
Distance (pc)		$1,035 \pm 55$

The masses and radii were derived from an analysis of our Ultracam photometry and UVES spectroscopy (Fig. 1, Supplementary Notes and Supplementary Table 2). The time of mid-eclipse is Barycentric Dynamical Time (TDB) given as a Julian date. We measured the effective temperatures of the stars by fitting models to the observed flux distribution of the binary from ultraviolet to infrared wavelengths, simultaneously with the constraints on the surface brightness ratio and luminosity ratio at the I_c band from the analysis of the eclipses (Supplementary Table 4 and Supplementary Fig. 4). The projected equatorial rotation velocity $v_{\text{rot}} \sin i$ is measured from the Doppler broadening of the spectral lines (Supplementary Figs 3 and 5).

¹Astrophysics Group, Keele University, Keele, Staffordshire ST5 5BG, UK. ²Instituto de Ciencias del Espacio (CSIC-IEEC), Facultat de Ciències, Campus UAB, Bellaterra 08193, Spain. ³School of Physics and Astronomy, University of Birmingham, Edgbaston, Birmingham B15 2TT, UK. ⁴Department of Physics, University of Warwick, Coventry CV4 7AL, UK. ⁵Dr Karl Remeis Observatory and ECAP, Astronomical Institute, Friedrich-Alexander University Erlangen-Nuremberg, Sternwartstrasse 7, 96049 Bamberg, Germany. ⁶Department of Physics and Astronomy, University of Sheffield, Sheffield S3 7RH, UK.

⁷Astrophysics Research Institute, Liverpool John Moores University, Twelve Quays House, Egerton Wharf, Birkenhead, Wirral CH41 1LD, UK. ⁸Institute for Astrophysics and Particle Physics, University of Innsbruck, Technikerstrasse 25/8, 6020 Innsbruck, Austria.

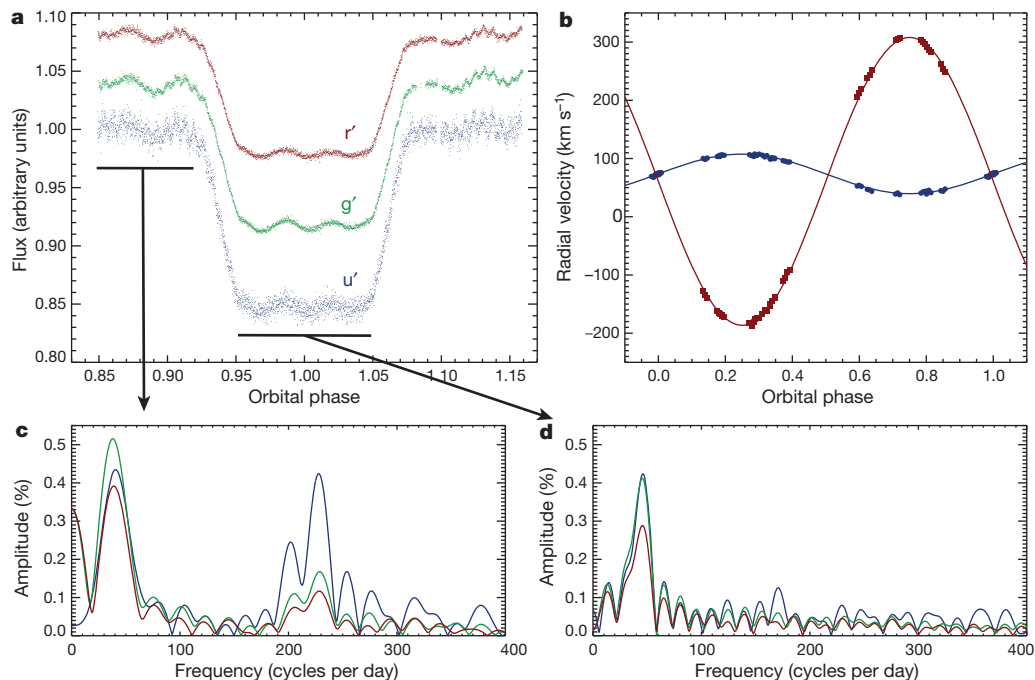


Figure 1 | Observations of J0247-25. **a**, Flux as a function of orbital phase for one primary eclipse of J0247-25 observed with Ultracam²⁶ on the 3.6-m New Technology Telescope at the European Southern Observatory (ESO). From bottom to top: u' band (356 nm), g' band (483 nm, offset by 0.04 units) and r' band (626 nm, offset 0.08 units). Each point corresponds to an integration time of 5 s. The primary eclipse is caused by the occultation of J0247-25B by the larger, cooler star J0247-25A. A secondary eclipse due to the transit of J0247-25B and a second primary eclipse were also observed (Supplementary Table 1). **b**, Radial velocity as a function of orbital phase for J0247-25A (circles) and J0247-25B (squares) measured from high-resolution spectra obtained with the Ultraviolet and Visual Echelle Spectrograph (UVES) on the ESO 8.2-m Very

Large Telescope. Solid lines show the predicted radial velocities for a circular orbit and our adopted values of the radial velocity semi-amplitudes, $K_A = 33.9 \text{ km s}^{-1}$ and $K_B = 247.2 \text{ km s}^{-1}$. **c**, Power spectra of the data shown in panel **a** (arrow) before eclipse (phase range, 0.85–0.92). The peaks near 240 cycles per day have the highest amplitude at u' band and the lowest amplitude at r' band. **d**, Power spectra of the data shown in panel **a** (arrow) obtained during total eclipse (phase range 0.95–1.05). The peaks near 220 cycles per day with amplitudes of 0.15% to 0.4% do not appear in the power spectrum during the eclipse and so must originate from J0247-25B. The pulsations near 40 cycles per day originate in J0247-25A, so this must be an SX Phe-type star (a metal-poor δ -Scuti star).

properties predicted by these models discussed below, we conclude that only models in which low-mass white dwarfs are born with thick hydrogen envelopes can match the observed properties of J0247-25B.

J0247-25B pulsates with at least three different frequencies around 2,500 μHz (Supplementary Fig. 2 and Supplementary Table 3). We have assessed the potential of this new class of pulsating star for asteroseismology, that is, for the study of the interior structure of stripped red giants based on an analysis of their pulsation frequencies. We have used the adiabatic approximation to calculate potential oscillation frequencies for our models of J0247-25B (Fig. 3). These calculations show that the observed frequencies are a mixture of radial modes and non-radial modes. The identification of the radial-mode frequencies

and of the angular degree l for the non-radial modes is required before the observed frequencies can be used for asteroseismology. Standard techniques exist to identify modes, although these identifications can be model dependent. The identification of modes from the analysis of the eclipses in an eclipsing binary like J0247-25 provides a rare opportunity to test standard mode identification techniques^{21,22}.

The non-radial modes in J0247-25B behave like gravity modes near the core and like pressure modes in the outer layers of the star. These mixed modes can be used to study the entire structure of the star: for example, to measure its internal rotation profile^{23,24}. Information on the interior structure of J0247-25B is also contained in the radial modes (Fig. 3). The pulsation periods are comparable to the thermal relaxation timescale in the second partial ionization zone of helium, so the change in opacity in this region (acting like a heat engine) may be driving these oscillations (the κ -mechanism). This suggests that other

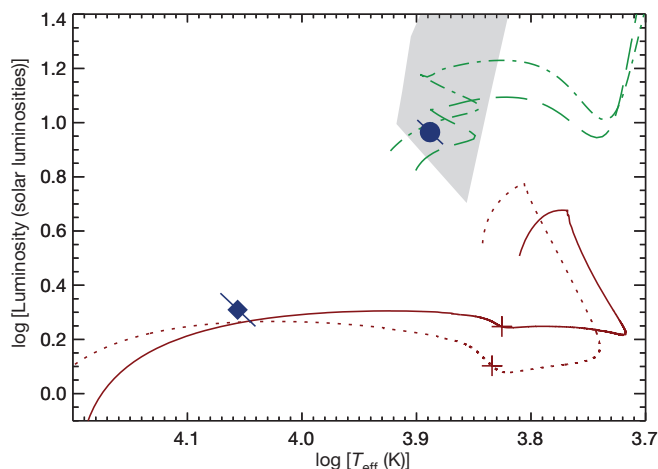


Figure 2 | Positions of J0247-25A and J0247-25B in the Hertzsprung–Russell diagram. J0247-25A is plotted as a filled circle, and J0247-25B as a filled diamond. The error on the luminosity is correlated with the effective temperature (T_{eff}) so the error range (1 s.d.) is plotted as a diagonal line. Two of our models for the formation of J0247-25B are shown, one including the effects of diffusion ($Z = 0.004$, solid line, final mass is 0.187 solar masses) and one without ($Z = 0.002$, dotted line, final mass is 0.185 solar masses). These models are plotted from the initiation of mass transfer at $\log[T_{\text{eff}}(\text{K})] \approx 3.8$, $\log[\text{Luminosity (solar luminosities)}] \approx 0.5$. The cross on each track marks the end of the mass transfer phase. A model for a star with a mass of 1.35 solar masses and a composition typical for thick-disk stars ($[\text{Fe}/\text{H}] = -1.0$, $[\alpha/\text{Fe}] = +0.6$, $Z = 0.005$) is plotted with a dashed line²⁷. A similar model for stars with $[\text{Fe}/\text{H}] = 0.0$ and a very high helium abundance ($Y = 0.4$, $Z = 0.019$) is plotted with a dot-dashed line. No match is found for any models with metal abundance outside the range $Z = 0.004$ –0.019. The instability strip for δ -Scuti-type pulsations with radial order $k = 4$ is indicated by light-grey shading²⁸.

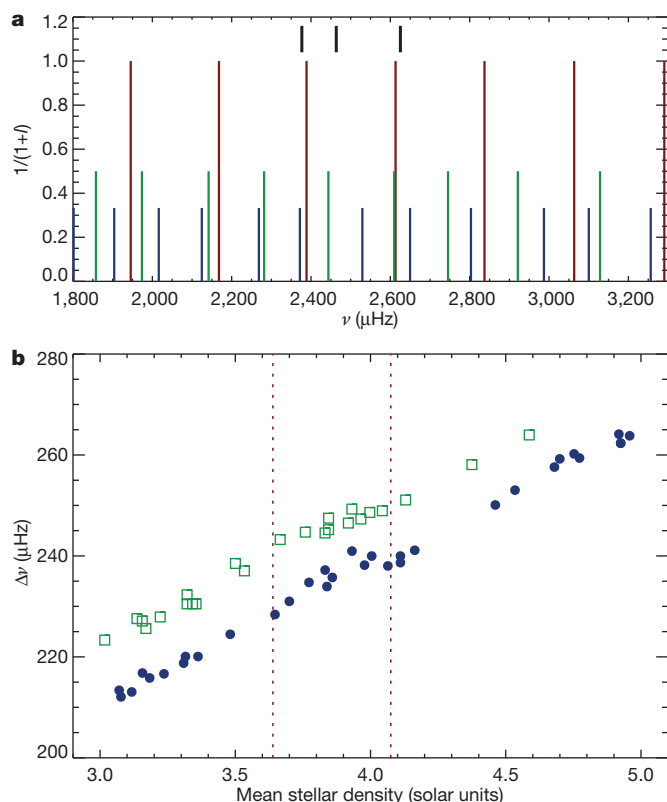


Figure 3 | Adiabatic pulsation frequencies for models of J0247-25B.

a, Pulsation frequencies for radial oscillation modes ($l = 0$) and non-radial modes with angular degree $l = 1$ and $l = 2$ calculated using the adiabatic approximation for a model of a star similar to J0247-25B. Short lines at the top of the plot indicate the observed pulsation frequencies of J0247-25B. The spacing of the three frequencies shown cannot be explained using radial modes only. The order of the radial modes shown is $k \approx 10$. **b**, The frequency spacing between two adjacent radial modes, $\Delta\nu$, as a function of the mean stellar density for models of J0247-25B with $Z = 0.0005$ – 0.004 . The results for models with and without diffusion are shown using filled and open symbols, respectively. The value of $\Delta\nu$ shown here is the mean value in the region of the theoretical power spectrum near the observed frequencies for J0247-25B. The difference in $\Delta\nu$ between models with and without diffusion is a result of the sharp change in the speed of sound in the second partial ionization zone for helium, due to the high helium abundance in this zone ($Y \approx 0.6$) for models without diffusion. The measured density of J0247-25B indicated using vertical dotted lines (± 1 s.d.), can be measured to high precision in this bright eclipsing binary star. As a result, models with and without diffusion can be distinguished if two of the observed pulsation frequencies are found to be radial modes.

low-mass white-dwarf precursors²⁵ with effective temperatures similar to J0247-25B may also show pulsations. Thus, the discovery of pulsations in J0247-25B opens up the possibility for a much-improved understanding of the structure and formation of low-mass white dwarfs and their environments through the application of asteroseismology to this new class of pulsating variable stars.

Received 19 September 2012; accepted 15 April 2013.

1. Lorimer, D. R. Binary and millisecond pulsars. *Liv. Rev. Rel.* **11**, 8 (2008).
2. Kilic, M. *et al.* The ELM Survey. II. Twelve binary white dwarf merger systems. *Astrophys. J.* **727**, 3 (2011).
3. Breton, R. P., Rappaport, S. A., van Kerkwijk, M. H. & Carter, J. A. KOI 1224: a fourth bloated hot white dwarf companion found with Kepler. *Astrophys. J.* **748**, 115 (2012).
4. Hermes, J. J., Kilic, M., Brown, W. R., Montgomery, M. H. & Winget, D. E. Two new tidally distorted white dwarfs. *Astrophys. J.* **749**, 42 (2012).
5. Webbink, R. F. Evolution of helium white dwarfs in close binaries. *Mon. Not. R. Astron. Soc.* **171**, 555–568 (1975).

6. Kiziltan, B. & Thorsett, S. E. Millisecond pulsar ages: implications of binary evolution and a maximum spin limit. *Astrophys. J.* **715**, 335–341 (2010).
7. van Kerkwijk, M. H., Bassa, C. G., Jacoby, B. A. & Jonker, P. G. Optical studies of companions to millisecond pulsars. *Astron. Soc. Pacif. Conf. Ser.* **328**, 357–370 (2005).
8. Gezari, S. *et al.* An ultraviolet-optical flare from the tidal disruption of a helium-rich stellar core. *Nature* **485**, 217–220 (2012).
9. Knigge, C. *et al.* Stellar exotica in 47 Tucanae. *Astrophys. J.* **683**, 1006–1030 (2008).
10. Strickler, R. R. *et al.* Helium-core white dwarfs in the globular cluster NGC 6397. *Astrophys. J.* **699**, 40–55 (2009).
11. Ergma, E., Sarna, M. J. & Gerškevičs-Antipova, J. The helium white dwarf in two pulsars: too cool in PSR J0751+1807 and too hot in PSR J1012+5307? *Mon. Not. R. Astron. Soc.* **321**, 71–76 (2001).
12. Breton, R. P. *et al.* Discovery of the optical counterparts to four energetic Fermi millisecond pulsars. *Astrophys. J.* **769**, 108 (2013).
13. Althaus, L. G., Serenelli, A. M. & Benvenuto, O. G. Diffusion and the occurrence of hydrogen-shell flashes in helium white dwarf stars. *Mon. Not. R. Astron. Soc.* **323**, 471–483 (2001).
14. Driebe, T., Schönberner, D., Blöcker, T. & Herwig, F. The evolution of helium white dwarfs. I. The companion of the millisecond pulsar PSR J1012+5307. *Astron. Astrophys.* **339**, 123–133 (1998).
15. Iben, I. Jr & Tutukov, A. V. On the formation and evolution of a helium degenerate dwarf in a close binary. *Astrophys. J.* **311**, 742–752 (1986).
16. Bassa, C. G., van Kerkwijk, M. H. & Kulkarni, S. R. The ultra-cool white dwarf companion of PSR J0751+1807. *Astron. Astrophys.* **450**, 295–303 (2006).
17. Espinoza, C. M., Lyne, A. G., Kramer, M., Manchester, R. N. & Kaspi, V. M. The braking index of PSR J1734–3333 and the magnetar population. *Astrophys. J.* **741**, L13 (2011).
18. Noutsos, A., Schnitzeler, D., Keane, E., Kramer, M. & Johnston, S. Pulsar spin-velocity alignment: kinematic ages, birth periods and braking indices. *Mon. Not. R. Astron. Soc.* **430**, 2281–2301 (2013).
19. Maxted, P. F. L. *et al.* Discovery of a stripped red giant core in a bright eclipsing binary system. *Mon. Not. R. Astron. Soc.* **418**, 1156–1164 (2011).
20. Nelson, L. A., Dubeau, E. & MacCannell, K. A. Evolutionary properties of helium-rich, degenerate dwarfs in binaries containing compact companions. *Astrophys. J.* **616**, 1124–1147 (2004).
21. Bíró, I. B. & Nuspl, J. Photometric mode identification methods of non-radial pulsations in eclipsing binaries—I. Dynamic eclipse mapping. *Mon. Not. R. Astron. Soc.* **416**, 1601–1615 (2011).
22. Aerts, C., Christensen-Dalsgaard, J. & Kurtz, D. W. *Asteroseismology* Ch. 6 (Springer, 2010).
23. Beck, P. G. *et al.* Fast core rotation in red-giant stars as revealed by gravity-dominated mixed modes. *Nature* **481**, 55–57 (2012).
24. Dupret, M.-A. *et al.* Asteroseismology of the β Cep star HD 129929. II. Seismic constraints on core overshooting, internal rotation and stellar parameters. *Astron. Astrophys.* **415**, 251–257 (2004).
25. Maxted, P. F. L. *et al.* Discovery of a stripped red-giant core in a bright eclipsing binary star. In *Fifth Meeting on Hot Subdwarf Stars and Related Objects* ASP Conf. Ser. Vol. 452, 137–146 (Astronomical Society of the Pacific, 2012).
26. Dhillion, V. *et al.* ULTRACAM: an ultrafast, triple-beam CCD camera for high-speed astrophysics. *Mon. Not. R. Astron. Soc.* **378**, 825–840 (2007).
27. Dotter, A. *et al.* The Dartmouth Stellar Evolution Database. *Astrophys. J.* **178** (Supp.), 89–101 (2008).
28. Dupret, M.-A., Grigahcène, A., Garrido, R., Gabriel, M. & Scuflaire, R. Theoretical instability strips for δ Scuti and γ Doradus stars. *Astron. Astrophys.* **414**, L17–L20 (2004).

Supplementary Information is available in the online version of the paper.

Acknowledgements We thank the ESO staff who obtained our UVES data for carefully scheduling the observations at the correct orbital phases. We thank A. Cherman and D. Kurtz for comments on a draft version of the paper. This work is based on observations collected at the ESO, Chile (program ID: 086.D-0194). A.M.S. is partially supported by a Re-integration Grant (PIRG-GA-2009-247732; FP7-People), and a MICINN grant (AYA2011-24704). V.S. acknowledges funding by the Deutsches Zentrum für Luft- und Raumfahrt (grant 50 OR 1110) and by the Erika-Giehl-Stiftung. T.R.M. acknowledges funding from the UK Science and Technology Facilities Council (ST/I001719/1).

Author Contributions P.F.L.M. analysed the light curves and spectroscopy and wrote the paper. A.M.S. calculated the models of the formation and evolution of J0247-25B. A.M. conducted the investigation into the pulsation properties of J0247-25B. T.R.M. and P.F.L.M. produced the light curves from the Ultracam images. U.H. calculated the synthetic stellar spectra used to check our effective temperature estimates for J0247-25B. T.R.M., V.S.D., S.L. and C.C. are responsible for the operation and maintenance of Ultracam and contributed to the planning and execution of the observations. B.S. calculated the synthetic stellar spectra and performed the comparison with the observed spectra for J0247-25A. V.S. and E.B. contributed to the execution of the observations.

Author Information Reprints and permissions information is available at www.nature.com/reprints. The authors declare no competing financial interests. Readers are welcome to comment on the online version of the paper. Correspondence and requests for materials should be addressed to P.F.L.M. (p.maxted@keele.ac.uk).

Entanglement between light and an optical atomic excitation

L. Li¹, Y. O. Dudin¹ & A. Kuzmich¹

The generation, distribution and control of entanglement across quantum networks is one of the main goals of quantum information science^{1,2}. In previous studies, hyperfine ground states of single atoms or atomic ensembles have been entangled with spontaneously emitted light^{3–6}. The probabilistic character of the spontaneous emission process leads to long entanglement generation times, limiting realized network implementations to just two nodes^{7–10}. The success probability for atom–photon entanglement protocols can be increased by confining a single atom in a high-finesse optical cavity^{11,12}. Alternatively, quantum networks with superior scaling properties could be achieved using entanglement between light fields and atoms in quantum superpositions of the ground and highly excited (Rydberg) electronic states^{2,13,14}. Here we report the generation of such entanglement. The dephasing of the optical atomic coherence is inhibited by state-insensitive confinement of both the ground and Rydberg states of an ultracold atomic gas in an optical lattice¹⁵. Our results pave the way for functional, many-node quantum networks capable of deterministic quantum logic operations between long-lived atomic memories.

Ensembles of ultracold atoms confined in conservative optical potentials are promising candidates for the realization of networks capable of quantum logic operations and long-term storage of quantum states². Such networks should enable intrinsically secure modes of communication¹ and distributed quantum computation³, and allow investigations of quantum phase transitions and entanglement percolation¹⁶. Atoms store quantum information that is transmitted by light, with atom–light entanglement being the key ingredient that underpins the networking protocols^{3–6,11}.

Although weak interactions between ground-level atoms make them ideal memories, implementations of deterministic quantum logic gates and entanglement demand strong atom–atom interactions. For Rydberg atoms of principal quantum number n , effective electric dipoles are larger by a factor of $\sim n^2$ compared to ground-level atoms. The strength of interaction between two atoms, V , is $\propto n^{11}$ in the van der Waals regime^{2,17}. For $n \gtrsim 70$ and atom separations of $\lesssim 10 \mu\text{m}$, $V \gtrsim 1 \text{ MHz}$, allowing entanglement operations in less than $1 \mu\text{s}$ (refs 18, 19). Broad-based efforts have been made to achieve quantum entanglement in mesoscopic ensembles with Rydberg interactions^{13,14,20,21}. Enhanced optical nonlinearity under conditions of electromagnetically induced transparency for Rydberg excitation has been realized²², as has a Rydberg single-photon source relying on the dephasing of multiply excited spin-waves²³. Many-body Rabi oscillations²⁴, interaction-induced spatial correlations of Rydberg atoms^{25,26}, and anti-bunching of light transmitted through the atomic gas^{27,28} have also been reported. In all these studies, ground-level atoms were initially trapped in conservative potentials $U_g(r)$ (here r is the atomic position vector), formed by far-off-resonance optical fields. However, whereas such potentials are attractive for ground atoms, $U_g(r) < 0$, they are generally repulsive for Rydberg atoms, $U_r(r) > 0$ (ref. 29). Therefore, they have to be switched off in order to maintain the coherent character of the

Rydberg excitation process, resulting in fast atom loss and a limited degree of quantum state control.

Building on the proposal of ref. 15, here we report realization of simultaneous, state-insensitive confinement of the ground and Rydberg atoms in the trapping potential of a one-dimensional optical lattice. The lattice wavelengths for which the differential energy shift $\delta U \equiv U_r(r) - U_g(r)$ between ground and Rydberg states is eliminated are called ‘magic’, and in our case they are 1,004 nm or 1,012 nm. The matched trapping potentials preserve the coherence between the ground and Rydberg atomic states, enabling the generation of entanglement of an optical atomic coherence and a light field. As illustrated in Fig. 1, an ensemble of atoms is driven in resonance between the ground atomic level $|g\rangle = |5s_{1/2}\rangle$ and a Rydberg level $|r\rangle = |90s_{1/2}\rangle$. As a result of the Rydberg excitation blockade¹³, the ensemble undergoes a many-body Rabi oscillation between the collective ground state $|G\rangle \equiv \prod_{i=1}^N |g\rangle_i$ and the singly-excited state $|R\rangle \equiv 1/\sqrt{N} \sum_{i=1}^N |g\rangle_{1\dots i} |r\rangle_{i\dots N}$ (ref. 24). By stopping the oscillation at half-period, we prepare the ensemble, in the ideal case, in state $|R\rangle$. This state is coherently mapped into an entangled atom–light state by illuminating the atoms with a retrieval field Ω_A , chosen such that a read-out of about one half of the Rydberg spin-wave into a retrieved field $|\Phi\rangle_A$ occurs: $|R\rangle \rightarrow |R\rangle|0\rangle_A + |G\rangle|1\rangle_A$. A phase dependent measurement of field $|\Phi\rangle_A$ is realized by mixing it with an orthogonally polarized coherent field $|\alpha\rangle_A = |\alpha| \exp(i\phi_A)$ using a beam splitter, with the outgoing (50:50 splitting) fields directed to a pair of single-photon detectors. After a storage period, the remaining atomic spin wave is mapped onto the second retrieved field $|\Phi\rangle_B$, and a phase-dependent measurement is done by mixing it with a coherent field $|\alpha\rangle_B = |\alpha| \exp(i\phi_B)$ and photoelectric detection of the resulting fields by the same single-photon detector pair. Atom–light entanglement is confirmed by analysing the correlations of photoelectric detection events in the two measurements as a function of varying phases ϕ_A and ϕ_B , and observing the violation of the Bell inequality³⁰.

In order to study state-insensitive trapping, we drive the ensemble into the collective state $|R\rangle$ by two-photon excitation with 795-nm field Ω_1 and a 474-nm field Ω_2 for a period $T_e = 1 \mu\text{s}$. After a storage period $T_s \approx 0.2 \mu\text{s}$, the atoms are coherently driven on the $|r\rangle \leftrightarrow |e\rangle$ transition by a retrieval field Ω_A . The ensuing cooperative emission on the $|e\rangle \leftrightarrow |g\rangle$ transition leads to atom–light mapping $|R\rangle \rightarrow |\Phi\rangle_A$ (ref. 14). We compare the excitation spectra for untrapped atoms with those taken at different values of lattice detuning, δ_L (Fig. 2a). The two peaks correspond to the Zeeman components of Rydberg level $|r\rangle$. The differential trap potential δU averaged over the atomic distribution gives the spectral line shift $\delta_2^s = \overline{\delta U}/h$, whereas the root-mean-square deviation of the differential trap potential $(\overline{\delta U^2} - \overline{\delta U}^2)^{1/2}$ increases the spectral linewidth, Γ . The fit for $\delta_L^m/2\pi \approx 51 \text{ MHz}$ (green curve in Fig. 2a) is nearly indistinguishable from the fit for untrapped atoms (black curve in Fig. 2a), with zero spectral shift ($\delta_2^s/2\pi = 0.01(2) \text{ MHz}$) and no line broadening (measured widths $\Gamma/2\pi = 0.71(1) \text{ MHz}$ and $0.74(2) \text{ MHz}$ for trapped and untrapped atoms, respectively). In contrast, when the lattice frequency is detuned from the magic value, the transition

¹School of Physics, Georgia Institute of Technology, Atlanta, Georgia 30332-0430, USA.

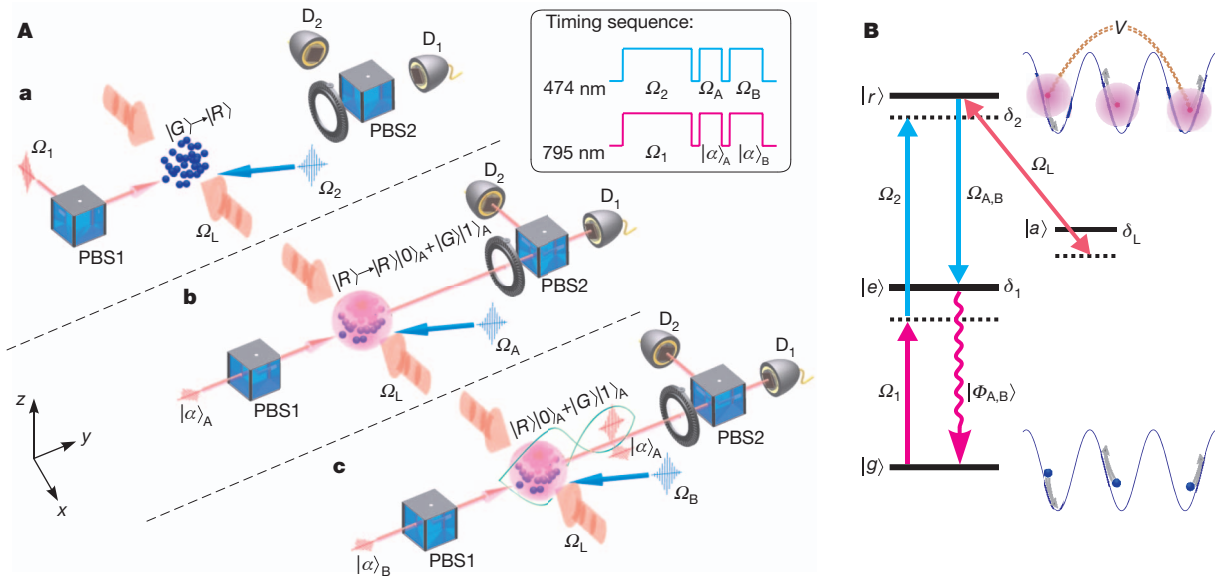


Figure 1 | Overview of the entanglement protocol. **A**, An ultracold gas is confined in a one-dimensional optical lattice at 1,004 nm. Three main steps of the entanglement protocol are illustrated. **a**, The atomic ensemble is driven from the collective ground state $|G\rangle$ into the singly-excited state $|R\rangle$. **b**, By applying a laser field Ω_A , an entangled state $|R\rangle|0_A\rangle + |G\rangle|1_A\rangle$ is generated. The retrieved field $|\Phi_A\rangle$ is mixed with coherent field $|\alpha_A\rangle$ using polarizing beam splitters PBS1 and PBS2, followed by measurement at single-photon detectors D_1 and D_2 . **c**, The remaining spin wave is mapped into field $|\Phi_B\rangle$ by the laser field Ω_B , mixed with $|\alpha_B\rangle$, and measured at D_1 and D_2 . A half-waveplate before PBS2 rotates polarizations of $|\Phi_{A,B}\rangle$ and $|\alpha_{A,B}\rangle$ by 45° . The inset shows the timing sequence for the 474-nm and 795-nm fields. **B**, Atomic levels of ^{87}Rb used in the experiment. The 1,004-nm lattice field is tuned to the

blue side of the $|r\rangle = |90s_{1/2}\rangle \leftrightarrow |a\rangle = |6p_{1/2}\rangle$ transition to equalize the trapping potentials of the ground $|g\rangle = |5s_{1/2}, F=2, m_F=0\rangle$ and $|r\rangle$ states (a lattice field at 1,012 nm can be tuned to the $|r\rangle \leftrightarrow |6p_{3/2}\rangle$ transition, see Supplementary Information). The large size of the electron wavefunction in the Rydberg state (pink spheres, not to scale) results in a ponderomotive contribution to the trapping potential. Laser fields Ω_1 at 795 nm and Ω_2 at 474 nm, detuned by δ_2 from the two-photon atomic resonance $|g\rangle \leftrightarrow |r\rangle$, and by $\delta_1/2\pi = -40$ MHz from the intermediate level $|e\rangle = 5p_{1/2}, F=1$, excite a collective atomic state $|R\rangle$ in the regime of the Rydberg excitation blockade caused by interaction between Rydberg atoms V . Laser fields $\Omega_{A,B}$, resonant on the $|r\rangle \leftrightarrow |e\rangle$ transition, map the collective atomic excitation into quantum fields $|\Phi_{A,B}\rangle$.

frequency is shifted ($\delta_2^s/2\pi = 2.75(2)$ MHz and $1.58(2)$ MHz) and $\Gamma/2\pi$ is increased to $0.95(1)$ and $0.86(1)$ MHz, for the red and blue lattice detuning, respectively. Lattice-induced off-resonant population $p_a \approx 0.02$ of level $|a\rangle$ causes a decay of Rydberg level $|r\rangle$ with lifetime $\tau_s \approx 6$ μs (Supplementary Information).

In Fig. 2b we display spectral shift as a function of lattice detuning. Positions of the $|6p_{1/2}\rangle$ hyperfine resonances are extracted from the fit (solid curve), as described in Supplementary Information. Using this fit and the measured atom temperature $T \approx 25$ μK , we obtain the maximum trap depth for the ground atoms, $U_g/k_B \approx 100$ μK . We estimate that the root-mean-square deviation of the differential trap potential averaged over the atom spatial positions and energies reaches its minimum value $(\overline{\delta U^2} - \overline{\delta U})^{1/2} / h|_{\min} \approx 0.03$ MHz at a detuning $\delta_L/2\pi = 58$ MHz where the average $\delta_2^s/2\pi \approx 0.33$ MHz (dashed horizontal line in Fig. 2b). This is a result of the ponderomotive part of the Rydberg trapping potential being only partially sensitive to the lattice intensity modulation, because the Rydberg atom size ~ 1 μm is greater than the 0.5 - μm lattice period.

Figure 2c displays the rate of photoelectric detection S as a function of δ_L . The two peaks correspond to the $|6p_{1/2}, F=1\rangle$ and $|6p_{1/2}, F=2\rangle$ hyperfine components. The peak value $S_p \approx 1,200$ s^{-1} for magic-valued detuning $\delta_L^m/2\pi \approx 58$ MHz and 294 MHz is more than two orders of magnitude higher compared to the value obtained using untrapped atoms^{23–25}. To investigate the temporal dynamics of atom confinement, we perform the Rydberg excitation-retrieval sequence with the lattice at a magic detuning $\delta_L^m/2\pi \approx 58$ MHz. As shown in Fig. 2d, we measure the probability of a photoelectric detection per experimental trial P as a function of atom holding time in the lattice, T_h (filled circles). An exponential fit gives the decay lifetime, $\tau_t = 74(3)$ ms. The decay is likely to be associated with atom loss due to light-induced collisions by way of the optical pumping fields, as the value of

the lifetime is strongly sensitive to the intensity of the latter. We are exploring polarization-gradient cooling within the Rydberg excitation sequence, aiming to extend the trap lifetime towards and beyond the atomic lattice lifetime $\tau_b = 0.3$ s set by background collisions with thermal Rb vapour.

In contrast to our near-resonant blue-detuned trap, typical far-off-resonance optical trapping potentials are repulsive for Rydberg levels, leading to fast dephasing of the ground–Rydberg optical coherence. Therefore an uncompensated lattice has to be turned off to avoid such dephasing, greatly reducing experimental rates^{23–25,27,28}. In Fig. 2d, values of P with the lattice shut off for the Rydberg excitation sequence are shown as diamonds. An exponential fit yields the decay constant $\tau_u = 0.76(1)$ ms, with the resulting rate of single photon detections $S_u \approx 10$ s^{-1} . The inset of Fig. 2d shows P as a function of the single-atom Rabi angle, $\theta \equiv \Omega_1\Omega_2T_e/(2\delta_1)$. The observed oscillation between the collective states $|G\rangle$ and $|R\rangle$ further confirms that our lattice preserves the quantum coherence between the ground and the Rydberg atom levels.

Our method to verify atom–light entanglement relies on the indistinguishability of the light fields $|\Phi_{A,B}\rangle$ mapped from the atomic coherence and of the coherent laser fields $|\alpha_{A,B}\rangle$. To characterize the mode-matching of these fields, we perform a two-photon quantum interference measurement between $|\Phi_A\rangle$ and $|\alpha_A\rangle$. The two fields are combined on the polarization beam splitter PBS2 (Fig. 1A), with the half-wave plate rotated to equalise the intensities of the two outputs. First, we determine probabilities of photoelectric detection at D_1 or D_2 , p_1 and $|\bar{\alpha}|^2/2$, respectively, with either field $|\Phi_A\rangle$ or field $|\alpha_A\rangle$ input to the beam splitter only. Next, we analyse the rate of joint photoelectric detection events between the detectors D_1 and D_2 within the $T_A = 100$ ns electronic detection window, when one coherent field $|\alpha\rangle$ and the single photon $|1\rangle$ are mixed on PBS2 (Fig. 3). We observe a non-classical (Hong–Ou–Mandel) suppression in this rate as a result of quantum two-photon interference. The

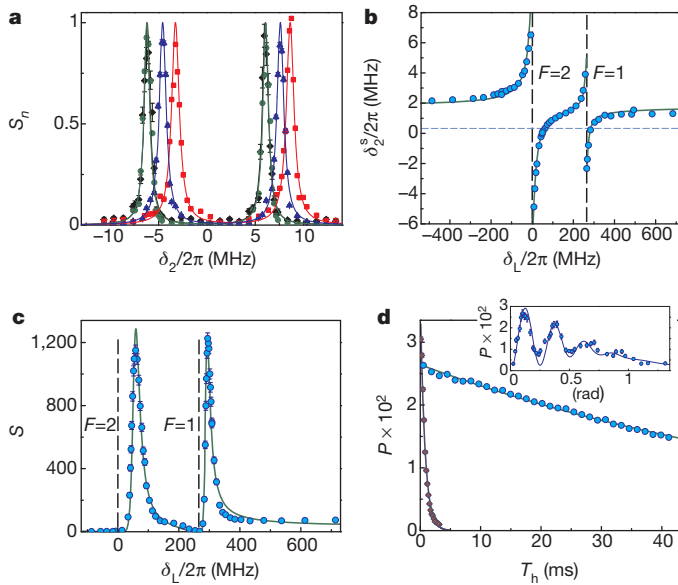


Figure 2 | State-insensitive optical trapping. **a**, Normalized Rydberg excitation spectra $S_n(\delta_2)$, for untrapped (black diamonds) and trapped atoms in a lattice with detuning $\delta_L/2\pi \approx (51, -100, 495 \text{ MHz})$ (green circles, red squares, blue triangles). The data are fitted by a pair of Lorentzian profiles. **b**, Spectral shift $\delta_2^s/2\pi$ as a function of lattice detuning, δ_L . Each data point and the associated error bar are extracted from a spectrum of the type shown in **a**. The dashed horizontal line indicates the spectral shift $\delta_2^s/2\pi = 0.33 \text{ MHz}$ for which the lifetime of the ground–Rydberg coherence is maximized. The data are fitted (solid curve) to the expected form, with the dashed vertical lines corresponding to the inferred positions of level $|a\rangle$ hyperfine components. **c**, The photoelectric detection rate S by detectors D_1 and D_2 . The solid curve is a theoretical fit. **d**, Probability of photoelectric detection P as a function of lattice holding time T_h . The data are fitted with an exponential function $\sim e^{-T_h/\tau}$. Inset, P as a function of the single-atom Rabi angle θ for lattice-confined atoms using a 50- μs data acquisition period per lattice loading to limit the effect of atom number variation. The solid curve is a damped oscillation fit. Error bars in **a**, **c** and **d**, ± 1 standard deviations (\sqrt{M}) for M photoelectric counting events.

degree of suppression allows us to infer the overlap of the two incoming light fields η , with $\eta = 1$ for fields that are indistinguishable within the detection window, and $\eta = 0$ for completely distinguishable fields. We define the visibility of the interference $V = 1 - p_{21}/w_{21}$. Here w_{21} is the

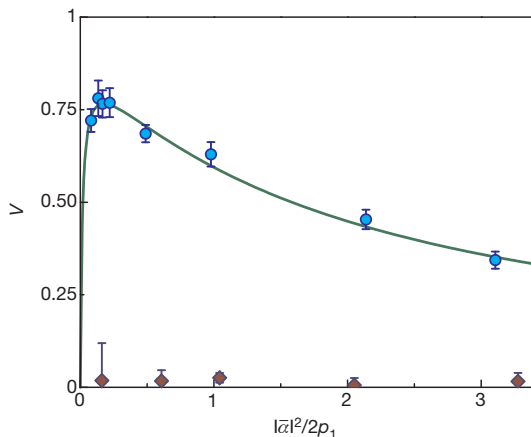


Figure 3 | Hong-Ou-Mandel interference between single-photon and coherent fields. Visibility V of two-photon interference between the retrieved field $|\Phi\rangle_A$ and the coherent field $|\alpha\rangle_A$ as a function of $|\alpha|^2/(2p_1)$. Data are for $|\alpha\rangle_A$ in resonance ($\delta \approx 0$; circles) and off resonance ($\delta/2\pi \approx -40 \text{ MHz}$; diamonds) with the field $|\Phi\rangle_A$. From the theoretical fit of our model (solid curve) we infer the overlap of the two fields, $\eta = 0.90(2)$. Error bars, ± 1 standard deviations (\sqrt{M}) for M photoelectric counting events.

expected level of two-photon coincidences if the retrieved and the laser fields are completely distinguishable. We determine w_{21} using one- and two-photon photoelectric detection probabilities for separate measurements using either of the two fields (Supplementary Information). When the frequency of the coherent field is matched to that of the retrieved light ($\delta \approx 0 \text{ MHz}$), high-visibility interference is observed. The data are fitted to a model that accounts for imperfect field matching and a finite value of $g^{(2)}(0)$ for the retrieved field, with the best-fit value of the field overlap $\eta = 0.90(2)$ (Supplementary Information). We approximate the case of distinguishable fields by introducing a frequency off-set $\delta/2\pi = -40 \text{ MHz}$ for the coherent field (diamonds in Fig. 3), and in this case find negligible overlap, $\eta_d = 0.03(2)$.

To generate atom–light entanglement, we coherently split part of the collective atomic excitation into a retrieved light field: $|R\rangle \rightarrow |R\rangle|0\rangle_A + |G\rangle|1\rangle_A$. Atom–light splitting is achieved by applying field Ω_A at about one-fifth of the intensity used to obtain full retrieval, investigated in Figs 2 and 3. The entanglement is verified by phase-sensitive measurement of both components of the quantum state³⁰ (Fig. 1). First, the retrieved field $|\Phi\rangle_A$ is interfered with a coherent field $|\alpha\rangle_A$ on a beam splitter, and the beam splitter outputs are measured by single-photon detectors D_1 and D_2 over a period A . To realize a phase-sensitive measurement of the atomic component, it is mapped, after a $0.1 \mu\text{s}$ delay, into a light field $|\Phi\rangle_B$ by application of the retrieval field Ω_B . This retrieved field $|\Phi\rangle_B$ is interfered with a coherent field $|\alpha\rangle_B$, and measured by detectors D_1 and D_2 over a period B . We evaluate the correlation function $E(\phi_A, \phi_B)$ defined by

$$\frac{C_{12}(\phi_A, \phi_B^\perp) + C_{21}(\phi_A, \phi_B^\perp) - C_{12}(\phi_A, \phi_B) - C_{21}(\phi_A, \phi_B)}{C_{12}(\phi_A, \phi_B^\perp) + C_{21}(\phi_A, \phi_B^\perp) + C_{12}(\phi_A, \phi_B) + C_{21}(\phi_A, \phi_B)} \quad (1)$$

where $C_{ij}(\phi_A, \phi_B)$ is the coincidence rate between detector D_i in detection period A and D_j in the detection period B , $\phi_B^\perp = \phi_B + \pi$. In Fig. 4 the correlation function E is displayed as a function of ϕ_A , when ϕ_B is fixed at $\pi/4$ and $3\pi/4$, together with sinusoidal fits of adjustable visibility, v . For our measured $g^{(2)}(0) \approx 0.02$ and $\alpha^2/(4p_1) \approx 0.08$, we expect $v \approx 0.79$ based on our model (Supplementary Information), in good agreement with the values $v_{\pi/4} = 0.80(4)$, $v_{3\pi/4} = 0.76(4)$ extracted from the fits.

From measurements of $E(\phi_A, \phi_B)$, we determine the Bell parameter $S = E(\phi_A, \phi_B) + E(\phi'_A, \phi_B) + E(\phi_A, \phi'_B) - E(\phi'_A, \phi'_B)$. We use canonical settings $\phi_A = \pi/2$, $\phi'_A = 0$, $\phi_B = \pi/4$, $\phi'_B = 3\pi/4$, which in the ideal case results in $S = 2\sqrt{2}$, maximally violating the Bell inequality $|S| \leq 2$. The measured values of $E(\phi_A, \phi_B)$ are displayed in Table 1. The value $S = 2.27(7) \not\leq 2$ is in a clear violation of the Bell inequality, and is

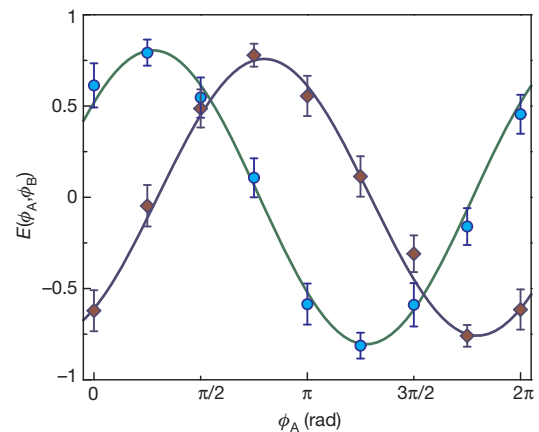


Figure 4 | Atom–light entanglement. Correlation function $E(\phi_A, \phi_B)$ as a function of ϕ_A ; circles are for $\phi_B = \pi/4$, diamonds are for $\phi_B = 3\pi/4$. The curves are sinusoidal fits with inferred visibility $v_{\pi/4} = 0.80(4)$, $v_{3\pi/4} = 0.76(4)$. Error bars, ± 1 standard deviations (\sqrt{M}) for M photoelectric counting events.

Table 1 | Entanglement verification by way of Bell's inequality

ϕ_A	ϕ_B	$E(\phi_A, \phi_B)$
0	$\pi/4$	0.57 ± 0.03
0	$3\pi/4$	-0.61 ± 0.04
$\pi/2$	$\pi/4$	0.57 ± 0.03
$\pi/2$	$3\pi/4$	0.53 ± 0.04
		$S = 2.27 \pm 0.07$

Correlation function $E(\phi_A, \phi_B)$ and S based on 4,254 events.

consistent with the visibility of the fringes shown in Fig. 4. We therefore verify unambiguously entanglement of an optical atomic coherence and a light field.

By normalizing the value of the initial photoelectric detection probability $P_t \approx 0.028$ (reduced by the $|6p_{1/2}\rangle$ level decay compared to the corresponding value $P_u \approx 0.032$ for untrapped atoms), Fig. 2d, with the linear transmission and detection efficiency $\zeta = 0.25$, we estimate efficiency $\xi = 0.11(3)$ with which the entangled atom–light state (see Supplementary Information) is prepared, with the average value $\bar{\xi} = 0.08(2)$. We emphasize that although photoelectric detection probabilities in our initial implementation are decreased from their ideal values by various preparation, transmission and detection inefficiencies, our entanglement generation and verification protocol is inherently deterministic.

To achieve long-term storage of atomic states, entanglement generation can be followed by mapping the Rydberg component of the atomic state into the $F = 1$, $m_F = 0$ hyperfine component of the ground state. The differential a.c. Stark shift between the $F = 2$, $m_F = 0$ and $F = 1$, $m_F = 0$ pair of ground states can be eliminated by directing a ‘magic’-valued bias magnetic field along the lattice (x) axis³¹. Matter–light mapping efficiency can be increased by enclosing the atomic ensemble into a low- to medium-finesse optical cavity, with values of $\xi = 0.8$ having already been demonstrated⁶.

We report the realization of entanglement between an optical atomic coherence and a light field. Our demonstration relies critically on achievement of state-insensitive optical confinement of atoms in their ground and Rydberg states. In contrast to prior probabilistic approaches where scalability is compromised by the need for multiple ‘repeat-until-success’ entanglement generation attempts^{1,4–6}, our protocol is intrinsically deterministic. Combined with already-demonstrated atomic memory on the scale of a minute³¹, our work leads to functional quantum networking architectures with superior scaling potential.

Received 11 March; accepted 24 April 2013.

Published online 19 June 2013.

- Duan, L.-M., Lukin, M. D., Cirac, J. I. & Zoller, P. Long-distance quantum communication with atomic ensembles and linear optics. *Nature* **414**, 413–418 (2001).
- Saffman, M., Walker, T. G. & Mølmer, K. Quantum information with Rydberg atoms. *Rev. Mod. Phys.* **82**, 2313–2363 (2010).
- Monroe, C. & Kim, J. Scaling the ion trap quantum processor. *Science* **339**, 1164–1169 (2013).
- Matsukevich, D. N. & Kuzmich, A. Quantum state transfer between matter and light. *Science* **306**, 663–666 (2004).

- Volz, J. *et al.* Observation of entanglement of a single photon with a trapped atom. *Phys. Rev. Lett.* **96**, 030404 (2006).
- Simon, J., Tanji, H., Ghosh, S. & Vuletic, V. Single-photon bus connecting spin-wave quantum memories. *Nature Phys.* **3**, 765–769 (2007).
- Chanelière, T. *et al.* Storage and retrieval of single photons transmitted between remote quantum memories. *Nature* **438**, 833–836 (2005).
- Eisaman, M. *et al.* Electromagnetically induced transparency with tunable single-photon pulses. *Nature* **438**, 837–841 (2005).
- Matsukevich, D. N. *et al.* Entanglement of remote atomic qubits. *Phys. Rev. Lett.* **96**, 030405 (2006).
- Hofmann, J. *et al.* Heralded entanglement between widely separated atoms. *Science* **337**, 72–75 (2012).
- Ritter, S. *et al.* An elementary quantum network of single atoms in optical cavities. *Nature* **484**, 195–200 (2012).
- Stute, A. *et al.* Tunable ion-photon entanglement in an optical cavity. *Nature* **485**, 482–485 (2012).
- Lukin, M. D. *et al.* Dipole blockade and quantum information processing in mesoscopic atomic ensembles. *Phys. Rev. Lett.* **87**, 037901 (2001).
- Saffman, M. & Walker, T. G. Creating single-atom and single-photon sources from entangled atomic ensembles. *Phys. Rev. A* **66**, 065403 (2002).
- Saffman, M. & Walker, T. G. Analysis of a quantum logic device based on dipole-dipole interactions of optically trapped Rydberg atoms. *Phys. Rev. A* **72**, 022347 (2005).
- Acín, A., Cirac, J. I. & Lewenstein, M. Entanglement percolation in quantum networks. *Nature Phys.* **3**, 256–259 (2007).
- Gallagher, T. F. *Rydberg Atoms* (Cambridge Univ. Press, 1994).
- Urban, E. *et al.* Observation of Rydberg blockade between two atoms. *Nature Phys.* **5**, 110–114 (2009).
- Gaëtan, A. *et al.* Observation of collective excitation of two individual atoms in the Rydberg blockade regime. *Nature Phys.* **5**, 115–118 (2009).
- Zhao, B., Mueller, M., Hammerer, K. & Zoller, P. Efficient quantum repeater based on deterministic Rydberg gates. *Phys. Rev. A* **81**, 052329 (2010).
- Brion, E., Carlier, F., Akulin, V. M. & Mølmer, K. Quantum repeater with Rydberg-blocked atomic ensembles in fiber-coupled cavities. *Phys. Rev. A* **85**, 042324 (2012).
- Mohapatra, A. K., Jackson, T. R. & Adams, C. S. Coherent optical detection of highly excited Rydberg states using electromagnetically induced transparency. *Phys. Rev. Lett.* **98**, 113003 (2007).
- Dudin, Y. O. & Kuzmich, A. Strongly interacting Rydberg excitations of a cold atomic gas. *Science* **336**, 887–889 (2012).
- Dudin, Y. O., Li, L., Bariani, F. & Kuzmich, A. Observation of coherent many-body Rabi oscillations. *Nature Phys.* **8**, 790–794 (2012).
- Dudin, Y. O., Bariani, F. & Kuzmich, A. Emergence of spatial spin-wave correlations in a cold atomic gas. *Phys. Rev. Lett.* **109**, 133602 (2012).
- Schäuf, P. *et al.* Observation of spatially ordered structures in a two-dimensional Rydberg gas. *Nature* **491**, 87–91 (2012).
- Peyronel, T. *et al.* Quantum nonlinear optics with single photons enabled by strongly interacting atoms. *Nature* **488**, 57–60 (2012).
- Maxwell, D. T. *et al.* Storage and control of optical photons using Rydberg polaritons. *Phys. Rev. Lett.* **110**, 103001 (2013).
- Anderson, S. E., Younge, K. C. & Raithel, G. Trapping Rydberg atoms in an optical lattice. *Phys. Rev. Lett.* **107**, 263001 (2011).
- Tan, S. M., Walls, D. F. & Collett, M. J. Nonlocality of a single photon. *Phys. Rev. Lett.* **66**, 252–255 (1991).
- Dudin, Y. O., Li, L. & Kuzmich, A. Light storage on the minute scale. *Phys. Rev. A* **87**, 031801(R) (2013).

Supplementary Information is available in the online version of the paper.

Acknowledgements This work was supported by the Atomic Physics Program and the Quantum Memories MURI of the Air Force Office of Scientific Research and the National Science Foundation.

Author Contributions All authors contributed substantially to all aspects of this work.

Author Information Reprints and permissions information is available at www.nature.com/reprints. The authors declare no competing financial interests. Readers are welcome to comment on the online version of the paper. Correspondence and requests for materials should be addressed to A.K. (alex.kuzmich@physics.gatech.edu).

A micrometre-scale Raman silicon laser with a microwatt threshold

Yasushi Takahashi^{1,2}, Yoshitaka Inui³, Masahiro Chihara¹, Takashi Asano³, Ryo Terawaki¹ & Susumu Noda^{3,4}

The application of novel technologies to silicon electronics has been intensively studied with a view to overcoming the physical limitations of Moore's law, that is, the observation that the number of components on integrated chips tends to double every two years. For example, silicon devices have enormous potential for photonic integrated circuits on chips compatible with complementary metal-oxide-semiconductor devices, with various key elements having been demonstrated in the past decade^{1–6}. In particular, a focus on the exploitation of the Raman effect has added active optical functionality to pure silicon^{7–10}, culminating in the realization of a continuous-wave all-silicon laser¹¹. This achievement is an important step towards silicon photonics, but the desired miniaturization to micrometre dimensions and the reduction of the threshold for laser action to microwatt powers have yet to be achieved: such lasers remain limited to centimetre-sized cavities with thresholds higher than 20 milliwatts¹², even with the assistance of reverse-biased p–i–n diodes. Here we demonstrate a continuous-wave Raman silicon laser using a photonic-crystal, high-quality-factor nanocavity without any p–i–n diodes, yielding a device with a cavity size of less than 10 micrometres and an unprecedentedly low lasing threshold of 1 microwatt. Our nanocavity design exploits the principle that the strength of light–matter interactions is proportional to the ratio of quality factor to the cavity volume and allows drastic enhancement of the Raman gain beyond that predicted theoretically^{13,14}. Such a device may make it possible to construct practical silicon lasers and amplifiers for large-scale integration in photonic circuits.

In 2002, stimulated Raman scattering in rib waveguides was proposed as a novel mechanism to generate optical gain in crystalline silicon⁷. However, the Raman gain is inherently small compared with the gain due to radiative recombination in direct-bandgap semiconductors^{15,16}. Therefore, Raman silicon lasers have thus far required long cavities and high excitation powers to generate net gain. Furthermore, free carrier absorption (FCA) induced by two-photon absorption^{17,18} (TPA) has a superlinear dependence on the excitation power, resulting in additional losses that compete with the Raman gain. The incorporation of reverse-biased p–i–n diodes along the waveguides has also been necessary to remove the carriers^{10–12}. To overcome all these disadvantages, the design of optical cavities with high quality factors (Q) and small volumes (V) is essential because high Q/V ratios yield strong light–matter interactions and enhance the Raman gain. From this point of view, the use of high- Q , photonic-crystal nanocavities^{19–23} is desirable. However, there have thus far been no experimental reports of stimulated Raman scattering in nanocavities and no feasible designs have been proposed for cavities in which continuous-wave lasing can be achieved. Progress in this area of research halted after a number of numerical studies on elementary cavity structures were unsuccessful in finding a design in which Raman emission can be detected^{13,14,24}. However, we now present a laser design that incorporates a heterostructure nanocavity, and demonstrate that it exhibits lasing with an unprecedentedly ultralow threshold of 1 μ W.

Figure 1a–c illustrates the basic features of the nanocavity Raman laser developed in this study. The photonic crystal has the well-known triangular lattice structure formed by circular air holes in a suspended silicon membrane. The heterostructure nanocavity is formed from a line-defect waveguide (Fig. 1d). This waveguide has two types of propagation mode within the photonic bandgap, an odd-waveguide mode and an even-waveguide mode. The low-loss propagation bands of these modes are shown in Fig. 1e. The modes are classified as 'odd' or 'even' by the symmetry of the electric field E_y , as schematically displayed. The corresponding band structure in wavenumber (k)-space is shown in Fig. 1f, where the blue and red curves show the dispersion relations for the odd-waveguide mode and even-waveguide mode, respectively. The dashed line represents the light line, below which the low-loss propagations are obtained (Supplementary Information, section A). The nanocavity is formed by a small increase (Δa) of the lattice constant in a short section of the waveguide, which moves the dispersion relation curves to a lower frequency. Accordingly, the frequency of the odd- and even-waveguide bands is lowered in this section²¹ (Fig. 1b), such that 'odd' and 'even' nanocavity modes are formed as a result of optical confinement by the mode-gap differences. (The mode gap is the frequency range with no low-loss waveguide modes.) In our Raman laser, we use these nanocavity modes to confine pump light and Stokes-Raman-scattered light, respectively (Fig. 1c).

Figure 1g shows the calculated x and y components of the electric field distribution of the odd nanocavity mode, which are denoted E_{x_pump} and E_{y_pump} , respectively. Figure 1h presents the analogous electric field distributions of the even nanocavity mode, denoted E_{x_Raman} and E_{y_Raman} . The E_{x_pump} and E_{x_Raman} distributions have different parities because they are generated from different waveguide modes. This is also the case for E_{y_pump} and E_{y_Raman} . Such pairs of modes initially seem unsuitable for Raman lasers owing to the small degree of overlap for stimulated Raman scattering. However, it can be seen from Fig. 1g, h that the 'cross components', E_{x_pump} and E_{y_Raman} (and E_{y_pump} and E_{x_Raman}), have the same line symmetry and similar distributions. This is a key observation, showing that the problem of cavity design can be solved by carefully selecting the crystallographic direction in which the nanocavity is formed, as discussed below. We will next demonstrate that the frequencies (f_p and f_R), Q values (Q_p and Q_R), modal volumes (V_p and V_R) and electric field distributions (E_p and E_R) associated with this unusual pair of modes allow dramatic enhancement of the Raman gain.

The first advantage of our design is that the frequency spacing ($\Delta f = f_p - f_R$) between these nanocavity modes can be tuned to the silicon Raman shift of 15.6 THz by changing the air-hole radius. This is because the electric field densities of the two modes within the air holes are fundamentally unequal owing to the difference in parity. It is fortuitous that the frequency spacing is close to 15.6 THz when the lattice constant (a) is set so that the even nanocavity mode has an operation wavelength in the telecommunications band between 1.30 and 1.60 μ m. Tuning the frequency spacing to exactly 15.6 THz is

¹Nanoscience and Nanotechnology Research Center, Research Organization for the 21st Century, Osaka Prefecture University, Sakai, Osaka 599-8570, Japan. ²Japan Science and Technology Agency, PRESTO, Kawaguchi, Saitama 332-0012, Japan. ³Department of Electronic Science and Engineering, Kyoto University, Kyoto 615-8510, Japan. ⁴Photonics and Electronics Science and Engineering Center, Kyoto University, Kyoto 615-8510, Japan.

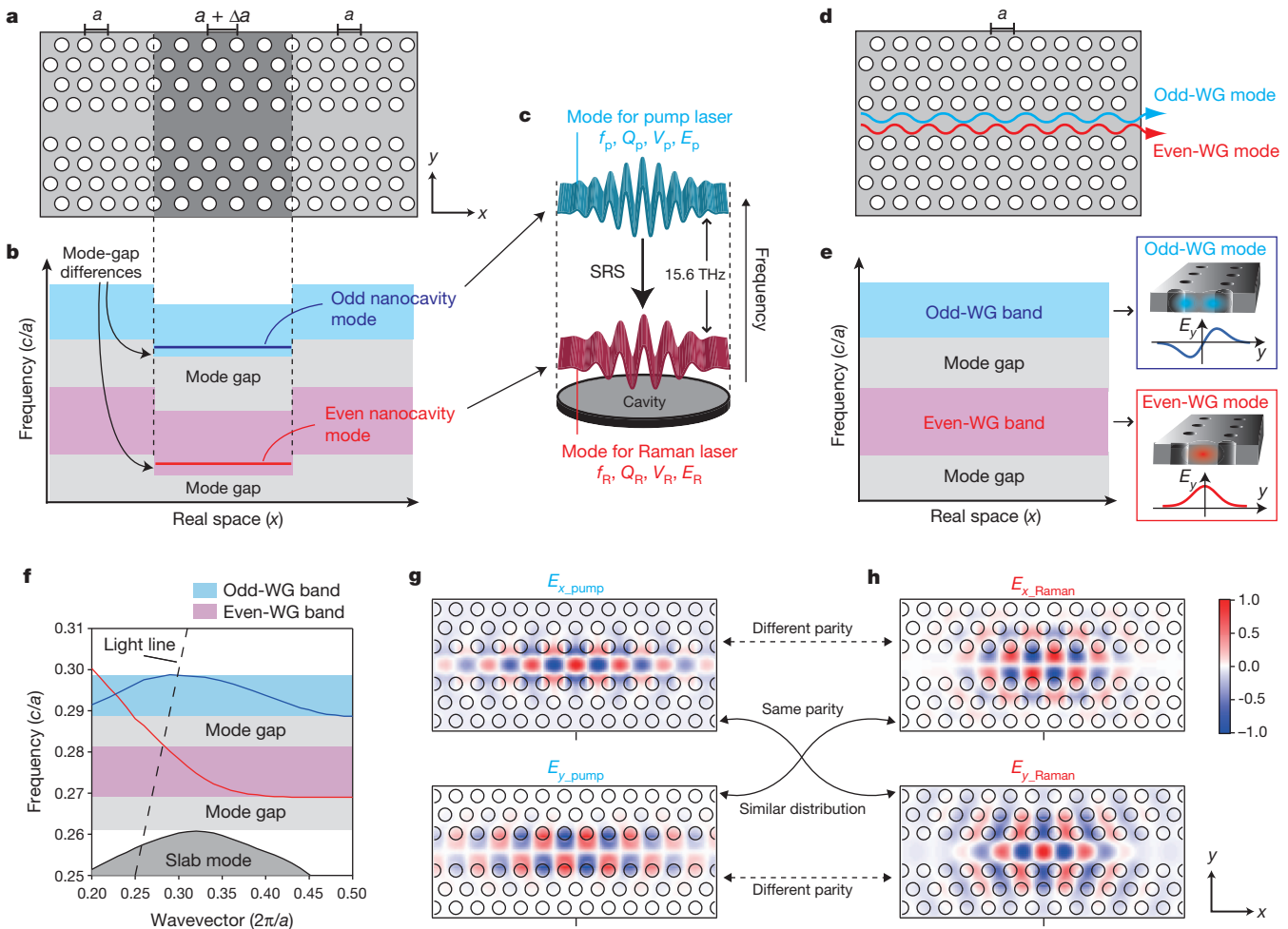


Figure 1 | Structure of Raman silicon laser based on a heterostructure nanocavity. **a**, Schematic picture of the heterostructure nanocavity in the photonic crystal slab. The lattice constant at the centre of the cavity is slightly larger in the x direction. **b**, Band diagram of the nanocavity along the x direction, where c is the speed of light in vacuum. Two high- Q nanocavity modes originating from odd- and even-waveguide modes are formed in the heterostructure. **c**, Configuration of Raman silicon laser using a small cavity. The two nanocavity modes in **b** are used to confine pump light and

Stokes-Raman-scattered light, respectively. SRS, stimulated Raman scattering. **d**, Line-defect waveguide formed by a missing row of air holes, in which two propagating waveguide modes are formed. WG, waveguide. **e**, Band diagram of the line-defect waveguide. The insets sketch the profiles of the propagating modes. **f**, Calculated band structure for the line-defect waveguide in k -space. **g, h**, Calculated electric field distributions for the odd nanocavity mode and the even nanocavity mode, respectively. The colour scale represents the intensity of the electric field.

essential for the efficient generation of Raman scattered light into the even nanocavity mode, and the flexibility of our design is thus an advantage over the alternatives^{13,14,24}.

Second, although the Q factor of the even nanocavity mode (Q_R) can be made as high as 4,000,000 in heterostructure nanocavities²³, the odd nanocavity mode has so far received little attention regarding its possible use as a high- Q resonant mode. However, we will show below that the Q factor of this mode (Q_P) can be higher than 100,000 in heterostructure nanocavities. Because the laser threshold is inversely proportional to the product of Q_P and Q_R , owing to the reduction of cavity loss, the characteristic of high Q factors for both modes is another advantage of our design. Below we demonstrate experimentally that the product $Q_P Q_R$ can exceed 10^{11} , which is 10,000 times higher than previously reported values^{13,14}. In addition, the cavity volumes of both modes (V_P and V_R) can be reduced to a cubic wavelength when Δf is at the desired value and $Q_P Q_R$ is high. This volume is 10,000 times smaller than in earlier rib-waveguide Raman lasers^{11,12}. Therefore, our design enables extraordinarily high $Q_P Q_R/V$ ratios, which no cavity design reported thus far has been able to achieve.

Last, our design allows high effective overlap for the Raman gain because the nanocavity is fabricated along a unique crystallographic direction of the silicon-on-insulator (SOI) substrate, which further

enhances the advantages discussed above. If the device is fabricated on a standard (001) SOI, then either the [100] or [110] direction can be chosen as the x axis of the nanocavity. Considering the Raman selection rules in silicon and that both nanocavity modes have transverse electric polarization with respect to the slab, in our design the Raman gain in each direction is as follows, where an asterisk denotes complex conjugate (Supplementary Information, section B):

$$G_{[100]} \propto \iiint_{\text{Si}} |E_{x_Raman}^* E_{y_pump} + E_{y_Raman}^* E_{x_pump}|^2 dx dy dz \quad (1)$$

$$G_{[110]} \propto \iiint_{\text{Si}} |E_{x_Raman}^* E_{x_pump} - E_{y_Raman}^* E_{y_pump}|^2 dx dy dz \quad (2)$$

Usually, SOI-based photonics devices are fabricated along [110] or its equivalent directions because the wafer is easily cleaved along [110]. The previously reported rib-waveguide lasers were indeed designed along [110] (refs 9–12) and the previous theoretical studies used the same direction^{14,24}. Although the Δf and Q factors are insensitive to the direction of fabrication, equation (1) indicates that the Raman gain will be higher for the [100] direction because there is a negative term in equation (2). The overlap involving the cross components is significant

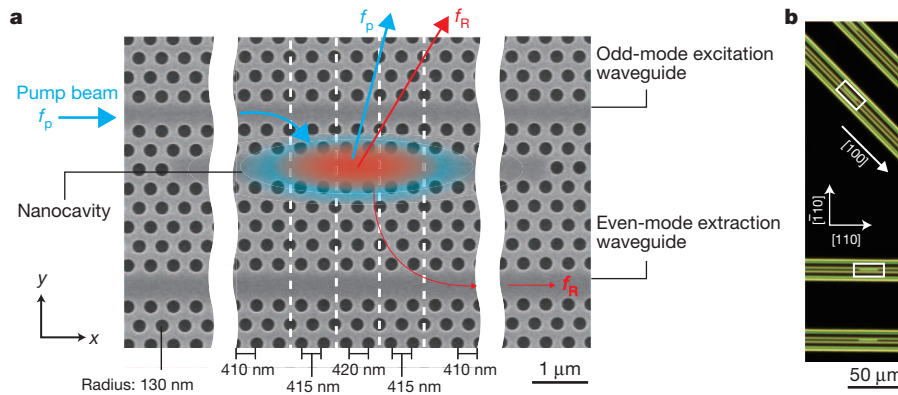


Figure 2 | Configuration of nanocavity Raman silicon laser. **a**, Scanning electron microscope image of the core region of the laser. The annotations show how laser light created from the pump beam is mainly emitted in the direction vertical to the slab. We refer to this as dropped light. A portion of the light is

in equation (1), which involves the odd and even nanocavity modes with the desirable parities and distributions indicated in Fig. 1g, h. Consequently, our design is also superior in terms of overlap and can drastically enhance the Raman gain when the device is fabricated along [100].

We now demonstrate the operation of a device fabricated according to our design strategy. Figure 2a shows a scanning electron microscope image of a nanocavity formed using well-established silicon nanofabrication technologies²⁵. The central line defect is the heterostructure nanocavity, and the upper and lower line defects are waveguides used to pump the odd nanocavity mode and to extract Raman laser light from the even nanocavity mode, respectively. The structural parameters were chosen such that the even nanocavity mode has a wavelength in the 1.55- μm band: the lattice constant is $a = 410$ nm, the air-hole radius is $r = 130$ nm, the silicon slab thickness is 220 nm and there are two

propagated along the even-mode extraction waveguide. **b**, Dark-field microscope image of the fabricated chip. Nanocavities oriented along [100] and [110] were fabricated. Patterned and unpatterned regions are clearly distinguishable. The rectangles indicate the areas shown in **a**.

successive 5-nm increases of a in the x direction. Figure 2b shows a microscope image of the chip. We also fabricated a nanocavity along [110] for reference. We note that no p-i-n diodes to reduce the TPA-induced FCA were incorporated.

We investigated the optical properties using the measurement set-up shown in Fig. 3a. Figure 3b, c show the measured resonant spectra of the two nanocavity modes for a sample with the x axis aligned to [100]. The even nanocavity mode was excited through the even-mode extraction waveguide. The linewidth ($\Delta\lambda$) of the odd nanocavity mode peak is 13.7 pm at the resonant wavelength $\lambda_p = 1424.99$ nm. A Q_p value of 104,000 is obtained from the relation $Q = \lambda/\Delta\lambda$. The Q_R value for the even nanocavity mode is estimated as 1,400,000 at the resonant wavelength $\lambda_R = 1540.13$ nm, and, thus, $Q_p Q_R = 1.5 \times 10^{11}$. The frequency spacing is $\Delta f = c(1/\lambda_p - 1/\lambda_R) = 15.74$ THz, which is not exactly matched to the silicon Raman shift of 15.6 THz.

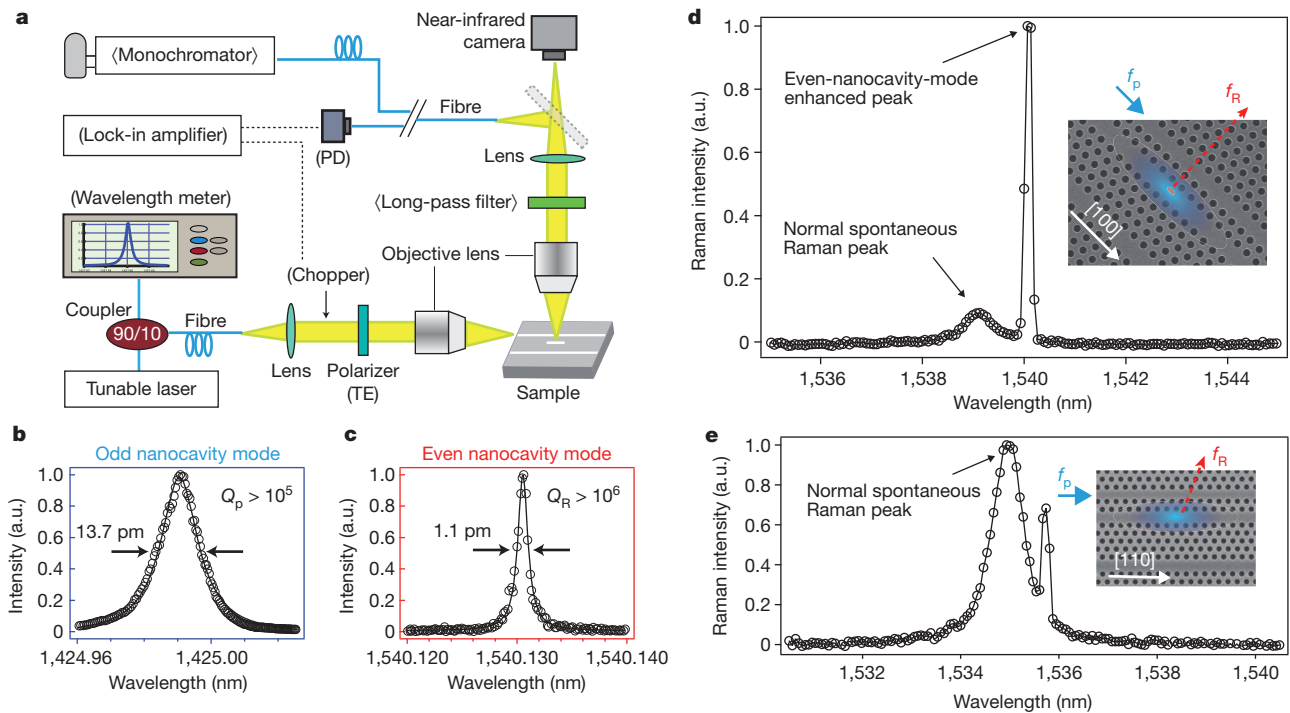


Figure 3 | Optical measurements on fabricated nanocavities. **a**, Set-up used to obtain resonant spectra and Raman-scattering spectra. The components enclosed in parentheses and angle brackets were used for resonant spectra and Raman spectra, respectively. TE, transverse electric. **b**, **c**, Resonant spectra for odd (**b**) and even (**c**) nanocavity modes. a.u., arbitrary units. **d**, Raman

spectrum for the [100] nanocavity, measured while pumping the odd nanocavity mode in **b** with an input power of 1 μW . **e**, Raman spectrum for the reference [110] nanocavity. The resolution limit of the monochromator is ~ 100 pm.

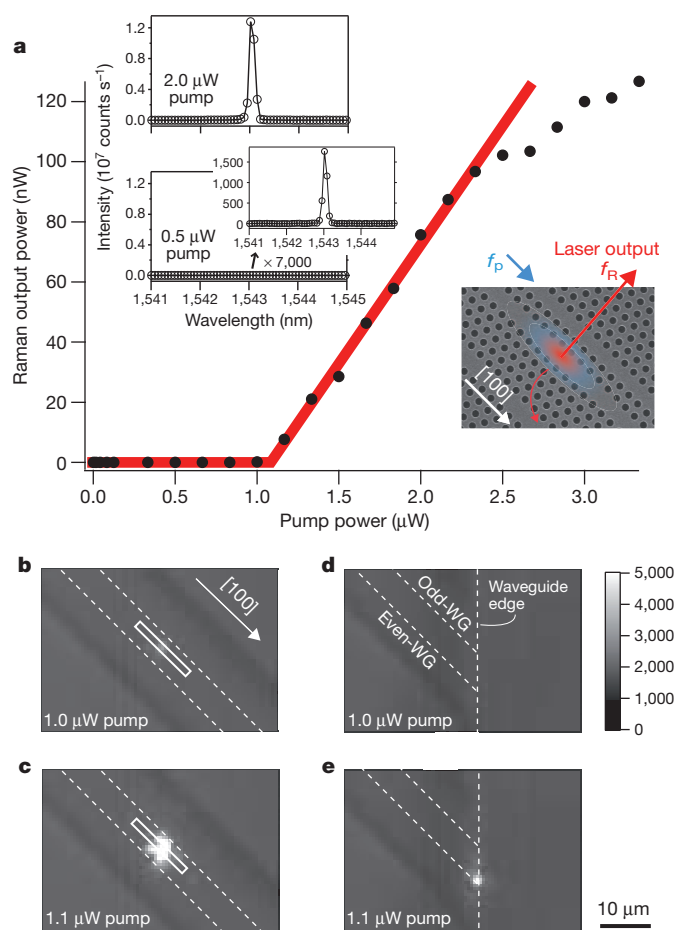


Figure 4 | Continuous-wave operation of fabricated nanocavity Raman silicon laser. **a**, Laser output power (black points) as a function of pump power coupled into the nanocavity. The absolute power was estimated from the dropped-light intensity, taking into account the loss from the experimental set-up. The red line shows the output of a typical laser with a slope efficiency of 8% above threshold. The insets show the Raman spectra below and above the threshold power on the same scale, demonstrating Raman laser action. **b**, **c**, Near-infrared camera images of the nanocavity Raman laser below and above the threshold, using a long-pass filter to eliminate the pump light. Dotted lines represent the waveguides. Rectangles indicate the nanocavity position. **d**, **e**, Near-infrared images at a waveguide edge. Images in **b–e** are shown on the same intensity scale.

Figure 3d shows the Raman scattering spectrum measured when the odd nanocavity mode in Fig. 3b was excited by a continuous-wave laser beam coupling only 1 μW of power into the cavity. Although the detuning, $\Delta f = 15.6$ THz, from the Raman shift is larger than the Raman gain width of silicon (~ 0.1 THz), a sharp Raman scattering peak is nevertheless observed. This is enhanced by the strong confinement of the even nanocavity mode at the tail of the normal spontaneous Raman emission peak. The linewidth of the normal spontaneous Raman peak is 750 pm, which is almost the same as the Raman gain width of silicon. As shown in Fig. 3e, the resonant peak is much smaller for the reference [110] nanocavity, which has similar Q values and Δf to the [100] nanocavity in Fig. 3d. Although the sample in Fig. 3d did not oscillate, owing to the residual mismatch of Δf , we were able to fabricate a sample with a Δf value of exactly 15.6 THz by carefully changing the radius of the air holes (Supplementary Information, section C). We separately confirmed that the rate of change of Δf with radius r is $(\partial \Delta f / \partial r) \approx 0.15$ THz nm^{-1} .

Finally, we present details of lasing in a sample with $Q_p = 140,000$, $Q_R = 1,500,000$, $\lambda_p = 1428.38$ nm and $\lambda_R = 1543.02$ nm. The laser output power is plotted in Fig. 4a as a function of the pump power coupled into the nanocavity, showing lasing oscillation above a threshold of

1 μW . This threshold is 20,000 times smaller than that previously reported for a rib-waveguide Raman silicon laser¹² and is also smaller than predicted by numerical studies^{13,14}. The spectral peak intensities in the insets indicate that the efficiency for Raman light generation above threshold is more than 1,000 times higher than that below threshold (Supplementary Information, section D). In addition, the slope efficiency is 8% and the laser efficiency is 4% without any p–i–n diodes (Supplementary Information, section E). The resolution limit of the monochromator (~ 100 pm) is much larger than the linewidth of the even nanocavity mode (~ 1 pm) and, thus, linewidth narrowing relative to the lasing could not be detected. We separately confirmed that sample heating due to increasing pump powers is negligible (see Supplementary Information, section F, for temperature dependence). Figure 4b and Fig. 4c show near-infrared camera images of the nanocavity below and above the threshold power, respectively. Figure 4d, e shows images of a waveguide facet, demonstrating that a portion of the Raman laser beam was successfully extracted from the even-mode extraction waveguide.

This low-threshold lasing result is a consequence of the fact that our nanocavity design produces net Raman gain in the low-excitation range before TPA-induced FCA becomes dominant. Because Raman gain has a linear dependence on pump power whereas TPA-induced FCA has a superlinear dependence, the Raman gain can exceed losses for low pump power in our design, where the high Q_R value and the large overlap between the nanocavity modes have especially important roles. Although the lasing output power gradually saturates with increasing pump power, most probably as a result of TPA-induced FCA, this effect could be reduced by reducing the free carrier lifetimes. There is also potential for further performance enhancement, including the reduction of threshold pump power ($\lesssim 100$ nW), for example by increasing the Q_p and Q_R factors²³ and modifying the volumes. Such an ultralow threshold is encouraging for a number of reasons. For instance, electrically driven silicon spontaneous-emission sources might be used for integrated pump light sources even though their efficiencies would be low, and Raman silicon laser chips without external pump sources could be realized in the future. The operational wavelength range could be extended above and below the 1.55- μm band²⁵. It will also be possible to make other Raman amplification devices based on photonic crystals^{26–28} using our design strategy. We believe that our device will stimulate silicon photonics research in a number of areas for the realization of compact photonic integrated circuit chips.

METHODS SUMMARY

We used the three-dimensional, finite-difference time-domain method²⁹ to calculate the band structure and the electric field distributions in Fig. 1, where the structural parameters in Fig. 2a were used. The calculated Q_p and Q_R values are 500,000 and 4,000,000, respectively. The experimental Q values obtained from Fig. 3b, c are smaller owing to the load of the two adjacent waveguides and imperfections in the fabricated samples^{29,30}.

The samples were fabricated using the following steps²⁵. A thin film of electron-beam resist was deposited by spin coating. The photonic-crystal patterns were drawn on the resist by electron-beam lithography. Next the samples were immersed in the developer at room temperature (22 °C) and the developed mask patterns were transferred to the top silicon slab using sulphur-hexafluoride-based dry etching. Finally the silicon dioxide layer underneath the patterned region was selectively removed using hydrofluoric acid to form an air-bridge structure.

In the optical measurements, the temperature of the sample stage was stabilized at room temperature using a Peltier controller. The nanocavity modes were excited by evanescent mode coupling with the corresponding waveguides, and dropped light from the nanocavity in the direction vertical to the slab was measured while scanning the wavelength-tunable laser with a narrow linewidth. The signal was collected from the 5- μm spot area at the centre of the nanocavity as shown in Fig. 2a. This measurement configuration is convenient for performing sensitive, quantitative analysis of the Raman laser (Supplementary Information, section E). The odd-mode excitation waveguide was fabricated close to the nanocavity because the $E_{y,\text{pump}}$ distribution is tightly confined in the y direction (Fig. 1g). For high-sensitivity Raman spectroscopy, we used a 500-mm-focal-length monochromator

with a liquid-nitrogen-cooled InGaAs-arrayed detector and a 0.65-numerical-aperture objective lens for the dropped light.

Received 21 February; accepted 30 April 2013.

1. Liu, A. *et al.* A high-speed silicon optical modulator based on a metal-oxide-semiconductor capacitor. *Nature* **427**, 615–618 (2004).
2. Jalali, B. & Fathpour, S. Silicon photonics. *J. Lightwave Technol.* **24**, 4600–4615 (2006).
3. Barkai, A. *et al.* Integrated silicon photonics for optical networks. *J. Opt. Netw.* **6**, 25–47 (2007).
4. Fang, A. W. *et al.* Hybrid silicon evanescent devices. *Mater. Today* **10**, 28–35 (2007).
5. Won, R. Integrating silicon photonics. *Nature Photon.* **4**, 498–499 (2010).
6. Michel, J., Liu, J. & Kimerling, L. C. High-performance Ge-on-Si photodetectors. *Nature Photon.* **4**, 527–534 (2010).
7. Claps, R., Dimitropoulos, D., Han, Y. & Jalali, B. Observation of Raman emission in silicon waveguides at 1.54 μm . *Opt. Express* **10**, 1305–1313 (2002).
8. Claps, R., Dimitropoulos, D., Raghunathan, V., Han, Y. & Jalali, B. Observation of stimulated Raman amplification in silicon waveguides. *Opt. Express* **11**, 1731–1739 (2003).
9. Boyraz, O. & Jalali, B. Demonstration of a silicon Raman laser. *Opt. Express* **12**, 5269–5273 (2004).
10. Rong, H. *et al.* An all-silicon Raman laser. *Nature* **433**, 292–294 (2005).
11. Rong, H. *et al.* A continuous-wave Raman silicon laser. *Nature* **433**, 725–728 (2005).
12. Rong, H. *et al.* Low-threshold continuous-wave Raman silicon laser. *Nature Photon.* **1**, 232–237 (2007).
13. Yang, X. & Wong, C. W. Design of photonic band gap nanocavities for stimulated Raman amplification and lasing in monolithic silicon. *Opt. Express* **13**, 4723–4730 (2005).
14. Yang, X. & Wong, C. W. Coupled-mode theory for stimulated Raman scattering in high- Q/V_m silicon photonic band gap defect cavity lasers. *Opt. Express* **15**, 4763–4780 (2007).
15. Loudon, R. The Raman effect in crystals. *Adv. Phys.* **13**, 423–482 (1964).
16. Ralston, J. M. & Chang, R. K. Spontaneous-Raman-scattering efficiency and stimulated scattering in silicon. *Phys. Rev. B* **2**, 1858–1862 (1970).
17. Liang, T. K. & Tsang, H. K. Role of free carriers from two-photon absorption in Raman amplification in silicon-on-insulator waveguides. *Appl. Phys. Lett.* **84**, 2745–2747 (2004).
18. Claps, R., Raghunathan, V., Dimitropoulos, D. & Jalali, B. Influence of nonlinear absorption on Raman amplification in silicon waveguides. *Opt. Express* **12**, 2774–2780 (2004).
19. Noda, S., Chutinan, A. & Imada, M. Trapping and emission of photons by a single defect in a photonic bandgap structure. *Nature* **407**, 608–610 (2000).
20. Akahane, Y., Asano, T., Song, B. S. & Noda, S. High- Q photonic nanocavity in a two-dimensional photonic crystal. *Nature* **425**, 944–947 (2003).
21. Song, B. S., Noda, S., Asano, T. & Akahane, Y. Ultra-high- Q photonic double-heterostructure nanocavity. *Nature Mater.* **4**, 207–210 (2005).
22. Takahashi, Y. *et al.* Design and demonstration of high- Q photonic heterostructure nanocavities suitable for integration. *Opt. Express* **17**, 18093–18102 (2009).
23. Taguchi, Y., Takahashi, Y., Sato, Y., Asano, T. & Noda, S. Statistical studies of photonic heterostructure nanocavities with an average Q factor of three million. *Opt. Express* **19**, 11916–11921 (2011).
24. Takano, H., Asano, T. & Noda, S. at *Spring Meeting Jpn Soc. Appl. Phys.*, abstr. 29a-ZB-8 (2007).
25. Terawaki, R., Takahashi, Y., Chihara, M., Inui, Y. & Noda, S. Ultrahigh- Q photonic crystal nanocavities in wide optical telecommunication bands. *Opt. Express* **20**, 22743–22752 (2012).
26. Song, B. S., Jeon, S. B. & Noda, S. Symmetrically glass-clad photonic crystal nanocavities with ultrahigh quality factors. *Opt. Lett.* **36**, 91–93 (2011).
27. Han, Z., Checoury, X., Haret, L.-D. & Boucaud, P. High quality factor in a two-dimensional photonic crystal cavity on silicon-on-insulator. *Opt. Lett.* **36**, 1749–1751 (2011).
28. Baba, T. Slow light in photonic crystals. *Nature Photon.* **2**, 465–473 (2008).
29. Hagino, H., Takahashi, Y., Tanaka, Y., Asano, T. & Noda, S. Effects of fluctuation in air hole radii and positions on optical characteristics in photonic crystal heterostructure nanocavities. *Phys. Rev. B* **79**, 085112 (2009).
30. Asano, T., Song, B. S. & Noda, S. Analysis of the experimental Q factors (~ 1 million) of photonic crystal nanocavities. *Opt. Express* **14**, 1996–2002 (2006).

Supplementary Information is available in the online version of the paper.

Acknowledgements We especially thank H. Takano for a preliminary calculation done before the start of this project. We thank K. Ishizaki and K. Kitamura for assistance in device fabrication, Y. Tanaka for assistance with finite-difference time-domain calculations, A. Oskooi and H. Ishihara for comments, and Y. Sakamoto for software assistance. Y.T. is supported by the NanoSquare programme, Funds for the Development of Human Resources in Science and Technology, commissioned by MEXT. This work was supported by JST, PRESTO, the NanoSquare programme and MEXT KAKENHI (grant numbers 23104721 and 21104512). The spectral measurements were partly supported by JSPS KAKENHI (grant number 23686015) and the Asahi Grass Foundation. The device fabrication was greatly supported by JSPS KAKENHI (grant number 20226002), the Ministry of Economy, Trade and Industry (METI) through its 'Future Pioneering Projects', and the CPHoST programme.

Author Contributions Y.T. designed the project, designed the original device, fabricated the samples, performed the measurements and wrote the paper. S.N. organized the contribution to the project from Kyoto University, where the fundamental studies to realize high- Q/V nanocavities and the initial investigation into Raman lasers was performed. S.N. also contributed greatly to writing the paper. Y.I. analytically determined the optimum crystalline direction for lasing and contributed to writing Supplementary Information, sections A and B. M.C. established the method to tune the nanocavity mode spacing, T.A. contributed to the theoretical analysis and R.T. contributed to the development of the measurement system.

Author Information Reprints and permissions information is available at www.nature.com/reprints. The authors declare no competing financial interests. Readers are welcome to comment on the online version of the paper. Correspondence and requests for materials should be addressed to Y.T. (y-takahashi@21c.osakafu-u.ac.jp) or S.N. (snoda@kuee.kyoto-u.ac.jp).

Lifespan of mountain ranges scaled by feedbacks between landsliding and erosion by rivers

David L. Egholm¹, Mads F. Knudsen¹ & Mike Sandiford²

An important challenge in geomorphology is the reconciliation of the high fluvial incision rates observed in tectonically active mountain ranges with the long-term preservation of significant mountain-range relief in ancient, tectonically inactive orogenic belts^{1–3}. River bedrock erosion and sediment transport are widely recognized to be the principal controls on the lifespan of mountain ranges. But the factors controlling the rate of erosion^{4–8} and the reasons why they seem to vary significantly as a function of tectonic activity remain controversial. Here we use computational simulations to show that the key to understanding variations in the rate of erosion between tectonically active and inactive mountain ranges may relate to a bi-directional coupling between bedrock river incision and landslides. Whereas fluvial incision steepens surrounding hillslopes and increases landslide frequency⁹, landsliding affects fluvial erosion rates in two fundamentally distinct ways. On the one hand, large landslides overwhelm the river transport capacity and cause upstream build up of sediment that protects the river bed from further erosion^{9–11}. On the other hand, in delivering abrasive agents to the streams^{4–6}, landslides help accelerate fluvial erosion. Our models illustrate how this coupling has fundamentally different implications for rates of fluvial incision in active and inactive mountain ranges. The coupling therefore provides a plausible physical explanation for the preservation of significant mountain-range relief in old orogenic belts, up to several hundred million years after tectonic activity has effectively ceased.

The erosive power of rivers incises bedrock in mountain belts and forms self-organizing patterns characteristic of dendritic drainage systems. Bedrock incision occurs by a combination of processes related to the transport of both water and sediment within the rivers^{4–8}. The balance between these erosion processes is poorly understood, and models for fluvial landscape evolution often rely on the assumption that river erosion rates scale with some measure of flow intensity, such as stream power¹² or shear stress¹³, which are both simple functions of local relief and water discharge. These models, collectively referred to as ‘stream-power models’, have found widespread favour in the modelling community, because they reproduce many features observed in natural landscapes^{12–15}.

However, stream-power models do not adequately capture the role of mobile sediment in fluvial erosion, and a number of recent studies of long-term erosion rates based on field measurements, low-temperature thermochronology and cosmogenic nuclides show that variations in precipitation rate^{16–19} and topographical relief^{20,21}, and, hence, stream power, do not always account for the long-term erosion rate of bedrock landscapes. Instead, measurements of average catchment denudation rates suggest that erosion is fast primarily where active tectonism constantly rejuvenates the topographic surface^{1,2,16,19–21} but slow in many high-relief passive orogens^{1,2,22,23}, which require nonlinear couplings between relief, discharge and erosion that are not easily explained by the stream-power concept. In particular, the long-term preservation of kilometre-scale mountainous relief in ancient, tectonically inactive, Palaeozoic orogenic belts, such as the Appalachian mountains in the United States, the Ural mountains in Russia and the Caledonian mountains in Greenland and Scandinavia (Supplementary Fig. 1), seems

directly at odds with the stream-power concept for river erosion. Although post-orogenic uplift processes related to mantle dynamics may possibly have influenced some of the Palaeozoic orogenic belts, the lifespan of mountainous relief in these old orogenic belts remains a long-standing problem in Earth sciences³.

A concept that more accurately describes the physics of erosional processes in rivers involves a process-based formalism for bedrock incision by saltating sediment particles in a river^{5,24}. In this saltation–abrasion model, the erosion rate is a direct function of abrasion per particle impact multiplied by the frequency of impacts and a sediment-cover factor²⁴ (Methods). The model captures the complex role of sediment concentration for the bedrock erosion rate and is supported by recent catchment-scale observations²⁵ and longitudinal river profiles^{26,27}, but has yet to be tested against long-term landscape evolution at orogenic scales.

To explore the fundamental implications of feedbacks between hillslope erosion, sediment delivery and channel incision in a non-glacial setting, we performed computational experiments that couple the full physics of the saltation–abrasion model with a stochastic model for bedrock landsliding and multi-component sediment transport on hillslopes and in rivers (Methods). We apply the saltation–abrasion formalism to model fluvial incision because of its solid foundation in physical principles based on experiments^{5,24}, but our findings apply to all sediment-flux-dependent fluvial incision models. Bedrock landsliding is incorporated because threshold-dominated hillslope processes, such as landsliding, have a dominant role in limiting the relief in tectonically active regions^{9,11,20,21} and because landslide magnitude and frequency are critical for providing abrasive agents to the fluvial system^{10,11,16,17,28}. Landslides are important for regulating the erosion budget of tectonically active mountain ranges, which is most evident in the distinct threshold landscapes presently found, for example, in Taiwan²⁸ and the Himalayas^{20,21}. In addition to fluvial incision and bedrock landsliding, our computational experiments include slope-independent hillslope weathering, nonlinear hillslope sediment transport and grain-size-dependent sediment transport in rivers (Methods).

The computational experiments are designed to investigate primarily the coupled impact of bedrock landsliding controlled by threshold slopes and fluvial erosion driven by the sediment flux in rivers. We note that lithological contrasts not addressed by our model experiments also influence river incision rates, and that, depending on the geological setting, the rock hardness may increase when long-term erosion exposes the deep and resistant core of mountain belts. Furthermore, additional erosion processes in rivers and on hillslopes may be of relevance in natural systems. The feedbacks between landslides and river incision that we address here are likely to dominate in settings where sediment-bed impacts drive bedrock abrasion or accelerate quarrying by producing fractures in the bedrock, but their significance will be less important in settings where other processes, such as chemical weathering, dominate^{1,4}. The aim here, however, is to demonstrate the fundamental impact of feedbacks between landslides and saltation–abrasion on fluvial incision rates in the context provided by the necessity to reconcile rapid incision rates in tectonically active orogens with

¹Department of Geoscience, Aarhus University, Høegh-Guldbergs Gade 2, 8000 Aarhus C, Denmark. ²School of Earth Sciences, University of Melbourne, Victoria 3010, Australia.

the long-term survival of significant orogenic relief after cessation of tectonic activity. To do so, we model a cross-section through an asymmetric mountain range generated by tectonic rock uplift in the shape of a two-sided wedge system (Fig. 1). We focus on the influence of tectonic uplift on river erosion rates, and find that the results are independent of bedrock lithology as long as saltation–abrasion remains the dominant driver of river erosion. The spatially variable uplift rate allows us to study the influence of uplift rate on the resulting relief (Supplementary Fig. 2). To demonstrate the key feedbacks, we performed identical experiments using both the stream-power model and the saltation–abrasion model with the same coupling to bedrock landsliding and sediment transport in both models (Methods).

Our results confirm that fluvial incision by saltation–abrasion generates landscape morphologies very similar to those predicted by stream-power models and observed in fluvial systems²⁹. Channel profiles are upwards concave and drainage following the steepest topographic descent paths leads naturally to a system defined by catchments with large and gently dipping valleys and a number of steeper tributaries (Fig. 1). During the tectonically active phase, both the saltation–abrasion model and the stream-power model reach a topographic steady state in which tectonic rock uplift is balanced by erosion everywhere in the modelled landscape. Both models are associated with poorly constrained rate-limiting parameters (Methods), which we calibrate to obtain steady-state landscapes of similar mean ($\sim 1,100$ m) and maximum ($\sim 3,500$ m) elevations. The scale of this steady-state configuration resembles those of relatively small orogens like, for example, Taiwan or the Southern Alps. In the steady-state configuration, bedrock landsliding represents a primary erosion mechanism in both models because hillslopes are

allowed to reach threshold slopes in many places (Supplementary Information and Supplementary Figs 2 and 3). The simulated landslide frequency-size distribution conforms to a power-law distribution (Supplementary Fig. 5), although the resolution of the numerical model limits the occurrence of small landslides. Of greater importance is, however, the bulk landslide erosion rate (Fig. 2), which represents the primary sediment flux from the hillslopes to the river network in the tectonically active phase.

Although the steady-state topographic patterns are largely similar for the two models, the temporal variations in erosion rate differ significantly. The saltation–abrasion model reveals a highly dynamic system with several feedbacks (Figs 2 and 3 and Supplementary Video 1). When the landslide frequency increases, rivers receive more sediment and accelerate fluvial incision while the landslide detritus is moved through the drainage network (Fig. 2). This further accelerates the landslide frequency because hillslopes steepen as the base level set by the channel elevation is lowered. This positive feedback terminates when excessive sediment supply protects the river bed from further erosion. At this point, fluvial incision slows, reducing the likelihood of landslides, and a negative feedback between fluvial erosion and landslides is established that helps to stabilize the relief temporarily (Fig. 2).

The pattern characterized by a highly oscillatory erosion flux during the active phase changes when tectonic activity ceases. At this point, continued rock uplift is due only to flexural-isostatic unloading, and the mean elevation of the landscape starts to decline. As hillslope gradients decrease below the critical threshold value for landsliding (Methods), the landslide frequency drops drastically (Fig. 3a). The landslide frequency decreases in our models simply because tectonic rock uplift no longer maintains the steep threshold slopes, and we note that the drop in landslide frequency may be even more dramatic in natural settings because earthquakes related to tectonic activity are

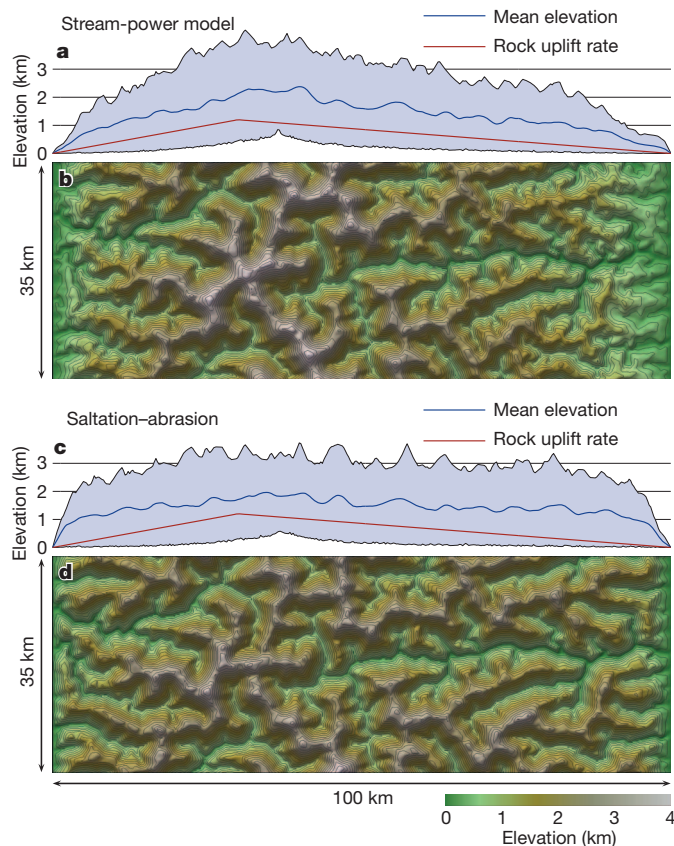


Figure 1 | Landscape morphology. **a**, Minimum, mean and maximum elevations along an east–west transect of the stream-power model. The red curve shows the variation in uplift rate, which peaks at 1 mm yr^{-1} . **b**, Detailed view of the resulting model landscape when bedrock landsliding is coupled to stream-power erosion. **c**, **d**, The same details, but for the saltation–abrasion model. The full model geometry is shown in Supplementary Fig. 4.

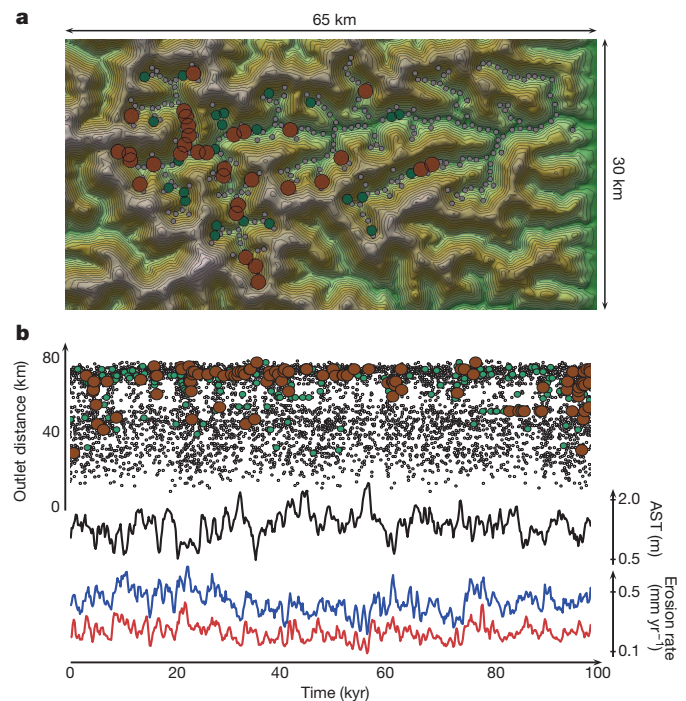


Figure 2 | Feedbacks between landsliding, fluvial incision and sediment transport. **a**, The location of large landslides in one of the model's major catchments during a 100-kyr period with tectonic uplift. The circles indicate the locations of the landslide initiation points. Circle size and colour indicate landslide volume (brown, $>0.3 \text{ km}^3$; green, $>0.2 \text{ km}^3$; grey, $>0.05 \text{ km}^3$). **b**, The temporal distribution of landslides (circles) with distance to catchment outlet along the vertical axis. The figure also shows catchment-averaged fluvial (red curve) and landslide (blue curve) erosion rates along with the averaged sediment thickness (AST) in the catchment (black curve).

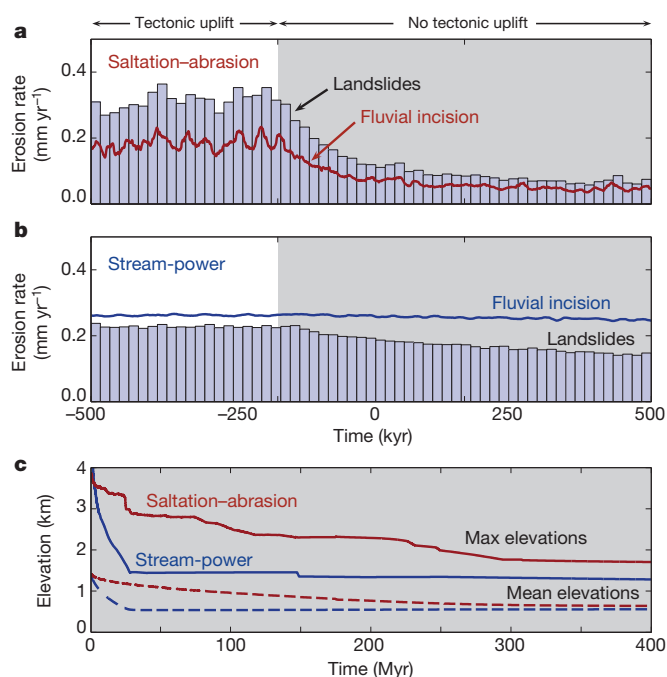


Figure 3 | Erosion rates and post-orogenic lifespan. **a**, Highly fluctuating erosion rates by saltation-abrasion and landsliding during the phase of tectonic uplift and slow erosion when tectonic activity stops. **b**, The combination of stream-power erosion and landslides does not include these feedbacks, and erosion rates are not directly affected by tectonic activity. The grey bars in **a** and **b** represent landslide erosion rates averaged over 10-kyr intervals. **c**, Results of model experiments covering 400 Myr of post-orogenic topographic evolution. The landscape of the saltation-abrasion model stays high for several hundred million years before a steady, transport-limited configuration is reached. The stream-power model achieves this configuration after only 25 Myr.

viewed as important landslide triggers¹¹. In the saltation-abrasion model, the decrease in landslide frequency leads to a corresponding decrease in the rate of fluvial incision, because of the associated decline in sediment input to the streams. The slowing fluvial erosion keeps channel elevations high and stalls both erosion processes by further reducing the landslide frequency. This is in stark contrast to the behaviour of the stream-power model (Fig. 3b), which exhibits a much more gradual decrease in erosion rate after tectonic uplift ceases, because the stream-power erosion rate is scaled only by the local channel slope and water discharge.

A sudden decrease in landslide frequency and saltation-abrasion erosion has a significant effect on the post-orogenic lifespan. Our scaled model results show that peaks can stand above an elevation of 2 km for more than 200 Myr following the cessation of tectonic activity (Fig. 3c). That contrasts with our scaled stream-power model in which elevations above 2 km last only 20 Myr because the stream-power erosion rates remain high in the absence of tectonic activity as long as significant relief persists. Both model experiments eventually terminate in similar transport-limited landscapes with main valleys that become permanently alluviated when the available stream power decreases below the threshold required for sediment transport³. At this stage, the two models converge, but the duration of the transition to a transport-limited stage differs by more than an order of magnitude because the mechanisms dictating the rate of post-orogenic river incision in the two models are fundamentally different. Landscapes in the stream-power model reach the transport-limited stage after only 25 Myr, whereas this transition takes more than ten times longer in the saltation-abrasion model. (Fig. 3c, Supplementary Information and Supplementary Fig. 4). These precise figures depend on the details of the parameterization, but the order-of-magnitude difference in post-orogenic topographical lifespan stands as a robust result of the different fluvial erosion mechanisms.

The prolonged lifespan of significant mountain-range topography in the saltation-abrasion model is caused by the reduced influx of sediment to the rivers³⁰ when tectonic activity stops, and we note that variations in the parameterization of saltation-abrasion, the sediment transport or the bedrock exposure estimates do not influence this result (Supplementary Fig. 6). Although other processes may substantially influence the post-orogenic lifespan in some geological settings, our results demonstrate that couplings between sediment-flux-dependent fluvial incision and threshold-dominated hillslope processes have the potential to explain the effects of tectonic uplift on long-term erosion rates^{1,2,17,19–21}. The interplay between hillslope processes and fluvial erosion by saltation-abrasion therefore provides a plausible physical mechanism for the preservation of several-hundred-million-year-old orogenic reliefs in tectonically inactive regions.

METHODS SUMMARY

The landscape evolution model used in this study computes the transport of water and sediment across a plan-form grid consisting of irregularly distributed Voronoi cells. Connecting neighbouring cells in the direction of steepest descent generates the fluvial surface transport network. Topographical depressions, which may for example arise from dams generated by landslides, are filled by water that form lakes and ensure continuous drainage from every grid cell to the model boundaries.

The rate of fluvial incision into bedrock is calculated from either the saltation-abrasion model or the stream-power model. For computing saltation-abrasion, we include the full physics of the model²⁴. Both types of fluvial erosion model are coupled to models for bedrock landsliding, sediment transport in rivers and on hillslopes, long-term hillslope weathering, and flexural isostasy. The various erosion components are coupled through their effects on bedrock topography and their contributions to a layer of transportable sediment. The fluvial sediment transport model operates with sediment of varying grain sizes to incorporate the effects of downstream fining on sediment transport capacity and saltation-abrasion erosion rate. The hillslope sediment transport model is independent of grain size, but includes nonlinear effects of slope. See Methods and Supplementary Information for additional references and more details on all model components.

Full Methods and any associated references are available in the online version of the paper.

Received 23 January; accepted 22 April 2013.

- Von Blanckenburg, F. The control mechanisms of erosion and weathering at basin scale from cosmogenic nuclides in river sediment. *Earth Planet. Sci. Lett.* **237**, 462–479 (2005).
- Molnar, P., Andersen, R. S. & Anderson, S. P. Tectonics, fracturing of rock, and erosion. *J. Geophys. Res.* **112**, F03014 (2007).
- Baldwin, J. A., Whipple, K. X. & Tucker, G. E. Implications of the shear stress river incision model for the timescale of postorogenic decay of topography. *J. Geophys. Res.* **108**, 2158 (2003).
- Whipple, K. X., Hancock, G. S. & Anderson, R. S. River incision into bedrock: mechanics and relative efficacy of plucking, abrasion, and cavitation. *Geol. Soc. Am. Bull.* **112**, 490–503 (2000).
- Sklar, L. S. & Dietrich, W. E. Sediment and rock strength controls on river incision into bedrock. *Geology* **29**, 1087–1090 (2001).
- Hancock, G. S. & Anderson, R. S. Numerical modelling of fluvial strath-terrace formation in response to oscillating climate. *Geol. Soc. Am. Bull.* **114**, 1131–1142 (2002).
- Turowski, J. M., Lague, D. & Hovius, N. Cover effects in bedrock abrasion: a new derivation and its implications for the modelling of bedrock channel morphology. *J. Geophys. Res.* **112**, F04006 (2007).
- Yanites, B. J. *et al.* The influence of sediment cover variability on long-term river incision rates: an example from Peikang River, central Taiwan. *J. Geophys. Res.* **116**, F03016 (2011).
- Larsen, I. J. & Montgomery, D. R. Landslide erosion coupled to tectonics and river incision. *Nat. Geosci.* **5**, 468–473 (2012).
- Quimet, W. B. *et al.* The influence of large landslides on river incision in a transient landscape: eastern margin of the Tibetan Plateau (Sichuan, China). *Geol. Soc. Am. Bull.* **119**, 1462–1476 (2007).
- Korup, O., Densmore, A. L. & Schlunegger, F. The role of landslides in mountain range evolution. *Geomorphology* **120**, 77–90 (2010).
- Seidl, M. A. & Dietrich, W. E. The problem of channel erosion into bedrock. *Catena* (Suppl.) **23**, 101–124 (1992).
- Howard, A. D. & Kerby, G. Channel changes in badlands. *Geol. Soc. Am. Bull.* **94**, 739–752 (1983).
- Whipple, K. X. *et al.* Geomorphic limits to climate-induced increases in topographic relief. *Nature* **401**, 39–43 (1999).
- Kirby, E. & Whipple, K. X. Quantifying differential rock-uplift rates via stream profile analysis. *Geology* **29**, 415–418 (2001).

16. Dadson, S. J. *et al.* Links between erosion, runoff variability and seismicity in the Taiwan orogen. *Nature* **426**, 648–651 (2003).
17. Stock, J. D. *et al.* Field measurements of incision rates following bedrock exposure: implications for process controls on the long profiles of valleys cut by rivers and debris flow. *Geol. Soc. Am. Bull.* **117**, 174–194 (2005).
18. Riebe, C. S. *et al.* Minimal climatic control on erosion rates in the Sierra Nevada. *Calif. Geol.* **29**, 447–450 (2001).
19. Burbank, D. W. *et al.* Decoupling of erosion and precipitation in the Himalayas. *Nature* **426**, 652–655 (2003).
20. Burbank, D. W. *et al.* Bedrock incision, rock uplift and threshold hillslopes in the northwestern Himalayas. *Nature* **379**, 505–510 (1996).
21. Montgomery, D. R. & Brandon, M. T. Topographic controls on erosion rates in tectonically active mountain ranges. *Earth Planet. Sci. Lett.* **201**, 481–489 (2002).
22. von Blanckenburg, F., Hewawasam, T. & Kubik, P. W. Cosmogenic nuclide evidence for low weathering and denudation in the wet, tropical highlands of Sri Lanka. *J. Geophys. Res.* **109**, F03008 (2004).
23. Scharf, T. E. *et al.* Strong rocks sustain ancient postorogenic topography in southern Africa. *Geology* **41**, 331–334 (2013).
24. Sklar, L. S. & Dietrich, W. E. A mechanistic model for river incision into bedrock by saltating bed load. *Wat. Resour. Res.* **40**, W06301 (2004).
25. Cowie, P. A. *et al.* New constraints on sediment-flux-dependent river incision: implications for extracting tectonic signals from river profiles. *Geology* **36**, 535–538 (2008).
26. Whipple, K. X. & Tucker, G. E. Implications of sediment-flux-dependent river incision models for landscape evolution. *J. Geophys. Res.* **107**, 2039 (2002).
27. Gasparini, N. M., Whipple, K. X. & Bras, R. L. Predictions of steady state and transient landscape morphology using sediment-flux-dependent river incision models. *J. Geophys. Res.* **112**, F03S09 (2007).
28. Hovius, N., Stark, C. P., Hao-Tsu, C. & Jiun-Chuan, L. Supply and removal of sediment in a landslide-dominated mountain belt: Central Range, Taiwan. *J. Geol.* **108**, 73–89 (2000).
29. Sklar, L. S. & Dietrich, W. E. Implications of the saltation-abrasion bedrock incision model for steady-state river longitudinal profile relief and concavity. *Earth Surf. Process. Landf.* **33**, 1129–1151 (2008).
30. Jansen, J. D. *et al.* Does decreasing paraglacial sediment supply slow knickpoint retreat? *Geology* **39**, 543–546 (2011).

Supplementary Information is available in the online version of the paper.

Acknowledgements D.L.E. acknowledges funding from the Danish Council for Independent Research under the Sapere Aude programme. M.F.K. acknowledges funding from the Carlsberg Foundation and the Villum Foundation. M.S. acknowledges funding from ARC DP110104098 and AISRF.

Author Contributions D.L.E. developed the computational modelling scheme and performed the modelling. All authors contributed equally to the design of the study and the writing of the paper.

Author Information Reprints and permissions information is available at www.nature.com/reprints. The authors declare no competing financial interests. Readers are welcome to comment on the online version of the paper. Correspondence and requests for materials should be addressed to D.L.E. (david@geo.au.dk).

METHODS

River dynamics. We modelled fluvial erosion and sediment transport across a two-dimensional plan form grid consisting of irregularly distributed Voronoi cells. The river pathways were established by connecting neighbouring cells in the direction of steepest descent in every time step following the CASCADE algorithm³¹. The precipitation rate, p_r , was uniform across the grid, implying that the volumetric water flux was $Q_w = p_r A$, where A is the upstream catchment area.

We followed ref. 32 in calculating the average bed shear stress as $\tau_b = \rho_w (g Q_w S)^{2/3} W^{-2/3}$, where ρ_w is the density of water, g is the acceleration due to gravity and S is the channel slope. The channel width, $W = k_w Q_w^{1/2}$, is a function of surface water discharge where k_w is a constant channel-width scaling factor³² (see Supplementary Table 1 for values of all model parameters).

Sediment transport. The applied landscape evolution model transports sediments in rivers and on hillslopes. The computational experiments therefore included a layer of mobile sediment of thickness H_s . The thickness of this sediment layer was updated by solving the continuity equation for volume conservation

$$\frac{\partial H_s}{\partial t} = -\nabla \cdot (q_{sf} + q_{sh}) + \frac{\rho_r}{\rho_s} (\dot{E}_f + \dot{E}_l + \dot{E}_h)$$

where q_{sf} and q_{sh} are the sediment flux vectors in rivers and on hillslopes, respectively; ∇ is the gradient operator; ρ_r and ρ_s are the densities of bedrock and sediment, respectively; and \dot{E}_f , \dot{E}_l and \dot{E}_h are the bedrock erosion rates due to rivers, landslides and hillslope weathering, respectively. These erosion mechanisms are described in separate sections below.

For the downstream sediment flux in rivers (q_{sf}), the transport model operated with sediment of varying grain sizes. This made it possible to incorporate the effects of downstream fining on sediment transport and bedrock erosion by saltation–abrasion. The total sediment volume was therefore binned according to grain size (D) from $\psi = 0, 1, 2, \dots, 8$, where $\psi = \log_2(D/D_0)$ is a logarithmic grain-size distribution³³ (Supplementary Table 2) and $D_0 = 1$ mm is a reference grain size. The sediments were then transported by the two-fraction model of ref. 34, in which the different grain sizes are combined in two groups: mixed sand ($D \leq 2$ mm) and mixed gravel ($D \geq 2$ mm). Carrying capacities for sand and gravel were calculated from the two-fraction model and rivers were assumed to run at capacity if enough sediment was available (see Supplementary Information for more information on the fluvial sediment transport model).

For sediment transport on hillslopes, we used a nonlinear flux model^{35,36} relating volumetric sediment flux, q_{sh} , to the bed gradient, ∇b :

$$q_{sh} = -K_s \frac{\nabla b}{1 - (|\nabla b|/s_c)^2}$$

where s_c is the critical slope and K_s is a constant (Supplementary Table 1). In this model, sediment transport is inefficient on flat surfaces and more efficient on steep slopes that approach the critical value, s_c .

River erosion by saltation–abrasion. The saltation–abrasion erosion rate, \dot{E}_f^{sa} , is expressed as the product of three terms²⁴, $\dot{E}_f^{\text{sa}} = V_i I_r F_c$, where V_i is the average volume of bedrock detached per particle impact; I_r is the rate of particle impact per unit area and F_c (the sediment cover factor) is the fraction of the river bed that is free of sediment and therefore exposed to erosion.

We followed the approach of ref. 24 closely, and consequently approximated \dot{E}_f^{sa} with

$$\dot{E}_f^{\text{sa}} = K_{sa} \frac{q_{sf}^{\psi}}{W} F_c (\tau' / \tau_c' - 1)^{-0.52} |1 - (u' / w_f)|^{1.5}$$

where K_{sa} is a lumped scaling parameter (Supplementary Information and Supplementary Table 1), q_{sf}^{ψ} is the sediment flux of a particular grain size, τ' is the non-dimensional Shield's stress, τ_c' is the non-dimensional critical threshold shear stress for sediment entrainment, $u' = \sqrt{\tau_b / \rho_w}$ is the shear velocity and w_f is the settling velocity of sediment grains. The sediment-free fraction of the river bed, F_c , was assumed to vary linearly between two endmember cases: (1) when the river runs at capacity and the bed is fully alluviated ($V_t = \Delta t Q_b$, where V_t is the volume of sediment available for transport, Q_t is the sediment transport capacity of the river segment and Δt is the length of the time step), and (2) when the river receives no sediment that can form patches of alluvial cover ($V_t = 0$):

$$F_c = \begin{cases} 1 - V_t / \Delta t Q_t & \text{for } V_t < \Delta t Q_t \\ 0 & \text{otherwise} \end{cases}$$

Importantly, apart from the sediment carried by the river, V_t includes sediment deposited on the river bed, which ensures that sediment not in transport also influences the sediment cover factor. Additional experiments with other types of functional form for F_c show that our conclusions are robust with respect to such variations (Supplementary Fig. 6).

The saltation–abrasion rate, \dot{E}_f^{sa} , depends on grain size, and we therefore computed the total erosion rate by summing the contributions to the erosion rate associated with the individual sediment grain-size bins (Supplementary Table 2). The values of q_{sf}^{ψ} , τ' , τ_c' and w_f were therefore calculated separately for each sediment grain size (see Supplementary Information for details on the grain-size dependence and for the full derivation of the saltation–abrasion relations above).

Stream-power erosion. For the model experiments using stream-power erosion, the fluvial erosion rate was calculated from $\dot{E}_f^{\text{sp}} = K_{sp} F_c Q_w^m S^n$, where K_{sp} is a rate-limiting constant³⁷, Q_w is the water discharge (volumetric flux), S is the channel slope, and m and n are constants (Supplementary Table 2). We note that we included in the stream-power model the protecting effect of sediment cover by incorporating F_c from the saltation–abrasion theory. By including the same protecting effects of sediments in all experiments, we effectively isolated the differences between the two incision models (saltation–abrasion and stream-power erosion). For example, by incorporating F_c in both models, we made sure that transport thresholds affected both model types similarly.

Bedrock landslides. We used the model in ref. 38 for simulating bedrock landslides. The model is stochastic in the sense that the probability of hillslope failure depends on the Culmann slope stability criterion³⁸. The Culmann criterion predicts the maximum stable height of a hillslope, H_c , from the angle of internal friction, ϕ , the hillslope cohesion, C , and the hillslope angle, β :

$$H_c = \frac{4C \sin(\beta) \cos(\phi)}{\rho_s g (1 - \cos(\beta - \phi))}$$

In every time step of the model run, a fixed number, N_c , of random cells were checked for landsliding. From each of these cells (target cells), the maximum extent of a stable plane was mapped by recursively collecting in a list the upslope cells with elevations above the cone-shaped plane that dips with angle ϕ and passes through the target cell. The stable plane must be continuous, meaning that only cells that neighbour a cell already on the list was added to the list.

After the list was generated, the hillslope height, H , and the hillslope angle, β , were established from the maximum elevation difference between the target cell and cells on the list. The failure probability was computed as $p_{\text{fail}} = H/H_c$. The hillslope fails if a randomly generated number between 0 and 1 falls below p_{fail} .

If failure occurred, the angle of the failure plane³⁸ was calculated from $\theta = (\beta + \phi)/2$. The failure plane was mapped by repeating the recursive procedure, now listing the cells with elevations above the cone-shaped failure plane dipping at angle θ . The rock mass above the failure plane was eroded and passed to the target cell as new sediment.

We assumed that the sediment generated in a landslide has a fractal distribution of grain sizes³⁹, such that $N_{\psi} \propto D_{\psi}^{-f}$, where N_{ψ} is the number of particles with diameter greater than D_{ψ} (Supplementary Table 2) and $f = 2.65$ is the fractal dimension⁴⁰. The fractal distribution was used to constrain the volume distribution of grain sizes within a landslide deposit: $V_s(\psi) = w_{\psi} V_{\text{landslide}}$, where $V_{\text{landslide}}$ is the total sediment volume generated by the landslide and w_{ψ} is the volume weight function associated with each grain-size bin ψ (Supplementary Table 2). We note that the volume weights were calculated to satisfy the fractal distribution.

Hillslope weathering. We followed ref. 38 by including nonlinear sediment (regolith) production to simulate slow hillslope erosion on bare bedrock surfaces⁴¹ (where $H_s = 0$), faster erosion under moderate sediment thicknesses⁴² ($H_s \leq H_s'$) and decreasing erosion rates under larger sediment thicknesses⁴³ ($H_s > H_s'$). In this model, the bedrock erosion rate is

$$\dot{E}_h = \begin{cases} \dot{E}_c + \frac{\dot{E}' - \dot{E}_0}{H_s'} H_s & \text{for } 0 \leq H_s < H_s' \\ \dot{E}' \exp\left(\frac{H_s' - H_s}{\Delta H}\right) & \text{for } H_s \geq H_s' \end{cases}$$

All parameters are listed in Supplementary Table 1.

We assumed that the grain sizes of the sediments produced by weathering is of the same fractal distribution as for landsliding, and the volume weights of Supplementary Table 2 were therefore reused. We note that grain sizes are likely to be smaller for sediments generated by weathering than by landsliding. However, using the same grain sizes for both erosion processes is a conservative assumption, because the saltation–abrasion erosion process preferentially weights the coarser fractions. Reducing sediment grain sizes for weathering would therefore further lower saltation–abrasion rates and amplify the difference between the saltation–abrasion and stream-power models.

Flexural isostasy. Flexural isostatic adjustments, $W_i(x, y)$, in response to erosional unloading and sediment deposition were performed according to the two-dimensional elastic thin-plate equation:

$$\frac{\partial^4 W_i}{\partial x^4} + 2 \frac{\partial^4 W_i}{\partial x^2 \partial y^2} + \frac{\partial^4 W_i}{\partial y^4} = \frac{L(x, y)}{D_i}$$

Here $D_f = YT_c^3/12(1 - \nu^2)$ is the flexural rigidity, Y is Young's modulus, ν is the Poisson ratio and T_c is the elastic thickness of the lithosphere (Supplementary Table 1). $L(x, y) = \rho_s g E(x, y) - \rho_s g H_s(x, y) - \rho_a g W_f(x, y)$ is the vertical load on the plate (positive upward), where $E(x, y)$ is the total bedrock erosion in each model cell, H_s is the amount of sediment present and ρ_a is the density of the isostatically compensating asthenosphere rocks.

31. Braun, J. & Sambridge, M. Modelling landscape evolution on geological time scales: a new method based on irregular spatial discretization. *Basin Res.* **9**, 27–52 (1997).
32. Tucker, G. E. & Slingerland, R. L. Predicting sediment flux from fold and thrust belts. *Basin Res.* **8**, 329–349 (1996).
33. Parker, G. & Andrews, E. D. Sorting of bedload sediment by flow in meander bends. *Wat. Resour. Res.* **21**, 1361–1373 (1985).
34. Wilcock, P. R. Two-fraction model of initial sediment motion in gravel-bed rivers. *Science* **280**, 410–412 (1998).
35. Andrews, D. J. & Bucknam, R. C. Fitting degradation of shoreline scarps by a nonlinear diffusion model. *J. Geophys. Res.* **92**, 12857–12867 (1987).
36. Roering, J. J., Kirchner, J. W. & Dietrich, W. E. Evidence for nonlinear, diffusive sediment transport and implications for landscape morphology. *Wat. Resour. Res.* **35**, 853–870 (1999).
37. Howard, A. D. A detachment-limited model of drainage basin evolution. *Wat. Resour. Res.* **30**, 2261–2285 (1994).
38. Densmore, A. L., Ellis, M. A. & Anderson, R. S. Landsliding and the evolution of normal-fault-bounded mountains. *J. Geophys. Res.* **103**, 15203–15219 (1998).
39. Turcotte, D. *Fractals and Chaos in Geology and Geophysics* 20–34 (Cambridge Univ. Press, 1992).
40. Crosta, G., Frattini, P. & Fusi, N. Fragmentation in the Val Pola rock avalanche, Italian Alps. *J. Geophys. Res.* **112**, F01006 (2007).
41. Small, E. E., Anderson, R. S. & Hancock, G. S. Estimates of the rate of regolith production using ^{10}Be and ^{26}Al from an alpine hillslope. *Geomorphology* **27**, 131–150 (1999).
42. Ahnert, F. Brief description of a comprehensive three-dimensional process-response model of landform development. *Z. Geomorphol.* **24**, 11–22 (1970).
43. Heimsath, A. M., Dietrich, W. E., Nishiizumi, K. & Finkel, R. C. The soil production function and landscape equilibrium. *Nature* **388**, 358–361 (1997).

Stability of active mantle upwelling revealed by net characteristics of plate tectonics

Clinton P. Conrad¹, Bernhard Steinberger^{2,3} & Trond H. Torsvik^{3,4,5}

Viscous convection within the mantle is linked to tectonic plate motions^{1–3} and deforms Earth's surface across wide areas^{4–6}. Such close links between surface geology and deep mantle dynamics presumably operated throughout Earth's history, but are difficult to investigate for past times because the history of mantle flow is poorly known⁷. Here we show that the time dependence of global-scale mantle flow can be deduced from the net behaviour of surface plate motions. In particular, we tracked the geographic locations of net convergence and divergence for harmonic degrees 1 and 2 by computing the dipole and quadrupole moments of plate motions from tectonic reconstructions^{8,9} extended back to the early Mesozoic era. For present-day plate motions, we find dipole convergence in eastern Asia and quadrupole divergence in both central Africa and the central Pacific. These orientations are nearly identical to the dipole and quadrupole orientations of underlying mantle flow, which indicates that these 'net characteristics' of plate motions reveal deeper flow patterns. The positions of quadrupole divergence have not moved significantly during the past 250 million years, which suggests long-term stability of mantle upwelling beneath Africa and the Pacific Ocean. These upwelling locations are positioned above two compositionally and seismologically distinct¹⁰ regions of the lowermost mantle, which may organize global mantle flow¹¹ as they remain stationary over geologic time¹².

Viscous convection of Earth's mantle dissipates our planet's internal heat, and, because it mobilizes Earth's surface, it is ultimately responsible for the Earth's long history of intense geological activity. Indeed, supercontinent formation and destruction¹³, epeirogeny^{4,5}, mountain-building⁶, intraplate volcanism¹² and plate tectonic motions^{1–3} have been linked directly to viscous flow in the mantle. Yet, despite these close links, the outlines of present-day global mantle flow have only recently become delineated using tomographic images of the mantle's heterogeneous density structure to inform viscous flow modelling of the mantle^{6,14}. Even this has been complicated by the uncertain interpretation of mantle tomography, especially concerning the role of two large low shear-wave velocity provinces (LLSVPs) observed in the lowermost mantle beneath Africa and the Pacific Ocean¹⁵. Active upwelling from these regions helps to explain patterns of seismic anisotropy¹⁴, plate motions³, orogeny^{5,6} and long-wavelength topography⁴, but seismological constraints suggest that these regions are compositionally dense^{6–18}. Under these conditions, thermochemical convection can help explain the geometry of upwellings¹⁹, but their stability depends on the interaction of the LLSVP regions with mantle flow²⁰. Our knowledge of mantle flow patterns is even poorer for past times, because direct geologic constraints on flow are few and past mantle-density heterogeneity can only be inferred from time-reversed flow models²¹ or inverse methods²² based on present-day mantle structure, or subduction models that do not include active mantle upwelling¹.

Because they are ultimately linked to mantle convection, plate motions should contain information about the underlying mantle flow patterns. Indeed, shear tractions exerted by mantle flow on the lithospheric base

may be a primary driver of plate motions^{1–3} and thus directly link surface tectonics to interior dynamics. We can exploit this link for past times by using tectonic reconstructions of plate motions, which are becoming increasingly better constrained^{8,9}, to infer patterns of past mantle flow. We achieve this by examining the net properties of plate motions, which should reflect the 'average' response of Earth's lithosphere to long-wavelength viscous mantle flow. Net rotation of the lithosphere (Fig. 1a) has previously been linked to present-day mantle flow¹⁴, but its utility for past times⁸ may be limited because observations of net rotation are highly dependent on the choice of mantle reference frame. By contrast, the relative motions between plates are less dependent on reference frame and are of larger amplitude than net rotation rates. To exploit these attributes, we define several new metrics of relative plate motions that are useful for constraining the interaction

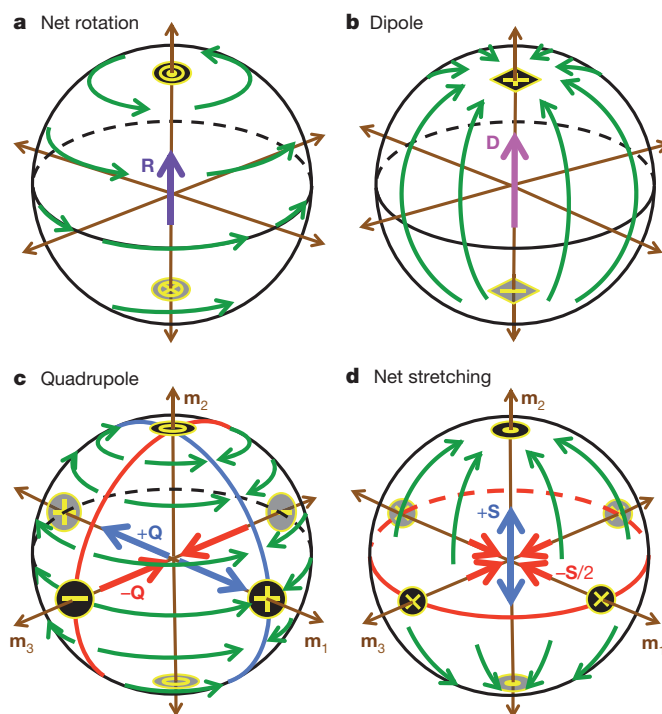


Figure 1 | Definitions of net characteristics. Plate motions for net rotation (a), net dipole (b), net quadrupole (c), and net stretching (d) (green arrows; see Supplementary Fig. 2), and their net characteristic vector definitions (R , D , $\pm Q$ and $+S$, respectively, and the m_1 , m_2 and m_3 eigenvectors; see Methods) are shown. The symbols used to denote pole locations are an encircled dot or cross for positive or negative net rotation poles (a), plus or minus within a diamond for positive or negative dipoles (b), plus, circle or minus signs within a circle for positive, null, or negative quadrupoles (c) and dots or crosses for compressive or extensional net stretching poles (d).

¹Department of Geology and Geophysics, SOEST, University of Hawaii at Mānoa, Honolulu, Hawaii 96822, USA. ²Helmholtz Centre Potsdam, GFZ German Research Centre for Geosciences, 14473 Potsdam, Germany. ³Centre for Earth Evolution and Dynamics (CEED), University of Oslo, 0316 Oslo, Norway. ⁴Geodynamics, Geological Survey of Norway, NO-7491, Trondheim, Norway. ⁵School of Geosciences, University of Witwatersrand, WITS 2050, Johannesburg, South Africa.

between plate tectonics and mantle flow, and apply them to published reconstructions of plate motions both for present and past times.

We defined three new ‘net characteristics’ of plate motions by performing different integrations of the tectonic plate motion vector field over the surface of the Earth (see Methods). The plate tectonic dipole vector **D** defines a ‘net convergence pole’ towards which plates are moving in an average sense away from an antipodal ‘net divergence pole’ (Fig. 1b). The plate tectonic quadrupole, defined by the quadrupole deformation matrix **Q** (see Methods), describes a second-order pattern of net plate motions associated with net hemispheric convergence towards two antipodal ‘positive’ poles and divergence away from two antipodal ‘negative’ poles located 90° away from the positive quadrupoles (Fig. 1c). This quadrupole motion occurs as revolution about two intermediate null poles (Fig. 1c). Plate tectonic net stretching, defined by deformation matrix **S** (see Methods), describes convergence towards the two null poles of the quadrupole and divergence away from an equator midway between them (Fig. 1d). These net characteristics describe plate motions at the largest scales; they are influenced by both rapid regional-scale (for example, northwestern North American convergence) and gradual global-scale deformations (for example, the circum-Africa ridge system), but are dominated by the longest-wavelength large-amplitude deformations.

We computed these net characteristics for present-day plate motions (Fig. 2a) and for vector fields associated with two major plate-driving forces: slab pull and basal shear tractions (Fig. 2b). The relevant pole locations for all three net characteristics (**D**, **Q** and **S**) are approximately co-located for both plate motions and plate-driving forces. For example, dipole convergence of plate tectonics occurs in eastern Asia,

dominated by convergent motion of the Pacific, Australian, Indian, African and Eurasian plates towards this location (Fig. 2a). The fact that slab pull also converges on average towards this location (Fig. 2b) is perhaps not surprising because subduction results from plate convergence. The convergence of basal tractions towards eastern Asia (Fig. 2b), however, reflects net motion of sub-lithospheric mantle flow towards this region. Within the mantle, downwelling occurs in this location (Fig. 2c), facilitated by a long history of subduction in the western Pacific that is observed tomographically²³. The co-location of these dipoles thus not only indicates the importance of basal tractions for driving plate motions^{1,3}, but also illustrates a direct link between plate motions and global-scale patterns of mantle flow.

The quadrupole moments for plate motions, slab pull and basal tractions are also aligned together (Fig. 2). In particular, quadrupole convergence for all three vector fields is centred in the western Pacific and South America (Fig. 2a), near regions of subduction and above major mantle downwellings (Fig. 2c). Similarly, quadrupole divergence is found in the central Pacific and eastern Africa (Fig. 2a, b), above major upwelling regions of the mantle (Fig. 2c) and just east of the location of the LLSVPs in the lowermost mantle (Fig. 2a). Poles orienting (negative) net stretching are also co-located near the geographic poles (Fig. 2a, b), which reflects the equatorial locations of the quadrupoles. As for the dipole, this co-location of quadrupoles reveals the direct link between surface plate motions and mantle flow patterns at depth. If we assume that this link also persisted for alternative plate configurations that existed in the past, then we can use dipole and quadrupole orientations computed for reconstructed past plate motions to infer the large-scale geometry of ancient mantle flow patterns.

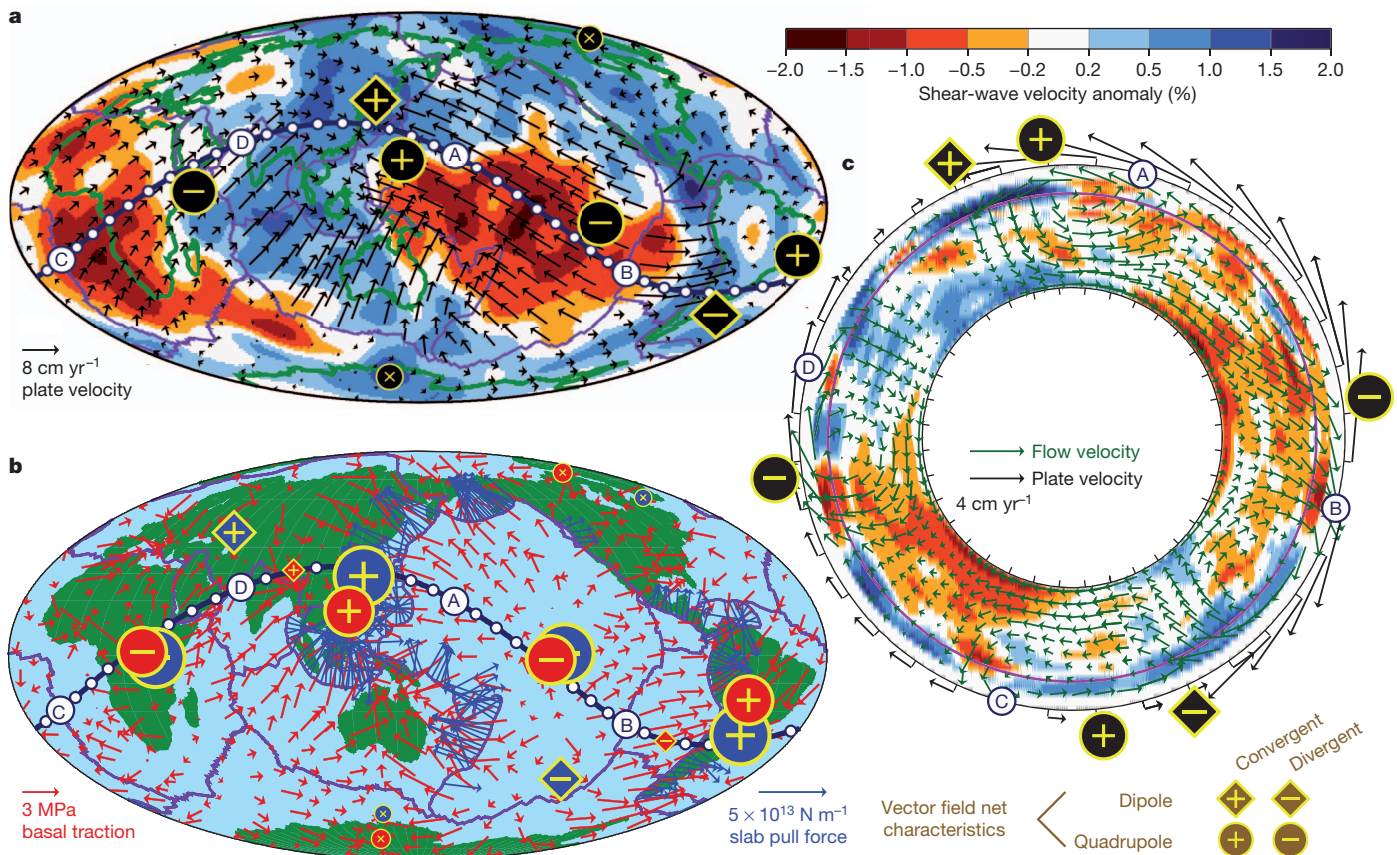


Figure 2 | Association of plate tectonic net characteristics with those of underlying mantle flow. **a**, **b**, Net characteristic pole locations (symbols as in Fig. 1) for the dipole, quadrupole and net stretching components of present-day surface plate motions²⁸ (black symbols) (**a**) and for plate tectonic driving forces associated with slab pull²⁹ (blue symbols) and basal tractions on plates³⁰ (red symbols) (**b**). **c**, A mantle cross-section cutting through great circle ABCD

(drawn on maps in all panels) shows the tomographic shear velocity anomaly²³ (colours, also drawn in map view in **a** at 2,800 km depth), the associated mantle flow field¹⁴ (green arrows), surface plate motion (black arrows), and net characteristic dipole and quadrupole locations for plate motions (black symbols).

To determine how dipole and quadrupole orientations have changed during Earth's recent history, we computed **D** and **Q** from a tectonic reconstruction of global plate motions for the past 150 million years (Myr) (ref. 8) that we have extended back to 250 Myr ago by combining palaeomagnetic constraints on absolute and relative plate motions in the African hemisphere^{24,25} with a reconstruction of the Pacific basin⁹. The latter is largely synthetic (and thus uncertain) because all Triassic sea floor and any Jurassic hotspot tracks for the Pacific have been lost to subduction. Nevertheless, since 250 Myr ago dipole convergence has generally remained near eastern Asia (Fig. 3a), reflecting the long-term stability of major downwelling beneath this area. Indeed, the stationary position of the Eurasian continent has been noted²⁶, and is consistent with persistent downwelling of slabs from the adjacent Panthalassa Ocean. The central Pacific and eastern Africa positions of quadrupole divergence have also remained stable above the eastern edges of the LLSVPs (Fig. 3b), which is consistent with the long-term stability of upwelling in these areas. In contrast, the locations of quadrupole convergence have circumscribed Panthalassa, finally resting along its northwestern (and southeastern) edges during the late Cretaceous period (Fig. 3b), about the time that subduction of increasingly younger lithosphere in the northern Pacific⁹ may have diminished downwelling flow beneath this region. While migration of the convergent quadrupoles reflects changes in the dominant location of subduction-induced downwelling flow, the stationary nature of the divergent quadrupoles reflects stability of the two major mantle upwellings.

The positioning of mantle upwelling above the African and Pacific LLSVP regions of the lowermost mantle is consistent with flow patterns observed in thermochemical convection models¹⁹. Our observation

that these upwellings have remained stably positioned above the current LLSVP regions may indicate that these LLSVPs form stable 'anchors' that organize mantle flow and surface tectonics¹¹. Indeed, plume ascent from the edges of the LLSVPs^{12,20} has been used to define an absolute reference frame for plate motions⁸ that allows palaeogeography to be reconstructed into the deep past²⁴. Our observation of quadrupole stability indicates that the two LLSVP regions have remained separate and in their current locations since at least the beginning of the Mesozoic era, and were not forced into these locations by flow patterns governed by supercontinental surface tectonics since then²⁷. Thus, if a transition from degree-1 to degree-2 convection occurred after the formation of Pangea⁷ (that is, after about 320 Myr ago), it probably occurred before about 250 Myr ago. The dipole and quadrupole amplitudes (Supplementary Fig. 3) have been decreasing slowly and in concert since the mid-Mesozoic and do not exhibit evidence of a transition between dominant modes (Supplementary Fig. 3). Dipole and quadrupole locations are also rarely co-located (Fig. 3 and Supplementary Fig. 6), which suggests that coupling between the two systems tends to suppress degree-1 upwelling in the vicinity of degree-2 downwelling. Instead, persistent degree-2 upwelling arising from the two LLSVP structures may induce convergent flow in the lowermost mantle that consolidates these structures into their current geometries²⁰, thus protecting and isolating them over geological timescales¹⁹. The surface expression of this flow pattern is recorded in the geologic record of plate tectonics.

METHODS SUMMARY

Dipole. We define the 'plate tectonic dipole' **D** as the direct integration of the plate motion velocity field **v** over the Earth's surface A_0 (Supplementary Fig. 1):

$$\mathbf{D} = \frac{3}{2A_0} \int_{A_0} \mathbf{v} dA \quad (1)$$

Here the normalization is chosen (see Supplementary Information) so that the amplitude of **D** represents the magnitude of motion of the 'pure' dipole on the equator midway between the positive and negative dipole locations (Supplementary Fig. 2b).

Quadrupole and net stretching. Higher-order net characteristics can be computed by integrating the outer product of the unit normal vector $\hat{\mathbf{r}}$ and **v** (Supplementary Fig. 1), and separating the resulting tensor **L** into symmetric (**M**) and antisymmetric (**N**) components:

$$\mathbf{M} + \mathbf{N} = \mathbf{L} = \frac{1}{A_0} \int_{A_0} \hat{\mathbf{r}} \otimes \mathbf{v} dA \quad (2)$$

Note that the diagonal components of **L** always sum to zero because $\text{tr}(\mathbf{L}) = \frac{1}{A_0} \int_{A_0} \hat{\mathbf{r}} \cdot \mathbf{v} dA$ and $\hat{\mathbf{r}} \perp \mathbf{v}$ everywhere (Supplementary Fig. 1). The three independent components of **N** form the net rotation vector according to $R_k = 3N_{ij}e_{ijk}/2$ (see Supplementary Information). The three eigenvalues of the symmetric **M** matrix ($\mu_1 > \mu_2 > \mu_3$) form the diagonalized matrix **M_D**, which is simply **M** expressed in a coordinate system defined by the corresponding eigenvectors **m₁**, **m₂**, and **m₃**. We can decompose **M_D** into 'quadrupole' (**Q**) and 'net stretching' (**S**) matrices as:

$$\begin{aligned} \mathbf{M}_D &= \begin{pmatrix} \mu_1 & 0 & 0 \\ 0 & \mu_2 & 0 \\ 0 & 0 & \mu_3 \end{pmatrix} = \frac{\mathbf{Q}}{6} + \frac{4\mathbf{S}}{15} \\ &= \frac{1}{6} \begin{pmatrix} Q & 0 & 0 \\ 0 & 0 & 0 \\ 0 & 0 & -Q \end{pmatrix} + \frac{4}{15} \begin{pmatrix} -S/2 & 0 & 0 \\ 0 & S & 0 \\ 0 & 0 & -S/2 \end{pmatrix} \end{aligned} \quad (3)$$

where the positive and negative elements of **Q** correspond to eigenvectors **m₁** and **m₃** respectively (Fig. 1c), and the unique (middle) element of **S** corresponds to eigenvector **m₂** (Fig. 1d). The piercing points of the eigenvectors $\pm \mathbf{m}_1$, $\pm \mathbf{m}_2$ and $\pm \mathbf{m}_3$ thus define the positive (convergent) quadrupoles, the net stretching poles (also null quadrupoles), and the negative (divergent) quadrupoles, respectively

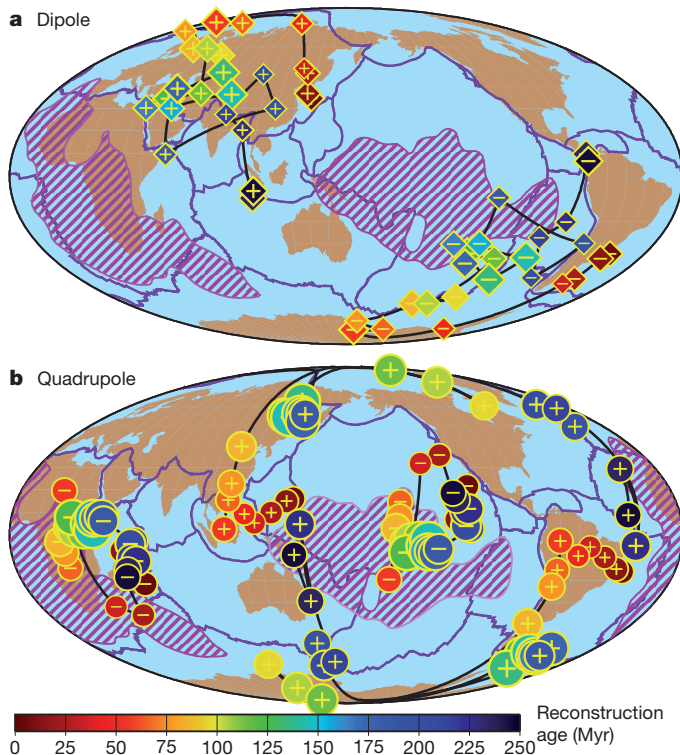


Figure 3 | Temporal evolution of plate tectonic net characteristics. **a, b**, Plate tectonic dipole (**a**) and quadrupole (**b**) locations as a function of age for a reconstruction of plate motions since the Triassic period (Supplementary Fig. 6). Symbols as in Fig. 1, with colours indicating reconstruction age and sizes indicating dipole or quadrupole magnitude (Supplementary Fig. 3). Notice the stability of the plate tectonic dipole near eastern Asia (**a**) and the divergent (negative) quadrupole above the eastern edges of the two LLSVPs (denoted here as pink hatching showing where shear waves at 2,800 km are $>1\%$ slow¹²) beneath Africa and the Pacific (**b**). Alternative reconstructions⁹ (Supplementary Figs 4 and 5) show similar stability of these features.

(Fig. 1c and 1d). We have defined $Q = 6\mu_1 + 3\mu_2$ and $S = 15\mu_2/4$ so that these values correspond to the maximum velocity magnitudes within the ‘pure’ quadrupole and net stretching velocity fields (see Supplementary Information). Note that the net stretching deformation (Fig. 1d) reverses to become ‘net flattening’ (polar extension and equatorial compression) if $S < 0$ ($\mu_2 < 0$).

Received 13 November 2012; accepted 18 April 2013.

- Lithgow-Bertelloni, C. & Richards, M. A. The dynamics of Cenozoic and Mesozoic plate motions. *Rev. Geophys.* **36**, 27–78 (1998).
- Stadler, G. *et al.* The dynamics of plate tectonics and mantle flow: from local to global scales. *Science* **329**, 1033–1038 (2010).
- van Summeren, J., Conrad, C. P. & Lithgow-Bertelloni, C. The importance of slab pull and a global asthenosphere to plate motions. *Geochim. Geophys. Geosyst.* **13**, Q0AK03 (2012).
- Lithgow-Bertelloni, C. & Silver, P. G. Dynamic topography, plate driving forces and the African superswell. *Nature* **395**, 269–272 (1998).
- Flowers, R. M., Ault, A. K., Kelley, S. A., Zhang, N. & Zhong, S. J. Epeirogeny or eustasy? Paleozoic–Mesozoic vertical motion of the North American continental interior from thermochronometry and implications for mantle dynamics. *Earth Planet. Sci. Lett.* **317–318**, 436–445 (2012).
- Becker, T. W. & Faccenna, C. Mantle conveyor beneath the Tethyan collisional belt. *Earth Planet. Sci. Lett.* **310**, 453–461 (2011).
- Zhang, N., Zhong, S. J., Leng, W. & Li, Z. X. A model for the evolution of the Earth's mantle structure since the Early Paleozoic. *J. Geophys. Res. Solid Earth* **115**, B06401 (2010).
- Torsvik, T. H., Steinberger, B., Gurnis, M. & Gaina, C. Plate tectonics and net lithosphere rotation over the past 150 My. *Earth Planet. Sci. Lett.* **291**, 106–112 (2010).
- Seton, M. *et al.* Global continental and ocean basin reconstructions since 200 Ma. *Earth Sci. Rev.* **113**, 212–270 (2012).
- Garnero, E. J. & McNamara, A. K. Structure and dynamics of Earth's lower mantle. *Science* **320**, 626–628 (2008).
- Dziewonski, A. M., Lekic, V. & Romanowicz, B. A. Mantle anchor structure: an argument for bottom up tectonics. *Earth Planet. Sci. Lett.* **299**, 69–79 (2010).
- Torsvik, T. H., Smethurst, M. A., Burke, K. & Steinberger, B. Large igneous provinces generated from the margins of the large low-velocity provinces in the deep mantle. *Geophys. J. Int.* **167**, 1447–1460 (2006).
- Li, Z.-X. & Zhong, S. Supercontinent–superplume coupling, true polar wander and plume mobility: plate dominance in whole-mantle tectonics. *Phys. Earth Planet. Inter.* **176**, 143–156 (2009).
- Conrad, C. P. & Behn, M. D. Constraints on lithosphere net rotation and asthenospheric viscosity from global mantle flow models and seismic anisotropy. *Geochim. Geophys. Geosyst.* **11**, Q05W05 (2010).
- Lassak, T. M., McNamara, A. K., Garnero, E. J. & Zhong, S. J. Core-mantle boundary topography as a possible constraint on lower mantle chemistry and dynamics. *Earth Planet. Sci. Lett.* **289**, 232–241 (2010).
- Kennett, B. L. N., Widiyantoro, S. & van der Hilst, R. D. Joint seismic tomography for bulk sound and shear wave speed in the Earth's mantle. *J. Geophys. Res.* **103**, 12469–12493 (1998).
- Ishii, M. & Tromp, J. Normal-mode and free-air gravity constraints on lateral variations in velocity and density of Earth's mantle. *Science* **285**, 1231–1236 (1999).
- Deschamps, F. & Trampert, J. Mantle tomography and its relation to temperature and composition. *Phys. Earth Planet. Inter.* **140**, 277–291 (2003).
- McNamara, A. K., Garnero, E. J. & Rost, S. Tracking deep mantle reservoirs with ultra-low velocity zones. *Earth Planet. Sci. Lett.* **299**, 1–9 (2010).
- Bower, D. J., Gurnis, M. & Seton, M. Lower mantle structure from paleogeographically constrained dynamic Earth models. *Geochim. Geophys. Geosyst.* **14**, 44–63 (2013).
- Steinberger, B. & O'Connell, R. J. Changes of the Earth's rotation axis owing to advection of mantle density heterogeneities. *Nature* **387**, 169–173 (1997).
- Liu, L. J., Spasojevic, S. & Gurnis, M. Reconstructing Farallon Plate subduction beneath North America back to the Late Cretaceous. *Science* **322**, 934–938 (2008).
- Ritsema, J., van Heijst, H. J. & Woodhouse, J. H. Global transition zone tomography. *J. Geophys. Res.* **109**, B02302 (2004).
- Torsvik, T. H., Müller, R. D., Van der Voo, R., Steinberger, B. & Gaina, C. Global plate motion frames: toward a unified model. *Rev. Geophys.* **46**, RG3004 (2008).
- Steinberger, B. & Torsvik, T. H. Absolute plate motions and true polar wander in the absence of hotspot tracks. *Nature* **452**, 620–623 (2008).
- Collins, W. J. Slab pull, mantle convection, and Pangaea assembly and dispersal. *Earth Planet. Sci. Lett.* **205**, 225–237 (2003).
- Zhong, S. J., Zhang, N., Li, Z. X. & Roberts, J. H. Supercontinent cycles, true polar wander, and very long-wavelength mantle convection. *Earth Planet. Sci. Lett.* **261**, 551–564 (2007).
- DeMets, C., Gordon, R. G., Argus, D. F. & Stein, S. Effect of recent revisions to the geomagnetic reversal time scale on estimates of current plate motions. *Geophys. Res. Lett.* **21**, 2191–2194 (1994).
- Wu, B. J., Conrad, C. P., Heuret, A., Lithgow-Bertelloni, C. & Lallemand, S. Reconciling strong slab pull and weak plate bending: the plate motion constraint on the strength of mantle slabs. *Earth Planet. Sci. Lett.* **272**, 412–421 (2008).
- Naliboff, J. B., Conrad, C. P. & Lithgow-Bertelloni, C. Modification of the lithospheric stress field by lateral variations in plate-mantle coupling. *Geophys. Res. Lett.* **36**, L22307 (2009).

Supplementary Information is available in the online version of the paper.

Acknowledgements We are grateful for NSF CAREER grant EAR-1151241 (to C.P.C.) and ERC grant 267631 (to T.H.T.), and to the Norwegian Centre for Advanced Study in Oslo for making this collaboration possible.

Author Contributions C.P.C. defined the method to compute net characteristics, B.S. and T.H.T. extended the plate reconstruction through the Mesozoic, all authors developed the geologic application and interpretation and C.P.C. prepared the manuscript with input, comments and review from all authors.

Author Information Reprints and permissions information is available at www.nature.com/reprints. The authors declare no competing financial interests. Readers are welcome to comment on the online version of the paper. Correspondence and requests for materials should be addressed to C.P.C. (clintc@hawaii.edu).

Elastic energy storage in the shoulder and the evolution of high-speed throwing in *Homo*

Neil T. Roach^{1,2}, Madhusudhan Venkadesan³, Michael J. Rainbow⁴ & Daniel E. Lieberman¹

Some primates, including chimpanzees, throw objects occasionally^{1,2}, but only humans regularly throw projectiles with high speed and accuracy. Darwin noted that the unique throwing abilities of humans, which were made possible when bipedalism emancipated the arms, enabled foragers to hunt effectively using projectiles³. However, there has been little consideration of the evolution of throwing in the years since Darwin made his observations, in part because of a lack of evidence of when, how and why hominins evolved the ability to generate high-speed throws^{4–8}. Here we use experimental studies of humans throwing projectiles to show that our throwing capabilities largely result from several derived anatomical features that enable elastic energy storage and release at the shoulder. These features first appear together approximately 2 million years ago in the species *Homo erectus*. Taking into consideration archaeological evidence suggesting that hunting activity intensified around this time⁹, we conclude that selection for throwing as a means to hunt probably had an important role in the evolution of the genus *Homo*.

Compared with other carnivores, hominins are slow, weak and lack natural weapons such as fangs and claws. However, hominins were eating meat at least 2.6 million years (Myr) ago, and were probably hunting large prey 1.9 Myr ago (Supplementary Note 1). Although contemporary hunter-gatherers rarely rely on throwing to kill prey, earlier hominins probably needed to throw projectiles frequently to acquire and defend carcasses before the relatively recent inventions of the atlatl and bow¹⁰. We can therefore surmise that the ability to throw well would confer a strong selective benefit to early hunters. However, to test when and how hominins evolved the ability to throw projectiles effectively, it is necessary to understand both throwing biomechanics and how changes in hominin anatomy affect throwing performance.

Throws are powered by rapid, sequential activation of many muscles, starting in the legs and progressing through the hips, torso, shoulder, elbow and wrist^{11–14}. Torques generated at each joint accelerate segmental masses, creating rapid angular movements that accumulate kinetic energy in the projectile until its release. It has been shown that internal (medial) rotation around the long axis of the humerus makes the largest contribution to projectile velocity¹⁵. This rotation, which occurs in a few milliseconds and can exceed 9,000° per s (ref. 13), is the fastest motion that the human body produces. Although previous research has focused on the internal rotator muscles of the shoulder^{11,16,17}, these muscles alone cannot explain how humans generate so much internal rotational power. Calculations of the maximum power-production capacity of all of the shoulder's internal rotator muscles indicate that these muscles can contribute, at most, half of the shoulder rotation power generated during the throwing motion (Supplementary Notes 2 and 3). Peak internal rotation torque also occurs well before the humerus starts to rotate internally¹². Furthermore, variation in muscle fibre orientation in these muscles produce actions other than internal humeral rotation that reduce power output for this action.

Elastic energy storage has been shown to be an important source of power amplification for many high-powered movements^{18,19}. We propose

that several evolutionarily novel features in the human shoulder help to store and release elastic energy to generate much of the power needed for rapid humeral rotation during human throwing. According to this model, energy storage occurs during the arm-cocking phase (Fig. 1a), which begins with completion of a large step towards the target. As the foot hits the ground, the arm is already externally rotated, horizontally extended, and abducted nearly 90° at the shoulder, with forearm flexion approaching 90° at the elbow¹³. As the cocking phase begins, large torques are generated by rapid rotation of the torso towards the target and by the activation of the major shoulder horizontal flexor, pectoralis major^{11,16}. The positioning of the shoulder and elbow at this time increases the mass moment of inertia around the long axis of the humerus, causing the forearm and hand to lag behind the accelerating torso. Furthermore, a flexed elbow during the cocking phase enables passive inertial forces to externally counter rotate the arm, stretching the short, parallel tendons, ligaments and elastic components of muscles that cross the shoulder, potentially storing elastic energy in the large aggregate cross-sectional area of these structures (Supplementary Note 4). When the biceps deactivate and elbow extension begins, the arm's moment of inertia is reduced, allowing these stretched elements to recoil, releasing energy and helping to power the extremely rapid internal rotation of the humerus (Supplementary Note 5).

Three derived morphological features of humans that are not present in chimpanzees, our closest extant relatives, have a major role in storing and releasing elastic energy during throwing (Supplementary Note 6). First, the tall, mobile waists of humans decouple the hips and thorax, permitting more torso rotation²⁰, in turn enabling high torque production over a large range of motion (ROM), which is needed to load the shoulder's elastic elements. Second, humeral torsion, the angle between humeral head orientation and the axis of the elbow, is 10–20° lower in human throwers' dominant arms compared to chimpanzee humeri⁵. Decreased torsion extends the rotational ROM at the shoulder externally^{21,22}, potentially enabling more elastic energy storage during the cocking phase. Finally, humans have a more laterally oriented glenohumeral joint, which aligns the pectoralis major flexion moment around the same axis as the torso rotation moment. This orientation allows humans to increase the arm's moment of inertia by abducting the humerus in line with the torso rotation and shoulder flexion torques, maximizing resistance to both (Fig. 1b, c, d). In contrast, chimpanzees have a more cranially oriented glenohumeral joint and limited ability to produce torso rotation torque, and this requires them to maximize inertial loading by abducting their humeri more than humans to bring their arm in line with the pectoralis major flexion moment. However, this increased abduction would force chimpanzees to position their elbow in a more extended posture to maximize the arm's moment of inertia, resulting in a costly reduction in elbow extension during the throw.

We tested the effects of these derived features on throwing performance using high-speed, three-dimensional kinematic and kinetic data from 20 human throwers with considerable prior training to quantify power production at the shoulder during overhand baseball throwing

¹Department of Human Evolutionary Biology, Harvard University, Cambridge, Massachusetts 02138, USA. ²Center for the Advanced Study of Hominid Paleobiology, Department of Anthropology, The George Washington University, Washington DC 20052, USA. ³National Centre for Biological Sciences, Tata Institute of Fundamental Research, Bangalore, Karnataka 560065, India. ⁴Spaulding National Running Center, Department of Physical Medicine and Rehabilitation, Harvard Medical School, Cambridge, Massachusetts 02138, USA.

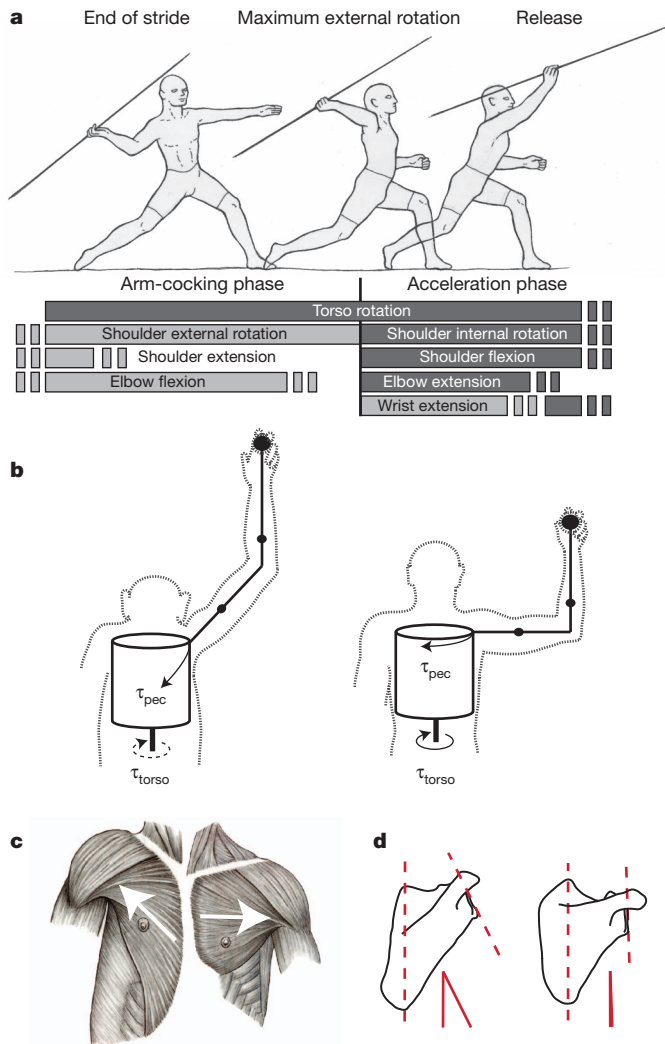


Figure 1 | Model of elastic energy storage. **a**, Arm-cocking and acceleration phases of the overhand throw. Light grey text boxes show the relative timing of the 'cocking' motions; dark grey boxes indicate the relative occurrence of the opposing 'acceleration' motions. Short boxes illustrate variation in timing of onset and cessation. **b**, **c**, Humans (right) and chimpanzees (left) differ in arm abduction and elbow flexion during throwing (**b**; a free-body diagram shows the torso (cylinder), arm and forearm, with black dots representing segmental centres of mass and τ vectors showing input torques), because of differences in shoulder orientation, that alter the major line of action (white arrows) of the pectoralis major (human, right; chimpanzee, left) (**c**). In humans, aligning the long axis of the humerus with the major axis of the pectoralis major and flexing the elbow maximizes inertia to shoulder flexion torque and loads the elastic elements in the shoulder. However, in chimpanzee morphology there is conflict between maximizing humeral rotation or maximizing elbow extension, hence chimpanzees are unable to achieve the same elastic energy storage. **d**, Signatures of shoulder orientation found in the scapula (human, right; chimpanzee, left) can be used to reconstruct hominin shoulder orientation; for example, the vertebral-glenoid angle is shown in red.

(Supplementary Note 7). During the arm-cocking phase, the throwers' humeri externally rotate $57 \pm 15^\circ$ (mean \pm s.d.) past the active ROM limit achieved using their own muscular power, indicating passive stretching of the ligaments, tendons and muscles crossing the shoulder. Inverse dynamics analysis shows that during this period, the shoulder produces an opposing internal rotation torque, causing a sustained period of power absorption (Fig. 2). During arm-cocking, the negative work of shoulder rotation averages -201 ± 70 J, with an average power of -631 ± 337 W. In contrast, the total rotational work of the subsequent internal rotation motion is 346 ± 116 J, with power during acceleration averaging $3,847 \pm 1,697$ W. If 90% of the negative work

during arm-cocking is stored and returned elastically²³, this energy can account for $54 \pm 15\%$ of the internal humeral rotation work done during a typical throw.

Elastic energy storage at the shoulder also augments the generation of joint velocity and power at the elbow. During acceleration, the elbow extends at very high angular velocities ($2,434 \pm 552^\circ$ per s) despite large amounts of negative power and work (-246 ± 63 J), indicating that the triceps alone are not powering this rapid extension (Fig. 2). As previous studies have shown, elbow extension is powered primarily by segments proximal to the elbow^{15,24}, particularly the shoulder.

An additional line of evidence to support the idea that elastic energy storage is important comes from experimentally limiting shoulder rotational ROM with therapeutic braces (Supplementary Notes 8–11); restricting external rotation by $24 \pm 9^\circ$. During brace trials, shoulder rotation beyond the active ROM decreased by $50 \pm 36\%$ and shoulder work during arm-cocking decreased by $39 \pm 16\%$ (repeated measures analysis of variance (ANOVA), $P < 0.001$) (Fig. 3). Shoulder rotation work during the subsequent acceleration phase was not significantly different between conditions, but average shoulder rotation power during acceleration decreased significantly ($-16 \pm 35\%$, repeated measures ANOVA, $P = 0.036$). Wearing a shoulder brace also decreased elbow negative work during acceleration by $20 \pm 21\%$ (repeated measures ANOVA, $P < 0.001$). Overall, these work and power reductions from less elastic energy exchange significantly reduced humeral rotation angular acceleration ($-24 \pm 29\%$, repeated measures ANOVA, $P < 0.001$) and elbow extension angular velocity ($-21 \pm 10\%$, repeated measures ANOVA, $P < 0.001$), reducing ball speed by $8 \pm 6\%$ (multivariate ANOVA, $P < 0.001$).

Natural variation in humeral torsion (Supplementary Note 12) produces similar performance effects. It has been known for a long time that athletes such as pitchers have lower degrees of humeral torsion, by

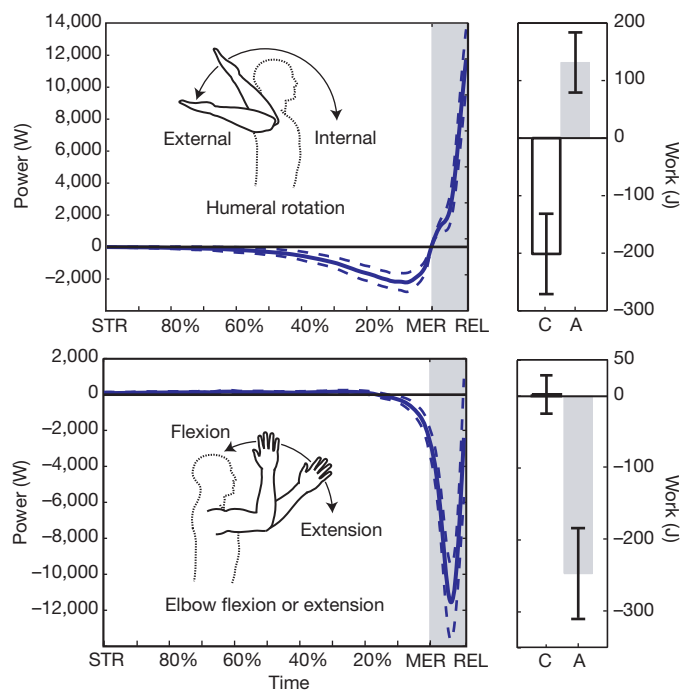


Figure 2 | Shoulder rotation and elbow flexion-extension power. Mean shoulder rotational power (solid blue line) with 95% confidence intervals (dotted blue lines) shows a sustained period (white) of negative power and work during arm-cocking (C), between stride (STR) and maximum external rotation (MER). This negative work is recovered (grey) during acceleration (A), between MER and release (REL). Recovered work powers both internal rotation at the shoulder and extension of the elbow. All power values are normalized by phase duration, with relative time and per cent arm-cocking duration shown on the x axis. Graphs on the right show the mean \pm s.d.

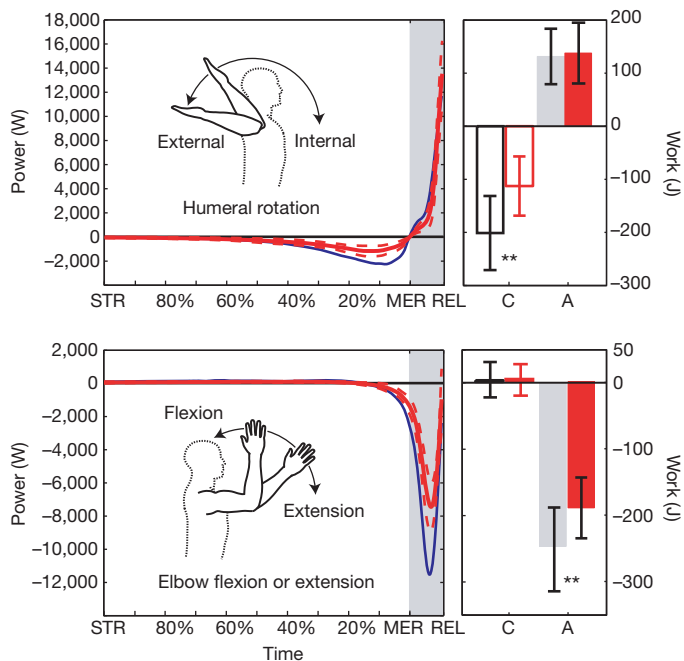


Figure 3 | Shoulder-brace restriction condition. Brace restricted mean power (solid red line) with 95% confidence intervals (dotted red lines) for shoulder rotation and elbow flexion-extension. Values for the unrestricted condition (no brace) are shown by the solid blue line. In the right panels, work values are shown in red bar and red solid bar (restricted using a brace) or white bar and solid grey bar (unrestricted). Significant reductions (** $P < 0.05$) in shoulder-rotation work occur during arm-cocking (C) and during elbow flexion-extension work when accelerating (A). Graphs on the right show the mean \pm s.d.

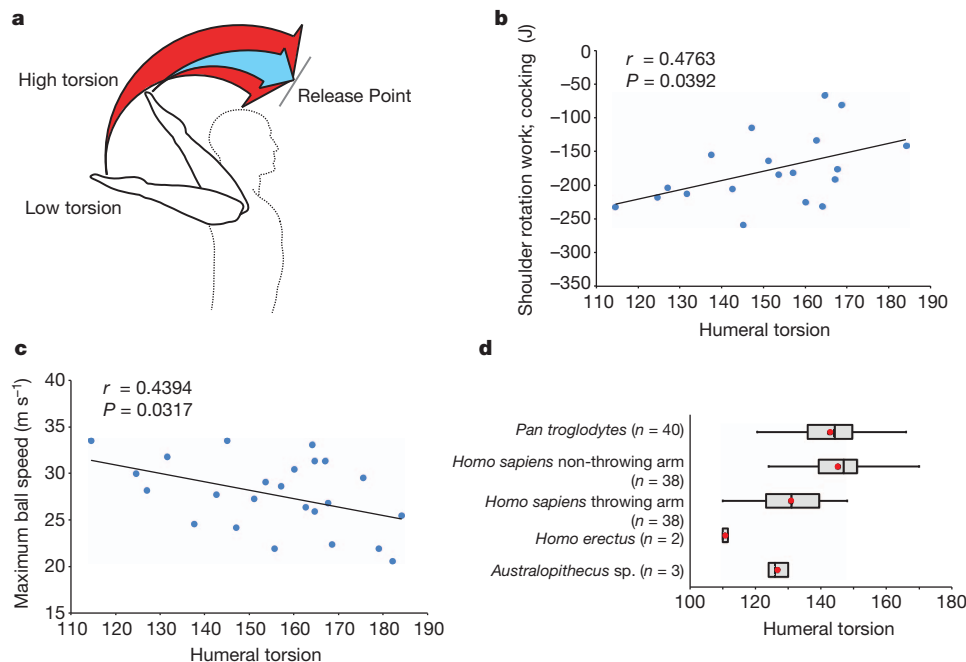


Figure 4 | Humeral torsion and throwing performance. a–c Low humeral torsion shifts the shoulder rotational ROM externally (a), enabling increased negative work during arm-cocking to be stored as elastic energy (b), and resulting in faster projectile speed (c). d, Humans and chimpanzees show comparable degrees of torsion⁵, although throwing athletes show reduced dominant-arm torsion²⁵ consistent with low torsion in *Australopithecus* and

10–15°, in their throwing versus non-throwing arms^{21,22,25}. By maintaining relatively lower, juvenile levels of torsion into adulthood²⁶, throwing athletes increase power generation by shifting the rotational ROM of the humerus externally^{21,22}. This shift enables further external rotation during arm-cocking and increases internal rotation during acceleration (Fig. 4a), permitting more elastic energy storage and release (Fig. 4b, c). It is unknown whether the plasticity of humeral torsion is greater in humans than in other taxa, but we speculate that plasticity in humans may be advantageous, enabling low torsion to persist in the throwing arm, whereas higher torsion (useful for manipulative tasks) develops in the non-throwing arm^{5,25}.

It is difficult to establish when high-speed throwing first evolved because the first projectiles were probably rocks and untipped wooden spears (Supplementary Notes 7 and 13). However, many of the derived morphological features that help human throwers to store elastic energy can be assessed in the fossil record (Supplementary Note 14). These features evolved in a mosaic fashion, some pre-dating the evolution of *Homo*. Tall, decoupled waists first appear in *Australopithecus* as adaptations for locomotion²⁰. Low humeral torsion also appears in *Australopithecus*, probably resulting from the release of the forelimbs from weight-bearing during quadrupedal locomotion, and is present in early *Homo*⁵ (Fig. 4d). Although variation in glenoid orientation exists within *Australopithecus*²⁷, a fully lateral glenoid position is first definitively present in *Homo erectus*²⁸ (Supplementary Notes 15 and 16). Such laterally oriented shoulders probably decreased the mechanical advantage of the scapular rotator muscles during climbing, and probably had little or no effect on stone-tool production. Throwing performance may also have benefited from low, wide shoulders, long legs, and hyperextendable wrists, which are all present in *H. erectus*^{20,29}. Although some of these features were probably selected for functions other than throwing, their combined configuration, first present in *H. erectus*, would have benefited throwing performance by enabling elastic energy storage in the shoulder, providing a selective advantage during hunting (Supplementary Note 1). Furthermore, high-speed

*Homo erectus*⁵. Chimpanzees are a combined sample as they do not show arm dominance, whereas human values are split between dominant and non-dominant arms as they show arm dominance. In d, the black and grey boxes and whiskers show torsion-angle quartiles, and the red dot shows the torsion-angle mean.

throwing was probably a critical component of a suite of hunting behaviours that enabled early members of the genus *Homo* to thrive in new and varied habitats both in and out of Africa.

Today, technological advances such as the bow and arrow, nets and firearms have reduced contemporary hunter-gatherers' reliance on thrown projectiles, but the human ability and proclivity to throw persists in many sports, in which athletes rely on the same mechanics (Supplementary Note 7). In this modern context, the evolution of adaptations for elastic energy storage during human throwing has implications for the high prevalence of injuries in throwing athletes. Paleolithic hunters almost certainly threw less frequently than modern athletes, who often deliver more than 100 high-speed throws over the course of a few hours. Unfortunately, the ligaments and tendons in the human shoulder and elbow are not well adapted to withstanding such repeated stretching from the high torques generated by throwing, and frequently suffer from laxity and tearing^{12,30}. Although humans' unique ability to power high-speed throws using elastic energy may have been critical in enabling early hunting, repeated overuse of this motion can result in serious injuries in modern throwers.

METHODS SUMMARY

Anthropometric and kinematic data were collected from 20 male subjects (Supplementary Note 17) after written consent was given in accordance with the Harvard Committee on the Use of Human Subjects. Kinematic data were collected at 1,000 Hz using an eight-camera Vicon T10s 3D infrared motion capture system (Vicon). Each subject had 21 passive reflective markers taped on the throwing arm and torso (Supplementary Note 18). Subjects were tasked to throw a 144-g baseball at a 1-m-radius target from 10 m away, both normally (8 to 10 pitches) and when restricted using a brace (Donjoy Shoulder Stabilizer, Donjoy) that limited external rotation ROM at the shoulder (8 to 20 pitches) (Supplementary Note 19). Ball speed was measured using a Sports Radar Model 3,600 radar gun. Ball release was timed using a synched FlexiForce A201 force sensor (Tekscan) collected at 1,000 Hz taped to the palmar side of the distal phalanx of the third digit and synchronized with a 30-Hz Canon Vixia HV30 digital video camera (Canon). A Butterworth second-order low-pass filter (cut-off of 25 Hz) was applied and marker gaps up to 100 frames were interpolated using C-Motion Visual3D software (v4) (Supplementary Note 20). For analysis, each motion was then subdivided into five phases of the throw¹⁴ and standardized by phase length (Supplementary Note 21). Joint Euler angles were calculated and inverse dynamics analyses were performed in Visual3D (Supplementary Note 22). Joint angular velocities, moments and power were calculated using each joint's instantaneous axis of rotation (Supplementary Note 23).

Full Methods and any associated references are available in the online version of the paper.

Received 11 January; accepted 2 May 2013.

- Goodall, J. *The Chimpanzees of Gombe: Patterns of Behavior* (Harvard Univ. Press, 1986).
- Westergaard, G. C., Liv, C., Haynie, M. K. & Suomi, S. J. A comparative study of aimed throwing by monkeys and humans. *Neuropsychologia* **38**, 1511–1517 (2000).
- Darwin, C. *The Descent of Man, and Selection in Relation to Sex* (John Murray, 1871).
- Churchill, S. E. & Rhodes, J. A. in *The Evolution of Hominin Diets: Integrating Approaches to the Study of Paleolithic Subsistence* (eds Hublin, J. J. & Richards, M. P.) 201–210 (Springer, 2009).
- Larson, S. G. Evolutionary transformation of the hominin shoulder. *Evol. Anthropol.* **16**, 172–187 (2007).
- Calvin, W. H. *The Throwing Madonna: Essays on the Brain* (Bantam, 1983).
- Fifer, F. C. The adoption of bipedalism by the hominids: a new hypothesis. *Hum. Evol.* **2**, 135–147 (1987).

- Bingham, P. M. Human evolution and human history: a complete theory. *Evol. Anthropol.* **9**, 248–257 (2000).
- Stanford, C. B. & Bunn, H. T. in *Human Evolution Series* (eds Ciochon, R. L. & Wood, B.) (Oxford Univ. Press, 2001).
- Shea, J. J. The origins of lithic projectile point technology: evidence from Africa, the Levant, and Europe. *J. Archaeol. Sci.* **33**, 823–846 (2006).
- Hirashima, M., Kadota, H., Sakurai, S., Kudo, K. & Ohtsuki, T. Sequential muscle activity and its functional role in the upper extremity and trunk during overarm throwing. *J. Sports Sci.* **20**, 301–310 (2002).
- Fleisig, G. S., Andrews, J. R., Dillman, C. J. & Escamilla, R. F. Kinetics of baseball pitching with implications about injury mechanisms. *Am. J. Sports Med.* **23**, 233–239 (1995).
- Pappas, A. M., Zawacki, R. M. & Sullivan, T. J. Biomechanics of baseball pitching. A preliminary report. *Am. J. Sports Med.* **13**, 216–222 (1985).
- Dillman, C. J., Fleisig, G. S. & Andrews, J. R. Biomechanics of pitching with emphasis upon shoulder kinematics. *J. Orthop. Sports Phys. Ther.* **18**, 402–408 (1993).
- Hirashima, M., Kudo, K., Watarai, K. & Ohtsuki, T. Control of 3D limb dynamics in unconstrained overarm throws of different speeds performed by skilled baseball players. *J. Neurophysiol.* **97**, 680–691 (2007).
- DiGiovine, N. M., Jobe, F. W., Pink, M. & Perry, J. An electromyography analysis of the upper extremity in pitching. *J. Shoulder Elbow Surg.* **1**, 15–25 (1992).
- Gowan, I. D., Jobe, F. W., Tibone, J. E., Perry, J. & Moynes, D. R. A comparative electromyographic analysis of the shoulder during pitching: professional versus amateur pitchers. *Am. J. Sports Med.* **15**, 586–590 (1987).
- Astley, H. C. & Roberts, T. J. Evidence for a vertebrate catapult: elastic energy storage in the plantaris tendon during frog jumping. *Biol. Lett.* **8**, 386–389 (2012).
- Patek, S. N., Nowroozi, B. N., Baio, J. E., Caldwell, R. L. & Summers, A. P. Linkage mechanics and power amplification of the mantis shrimp's strike. *J. Exp. Biol.* **210**, 3677–3688 (2007).
- Bramble, D. M. & Lieberman, D. E. Endurance running and the evolution of *Homo*. *Nature* **432**, 345–352 (2004).
- Osbahr, D. C., Cannon, D. L. & Speer, K. P. Retroversion of the humerus in the throwing shoulder of college baseball pitchers. *Am. J. Sports Med.* **30**, 347–353 (2002).
- Reagan, K. M. *et al.* Humeral retroversion and its relationship to glenohumeral rotation in the shoulder of college baseball players. *Am. J. Sports Med.* **30**, 354–360 (2002).
- Bennett, M. B., Ker, R. F., Dimery, N. J. & Alexander, R. M. Mechanical properties of various mammalian tendons. *J. Zool.* **209**, 537–548 (1986).
- Werner, S. L., Fleisig, G. S., Dillman, C. J. & Andrews, J. R. Biomechanics of the elbow during baseball pitching. *J. Orthop. Sports Phys. Ther.* **17**, 274–278 (1993).
- Pieper, H. G. Humeral torsion in the throwing arm of handball players. *Am. J. Sports Med.* **26**, 247–253 (1998).
- Cowgill, L. W. Humeral torsion revisited: a functional and ontogenetic model for populational variation. *Am. J. Phys. Anthropol.* **134**, 472–480 (2007).
- Haile-Selassie, Y. *et al.* An early *Australopithecus afarensis* postcranium from Woranso-Mille, Ethiopia. *Proc. Natl Acad. Sci. USA* **107**, 12121–12126 (2010).
- Walker, A. & Leakey, R. E. *The Nariokotome Homo erectus Skeleton* (Harvard Univ. Press, 1993).
- Richmond, B. G., Begun, D. R. & Strait, D. S. Origin of human bipedalism: the knuckle-walking hypothesis revisited. *Am. J. Phys. Anthropol.* **44** (Suppl.), 70–105 (2001).
- Snyder, S. J., Karzel, R. P., Del Pizzo, W., Ferkel, R. D. & Friedman, M. J. SLAP lesions of the shoulder. *Arthroscopy* **6**, 274–279 (1990).

Supplementary Information is available in the online version of the paper.

Acknowledgements We would like to thank the Wyss Institute, L. Stirling, A. Biewener, R. Wrangham, S. Larson, B. Roach, L. Meszoly, A. Lobell and many undergraduate research assistants for their feedback, help and support. Funding was provided by the National Science Foundation (BCS-0961943 to N.T.R. and D.E.L.), the American School for Prehistoric Research (to N.T.R. and D.E.L.) and the Wellcome Trust/DBT India Alliance (500158/Z/09/Z to M.V.).

Author Contributions N.T.R. and D.E.L. designed the study and wrote the paper. N.T.R. collected and analysed the data with help from D.E.L., M.V. and M.J.R. All authors helped to edit the paper.

Author Information Reprints and permissions information is available at www.nature.com/reprints. The authors declare no competing financial interests. Readers are welcome to comment on the online version of the paper. Correspondence and requests for materials should be addressed to N.T.R. (ntroach@email.gwu.edu).

METHODS

Subjects. Data were collected from 20 male subjects (aged between 19 and 23 years). Nineteen of the subjects were collegiate athletes (16 baseball players, 3 non-throwing athletes). Prior to enrolment in the study, all participants were required to pass a throwing performance task (Supplementary Note 17) to exclude poor throwers. For all subjects, we collected information on relevant injury, medical history, and basic anthropometric data (height, weight, segment lengths and circumferences, joint ROM). Humeral torsion was estimated using ROM measures³¹. All subjects provided informed written consent in accordance with the Harvard Committee on the Use of Human Subjects.

Kinematics. Kinematic data were collected at 1,000 Hz using an eight-camera Vicon T10s 3D infrared motion capture system (Vicon). Each subject had twenty-one passive reflective markers taped on the throwing arm and torso (Supplementary Note 18). Subjects were given approximately 5 min to stretch and warm up before recording. After the warm-up period, subjects were tasked to throw a 144-g baseball at a 1-m-radius target from 10 m away. The subject then threw 8 to 10 normal pitches and 8 to 20 pitches using a Donjoy Shoulder Stabilizer (Donjoy) brace that restricts external rotational ROM at the shoulder (Supplementary Note 19). As a control, data were collected for an intermediate (sham) condition in which the brace was applied but not tightened (Supplementary Note 8). Ball speed was measured using a Sports Radar Model 3,600 radar gun. Ball release was timed using a synched FlexiForce A201 force sensor (Tekscan) collected at 1,000 Hz taped to the palmar side of the distal phalanx of the third digit and synched with a 30-Hz Canon Vixia HV30 digital video camera (Canon). To filter the kinematic data, a residual analysis³² of the entire throwing trial and the critical period during

the humeral internal rotation motion was calculated in MATLAB (version R2010b) (Supplementary Note 20). A Butterworth second-order low-pass filter (cut-off of 25 Hz) was applied and marker gaps up to 100 frames were interpolated using C-Motion Visual3D software (v4). For analysis, each motion was then subdivided into five standard phases of the throw: windup-stride, arm cocking, arm acceleration, arm deceleration and follow through¹⁴.

Kinetics. Joint Euler angles were calculated and inverse dynamics analyses were carried out using mass distribution data from Dempster³³ in Visual3D. Joint angular velocities, moments and power were calculated using each joint's instantaneous axis of rotation (Supplementary Note 23). The sequence of rotations at each joint is described in Supplementary Note 22. Joint work was calculated in MATLAB using the trapz function.

Statistics. Kinetic data were standardized to phase length, interpolated and resampled using custom MATLAB code to produce comparable data across all trials and subjects (Supplementary Note 21). Individual subject means were compared across experimental conditions using repeated measures ANOVA or multivariate ANOVA as appropriate. All statistical analyses were conducted using JMP software (v5). Differences were considered to be significant at $\alpha < 0.05$.

31. Roach, N. T., Lieberman, D. E., Gill, T. J., IV, Palmer W. E. & Gill, T. J. III. The effect of humeral torsion on rotational range of motion in the shoulder and throwing performance. *J. Anat.* **220**, 293–301 (2012).
32. Winter, D. A. *Biomechanics and Motor Control of Human Movement* 2nd edn (Wiley-Interscience, 1990).
33. Dempster, W. T. *Space Requirements for the Seated Operator* (Wright Air Development Center, 1955).

orco mutant mosquitoes lose strong preference for humans and are not repelled by volatile DEET

Matthew DeGennaro^{1,2}, Carolyn S. McBride¹, Laura Seeholzer¹, Takao Nakagawa^{1†}, Emily J. Dennis¹, Chloe Goldman¹, Nijole Jasinskiene³, Anthony A. James^{3,4} & Leslie B. Vosshall^{1,2}

Female mosquitoes of some species are generalists and will blood-feed on a variety of vertebrate hosts, whereas others display marked host preference. *Anopheles gambiae* and *Aedes aegypti* have evolved a strong preference for humans, making them dangerously efficient vectors of malaria and Dengue haemorrhagic fever¹. Specific host odours probably drive this strong preference because other attractive cues, including body heat and exhaled carbon dioxide (CO₂), are common to all warm-blooded hosts^{2,3}. Insects sense odours via several chemosensory receptor families, including the odorant receptors (ORs), membrane proteins that form heteromeric odour-gated ion channels^{4,5} comprising a variable ligand-selective subunit and an obligate co-receptor called Orco (ref. 6). Here we use zinc-finger nucleases to generate targeted mutations in the *orco* gene of *A. aegypti* to examine the contribution of Orco and the odorant receptor pathway to mosquito host selection and sensitivity to the insect repellent DEET (*N,N*-diethyl-*meta*-toluamide).

orco mutant olfactory sensory neurons have greatly reduced spontaneous activity and lack odour-evoked responses. Behaviourally, *orco* mutant mosquitoes have severely reduced attraction to honey, an odour cue related to floral nectar, and do not respond to human scent in the absence of CO₂. However, in the presence of CO₂, female *orco* mutant mosquitoes retain strong attraction to both human and animal hosts, but no longer strongly prefer humans. *orco* mutant females are attracted to human hosts even in the presence of DEET, but are repelled upon contact, indicating that olfactory- and contact-mediated effects of DEET are mechanistically distinct. We conclude that the odorant receptor pathway is crucial for an anthropophilic vector mosquito to discriminate human from non-human hosts and to be effectively repelled by volatile DEET.

In the vinegar fly, *Drosophila melanogaster*, Orco is an obligate olfactory co-receptor⁷ that forms a complex with all ligand-selective odorant receptors and is required for efficient trafficking to olfactory sensory

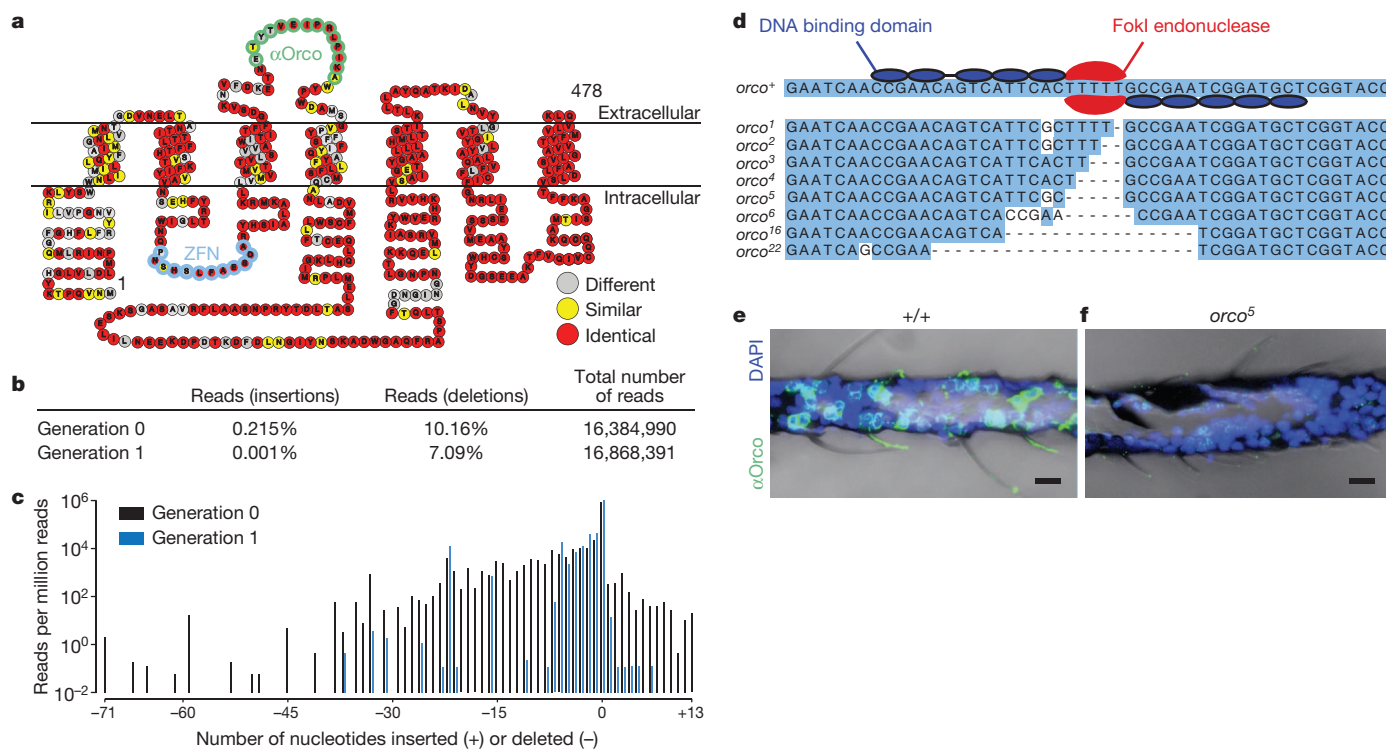


Figure 1 | Targeted mutagenesis of *orco* in *A. aegypti*. **a**, Snake plot of *A. aegypti* Orco with amino acids colour-coded to indicate conservation with *D. melanogaster*. The amino acids encoded by the DNA bound by the *orco* ZFN (blue) and the epitope of the *Drosophila* anti-Orco antibody (green) are indicated. **b**, Analysis of *orco* ZFN mutagenesis in *A. aegypti* G₀ and G₁ animals assayed by Illumina sequencing of an amplicon containing the ZFN cut site.

c, Frequency of insertions or deletions expressed as the number of sequence reads per million reads. **d**, Schematic of *orco* ZFN pair binding to *orco* DNA (top). *orco* mutant alleles (bottom). **e**, **f**, Immunofluorescence of frozen sections of wild-type (**e**) and *orco*⁵ mutant (**f**) antennae (*D. melanogaster* Orco antibody staining, green; DAPI (4',6-diamidino-2-phenylindole) nuclear stain, blue). Scale bar, 10 μm.

¹Laboratory of Neurogenetics and Behavior, The Rockefeller University, New York, New York 10065, USA. ²Howard Hughes Medical Institute, The Rockefeller University, New York, New York 10065, USA. ³Department of Molecular Biology & Biochemistry, University of California, Irvine, California 92697, USA. ⁴Department of Microbiology & Molecular Genetics and Molecular Biology & Biochemistry, University of California, Irvine, California 92697, USA. [†]Present address: Kansei Laboratories, KAO Corporation, Tochigi 321-3497, Japan.

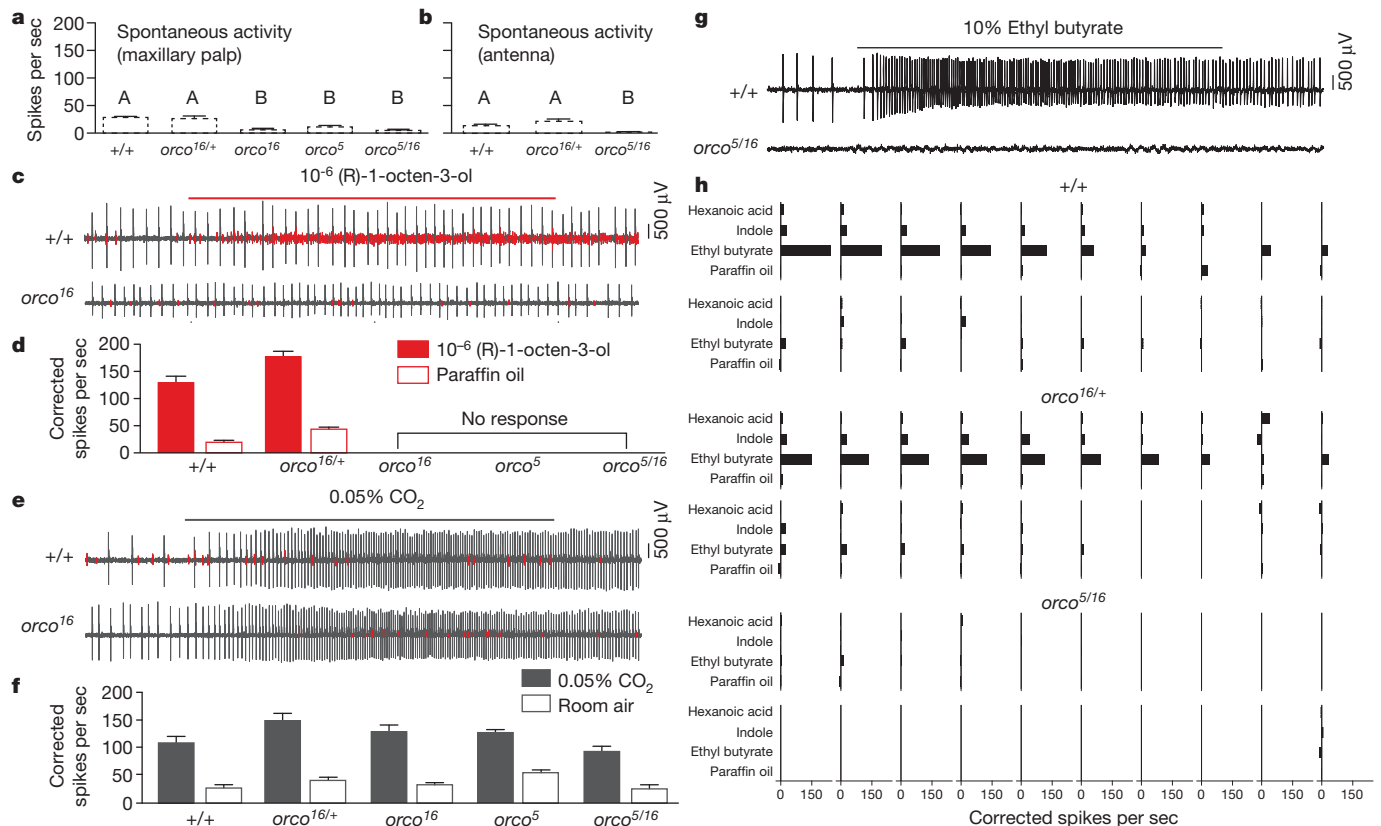


Figure 2 | Reduced spontaneous activity and loss of odour-evoked responses in *orco* mutant olfactory neurons. **a, b**, Spontaneous activity in the small-amplitude cell in capitate-peg sensilla on the maxillary palp (**a**) or in the large-amplitude cell in short blunt-tipped sensilla on the antenna (**b**) recorded from the indicated genotypes. Data are plotted as mean \pm s.e.m. (maxillary palp $n = 19$ ($+/+$), $n = 5$ ($orco^{16/+}$), $n = 21$ ($orco^{16}$), $n = 25$ ($orco^5$), $n = 15$ ($orco^{5/16}$); antenna $n = 20$ ($+/+$), $n = 20$ ($orco^{16/+}$), $n = 20$ ($orco^{5/16}$)). Values that are significantly different are labelled with different letters (one-way ANOVA for both comparisons, $P < 0.0001$ followed by Tukey's HSD test). **c**, Representative spike traces of maxillary palp neurons stimulated with (R)-1-octen-3-ol (10^{-6} dilution in paraffin oil) for 1 s (red bar). Small-amplitude spikes are in red. **d**, Summary of small-amplitude spikes evoked by (R)-1-octen-

neuron dendrites⁸. We reasoned that mutations in the *orco* gene of *A. aegypti* should eliminate signalling mediated by all 131 ligand-selective ORs in this mosquito⁹. To obtain *A. aegypti* heritable targeted null mutations in the *orco* gene, we used zinc-finger nucleases (ZFNs), which are fusion proteins of a sequence-specific DNA binding protein and a nuclease that induces mutagenic double-stranded breaks^{10,11}.

We first used ZFNs¹² to disrupt green fluorescent protein (GFP) in a transgenic strain of *A. aegypti* and detected a wide range of insertion and deletion events in GFP (Supplementary Fig. 1). We next injected ZFNs designed to target the *orco* locus (Fig. 1a) into wild-type mosquito embryos. The *orco* ZFNs induced mutations at high efficiency in adults derived from injected embryos (G_0) as well as their progeny (G_1) (Fig. 1b–d). Three mutant alleles were characterized, *orco*², *orco*⁵ and *orco*¹⁶, and these are predicted to produce truncated Orco protein. We did not detect Orco expression in antennae in any of these homozygous *orco* mutant alleles (Fig. 1e, f and data not shown). Using these homozygous mutants, we further generated heteroallelic *orco* mutant combinations to control for independent background mutations.

orco mutants exhibited severely impaired electrophysiological responses (Fig. 2). Spontaneous activity in maxillary palp (Fig. 2a) and antennal (Fig. 2b) sensilla was reduced relative to wild-type and heterozygous controls, as observed previously in *D. melanogaster orco* mutants⁷. We were unable to locate any maxillary palp capitate-peg sensilla responsive to a ligand for OR8/Orco, (R)-1-octen-3-ol^{13–15}, in

3-ol (solid bars) or paraffin oil solvent (open bars). Data are presented as mean \pm s.e.m. **e**, Representative spike traces of maxillary palp neurons stimulated with CO₂ (0.05%) for 1 s (grey bar). Large amplitude spikes are in grey. **f**, Summary of large-amplitude spikes evoked by CO₂ (solid bars) or air (open bars). Data are plotted as mean \pm s.e.m. ($n = 7$ ($+/+$), $n = 6$ ($orco^{16/+}$), $n = 9$ ($orco^{16}$), $n = 8$ ($orco^5$), $n = 6$ ($orco^{5/16}$)). There was no difference in CO₂-evoked spikes between genotypes except for those between *orco*^{16/+} and *orco*^{5/16} (one-way ANOVA, $P = 0.0232$). **g**, Representative spike traces of short blunt-tipped antennal neurons of the indicated genotypes stimulated for 1 s (black bar) with 10% ethyl butyrate. **h**, Odour-evoked responses of 20 short blunt-tipped sensilla for each of the indicated genotypes.

*orco*⁵, *orco*¹⁶ or *orco*^{5/16} mutant mosquitoes (0/25, 0/21 and 0/15 sensilla tested, respectively), but readily detected them in wild-type and heterozygous *orco*^{16/+} animals (19/29 and 5/7 sensilla tested, respectively) (Fig. 2c, d). Insect chemosensory responses to carbon dioxide (CO₂) are *orco*-independent¹⁶ and capitate-peg sensilla in all genotypes responded normally to CO₂ (Fig. 2e, f). On the antennae of *orco* mutants, we were unable to locate any short blunt-tipped trichoid sensilla responding to a panel of odors selected from those previously shown to activate neurons in subsets of these sensilla¹⁷ (Fig. 2g, h). As expected, a subset of short blunt-tipped sensilla from wild-type (13/20) and heterozygous (13/20) control mosquitoes responded to one or more odors in the panel (Fig. 2g, h). Our results show that in *orco* mutants, both antennal and maxillary palp neurons fail to respond to the odors tested, suggesting that as in *D. melanogaster*, *orco* is required for the function of ligand-selective ORs.

We investigated whether these electrophysiological defects translate into altered responses to important olfactory cues using a modified two-port Gouck olfactometer¹⁸ (Fig. 3a). Both male and female mosquitoes feed on nectar to satisfy their metabolic needs and are attracted to floral and honey odors¹⁹. We quantified attraction of fasted male and female mosquitoes to honey or glycerol, which is odourless and has a viscosity and water content similar to honey. Although wild-type and heterozygous control mosquitoes responded to honey, heteroallelic *orco* mutant mosquitoes showed little to no response (Fig. 3b, c).

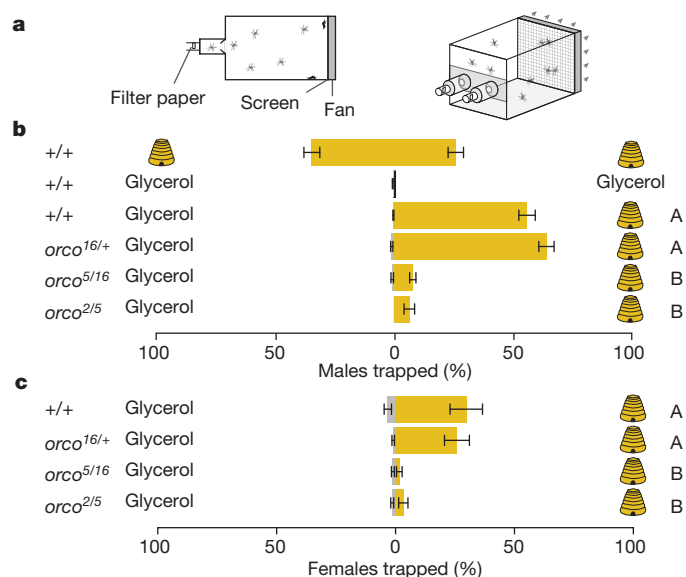


Figure 3 | Disruption of honey odour detection in *orco* mutants. **a**, Diagram of two-port olfactometer used for honey response assay. **b, c**, Response of male (**b**) or female (**c**) mosquitoes to honey (beehive) or glycerol by the indicated genotypes. Wild-type males distributed evenly between the two ports when both contained honey (Student's *t*-test, $P = 0.13$; $n = 8$), and did not respond to glycerol ($n = 7$). Genotypes varied significantly in their response to honey (one-way ANOVA, $P < 0.001$; n (males) = 10–11; n (females) = 7–11). Genotypes marked with different letters are significantly different by post hoc Tukey's HSD test.

When fasted, we found no reduction in survival or locomotor activity in *orco* mutants relative to controls (Supplementary Fig. 2). Thus, these weak responses cannot be explained by a locomotion defect in the mutants.

female mosquitoes did not respond to unworn sleeves, but showed moderate attraction to human-scented sleeves (Fig. 4b). In contrast, *orco* mutant females showed little or no response to host odour (Fig. 4b). Because live hosts emit both odour and CO₂, we repeated these experiments in the presence of CO₂ (Fig. 4c). Wild-type female mosquitoes showed moderate attraction to CO₂ alone, and this response was greatly enhanced when human-scented sleeves were presented along with CO₂ (Fig. 4c). Contrary to the defect seen in the absence of CO₂, *orco* mutant females exhibited the same robust response to human odour in the presence of CO₂ as controls (Fig. 4c). Likewise, *orco* mutant females responded at the same robust levels as controls to air that had passed over a live human arm, supplemented with human breath, and tested in a modified version of the same olfactometer (Fig. 4a, d).

These results indicate that CO₂ synergizes with host odour to rescue the defect in *orco* mutant attraction, suggesting that mosquitoes possess redundant mechanisms for host odour detection that can only be activated in the presence of CO₂. Further, this indicates that olfactory signalling mediated through a second family of chemosensory receptors, the ionotropic receptors, cannot compensate for the loss of OR function in *orco* mutants in the absence of CO₂.

Most populations of *A. aegypti* strongly prefer human over non-human hosts, prompting us to ask whether the OR pathway is required for host discrimination. We assayed host discrimination between human and guinea-pig (*Cavia porcellus*)—an animal host to which *A. aegypti* has been shown to respond¹⁸. Both wild-type and *orco* mutants showed moderate levels of baseline attraction to a live guinea-pig (Fig. 4e). We were intrigued by the stronger attraction of *orco* mutants to guinea-pig relative to controls, but note that this difference was statistically significant for only *orco*^{5/16}. We then offered mosquitoes a choice between air that had passed over a live guinea-pig or the arm of one of 14 live human subjects (Fig. 4f). *orco* mutants were less likely than wild-type to choose the human host, resulting in a statistically significant lower mean preference index (Fig. 4f). To determine if the reduced preference of mutant mosquitoes for humans depended on host-specific odours alone, we repeated the choice assay but replaced live hosts with host odour collected on nylon sleeves, supplemented with CO₂ (Fig. 4g). Under these conditions, control

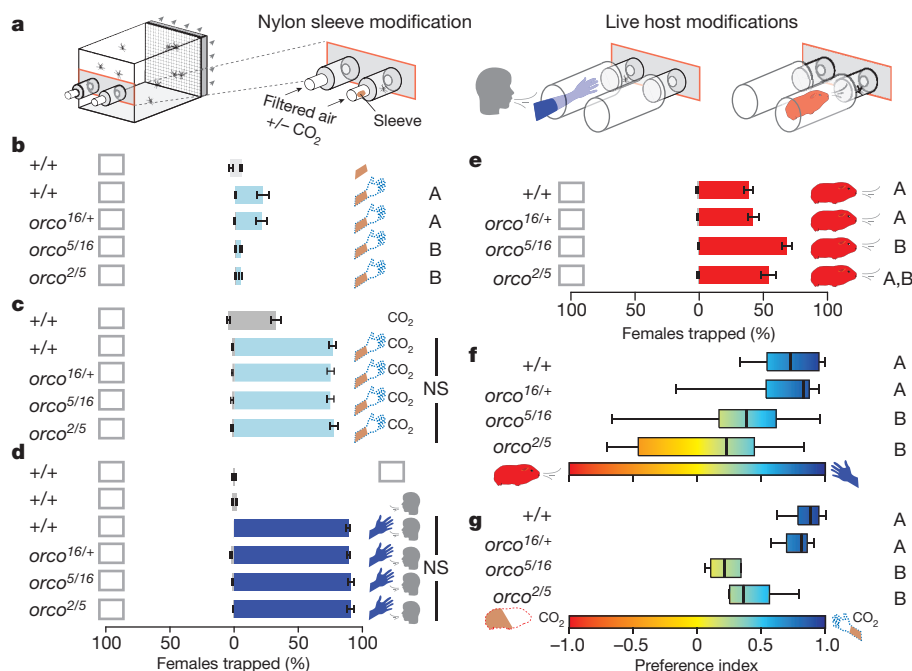


Figure 4 | Disruption of host detection and discrimination in *orco* mutants. **a**, Diagram of modifications to the two-port olfactometer for host assays with female mosquitoes. **b**, Response to no stimulus (open box), unworn nylon sleeve (sleeve cartoon), or human scented nylon sleeve (dotted hand cartoon) without CO₂. Genotypes varied significantly (one-way ANOVA, $P < 0.0001$; $n = 15$). **c**, Response to CO₂ or human scented nylon sleeve with CO₂. Genotypes did not differ in their response to human scented nylon sleeves with CO₂ (one-way ANOVA, $P = 0.8881$; $n = 15$). **d**, Response to no stimulus, human breath (face cartoon), or live human (blue). Genotypes did not differ (one-way ANOVA, $P = 0.8$; $n = 7$). **e**, Response to no stimulus or guinea-pig (red). Genotypes differed in responses (one-way ANOVA, $P = 0.0001$; $n = 12-13$). **f**, Preference index for live human or guinea-pig. Variation was significant among both genotypes and human subjects tested (two-way ANOVA, $P < 0.0001$ for genotype and $P = 0.0015$ for subject). **g**, Preference index for human or guinea-pig-scented nylon sleeve. Variation among genotypes was significant (one-way ANOVA; $P < 0.0001$; $n = 5-6$). Data in **b-e** are plotted as mean \pm s.e.m. and data in **f, g** are presented as box plots (black line, median; bounds of boxes, first and third quartiles; bars, range). In **b** and **e-g**, genotypes marked with different letters are significantly different by post hoc Tukey's HSD test. NS, not significant.

mosquitoes strongly preferred human odour, whereas *orco* mutants again showed only a weak preference (Fig. 4g). Overall response rates did not differ between genotypes in either assay (Supplementary Fig. 3a–d). We speculate that *orco* mutants are attracted to vertebrate hosts, but are impaired in their ability to discriminate between them.

ORs have been proposed to be the major target of the olfactory effect of the insect repellent DEET^{20–25}. To investigate whether DEET can interfere with the strong attraction to human hosts in *orco* mutants, we tested female *orco* mutant and control mosquitoes in a two-port olfactometer DEET choice assay (Fig. 5a). Wild-type and heterozygous mosquitoes avoided the port with 10% DEET and accumulated in the solvent port (Fig. 5a). In contrast, *orco* mutants were insensitive to DEET and accumulated equally in both ports. Differences in the overall response rate were not statistically significant (Supplementary Fig. 3e, f).

The DEET choice assay tests mosquito response over a distance of 20 to 100 cm. To test the olfactory effect of DEET at close range, we used a host proximity assay that measures the effects of DEET over a distance of 2.5 to 32.5 cm (Fig. 5b). In this assay, a human arm treated with solvent or 10% DEET was placed 2.5 cm from the side of a screened cage. Control mosquitoes were attracted to the arm when it was treated with solvent, but strongly avoided it when it was treated with DEET. In contrast, *orco* mutants showed equal attraction to the solvent- and DEET-treated arm (Fig. 5b and Supplementary Video 1). These results indicate that the olfactory attraction of *orco* mutants for humans cannot be inhibited by DEET, even at close range.

Upon landing on a host, mosquitoes are exposed to taste cues and become susceptible to the contact-mediated repellent effects of DEET. Work in *D. melanogaster* indicates that DEET acts on gustatory receptors to induce taste avoidance²⁶. To investigate whether *orco* mutants are sensitive to the contact-mediated effects of DEET, we carried out an arm-in-cage biting assay in which subjects inserted a solvent- or DEET-treated arm into a mosquito cage (Fig. 5c). DEET treatment inhibited blood feeding of both wild-type and *orco* mutant females (Fig. 5c). To detect *orco* mutants contacting DEET-treated skin, we designed a landing assay to image female mosquitoes interacting with exposed skin treated with DEET or solvent (Fig. 5d). In contrast to controls, *orco* mutants approached the host and briefly contacted the DEET-treated skin as often as solvent-treated skin (Fig. 5d). A representative *orco*^{2/5} mutant mosquito is repelled within 60 msec of contact with DEET-treated skin (Fig. 5e). These results support the conclusion that although the olfactory effect of DEET requires an intact OR pathway, the contact repellent activity of DEET is independent of *orco* function.

In this study, we investigated the requirement for *orco* and the OR pathway in mosquito appetitive behaviour and sensitivity to the insect repellent DEET. *orco* mutants are impaired in both honey and host odour attraction. Despite this defect in host odour detection, *orco* mutants can still respond to live hosts. We propose that CO₂, along with odours that are detected by the ionotropic receptor pathway, may constitute more generic vertebrate signals that are sufficient to drive attraction.

The impairment in host preference in *orco* mutant females suggests a specialization of the OR pathway in *A. aegypti* for host odour discrimination. We speculate that the OR/*Orco* pathway provides information about the specific identity of the host and that specific ORs may mediate preference for humans in this anthropophilic disease vector. A role for ORs in host discrimination is consistent with the broader range of ligands that activates this class of receptors^{27,28} compared to ionotropic receptors²⁹.

Our results also provide proof that *orco* and the OR pathway are necessary for the olfactory effects of DEET on mosquitoes. A previous study used RNA interference to knock down *orco* in *A. gambiae* larvae²³ and found that these animals no longer responded to DEET. However, because mosquito larvae are aquatic, these experiments could not distinguish olfactory- and contact-mediated effects. Three

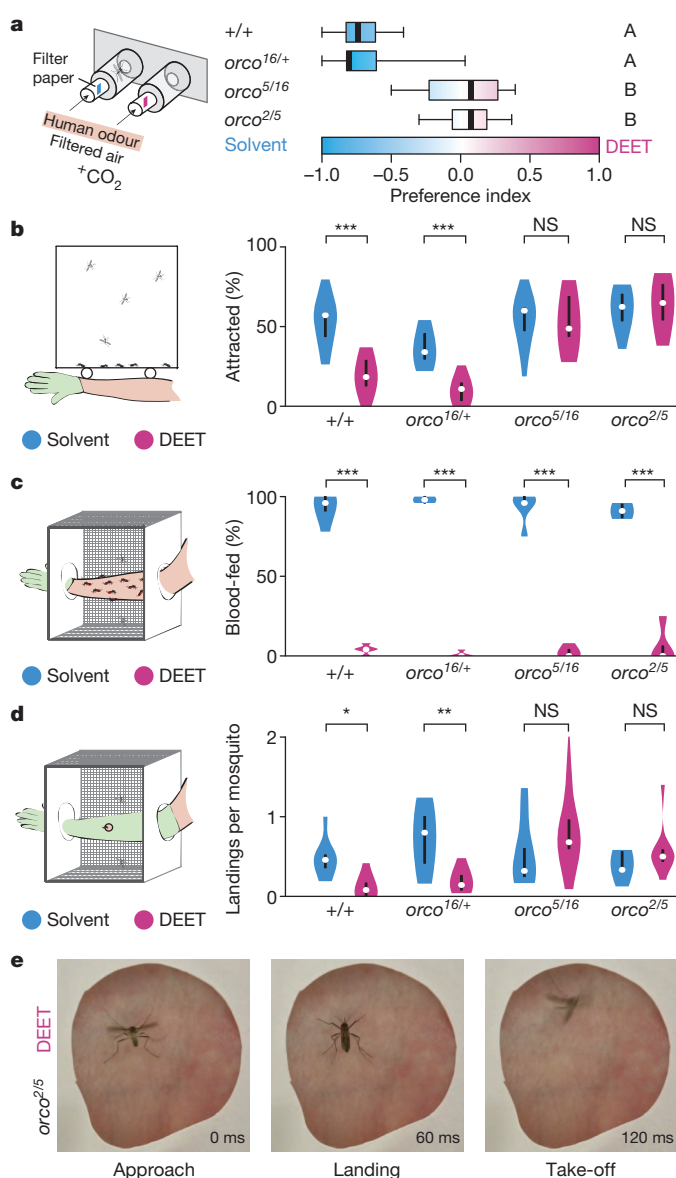


Figure 5 | Female *orco* mutants are insensitive to volatile DEET but are repelled on contact. **a**, Preference for human host-scented traps containing either solvent (cyan) or 10% DEET (magenta). Data are presented as box plots (black line, median; bounds of boxes, first and third quartiles; bars, range). Genotypes marked with different letters are significantly different by post hoc Tukey's HSD test (one-way ANOVA; $P < 0.0001$; $n = 7$ –16). *orco* mutant preference is not significantly different from zero (one sample Student's *t*-test; *orco*^{2/5}, $P = 0.3$; *orco*^{5/16}, $P = 0.9$). **b**, Per cent mosquitoes attracted to a human arm treated either with solvent or 10% DEET (Bonferroni corrected *t*-test comparing solvent and DEET; *** $P < 0.00025$; NS, not significant; $n = 12$ –14). **c**, Per cent females blood-fed on a human arm treated with solvent or 10% DEET (Bonferroni corrected *t*-test comparing solvent and DEET: *** $P < 0.00025$; $n = 4$ –5). **d**, Per cent landing on human skin treated either with solvent or 10% DEET (Bonferroni corrected *t*-test comparing solvent and DEET; * $P < 0.0125$, ** $P < 0.0025$; $n = 9$). The violin plots in **b**–**d** show the median as a white dot and the first and third quartile by the bounds of the black bar. The violins are clipped at the range of the data, except in **d**, in which the *orco*^{5/16} DEET violin is further clipped at 2.0, excluding a single outlier at 3.76. **e**, Video stills separated by 60 msec of an *orco*^{2/5} mutant mosquito responding to DEET-treated skin.

mechanisms have been suggested to explain the olfactory repellency of DEET, but no clear consensus has emerged. First, DEET may silence ORs tuned to attractive odours^{20,21}. Second, DEET may activate one or a few ORs to trigger repulsion^{22,23}. Third, DEET may act as a 'confusant' to modulate the activity of many ORs^{24,25}. The fact that *orco*

mutants retain very strong olfactory host attraction indicates that the first hypothesis cannot be correct. If the olfactory repellency of DEET acted solely to inhibit the OR pathway, DEET would not be an effective insect repellent. Instead, our results are consistent with the second or third hypotheses. Our genetic analysis of *orco* mutants indicates that either mechanism must overcome the strong baseline attraction to hosts in the presence of CO₂ seen in *orco* mutants. Finally, we note that the development of an efficient method to generate targeted mutations in *A. aegypti* opens up this important disease vector to comprehensive genetic analysis.

METHODS SUMMARY

orco ZFNs were generated using the CompoZr Custom ZFN Service (Sigma-Aldrich). Of the 16 ZFN pairs screened, the *orco* exon 1 ZFN pair used in this study had the greatest activity, comparable to a highly active positive control ZFN pair that targets CCR5. Mutant alleles were detected by Illumina sequencing of an amplicon that contained the ZFN cut site. Mutant alleles were isolated using size-based genotyping of amplicons surrounding the deletion site, allowing us to discriminate heterozygous from homozygous individuals. Mosquitoes were tested for their response to odour cues in a modified version of a Gouck two-port olfactometer¹⁸. Full Methods are described in the Supplementary Information.

Received 23 August 2012; accepted 19 April 2013.

Published online 29 May 2013.

- Besansky, N. J., Hill, C. A. & Costantini, C. No accounting for taste: host preference in malaria vectors. *Trends Parasitol.* **20**, 249–251 (2004).
- Skinner, W. A., Tong, H., Pearson, T., Strauss, W. & Maibach, H. Human sweat components attractive to mosquitoes. *Nature* **207**, 661–662 (1965).
- Takken, W. & Knols, B. G. Odor-mediated behavior of Afrotropical malaria mosquitoes. *Annu. Rev. Entomol.* **44**, 131–157 (1999).
- Sato, K. *et al.* Insect olfactory receptors are heteromeric ligand-gated ion channels. *Nature* **452**, 1002–1006 (2008).
- Wicher, D. *et al.* *Drosophila* odorant receptors are both ligand-gated and cyclic-nucleotide-activated cation channels. *Nature* **452**, 1007–1011 (2008).
- Vosshall, L. B. & Hansson, B. S. A unified nomenclature system for the insect olfactory co-receptor. *Chem. Senses* **36**, 497–498 (2011).
- Larsson, M. C. *et al.* *Or83b* encodes a broadly expressed odorant receptor essential for *Drosophila* olfaction. *Neuron* **43**, 703–714 (2004).
- Benton, R., Sachse, S., Michnick, S. W. & Vosshall, L. B. Atypical membrane topology and heteromeric function of *Drosophila* odorant receptors *in vivo*. *PLoS Biol.* **4**, e20 (2006).
- Bohbot, J. *et al.* Molecular characterization of the *Aedes aegypti* odorant receptor gene family. *Insect Mol. Biol.* **16**, 525–537 (2007).
- Kim, Y. G., Cha, J. & Chandrasegaran, S. Hybrid restriction enzymes: zinc finger fusions to Fok I cleavage domain. *Proc. Natl Acad. Sci. USA* **93**, 1156–1160 (1996).
- Rémy, S. *et al.* Zinc-finger nucleases: a powerful tool for genetic engineering of animals. *Transgenic Res.* **19**, 363–371 (2010).
- Geurts, A. M. *et al.* Knockout rats via embryo microinjection of zinc-finger nucleases. *Science* **325**, 433 (2009).
- Grant, A. J. & Dickens, J. C. Functional characterization of the octenol receptor neuron on the maxillary palps of the yellow fever mosquito, *Aedes aegypti*. *PLoS ONE* **6**, e21785 (2011).
- Bohbot, J. D. & Dickens, J. C. Characterization of an enantioselective odorant receptor in the yellow fever mosquito *Aedes aegypti*. *PLoS ONE* **4**, e7032 (2009).
- Lu, T. *et al.* Odor coding in the maxillary palp of the malaria vector mosquito *Anopheles gambiae*. *Curr. Biol.* **17**, 1533–1544 (2007).
- Jones, W. D., Cayirlioglu, P., Kadow, I. G. & Vosshall, L. B. Two chemosensory receptors together mediate carbon dioxide detection in *Drosophila*. *Nature* **445**, 86–90 (2007).
- Ghaninia, M., Ignell, R. & Hansson, B. S. Functional classification and central nervous projections of olfactory receptor neurons housed in antennal trichoid sensilla of female yellow fever mosquitoes, *Aedes aegypti*. *Eur. J. Neurosci.* **26**, 1611–1623 (2007).
- Gouck, H. K. Host preferences of various strains of *Aedes aegypti* and *Aedes simpsoni* as determined by an olfactometer. *Bull. World Health Organ.* **47**, 680–683 (1972).
- Foster, W. A. & Takken, W. Nectar-related vs. human-related volatiles: behavioural response and choice by female and male *Anopheles gambiae* (Diptera: Culicidae) between emergence and first feeding. *Bull. Entomol. Res.* **94**, 145–157 (2004).
- Dogan, E. B., Ayres, J. W. & Rossignol, P. A. Behavioural mode of action of deet: inhibition of lactic acid attraction. *Med. Vet. Entomol.* **13**, 97–100 (1999).
- Ditzen, M., Pellegrino, M. & Vosshall, L. B. Insect odorant receptors are molecular targets of the insect repellent DEET. *Science* **319**, 1838–1842 (2008).
- Syed, Z. & Leal, W. S. Mosquitoes smell and avoid the insect repellent DEET. *Proc. Natl Acad. Sci. USA* **105**, 13598–13603 (2008).
- Liu, C. *et al.* Distinct olfactory signaling mechanisms in the malaria vector mosquito *Anopheles gambiae*. *PLoS Biol.* **8**, e1000467 (2010).
- Bohbot, J. D. & Dickens, J. C. Insect repellents: Modulators of mosquito odorant receptor activity. *PLoS ONE* **5**, e12138 (2010).
- Pellegrino, M., Steinbach, N., Stensmyr, M. C., Hansson, B. S. & Vosshall, L. B. A natural polymorphism alters odour and DEET sensitivity in an insect odorant receptor. *Nature* **478**, 511–514 (2011).
- Lee, Y., Kim, S. H. & Montell, C. Avoiding DEET through insect gustatory receptors. *Neuron* **67**, 555–561 (2010).
- Hallam, E. A. & Carlson, J. R. Coding of odors by a receptor repertoire. *Cell* **125**, 143–160 (2006).
- Carey, A. F., Wang, G., Su, C. Y., Zwiebel, L. J. & Carlson, J. R. Odorant reception in the malaria mosquito *Anopheles gambiae*. *Nature* **464**, 66–71 (2010).
- Silbering, A. F. *et al.* Complementary function and integrated wiring of the evolutionarily distinct *Drosophila* olfactory subsystems. *J. Neurosci.* **31**, 13357–13375 (2011).

Supplementary Information is available in the online version of the paper.

Acknowledgements We thank K. J. Lee and members of the Vosshall lab for comments on the manuscript. F. Urnov of Sangamo BioSciences suggested the experiments in Supplementary Fig. 1. We thank C. McMeniman for initiating the *A. aegypti* GFP ZFN disruption project together with M.D. and for establishing mosquito microinjection at Genetic Services Inc. S. Dewell of the Rockefeller University Genomics Resource Center provided bioinformatic assistance. W. Takken and N. Verhulst suggested the use of nylon stockings in Figs 4 and 5. Román Corfas provided advice on imaging in Fig. 5b. This work was funded in part by a grant to R. Axel and L.B.V. from the Foundation for the National Institutes of Health through the Grand Challenges in Global Health Initiative. This work was supported in part by grants from the National Institutes of Health to C.S.M. (DC012069) and N.J. and A.A.J. (AI29746). L.B.V. is an investigator of the Howard Hughes Medical Institute.

Author Contributions M.D. carried out the experiments in Fig. 1 and Supplementary Fig. 1 and Supplementary Fig. 2b, c. E.J.D. carried out the experiments in Supplementary Fig. 2a. N.J. generated the GFP transgenic *A. aegypti* and injected the GFP ZFN for Supplementary Fig. 1 and was supervised by A.A.J. T.N. carried out the experiments in Fig. 2. C.G. reared mosquitoes and genotyped *orco* mutants. C.S.M. developed the assays used in Figs 3 and 4 with M.D. and L.S. L.S., M.D. and C.S.M. carried out the experiments in Figs 3 and 4. L.S., E.J.D. and M.D. developed and carried out the assays in Fig. 5. M.D., C.S.M. and L.B.V. wrote the paper.

Author Information Reprints and permissions information is available at www.nature.com/reprints. The authors declare no competing financial interests. Readers are welcome to comment on the online version of the paper. Correspondence and requests for materials should be addressed to L.B.V. (Leslie.Vosshall@rockefeller.edu).

EndMT contributes to the onset and progression of cerebral cavernous malformations

Luigi Maddaluno^{1*}, Noemi Rudini^{1*}, Roberto Cuttano¹, Luca Bravi¹, Costanza Giampietro¹, Monica Corada¹, Luca Ferrarini¹, Fabrizio Orsenigo¹, Eleanna Papa¹, Gwenola Boulday^{2,3}, Elisabeth Tournier-Lasserre^{2,3,4}, Françoise Chapon⁵, Cristina Richichi⁶, Saverio Francesco Retta⁷, Maria Grazia Lampugnani^{1,8} & Elisabetta Dejana^{1,9}

Cerebral cavernous malformation (CCM) is a vascular dysplasia, mainly localized within the brain and affecting up to 0.5% of the human population. CCM lesions are formed by enlarged and irregular blood vessels that often result in cerebral haemorrhages. CCM is caused by loss-of-function mutations in one of three genes, namely *CCM1* (also known as *KRIT1*), *CCM2* (*OSM*) and *CCM3* (*PDCD10*), and occurs in both sporadic and familial forms¹. Recent studies^{2–7} have investigated the cause of vascular dysplasia and fragility in CCM, but the *in vivo* functions of this ternary complex remain unclear⁸. Postnatal deletion of any of the three *Ccm* genes in mouse endothelium results in a severe phenotype, characterized by multiple brain vascular malformations that are markedly similar to human CCM lesions⁹. Endothelial-to-mesenchymal transition (EndMT) has been described in different pathologies, and it is defined as the acquisition of mesenchymal and stem-cell-like characteristics by the endothelium^{10–12}. Here we show that endothelial-specific disruption of the *Ccm1* gene in mice induces EndMT, which contributes to the development of vascular malformations. EndMT in *CCM1*-ablated endothelial cells is mediated by the upregulation of endogenous BMP6 that, in turn, activates the transforming growth factor- β (TGF- β) and bone morphogenetic protein (BMP) signalling pathway. Inhibitors of the TGF- β and BMP pathway prevent EndMT both *in vitro* and *in vivo* and reduce the number and size of vascular lesions in *CCM1*-deficient mice. Thus, increased TGF- β and BMP signalling, and the consequent EndMT of *CCM1*-null endothelial cells, are crucial events in the onset and progression of CCM disease. These studies offer novel therapeutic opportunities for this severe, and so far incurable, pathology.

To study the role of *CCM1* *in vivo*, we generated endothelial-specific tamoxifen-inducible *Ccm1* loss-of-function (iCCM1) mice. *Ccm1* deletion resulted in the development of vascular lesions within the central nervous system. The lesions were mostly concentrated in the cerebellum (Supplementary Fig. 1a), and were composed of dilated vessels with multiple lumens, sometimes with signs of vascular leakage as hemosiderin accumulation (Supplementary Fig. 1a, b). We also observed a marked inflammatory reaction, characterized by infiltration of leukocytes and increased expression of the adhesion molecules intercellular adhesion molecule 1 (ICAM1) and vascular cell adhesion molecule-1 (VCAM1) (Supplementary Fig. 1c–h). As in patients with CCM¹³, iCCM1 mice presented venous malformations at the periphery of the retinal vascular plexus (Supplementary Fig. 1i). Enhanced yellow fluorescent protein (eYFP) staining confirmed the high gene recombination efficiency (Supplementary Fig. 1j). To investigate the phenotype of endothelial cells lining the vascular lesions, we analysed the expression and the localization of junctional proteins. In these cells the adherens junction protein VE-cadherin was strongly

disorganized whereas N-cadherin was markedly upregulated (Fig. 1a, b) as compared with cadherin distribution in endothelial cells of the normal vessels surrounding the lesions. This type of cadherin switch has been associated with EndMT^{14,15}. To test the hypothesis of the occurring EndMT, we evaluated the expression of typical mesenchymal markers, such as SLUG (also known as *SNAI2*), inhibitor of DNA binding 1 (ID1) and α -smooth muscle actin (α SMA)^{16,17}. We found that these proteins were strongly upregulated in the endothelial cells forming the vascular malformations (Fig. 1c–e). The stem-cell markers stem cell antigen 1 (SCA1) and CD44 were also strongly expressed by cells lining the lesions, but not by endothelial cells in the surrounding normal vessels (Fig. 1f, g). KLF4, a transcription factor involved in cell differentiation¹⁸, was the only investigated marker that was upregulated both in the lesions and the normal vasculature of the iCCM1 mice (Fig. 1h, i). In iCCM1 malformations, endothelial expression of mesenchymal and stem-cell markers increased with the size of the lesion, with the exception of KLF4, SLUG and ID1 (Fig. 1j). Furthermore, the upregulation of mesenchymal and stem-cell markers and leukocyte adhesion molecules was confirmed in freshly isolated mouse brain endothelial cells (Fig. 1k) and in the retina of iCCM1 mice (Supplementary Fig. 2a–f). Importantly, the acquisition of the mesenchymal and stem-cell phenotype occurs only in endothelial cells expressing eYFP, confirming *Ccm1* recombination (Supplementary Fig. 2g for KLF4). Thus, *Ccm1* ablation *in vivo* confers EndMT traits to endothelial cells.

To investigate whether EndMT in CCM lesions is a cell-autonomous process, we treated cultured endothelial cells from *Ccm1*^{fl/fl} mice with Tat-Cre recombinase. *CCM1* downregulation in lung (CCM1 knock-out) and primary brain microvascular endothelial cells (BMECs) (CCM1 knockdown) (Supplementary Fig. 3a, e) caused a switch in phenotype, which recapitulates the findings observed *in vivo* (Supplementary Fig. 3b–g). Cell transition to a mesenchymal state is accompanied by increased proliferation and invasiveness¹². We found that loss of CCM1 caused a significant enhancement of endothelial cell proliferation and a greater invasive/sprouting capacity (Supplementary Fig. 4).

Because the TGF- β pathway is a major inducer of EndMT¹⁰, we investigated whether the EndMT switch in CCM1-knockout endothelial cells is due to a greater sensitivity of these cells to this factor. TGF- β signalling is mediated by phosphorylation of receptor-activated SMAD proteins, which, once phosphorylated (pSMADs), translocate to the nucleus and regulate the transcription of target genes. Phosphorylation of SMAD1 and SMAD3 was enhanced after loss of CCM1 (Fig. 2a, quantification in Supplementary Fig. 11). In addition, TGF- β 1 stimulation of CCM1-knockout endothelial cells showed a stronger and more prolonged SMAD phosphorylation and transcriptional activity compared to control endothelial cells (Fig. 2b, c). The higher

¹IFOM Fondazione, FIRC Institute of Molecular Oncology, 20139 Milan, Italy. ²INSERM, UMR-S740, F-75010 Paris, France. ³Université Paris Diderot, Sorbonne Paris Cité, Génomique des Maladies Vasculaires UMR-S740, F-75010 Paris, France. ⁴AP-HP, Groupe Hospitalier Saint-Louis Lariboisière-Fernand-Widal, F-75010 Paris, France. ⁵Department of Pathology, Centre Hospitalier Universitaire, Avenue Côte de Nacre, 14032 Caen, France. ⁶IEO – European Institute of Oncology, 20139 Milan, Italy. ⁷CCM Italia - Department of Clinical and Biological Sciences, University of Turin, 10043 Orbassano, Turin, Italy. ⁸Mario Negri Institute of Pharmacological Research, 20156 Milan, Italy. ⁹Department of Biosciences, University of Milan, 20133 Milan, Italy.

*These authors contributed equally to this work.

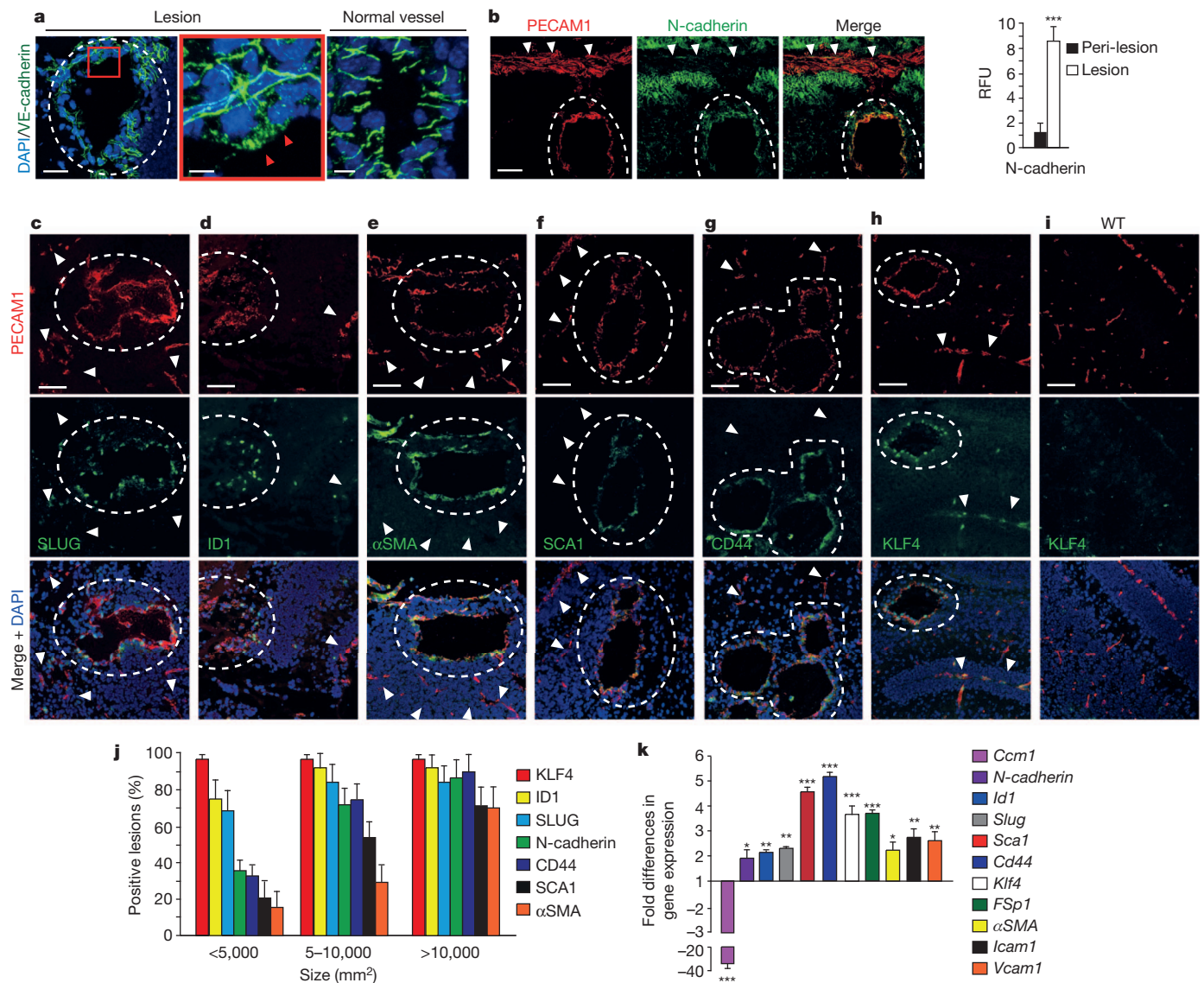


Figure 1 | *Ccm1* deletion causes EndMT *in vivo*. **a, b**, VE- and N-cadherin in normal vessels and vascular lesions of iCCM1 mouse brains. Red arrowheads denote VE-cadherin out of the junctions. DAPI, 4',6-diamidino-2-phenylindole; RFU, relative fluorescent units. **c–h**, Mesenchymal and stem-cell markers in the vascular lesions of iCCM1 mouse brains. **i**, KLF4 expression in wild-type (WT) mouse brain. Data are representative of three independent observations ($n = 5$ in each group, from two different litters). In **a–i**, white arrowheads denote normal peri-lesion vessels; dotted areas denote vascular

lesions. **j**, Analysis of EndMT markers in CCM lesions in eight iCCM1 mice. **k**, Quantitative reverse transcriptase PCR (qRT-PCR) analysis of EndMT markers in freshly isolated brain endothelial cells (fold difference in gene expression in iCCM1 versus wild type). Data are mean \pm s.d. from three independent experiments. α SMA is also known as *Acta2*; *Fsp1* is also known as *S100a4*; *N-cadherin* is also known as *Cdh2*; *Sca1* is also known as *Ly6a*. $*P < 0.05$; $**P < 0.01$; $***P < 0.001$. Scale bars, 50 μ m (**a**, left); 60 μ m (**b–i**); 8 μ m (**a**, middle and right).

sensitivity of CCM1-knockout endothelial cells was not due to a basal increased production of TGF- β 1 and TGF- β 2, nor to an altered expression of SMAD4, TGF- β type II receptor (T β RII) and the two TGF- β type I (T β RI) receptors, ALK5 and ALK1 (Supplementary Fig. 5 and data not shown). Treatment of CCM1-knockout endothelial cells with the T β RI and pSMAD signalling inhibitor LY-364947 (ref. 19) strongly reduced pSMAD1 and 3 levels, and inhibited the EndMT switch (Fig. 2d–f and Supplementary Fig. 6a–c and quantification in Supplementary Fig. 11). Similar results were obtained with the T β RI/II inhibitor LY-2109761 (ref. 20; Supplementary Fig. 6d, e). Inhibition of TGF- β signalling in iCCM1 mice by the combination of LY-364947 and SB-431542 (another inhibitor of pSMAD signalling active *in vivo*)²¹ macroscopically reduced the number and extension of the vascular malformations and prevented vascular leakage (Fig. 3a, b). This treatment also restored a correct endothelial-cell–astrocyte interaction in the

vascular lesions (Fig. 3c, yellow and magenta outlined magnifications) and markedly reduced mesenchymal marker expression and SMAD phosphorylation (Supplementary Fig. 7).

Importantly, the analysis of lesions from patients carrying CCM1 or CCM2 mutations showed that, in parallel with increased nuclear staining of pSMAD3 (Supplementary Fig. 8b, d), VE-cadherin was delocalized from the endothelial junctions (Supplementary Fig. 8d, asterisks), whereas N-cadherin expression was enhanced (Supplementary Fig. 8a, c). These data support the concept of increased TGF- β signalling and EndMT switch in endothelial cells also in human CCM lesions.

To investigate the mechanism of the increased sensitivity of CCM1-knockout endothelial cells to TGF- β , we analysed the endogenous expression of members of the TGF- β signalling superfamily. Among all the genes examined, *Bmp6* was specifically and strongly upregulated after CCM1 ablation in cultured or freshly isolated brain endothelial

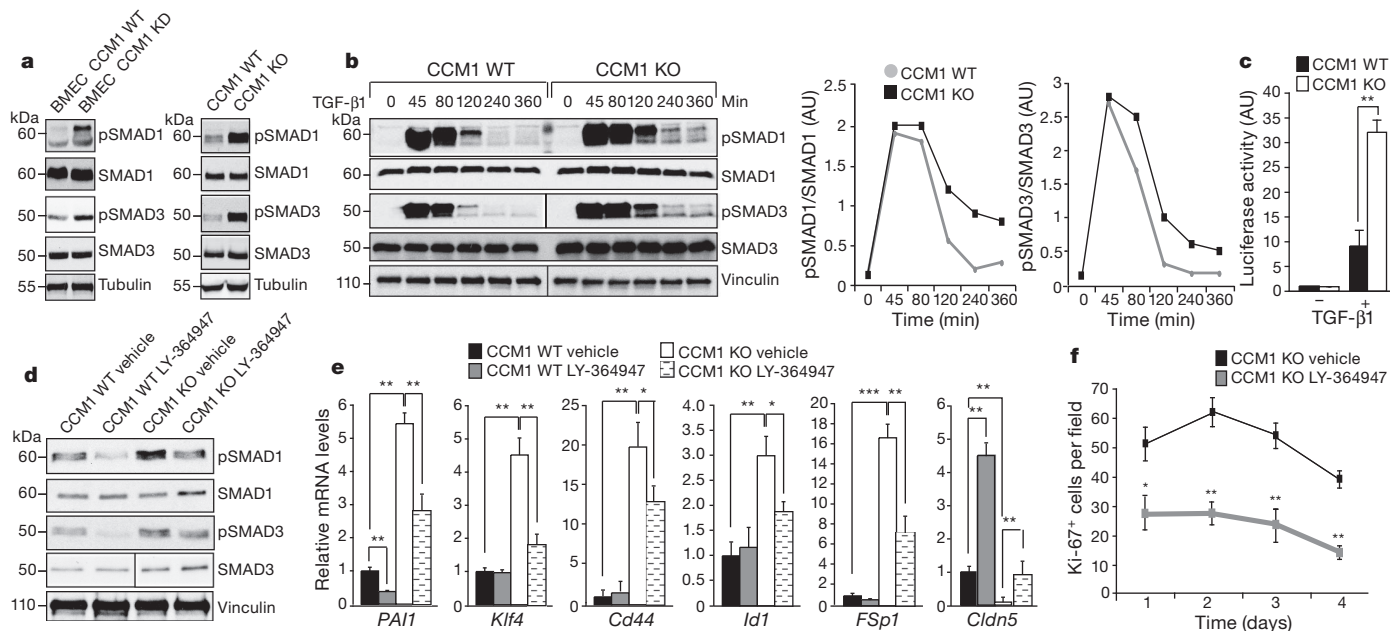
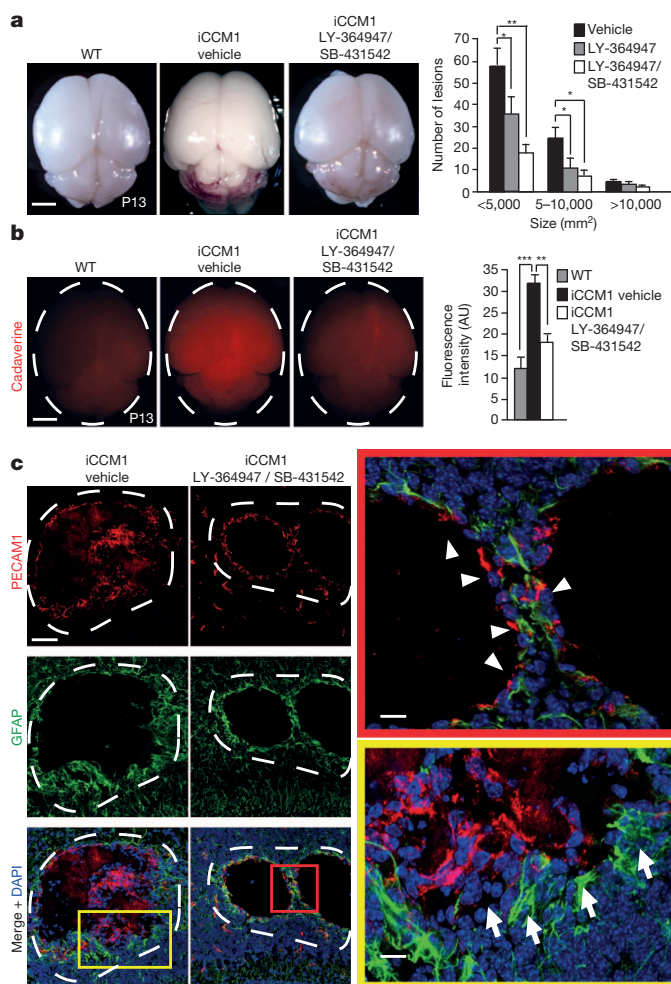


Figure 2 | *Ccm1* deletion induces EndMT via TGF- β signalling activation. **a**, Western blot of pSMAD proteins in CCM1 wild-type and knockdown (KD) BMECs (left), and in CCM1 wild-type and knockout (KO) lung endothelial cells (right) (see Methods). **b**, Left, TGF- β -induced SMAD phosphorylation in CCM1 wild-type and knockout lung endothelial cells. Right, pSMAD quantification by densitometry scan. AU, arbitrary units. **c**, TGF- β -induced transcriptional reporter activity in CCM1 wild-type and knockout lung endothelial cells.

d, Western blot of pSMAD proteins after LY-364947-mediated TGF- β pathway inhibition. **e**, Effect of LY-364947 on EndMT markers and claudin 5 (*Cldn5*) in CCM1-positive and knockout endothelial cells. Data are mean \pm s.d. from three independent experiments. *PAI1* is also known as *Serpine1*. **f**, Proliferation of vehicle- or LY-364947-treated CCM1-knockout endothelial cells quantified by counting Ki-67-positive cells. Data are mean \pm s.d. from three independent experiments. * P < 0.05; ** P < 0.01; *** P < 0.001.



cells (Fig. 4a, i). BMPs are secreted proteins that, after binding to their receptors, lead to SMAD phosphorylation. BMPs have been associated with epithelial-to-mesenchymal transition²², and treatment of endothelial cells with recombinant BMP6 increased SMAD1 and SMAD3 phosphorylation and induced the expression of EndMT markers (Fig. 4b, c). Furthermore, DMH1, an inhibitor of BMP signalling²³, abrogated SMAD1 and SMAD3 phosphorylation and the EndMT switch (Fig. 4d–f). Finally, knockdown of BMP6 expression in CCM1-knockout endothelial cells resulted in decreased pSMAD levels together with a significant reduction of the EndMT markers (Fig. 4g, h).

One of the unsolved questions in CCM pathology is why the appearance of vascular lesions is confined to the brain. We therefore compared freshly isolated endothelial cells from wild-type and iCCM1 brains and lungs after gene recombination. These cells have been lysed after isolation and were not exposed to culture conditions. We found that only iCCM1 freshly isolated brain endothelial cells expressed high levels of BMP6 and EndMT markers, whereas freshly isolated lung endothelial cells did not, with the exception of KLF4 (Fig. 4i).

CCM1 acts as a Notch activator⁷. Accordingly, we found that both CCM1-knockdown BMECs and freshly isolated brain endothelial cells from iCCM1 mice showed a significantly lower expression of the Notch-dependent transcription factors HEY1 and HEY2 compared

Figure 3 | TGF- β signalling inhibition reduces number and size of lesions and vessel leakage. **a**, Wild-type, iCCM1 vehicle-treated and LY-364947/SB-431542-treated mouse brains after dissection (left) and quantification of number and size of lesions (right) (n = 4 in each group from three different litters). **b**, Whole brains photographed after fluorescent cadaverine injection (left) and quantification of the recovered fluorescence (right). Data are mean \pm s.d. **c**, Confocal microscopy of astrocytes (GFAP staining) in CCM1 lesions (dotted areas) of iCCM1 vehicle- and LY-364947/SB-431542-treated animals. Arrowheads denote normal astrocyte coverage in a LY-364947/SB-431542-treated mouse (red magnification). Arrows denote astrocyte detachment from a vascular lesion of a vehicle treated mouse (yellow magnification). Data are mean \pm s.d. Scale bars, 500 μ m (**a**, **b**); 60 μ m (**c**); 20 μ m (magnifications in **c**). * P < 0.05; ** P < 0.01; *** P < 0.001.

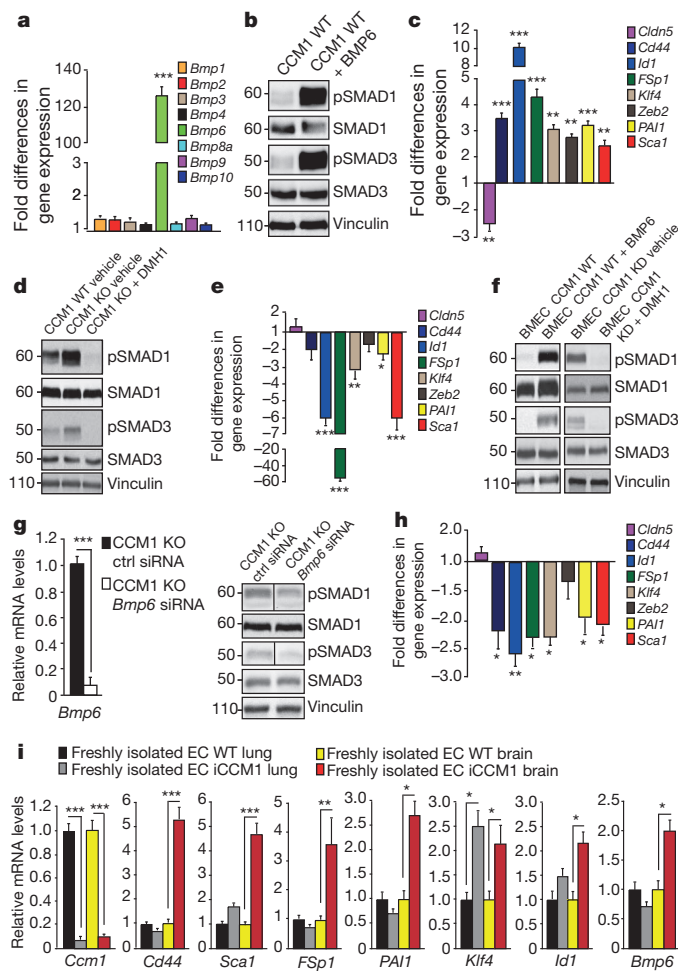


Figure 4 | CCM1 deletion induces EndMT via BMP6 upregulation. **a**, *Bmp* gene expression profile in CCM1 wild-type and knockout endothelial cells (fold changes in knockout versus wild type). *Bmp9* is also known as *Gdf2*. **b**, **c**, BMP6-mediated SMAD phosphorylation and upregulation of mesenchymal and stem-cell makers in wild-type lung endothelial cells. Fold changes in gene expression in BMP6-treated versus control (**c**). **d**, **e**, DMH1-mediated BMP pathway inhibition and downregulation of mesenchymal and stem-cell makers in CCM1-knockout endothelial cells. Fold difference in DMH1-treated versus control. **f**, BMP6- and DMH1-mediated effects on SMAD phosphorylation in wild-type and CCM1-knockdown BMECs. **g**, *Bmp6* relative mRNA levels (left) and SMAD phosphorylation (right) in *Bmp6* and control (ctrl) short interfering RNA (siRNA)-treated CCM1-knockout endothelial cells. **h**, Gene expression levels of EndMT molecules in *Bmp6* and control siRNA-treated CCM1-knockout endothelial cells. Fold change in *Bmp6* siRNA versus control. **i**, qRT-PCR analysis of mesenchymal and stem-cell markers and *Bmp6* in freshly isolated brain and lung endothelial cells (EC) from wild-type and iCCM1 mice. Data are mean \pm s.d. from three independent observations. * $P < 0.05$; ** $P < 0.01$; *** $P < 0.001$. Lane markers denote kilodaltons.

to relative wild-type endothelial cells (Supplementary Fig. 9a). Notch activation of BMECs by upregulation of an intracellular fragment of the murine Notch1 receptor (NotchIC)²⁴ abrogated BMP6 expression (Supplementary Fig. 9b, c). Conversely, inhibition of Notch signalling by DAPT (*N*-[*N*-(3,5-difluorophenyl)-*L*-alanyl]-*S*-phenylglycine *t*-butyl ester), resulted in strong BMP6 upregulation (Supplementary Fig. 9c). Thus, our data suggest that: (1) loss of CCM1 mediates Notch inhibition; (2) Notch inhibition upregulates BMP6 expression in the brain endothelium; and (3) autocrine BMP6 activity strongly contributes to the observed EndMT (Supplementary Fig. 9d).

Patients with loss-of-function mutations in any of the three CCM genes develop similar brain vascular lesions. This observation supports the idea of a common mechanism of action for the three CCM

proteins. To investigate this aspect, we ablated CCM3 in endothelial cells derived from *Ccm3*^{fl/fl} mice and observed a similar phenotype to CCM1-knockout cells (Supplementary Fig. 10). This suggests that the EndMT transition is a common feature of loss-of-function mutations of members of the CCM complex. Altogether, these findings support a model in which CCM lesions are formed by endothelial cells undergoing EndMT. The process of EndMT is characterized by altered junction organization, loss of cell polarity, increased cell proliferation and migratory capacity¹². The EndMT may, therefore, explain most of the previously observed changes in the phenotype of CCM-deficient endothelial cells^{2,4-6,9} that have been associated with vascular dysplasia and fragility of CCM lesions. These findings introduce novel and unexpected therapeutic opportunities to reduce CCM vascular malformations and consequent intracerebral haemorrhages. Inhibition of pSMAD signalling effectively reduces CCM lesions. Therefore, it is conceivable to use currently available inhibitors of different steps of the TGF- β and BMP signalling pathway^{25,26} to reduce or reverse the development of CCM lesions. Other pathways may contribute to the EndMT phenotype and offer potential pharmacological targets. These include the Notch pathway that is inhibited in the absence of CCM1.

Canonical Wnt signalling may also be implicated. Deletion of CCM1 increases β -catenin nuclear translocation and transcriptional signalling²⁷. Wnt signalling is known to act synergistically with the TGF- β pathway to promote EndMT in endocardial cells²⁸. Chemical inhibitors of β -catenin are at present under evaluation for clinical studies, and may lead to new treatments for CCM disease.

CCM lesions are mostly localized in the brain vasculature although the gene is inactivated in all types of endothelial cell. The brain vasculature requires a continuous cross talk with astrocytes to maintain the organization of the neurovascular unit²⁹. As reported here, a correct communication of the endothelium with astrocytes is lost in iCCM1 mice, but is restored by inhibiting TGF- β and BMP signalling. The lack of an appropriate interaction with neural cells may strongly influence the development of lesions³⁰. This interaction is unique for the brain vessels and may explain why in other organs the appearance of vascular malformations is much less frequent.

METHODS SUMMARY

Mutant mice, inducible genetic experiments, pharmacological inhibition and cell treatments. For inducible and endothelial-cell-specific genetic loss-of-function experiments, we crossed *Cdh5*(PAC)-CreERT2 and *loxP*-flanked *Ccm1* allele transgenic mice (named *Ccm1*^{fl/fl}) (see Methods). For the *in vivo* tamoxifen-induced *Ccm1* deletion, tamoxifen (Sigma) was diluted and used as described⁹. For the *in vivo* inhibition of the TGF- β signalling, after tamoxifen-induced *Ccm1* gene-recombination (at postnatal day (P) 1), LY-364947 (Sigma; 10 mg per kg) and SB-431542 (SelleckBio; 10 mg per kg) were intraperitoneally injected daily, starting from P3, and the animals were killed at P13. For TGF- β 1 stimulation, confluent endothelial cells were serum-starved and incubated with 0.75 ng ml⁻¹ TGF- β 1 (PeproTech). For LY-364947, LY-2109761 (SelleckBio), BMP6 (R&D), DMH1 (4-[6-[4-(1-Methylethoxy)phenyl]pyrazolo[1,5-*a*]pyrimidin-3-yl]-quinoline, TOCRIS Bioscience) and DAPT (Alexis) treatments, endothelial cells were grown in MCDB with 5% FCS. Cells were stimulated daily for the indicated times with: LY-364947 (40 μ M for 6 days); LY-2109761 (5–10 μ M up to 72 h); BMP6 (100 ng ml⁻¹ for 96 h); DMH1 (2 μ M for 96 h); and DAPT (10 μ M for 48 h).

Full Methods and any associated references are available in the online version of the paper.

Received 16 May 2012; accepted 19 April 2013.

Published online 9 June 2013.

- Bergametti, F. *et al.* Mutations within the programmed cell death 10 gene cause cerebral cavernous malformations. *Am. J. Hum. Genet.* **76**, 42–51 (2005).
- Whitehead, K. J. *et al.* The cerebral cavernous malformation signaling pathway promotes vascular integrity via Rho GTPases. *Nature Med.* **15**, 177–184 (2009).
- Chan, A. C. *et al.* Mutations in 2 distinct genetic pathways result in cerebral cavernous malformations in mice. *J. Clin. Invest.* **121**, 1871–1881 (2011).
- Glading, A., Han, J., Stockton, R. A. & Ginsberg, M. H. KRIT-1/CCM1 is a Rap1 effector that regulates endothelial cell cell junctions. *J. Cell Biol.* **179**, 247–254 (2007).

5. Stockton, R. A., Shenkar, R., Awad, I. A. & Ginsberg, M. H. Cerebral cavernous malformations proteins inhibit Rho kinase to stabilize vascular integrity. *J. Exp. Med.* **207**, 881–896 (2010).
6. Lampugnani, M. G. *et al.* CCM1 regulates vascular-lumen organization by inducing endothelial polarity. *J. Cell Sci.* **123**, 1073–1080 (2010).
7. Wüsthube, J. *et al.* Cerebral cavernous malformation protein CCM1 inhibits sprouting angiogenesis by activating DELTA-NOTCH signaling. *Proc. Natl Acad. Sci. USA* **107**, 12640–12645 (2010).
8. Faurobert, E. & Albiges-Rizo, C. Recent insights into cerebral cavernous malformations: a complex jigsaw puzzle under construction. *FEBS J.* **277**, 1084–1096 (2010).
9. Bouliday, G. *et al.* Developmental timing of CCM2 loss influences cerebral cavernous malformations in mice. *J. Exp. Med.* **208**, 1835–1847 (2011).
10. Zeisberg, E. M. *et al.* Endothelial-to-mesenchymal transition contributes to cardiac fibrosis. *Nature Med.* **13**, 952–961 (2007).
11. Medici, D. *et al.* Conversion of vascular endothelial cells into multipotent stem-like cells. *Nature Med.* **16**, 1400–1406 (2010).
12. Kalluri, R. & Weinberg, R. A. The basics of epithelial-mesenchymal transition. *J. Clin. Invest.* **119**, 1420–1428 (2009).
13. Labauge, P., Denier, C., Bergametti, F. & Tournier-Lasserre, E. Genetics of cavernous angiomas. *Lancet Neurol.* **6**, 237–244 (2007).
14. Lopez, D., Niu, G., Huber, P. & Carter, W. B. Tumor-induced upregulation of Twist, Snail, and Slug represses the activity of the human VE-cadherin promoter. *Arch. Biochem. Biophys.* **482**, 77–82 (2009).
15. Mariotti, A., Perotti, A., Sessa, C. & Ruegg, C. N-cadherin as a therapeutic target in cancer. *Expert Opin. Investig. Drugs* **16**, 451–465 (2007).
16. Thiery, J. P., Acloque, H., Huang, R. Y. & Nieto, M. A. Epithelial-mesenchymal transitions in development and disease. *Cell* **139**, 871–890 (2009).
17. Li, Y., Yang, J., Luo, J. H., Dedhar, S. & Liu, Y. Tubular epithelial cell dedifferentiation is driven by the helix-loop-helix transcriptional inhibitor Id1. *J. Am. Soc. Nephrol.* **18**, 449–460 (2007).
18. Vivien, C. *et al.* Non-viral expression of mouse Oct4, Sox2, and Klf4 transcription factors efficiently reprograms tadpole muscle fibers *in vivo*. *J. Biol. Chem.* **287**, 7427–7435 (2012).
19. Gauger, K. J., Chenausky, K. L., Murray, M. E. & Schneider, S. S. SFRP1 reduction results in an increased sensitivity to TGF- β signaling. *BMC Cancer* **11**, 59 (2011).
20. Melisi, D. *et al.* LY2109761, a novel transforming growth factor β receptor type I and type II dual inhibitor, as a therapeutic approach to suppressing pancreatic cancer metastasis. *Mol. Cancer Ther.* **7**, 829–840 (2008).
21. Tanaka, H. *et al.* Transforming growth factor beta signaling inhibitor, SB-431542, induces maturation of dendritic cells and enhances anti-tumor activity. *Oncol. Rep.* **24**, 1637–1643 (2010).
22. McLean, K. *et al.* Human ovarian carcinoma-associated mesenchymal stem cells regulate cancer stem cells and tumorigenesis via altered BMP production. *J. Clin. Invest.* **121**, 3206–3219 (2011).
23. Ao, A., Hao, J., Hopkins, C. R. & Hong, C. C. DMH1, a novel BMP small molecule inhibitor, increases cardiomyocyte progenitors and promotes cardiac differentiation in mouse embryonic stem cells. *PLoS ONE* **7**, e41627 (2012).
24. Murtaugh, L. C., Stanger, B. Z., Kwan, K. M. & Melton, D. A. Notch signaling controls multiple steps of pancreatic differentiation. *Proc. Natl Acad. Sci. USA* **100**, 14920–14925 (2003).
25. Korpai, M. & Kang, Y. Targeting the transforming growth factor-beta signalling pathway in metastatic cancer. *Eur. J. Cancer* **46**, 1232–1240 (2010).
26. Yuan, Q. *et al.* Fluorofenidone suppresses epithelial-mesenchymal transition and the expression of connective tissue growth factor via inhibiting TGF- β /Smads signaling in human proximal tubular epithelial cells. *Pharmazie* **66**, 961–967 (2011).
27. Glading, A. J. & Ginsberg, M. H. Rap1 and its effector KRIT1/CCM1 regulate β -catenin signaling. *Dis. Model Mech.* **3**, 73–83 (2010).
28. Liebner, S. *et al.* β -catenin is required for endothelial-mesenchymal transformation during heart cushion development in the mouse. *J. Cell Biol.* **166**, 359–367 (2004).
29. Liebner, S., Czupalla, C. J. & Wolburg, H. Current concepts of blood-brain barrier development. *Int. J. Dev. Biol.* **55**, 467–476 (2011).
30. Louvi, A. *et al.* Loss of cerebral cavernous malformation 3 (Ccm3) in neuroglia leads to CCM and vascular pathology. *Proc. Natl Acad. Sci. USA* **108**, 3737–3742 (2011).

Supplementary Information is available in the online version of the paper.

Acknowledgements This work was supported by grants from: Fondation Leducq Transatlantic Network of Excellence, Associazione Italiana per la Ricerca sul Cancro (AIRC) and a 'Special Program Molecular Clinical Oncology 5x1000' to AIRC-Gruppo Italiano Malattie Mieloproliferative (AGIMM); the European Community: European Research Council (ERC grant 268870 call identifier ERC-2010-SdG) (EU Networks: EUSTROKE-contract-202213, OPTISTEM-contract-223098, ENDOSTEM-HEALTH-2009-241440, ENDOSTEM-HEALTH-2009-241440, JUSTBRAIN-HEALTH-2009-241861, ITN-VESSEL), and the CARIPLO Foundation. We are strongly indebted to R. Adams and D. A. Melton for sharing *Cdh5(PAC)-CreERT2* and *Notch1C* mice, respectively. We are grateful to M. Forni and the Italian research network for Cerebral Cavernous Malformation (CCM Italia; <http://www.ccmitalia.unito.it>) for contributing to the study with important biological materials.

Author Contributions Experiments were designed by L.M., N.R. and E.D.; *in vivo* treatments were performed by L.M., N.R., R.C., M.C. and L.B.; G.B. and E.T.-L. contributed to the scientific discussion and the setting-up of the *in vivo* experiments. Cell isolation and treatments were performed by L.M., N.R., E.P., M.G.L., C.G. and M.C.; qRT-PCR analyses were performed by L.M., N.R. and L.F.; F.O., R.C., C.R. and L.M. performed analysis of the retinas; human samples were analysed by L.M. with the help of F.C. and S.F.R.; the manuscript was assembled and written by L.M., N.R., C.G. and E.D.

Author Information Reprints and permissions information is available at www.nature.com/reprints. The authors declare no competing financial interests. Readers are welcome to comment on the online version of the paper. Correspondence and requests for materials should be addressed to E.D. (elisabetta.dejana@ifom.eu) or L.M. (luigi.maddaluno@ifom.eu).

METHODS

Antibodies. For immunofluorescence, western blotting and immunoprecipitation, the following antibodies were used: VE-cadherin rat (550548, BD Biosciences); VE-cadherin goat (sc-6458, Santa Cruz); N-cadherin mouse (610920, BD Biosciences); PECAM1 hamster (MAB1398Z, Millipore); CD3 hamster (140033, eBiosciences); CD11b rat (553310, BD Biosciences); VCAM1 rat (ab19569, Abcam); ICAM1 rat (116111, BioLegend); CD44 rat (553131, BD Biosciences); KLF4 goat (AF3158, R&D); FSP1 rabbit (07-2274, Millipore); ID1 rabbit (sc-488, Santa Cruz); SLUG rabbit (9585, Cell Signaling); SCA1 goat (AF1226, R&D); STRO-1 mouse (Invitrogen); α SMA mouse (F3777, Sigma); GFP rabbit (A-6455, Invitrogen); CCM1 rabbit (gift from F. Retta); L1 rabbit (gift from U. Cavallaro); CCM3 rabbit (produced by Eurogentec); Ki-67 mouse (558616, BD Biosciences); GFAP (Z0334, Dako); claudin 5 mouse (352588, Invitrogen); claudin 5 rabbit (gift from H. Wolburg); ALK5 rabbit (sc-398, Santa Cruz); T β RII rabbit (sc-220, Santa Cruz); pSMAD1/5 rabbit (9516, Cell Signaling); pSMAD3 rabbit (9520, Cell Signaling); pSMAD3 rabbit (1880-1, Epitomics); SMAD1 rabbit (9743, Cell Signaling); SMAD3 rabbit (9523, Cell Signaling); α -tubulin mouse (T9026, Sigma); vinculin mouse (V9264, Sigma); horseradish peroxidase (HRP)-linked anti-mouse, anti-rat and anti-rabbit (Cell Signaling); HRP-linked anti-goat (Promega); Alexa Fluor 555-conjugated donkey anti-rat, anti-goat, anti-rabbit and anti-mouse (Invitrogen); Cy3-conjugated goat anti-hamster (Jackson ImmunoResearch); Alexa Fluor 488-conjugated donkey anti-rat, anti-goat, anti-rabbit and anti-mouse (Invitrogen).

Mouse lines. *Ccm1*^{fl/fl} and *Ccm3*^{fl/fl} mice, in which exons 4–5 of the *Ccm1* and *Ccm3* genes, respectively, are flanked by *loxP* sites, were produced by Artemis Taconis. Deletion of exons by Cre-mediated recombination produces loss-of-function alleles. The *Cdh5*(PAC)-CreERT2 mouse line was previously reported³¹. The *Cdh5*(PAC)-CreERT2; *Ccm1*^{fl/fl} mice were bred with *Rosa26-Stop*^{fl}-EYFP reporter mice³² to monitor tamoxifen-induced Cre/*loxP* recombination. *Rosa26-Stop*^{fl}-EYFP mice were purchased from the Jackson Laboratory. Mice were all bred on a C57BL/6 background. The genotype of iCCM1 animals was *Cdh5*(PAC)-CreERT2; *Ccm1*^{fl/fl}; *Rosa26-Stop*^{fl}-EYFP. Control mice were *Cdh5*(PAC)-CreERT2; *Ccm1*^{fl/+}; *Rosa26-Stop*^{fl}-EYFP. *Rosa26*^{Notch1C} mice²⁴ were a gift from D. A. Melton. All procedures described in this study were in full accordance with the guidelines established in the Principles of Laboratory Animal Care (directive 86/609/EEC) and approved by the Italian Ministry of Health.

Treatment with TGF- β and BMP signalling inhibitors. LY-364947 (Sigma), SB-431542 (SelleckBio), LY-2109761 (SelleckBio) and DMH1 (TOCRIS Bioscience) were dissolved in dimethylsulphoxide (DMSO). Endothelial cells were grown in MCDB with 5% FCS, and stimulated daily with: LY-364947 (40 μ M for 6 days); LY-2109761 (5–10 μ M up to 72 h); and DMH1 (2 μ M for 96 h). For the *in vivo* inhibition of the TGF- β signalling, LY-364947 (Sigma; 10 mg per kg) and SB-431542 (SelleckBio; 10 mg per kg) were intraperitoneally injected daily starting 2 days after the *Ccm1* recombination. The control mice were treated in parallel with vehicle only. The animals were killed at P13.

Cell treatments. For TGF- β 1 stimulation, confluent endothelial cells were serum-starved and incubated with 0.75 ng ml⁻¹ TGF- β 1 (PeproTech). For BMP6 (R&D) and DAPT (Alexis) treatments, endothelial cells were grown in MCDB with 5% FCS and stimulated daily with BMP6 (100 ng ml⁻¹ for 96 h) and DAPT (10 μ M for 48 h).

Western blotting. Confluent cells were lysated by boiling in a modified Laemmli sample buffer (2% SDS, 20% glycerol, and 125 mM Tris-HCl, pH 6.8). Equal amount of proteins were loaded on gel and separated by SDS-PAGE and transferred to a Protran nitrocellulose membrane (Whatman). After blocking, primary and HRP-linked secondary antibodies, specific bindings were detected by chemiluminescence system (GE Healthcare).

RNA interference. For small RNA interference (siRNA) the following anti-BMP6 oligonucleotides (10620318, Invitrogen) were used: MSS-236054 (5'-GCCAACUACUGUGAGAGAGUGUU-3'), MSS-236055 (5'-GCCUCAGAAGAAGGUUGGCUGGAAU-3'), MSS-236056 (5'-CCUUUCUUAUCAGCAUUUACCAAGU-3') and negative control siRNA Med GC (12935-300, Invitrogen). For oligonucleotide transfection, cells were seeded at a density of 10⁴ cm⁻². After 20 h, they were transfected with a combination of the three anti-BMP6 siRNA oligonucleotides (20 nM each) for 5 h in OptiMem (Invitrogen) using Lipofectamine 2000 (Invitrogen).

Immunoprecipitation. For analysis of endogenous receptors, confluent endothelial cells were solubilized in lysis buffer (20 mM Tris-HCl, pH 7.6, 150 mM NaCl, 1 mM CaCl₂, 0.5% Triton X-100, protease/phosphatase inhibitors) on ice for 30 min. Pre-cleared cell extracts were subjected to anti-T β RII and anti-ALK5 precipitation overnight at 4 °C, and immune complexes captured by protein A-sepharose beads (Amersham). Immunoprecipitated material was separated on Tris-glycine SDS-PAGE, blotted onto nitrocellulose membranes and analysed by standard methodologies.

qRT-PCR analysis. Total RNA was isolated by extraction with the RNeasy mini kit (Qiagen) and 1 μ g was reverse transcribed with random hexamers (High Capacity cDNA Archive kit; Applied Biosystems). cDNA was amplified with the TaqMan Gene Expression assay (Applied Biosystems) and an ABI/Prism 7900 HT thermocycler. For any sample the expression level, normalized to the housekeeping genes encoding *18S* and *GAPDH*, was determined by the comparative threshold cycle (*C_t*) method as described previously³³. The probe to identify the *Ccm1* mRNA has been purchased by Applied Biosystem TaqMan gene expression assays (Mm 01316552_m1).

Histology and tissue immunofluorescence. Mouse brains were embedded in Tissue-Tek OCT (Sakura) and snap frozen. Paraffin embedded human brain samples from patients with CCM were provided by S. F. Retta and F. Chapon. Five-micrometre-thick sections were fixed in cold methanol or 4% paraformaldehyde and subjected to immunofluorescence. Blocking (2 h), primary (overnight) and secondary (3 h) antibodies were in PBS with 2% BSA. Sections were then counterstained with DAPI and mounted in Vectashield. Microscopy was performed with a Leica TCS AOBS confocal microscope. For quantification of the number and size of CCM1 lesions, serial sagittal sections (50 μ m) from frozen brain of iCCM1 vehicle-, LY-364947- and LY-364947/SB-431542-treated animals were performed. Each section was stained with haematoxylin and eosin. Analysis of the number/size of the CCM caverns was performed using an Olympus BX51 microscope and the NIS Element imaging software (Nikon). Three different groups of caverns were defined according to their size.

Transient transfection and transcriptional reporter assay. Transient transfection and reporter assay were performed as previously described³⁴. In all the reporter assays, a β -galactosidase (β -gal) expression vector was used as an internal control for the transfection efficiency. For the detection of SMAD-dependent transcription, cells were seeded at a density of 2×10^4 cm⁻² and transfected with 0.75 μ g (CAGA)12-luc and 0.25 μ g pCMV- β -gal using LipofectAMINE 2000 (Invitrogen) as the transfecting reagent. The luciferase activity was measured 24 h after the addition of 0.75 ng ml⁻¹ TGF- β 1. The dual-light reporter gene assay system (Applied Biosystems) for the combined detection of firefly luciferase and β -gal was used. The cell extraction and detection of chemiluminescence (Glomax 96 microplate luminometer; Promega) was carried out according to the manufacturer's instructions.

Intravenous injection and detection of fluorescent tracer. Animals (P13) received intraperitoneal injection of cadaverine conjugated to Alexa Fluor 555 (Invitrogen) (12.5 μ g per 1 g). Two hours after cadaverine circulation, anaesthetized animals (Avertin, 20 μ l g⁻¹, intraperitoneal) were perfused for 5 min with PBS to wash out the tracer from vessels. Brains were dissected and post-fixed in 4% paraformaldehyde at 4 °C overnight. Cadaverine extravasation in brain parenchyma was measured by software analysis (ImageJ) of brain images acquired under a stereomicroscope equipped with HBO 100 lamp and a Filter Set Lumar 43 HE.

Cells. Lung endothelial cells from *Ccm1*^{fl/fl} and *Ccm3*^{fl/fl} mice were isolated, immortalized and cultured as described³⁵. *Ccm1* or *Ccm3* were inactivated by treating cultured endothelial cells with Tat-Cre recombinase³⁶. To obtain primary BMECs, brain microvascular fragments from *Ccm1*^{fl/fl} mice were processed and cultured as published³⁶. To obtain freshly isolated endothelial cells, lungs and brain were dissected from control and iCCM1 mice (P13). These cells were lysed after isolation and were not exposed to culture conditions. Lungs were treated with collagenase type I and DNase (respectively, 1.5 mg ml⁻¹ and 25 μ g ml⁻¹, Roche) in HEPES-buffered DMEM (Life Technology) for 1 h at 37 °C with occasionally shaking and pipetting. The cell suspension was passed through a 70- μ m strainer and collected by centrifugation (5 min, 1,200 r.p.m.). Then, cell pellets were resuspended in 0.1% BSA and 2 mM EDTA in PBS, pH 7.4, and incubated for 45–60 min at 4 °C with Dynabeads (Invitrogen) previously coated with rat-anti mouse PECAM1 antibody (BD). Endothelial cells were then separated using a magnet.

Retinal immunohistochemistry. Eyes from wild-type and iCCM1 pups were fixed in 2% paraformaldehyde overnight before retinas were dissected. Retinas were incubated in 5% donkey serum, 1% BSA and 0.5% Triton-X100 in PBS overnight and the day after stained with PECAM1 (Millipore) or biotinylated isolectin B4 (IB4) (Vector Lab) (both used for vessel detection) and primary antibodies overnight. Then retinas were incubated with fluorophore-conjugated antibodies and with Alexa Fluor 405/488/555 streptavidin (Invitrogen) and mounted with ProLong Gold (Invitrogen).

Generation of endothelial spheroids and three-dimensional migration assay. To generate endothelial cell spheroids, 1,500 lung-derived endothelial cells were suspended in culture medium containing 0.25% (w/v) carboxymethylcellulose and seeded in non-adherent round-bottom 96-well plates (Greiner). Under these conditions, all suspended cells contribute to the formation of a single endothelial cell spheroid. These standardised spheroids were collected within 24 h. Cell spheroids were then embedded into a collagen gel as described³⁷. After gel polymerization,

0.15 ml of complete cell medium containing 10 ng ml^{-1} VEGF-A (PeproTech) and 10 ng ml^{-1} FGF-2 (PeproTech) was added. The gels were incubated at 37°C in 5% CO_2 . After 24 h spheroids were fixed in 4% paraformaldehyde, and cell sprouting and migration were visualized by actin staining (TRITC-phalloidin, Sigma). The cumulative length of capillary-like sprouts originating from the central plane of the spheroid was measured using a digitised imaging system connected to an inverted microscope (IX50, Olympus). At least 10 spheroids per experimental group and experiment were analysed.

Statistics. Student's two-tailed non-paired *t*-tests were used to determine the statistical significance for the *in vitro* analysis. The significance level was set at $P < 0.05$.

31. Corada, M. *et al.* The Wnt/ β -catenin pathway modulates vascular remodeling and specification by upregulating Dll4/Notch signaling. *Dev. Cell* **18**, 938–949 (2010).
32. Soriano, P. Generalized lacZ expression with the ROSA26 Cre reporter strain. *Nature Genet.* **21**, 70–71 (1999).
33. Spagnuolo, R. *et al.* Gas1 is induced by VE-cadherin and vascular endothelial growth factor and inhibits endothelial cell apoptosis. *Blood* **103**, 3005–3012 (2004).
34. Felici, A. *et al.* TLP, a novel modulator of TGF- β signaling, has opposite effects on Smad2- and Smad3-dependent signaling. *EMBO J.* **22**, 4465–4477 (2003).
35. Bussolino, F. *et al.* Murine endothelioma cell lines transformed by polyoma middle T oncogene as target for and producers of cytokines. *J. Immunol.* **147**, 2122–2129 (1991).
36. Liebner, S. *et al.* Wnt/ β -catenin signaling controls development of the blood-brain barrier. *J. Cell Biol.* **183**, 409–417 (2008).
37. Korff, T. & Augustin, H. G. Tensional forces in fibrillar extracellular matrices control directional capillary sprouting. *J. Cell Sci.* **112**, 3249–3258 (1999).

In vivo cardiac reprogramming contributes to zebrafish heart regeneration

Ruilin Zhang¹, Peidong Han¹, Hongbo Yang¹, Kunfu Ouyang¹, Derek Lee¹, Yi-Fan Lin², Karen Ocorr³, Guson Kang⁴, Ju Chen¹, Didier Y. R. Stainier^{4,†}, Deborah Yelon² & Neil C. Chi^{1,5}

Despite current treatment regimens, heart failure remains the leading cause of morbidity and mortality in the developed world due to the limited capacity of adult mammalian ventricular cardiomyocytes to divide and replace ventricular myocardium lost from ischaemia-induced infarct^{1,2}. Hence there is great interest to identify potential cellular sources and strategies to generate new ventricular myocardium³. Past studies have shown that fish and amphibians and early postnatal mammalian ventricular cardiomyocytes can proliferate to help regenerate injured ventricles^{4–6}; however, recent studies have suggested that additional endogenous cellular sources may contribute to this overall ventricular regeneration³. Here we have developed, in the zebrafish (*Danio rerio*), a combination of fluorescent reporter transgenes, genetic fate-mapping strategies and a ventricle-specific genetic ablation system to discover that differentiated atrial cardiomyocytes can transdifferentiate into ventricular cardiomyocytes to contribute to zebrafish cardiac ventricular regeneration. Using *in vivo* time-lapse and confocal imaging, we monitored the dynamic cellular events during atrial-to-ventricular cardiomyocyte transdifferentiation to define intermediate cardiac reprogramming stages. We observed that Notch signalling becomes activated in the atrial endocardium following ventricular ablation, and discovered that inhibiting Notch signalling blocked the atrial-to-ventricular transdifferentiation and cardiac regeneration. Overall, these studies not only provide evidence for the plasticity of cardiac lineages during myocardial injury, but more importantly reveal an abundant new potential cardiac resident cellular source for cardiac ventricular regeneration.

Atrial cardiomyocytes appear to have the remarkable capacity to divide in many adult vertebrate hearts including mammals during cardiac ventricular injury^{7,8}; however, the role of these proliferating atrial cardiomyocytes remains unclear. To address this issue, we have generated in the zebrafish, a genetic cardiac ventricle-specific nitroreductase (NTR)-mediated ablation system⁹, *Tg(vmhc:mCherry-NTR)*^{s957}, using the ventricular *myosin heavy chain* (*vmhc*) promoter¹⁰. Thus, this ablation system permits the targeted destruction of ventricular cardiomyocytes after metronidazole (MTZ) treatment (Fig. 1). To track both atrial and ventricular cardiomyocytes during ventricular injury, we fused the mCherry fluorescent protein to NTR to label ventricular cardiomyocytes in red (venCherry), as well as using the atrial *myosin heavy chain* (*amhc*) promoter to create the *Tg(amhc:eGFP)*^{s958} transgenic line, which marks with enhanced green fluorescent protein the atrial cardiomyocytes (atrGFP). As a result, we observed that the expression of mCherry and GFP in these reporter lines were restricted to ventricular and atrial cardiomyocytes, respectively, throughout development (Supplementary Fig. 1a–d). In order to visually monitor *in vivo* the dynamic cellular events that transpire throughout ventricular injury and regeneration within the same animal, the ventricles of *Tg(vmhc:mCherry-NTR)*; *Tg(amhc:eGFP)* hearts were ablated at 3–4 days post-fertilization (dpf),

an age when the zebrafish heart has completed cardiac looping and cardiac chamber cardiomyocytes have fully differentiated¹¹, but the zebrafish remains optically clear. As a result, 4 dpf ablated *vmhc:mCherry-NTR* ventricles displayed statistically significant reduction in venCherry fluorescence by 24 h post MTZ treatment (hours post treatment, hpt) (Fig. 1b, Supplementary Fig. 2a). This rapid decrease in venCherry fluorescence was accompanied by a reduction in ventricular size (Fig. 1b, Supplementary Fig. 2b) and function (fractional area change decreased from 42% to 16% at 24 hpt, $n = 5$, $P = 0.004$; Supplementary Videos 1 and 2; Supplementary Fig. 3a–c), leading to pericardial oedema and overall decreased blood circulation. TUNEL (TdT-mediated dUTP nick end labelling) cell-death assays revealed that this decrease in ventricular function and size was due to an increase in ventricular cardiomyocyte death (Fig. 1f). Conversely, we observed that the atria significantly enlarged (Supplementary Fig. 2b) and maintained normal contractile function (Supplementary Fig. 3d) during this reduction in ventricular size and function.

By 48 hpt, we observed in these injured ventricles an accretion of new venCherry⁺ cardiomyocytes adjacent to the atrioventricular canal (AVC) (Fig. 1c, asterisk), which continued to expand across the ventricle over the next 48 h to restore lost ventricular myocardium nearest

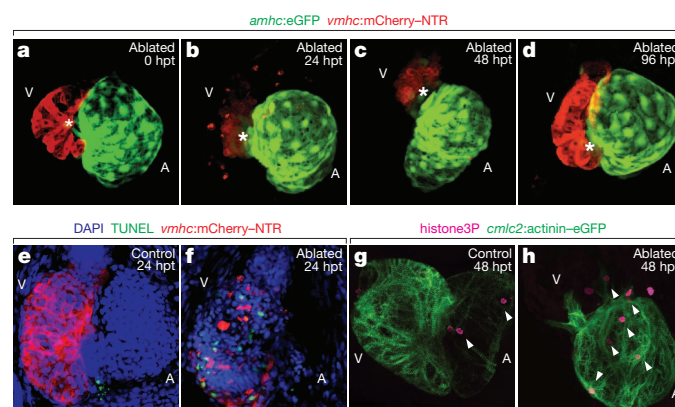


Figure 1 | Genetic ventricular-specific cardiomyocyte ablation results in ventricular cardiomyocyte death and subsequent regeneration.

a–d, Metronidazole (MTZ)-ablated *Tg(vmhc:mCherry-NTR)*; *amhc:eGFP* ventricular cardiomyocytes at 0 h (**a**), 24 h (**b**), 48 h (**c**) and 96 h (**d**) post-treatment (hpt). Ventricular cardiomyocytes (red), atrial cardiomyocytes (green), AVC (asterisks). **e, f**, TUNEL staining (green) in 24 hpt *Tg(vmhc:mCherry-NTR)* control (**e**) and ablated (**f**) ventricles (red) at 4 dpf. DAPI (4',6-diamidino-2-phenylindole), blue. **g, h**, Anti-phospho-histone H3 staining (magenta) in 48 hpt *Tg(vmhc:mCherry-NTR)*; *cmlc2:actinin-eGFP* control (**g**) and ablated (**h**) hearts (green). Arrowheads indicate anti-phospho-histone H3 positive cells. A, atrium; V, ventricle. Magnification, $\times 40$ objective.

¹Department of Medicine, Division of Cardiology, University of California, San Diego, La Jolla, California 92093, USA. ²Division of Biological Sciences, University of California, San Diego, La Jolla, California 92093, USA. ³Development and Aging Program, Sanford-Burnham Institute for Medical Research, La Jolla, California 92037, USA. ⁴Department of Biochemistry and Biophysics, University of California, San Francisco, San Francisco, California 94158, USA. ⁵Institute of Genomic Medicine, University of California, San Diego, La Jolla, California 92093, USA. [†]Present address: Department of Developmental Genetics, Max Planck Institute for Heart and Lung Research, Ludwigstrasse 43, 61231 Bad Nauheim, Germany.

the AVC by 96 hpt (Fig. 1d, asterisk). Subsequently, ventricular cardiac function recovered in these injured hearts to nearly that of age-matched controls by 96 hpt (fractional area change of ablated and control ventricle was 38% and 39%, respectively; $n = 5$, $P = 0.49$; Supplementary Fig. 3c), allowing for survival of these ventricle-ablated fish into adulthood. Anti-phospho-histone H3 immunostaining revealed that ventricular injury resulted in not only ventricular but also atrial cardiomyocyte proliferation (Fig. 1g, h; Supplementary Fig. 4), as observed in other cardiac injury and regeneration models^{4,6,12}. Although this cardiomyocyte cell division peaked by 48 hpt in both cardiac chambers (Supplementary Fig. 4d, e), there was a particularly significant atrial cardiomyocyte proliferative increase that remained elevated up to 84 hpt.

During the ventricular recovery, we observed the presence of low expressing atrGFP cardiomyocytes (atrGFP^{lo}) within the injured ventricle near the AVC between 24–48 hpt (Fig. 1b, c and 2b), whereas atrGFP cardiomyocytes were never observed in the ventricle of control hearts (Fig. 2a). Optical sections of the AVC region revealed that these atrGFP^{lo} cardiomyocytes co-expressed the venCherry marker in the ablated ventricles (Fig. 2b, right panel, arrowheads), but were not detected in unablated ventricles (Fig. 2a, right panel). To further confirm these findings, we examined the gene expression of *amhc* and *vmhc* in the hearts of these ablated ventricles and observed that *amhc* was expressed throughout the atrium and frequently in the ventricle at the AVC by 24–48 hpt, where we observed the double-labelled

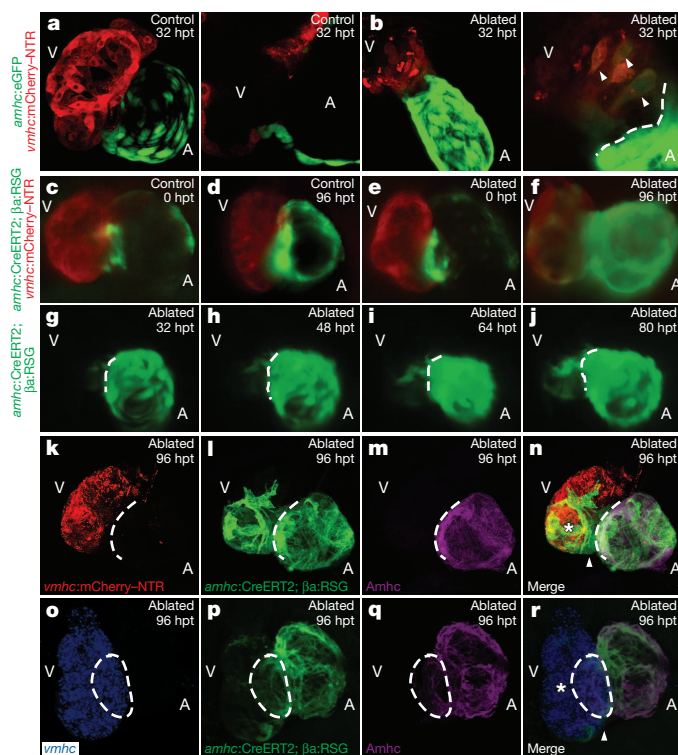


Figure 2 | In vivo cardiac reprogramming contributes to zebrafish ventricular regeneration. **a, b**, 32 hpt *Tg(vmhc:mCherry-NTR; amhc:eGFP)* control (**a**) and ablated (**b**) hearts. The AVC section of **a** and **b** are shown in the respective right images of these panels. Arrowheads indicate mCherry⁺ GFP⁺ cardiomyocytes. **c–j**, 4-HT-treated *Tg(vmhc:mCherry-NTR; amhc:CreERT2; β-actin2:RSG)* zebrafish in control (**c, d**) or ablated (**e–j**) hearts at 0 hpt (**c, e**), 32 hpt (**g, h**), 48 hpt (**i, j**), 64 hpt (**k, l**) and 80 hpt (**m, n**). **g–j**, 32–80 hpt GFP time-lapse imaging. **k–r**, 4-HT-treated *Tg(vmhc:mCherry-NTR; amhc:CreERT2; β-actin2:RSG)* ablated hearts at 96 hpt; venCherry⁺ (red) (**k**); cre-atrGFP⁺ (green) (**l, p**); anti-Amhc (S46) (magenta) (**m, q**); merge (**n, r**) and *vmhc* RNA (blue) (**o**). Asterisk indicates venCherry⁺ cre-atrGFP⁺ Amhc⁺ (**n**) or *vmhc*⁺ cre-atrGFP⁺ Amhc⁺ (**r**) ventricular cardiomyocytes. Arrowhead indicates venCherry⁺ cre-atrGFP⁺ Amhc⁺ (**n**) or *vmhc*⁺ cre-atrGFP⁺ Amhc⁺ (**r**) ventricular cardiomyocytes. A, atrium; V, ventricle; dashed lines indicate the atrioventricular boundary.

atrGFP^{lo} venCherry⁺ cardiomyocytes; whereas *vmhc* was expressed throughout the ventricle, but rarely in the atrium and only at 12–24 hpt. (Supplementary Fig. 5). Thus, these findings indicate that during injury, pre-existing atrial cardiomyocytes may migrate to the ventricle to transdifferentiate into ventricular cardiomyocytes, or alternatively, proliferating dedifferentiated ventricular cardiomyocytes may need to activate an atrial program before fully differentiating into ventricular cardiomyocytes. Given that we still observe some proliferating pre-existing venCherry cardiomyocytes that never express the atrGFP marker, we speculate that the atrial-to-ventricular cardiomyocyte transdifferentiation model may be more plausible.

To further investigate this transdifferentiation model, we performed genetic lineage tracing of atrial cardiomyocytes in the *Tg(vmhc:mCherry-NTR)* ventricle ablation model using an atrial cardiomyocyte specific tamoxifen-inducible Cre transgenic line, *Tg(amhc:CreERT2)^{sd20}*, and the indicator transgenic line, *Tg(β-actin2:loxP-DsRed-STOP-loxP-eGFP)^{s928}*, hereafter referred to as *β-actin2:RSG* (*β-actin2* is also known as *actb2*), which can effectively label most cells, including cardiomyocytes and endocardial cells, with GFP after tissue-specific Cre-mediated excision of the floxed dsRed cassette^{5,13}. Treating the *Tg(vmhc:mCherry-NTR; amhc:CreERT2; β-actin2:RSG)* fish with 4-hydroxytamoxifen (4-HT) at 3 dpf for 4–6 h, effectively GFP labelled all atrial cardiomyocytes by Cre recombination (cre-atrGFP⁺) without ectopic GFP-labelling of ventricular cardiomyocytes by 5 dpf (Fig. 2c, e; Supplementary Fig. 6a–c); whereas vehicle control treatment resulted in no Cre-mediated GFP labelling of any cells (Supplementary Fig. 6d). We subsequently MTZ-ablated the ventricles of these cre-atrGFP-labelled hearts at 5 dpf (Fig. 2e). In the ablated group, these cre-atrGFP⁺ cardiomyocytes at 96 hpt and at 12 months were present in not only the atrium but also in the ventricle where many of them also co-expressed venCherry ($n = 73/76$; Fig. 2f, Supplementary Figs 7i, j and 8b, c). However, in the control non-ablated group at 96 hpt and at 12 months, cre-atrGFP⁺ cardiomyocytes were only observed in the atrium but never in the ventricle ($n = 0/54$; Fig. 2d; Supplementary Figs 6c and 8a). Using time-lapse imaging within the same ventricle-ablated *Tg(vmhc:mCherry-NTR; amhc:CreERT2; β-actin2:RSG)* hearts, we observed the gradual and contiguous extension of these cre-atrGFP⁺ cardiomyocytes at the AVC into the ventricle where they began to restore ventricular contractile function nearest the AVC and also to exhibit venCherry expression, indicating that they were transdifferentiating from atrial to ventricular cardiomyocytes (Fig. 2g–j, Supplementary Videos 3–5). Electrophysiologic intracellular recordings revealed that these cre-atrGFP⁺ venCherry⁺ cardiomyocytes within the regenerating ventricle exhibited electrical attributes similar to endogenous cre-atrGFP⁺ venCherry⁺ ventricular cardiomyocytes and distinct from atrial cardiomyocytes (that is, cre-atrGFP⁺ venCherry⁺) (Supplementary Fig. 9). Furthermore, *in situ* analysis showed that the ventricular specific markers *irx1a* and *vmhc* were expressed in ventricular cardiomyocytes at the AVC where cre-atrGFP⁺ ventricular cardiomyocytes reside (Supplementary Fig. 10). Moreover, we also observed that the atrial chamber cre-atrGFP⁺ fluorescence intensity and size in hearts with ablated ventricles appeared to be significantly greater than that of control hearts (compare Fig. 2f to 2d, Supplementary Fig. 7k, l), an observation consistent with the increased atrial size, fluorescence intensity and cardiomyocyte proliferation observed after ventricular injury (Supplementary Figs 2a, b and 4d). Finally, in adult zebrafish ventricles ablated at 4 months, we discovered that the contribution of transdifferentiated atrial cardiomyocytes to the regenerating ventricle was diminished (Supplementary Fig. 11), indicating that this cardiac transdifferentiation process may be age-dependent.

To investigate whether these atrial-derived ventricular cardiomyocytes maintained the atrial program, we examined Amhc protein expression by S46 antibody immunostaining in the ventricle-ablated *Tg(vmhc:mCherry-NTR; amhc:CreERT2; β-actin2:RSG)* hearts, and observed that cre-atrGFP⁺ atrial cardiomyocytes continued to express Amhc in the atrium (Fig. 2m, n), but not in the ventricle. However, before their subsequent differentiation into ventricular cardiomyocytes

(cre-*atrGFP*⁺ *Amhc*⁻ *venCherry*⁺ Fig. 2n, Supplementary Fig. 7d, asterisk), we discovered that cre-*atrGFP*⁺ cardiomyocytes may first exist in an intermediate dedifferentiation stage (cre-*atrGFP*⁺ *Amhc*⁻ *venCherry*⁻, Fig. 2n, Supplementary Fig. 7d, arrowheads), in which they no longer maintain the atrial program (*Amhc*⁻) but have not yet activated the ventricular program (*venCherry*⁻). Consistent with these findings, *vmhc* fluorescent *in situ* hybridization also revealed a population of cre-*atrGFP*⁺ cardiomyocytes devoid of *vmhc* expression within the recovering ventricle (Fig. 2r, Supplementary Fig. 7h, d arrowheads). Because of this possible dedifferentiation of atrial cardiomyocytes, we also examined the expression of cardiac progenitor markers in the ventricle-ablated hearts. Although we did not detect *Isl1* in the injured hearts (data not shown), we did observe the re-expression of *gata4*, *hand2*, *nkx2.5*, *tbx5a* and *tbx20* (Supplementary Fig. 12), as well as increased expression of *Mef2* in the atrium, ventricle and outflow tract of the recovering ventricle-ablated hearts (Supplementary Fig. 13). Furthermore, *Mef2* immunofluorescence revealed not only that many of the intermediate dedifferentiated cre-*atrGFP*⁺ cardiomyocytes within the recovering ventricle (that is, cre-*atrGFP*⁺ *venCherry*⁻) expressed *Mef2* (Supplementary Fig. 13p, arrowheads), but also that the new *Mef2*⁺ cells at the outflow tract did not express myosin heavy chain (Supplementary Fig. 13e–h), indicating that these cells may be cardiac progenitor cells, which have not yet differentiated into mature cardiomyocytes. Overall, these data indicate that atrial cardiomyocytes may acquire cardiac progenitor cell attributes to become ventricular cardiomyocytes and moreover that the zebrafish second heart field residing near the outflow tract^{14,15} may also contribute ventricular cardiomyocytes to recover the distal portion of the injured ventricle.

To further elucidate the cellular events that take place during ventricular injury and recovery including the atrial-to-ventricular cardiac lineage switch, we analysed the cardiomyocyte structural and morphologic changes after ventricular ablation. To study this, we crossed the *Tg(vmhc:mCherry-NTR)* fish to the reporter lines, *Tg(cmlc2:actinin-eGFP)*^{sd10} (*cmlc2* is also known as *myl7*) or *Tg(cmlc2:eGFP-ras)*^{s883}, which labels sarcomeric structures¹⁶ or outlines cardiomyocytes¹⁷, respectively (Fig. 3a–j, Supplementary Fig. 14), as well as performed N-cadherin immunostaining to examine cardiomyocyte cell–cell junctions (Fig. 3k–o). During ventricular injury, damaged ventricular cardiomyocytes lost their rod-like shape¹⁸, particularly at the outer curvature (Fig. 3g, h, asterisks), and as reported^{4,5}, exhibited disorganized or

complete loss of sarcomeres and cell junctions between 12–24 hpt (Fig. 3b, c, l, m, asterisks), when ventricular function has reached its lowest point. In contrast, during ventricular recovery (36–48 hpt), we observed the reorganization of not only ventricular but also atrial cardiomyocyte sarcomeres, morphologies and adhesion junctions (Fig. 3d, i, n, Supplementary Fig. 14e). In particular, atrial cardiomyocytes at the AVC became more circular (Supplementary Fig. 14b, e) and lost N-cadherin localization at their cell junctions when they began to extend into the ventricle and differentiate into ventricular cardiomyocytes (Fig. 3n). Moreover, we also observed that these migrating atrial cardiomyocytes at the AVC initially displayed disorganized sarcomeric structures (Supplementary Fig. 14d, asterisk), but after populating the ventricle, exhibited enriched actinin-eGFP at the cell periphery/cortex (Fig. 3d, Supplementary Fig. 14d arrow) and frequently short bundles of actinin-eGFP labelled z-line structures (Fig. 3d, Supplementary Fig. 14d, arrowhead), closely resembling *de novo* sarcomere assembly¹⁶. By 96 hpt when the ventricle has functionally recovered, the ventricular cardiomyocytes derived from reprogrammed atrial cardiomyocytes exhibited not only organized sarcomeres that align with other ventricular cardiomyocytes, but also localization of N-cadherin at the cell junctions (Fig. 3e, o). Overall, these results reveal that atrial cardiomyocytes undergo activated cellular reprogramming following ventricular myocardial injury in order to initiate cellular events that permit their proliferation, migration and transdifferentiation to facilitate ventricular regeneration.

Because previous studies have shown that endocardial activation may be essential to regulate cardiac regeneration¹⁹, we examined *Raldh2* (also known as *Aldh1a2*) expression in ventricle ablated *Tg(vmhc:mCherry-NTR)* fish. Although *Raldh2* is expressed weakly in control treated hearts (Supplementary Fig. 15a, c, g, h), its expression is induced throughout the endocardium of the ventricle-ablated hearts by 24–48 hpt (Supplementary Fig. 15b, d, k, l). Using the *Tg(tp1:eGFP)*^{um14} Notch reporter line²⁰, we also observed that Notch signalling (that is, *tp1:eGFP* expression) was specifically activated in atrial endocardial cells of *Tg(vmhc:mCherry-NTR)* MTZ-ablated hearts, as detected by the overlapping expression between *tp1:eGFP* and *kdr1:mCherry* (*Tg(kdr1:ras-mCherry)*^{s896}), which labels endothelial and endocardial cell membranes in red²¹ (compare Fig. 4a to b, 4e to f). Whole mount *in situ* hybridization of Notch signalling components revealed that *notch1b* and *deltaD*, which are normally present in the AVC and outflow tract

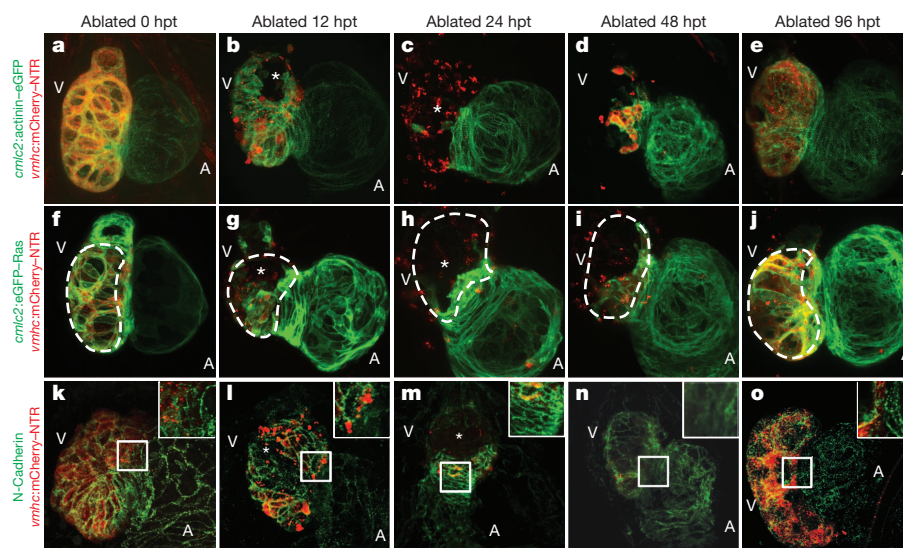


Figure 3 | Dynamic cellular remodelling occurs during zebrafish cardiac regeneration. a–o, MTZ-treated zebrafish: *Tg(vmhc:mCherry-NTR; cmlc2:actinin-eGFP)* (a–e), *Tg(vmhc:mCherry-NTR; cmlc2:eGFP-ras)* (f–j), N-cadherin immunostained *Tg(vmhc:mCherry-NTR)* (k–o). 0 hpt (a, f, k); 12 hpt (b, g, l); 24 hpt (c, h, m); 48 hpt (d, i, n) and 96 hpt

(e, j, o). Asterisks indicate ventricular cardiomyocyte injury and death due to ablation. Dashed lines indicate the outer curvature ventricular cardiomyocytes. Inset shows the enlargement of the boxed area in k–o at the AVC. A, atrium; V, ventricle.

of uninjured hearts (Fig. 4i, m), exhibited increased AVC expression as well as activated atrial expression in ventricular-ablated hearts (Fig. 4j, n); however, *deltaC* was absent (Supplementary Fig. 16). Because *tp1:eGFP* expression was strong in the ventricle (Fig. 4a, b), but *notch1b* and *deltaD* expression was not, we performed *gfp* RNA *in situ* analysis to confirm this *tp1:eGFP* ventricular fluorescence and discovered that RNA expression of *gfp* was weak to negligible in both uninjured and injured ventricles (Supplementary Fig. 17a, b), indicating that the relatively robust *tp1:eGFP* ventricular fluorescence may be due to eGFP protein perdurance. Finally, we investigated whether these Notch-activated atrial endocardial cells genetically marked by *Tg(kdrl:Cre)^{s898}*; *Tg(β -actin2:RSG)¹³* could reprogram into cardiomyocytes to contribute to the regeneration of the ventricle-injured heart, but found no evidence for such an event (data not shown). Conversely, we did not observe any of the genetically marked atrial cardiomyocytes (*cre-atrGFP⁺*) becoming endocardial cells (Supplementary Fig. 15i–l).

Thus, to further investigate the importance of this injury-induced atrial Notch activation, we treated ventricle-ablated hearts with the γ -secretase inhibitor, DAPT. As a result, DAPT treatment decreased the ability of these hearts to restore their ventricular morphology and function after injury (control 81%, $n = 96/119$ vs. DAPT-treated 39%, $n = 52/132$; Fig. 4h), which may be due to overall decreased atrial and ventricular cardiomyocyte proliferation (Supplementary Fig. 18). To determine how DAPT impairs this recovery process, we examined the expression of *tp1:eGFP* as well as the migration of genetically labelled atrial cardiomyocytes in DAPT-treated ventricle-injured hearts. We observed not only decreased *tp1:eGFP* expression in the atrium (Fig. 4d),

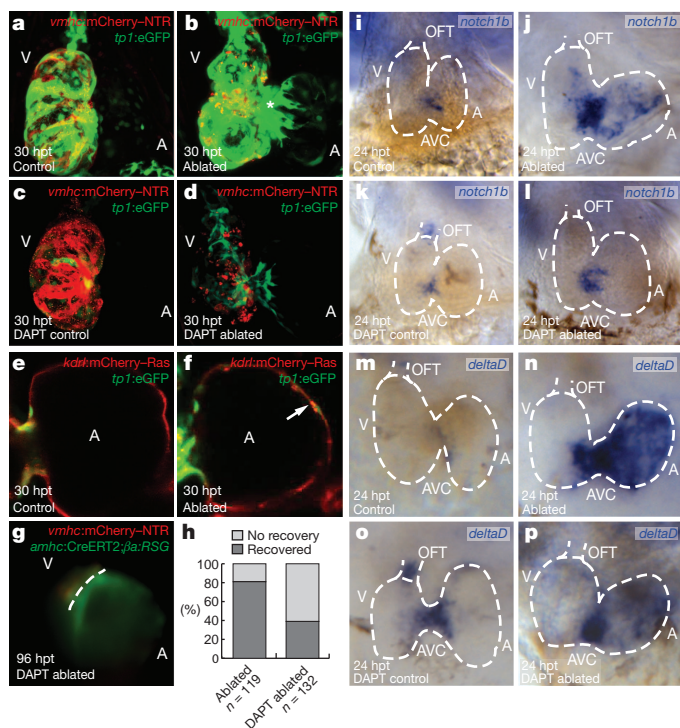


Figure 4 | Notch signalling is required for zebrafish cardiac regeneration. a–d, 30 hpt *Tg(vmh:mCherry-NTR; tp1:eGFP)* control (a); ablated (b); DAPT-treated control (c); DAPT-treated ablated (d) hearts. e, f, Atrium of 30 hpt *Tg(vmh:mCherry-NTR; tp1:eGFP; kdrl:mCherry)* control (e) and ablated (f) hearts. Arrow indicates endocardial *tp1:eGFP* expression. g, DAPT-treated 96 hpt *Tg(vmh:mCherry-NTR; amhc:CreERT2; β -actin2:RSG)* ablated ventricles. Dashed line indicates atrioventricular boundary. h, Recovery of 96 hpt control and DAPT-treated *Tg(vmh:mCherry-NTR; amhc:CreERT2; β -actin2:RSG)* ablated fish. i–p, *notch1b* (i–l) and *deltaD* (m–p) *in situ* hybridization on control (i, k, m, o) or ablated (j, l, n, p) *Tg(vmh:mCherry-NTR)* hearts (dashed lines) at 24 hpt. DAPT-treated (k, l, o, p). A, atrium; AVC, atrioventricular canal; OFT, outflow tract; V, ventricle.

but also a reduction in the migration of *cre-atrGFP⁺* atrial cardiomyocytes into the injured ventricle (Fig. 4g). Consistent with these findings, DAPT also inhibited *notch1b*, *deltaD* and *tp1:egfp* expression in the atrium of ventricle-injured hearts (Fig. 4l, p, Supplementary Fig. 17d), but increased *notch1b* and *deltaD* in the outflow tract of uninjured hearts (Fig. 4k, o). Thus, these data indicate that atrial endocardial Notch activation may be crucial to non-cell-autonomously regulate ventricle regeneration through the modulation of atrial-to-ventricular transdifferentiation.

Overall, these results reveal that *in vivo* reprogramming of differentiated atrial cardiomyocytes can be induced by cardiac ventricular injury through Notch-mediated signalling and proceeds in distinct intermediate stages (Supplementary Fig. 19) in order to provide a novel endogenous cellular source for cardiac ventricular regeneration in zebrafish. Similar to recent cardiac-injury studies in zebrafish and mouse neonatal hearts, this process may be mediated through the activation of *Raldh2* and Notch pathways^{19,22}, which may lead to sarcomeric reorganization^{4,5}, cardiomyocyte migration^{4,5}, and the re-expression of key early cardiac transcriptional regulators such as *Gata4*, *Hand2*, *Mef2*, *Nkx2.5*, *Tbx5*, and *Tbx20*^{5,6,23}. Although *Raldh2* was expressed throughout the endocardium of the ventricle-injured heart as previously described^{6,19}, Notch signalling was activated primarily in the atrial endocardium. As a result, we speculate that Notch-activated atrial endocardium may influence the atrial myocardium, just as Notch signalling in the ventricular endocardium influences ventricular trabeculation²⁴. Given that previous studies have shown that specific congenital heart diseases can arise from aberrant Notch signalling²⁵, our studies also raise the possibility that abnormal reprogramming of cardiac lineages may be partially responsible for these heart defects.

Although it remains to be elucidated whether mammalian atrial cardiomyocytes may also have a comparable transdifferentiation capacity, recent studies have indicated that mammalian cardiomyocyte progenitor cells (CPMCs) appear to be enriched in the atrium^{26–28} suggesting that the zebrafish transdifferentiating atrial cardiomyocytes may be analogous to the atrial-resident adult CPMCs. Alternatively, mammalian atrial cardiomyocytes could reprogram into ventricular cardiomyocytes through the reactivation of early cardiac transcriptional factors, a process recently reported to reprogram cardiac fibroblasts into ventricular cardiomyocytes in mouse hearts^{29,30}. Thus, future studies in mammalian ventricular injury models⁶ using similar atrial genetic lineage tracing strategies as presented here, are warranted to further investigate the potential of this cardiac reprogramming process as an endogenous cellular regenerative therapy in human heart failure patients. Such a cardiac regenerative strategy could overcome current obstacles facing the translation of stem-cell therapies for heart failure patients, including the differentiation of autologous cardiac progenitor cells into ventricular cardiomyocytes as well as the delivery and integration of these differentiated ventricular cardiomyocytes into the patient's ventricular myocardium.

METHODS SUMMARY

Chamber-specific ablation and reporter lines were generated using the standard I-SceI meganuclease transgenesis technique (details in Methods). To perform ventricular cardiomyocyte ablation, *Tg(vmh:mCherry-NTR)* zebrafish were treated with 5 mM MTZ as previously described⁹. For lineage tracing experiments, *Tg(vmh:mCherry-NTR; amhc:CreERT2; β -actin2:RSG)* zebrafish were treated with 10 μ M 4-hydroxytamoxifen as previously described⁵. For Notch inhibition studies, zebrafish were treated with 100 μ M DAPT. Live imaging, heart contraction, immunofluorescence and whole mount *in situ* hybridization were performed as described in the Methods.

Full Methods and any associated references are available in the online version of the paper.

Received 23 July 2012; accepted 23 May 2013.

Published online 19 June 2013.

- Bergmann, O. *et al.* Evidence for cardiomyocyte renewal in humans. *Science* **324**, 98–102 (2009).
- Senyo, S. E. *et al.* Mammalian heart renewal by pre-existing cardiomyocytes. *Nature* **493**, 433–436 (2013).

3. Laflamme, M. A. & Murry, C. E. Heart regeneration. *Nature* **473**, 326–335 (2011).
4. Jopling, C. *et al.* Zebrafish heart regeneration occurs by cardiomyocyte dedifferentiation and proliferation. *Nature* **464**, 606–609 (2010).
5. Kikuchi, K. *et al.* Primary contribution to zebrafish heart regeneration by *gata4*⁺ cardiomyocytes. *Nature* **464**, 601–605 (2010).
6. Porrello, E. R. *et al.* Transient regenerative potential of the neonatal mouse heart. *Science* **331**, 1078–1080 (2011).
7. McDonnell, T. J. & Oberpriller, J. O. The response of the atrium to direct mechanical wounding in the adult heart of the newt, *Notophthalmus viridescens*. An electron-microscopic and autoradiographic study. *Cell Tissue Res.* **235**, 583–592 (1984).
8. Oberpriller, J. O., Oberpriller, J. C. & Aafedt, B. C. Changes in binucleation and cellular dimensions of rat left atrial myocytes after induced left ventricular infarction. *Am. J. Anat.* **179**, 285–290 (1987).
9. Curado, S. *et al.* Conditional targeted cell ablation in zebrafish: a new tool for regeneration studies. *Dev. Dyn.* **236**, 1025–1035 (2007).
10. Zhang, R. & Xu, X. Transient and transgenic analysis of the zebrafish ventricular myosin heavy chain (*vmhc*) promoter: an inhibitory mechanism of ventricle-specific gene expression. *Dev. Dyn.* **238**, 1564–1573 (2009).
11. de Pater, E. *et al.* Distinct phases of cardiomyocyte differentiation regulate growth of the zebrafish heart. *Development* **136**, 1633–1641 (2009).
12. Poss, K. D., Wilson, L. G. & Keating, M. T. Heart regeneration in zebrafish. *Science* **298**, 2188–2190 (2002).
13. Bertrand, J. Y. *et al.* Haematopoietic stem cells derive directly from aortic endothelium during development. *Nature* **464**, 108–111 (2010).
14. Zhou, Y. *et al.* Latent TGF- β binding protein 3 identifies a second heart field in zebrafish. *Nature* **474**, 645–648 (2011).
15. Hinitz, Y. *et al.* Zebrafish Mef2ca and Mef2cb are essential for both first and second heart field cardiomyocyte differentiation. *Dev. Biol.* **369**, 199–210 (2012).
16. Lin, Y. F., Swinburne, I. & Yelon, D. Multiple influences of blood flow on cardiomyocyte hypertrophy in the embryonic zebrafish heart. *Dev. Biol.* **362**, 242–253 (2012).
17. D'Amico, L., Scott, I. C., Jungblut, B. & Stainier, D. Y. A mutation in zebrafish *hmgcr1b* reveals a role for isoprenoids in vertebrate heart-tube formation. *Curr. Biol.* **17**, 252–259 (2007).
18. Chi, N. C. *et al.* Genetic and physiologic dissection of the vertebrate cardiac conduction system. *PLoS Biol.* **6**, e109 (2008).
19. Kikuchi, K. *et al.* Retinoic acid production by endocardium and epicardium is an injury response essential for zebrafish heart regeneration. *Dev. Cell* **20**, 397–404 (2011).
20. Parsons, M. J. *et al.* Notch-responsive cells initiate the secondary transition in larval zebrafish pancreas. *Mech. Dev.* **126**, 898–912 (2009).
21. Chi, N. C. *et al.* Foxn4 directly regulates *tbx2b* expression and atrioventricular canal formation. *Genes Dev.* **22**, 734–739 (2008).
22. Raya, A. *et al.* Activation of Notch signaling pathway precedes heart regeneration in zebrafish. *Proc. Natl Acad. Sci. USA* **100** (suppl 1), 11889–11895 (2003).
23. Lepilina, A. *et al.* A dynamic epicardial injury response supports progenitor cell activity during zebrafish heart regeneration. *Cell* **127**, 607–619 (2006).
24. Grego-Bessa, J. *et al.* Notch signaling is essential for ventricular chamber development. *Dev. Cell* **12**, 415–429 (2007).
25. Luxán, G. *et al.* Mutations in the NOTCH pathway regulator *MIB1* cause left ventricular noncompaction cardiomyopathy. *Nature Med.* **19**, 193–201 (2013).
26. Bu, L. *et al.* Human ISL1 heart progenitors generate diverse multipotent cardiovascular cell lineages. *Nature* **460**, 113–117 (2009).
27. Laugwitz, K. L. *et al.* Postnatal isl1⁺ cardioblasts enter fully differentiated cardiomyocyte lineages. *Nature* **433**, 647–653 (2005).
28. Genead, R. *et al.* Early first trimester human embryonic cardiac Islet-1 progenitor cells and cardiomyocytes: Immunohistochemical and electrophysiological characterization. *Stem Cell Res.* **4**, 69–76 (2010).
29. Song, K. *et al.* Heart repair by reprogramming non-myocytes with cardiac transcription factors. *Nature* **485**, 599–604 (2012).
30. Qian, L. *et al.* *In vivo* reprogramming of murine cardiac fibroblasts into induced cardiomyocytes. *Nature* **485**, 593–598 (2012).

Supplementary Information is available in the online version of the paper.

Acknowledgements We thank N. Tedeschi, L. Pandolfo and A. Ayala for fish care; O. Huang, J. Kim, T. Kuo and J. Sun for experimental assistance; S. Tu and other laboratory members for comments on the manuscript; Q. Liu for anti-N-cadherin antibody; M. Lardelli, J. Lenis and W. Clements for plasmids; and N. Lawson for the Notch reporter line. This work was supported in part by grants from the American Heart Association to D.Y. (0940041N), R.Z. (11POST7090024) and H.Y. (12POST12050080); the Packard Foundation and the National Institutes of Health (NIH) (HL54737) to D.Y.R.S.; NIH/NHLBI (NIH Heart, Lung, and Blood Institute) to J.C.; and the NIH (OD007464, HL104239) to N.C.C.

Author Contributions N.C.C. initiated the project when he was in the laboratory of D.Y.R.S. by generating and validating some of the cardiac chamber specific transgenic lines. Additional experimental design was done with the help of R.Z. and D.Y. R.Z., P.H., Ku.Ou., D.L., G.K. and N.C.C. conducted experiments. R.Z., H.Y. and N.C.C. generated and characterized transgenic lines for lineage tracing. Ka.Oc. and J.C. helped with cardiac function analysis. Y.-F.L. and D.Y. provided key reagents. R.Z., P.H., D.L., D.Y. and N.C.C. prepared the manuscript. All authors commented on the manuscript.

Author Information Reprints and permissions information is available at www.nature.com/reprints. The authors declare no competing financial interests. Readers are welcome to comment on the online version of the paper. Correspondence and requests for materials should be addressed to N.C.C. (nchi@ucsd.edu).

METHODS

Zebrafish husbandry and generation of transgenic fish lines. Zebrafish were raised under standard laboratory conditions at 28 °C. We used the following transgenic lines: *Tg(β-actin2:loxP-DsRed-STOP-loxP-eGFP)*⁹²⁸, *Tg(β-actin2:RSG)*⁵, *Tg(cmlc2:actinin-eGFP)*^{sd10} (ref. 16), *Tg(cmlc2:eGFP-ras)*⁸⁸³ (ref. 17), *Tg(tp1:eGFP)*^{um14} (ref. 20), *Tg(kdr:ras-mCherry)*⁸⁹⁶ (ref. 21) and *Tg(kdr:Cre)*⁸⁹⁸ (ref. 13). The *Tg(tp1:eGFP)*^{um14} Notch reporter line used for these studies was previously confirmed for reporting Notch activity in the heart as well as other tissues using the mindbomb mutant^{25,31,32}. The construct to create *Tg(vmhc:mCherry-NTR)*⁹⁵⁷ was generated by cloning a 2 kilobase (kb) *vmhc* promoter¹⁰ into the pBSK1 vector³³, and the mCherry-nitroreductase fusion gene was then cloned downstream of the *vmhc* promoter. The construct used to create *Tg(amhc:eGFP)*⁹⁵⁸ was generated by cloning a 982 base pair (bp) *amhc* promoter (forward primer: 5'-GCTAAAGTGGCAGTGTGCCG-3' and reverse primer: 5'-CGTGAATATGGTTTTCAGGAG-3') into the pBSK1 vector, and GFP was cloned downstream of the *amhc* promoter. The construct to create *Tg(amhc:CreERT2)*^{sd20} was generated by cloning a 4.5 kb *amhc* promoter (forward primer: 5'-CCTGGAACCTCAACAATGCTC-3' and reverse primer: 5'-GATCTGGATCTCTCCTCAGTTG-3') into the pBSK1 vector, and CreERT2³⁴ was cloned downstream of the *amhc* promoter. We injected 200 pg of each linearized DNA into one-cell-stage embryos and selected individual transgenic carrier adults by screening for fluorescent progeny.

MTZ treatment. *Tg(vmhc:mCherry-NTR)* larval and adult zebrafish were treated with 5 or 10 mM MTZ in egg or zebrafish system water for four hours and two days, respectively, at 28 °C in the dark as previously described³⁵. As controls, age-matched *Tg(vmhc:mCherry-NTR)* siblings were incubated in 0.2% DMSO (dimethylsulphoxide) in egg or zebrafish system water. Treated zebrafish were washed with several changes of fresh egg or zebrafish system water at the end of ablation and then allowed to continue to grow in fresh egg or zebrafish system water.

TUNEL. Using the *in situ* cell death detection kit, fluorescein from Roche (11684795910), fish hearts were examined for cell death by TUNEL staining. Specifically, zebrafish at the indicated stages were fixed with 4% paraformaldehyde (PFA), permeabilized with PBS with 0.5% TritonX-100 and then incubated in TUNEL staining solution at 37 °C for 2 h.

Immunofluorescence. Immunofluorescence staining was performed as previously described³⁶. The primary antibodies used in this study include: anti-GFP (chicken; Aves Labs); anti-Isl (ref. 11) (mouse; Developmental Studies Hybridoma Bank); anti-Mef2/C-21 (ref. 15) (rabbit; Santa Cruz Biotechnology); MF20/anti-MHC (ref. 37) (mouse; Developmental Studies Hybridoma Bank); anti-N-cadherin (ref. 38) (rabbit; courtesy of Q. Liu); anti-phospho-histone H3 (rabbit; Upstate), anti-Raldh2 (ref. 19) (rabbit; Abmart); and anti-Amhc (S46) (ref. 37) (mouse; Developmental Studies Hybridoma Bank). For the *vmhc* fluorescent *in situ* hybridization studies, GFP antibody was used to detect the GFP genetically labelled atrial cardiomyocytes. Raldh2 antibody was used to examine endocardial and epicardial activation during cardiac injury¹⁹. The secondary antibodies used in this study include: Alexa Fluor 488 goat anti-mouse IgG, Alexa Fluor 488 goat anti-rabbit IgG, Alexa Fluor 594 goat anti-mouse IgG, Alexa Fluor 633 goat anti-mouse IgG, Alexa Fluor 647 goat anti-rabbit IgG from Invitrogen and anti-chicken IgY-FITC from Sigma. Fluorescent images were obtained using a Leica SP5 or Nikon C2 confocal microscope.

***in situ* hybridization.** Whole mount *in situ* hybridization was performed as previously described¹⁸, using the following probes: *amhc*, *deltaC* (courtesy of J. Lenis), *deltaD* (courtesy of W. Clements), *gata4*, *gfp*, *hand2*, *irx1a*, *nkx2.5*, *notch1b* (courtesy of M. Lardelli), *tbx5a*, *tbx20* and *vmhc*. *vmhc* fluorescent *in situ* hybridization³⁷ was performed as previously described³⁹ using single digoxigenin-labelled riboprobe and detected by TSA Plus Cy5 Solution (Perkin Elmer).

Cardiac contractile analysis. Live zebrafish were embedded in 1% low melting agarose in a glass bottom culture dish (MatTek), and the heart contraction was recorded by a high speed EMCCD camera (Hamamatsu). The heart function was analysed as previously described⁴⁰. The fractional area change was calculated as FC = (End diastolic area – End systolic area)/End diastolic area × 100%.

Intracellular action potential recording. Adult zebrafish hearts were mounted in a chamber containing Tyrode's solution of the following composition (mM): NaCl 150, KCl 5.4, MgSO₄ 1.5, NaH₂PO₄ 0.4, CaCl₂ 2, Glucose 10, HEPES 10. The pH of the solution was adjusted to pH 7.4 with NaOH. Glass pipettes with tip resistance 30–40 MΩ were filled with 3M KCl solutions. The hearts were allowed to equilibrate for 10 min before spontaneous intracellular action potentials were recorded using an Axopatch 200B amplifier and pClamp10.3 software (Molecular Devices, LLC). Electrophysiologic intracellular recordings were performed on transdifferentiated ventricular cardiomyocytes (cre-*atrGFP*⁺ *venCherry*⁺), endogenous ventricular cardiomyocytes (cre-*atrGFP*⁺ *venCherry*⁺) and atrial cardiomyocytes

(cre-*atrGFP*⁺ *venCherry*⁺). All experiments were performed at room temperature (20–22 °C). *n* = 5 hearts.

Tamoxifen treatment and lineage tracing. *Tg(vmhc:mCherry-NTR; amhc:CreERT2; β-actin2:RSG)* zebrafish were treated with 10 μM 4-hydroxytamoxifen (4-HT) solution (Sigma) or 0.1% ethanol alone (control) at 72 hpf for 6 h at 28 °C and then washed with fresh egg water several times. The ventricles of hearts with GFP genetically labelled atrial cardiomyocytes were then ablated at 96–120 hpf (*n* = 76) or at 4 months (*n* = 23). Live zebrafish were embedded in 0.5% low melting agarose in a glass bottom culture dish as previously described⁴¹ for time-lapse imaging using a Leica M205FA stereomicroscope with a DFC310FX camera. The hearts were then collected at indicated time points post treatment, cryosectioned and examined under a Nikon C2 confocal microscope.

Cryosection and histology staining. Adult zebrafish hearts were fixed in 4% PFA for 2 h at room temperature and equilibrated through 15% and then 30% sucrose in PBS for several hours until they sank down to the bottom. Hearts were embedded in O.C.T. compound (Tissue-Tek, 4583) and frozen in liquid nitrogen. 10-μm cryosections were prepared on a Leica CM3050 S cryostat. Masson's trichrome staining was performed using the Sigma HT15 kit.

DAPT treatment. Zebrafish were incubated in egg water with 100 μM DAPT (Sigma) or 0.1% DMSO alone (control) right after ablation until the zebrafish were fixed or examined at indicated stages. Treated zebrafish were washed several times in egg water after DAPT or DMSO treatment.

Quantification and statistical analysis. To measure cardiac chamber size, *Tg(vmhc:mCherry-NTR)* hearts were visualized by bright field microscopy at the indicated conditions, and the cardiac chamber size was calculated by measuring the surface area of outlined chambers using Leica LAS AF software (*n* = 10). To determine average fluorescence intensity for each chamber, *Tg(vmhc:mCherry-NTR; cmlc2:actinin-eGFP)* hearts were visualized by confocal microscopy at the indicated stages, and average fluorescence intensity was calculated by measuring the fluorescence intensity of outlined maximal projections of cardiac chambers using Nikon NIS Elements software (*n* = 5). Cardiomyocyte surface area and circularity were measured by outlining single cardiomyocytes on confocal maximal projection images of *Tg(vmhc:mCherry-NTR; cmlc2:eGFP-ras)* hearts using the Nikon NIS Elements software (*n* = 15, 5 cells per heart, 3 hearts) as previously described¹⁸. Circularity was calculated as circularity = 4 × π area/perimeters². To determine the percentage of the *Tg(vmhc:mCherry-NTR; amhc:CreERT2; β-actin2:RSG)* ventricles that was GFP positive, the measured GFP positive surface area of the cardiac ventricles as detected by confocal microscopy was divided by the measured total surface area of the cardiac ventricles as detected by brightfield microscopy. To determine the surface area and average fluorescence intensity of the *Tg(vmhc:mCherry-NTR; amhc:CreERT2; β-actin2:RSG)* atria, the atrial chamber surface area and fluorescence were measured in the bright field and GFP channel using the Nikon NIS Elements software (*n* = 5). *P* values were obtained by unpaired two-tailed Student's *t*-test.

- Ninov, N., Borius, M. & Stainier, D. Y. Different levels of Notch signaling regulate quiescence, renewal and differentiation in pancreatic endocrine progenitors. *Development* **139**, 1557–1567 (2012).
- Wang, Y., Rovira, M., Yusuff, S. & Parsons, M. J. Genetic inducible fate mapping in larval zebrafish reveals origins of adult insulin-producing β-cells. *Development* **138**, 609–617 (2011).
- Thermes, V. et al. I-SceI meganuclease mediates highly efficient transgenesis in fish. *Mech. Dev.* **118**, 91–98 (2002).
- Feil, R. et al. Ligand-activated site-specific recombination in mice. *Proc. Natl Acad. Sci. USA* **93**, 10887–10890 (1996).
- Curado, S., Stainier, D. Y. & Anderson, R. M. Nitroreductase-mediated cell/tissue ablation in zebrafish: a spatially and temporally controlled ablation method with applications in developmental and regeneration studies. *Nature Protocols* **3**, 948–954 (2008).
- Huang, W., Zhang, R. & Xu, X. Myofibrillogenesis in the developing zebrafish heart: A functional study of *tnnt2*. *Dev. Biol.* **331**, 237–249 (2009).
- Stainier, D. Y. & Fishman, M. C. Patterning the zebrafish heart tube: acquisition of anteroposterior polarity. *Dev. Biol.* **153**, 91–101 (1992).
- Kerstetter, A. E., Azodi, E., Marrs, J. A. & Liu, Q. Cadherin-2 function in the cranial ganglia and lateral line system of developing zebrafish. *Dev. Dyn.* **230**, 137–143 (2004).
- Brend, T. & Holley, S. A. Zebrafish whole mount high-resolution double fluorescent *in situ* hybridization. *J. Vis. Exp.* <http://dx.doi.org/10.3791/1229> (2009).
- Fink, M. et al. A new method for detection and quantification of heartbeat parameters in Drosophila, zebrafish, and embryonic mouse hearts. *Biotechniques* **46**, 101–113 (2009).
- Dong, Z., Wagle, M. & Guo, S. Time-lapse live imaging of clonally related neural progenitor cells in the developing zebrafish forebrain. *J. Vis. Exp.* <http://dx.doi.org/10.3791/2594> (2011).

Severe malaria is associated with parasite binding to endothelial protein C receptor

Louise Turner^{1*}, Thomas Lavstsen^{1*}, Sanne S. Berger¹, Christian W. Wang¹, Jens E. V. Petersen¹, Marion Avril², Andrew J. Brazier², Jim Freeth³, Jakob S. Jespersen¹, Morten A. Nielsen¹, Pamela Magistrado⁴, John Lusingu⁴, Joseph D. Smith^{2,5}, Matthew K. Higgins⁶ & Thor G. Theander¹

Sequestration of *Plasmodium falciparum*-infected erythrocytes in host blood vessels is a key triggering event in the pathogenesis of severe childhood malaria, which is responsible for about one million deaths every year¹. Sequestration is mediated by specific interactions between members of the *P. falciparum* erythrocyte membrane protein 1 (PfEMP1) family and receptors on the endothelial lining². Severe childhood malaria is associated with expression of specific PfEMP1 subtypes containing domain cassettes (DCs) 8 and 13 (ref. 3), but the endothelial receptor for parasites expressing these proteins was unknown^{4,5}. Here we identify endothelial protein C receptor (EPCR), which mediates the cytoprotective effects of activated protein C⁶, as the endothelial receptor for DC8 and DC13 PfEMP1. We show that EPCR binding is mediated through the amino-terminal cysteine-rich interdomain region (CIDR α 1) of DC8 and group A PfEMP1 subfamilies, and that CIDR α 1 interferes with protein C binding to EPCR. This PfEMP1 adhesive property links *P. falciparum* cytoadhesion to a host receptor involved in anticoagulation and endothelial cytoprotective pathways, and has implications for understanding malaria pathology and the development of new malaria interventions.

Each *P. falciparum* parasite genome harbours about 60 *var* genes encoding different PfEMP1 types, enabling the parasite to attach infected erythrocytes to different receptors on the vascular lining². This attachment drives malaria pathologies, but also prevents the passage of mature-stage infected erythrocytes through the spleen, where they are destroyed. On the basis of the *var* 5' upstream regions (UPS), PfEMP1 can be divided into groups A–E. In addition, the Duffy-binding-like (DBL) and CIDR adhesion domains are subdivided into 147 subclasses (for example, CIDR α 1.1)⁷. Despite a high rate of *var* gene recombination, many tandem domain arrangements—DCs—have been maintained through evolution, and are therefore thought to be of functional importance. The best example is DC2, also known as VAR2CSA, which mediates binding in the placenta⁸ and is of key importance to the pathogenesis of malaria in pregnancy. Severe malaria in children is associated with expression of a subset of PfEMP1 molecules characterized by DC8 (a unique group B/A chimaeric gene) and DC13 (group A)³, but the endothelial receptor(s) for these proteins have remained undefined^{4,5}.

To identify the DC8–PfEMP1 receptor, we produced a full-length DC8-containing PfEMP1 protein encoded by *var* gene *IT4var20* from the FCR3/IT4 parasite. This 288 kilodalton (kDa) His-tagged recombinant protein (rIT4VAR20) was screened against an array of 2,505 full-length human plasma membrane proteins expressed on HEK293 cells (Supplementary Table 1) using the Retrogenix Cell Microarray. One specific hit for rIT4VAR20 identified EPCR as a potential binding partner⁹. EPCR is encoded by the *PROCR* gene, and is expressed on endothelial cells in most tissues¹⁰. Protein C binds EPCR, promoting its

conversion to activated protein C (APC)¹¹. On endothelial cells, APC cleaves protease activated receptor 1 (PAR1) resulting in broad endothelial cytoprotective¹² and anti-inflammatory effects¹³. In the absence of APC–EPCR engagement, PAR1 activation can result in barrier-disruptive effects and activation of pro-inflammatory pathways¹³. In plasma, soluble APC exerts anticoagulative effects by the proteolytic inactivation of blood coagulation factors Va and VIIIa¹³.

To identify the EPCR-binding region in DC8–PfEMP1 variants, we expressed individual recombinant protein domains (Supplementary Table 2) from IT4VAR20 and two other DC8 variants (IT4VAR19 and 3D7-PFD0020c), and evaluated binding to recombinant EPCR (rEPCR) by enzyme-linked immunosorbent assay (ELISA) (Fig. 1a). For all three proteins, EPCR binding mapped to the CIDR α 1.1 domain within DC8 and not to other extracellular domains. Using surface plasmon resonance (SPR) (Fig. 1c and Supplementary Fig. 2), the binding kinetics of the IT4VAR20CIDR α 1.1::EPCR interaction (dissociation constant (K_d) \sim 29 nM) was similar to that of the full-length protein (K_d \sim 10 nM). This affinity is comparable to the binding of APC to EPCR, for which a K_d of 32 nM has been reported¹⁴. These data confirmed that the DC8 CIDR α 1.1 domain binds EPCR with a high and physiologically relevant affinity.

Previous work has shown that the N-terminal CIDR domain of PfEMP1 has diverged in sequence and functional properties. Whereas group B and C PfEMP1 variants bind CD36, group A and B/A PfEMP1 variants do not¹⁵. To investigate EPCR binding, a panel of 28 different CIDR variants representing both CD36-binding (CIDR α 2–6) and non-CD36-binding subtypes (CIDR α 1, δ subtypes) were tested. Also included were full-length VAR2CSA and VAR3 (DC3) (Fig. 1b). All of the CIDR α 1.1 and CIDR α 1.4 proteins, representing DC8 and DC13 from different parasite genomes, bound EPCR (Fig. 1 and Supplementary Fig. 2). In addition, the group A CIDR α 1.5 (DC15) and CIDR α 1.7 proteins also bound EPCR. By contrast, other group A CIDR domains representing DC1 (CIDR α 1.2/1.3), DC4 (CIDR α 1.6), and PfEMP1 variants that facilitate rosetting between infected and uninfected erythrocytes (CIDR δ)¹⁶ did not bind EPCR; neither did group B CIDR α domains, VAR2CSA or VAR3 (Fig. 1b). As expected, the two group B CIDR α domains bound with high affinity to CD36 (K_d \sim 12 nM) (Fig. 1c and Supplementary Fig. 2). These results show that most PfEMP1 proteins have diverged into CD36-binding (group B and C) and EPCR-binding types (group A and DC8), although the binding properties of a small subset of group A variants containing CIDR α 1.2, 1.3 or 1.6, or atypical CIDR sequence types (CIDR β , γ , δ) remain unknown.

Next we tested whether *P. falciparum*-infected erythrocytes expressing native DC8 PfEMP1 bound EPCR on endothelial cells. An FCR3/IT parasite line expressing IT4VAR20 was generated (Supplementary Fig. 3) and found to bind human brain microvascular endothelial cells

¹Centre for Medical Parasitology, Department of International Health, Immunology & Microbiology, University of Copenhagen and Department of Infectious Diseases, Rigshospitalet, Copenhagen, Denmark.

²Seattle Biomedical Research Institute, Seattle, Washington 98109-5219, USA. ³Retrogenix, Crown House, Bingswood Estate, Whaley Bridge, High Peak SK23 7LY, UK. ⁴National Institute of Medical Research, Tanga Centre, Tanga, Tanzania. ⁵Department of Global Health, University of Washington, Seattle, Washington 98195, USA. ⁶Department of Biochemistry, University of Oxford, South Parks Road, Oxford OX1 3QU, UK.

*These authors contributed equally to this work.

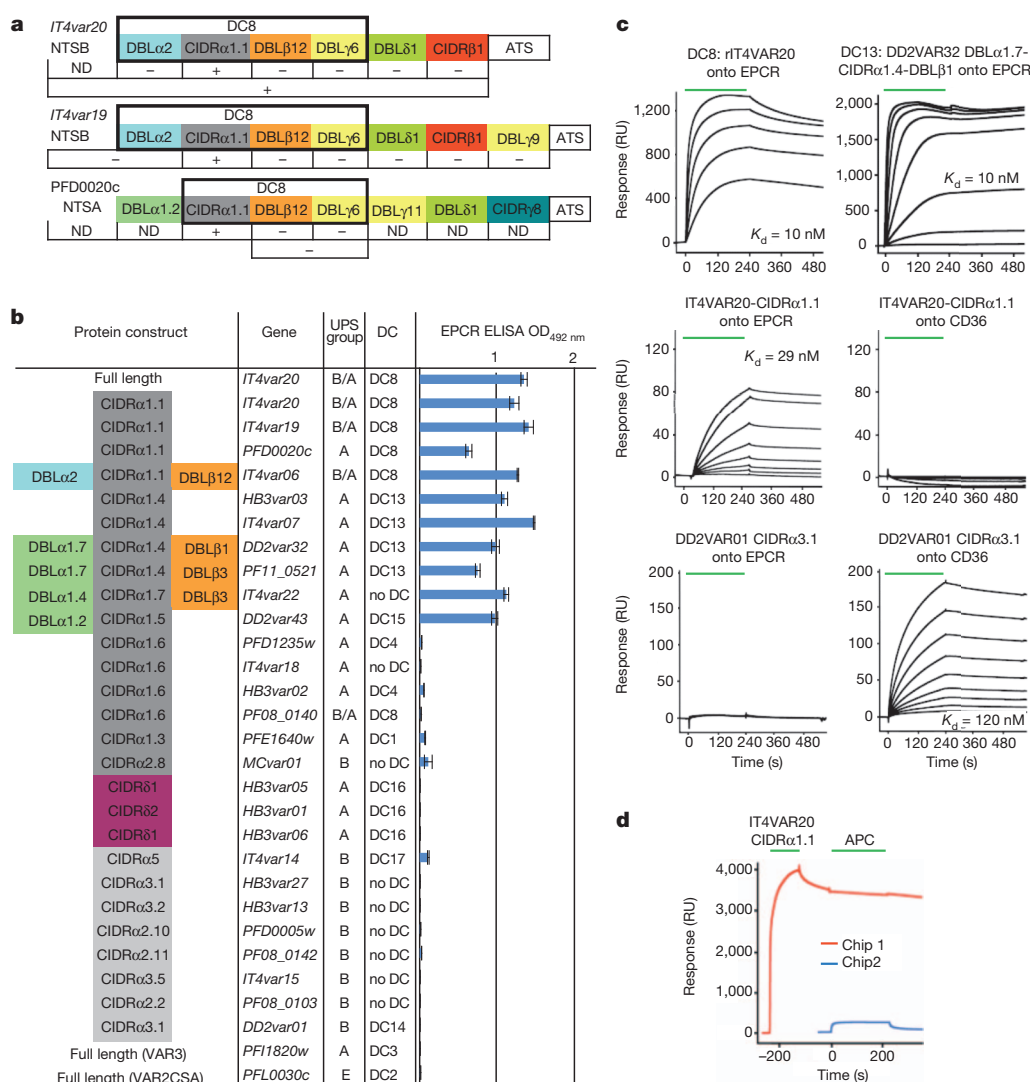


Figure 1 | Binding between recombinant PfEMP1 and EPCR. a, Protein domain architectures (coloured boxes) and their ability to bind EPCR by ELISA (+/-). ATS, acidic terminal segment; ND, not done; NTS, N-terminal segment. **b**, EPCR binding (ELISA optical density (OD_{492nm}), \pm s.d.) of 30 recombinant PfEMP1 proteins. **c**, SPR sensorgrams of PfEMP1 binding to EPCR and CD36. Binding was tested in twofold dilutions of PfEMP1 from

125 nM for rIT4VAR20, 0.5 μ M for DD2VAR32 and DD2VAR01, and 1 μ M for the rest. Green, protein infusion. RU, response units. **d**, Sensorgrams for two chips coated with EPCR. Red, EPCR-coated chip sequentially flushed with DC8 CIDR α 1.1 (2 μ M), buffer alone, APC (2 μ M), then buffer alone. Blue, EPCR-coated chip flushed with APC only.

(HBMECs) via the PfEMP1::EPCR interaction, as demonstrated by reversal of binding by rEPCR, anti-EPCR antibodies and antibodies against either the full-length rIT4VAR20 or the IT4VAR20-CIDR α 1.1 domain (Fig. 2 and Supplementary Figs 4 and 5). Recombinant intercellular adhesion molecule 1 (ICAM1), anti-ICAM1 antibodies, or antibodies against heterologous PfEMP1 domains did not inhibit binding. The binding of VAR2CSA-expressing parasites to chondroitin sulphate A (CSA), or platelet endothelial cell adhesion molecule 1 (PECAM1)-mediated binding of IT4VAR02 (DC16-DC5 PfEMP1)-expressing parasites to transformed human bone marrow endothelial cells, were not inhibited by rEPCR, anti-EPCR-antibodies or the antibodies against recombinant IT4VAR20 (Supplementary Table 3). To confirm these findings, a further three DC8-expressing parasite lines (FCR3 IT4VAR19, FCR3 IT4VAR06 and 3D7 PFD0020c) were generated (Supplementary Fig. 3) and all were found to bind brain-derived endothelial cells via EPCR (Supplementary Table 3). Previous work has shown that DC8 and DC13 variants selected on brain endothelial cells also bind to non-brain microvascular endothelial cells from the heart and lung^{4,5}. Binding of the FCR3 IT4VAR19b parasite line (previously described⁴) to brain, heart, lung and bone marrow

endothelial cells was evaluated and found to be mediated by EPCR (Supplementary Table 3). Altogether, these results demonstrate cytoadhesion of DC8-PfEMP1-expressing infected erythrocytes via EPCR on endothelial cells of diverse tissue origin.

Next, we explored the EPCR-binding phenotype of two parasite isolates (1983 and 1965) from African children with severe malaria. As reported previously³, the *ex vivo* var transcript profiles of these isolates were dominated by DC8-coding transcripts. The isolates cryopreserved at diagnosis were thawed, cultured and selected on rEPCR before the var transcript profile and binding phenotypes were established. The analyses showed that the cultured parasites predominantly expressed the DC8-encoding genes detected when the children were diagnosed (Supplementary Fig. 6), and that the parasite lines bound to brain endothelial cells via EPCR (Supplementary Table 3). This suggests that the parasites causing severe malaria in these children expressed EPCR-binding PfEMP1. To extend this observation, the binding phenotypes of 15 severe malaria, 5 uncomplicated and 10 mild malaria isolates were compared (Table 1 and Supplementary Table 4). Parasites were snap frozen at diagnosis, thawed and exposed to short-term *in vitro* culture (2–12 parasite divisions, without rEPCR selection)

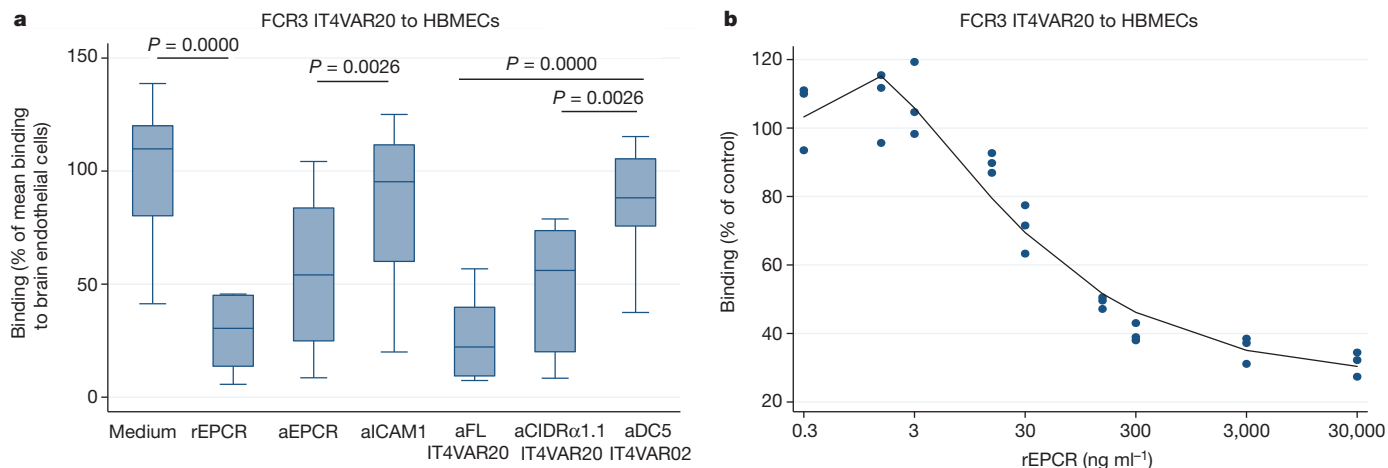


Figure 2 | Binding of DC8-expressing parasites to human brain microvascular endothelial cells. **a, b,** Binding characteristics of IT4VAR20-expressing FCR3 parasites shown as median binding (percentiles: 10, 25, 75, 90) of $n = 10$ independent experiments in relation to the mean control binding in medium (**a**) and triplicate measures in one representative experiment of three (**b**). HBMECs, human brain microvascular endothelial cells. Binding was

to give them an opportunity to recover and expand in sufficient numbers for the binding assay. As previously reported¹⁷, binding to ICAM1 was higher in parasites causing severe malaria than in the control parasites ($P < 0.03$ and $P = 0.0016$ for parasites from children with uncomplicated and mild malaria, respectively). Among parasites from patients with severe malaria, EPCR binding was significantly higher than ICAM1 binding as measured in two independent assays ($P = 0.01$ and $P < 0.05$, respectively), and EPCR binding was significantly higher among parasites causing severe malaria than in control parasites ($P = 0.0078$ and $P = 0.0009$ for parasites from children with uncomplicated and mild malaria, respectively). These data show that EPCR binding is a common phenotype of parasites causing severe malaria, although studies including a larger number of children with different clinical manifestations will be needed to disentangle the role of EPCR binding in different forms of severe malaria.

The pathogenesis of complicated malaria is far from completely understood and it is likely that there are several paths leading to severe outcomes. However, most of the pathology seems to be linked to an unrestrained inflammatory reaction in response to unchecked parasite growth. EPCR has been described as the “cell surface conductor of cytoprotective coagulation factor signaling”¹³ and, interestingly, APC–EPCR-induced PAR1 signalling downregulates 5 of the 13 previously described PfEMP1 ligands, including ICAM1 (ref. 6). We used SPR to investigate whether PfEMP1 might interfere with EPCR-mediated activation of APC. Pre-incubation of EPCR with either DC8–CIDRα1.1 or DC13–CIDRα1.4 domains prevented binding of APC (Fig. 1d and Supplementary Fig. 2b). This indicated that the DC8 domain and APC competed for the same binding site. This was confirmed by showing that monoclonal antibody RCR-252 (ref. 18), an

measured in medium and in the presence of rEPCR (60 $\mu\text{g ml}^{-1}$ or as indicated), anti-EPCR IgG (aEPCR, 20 $\mu\text{g ml}^{-1}$), anti-ICAM1 IgG (aICAM1, 20 $\mu\text{g ml}^{-1}$), anti-rIT4VAR20 IgG (aFL IT4VAR20, 500 $\mu\text{g ml}^{-1}$), anti-CIDRα1.1 IgG (aCIDRα1.1, 500 $\mu\text{g ml}^{-1}$) or control IgG against a recombinant PfEMP1 containing DC5 (aDC5 IT4VAR20, 500 $\mu\text{g ml}^{-1}$). P values for comparisons were evaluated using the Wilcoxon test for paired differences.

antibody that blocks APC binding to EPCR, also prevented parasite binding to endothelial cells (Supplementary Fig. 4). However, the affinity ($K_d = 1 \mu\text{M}$) of the commercial human purified APC used here was lower than that reported earlier for native APC¹⁴. Thus, the extent to which native soluble APC can inhibit parasite binding remains to be explored. Taken together, these findings indicate that adhesion of DC8-expressing parasites to brain endothelial cells is mediated by PfEMP1 interacting with EPCR at or close to the RCR-252 antibody-binding site. It further suggests that PfEMP1 binds EPCR near or at the same region as APC. Thus, EPCR-mediated parasite cytoadhesion could interfere with activation of cytoprotective and anti-inflammatory pathways, which in turn may contribute to severe malaria pathology (Supplementary Fig. 1).

Soluble EPCR is shed from endothelial cells by the metalloproteinase tumour necrosis factor- α converting enzyme (TACE) (also known as a disintegrin and metalloproteinase-17 (ADAM17)) and circulates in plasma¹⁹. The levels of soluble EPCR differ between individuals, and high plasma levels of EPCR (up to 500 ng ml^{-1}) are associated with specific *PROCR* haplotypes²⁰, which in turn are associated with a higher risk of contracting venous thrombosis²¹. Of interest, with the addition of soluble rEPCR at levels between 15–300 ng ml^{-1} , a progressively higher inhibition of the binding between DC8-expressing parasites and endothelial cells was seen (Fig. 2b). It is a possibility worthy of further exploration that human polymorphism in EPCR is a balanced polymorphism protecting individuals against severe malaria at the expense of a higher risk of thrombotic disease.

Our findings identify EPCR binding as a property of PfEMP1. Previous studies that aimed to link parasite-binding phenotypes to disease outcome have not tested for binding to EPCR and results have

Table 1 | Binding characteristics of malaria parasites from patients

Parasites**	HBMEC binding* (95% CI)	HBMEC via EPCR† (95% CI)	HBMEC via ICAM1† (95% CI)	CHO ICAM1‡ (95% CI)	CHO CD36‡ (95% CI)
Severe malaria ($N = 15$)	58 (40;80)	40§ (20;50)	27 (8;48)	26 (10;42)	19 (8;34)
Uncomplicated ($N = 5$) (P value)	25 (14;34) ($P = 0.021$)	7 (4;19) ($P = 0.078$)	4 (1;20) ($P = 0.027$)	4 (0;6) ($P = 0.020$)	21 (12;25) ($P = 0.75$)
Mild malaria ($N = 10$) (P value)	24 (12;45) ($P = 0.0039$)	8 (4;17) ($P = 0.0009$)	2 (0;6) ($P = 0.0016$)	0 (0;1) ($P = 0.0008$)	10 (2;37) ($P = 0.39$)

** Parasites were isolated from children admitted to hospital with cerebral malaria and/or severe anaemia (severe malaria), children admitted with uncomplicated malaria (uncomplicated) or individuals diagnosed during village surveys (mild malaria).

* Median units. One hundred units representing optimal binding defined as the HBMEC binding observed with the IT4 parasite line selected to express IT4VAR20 (Fig. 2). CI, confidence interval.

† Reduction in HBMEC binding by incubating parasites in the presence of soluble EPCR (30 $\mu\text{g ml}^{-1}$) or anti-ICAM1 monoclonal antibody (50 $\mu\text{g ml}^{-1}$) given as delta binding units (HBMEC binding subtracted from HBMEC binding in the presence of soluble EPCR or anti-ICAM1).

‡ Binding to Chinese hamster ovary cells (CHO) transfected with ICAM1 or CD36.

§ Among parasites from patients with severe disease, EPCR binding was statistically significantly higher (Wilcoxon test for paired data) than HBMEC ICAM1 binding ($P = 0.01$) or binding to CHO ICAM1 ($P < 0.05$).

|| Wilcoxon rank sum test for comparison to parasites from patients with severe malaria.

been conflicting. Most consistently, ICAM1 binding and rosetting have been identified as virulence factors²². However, the fact that DC8 and other EPCR-binding variants are frequently expressed in parasites infecting young children with limited malaria immunity^{23,24}, and the ubiquity of endothelial cells expressing EPCR, suggest that CIDR α 1::EPCR-mediated *P. falciparum* cytoadhesion is the major virulence phenotype for severe malaria. Intriguingly, in a small number of case reports a recombinant form of APC (drotrecogin alfa)^{25–27} was used successfully to treat severe malaria infections with remarkable recoveries. The results presented here open new avenues for studies of malaria pathogenesis, and possibilities for the development of new adjunct therapy and vaccines to treat or protect children from death from malaria.

METHODS SUMMARY

Recombinant proteins were produced in insect²³ or *Escherichia coli*⁴ cells (Supplementary Table 2), and anti-PfEMP1 antibodies were prepared as described^{4,5,28}. Potential PfEMP1-binding partners were screened using Retrogenix methodology. PfEMP1::EPCR interactions were analysed by ELISA and SPR. Malaria parasites were cultured and PfEMP1 expression was determined using quantitative PCR, DBL α tag determination and flow cytometry^{3,28}. The history of each parasite line is given in Methods. In Copenhagen, parasite adhesion assays were performed using robotic washing and radioactively labelled parasites. HBMECs²⁹ were provided by M. Stins (Johns Hopkins University). In Seattle, parasite binding assays were performed using endothelial cells from different tissues on glass slides. Unbound parasites were moved by inverting slides in medium and binding quantified by microscopy. Bone marrow endothelial cells were provided by K. Kellar (Centers for Disease Control and Prevention).

Full Methods and any associated references are available in the online version of the paper.

Received 15 January; accepted 24 April 2013.

Published online 5 June 2013.

- Murray, C. J. *et al.* Global malaria mortality between 1980 and 2010: a systematic analysis. *Lancet* **379**, 413–431 (2012).
- Kraemer, S. M. & Smith, J. D. A family affair: *var* genes, PfEMP1 binding, and malaria disease. *Curr. Opin. Microbiol.* **9**, 374–380 (2006).
- Lavstsen, T. *et al.* *Plasmodium falciparum* erythrocyte membrane protein 1 domain cassettes 8 and 13 are associated with severe malaria in children. *Proc. Natl Acad. Sci. USA* **109**, E1791–E1800 (2012).
- Avril, M. *et al.* A restricted subset of *var* genes mediates adherence of *Plasmodium falciparum*-infected erythrocytes to brain endothelial cells. *Proc. Natl Acad. Sci. USA* **109**, E1782–E1790 (2012).
- Claessens, A. *et al.* A subset of group A-like *var* genes encodes the malaria parasite ligands for binding to human brain endothelial cells. *Proc. Natl Acad. Sci. USA* **109**, E1772–E1781 (2012).
- Mosnier, L. O., Zlokovic, B. V. & Griffin, J. H. The cytoprotective protein C pathway. *Blood* **109**, 3161–3172 (2007).
- Rask, T. S., Hansen, D. A., Theander, T. G., Gorm Pedersen, A. & Lavstsen, T. *Plasmodium falciparum* erythrocyte membrane protein 1 diversity in seven genomes—divide and conquer. *PLoS Comput. Biol.* **6** (2010).
- Salanti, A. *et al.* Evidence for the involvement of VAR2CSA in pregnancy-associated malaria. *J. Exp. Med.* **200**, 1197–1203 (2004).
- Fukudome, K. & Esmon, C. T. Identification, cloning, and regulation of a novel endothelial cell protein C/activated protein C receptor. *J. Biol. Chem.* **269**, 26486–26491 (1994).
- Simmonds, R. E. & Lane, D. A. Structural and functional implications of the intron/exon organization of the human endothelial cell protein C/activated protein C receptor (EPCR) gene: comparison with the structure of CD1/major histocompatibility complex α 1 and α 2 domains. *Blood* **94**, 632–641 (1999).
- Stearns-Kurosawa, D. J., Kurosawa, S., Mollica, J. S., Ferrell, G. L. & Esmon, C. T. The endothelial cell protein C receptor augments protein C activation by the thrombin-thrombomodulin complex. *Proc. Natl Acad. Sci. USA* **93**, 10212–10216 (1996).

- Schuepbach, R. A., Feistritzer, C., Fernandez, J. A., Griffin, J. H. & Riewald, M. Protection of vascular barrier integrity by activated protein C in murine models depends on protease-activated receptor-1. *Thromb. Haemost.* **101**, 724–733 (2009).
- Gleeson, E. M., O'Donnell, J. S. & Preston, R. J. The endothelial cell protein C receptor: cell surface conductor of cytoprotective coagulation factor signaling. *Cell. Mol. Life Sci.* **69**, 717–726 (2012).
- Fukudome, K. *et al.* The endothelial cell protein C receptor. Cell surface expression and direct ligand binding by the soluble receptor. *J. Biol. Chem.* **271**, 17491–17498 (1996).
- Robinson, B. A., Welch, T. L. & Smith, J. D. Widespread functional specialization of *Plasmodium falciparum* erythrocyte membrane protein 1 family members to bind CD36 analysed across a parasite genome. *Mol. Microbiol.* **47**, 1265–1278 (2003).
- Ghumra, A. *et al.* Induction of strain-transcending antibodies against Group A PfEMP1 surface antigens from virulent malaria parasites. *PLoS Pathog.* **8**, e1002665 (2012).
- Ochola, L. B. *et al.* Specific receptor usage in *Plasmodium falciparum* cytoadherence is associated with disease outcome. *PLoS ONE* **6**, e14741 (2011).
- Sturn, D. H. *et al.* Expression and function of the endothelial protein C receptor in human neutrophils. *Blood* **102**, 1499–1505 (2003).
- Xu, J., Qu, D., Esmon, N. L. & Esmon, C. T. Metalloproteolytic release of endothelial cell protein C receptor. *J. Biol. Chem.* **275**, 6038–6044 (2000).
- Pintao, M. C. *et al.* High levels of protein C are determined by PROCR haplotype 3. *J. Thromb. Haemost.* **9**, 969–976 (2011).
- Dennis, J. *et al.* The endothelial protein C receptor (PROCR) Ser219Gly variant and risk of common thrombotic disorders: a HuGE review and meta-analysis of evidence from observational studies. *Blood* **119**, 2392–2400 (2012).
- Rowe, J. A., Claessens, A., Corrigan, R. A. & Arman, M. Adhesion of *Plasmodium falciparum*-infected erythrocytes to human cells: molecular mechanisms and therapeutic implications. *Expert Rev. Mol. Med.* **11**, e16 (2009).
- Cham, G. K. *et al.* Sequential, ordered acquisition of antibodies to *Plasmodium falciparum* erythrocyte membrane protein 1 domains. *J. Immunol.* **183**, 3356–3363 (2009).
- Cham, G. K. *et al.* Hierarchical, domain type-specific acquisition of antibodies to *Plasmodium falciparum* erythrocyte membrane protein 1 in Tanzanian children. *Infect. Immun.* **78**, 4653–4659 (2010).
- Kendrick, B. J., Gray, A. G., Pickworth, A. & Watters, M. P. Drotrecogin alfa (activated) in severe falciparum malaria. *Anaesthesia* **61**, 899–902 (2006).
- Rankin, L. G. & Austin, D. L. The use of activated protein C in severe *Plasmodium falciparum* malaria. *Anaesth. Intensive Care* **35**, 428–432 (2007).
- Robak, O. *et al.* The use of drotrecogin alfa in severe falciparum malaria. *Anaesth. Intensive Care* **38**, 751–754 (2010).
- Wang, C. W. *et al.* Evidence for *in vitro* and *in vivo* expression of the conserved VAR3 (type 3) *Plasmodium falciparum* erythrocyte membrane protein 1. *Malar. J.* **11**, 129 (2012).
- Stins, M. F., Gilles, F. & Kim, K. S. Selective expression of adhesion molecules on human brain microvascular endothelial cells. *J. Neuroimmunol.* **76**, 81–90 (1997).

Supplementary Information is available in the online version of the paper.

Acknowledgements We thank A. Salanti for supplying the full-length VAR2CSA protein and S. Lücking Nielsen for technical assistance. The work was supported by the University of Copenhagen Program of Excellence, Lundbeck Foundation, Danish International Development Agency, Augustinus Fonden, Malaria Capacity Development Consortium and The Danish Medical Research Council, as well as the National Institutes of Health (R01 AI47953 and U19 AI089688 to J.D.S.). M.K.H. was funded by a research grant from the Medical Research Council.

Author Contributions L.T., T.L., J.D.S. and A.J.B. produced recombinant proteins; J.F. performed the cell microarray experiments; S.S.B., C.W.W., J.E.V.P., M.A.N., M.A. and J.S.J. performed the work with malaria parasites; P.M., J.L. and T.G.T. organized clinical work and processed clinical samples; M.K.H. performed the SPR studies; L.T. performed the ELISA studies. The study was conceived and planned by L.T., T.L. and T.G.T. The manuscript was written by T.L., T.G.T., L.T., J.D.S. and M.K.H. All authors read and commented on the manuscript. L.T. and T.L. contributed equally to this work.

Author Information Reprints and permissions information is available at www.nature.com/reprints. The authors declare no competing financial interests. Readers are welcome to comment on the online version of the paper. Correspondence and requests for materials should be addressed to T.L. (thomasl@sund.ku.dk) or L.T. (lturner@sund.ku.dk).

METHODS

Recombinant PfEMP1 proteins and anti-PfEMP1 antibodies. Recombinant proteins were produced in insect²³ or *Escherichia coli*⁴ cells (Supplementary Table 2), and anti-PfEMP1 antibodies were prepared as described^{4,5,28}. In brief, the full-length exon 1 sequences of FCR3 *IT4var20* and *IT4var13* genes were codon-optimized for expression in *Trichoplusia ni* cells using the software GeneOptimizer. DNA constructs containing a His tag at the C-terminal end were synthesized by Geneart and subcloned into the baculovirus expression vector pAcGP67-A (BD Biosciences) modified to contain a His tag at the C-terminal end of the construct, by Geneart. Other insect-cell-produced proteins were generated by PCR from genomic DNA using the primers shown in Supplementary Table 2, as described previously^{4,5,30}. Recombinant *Escherichia coli* proteins were generated as described previously⁴. Rat and rabbit immunizations and IgG preparations were as described previously⁵. Animal immunizations were conducted according to and approved by the Danish national Animal Experiments Inspectorate.

Human receptor interaction microarray screening. Screening for human protein ligands of DC8 PfEMP1 was performed using the Retrogenix Cell Microarray technology. Detection of recombinant His-tagged PfEMP1 interactions with the vector-transfected HEK293-cell glass slide microarray was first optimized using an ICAM-binding recombinant full-length IT4VAR13 protein (rIT4VAR13).

Retrogenix's expression vectors encoding ICAM1 or CD28 (negative control) were each spotted onto glass slides, and a human HEK293 monolayer was grown on top and reverse transfected using Retrogenix's optimized methodology. Slides were incubated with $10.5 \mu\text{g ml}^{-1}$ His-tagged rIT4VAR13, and interactions were detected using a mouse anti-His antibody (Millipore) followed by an AlexaFluor 647 anti-mouse antibody (Life Technologies). Slides were then imaged for fluorescence and analysed using ImageQuant software (GE). For rIT4VAR20 receptor screening, 2,505 expression vectors, each encoding a full-length human plasma membrane protein, were arrayed across seven microarray slides, and human HEK293 cells were reverse transfected. See Supplementary Table 1 for the list of proteins screened. Each slide was incubated with $10.5 \mu\text{g ml}^{-1}$ rIT4VAR20. Detection of binding was performed using the mouse anti-His antibody followed by the AlexaFluor 647 anti-mouse antibody. Protein 'hits' were identified by visual inspection using ImageQuant software (GE). This primary screen produced a total of 16 hits to rIT4VAR20. The vectors encoding each of the 16 hits were sequenced, confirming their identities. A confirmation/specificity screen was done, with each of the 16 vectors re-spotted and re-probed with rIT4VAR20, rIT4VAR13, or detection anti-His antibody alone, to determine which hits were specific for rIT4VAR20. In this screen only one hit, EPCR (*PROCR* gene) was specific for rIT4VAR20.

ELISA. MaxiSorp immunoplates (Nunc) were coated with recombinant human EPCR (250 ng per well, Sino Biological, 13320-H08H, consisting of the extracellular domain of human EPCR Met1–Thr209 fused with a C-terminal poly-histidine tag) in PBS buffer pH 7.4 and blocked with PBS 3% skimmed milk. PfEMP1 proteins were added at a concentration of $10 \mu\text{g ml}^{-1}$ per DBL or CIDR domain in PBS, 1% skimmed milk and incubated for 1 h at 37 °C with gentle shaking. Peroxidase-conjugated anti-V5 antibodies (Invitrogen, R961-25) were added at a dilution of 1:3,000 for 1 h at 37 °C (baculovirus-produced proteins) or $0.375 \mu\text{g ml}^{-1}$ rabbit anti-StrepII antibody (Genscript no. A00626) (*E. coli*-produced proteins). Secondary incubation with 1:400 anti-rabbit IgG/HRP (Alpha Diagnostics no. 20321) was carried out for *E. coli* proteins. Plates were developed with phosphate solution with 0.012% H_2O_2 substrate and O-phenylenediamine (baculovirus) or TMB Substrate (Alpha Diagnostics no. 80091) (*E. coli*). The colorimetric reaction was stopped with 3 M H_2SO_4 after 10 min and the OD was measured at 492 nm (baculovirus) or 1 × stop solution (Alpha Diagnostics no. 80100) and read at 450 nm (*E. coli*). Reactivity with EPCR was tested in triplicates twice for *E. coli*-produced proteins and at least twice in duplicates for insect-cell-produced proteins, results from one representative experiment are given.

SPR. SPR experiments were carried out using a BIAcore T100 instrument (GE Healthcare). All experiments were performed in 10 mM HEPES pH 7.5, 150 mM NaCl at 25 °C. Recombinant EPCR was immobilized on a CM5 chip (GE Healthcare) by amine coupling to a total loading of 1,200 RU. Binding partners were buffer exchanged into 10 mM HEPES pH 7.5, 150 mM NaCl and dilution series were injected over the rEPCR-coated chip. Injections were 240 s with 300 s dissociation. The chip surface was regenerated in between injections with a 60 s pulse of 10 mM NaOH. Repeat injections showed that this treatment left the rEPCR-coated surface undamaged. The specific binding response to rEPCR was obtained by subtracting the response given by analytes to an uncoupled surface. The kinetic sensorgrams were fitted to a global 1:1 interaction model to allow calculation of the association rate constant, k_a ; dissociation rate constant, k_d ; and dissociation constant, K_d using BIAevaluation software 2.0.3 (GE Healthcare).

Clinical parasite isolates. The clinical parasite isolates were collected during studies conducted in Korogwe District in northeastern Tanzania about 100 km from the Indian Ocean³. Children admitted to Korogwe District Hospital with malaria symptoms were enrolled after obtaining informed consent from a parent or guardian. Children were immediately subjected to a clinical investigation, and a blood sample was collected for diagnostic and research purposes, after which treatment was instigated according to the national guidelines. Samples were also collected from patients recruited in two study villages during malaria surveys and diagnosed by a rapid diagnostic test. None of these patients had severe symptoms, and they were all treated as outpatients at the village clinic. The study received ethical clearance from the Ethical Review Board of the National Institute for Medical Research, Tanzania (National Institute of Medical Research/HQ/R.8a/Vol.IX/559) and informed consent was obtained from all study participant and/or parents or guardians. The patient samples representing severe malaria parasites were selected from a database among patients having a Blantyre coma score <3 and/or a blood haemoglobin <5 g dl⁻¹ (Supplementary Table 4). The samples from patients with mild malaria were selected on the basis of having a reasonable high parasite density to ensure a high culture success rate. Knowledge about *ex vivo* var gene transcription was not available when selecting the parasites to be tested for EPCR binding. At diagnosis pelleted erythrocytes (25–50 μl) from venous blood were preserved for later parasite culturing by adding an equal volume of freezing medium (28% glycerol and 3% D-sorbitol in a 0.65% saline solution) and then snap frozen in liquid nitrogen. Cultures of live parasite isolates were re-established by thawing in an equal volume of 3.5% saline solution, washing in RPMI and cultured with fresh uninfected red blood cells to allow reinvasion. Parasites were cultured for 4–22 days without any selection for binding phenotype until sufficient material was available for the binding assays.

Malaria parasite culture, phenotype determination and manipulation. Malaria parasites were cultured and PfEMP1 expression phenotypes were determined by quantitative PCR and var gene or var gene type-specific primers to determine the transcript level of var genes in relation to two internal control genes, seryl-tRNA synthetase and aldolase, as well as by flow cytometry using PfEMP1-specific polyclonal antibodies as previously described^{3,28}. The var transcript distribution of 1965 and 1983 parasite isolates were determined by counting unique DBL α var tags from 48 clones obtained by capillary sequencing (Macrogen) of PCR products generated as previously described³ and cloned into pCR2.1 vectors.

Parasites were selected for either specific PfEMP1 expression using antibodies to recombinant PfEMP1 constructs as described previously²⁸ and/or by selection for binding to HBMECs and rEPCR. $50 \mu\text{g ml}^{-1}$ rEPCR was added in three spots (10 μl) onto the bottom of a 25 cm² culture flask and allowed to adsorb to the plastic surface (2 h, room temperature (24 °C)). The spotting liquid was gently aspirated and the bottom of the flask washed twice with PBS and blocked with skimmed milk (3%) in PBS (overnight, 4 °C). The flask was washed twice with parasite medium and 3 ml of infected erythrocytes (parasitaemia \geq 2%, haematocrit 2%) were added. The flask was then gassed with parasite gas mixture for 30 s, tightly capped and incubated on a rocking platform (10 r.p.m., 1 h, 37 °C). Unbound erythrocytes were washed away using parasite medium and binding to spots was assessed using an inverted microscope. Ten millilitres of parasite medium and 200 μl fresh human type O⁺ erythrocytes were added to the flask, which was gassed and incubated overnight (37 °C). The parasitaemia was recorded the following day.

History of parasite lines. The FCR3 IT4VAR20 line was generated by alternate antibody selection using rat anti-rIT4VAR20 antibodies and panning on HBMECs. The FCR3 IT4VAR19a line was generated by rEPCR selection from an IT4VAR03-expressing FCR3 (FCR3 IT4VAR03) line²⁹ by three continuous selections for rEPCR binding as described earlier. The FCR3 IT4VAR19b and FCR3 IT4VAR06 lines were generated by limiting dilution from the ItG-ICAM1 line panned on immortalized transformed human brain microvascular endothelial cells (THBMECs). The FCR3 IT4VAR06 line was further enriched by selection for binding to rEPCR as described earlier. The 3D7 PFD0020c line was generated by alternating antibody (rat anti-DBL γ 6-PFD0020c antibodies) and rEPCR-binding selections. The FCR3 IT4VAR02 parasites were generated by antibody selection (rabbit anti-DC5-IT4VAR02 serum), and FCR3 VAR2CSA lines were generated by panning on BeWo cells. Parasite isolates 1965 and 1983 were obtained from two patients diagnosed with severe malaria (described previously³). The 1965 and 1983 parasite isolates were selected for rEPCR binding as described earlier.

Parasite adhesion to HBMECs and CHO cells. In Copenhagen, parasite adhesion assays (Fig. 2 and Table 1, and Supplementary Fig. 4 and Supplementary Table 3) were carried out as follows. HBMECs²⁹ were grown in Endothelial Cell Medium (1001, ScienCell), and CHO cells (CHO wild type, CHO CD36 and CHO ICAM1; from ATCC) were grown in RPMI 1640 supplemented with 10% fetal bovine serum (Lonza), 0.125 $\mu\text{g ml}^{-1}$ gentamycin (Lonza) and 2 mmol l⁻¹ L-glutamine

(Sigma-Aldrich). Wells in flat-bottomed 96-well plates destined for HBMECs were pre-coated with 100 μ l fibronectin ($2 \mu\text{g cm}^{-2}$) (1918-FN-02M, R&D Systems) (overnight, 37°C). One-hundred microlitres of endothelial cells or CHO cells with 80,000 cells per ml were seeded per well and grown to a monolayer over 2 days. The day before the adhesion assay, ring-stage infected erythrocytes were radioactively labelled with tritiated hypoxanthine (^3H) (Amersham; 8.75 MBq ml^{-1} packed erythrocytes) in hypoxanthine-free parasite medium and cultured overnight. Radioactively labelled late trophozoite and schizont stages were purified using magnetic cell sorting (MACS, Miltenyi Biotec) and adjusted to 1.25×10^7 cells ml^{-1} in 2% FCS (in RPMI 1640). Before the adhesion assay, HBMECs were washed once with PBS followed by addition of 20 μ l 2% FCS in RPMI per well. For binding inhibition, 20 μ l of antibodies or proteins diluted in PBS were added to HBMECs in triplicates and PBS alone was added as a control. IgG-purified anti-PfEMP1 rat or rabbit antibodies were added to a final concentration of $500 \mu\text{g ml}^{-1}$. Polyclonal human EPCR antibodies (AF2245, R&D) and monoclonal antibody to ICAM1 (MCA1615EL, AbDSerotec) were added at a final concentration of $50 \mu\text{g ml}^{-1}$. Monoclonal antibody (RCR-252) to human EPCR (HM2145, Hycult Biotech) was added at final concentrations of 5, 10, 20 and $30 \mu\text{g ml}^{-1}$. rEPCR and ICAM1 (ADP4, R&D Systems) were added at a final concentration of $30,000 \text{ ng ml}^{-1}$ (titration with human EPCR: 0.3, 3, 30, 300, 3,000 or $30,000 \text{ ng ml}^{-1}$). Twenty microlitres of late-stage infected erythrocytes were added to HBMECs and co-incubated on a rocking table for 0.25 h to 1.5 h at 37°C . Unbound infected erythrocytes were removed with a washing robot (Biomek 2000, Beckman Coulter). Radioactive material was harvested (Filtermate Harvester, PerkinElmer) and scintillation liquid added (Microscint 20, PerkinElmer). Radioactivity was measured in counts per minute (Topcount NXT, PerkinElmer). Adhesion to wells blocked with 2% human albumin (A-1887, Sigma-Aldrich) was also measured in addition to the total amount of radioactivity added per well (max-value). Adhesion was calculated as the proportion (percentage) of bound radioactively labelled infected erythrocytes out of the total

amount of radioactively labelled infected erythrocytes added per well. The binding was then normalized into units by assigning the value 100 to the percentage radioactivity bound and recovered under optimal conditions. The binding of FCR3 IT4VAR02 and FCR3 VAR2CSA parasite lines to transformed human bone marrow endothelial cells (TrHBMECs) or BeWo cells, respectively, was performed as described earlier for the HBMEC-binding assay. Anti-PECAM1 antibodies (BBA7, R&D Systems) were used at a final concentration of $20 \mu\text{g ml}^{-1}$.

In Seattle, parasite adhesion assays (Supplementary Table 3) were carried out as follows. Endothelial cell culture and adhesion of the FCR3 IT4VAR19b infected erythrocytes were performed as described⁴. Endothelial cells were primary human pulmonary microvascular endothelial cells (HPMECs) and human cardiac microvascular endothelial cells (HCMECs) (ScienCell), and immortalized THBMECs and bone marrow endothelial cells (BMECs; CDC) provided by K. Kellar. In brief, endothelial cells were grown to a confluent monolayer on either collagen- (THBMECs and BMECs) or fibronectin- (HPMECs and HCMECs) coated flasks, or on 8-well slides. The endothelial cells were incubated statically with gelatin-purified late-stage parasite. Unbound parasites were removed by inverting slides upside down for 10 min in binding medium, and bound parasites were quantified by counting. All binding assays were done at least in duplicate. For antibody inhibition assays, cells were pre-incubated for 15 min with $5 \mu\text{g ml}^{-1}$ of mouse monoclonal anti-human ICAM1 (clone 15.2, Abcam ab20), 0.1 mg ml^{-1} of polyclonal goat anti-EPCR (AF2245, R&D) or $50 \mu\text{g ml}^{-1}$ of APC (Sigma P2200). For inhibition with rEPCR, gelatin-enriched infected erythrocytes were pre-incubated for 15 min with $50 \mu\text{l ml}^{-1}$ of rEPCR before they were added to the cells.

30. Turner, L. *et al.* Antibodies against PfEMP1, RIFIN, MSP3 and GLURP are acquired during controlled *Plasmodium falciparum* malaria infections in naive volunteers. *PLoS ONE* **6**, e29025 (2011).

BACH2 represses effector programs to stabilize T_{reg} -mediated immune homeostasis

Rahul Roychoudhuri^{1*}, Kiyoshi Hirahara^{2†*}, Kambiz Mousavi^{3*}, David Clever¹, Christopher A. Klebanoff¹, Michael Bonelli², Giuseppe Sciumè², Hossein Zare³, Golnaz Vahedi², Barbara Dema⁴, Zhiya Yu¹, Hui Liu⁵, Hayato Takahashi², Mahadev Rao¹, Pawel Muranski¹, Joseph G. Crompton¹, George Punkosdy⁶, Davide Bedognetti⁵, Ena Wang⁵, Victoria Hoffmann⁷, Juan Rivera⁴, Francesco M. Marincola^{5,8}, Atsushi Nakamura^{9,10}, Vittorio Sartorelli³, Yuka Kanno², Luca Gattinoni¹, Akihiko Muto^{9,10}, Kazuhiko Igarashi^{9,10}, John J. O'Shea^{2*} & Nicholas P. Restifo^{1,11*}

Through their functional diversification, distinct lineages of $CD4^+$ T cells can act to either drive or constrain immune-mediated pathology. Transcription factors are critical in the generation of cellular diversity, and negative regulators antagonistic to alternate fates often act in conjunction with positive regulators to stabilize lineage commitment¹. Genetic polymorphisms within a single locus encoding the transcription factor BACH2 are associated with numerous autoimmune and allergic diseases including asthma², Crohn's disease^{3,4}, coeliac disease⁵, vitiligo⁶, multiple sclerosis⁷ and type 1 diabetes⁸. Although these associations point to a shared mechanism underlying susceptibility to diverse immune-mediated diseases, a function for BACH2 in the maintenance of immune homeostasis has not been established. Here, by studying mice in which the *Bach2* gene is disrupted, we define BACH2 as a broad regulator of immune activation that stabilizes immunoregulatory capacity while repressing the differentiation programs of multiple effector lineages in $CD4^+$ T cells. BACH2 was required for efficient formation of regulatory (T_{reg}) cells and consequently for suppression of lethal inflammation in a manner that was T_{reg} -cell-dependent. Assessment of the genome-wide function of BACH2, however, revealed that it represses genes associated with effector cell differentiation. Consequently, its absence during T_{reg} polarization resulted in inappropriate diversion to effector lineages. In addition, BACH2 constrained full effector differentiation within $T_{\text{H}}1$, $T_{\text{H}}2$ and $T_{\text{H}}17$ cell lineages. These findings identify BACH2 as a key regulator of $CD4^+$ T-cell differentiation that prevents inflammatory disease by controlling the balance between tolerance and immunity.

BACH2 is expressed in B cells where it acts as a transcriptional repressor of Blimp-1 (also known as PR domain zinc finger 1) and is critical for somatic hypermutation and class switch recombination^{9–11}. Given the association of polymorphisms in the *BACH2* locus with multiple inflammatory diseases in humans, however, we proposed a role for the transcription factor in the prevention of inflammation. To test this hypothesis, we characterized the phenotype of knockout (KO) mice in which the *Bach2* gene had been disrupted⁹. Although pups appeared normal at birth, they developed a progressive wasting disease (Fig. 1a and Supplementary Fig. 1a) that resulted in diminished survival compared to wild-type (WT) littermates (Fig. 1b). Sera from KO mice at 3 months of age contained elevated levels of anti-nuclear and anti-double stranded DNA autoantibodies (Fig. 1c). Gross examination revealed enlargement of the lungs (Fig. 1d and Supplementary Fig. 1b) with highly penetrant histopathological changes (Fig. 1e), including extensive perivascular and alveolar infiltration by lymphocytes

and macrophages (Fig. 1f). Examination of the gut revealed less severe and incompletely penetrant inflammatory pathology of the small intestine and stomach also associated with lymphocytic and macrophage infiltration (Fig. 1g and Supplementary Fig. 2). Consistently, we measured elevated expression of the C-C chemokine receptors CCR4 and CCR9 on splenic $CD4^+$ T cells that guide migration to the lung and gut, respectively (Fig. 1h)^{12,13}. Accordingly, we found a striking increase in the number of $CD4^+$ T cells in the lungs of KO animals, whereas peripheral lymphoid organs contained similar or decreased numbers (Fig. 1i and Supplementary Fig. 3). We also observed increased proportions of effector cells in both the spleen and lungs of KO animals (Supplementary Fig. 4a) and a substantial proportion of $CD4^+$ T cells in the lungs expressed the acute activation marker CD69 (Fig. 1j and Supplementary Fig. 4b), a finding indicative of their involvement in the inflammatory process affecting this organ.

$CD4^+$ T cells can be characterized into a number of functionally specialized subsets depending upon expression of lineage-specific transcription factors and cytokines¹⁴. $T_{\text{H}}2$ cells have a central role in allergic inflammation and airway disease and are characterized by expression of the transcription factor GATA3 and cytokines such as interleukin (IL)-4 and IL-13 (ref. 15). Consistent with the presence of $T_{\text{H}}2$ inflammation, there were increased proportions of GATA3⁺ $CD4^+$ T cells in the spleen and lungs (Fig. 1k and Supplementary Fig. 5) and elevated expression of IL-13 and IL-4 in the spleen, lungs and lymph nodes of KO animals (Fig. 1l and Supplementary Fig. 6a). By contrast, we observed no differences in the frequency of IL-17A⁺ cells in these organs and only a minor increase in interferon (IFN)- γ ⁺ cells in the lymph nodes (Supplementary Fig. 6b).

$CD4^+$ T cells can function to both drive and constrain immune-mediated pathology. Whereas effector (T_{eff}) cells are often implicated in immune-mediated disease, FOXP3⁺ T_{reg} cells suppress inflammatory reactions and have a non-redundant role in maintaining immune homeostasis^{16,17}. Given dysregulated immune reactions in *Bach2*-deficient animals, we measured the expression of *Bach2* messenger RNA (mRNA) in conventional and regulatory $CD4^+$ T-cell subsets and their thymic precursors from *Foxp3*^{GFP} reporter mice, which express GFP under the control of the endogenous *Foxp3* promoter. *Bach2* mRNA was expressed at high levels in both conventional FOXP3[−] and FOXP3⁺ (T_{reg}) $CD4^+$ thymocytes in addition to naive ($T_{\text{naï}}$) and T_{reg} cells in the spleen (Fig. 2a).

Evaluation of conventional thymic maturation in KO animals revealed similar proportions of $CD4^+$ SP, $CD8^+$ SP and TCR β ⁺ cells (Supplementary Fig. 7). Given high levels of expression of *Bach2*

¹Center for Cancer Research, National Cancer Institute, National Institutes of Health (NIH), Bethesda, Maryland 20892, USA. ²Molecular Immunology and Inflammation Branch, National Institute of Arthritis and Musculoskeletal and Skin Diseases (NIAMS), NIH, Bethesda, Maryland 20892, USA. ³Laboratory of Muscle Stem Cells and Gene Regulation, NIAMS, NIH, Bethesda, Maryland 20892, USA. ⁴Laboratory of Molecular Immunogenetics, NIAMS, NIH, Bethesda, Maryland 20892, USA. ⁵Department of Transfusion Medicine, NIH, Bethesda, Maryland 20892, USA. ⁶National Institutes of Allergy and Infectious Diseases, NIH, Bethesda, Maryland 20892, USA. ⁷Division of Veterinary Resources, NIH, Bethesda, Maryland 20892, USA. ⁸Sidra Medical and Research Centre, Doha, Qatar. ⁹Department of Biochemistry, Tohoku University Graduate School of Medicine, Sendai 980-8575, Japan. ¹⁰CREST, Japan Science and Technology Agency, Sendai 980-8575, Japan. ¹¹NIH Center for Regenerative Medicine, NIH, Bethesda, Maryland 20892, USA. †Present address: Department of Advanced Allergology of the Airway, Graduate School of Medicine, Chiba University, Chiba 260-8670, Japan.

*These authors contributed equally to this work.

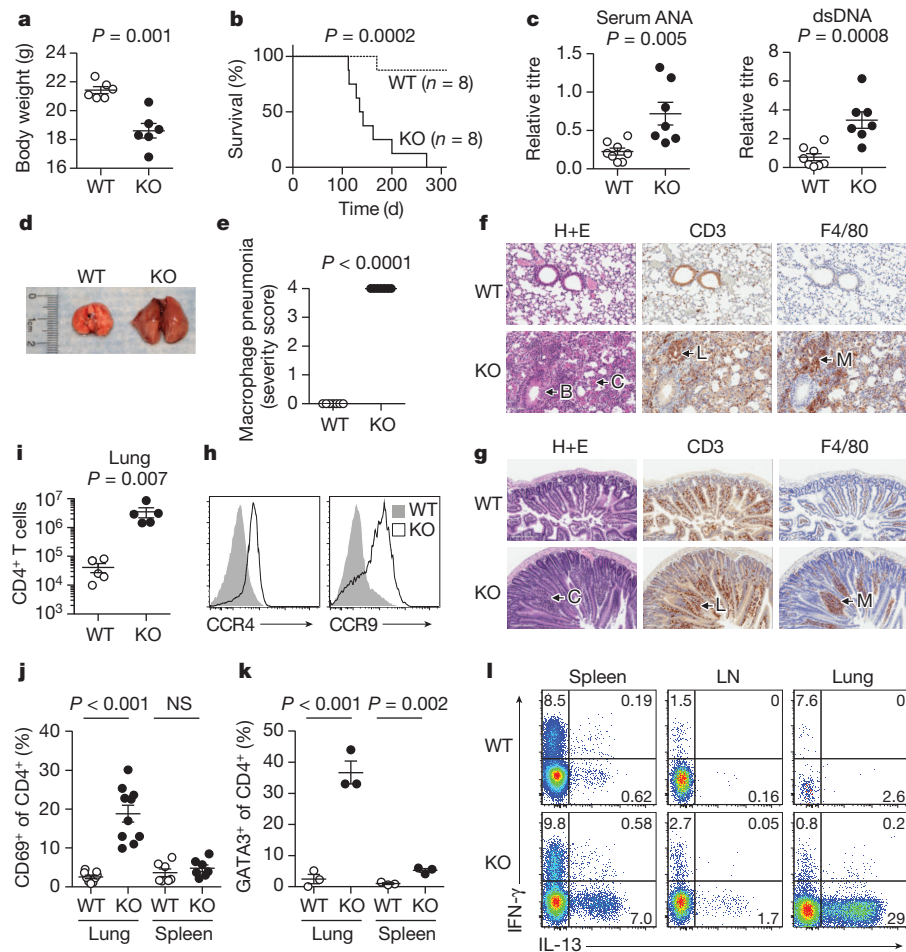


Figure 1 | Spontaneous lethal inflammation in *Bach2* knockout animals.

a, b, Body weight at 3 months of age (**a**) and survival (**b**) of *Bach2* knockout (KO) and wild-type (WT) littermate females. **c**, Titre of anti-dsDNA antibodies and anti-nuclear antibodies (ANA) in the sera of WT and KO animals. **d**, Gross morphology of lungs from WT and KO mice. **e**, Histopathology scoring of lung tissue from WT and KO mice ($n = 7$ per group). **f**, Haematoxylin and eosin (H+E) and immunohistochemical (IHC) stains of WT and KO lung tissue with hypertrophy of bronchial epithelium (B), eosinophilic crystals (C), perivascular lymphocytic infiltration (L) and macrophage infiltration (M). **g**, H+E and IHC

stains of small intestinal tissue lesions with hypertrophic crypts (C), lymphocytic infiltration (L) and macrophage infiltration (M). **h**, Expression of CCR4 and CCR9 on the surface of splenic CD4⁺ T cells. **i**, Quantification of CD4⁺ T cells in lungs of WT and KO animals. **j, k**, Percentage of CD4⁺ T cells expressing CD69 (**j**) and GATA3 (**k**) in lungs and spleen. **l**, Flow cytometry of IFN- γ and IL-13 expression by CD4⁺ T cells from spleen, lymph nodes (LN) and lungs. Mice were analysed at 3 months of age unless otherwise specified. Data are representative of ≥ 2 independent experiments with ≥ 3 mice per genotype. Error bars, s.e.m.; *P* values (Student's *t*-test).

mRNA in CD4SP thymocytes, however, we wished to determine the cell-intrinsic function of BACH2 in regulating gene transcription within these cells. We reconstituted *Rag1*^{-/-} hosts with equal mixtures of lineage-depleted bone marrow cells (hereafter BM) from congenically distinguishable Ly5.1⁺ WT and Ly5.1⁻ KO animals and measured global gene expression in WT and KO CD4SP cells that had developed within the same host (Supplementary Fig. 8 and Supplementary Table 1). Gene set enrichment analysis (GSEA) of this data set (Supplementary Tables 2–6) indicated the loss of genes known to be dependent upon FOXP3 (ref. 2) or directly bound by FOXP3 (Supplementary Fig. 9a)¹⁸. Consistent with these observations, *Foxp3* mRNA itself showed the greatest fold-reduction in expression amongst all transcripts measured (Fig. 2b and Supplementary Fig. 9b). Consequently, we observed a near complete absence of FOXP3⁺ cells amongst KO CD4SP thymocytes in WT:KO mixed BM chimaeric animals (Fig. 2c and Supplementary Fig. 10). In animals reconstituted with either KO BM alone (Fig. 2c) or equal mixtures of KO and *Foxp3*^{3f} BM (Supplementary Fig. 11), however, FOXP3⁺ KO cells were present in both the thymus and spleen but at a lower frequency than when WT cells were transferred. Taken together, these findings indicated a cell-autonomous requirement for BACH2 in the formation of T_{reg} cells in the thymus with an incomplete defect in non-competitive environments.

Whereas a proportion of T_{reg} cells found in peripheral tissues arise in the thymus (thymic T_{reg} or tT_{reg})¹⁶, induced T_{reg} (iT_{reg}) cells develop from conventional FOXP3⁻ CD4⁺ T cells in extrathymic tissues. To test whether BACH2 was required for efficient formation of iT_{reg} cells, we tracked the fate of naive CD4⁺ T cells upon transfer into *Rag1*^{-/-} hosts. Although a proportion of WT CD4⁺ T cells converted into FOXP3⁺ iT_{reg} cells, significantly fewer KO cells underwent similar conversion (Supplementary Fig. 12). By contrast, KO cells showed similar stability of FOXP3 expression and survival upon transfer into *Rag1*^{-/-} hosts over acute time points (Supplementary Fig. 13). Consistent with *in vivo* data, KO naive CD4⁺ T cells were markedly impaired in their ability to induce *Foxp3* mRNA and form FOXP3⁺ iT_{reg} cells upon stimulation in the presence of TGF- β *in vitro* (Fig. 2d, Supplementary Fig. 14). Despite this, KO cells exhibited intact TGF- β and IL-2 signalling (Supplementary Fig. 15). Importantly, defective iT_{reg} induction in KO cells was rescued by reconstitution with *Bach2*-expressing retroviruses (Fig. 2e), confirming that BACH2 is required during induction for the formation of iT_{reg} cells. In addition, *Bach2* overexpression in WT cells enhanced FOXP3 induction under suboptimal polarizing conditions (Supplementary Fig. 16).

Taken together, our results demonstrated a requirement for BACH2 in the efficient generation of both tT_{reg} and iT_{reg} cells. Accordingly,

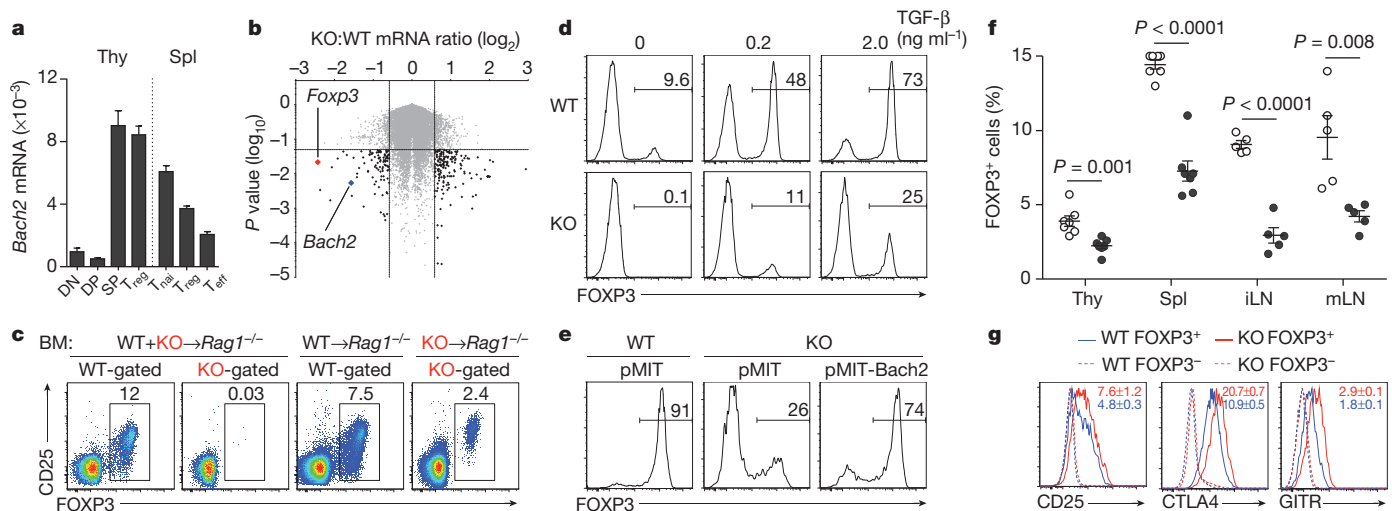


Figure 2 | BACH2 is required for efficient formation of T_{reg} cells.

a, Expression of *Bach2* mRNA in thymic $\text{Foxp3}^{\text{GFP}+}$ DP and CD4SP (SP), and $\text{Foxp3}^{\text{GFP}+}$ CD4SP T_{reg} cells and splenic CD4 $^{+}$ $\text{Foxp3}^{\text{GFP}+}$ $\text{T}_{\text{naï}}$ and T_{eff} and $\text{Foxp3}^{\text{GFP}+}$ T_{reg} cells isolated from *Foxp3* $^{\text{GFP}}$ reporter mice relative to *Actb* mRNA. Thy, thymus; Spl, spleen. **b**, Volcano plot indicating differentially expressed genes in KO compared with WT CD4SP thymocytes from WT:KO mixed BM chimaeric animals. **c**, Intracellular FOXP3 expression in CD4SP thymocytes from mice reconstituted with individual or mixed transfers of WT and KO BM. **d**, FOXP3 expression in WT and KO naive splenic CD4 $^{+}$ T cells stimulated in the presence of indicated amounts of TGF- β *in vitro*. **e**, FOXP3

expression in Thy1.1 $^{+}$ (transduced) WT and KO naive splenic CD4 $^{+}$ T cells stimulated in the presence of 2 ng ml $^{-1}$ TGF- β and transduced with indicated retroviruses. **f**, Ratio of FOXP3 $^{+}$ cells in thymic (gated on CD4SP) and extrathymic tissues (gated on CD3 $^{+}$ CD4 $^{+}$ cells) of 3-month-old WT (open circles) and KO (closed circles) littermates. iLN, inguinal lymph nodes. **g**, Expression of CD25, CTLA4 and GITR on the surface of splenic FOXP3 $^{+}$ and FOXP3 $^{-}$ CD4 $^{+}$ cells from WT and KO mice. Error bars, s.e.m.; *P* values (Student's *t*-test). All data are representative ≥ 2 independent experiments with ≥ 3 mice per genotype (**a–c**, **f**, **g**) or ≥ 4 experiments (**d**, **e**).

analysis of primary and secondary lymphatic tissues from KO mice at 3 months of age revealed a deficiency in T_{reg} cells resembling that in mice individually reconstituted with KO BM (Fig. 2f). Similar reduction in thymic T_{reg} cell frequency was observed in neonatal mice before evidence of autoimmune disease (Supplementary Fig. 17). Furthermore, T_{reg} cell formation was *Bach2* gene-dose dependent because mice heterozygous for the KO allele had reduced frequencies of T_{reg} cells (Supplementary Fig. 18). Thus, T_{reg} cells are found at low frequencies in KO mice despite the presence of inflammation in these animals. Characterization of these cells revealed higher levels of expression of T_{reg} cell suppressive molecules CD25, CTLA4 and GITR (also known as TNFRSF18), the activation marker CD69 and the marker of terminal differentiation, KLRG1 (Fig. 2g and Supplementary Fig. 19; *P* < 0.05) 19 . Consistent with this terminally differentiated phenotype, T_{reg} cells from *Bach2*-deficient mice failed to prevent colitis in long-term assays despite possessing acute suppressive function (Supplementary Fig. 20a–e) 19 .

Because T_{reg} cells maintain immune homeostasis in an immunodominant fashion, disorders resulting from their deficiency are amenable to rescue by provision of wild-type T_{reg} cells. To test whether failure to maintain immune homeostasis in the absence of BACH2 was a consequence of defective immunoregulatory capacity, we reconstituted lethally irradiated *Rag1* $^{-/-}$ mice with KO BM in the presence or absence of WT BM. Strikingly, although we observed massive induction of effector differentiation amongst KO CD4 $^{+}$ T cells and mucosal thickening of the large intestine accompanied by infiltration of KO cells when KO BM was transferred independently, these changes were prevented by co-transfer of WT BM (Fig. 3a, b and Supplementary Fig. 21a). Consequently, animals reconstituted with KO BM showed profound weight loss and diminished survival whereas co-transfer of WT BM prevented the induction of disease (Supplementary Fig. 21b, c). The dominant immunoregulatory effect exerted by *Bach2*-sufficient (WT) BM was dependent upon FOXP3 because BM from mice which possess an intact *Bach2* locus but lack functional FOXP3 protein (*Foxp3* $^{\text{sf}}$) 20 could not rescue the phenotype induced by KO BM (Fig. 3c). Moreover, the lethal phenotype induced by KO

BM was rescued by transfer of purified splenic CD4 $^{+}$ CD25 $^{+}$ T_{reg} cells from WT mice. Thus, BACH2 is required for the prevention of lethal autoimmunity through its role in T_{reg} cell formation.

Taken together, these results demonstrated a non-redundant role for BACH2 in T_{reg} -mediated immune homeostasis. For transcriptional repression, BACH2 is dependent upon a DNA-binding basic leucine zipper region located near the carboxy terminus of the protein 21 .

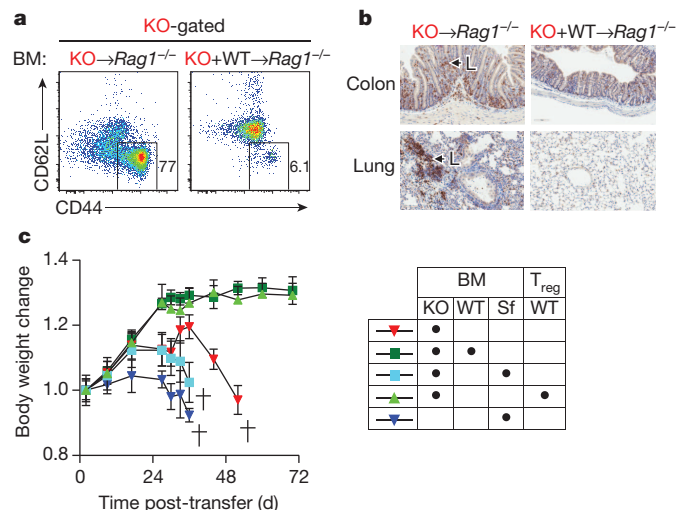


Figure 3 | BACH2 is required for suppression of lethal inflammation in a T_{reg} -dependent manner. **a**, CD44 and CD62L expression on splenic CD4 $^{+}$ T cells descended from KO BM 6 weeks following individual or mixed reconstitution of *Rag1* $^{-/-}$ mice with KO and WT BM. **b**, CD3 staining of large intestine and lung tissue from mice 6 weeks following reconstitution with indicated BM. Arrows indicate KO T cells (L). **c**, Mass of mice following individual or mixed reconstitution of *Rag1* $^{-/-}$ animals with BM from Scurfy (*Foxp3* $^{\text{sf}}$), KO or WT mice with or without transfer of 4×10^5 purified splenic CD4 $^{+}$ CD25 $^{+}$ T_{reg} cells. Data are representative of ≥ 3 independent experiments. Mass measurements were continued until < 3 mice were remaining (**c**). Error bars, s.e.m.

We found that overexpression of a truncation mutant deficient in this region (*Bach2*^{ΔZip}) did not complement defective *iT*_{reg} induction in KO CD4⁺ T cells (Fig. 4a), implicating its function as a transcriptional regulator in *T*_{reg} cell formation. To identify genes whose expression is controlled by BACH2, we performed massively parallel RNA sequencing of KO naive CD4⁺ T cells stimulated under *iT*_{reg} polarizing conditions. Consistent with its role as a transcriptional repressor, a majority of differentially expressed genes were upregulated in *Bach2*-deficient cells (Supplementary Fig. 22). Strikingly, when we compared these genes with transcripts that were induced upon differentiation of naive cells into effector-lineage *T*_H1, *T*_H2 or *T*_H17 cells, we found that 31.8% (877) of all upregulated genes (2,754) in *Bach2*-deficient cells were effector-lineage-associated genes (Fig. 4b, c).

To test whether BACH2 has a direct role in mediating these transcriptional differences, we measured genome-wide BACH2 binding in *iT*_{reg} cells by chromatin immunoprecipitation with massively parallel sequencing (ChIP-Seq), validating selected loci by quantitative PCR (Supplementary Fig. 23 and Supplementary Table 7). Remarkably, BACH2 bound 43.6% of all derepressed genes, including 408 derepressed effector lineage-associated genes (Fig. 4b, c). Examples from this group of genes are provided (Fig. 4d and Supplementary Fig. 24a), notably, BACH2 bound and repressed *Prdm1*, which encodes Blimp-1, a transcription factor critical in driving full effector differentiation in CD4⁺ T cells²². BACH2 also repressed genes with

effector-lineage-specific functions such as *Gata3*, *Irf4* and *Nfil3*, and *Il12rb1*, *Il12rb2*, *Map3k8* and *Gadd45g*, which have important roles in *T*_H2 and *T*_H1 differentiation, respectively^{23–27}. Additionally, BACH2 repressed *Ahr*, which is involved in *T*_H17 differentiation²⁸. Importantly, a number of effector-lineage-associated genes repressed by BACH2 encode proteins that transduce signals antagonistic to *T*_{reg} cell differentiation itself, including *Il12rb1*, *Il12rb2* and *Tnfrsf4*^{29,30}. Repression of *Ccr4* and *Ccr9* by BACH2 (Supplementary Fig. 24b) was also of interest since it provides some explanation for the predominance of lung and gut immunopathology in KO animals.

These data indicated that an important aspect of the function of BACH2 is to repress the differentiation programs of multiple effector lineages during *iT*_{reg} cell development. Accordingly, KO CD4⁺ T cells stimulated under *iT*_{reg} conditions aberrantly expressed cytokines associated with effector lineages (Fig. 4e). To test whether BACH2 stabilizes *iT*_{reg} cell development through repression of effector differentiation, we examined whether blockade of effector cytokines, which play an important role in positive reinforcement of effector cell differentiation, could restore *iT*_{reg} induction in KO cells. Whereas KO cells stimulated under *iT*_{reg} conditions preferentially differentiated into FOXP3⁺ cells expressing T-bet, GATA3 or RORγt, master regulators of the *T*_H1, *T*_H2 and *T*_H17 differentiation programs, respectively (Fig. 4f), addition of neutralizing antibodies against IFN-γ and IL-4 partially reverted this phenotype, preventing aberrant induction of

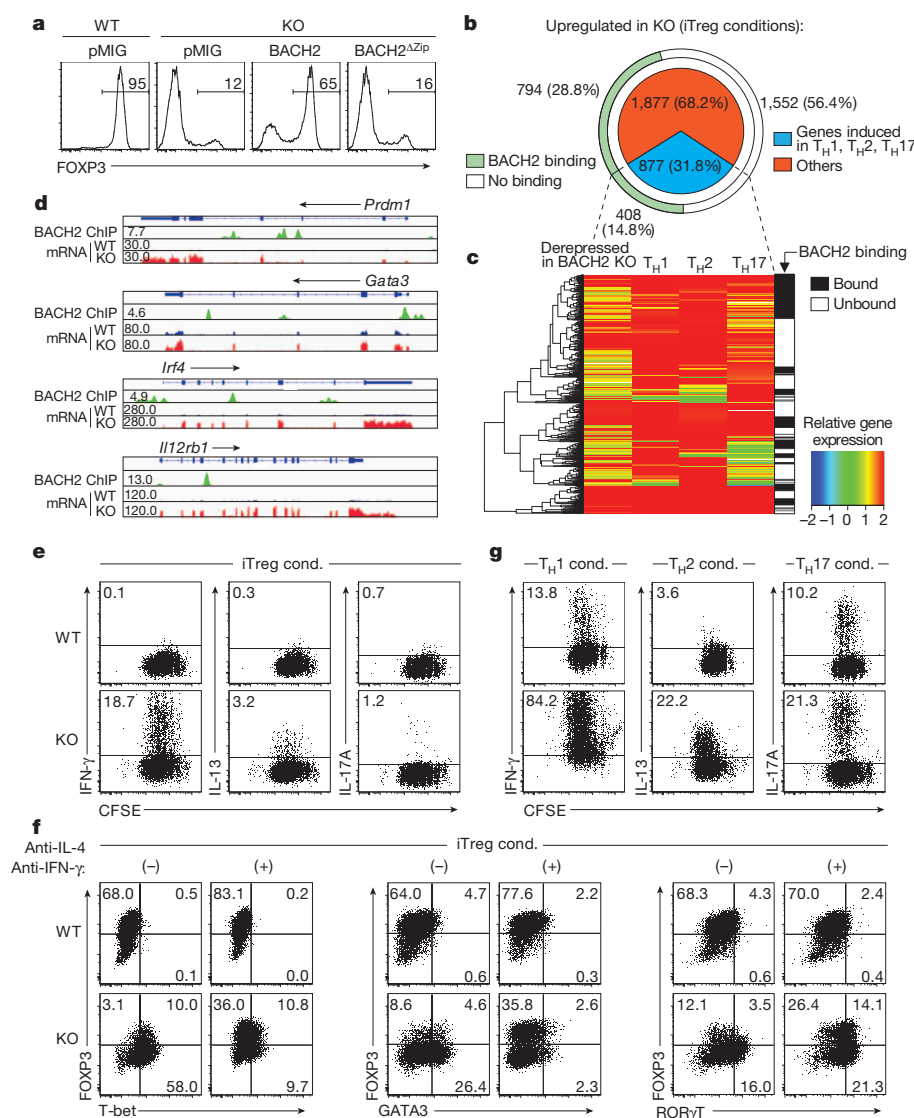


Figure 4 | BACH2 represses effector programs to stabilize *iT*_{reg} cell development. **a**, FOXP3 expression in GFP⁺ (transduced) WT and KO naive splenic CD4⁺ T cells stimulated in the presence of 2 ng ml⁻¹ TGF-β and transduced with indicated retroviruses. **b**, Derepressed genes in KO compared with WT naive CD4⁺ T cells stimulated under *iT*_{reg} polarizing conditions. Proportion of effector-lineage-associated transcripts (upregulated upon stimulation of naive CD4⁺ T cells in *T*_H1, *T*_H2 or *T*_H17 conditions respectively (pie chart) and genes that are directly bound by BACH2 in *iT*_{reg} cells (outer arc) are shown. **c**, Heat map indicating expression of effector-lineage-associated transcripts derepressed in KO cells (*iT*_{reg} conditions), their expression in wild-type *T*_H1, *T*_H2 and *T*_H17 cells and binding at their respective gene loci by BACH2 (gene-body ± 2 kb). **d**, Alignments showing binding of BACH2 to selected genes and their mRNA expression in WT and KO cells cultured under *iT*_{reg} conditions. **e**, Proliferation and effector cytokine expression in CFSE-labelled WT and KO naive CD4⁺ T cells stimulated under *iT*_{reg} conditions (cond.) for 3 days. **f**, Transcription factor expression upon stimulation of WT and KO naive CD4⁺ T cells under *iT*_{reg} conditions for 3 days in the presence or absence of indicated anti-cytokine neutralizing antibodies. **g**, Proliferation and effector cytokine expression in CFSE-labelled WT and KO naive CD4⁺ T cells stimulated under indicated polarizing conditions for 3 days. Data are representative of ≥ 2 independently repeated experiments (**a**, **e**–**g**).

T-bet and GATA3 and restoring FOXP3 expression. Interestingly, ROR γ t expression in KO cells increased in the presence of anti-IFN- γ and anti-IL-4 antibodies, consistent with the recognized ability of IFN- γ and IL-4 to block T_H17 differentiation. Consequently, higher levels of IL-17A were expressed by KO cells under these conditions (Supplementary Fig. 25). These observations raised the possibility that BACH2 might also constrain full effector differentiation amongst conventional T-cell subsets. Strikingly, and consistent with this hypothesis, we observed increased IFN- γ , IL-13 and IL-17A expression when KO naive CD4⁺ cells were stimulated under T_H1, T_H2 and T_H17 conditions, respectively. Thus, additional to its role in T_{reg} cell development, BACH2 limits full effector differentiation in conventional CD4⁺ T cells (Fig. 4g).

During specification of a variety of tissues, negative regulators antagonistic to alternative fates often act in conjunction with positive regulators to stabilize lineage identity¹. We have identified a function of BACH2 in repressing the differentiation programs of multiple effector lineages in CD4⁺ T cells. By doing so, BACH2 stabilizes the development of T_{reg} cells while limiting full effector differentiation in conventional T cell lineages. Thus, at both a cellular and molecular level, BACH2 functions to constrain immune activation, enabling it to play a critical role in the maintenance of immune homeostasis. These findings help explain the emergence of BACH2 as a key node in human autoimmunity.

METHODS SUMMARY

Experiments were approved by the Institutional Animal Care and Use Committees of the NCI and NIAMS and performed in accordance with NIH guidelines. C57BL/6J, *Rag1*^{-/-} (B6.129S7-Rag1^{tm1Mom/J}), *Ly5.1*^{+/+} (B6.SJL-Ptprc^{ab}/BoyJ) and *Foxp3*^{GFP} (B6.Cg-Foxp3^{tm2Tch/J}) mice were purchased from The Jackson Laboratory. *Bach2* KO mice, which have been previously described⁹, were backcrossed >16 times with C57BL/6 mice.

Full Methods and any associated references are available in the online version of the paper.

Received 22 November 2012; accepted 17 April 2013.

Published online 2 June 2013.

1. Rothenberg, E. V., Scripture-Adams, D. D., Competition and collaboration. GATA-3, PU.1, and Notch signaling in early T-cell fate determination. *Semin. Immunol.* **20**, 236–246 (2008).
2. Ferreira, M. A. et al. Identification of *IL6R* and chromosome 11q13.5 as risk loci for asthma. *Lancet* **378**, 1006–1014 (2011).
3. Franke, A. et al. Genome-wide meta-analysis increases to 71 the number of confirmed Crohn's disease susceptibility loci. *Nature Genet.* **42**, 1118–1125 (2010).
4. Christodoulou, K. et al. Next generation exome sequencing of paediatric inflammatory bowel disease patients identifies rare and novel variants in candidate genes. *Gut* <http://dx.doi.org/10.1136/gutjnl-2011-301833> (28 April 2012).
5. Dubois, P. C. et al. Multiple common variants for celiac disease influencing immune gene expression. *Nature Genet.* **42**, 295–302 (2010).
6. Jin, Y. et al. Genome-wide association analyses identify 13 new susceptibility loci for generalized vitiligo. *Nature Genet.* **44**, 676–680 (2012).
7. International Multiple Sclerosis Genetics Consortium & The Wellcome Trust Case Control Consortium 2. Genetic risk and a primary role for cell-mediated immune mechanisms in multiple sclerosis. *Nature* **476**, 214–219 (2011).
8. Cooper, J. D. et al. Meta-analysis of genome-wide association study data identifies additional type 1 diabetes risk loci. *Nature Genet.* **40**, 1399–1401 (2008).
9. Muto, A. et al. The transcriptional programme of antibody class switching involves the repressor Bach2. *Nature* **429**, 566–571 (2004).
10. Ochiai, K. et al. Plasmacytic transcription factor Blimp-1 is repressed by Bach2 in B cells. *J. Biol. Chem.* **281**, 38226–38234 (2006).
11. Muto, A. et al. Bach2 represses plasma cell gene regulatory network in B cells to promote antibody class switch. *EMBO J.* **29**, 4048–4061 (2010).
12. Sigmundsdottir, H. & Butcher, E. C. Environmental cues, dendritic cells and the programming of tissue-selective lymphocyte trafficking. *Nature Immunol.* **9**, 981–987 (2008).
13. Lloyd, C. M. et al. CC chemokine receptor (CCR)3/Eotaxin is followed by CCR4/monocyte-derived chemokine in mediating pulmonary T helper lymphocyte type 2 recruitment after serial antigen challenge *in vivo*. *J. Exp. Med.* **191**, 265–274 (2000).
14. O'Shea, J. J. & Paul, W. E. Mechanisms underlying lineage commitment and plasticity of helper CD4⁺ T cells. *Science* **327**, 1098–1102 (2010).
15. Zhu, J., Yamane, H. & Paul, W. E. Differentiation of effector CD4 T cell populations. *Annu. Rev. Immunol.* **28**, 445–489 (2010).
16. Sakaguchi, S., Fukuma, K., Kuribayashi, K. & Masuda, T. Organ-specific autoimmune diseases induced in mice by elimination of T cell subset. I. Evidence for the active participation of T cells in natural self-tolerance; deficit of a T cell subset as a possible cause of autoimmune disease. *J. Exp. Med.* **161**, 72–87 (1985).
17. Gavin, M. A. et al. Foxp3-dependent programme of regulatory T-cell differentiation. *Nature* **445**, 771–775 (2007).
18. Zheng, Y. et al. Genome-wide analysis of Foxp3 target genes in developing and mature regulatory T cells. *Nature* **445**, 936–940 (2007).
19. Cheng, G. et al. IL-2 receptor signaling is essential for the development of Klrp1⁺ terminally differentiated T regulatory cells. *J. Immunol.* **189**, 1780–1791 (2012).
20. Brunkow, M. E. et al. Disruption of a new forkhead/winged-helix protein, scurf, results in the fatal lymphoproliferative disorder of the scurfy mouse. *Nature Genet.* **27**, 68–73 (2001).
21. Oyake, T. et al. Bach proteins belong to a novel family of BTB-basic leucine zipper transcription factors that interact with Mafk and regulate transcription through the NF-E2 site. *Mol. Cell. Biol.* **16**, 6083–6095 (1996).
22. Crotty, S., Johnston, R. J. & Schoenberger, S. P. Effectors and memories: Bcl-6 and Blimp-1 in T and B lymphocyte differentiation. *Nature Immunol.* **11**, 114–120 (2010).
23. Rengarajan, J. et al. Interferon regulatory factor 4 (IRF4) interacts with NFATc2 to modulate interleukin 4 gene expression. *J. Exp. Med.* **195**, 1003–1012 (2002).
24. Zheng, W. & Flavell, R. A. The transcription factor GATA-3 is necessary and sufficient for Th2 cytokine gene expression in CD4 T cells. *Cell* **89**, 587–596 (1997).
25. Murphy, K. M. et al. Signaling and transcription in T helper development. *Annu. Rev. Immunol.* **18**, 451–494 (2000).
26. Watford, W. T. et al. Tpl2 kinase regulates T cell interferon- γ production and host resistance to *Toxoplasma gondii*. *J. Exp. Med.* **205**, 2803–2812 (2008).
27. Kashiwada, M., Cassel, S. L., Colgan, J. D. & Rothman, P. B. NFIL3/E4BP4 controls type 2 T helper cell cytokine expression. *EMBO J.* **30**, 2071–2082 (2011).
28. Veldhoen, M. et al. The aryl hydrocarbon receptor links T_H17-cell-mediated autoimmunity to environmental toxins. *Nature* **453**, 106–109 (2008).
29. Xiao, X. et al. OX40 signaling favors the induction of T_H9 cells and airway inflammation. *Nature Immunol.* **13**, 981–990 (2012).
30. Oldenhove, G. et al. Decrease of Foxp3⁺ Treg cell number and acquisition of effector cell phenotype during lethal infection. *Immunity* **31**, 772–786 (2009).

Supplementary Information is available in the online version of the paper.

Acknowledgements This research was supported by the Intramural Research Programs of the National Cancer Institute (NIH) and the National Institute of Arthritis and Musculoskeletal and Skin Diseases, the NIH Center for Regenerative Medicine and the JSPS Research Fellowship for Japanese Biomedical and Behavioural Researchers at NIH. We thank D. N. Roychoudhuri, D. C. Macallan, G. E. Griffin, S.A. Rosenberg, M.S. Rao, Y. Ji, D. Palmer, M. Sukumar, G. Fabozzi, K. Hanada, E. Lugli, J. H. Pan and N. Van Panhuys for discussions, A. Mixon and S. Farid for cell sorting, G. McMullen for mouse handling and Y. Luo, Y. Wakabayashi, J. Zhu, G. Gutierrez-Cruz and H. W. Sun for help with sequencing and analysis.

Author Contributions R.R., K.H., J.J.O'S. and N.P.R. wrote the manuscript and designed experiments; R.R., K.H., K.M., D.C., M.B., G.S., Y.K., B.D., Z.Y., H.T. and H.L. carried out experiments; R.R., H.Z., G.V., E.W., V.S., J.J.O'S. and N.P.R. analysed experiments; V.H. performed histopathological evaluations; G.P., A.N., A.M. and K.I. contributed reagents; C.A.K., M.R., P.M., J.G.C., J.R., D.B., A.N., A.M., F.M.M., L.G., V.S. and K.I. edited the manuscript.

Author Information Massively parallel RNA and ChIP sequencing data have been deposited to the Gene Expression Omnibus under the accession number GSE45975. Reprints and permissions information is available at www.nature.com/reprints. The authors declare no competing financial interests. Readers are welcome to comment on the online version of the paper. Correspondence and requests for materials should be addressed to R.R. (roychoudhuri@mail.nih.gov), J.J.O'S. (osheajo@mail.nih.gov) or N.P.R. (restifo@nih.gov).

METHODS

Mice. Experiments were approved by the Institutional Animal Care and Use Committees of the NCI and NIAMS and performed in accordance with NIH guidelines. C57BL/6J, *Rag1*^{-/-} (B6.129S7-*Rag1*^{tm1Mom/J}), *Ly5.1*^{+/+} (B6.SJL-Ptprc^{pep}/BoyJ) and *Foxp3*^{GFP} (B6.Cg-*Foxp3*^{tm2Tch/J}) mice were purchased from The Jackson Laboratory. *Bach2* KO mice, which have been previously described⁹, were backcrossed >16 times with C57BL/6 mice.

Plasmid DNA and cloning. For the generation of pMSCV-IRES-Bach2-Thy1.1, a fragment of *Bach2* cDNA was amplified by PCR from pMSCV-IRES-Bach2-EGFP¹ using the following primers: forward, 5'-GTATTAGCGCGCCGACAGCATGGACTACAAGGACGACGATGACAAG-3' and reverse, 5'-GATGAAATC GATCTAGGCATAATCTTCTCTGGGCTGTCGTCG-3' and cloned between the NotI and ClaI sites within the multiple cloning site of pMSCV-IRES-Thy1.1-DEST (pMIT; Addgene 17442). pMIG-Bach2 and pMIG-Bach2^{ΔZfp} have been described previously¹⁰.

Cell culture. CD4⁺ T cells from spleens and lymph nodes of 6–8-week-old mice were purified by negative magnetic selection (Miltenyi) followed by sorting of naive CD4⁺ CD62L^{high} CD44^{low} CD25^{low} cells using a FACSAria II sorter (BD). For isolation of T_{reg} cells, CD4⁺ GFP⁺ cells were sorted from *Foxp3*^{GFP} reporter mice or CD4⁺ CD25^{high} cells were sorted from WT mice. Naive CD4⁺ T cells were activated with plate-bound anti-CD3 and soluble anti-CD28 (10 μg ml⁻¹ each; eBioscience) in media for 3 days either under: Th0 conditions (media alone); Th1 conditions (IL-12 (20 ng ml⁻¹, R&D Systems) and anti-IL-4 neutralizing antibodies (10 μg ml⁻¹, BioXCell); Th2 conditions (IL-4 (20 ng ml⁻¹, R&D Systems) and anti-IFN-γ neutralizing antibodies (10 μg ml⁻¹, BD Pharmingen); Th17 conditions (IL-6 (20 ng ml⁻¹, R&D Systems), human TGF-β1 (2 ng ml⁻¹, R&D Systems), anti-IFN-γ neutralizing antibodies (10 μg ml⁻¹) and anti-IL-4 neutralizing antibodies (10 μg ml⁻¹)) or iTreg conditions (IL-2 (100 IU ml⁻¹, R&D Systems) and human TGF-β1 (5 ng ml⁻¹)). Where indicated, purified naive CD4⁺ T cells were labelled with carboxyfluorescein succinimidyl ester (CFSE, 1 mM, Molecular Probes) for 8 min at room temperature. The labelling reaction was quenched by washing in FCS.

Retroviral transduction. 20 μg of retroviral plasmid DNA along with 6 μg pCL-Eco plasmid DNA were transfected using 60 μl Lipofectamine 2000 in 3 ml OptiMEM (Invitrogen) for 8 h in antibiotic-free media into Platinum-E ecotropic packaging cells (Cell Biolabs) plated a day prior on poly-D-lysine-coated 10-cm plates (Becton Dickinson) at a concentration of 6 × 10⁶ cells per plate. Media were replaced 8 h after transfection and cells were incubated for a further 48 h. Retroviral supernatants were collected and spun at 2,000g for 2 h at 32 °C onto 24-well non-tissue culture treated plates coated overnight in Retronectin (20 μg ml⁻¹; Takara Bio) and 5 μg ml⁻¹ anti-CD3 (2C11) and 5 μg ml⁻¹ anti-CD28 (37.51) (eBioscience). Supernatant was discarded and cells were applied to plates 1 day after stimulation in triplicate wells for 24 h in the presence of polarizing cytokines. Following transduction, cells were cultured on fresh anti-CD3 coated plates until analysis at day 5 post-stimulation.

Antibodies and flow cytometry. The following fluorescent dye-conjugated antibodies against surface and intracellular antigens were used: anti-FOXP3 (FJK-16s), anti-IL-13 (eBio13A), anti-IL-17A clone eBio17B7 and anti-GATA3 clone TWAJ (eBioscience); anti-Thy1.1 (OX-7), anti-Ly5.1 (A20), anti-KLRG1 (2F1), anti-B220 (RA3-6B2), anti-NK1.1 (PK136), anti-CTLA4 (UC10-4F10-11), anti-CD4 (RM4-5), anti-CD25 (PC61), anti-CD62L (MEL-14), anti-IFN-γ (Cat 554413), anti-IL-4 (Cat 554435), anti-CD44 (IM7) and anti-CD8a clone 53-6.7 (BD Biosciences); anti-GITR Cat. FAB5241A (R&D Systems) and anti-CD19 clone 6D5 (Biolegend). Cells were incubated with specific antibodies for 30 min on ice in the presence of 2.4G2 monoclonal antibody to block FcγR binding. All samples were acquired with a Canto II flow cytometer (Becton Dickinson) and analysed using FlowJo software (TreeStar). Intracellular staining for FOXP3 was carried out using the FOXP3 staining kit (eBioscience). To determine cytokine expression, cellular suspensions containing T cells were stimulated in media containing phorbol 12-myristate 13-acetate, ionomycin and brefeldin-A (Leukocyte activation cocktail with Golgiplug; BD biosciences) for 4 h. After stimulation, cells were stained an amine-reactive exclusion-based viability dye (Invitrogen) and with antibodies against cell-surface antigens, fixed and permeabilized followed by intracellular staining with specific anti-cytokine antibodies. Single-cell suspensions from lung tissues were prepared by mechanical disruption (GentleMACS, Miltenyi). CountBright beads were spiked-in for the flow cytometric quantification of absolute cell number (Invitrogen).

Autoantibody enzyme-linked immunosorbent assay (ELISA). For measurement of antinuclear antibodies (ANAs), ELISA assays were performed on mouse serum according to manufacturer's instructions (Alpha Diagnostic International). For the measurement of anti-dsDNA autoantibodies, dsDNA-coated plates (Calbiotech) were incubated with serum samples and anti-dsDNA titres were

evaluated using a horseradish peroxidase-conjugated anti-mouse antibody (IgG, IgM, IgA) (Alpha Diagnostic International).

Quantitative reverse-transcription polymerase chain reaction (qRT-PCR). Cells were sorted or transferred into RNeasy lysis solution (Ambion) and stored at -80 °C. Total RNA from pelleted cells was isolated using the RNeasy Plus mini kit (Qiagen). First-strand cDNA synthesis was performed using random priming with the high-capacity cDNA synthesis kit (Applied Biosystems) in the presence of Superscript RNase inhibitor (Ambion). cDNA was used as a template for quantitative PCR reactions using the following Taqman primer-probes (Applied Biosystems): *Actb* (mm00607939_s1), *Bach2* (mm00464379_m1) and *Foxp3* (mm00475162_m1). Reactions were performed using Fast Universal PCR Mastermix (Applied Biosystems) according to the manufacturer's instructions and thermocycled in quadruplicate 10 μl reactions in 384-well plates. Signals in the FAM channel were normalized to ROX intensity, and *C_t* values were calculated using automatically determined threshold values using SDS software (Applied Biosystems).

Bone marrow chimaeras and T_{reg} cell rescue experiments. For bone marrow reconstitution experiments, *Rag1*^{-/-} mice were administered 1,000 Gy total-body γ-radiation from a ¹³⁷Cs source before intravenous injection of BM cells depleted of mature lineages from single-cell bone-marrow preparations using antibody-coupled magnetic beads (Miltenyi). Bone marrow from 6–10-week-old donor mice were used except with Scurfy mice where 12 day old pups were used as donors. Where indicated, 4 × 10⁵ fluorescence-activated cell sorting (FACS)-purified CD4⁺ CD25⁺ T cells were transferred intravenously into mice 1 day after transfer of bone marrow cells.

In vivo iT_{reg} induction. *Rag1*^{-/-} mice were injected intravenously with 4 × 10⁵ CD4⁺ CD25⁺ CD45RB^{high} cells from wild-type or *Bach2*-deficient mice. On day 21 to 23, cells were isolated and analysed for FOXP3 expression.

In vitro suppression assay. Varying numbers of WT and KO CD4⁺ CD25⁺ T_{reg} cells were cultured in 96-well round-bottom plates with 5 × 10⁴ CFSE-labelled naive CD4⁺ CD62L^{high} CD44^{low} responder (T_{resp}) cells along with 1 × 10⁴ CD11c⁺ dendritic cells used as antigen-presenting cells, isolated by immunomagnetic selection (Miltenyi). Cells were stimulated with 1 μg ml⁻¹ anti-CD3 antibody (BD Biosciences) for 72 h at 37 °C and 5% CO₂. T_{resp} cell proliferation was measured by flow cytometry.

In vivo suppression assay. *In vivo* suppression assays were done as previously described³¹. Briefly, *Rag2*^{-/-} mice were injected intravenously with 1 × 10⁵ CFSE-labelled naive CD4⁺ CD25⁺ CD45RB^{hi} (T_{resp}) cells from CD45.1 mice with or without 1 × 10⁵ wild type or *BACH2*-deficient CD4⁺ *Foxp3*^{GFP+} T_{reg} cells. Mice were analysed on day seven for T_{resp} cell proliferation by flow cytometry.

Transfer colitis model. The transfer colitis model has been described previously³². Briefly, *Rag1*^{-/-} mice were injected intravenously with 4 × 10⁵ FACS-sorted naive CD4⁺ CD25⁺ CD45RB^{high} cells from CD45.1⁺ mice with or without 1 × 10⁵ WT or KO CD4⁺ CD25^{high} T_{reg} cells. Mice were monitored weekly for weight loss and signs of disease, and killed at week 6. Sections of the proximal, mid-, and distal colon were fixed in buffered 10% formalin and stained with haematoxylin and eosin (H&E).

RNA sequencing. RNA sequencing was performed and analysed as described previously³³. Total RNA was prepared from approximately 1 million cells by using mirVana miRNA Isolation Kit (AM1560, ABI). 200 ng of total RNA was subsequently used to prepare RNA-seq libraries by using TruSeq SRRNA sample prep kit (FC-122-1001, Illumina) according to the manufacturer's instructions. The libraries were sequenced for 50 cycles (single read) using a HiSeq 2000 sequencer (Illumina). Sequence reads from each cDNA library were mapped onto the mouse genome build mm9 by using Tophat, and the mappable data were then processed by Cufflinks³⁴. The obtained data were normalized based on RPKM (reads per kilobase exon model per million mapped reads). To find differentially regulated genes, we used a 1.5-fold change difference between genotypes and a fourfold change difference between different lineages.

Chromatin immunoprecipitation. T cells were chemically crosslinked and sonicated to generate fragmented genomic DNA. Chromatin immunoprecipitation was performed using an anti-BACH2 antibody (N-2; Tohoku University). For sequencing of immunoprecipitated DNA, DNA fragments were blunt-end ligated to the Illumina adaptors, amplified, and sequenced by using the Hi-Seq 2000 sequencer (Illumina). Sequence reads of 50 base pairs were obtained by using the Illumina Analysis Pipeline. All reads were mapped to the mouse genome (mm9), and only uniquely matching reads were retained. After removal of redundant reads, enriched peaks were called using ChIP-Seq analysis tool MACS³⁵. Around 20,000 peaks were detected at a *P*-value level of less than 1 × 10⁻⁴ and false discovery rate of less than 5%. Peaks in ±2 kb vicinity of gene bodies were assigned to genes to identify the bound target genes. For PCR-based confirmation of BACH2 binding, chromatin immunoprecipitation was performed as described above, and qPCR reactions were carried out on input and immunoprecipitated

DNA using the Power SYBR Green kit (Applied Biosystems) and primers as specified in Supplementary Table 7.

Microarray analysis. 100 ng of total RNA extracted as previously described was amplified using Ovation Pico WTA System V2 (NuGEN) according to the manufacturer's instructions. Briefly, first-strand cDNA was synthesized using the SPIA tagged random and oligo dT primer mix in 10 µl reactions after denaturation and incubated at 65 °C for 2 min and priming at 4 °C followed by extension at 25 °C for 30 min, 42 °C for 15 min and 77 °C for 15 min. Second strand cDNA synthesis of fragmented RNA was performed using DNA polymerase at 4 °C for 1 min, 25 °C for 10 min, 50 °C for 30 min and 80 °C for 20 min. 5' double stranded cDNA was used as the template for isothermal single-strand cDNA amplification following a cycle of DNA/RNA primer binding, DNA replication, strand displacement and RNA cleavage at 4 °C for 1 min, 47 °C for 75 min and 95 °C for 5 min in total 100 µl reaction. Samples were fragmented and biotinylated using the Encore Biotin Module (NuGEN) according to the manufacturer's instructions. Biotinylated cDNA was then hybridized to Mouse Gene 1.0 ST arrays (Affymetrix) overnight at 45 °C and stained on a Genechip Fluidics Station 450 (Affymetrix), according to the respective manufacturers' instructions. Arrays were scanned on a GeneChip Scanner 3000 7G (Affymetrix). Global gene expression profiles rank ordered by

relative fold-change values were analysed by using Gene set enrichment analysis software (Broad Institute, MIT). *P* values were calculated using Student's *t*-test using Partek Genomic Suite after Robust Multiarray Average normalization.

Statistical analysis. Student's *t*-test was used unless otherwise specified to calculate statistical significance of the difference in mean values and *P* values are provided. For calculation of statistical significance of differences in clinical histopathology scores, the Wilcoxon rank-sum test was used.

31. Pesu, M. *et al.* T-cell-expressed proprotein convertase furin is essential for maintenance of peripheral immune tolerance. *Nature* **455**, 246–250 (2008).
32. Powrie, F., Carlino, J., Leach, M. W., Mauze, S. & Coffman, R. L. A critical role for transforming growth factor- β but not interleukin 4 in the suppression of T helper type 1-mediated colitis by CD45RB^{low} CD4⁺ T cells. *J. Exp. Med.* **183**, 2669–2674 (1996).
33. Vahedi, G. *et al.* STATs shape the active enhancer landscape of T cell populations. *Cell* **151**, 981–993 (2012).
34. Trapnell, C. *et al.* Transcript assembly and quantification by RNA-Seq reveals unannotated transcripts and isoform switching during cell differentiation. *Nature Biotechnol.* **28**, 511–515 (2010).
35. Zhang, Y. *et al.* Model-based analysis of ChIP-Seq (MACS). *Genome Biol.* **9**, R137 (2008).

Rev-Erbs repress macrophage gene expression by inhibiting enhancer-directed transcription

Michael T. Y. Lam¹, Han Cho², Hanna P. Lesch¹, David Gosselin¹, Sven Heinz¹, Yumiko Tanaka-Oishi¹, Christopher Benner¹, Minna U. Kaikkonen¹, Aneesa S. Kim³, Mika Kosaka¹, Cindy Y. Lee¹, Andy Watt³, Tamar R. Grossman³, Michael G. Rosenfeld^{4,5}, Ronald M. Evans^{2,5} & Christopher K. Glass^{1,4}

Rev-Erb- α and Rev-Erb- β are nuclear receptors that regulate the expression of genes involved in the control of circadian rhythm^{1,2}, metabolism^{3,4} and inflammatory responses⁵. Rev-Erbs function as transcriptional repressors by recruiting nuclear receptor co-repressor (NCoR)–HDAC3 complexes to Rev-Erb response elements in enhancers and promoters of target genes^{6–8}, but the molecular basis for cell-specific programs of repression is not known. Here we present evidence that in mouse macrophages Rev-Erbs regulate target gene expression by inhibiting the functions of distal enhancers that are selected by macrophage-lineage-determining factors, thereby establishing a macrophage-specific program of repression. Remarkably, the repressive functions of Rev-Erbs are associated with their ability to inhibit the transcription of enhancer-derived RNAs (eRNAs). Furthermore, targeted degradation of eRNAs at two enhancers subject to negative regulation by Rev-Erbs resulted in reduced expression of nearby messenger RNAs, suggesting a direct role of these eRNAs in enhancer function. By precisely defining eRNA start sites using a modified form of global run-on sequencing that quantifies nascent 5' ends, we show that transfer of full enhancer activity to a target promoter requires both the sequences mediating transcription-factor binding and the specific sequences encoding the eRNA transcript. These studies provide evidence for a direct role of eRNAs in contributing to enhancer functions and suggest that Rev-Erbs act to suppress gene expression at a distance by repressing eRNA transcription.

To study the mechanisms underlying Rev-Erb regulation of macrophage gene expression, we first determined genome-wide binding profiles in mouse RAW264.7 macrophages engineered to contain biotin-tagged Rev-Erb- α and Rev-Erb- β . Chromatin immunoprecipitation linked to deep sequencing (ChIP-Seq) indicated enrichment for both Rev-Erb- α and Rev-Erb- β at the promoter of the circadian target gene *Bmal1* (also known as *Arntl*) (Supplementary Fig. 1a), in accordance with previous studies^{1,7}. We focused on a core set of highest confidence peaks ($n = 1,544$) occupied by both proteins for detailed analysis (Fig. 1a and Supplementary Fig. 1b). Most (~90%) Rev-Erb peaks were in intra- and intergenic regions at least 1 kilobase (kb) away from annotated transcription start sites (TSSs) (Supplementary Fig. 1c), exemplified by binding sites vicinal to the *Mmp9* and *Cx3cr1* genes (Fig. 1b). In addition, ~70% of Rev-Erb-bound sites were in regions demarcated by high H3K4me1 and low H3K4me3, a combination characteristic of enhancer elements⁹ (Fig. 1a). *De novo* motif discovery of Rev-Erb-bound loci returned significant enrichment for binding sites for Rev-Erb, PU.1, API1 and C/EBP (Fig. 1c). PU.1, API1 and C/EBP transcription factors are required for macrophage differentiation¹⁰ and have recently been shown to select the majority of the enhancer-like elements in macrophages¹¹. Colocalization of Rev-Erbs with PU.1 and C/EBP in macrophages was confirmed by comparison with direct binding data for these factors¹¹ (Fig. 1a, b). Consistent with these findings, most of the Rev-Erb-bound sites

defined here localize to enhancer-like elements specific for macrophages (Supplementary Fig. 2a, b).

We next performed global run-on sequencing (GRO-seq)¹² in Rev-Erb- α /Rev-Erb- β -deficient and wild-type bone-marrow-derived macrophages (BMDMs) from *Tie2-Cre*; *Rev-Erb α ^{fllox/fllox}*; *Rev-Erb β ^{fllox/fllox}* (double knockout; DKO) animals and Cre-negative littermates (wild type). *Tie2-Cre* expression in haematopoietic stem cells¹³ resulted in excision efficiencies in DKO macrophages of 85% for Rev-Erb- α and 92% for Rev-Erb- β (Supplementary Fig. 3). GRO-seq analysis indicated that 142 mRNAs were significantly upregulated in DKO macrophages (P value <0.005), and 71 genes were downregulated (P value <0.005) (Supplementary Table 1). Quantitative polymerase chain reaction with reverse transcription (qRT-PCR) confirmed upregulation of *Mmp9* and *Cx3cr1* mRNAs in Rev-Erb DKO macrophages (Fig. 1d). Conversely, constitutive expression of either Rev-Erb- α or Rev-Erb- β in RAW264.7 macrophages resulted in repression of *Mmp9* and *Cx3cr1* expression (Fig. 1e and Supplementary Fig. 4a, b). Analysis of multiple independent clones indicated that the extent of *Mmp9* and *Cx3cr1* repression correlated with Rev-Erb expression levels (Supplementary Fig. 4c–f). Genes that were upregulated in DKO macrophages were significantly closer to Rev-Erb-binding sites than downregulated genes (Fig. 1f), consistent with primary roles of Rev-Erbs as transcriptional repressors. However, only 3 of the 142 upregulated genes had Rev-Erb peaks within 2 kb of annotated TSSs, suggesting that Rev-Erbs primarily act to repress gene expression at distant enhancer-like elements.

We next tested genomic regions containing Rev-Erb-binding sites for enhancer activity. A 983 base pair (bp) region surrounding the Rev-Erb-bound site at –5 kb from the *Mmp9* TSS was cloned downstream of a luciferase reporter driven by a TATA-like promoter (Fig. 1g). This region increased reporter gene activity in RAW264.7 macrophages and was sensitive to Rev-Erb repression (Fig. 1g). By contrast, this element is inactive in a hepatoma cell line that lacks expression of PU.1 (Supplementary Fig. 5). RAR-related orphan nuclear receptors (RORs) also bind to Rev-Erb response elements and constitutively activate gene expression¹⁴. Consistent with this, we found that constitutive expression of ROR- α increased activity of the *Mmp9* enhancer element (Supplementary Fig. 6). Co-expression of wild-type Rev-Erb- β , but not Rev-Erb- β with a mutation disrupting sequence-specific DNA binding, antagonized ROR- α activation (Supplementary Fig. 6). Six of six other Rev-Erb-bound distal regions chosen for analysis were activated by ROR- α , four of which were antagonized by Rev-Erb co-transfection.

Examination of GRO-seq data at intergenic Rev-Erb-binding sites exhibiting the enhancer histone signature H3K4me1^{hi}/H3K4me3^{lo} indicated the presence of bidirectional transcripts (Fig. 2a–c), consistent with recent studies indicating that RNAs are transcribed from distal enhancer elements on a genome-wide scale^{15–17}. To determine whether transcripts were being initiated at enhancers, we modified the GRO-seq

¹Department of Cellular and Molecular Medicine, University of California, San Diego, 9500 Gilman Drive, La Jolla, California 92093, USA. ²Salk Institute for Biological Studies, 10010 North Torrey Pines Road, La Jolla, California 92037, USA. ³Isis Pharmaceuticals, Inc., 2855 Gazelle Court, Carlsbad, California 92010, USA. ⁴Department of Medicine, University of California, San Diego, 9500 Gilman Drive, La Jolla, California 92093, USA. ⁵Howard Hughes Medical Institute, 4000 Jones Bridge Road, Chevy Chase, Maryland 20815-6789, USA.

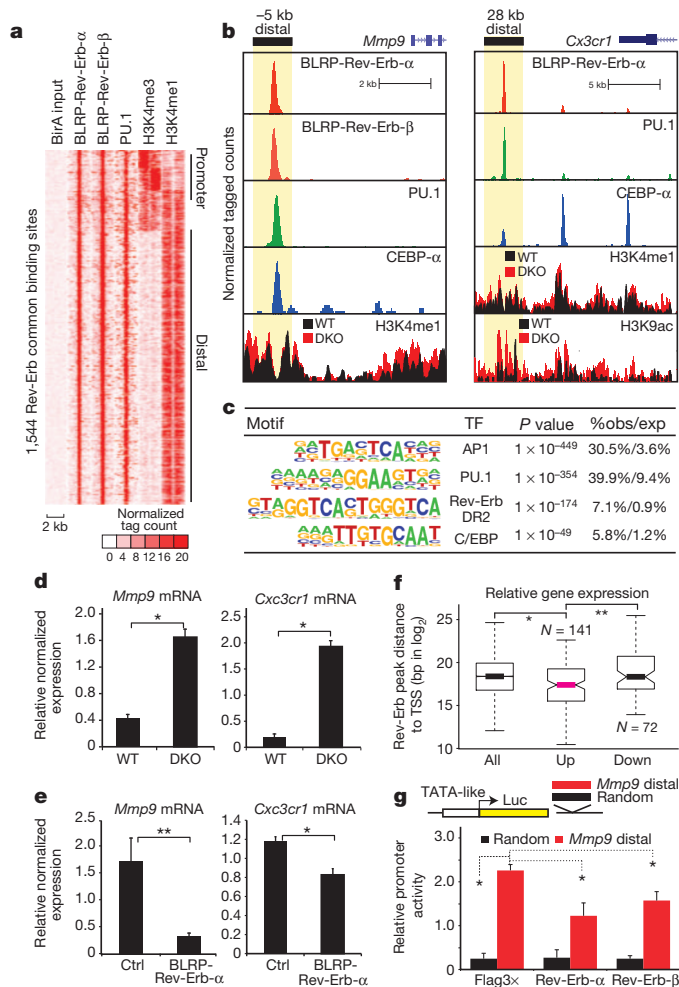


Figure 1 | Rev-Erb binding and function at macrophage-specific enhancers. **a**, Cluster plot of tag counts for H3K4me1 and H3K4me3 ChIP-Seq, 5'-GRO-seq and GRO-seq at 544 intergenic Rev-Erb-bound, H3K4me1^{hi}/H3K4me3^{lo} regions. **b**, Genomic loci for *Mmp9* and *Cx3cr1* showing indicated tag counts for GRO-seq, 5'-GRO-seq and Rev-Erb- β . **c**, Distribution of averaged macrophage GRO-seq eRNA signal in macrophages flanking Rev-Erb intergenic sites defined in BMDMs ($n = 544$, blue) and Rev-Erb intergenic sites defined in liver ($n = 521$, red*). Mac, macrophage. 'Plus' and 'minus' refer to the direction of DNA sequences. **d**, Distribution of average 5'-GRO-seq signal from Rev-Erb- α -overexpressing (green) and control RAW264.7 macrophages (black) flanking the top 100 Rev-Erb sites. **e**, **f**, qPCR analysis of the -5 kb *Mmp9* and 28 kb *Cx3cr1* eRNAs in Rev-Erb DKO (wild type, $N = 6$; DKO, $N = 5$) (**e**) and Rev-Erb- α -overexpressing RAW264.7 macrophages (control, $N = 13$; Rev-Erb- α , $N = 14$; independent lines) (**f**). Data represent mean \pm s.e.m. * $P < 0.01$, ** $P < 0.005$ versus control by two-tailed Student's *t*-test.

protocol to detect nascent RNA with a 5' 7-methylguanylated cap (5'-GRO-seq). This methodology precisely localized start sites of well-characterized mRNAs (Supplementary Fig. 7) and identified eRNA initiation at 76% of the Rev-Erb-binding sites at enhancer-like regions of the genome (Fig. 2a). Most (56%) of these sites direct bidirectional transcription, exemplified by the *Mmp9* -5 kb and *Cx3cr1* 28 kb enhancers (Fig. 2b). No significant GRO-seq signal was detected in macrophages at locations of intergenic Rev-Erb- α peaks in liver⁸ (Fig. 2c), consistent with cell-type-specific eRNA expression.

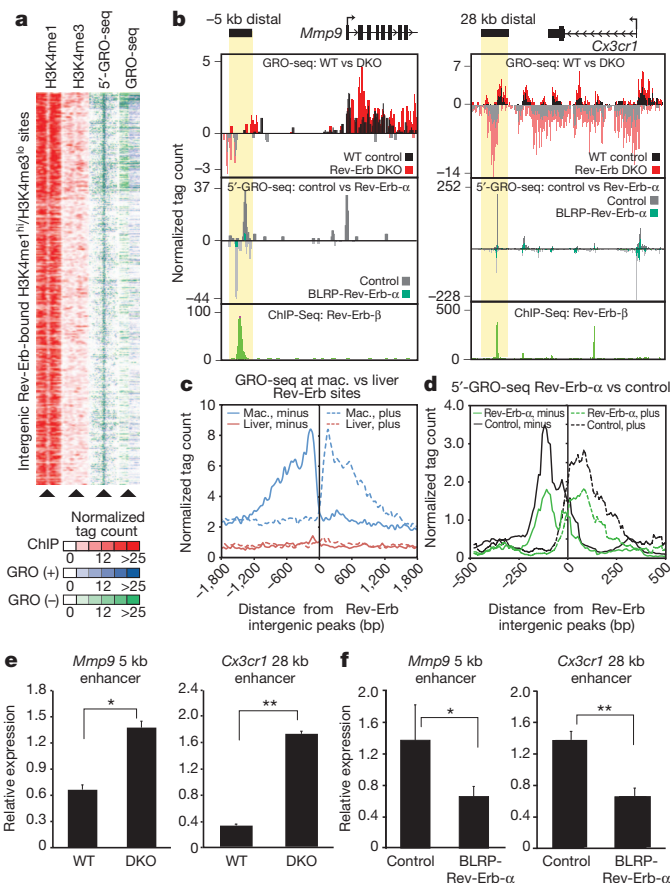


Figure 2 | Rev-Erb negatively regulates enhancer transcription. **a**, Cluster plot of tag counts for H3K4me1 and H3K4me3 ChIP-Seq, 5'-GRO-seq and GRO-seq at 544 intergenic Rev-Erb-bound, H3K4me1^{hi}/H3K4me3^{lo} regions. **b**, Genomic loci for *Mmp9* and *Cx3cr1* showing indicated tag counts for GRO-seq, 5'-GRO-seq and Rev-Erb- β . **c**, Distribution of averaged macrophage GRO-seq eRNA signal in macrophages flanking Rev-Erb intergenic sites defined in BMDMs ($n = 544$, blue) and Rev-Erb intergenic sites defined in liver ($n = 521$, red*). Mac, macrophage. 'Plus' and 'minus' refer to the direction of DNA sequences. **d**, Distribution of average 5'-GRO-seq signal from Rev-Erb- α -overexpressing (green) and control RAW264.7 macrophages (black) flanking the top 100 Rev-Erb sites. **e**, **f**, qPCR analysis of the -5 kb *Mmp9* and 28 kb *Cx3cr1* eRNAs in Rev-Erb DKO (wild type, $N = 6$; DKO, $N = 5$) (**e**) and Rev-Erb- α -overexpressing RAW264.7 macrophages (control, $N = 13$; Rev-Erb- α , $N = 14$; independent lines) (**f**). Data represent mean \pm s.e.m. * $P < 0.01$, ** $P < 0.005$ versus control by two-tailed Student's *t*-test.

To determine whether Rev-Erbs regulate eRNA expression, transcription of nascent RNA at Rev-Erb-bound enhancers was examined in both loss- and gain-of-function models. Rev-Erb- β binding was strongly associated with a reduced 5'-GRO-seq signal at the most confident Rev-Erb- β -binding sites (Supplementary Fig. 8a). Analysis of the averaged 5'-GRO-seq signal at the top 100 Rev-Erb intergenic enhancers showed a marked decrease of eRNA initiation in macrophages overexpressing Rev-Erb- α compared with control macrophages (Fig. 2d). Conversely, the GRO-seq RNA signal was increased overall in these same intergenic enhancers in Rev-Erb DKO macrophages (Supplementary Fig. 9a). In both loss- and gain-of-function experiments, the eRNA signal at the top 100 PU.1-bound enhancers showed no significant change (for example, Supplementary Fig. 9b), indicating that changes in eRNA are specific to Rev-Erb-bound elements. The effects of gain or loss of Rev-Erb function on eRNA expression at the *Mmp9* -5 kb and *Cx3cr1* 28 kb enhancers were confirmed by RT-PCR (Fig. 2e, f). Overall, levels of de-repressed eRNAs in Rev-Erb DKO macrophages were inversely correlated to levels of eRNA repression upon constitutive expression of Rev-Erb- α (Supplementary Fig. 8b).

ChIP-Seq experiments demonstrated that gain or loss of Rev-Erb function also resulted in reciprocal loss or gain of H3K9 acetylation (H3K9ac) at Rev-Erb-occupied enhancers, respectively (Fig. 1b and Supplementary Fig. 10a, c, e–g), consistent with Rev-Erb-mediated recruitment of NCoR–HDAC3 complexes⁷. By contrast, H3K9ac was not changed at the global set of PU.1 enhancers (Supplementary Fig. 10b, d). Notably, constitutive expression of Rev-Erb- α had no significant effect on H3K4me1 or PU.1 binding at Rev-Erb-bound

enhancer elements (Supplementary Fig. 11a, b), despite the profound changes in eRNA initiation (Fig. 2b, d).

Collectively, these results raised the possibility that Rev-Erbs repressed gene expression at a distance by regulating enhancer-directed transcription. Consistent with this possibility, changes in eRNA expression at Rev-Erb-bound sites due to gain or loss of Rev-Erb function were associated with changes in expression of the nearest mRNA (Supplementary Fig. 12a, b), and were better predictors than Rev-Erb binding itself (Supplementary Fig. 12c, d). In addition, although levels of eRNAs are low at steady state¹⁵, 5'-GRO-seq data suggest that the extent of engaged RNA polymerase II (RNAPII) at enhancers is often comparable to that at promoters, as exemplified by *Cx3cr1* and *Mmp9* (Fig. 2b). Three experimental approaches were used to investigate whether the synthesis of enhancer-directed RNA transcripts contributed to enhancer activity. First, we designed short interfering RNAs (siRNAs) that specifically reduced expression of eRNAs associated with the *Mmp9* or *Cx3cr1* enhancers in primary wild-type macrophages. Reduced eRNA expression was associated with a corresponding reduction of *Mmp9* and *Cx3cr1* mRNAs, but not mRNAs from their nearest expressing genes, *Ncoa5* and *Csrnp1*, respectively (Fig. 3a, b). Furthermore, these siRNAs reversed the de-repression phenotype associated with increased eRNA expression in Rev-Erb DKO macrophages. Importantly, the siRNA directed against the sense-strand *Mmp9* eRNA had no effect on expression of the antisense-strand eRNA or binding of PU.1 to the *Mmp9* –5 kb enhancer (Supplementary Fig. 13), thereby excluding potential silencing effects of the siRNA on the transcriptional activity of the –5 kb enhancer itself.

As a second approach, we used antisense oligonucleotides (ASOs) to knock down *Mmp9* –5 kb and *Cx3cr1* 28 kb enhancer eRNAs. ASOs mediate nuclear RNA degradation via an RNaseH pathway¹⁸. This provides an independent method for eRNA targeting, as siRNA-directed silencing may alter enhancer function through ways other than RNA degradation^{19,20}. We systematically screened ASOs targeting the *Mmp9* –5 kb and *Cx3cr1* 28 kb eRNAs (Supplementary Fig. 14) and selected subsets of the most effective ASOs for detailed analysis. ASOs with the ability to reduce *Mmp9* –5 kb sense-strand eRNA expression resulted in dose-dependent reduction of the corresponding *Mmp9* mRNA, but did not affect the *Cx3cr1* mRNA (Fig. 3c). ASOs with the ability to knock down the antisense-strand *Cx3cr1* 28 kb eRNA reduced *Cx3cr1*, but not *Mmp9* or *Csrnp1* expression (Fig. 3d).

As a third approach, we examined the functional significance of the *Mmp9* and *Cx3cr1* eRNAs using an enhancer assay guided by 5'-GRO-seq definition of eRNA start sites. The 983 bp sequence upstream of *Mmp9* that confers Rev-Erb-regulated enhancer activity in RAW264.7 cells encompasses a 388 bp central region containing the binding sites for PU.1, C/EBPs, AP-1 and Rev-Erbs, as well as start sites of sense- and antisense-strand eRNAs (Fig. 4a). Notably, the 388 bp core was significantly less active than the 983 bp sequence, which encodes the eRNAs (Fig. 4b). Expression of the sense-strand eRNA from the 983 bp enhancer was confirmed by RT-PCR using a reporter-specific primer for first-strand complementary DNA synthesis (Fig. 4c). Addition of DNA encoding the sense-strand eRNA, but not the antisense-strand eRNA, restored transcriptional activity to the 388 bp core (Fig. 4d), consistent with the finding that siRNAs and ASOs directed against the sense-strand eRNA resulted in reduction of *Mmp9* mRNA expression. A similar activity of the sense-strand eRNA was observed when the 983 bp or core enhancer elements were inserted in the reverse orientation (Supplementary Fig. 15). Similarly, the central 210 bp of the *Cx3cr1* 28 kb enhancer containing PU.1- and Rev-Erb-binding sites was less active than a 967 bp fragment encoding sense- and antisense-strand eRNAs. Adding back the antisense-strand eRNA, but not the sense-strand eRNA, restored the activity of the enhancer core (Supplementary Fig. 16), consistent with the results of the siRNA and ASO experiments.

We next reversed the orientation of the eRNA-coding sequences relative to the enhancer cores, thereby retaining any putative transcription-factor-binding sites but completely changing the sequence of any

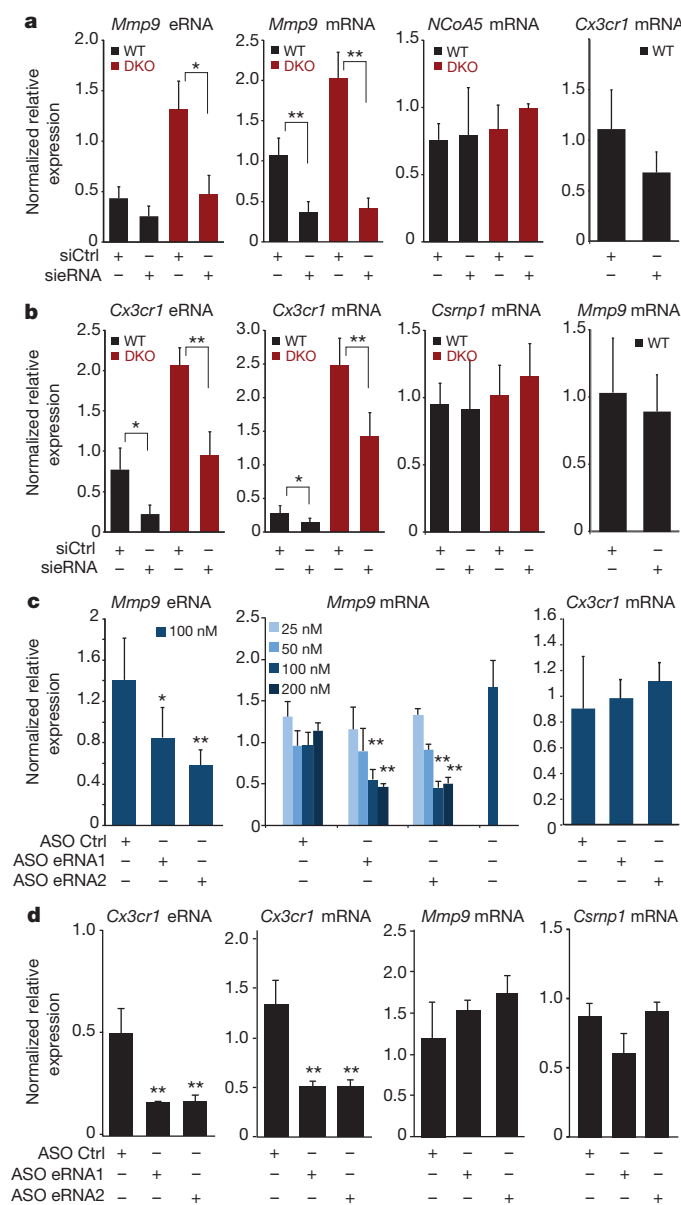


Figure 3 | Reduction of eRNA expression results in reduced expression of nearby mRNAs. **a**, qRT-PCR analysis of *Mmp9* eRNA, and *Mmp9*, *Ncoa5* and *Cx3cr1* mRNAs for wild-type and Rev-Erb DKO thioglycollate-elicited macrophages transfected with control (siCtrl) or *Mmp9* eRNA (sieRNA) siRNA (wild type, $N = 4$; DKO, $N = 4$). **b**, qRT-PCR analysis of *Cx3cr1* eRNA, and *Cx3cr1*, *Csrnp1* and *Mmp9* mRNAs for wild-type and Rev-Erb DKO BMDMs transfected with siRNA targeting *Cx3cr1* eRNA (wild type, $N = 6$; DKO, $N = 5$). **c**, qRT-PCR analysis of *Mmp9* eRNA and *Mmp9* and *Cx3cr1* mRNAs in thioglycollate-elicited macrophages transfected with the indicated ASOs ($n = 3$ –7 per condition). Ctrl, control. **d**, qRT-PCR analysis of *Cx3cr1* eRNA and *Cx3cr1*, *Mmp9* and *Csrnp1* mRNAs in BMDMs transfected with the indicated ASOs ($n = 3$ –7 per condition). Data represent mean \pm s.d., with expression normalized to 36B4 in all cases. **a**, **b**, Statistical significance was determined by two-tailed Student's *t*-test. **c**, **d**, Significance was determined by one-way ANOVA with Tukey HSD test. * $P < 0.05$, ** $P < 0.005$ versus control.

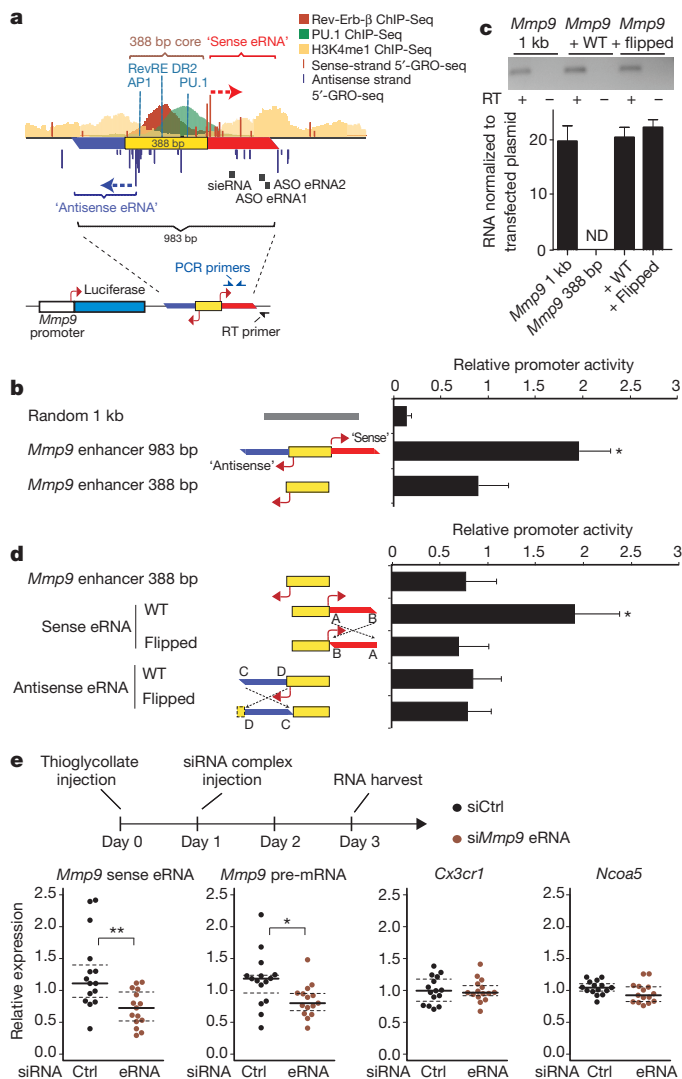


Figure 4 | eRNA contribution to enhancer activity and consequences of knockdown in vivo. **a**, Experimental design for testing eRNA coding sequences. 983 bp of the *Mmp9* enhancer was cloned downstream of the luciferase reporter gene driven by the *Mmp9* promoter. The yellow box represents the 388 bp core mediating transcription-factor binding as indicated by the ChIP-Seq tracks. Positions of transcription factor motifs are indicated in blue. Directional arrows represent eRNA TSSs defined by 5'-GRO-seq that give rise to 'sense eRNA' and 'antisense eRNA' as indicated. The locations of RT and PCR primers for detecting plasmid-directed eRNAs are indicated. **b**, Luciferase activity of the indicated reporter constructs in RAW264.7 macrophages. Bars represent mean normalized values from eight independent experiments \pm s.d. (* $P < 0.005$ versus all other indicated conditions). **c**, RT-PCR of *Mmp9* plus eRNA normalized to the copy number of the indicated transfected plasmid DNA. Gel electrophoresis of PCR with or without RT is indicated on top. ND, not detected; WT, wild type. **d**, Enhancer reporter assays performed as in **b** with the indicated luciferase reporters. Dashed lines represent inversions of the sense or antisense DNA sequence relative to the core enhancer element (yellow) (bars represent mean normalized values from five independent experiments \pm s.d.; * $P < 0.005$ versus all other indicated conditions). Statistical significance was determined by one-way ANOVA followed by Tukey HSD test. **e**, Sterile peritonitis was initiated by intraperitoneal injection of thioglycollate on day 0. Mice were injected with lipofectamine-siRNA complexes on day 1, and peritoneal exudate cells were recovered for analysis of *Mmp9* eRNA, *Mmp9* primary transcript (pre-mRNA), *Ncoa5* and *Cx3cr1* mRNA on day 3 ($n = 15$ per condition). Ctrl, control. Values were normalized to the average of *36B4* and cyclophilin A mRNA. * $P < 0.05$, ** $P < 0.005$ versus siCtrl as determined by two-tailed Student's *t*-test.

potential eRNA product. In the 'flipped' *Mmp9* plus eRNA construct, *Mmp9* enhancer activity was reduced to a level comparable to the 388 bp core (Fig. 4d), despite production of a 'flipped' eRNA (Fig. 4c

and Supplementary Fig. 15). Corresponding results were obtained for the *Cx3cr1* enhancer (Supplementary Fig. 16).

As even broadly expressed genes are often under the control of cell-specific enhancers, these findings raised the question of whether enhancers might be considered as targets for cell-specific manipulation of gene expression *in vivo*. To explore this possibility, we induced sterile peritonitis in mice and investigated the ability of siRNAs directed against the *Mmp9* -5 kb sense-strand eRNA to alter *Mmp9* mRNA expression. Using lipofectamine-siRNA delivery²¹, the eRNA-specific siRNA, but not a control siRNA, reduced expression of the -5 kb sense-strand eRNA and the *Mmp9* primary transcript, as was observed in *in vitro* (Fig. 4e).

We provide evidence that Rev-Erbs function to repress macrophage gene expression by repressing transcription from enhancers that are selected by macrophage-lineage-determining factors. The recent finding of widespread enhancer transcription raises the question of whether eRNAs represent 'noise' due to spurious transcription from regions of open chromatin, reflect an important role of enhancer transcription itself, or directly contribute to enhancer function. Our findings suggest that at least some eRNAs make a quantitative contribution to enhancer function, in agreement with findings for noncoding RNAs expressed in the vicinity of the *p53* and *SNAI1* genes^{22,23}. These results do not exclude transcription-independent functions of the enhancer core or roles of enhancer transcription unrelated to the eRNA product. A major goal for the future will be to establish the functional relevance of eRNAs *in vivo*. As the expression of many widely transcribed genes seems to be controlled by cell-restricted enhancers, the expression of such genes might be altered in a cell-restricted manner by targeting corresponding functional eRNAs. Recent advances in the development of chemically modified ASOs that can effectively reduce RNA expression *in vivo*²⁴ could potentially enable this effort, suggesting the possibility of an 'enhancer therapy' approach to the treatment of disease.

METHODS SUMMARY

BMDMs and thioglycollate-elicited macrophages (ThioMac) were generated from 4–6-week-old *Rev-Erb α /flax/flax*; *Rev-Erb β /flax/flax* mice with or without *Tie2-Cre* as previously described²¹. *Rev-Erb α* and *Rev-Erb β* were tagged with BLP for *in vivo* biotinylation in RAW264.7 macrophages expressing *Escherichia coli* biotin ligase¹¹. Biotin-based or antibody-based ChIP-Seq were performed as described¹¹. Preparation for GRO and library sequencing was performed as described previously¹⁶. 5'-GRO-seq was performed using modifications of the GRO-seq protocol enabling specific amplification of the 5' ends of capped transcripts. Identification and quantitation of ChIP-Seq peaks, GRO-seq and 5'-GRO-seq transcripts and *de novo* transcription factor motif discovery were performed using HOMER (<http://biowhat.ucsd.edu/homer>)^{11,16}. For expression analysis, RNA was harvested from macrophages using RNeasy kit (Qiagen), treated with Turbo-DNases (Ambion) and reverse transcribed using SuperScript III Reverse-Transcriptase (Invitrogen) with random hexamers. Values determined for mRNA or eRNA, using qPCR, are normalized to *36B4* mRNA content from at least three independent experiments in triplicates. For RNA interference (RNAi) experiments, non-targeting siRNA oligonucleotides or siRNA directed against *Mmp9* and *Cx3cr1* eRNA (Dharmacon) were transfected using DeliverX (Affymetrix) or Lipofectamine 2000 (Invitrogen) into ThioMac or BMDMs, respectively. For ASO experiments, non-target ASO (ASO control, Isis Pharmaceuticals no. 129700) or *Mmp9*-directed ASO (*Mmp9* eRNA1, Isis no. 566237; *Mmp9* eRNA2, Isis no. 566241) were transfected into ThioMac using Cytofectin (Gene Therapy System). *Rev-Erb*-bound enhancers were cloned into pGL4-based reporter and tested in RAW264.7 macrophages as described¹¹. Thioglycollate-elicited sterile peritonitis and *in vivo* RNAi experiments were performed as described²¹.

Full Methods and any associated references are available in the online version of the paper.

Received 17 May 2012; accepted 22 April 2013.

Published online 2 June 2013.

1. Preitner, N. *et al.* The orphan nuclear receptor REV-ERB α controls circadian transcription within the positive limb of the mammalian circadian oscillator. *Cell* **110**, 251–260 (2002).

2. Liu, A. C. *et al.* Redundant function of REV-ERB α and β and non-essential role for Bmal1 cycling in transcriptional regulation of intracellular circadian rhythms. *PLoS Genet.* **4**, e1000023 (2008).
3. Ráspé, E. *et al.* Identification of Rev-erba as a physiological repressor of apoC-III gene transcription. *J. Lipid Res.* **43**, 2172–2179 (2002).
4. Le Martelot, G. *et al.* REV-ERB α participates in circadian SREBP signaling and bile acid homeostasis. *PLoS Biol.* **7**, e1000181 (2009).
5. Gibbs, J. E. *et al.* The nuclear receptor REV-ERB α mediates circadian regulation of innate immunity through selective regulation of inflammatory cytokines. *Proc. Natl Acad. Sci. USA* **109**, 582–587 (2012).
6. Zamir, I. *et al.* A nuclear hormone receptor corepressor mediates transcriptional silencing by receptors with distinct repression domains. *Mol. Cell. Biol.* **16**, 5458–5465 (1996).
7. Yin, L. & Lazar, M. A. The orphan nuclear receptor Rev-erba recruits the N-CoR/histone deacetylase 3 corepressor to regulate the circadian *Bmal1* gene. *Mol. Endocrinol.* **19**, 1452–1459 (2005).
8. Feng, D. *et al.* A circadian rhythm orchestrated by histone deacetylase 3 controls hepatic lipid metabolism. *Science* **331**, 1315–1319 (2011).
9. Heintzman, N. D. *et al.* Histone modifications at human enhancers reflect global cell-type-specific gene expression. *Nature* **459**, 108–112 (2009).
10. Friedman, A. D. Transcriptional control of granulocyte and monocyte development. *Oncogene* **26**, 6816–6828 (2007).
11. Heinz, S. *et al.* Simple combinations of lineage-determining transcription factors prime *cis*-regulatory elements required for macrophage and B cell identities. *Mol. Cell* **38**, 576–589 (2010).
12. Core, L. J., Waterfall, J. J. & Lis, J. T. Nascent RNA sequencing reveals widespread pausing and divergent initiation at human promoters. *Science* **322**, 1845–1848 (2008).
13. Schlaeger, T. M., Mikkola, H. K., Gekas, C., Helgadottir, H. B. & Orkin, S. H. Tie2-Cre-mediated gene ablation defines the stem-cell leukemia gene (*SCL/tal1*)-dependent window during hematopoietic stem-cell development. *Blood* **105**, 3871–3874 (2005).
14. Giguere, V. *et al.* Isoform-specific amino-terminal domains dictate DNA-binding properties of ROR α , a novel family of orphan hormone nuclear receptors. *Genes Dev.* **8**, 538–553 (1994).
15. Kim, T.-K. *et al.* Widespread transcription at neuronal activity-regulated enhancers. *Nature* **465**, 182–187 (2010).
16. Wang, D. *et al.* Reprogramming transcription by distinct classes of enhancers functionally defined by eRNA. *Nature* **474**, 390–394 (2011).
17. Hah, N. *et al.* A rapid, extensive, and transient transcriptional response to estrogen signaling in breast cancer cells. *Cell* **145**, 622–634 (2011).
18. Bennett, C. F. & Swayze, E. E. RNA targeting therapeutics: molecular mechanisms of antisense oligonucleotides as a therapeutic platform. *Annu. Rev. Pharmacol. Toxicol.* **50**, 259–293 (2010).
19. Guang, S. *et al.* Small regulatory RNAs inhibit RNA polymerase II during the elongation phase of transcription. *Nature* **465**, 1097–1101 (2010).
20. Gu, S. G. *et al.* Amplification of siRNA in *Caenorhabditis elegans* generates a transgenerational sequence-targeted histone H3 lysine 9 methylation footprint. *Nature Genet.* **44**, 157–164 (2012).
21. Huang, W. *et al.* Coronin 2A mediates actin-dependent de-repression of inflammatory response genes. *Nature* **470**, 414–418 (2011).
22. Lai, F. *et al.* Activating RNAs associate with Mediator to enhance chromatin architecture and transcription. *Nature* **494**, 497–501 (2013).
23. Melo, C. A. *et al.* eRNAs are required for p53-dependent enhancer activity and gene transcription. *Mol. Cell* **49**, 524–535 (2013).
24. Raal, F. J. *et al.* Mipomersen, an apolipoprotein B synthesis inhibitor, for lowering of LDL cholesterol concentrations in patients with homozygous familial hypercholesterolaemia: a randomised, double-blind, placebo-controlled trial. *Lancet* **375**, 998–1006 (2010).

Supplementary Information is available in the online version of the paper.

Acknowledgements We thank L. Bautista for assistance with figure preparation. These studies were supported by National Institutes of Health grants CA17390, U19DK62434, DK091183, DK063491, CA014195, DK057978, HL088093, HL105278 and CA52599. M.G.R. and R.M.E. are Investigators of the Howard Hughes Medical Institute. M.T.Y.L. is supported by the University of California, San Diego Medical Scientist Training Program T32 GM007198-37, and Genetics Training Program T32 GM008666, National Institute of General Medical Sciences. M.U.K. was supported by a LeDucq Foundation Fellowship. H.P.L. was supported by the Finnish Cultural Foundation, Instrumentarium Foundation, The Paulo Foundation, Paavo Nurmi Foundation, Finnish Foundation for Cardiovascular Research, The Maud Kuistila Memorial Foundation and The Fulbright Center. These studies were also supported by grants from the Leona M. and Harry B. Helmsley Charitable Trust, Samuel Waxman Cancer Research Foundation, the Glenn Foundation for Medical Research, the Ellison Medical Foundation and Ipsen/Biomeasure.

Author Contributions M.T.Y.L., S.H., C.B., A.W., T.R.G., M.G.R., R.M.E. and C.K.G. conceived the project and planned experiments, which were performed by M.T.Y.L., H.C., H.P.L., D.G., S.H., Y.T.-O., M.U.K., A.S.K., M.K. and C.Y.L., and analysed by M.T.Y.L., H.P.L., D.G., C.B. and C.K.G. The project was supervised by C.K.G., who wrote the manuscript with M.T.Y.L.

Author Information Sequencing data have been deposited in the Gene Expression Omnibus under accession GSE45914. Reprints and permissions information is available at www.nature.com/reprints. The authors declare competing financial interests: details are available in the online version of the paper. Readers are welcome to comment on the online version of the paper. Correspondence and requests for materials should be addressed to C.K.G. (ckg@ucsd.edu).

METHODS

Reagents and expression plasmids. Rabbit anti-PU.1 (SC-352) was from Santa Cruz Biotechnology. Rabbit anti-H3K4me1 (8895) was purchased from Abcam. Rabbit anti-H3K9ac (07-352) was purchased from Millipore. Expression constructs for Rev-Erb- α (amino acid 1–614), Rev-Erb- β (amino acid 1–576) and ROR- α (amino acid 1–460) were cloned into p3 \times Flag-CMV7.1 (Sigma) at NotI and BamHI sites. The following primers were used. Rev-Erb- α : 5'-AGCTTGGCGCCGCTATGACGACCCTGGACTCC-3', 5'-ATTACGGATCCTCACTGGGCGTCCACC CG-3'; Rev-Erb- β : 5'-AGCTTGGCGCCGCTATGGAGCTGAACGACGAGGA-3', 5'-ATTACGGATCCTTAAGGATGAACCTTTAA-3'; ROR- α : 5'-AGCTTGGCGCCGCTATGAAAGCTCAAATTGAA-3', 5'-ACCGGGATCCTTACCCATCGATTTCATG-3'. Mutation of the DNA-binding domain of Rev-Erb- β was generated using QuickChange II site-directed mutagenesis (Stratagene). The cysteines in the zinc finger domain (Rev-Erb- β , amino acid 133 and 136) were mutated to alanines using the following oligonucleotides, with mutated sequence in bold: Rev-Erb- β sense: 5'-AGTGGCATGGTTCTACTGGCTAAAGTCGCTGGGATGTGGCATCAGG-3'; antisense: 5'-CCTGATGCCACATCCCCAGCGACTTTAGCCAGTAGAACCATGCCACT-3'.

Rev-Erb DKO mice and genotyping. Mice with floxed alleles for Rev-Erb- α and Rev-Erb- β were prepared as described²⁵. *Rev-Erb α ^{flox/flox}*; *Rev-Erb β ^{flox/flox}* mice were crossed with *Tie2-Cre*; *Rev-Erb α ^{flox/flox}*; *Rev-Erb β ^{flox/flox}* mice to obtain haematopoietic-specific knockout of Rev-Erbs. Littermates without the *Tie2-Cre* transgene were used as controls. DNA was harvested from mouse tails or from macrophages, and standard PCR protocol was used for genotyping. The *Tie2-Cre* transgene was detected using primers 5'-GCATTACCGGTTCGATGCAACGAGTGATGAG-3' and 5'-GAGTGAACGAACCTGGTCGAAATCAGTGCG-3', yielding a 408 bp PCR product. Genotyping PCR primers 5'-TCTCCGTTGGCATGTCTAGAGATGG-3' and 5'-GAAGAGTGTGTGTTTGCCCAAGAGG-3' were used to distinguish wild-type (191 bp) and floxed (332 bp) alleles in the *Rev-Erb α* locus. Genotyping PCR primers 5'-GGTTAGGTTTGTGAGTGTCCACAGC-3' and 5'-AAGTGCTCCAACAAGGTAGTGCA-3' were used to distinguish wild-type (236 bp) and floxed (377 bp) alleles in the *Rev-Erb β* locus.

Generation of biotin-tagged Rev-Erb- α and Rev-Erb- β . Details on generating biotin-tagged proteins stably expressed in RAW264.7 macrophages were previously published¹¹. Briefly, Rev-Erbs were fused in-frame at the N terminus with amino acid peptide MAGGLNDIFEAKIEWHEDTGGGGSGGGSGENLYFQS containing a BLRP and a TEV-protease-specific cleavage sequence (in bold). BLRP-empty, BLRP-Rev-Erb- α or BLRP-Rev-Erb- β expression plasmid was transfected into RAW264.7 macrophages engineered to stably express BirA. G418 (275 ng ml⁻¹) and puromycin (2.5 μ g ml⁻¹) were used for stable selection. Multiple stable cell lines were isolated and screened for BLRP-Rev-Erb expression and biotinylation by western blot using anti-Avi-tag antibody specifically recognizing the BLRP tag (Genscript) or HRP-streptavidin (Jackson ImmunoResearch), respectively.

The following primers were used for cloning full-length Rev-Erb- α and Rev-Erb- β at the NotI/PmeII sites in the BLRP expression constructs. BLRP-Rev-Erb- α , AGCTTGGCGCCGCTATGACGACCCTGGACTCC, AGCTTTGTTAAACTCACTGGGCGTCCACCCG; BLRP-Rev-Erb- β , AGCTTGGCGCCGCTATGGAGCTGAACGACGAGGA, AGCTTTGTTAAACTTAAGGATGAACCTTAA.

ChIP-Seq. Detailed protocols for antibody-based ChIP experiments were previously described¹¹. ChIP for biotinylated Rev-Erbs was performed as described¹¹ with the following modifications. Sonicated chromatin was incubated with BSA-blocked streptavidin T1 Dynabeads (Invitrogen) overnight at 4 °C with rotation. The captured biotin-streptavidin complexes were washed, and samples were equilibrated in TEV buffer (50 mM Tris-HCl, pH 8.0, 100 mM NaCl, 0.1% NP-40 (CA630), 0.5 mM EDTA) for 5 min at room temperature (25 °C), followed by AcTEV protease (Invitrogen) digestion (5–10 U) for 1 h at room temperature in 40 μ l TEV buffer. The streptavidin-conjugated beads were eluted again with TEV buffer with 10 min incubation at room temperature. Eluted samples were reverse cross-linked and RNaseA- and proteinase-K-treated following a standard ChIP protocol¹¹. ChIP fragments were ligated to Genomic adaptor (Illumina) or NEXTflex DNA barcode adaptors (BioO Scientific). Adaptor ligated DNA fragments were size selected (150–250 bp), PCR amplified and sequenced on the Illumina Genome Analyzer or HiSeq system according to the manufacturer's instructions.

ChIP-Seq analysis and de novo motif discovery. ChIP-Seq peak identification, quality control, and motif analysis were performed using HOMER (<http://biowhat.ucsd.edu/homer>) as described^{11,16}. Peaks from separate experiments were considered co-bound if their peak centres were located within 200 bp of each other. For de novo motif analysis, transcription factor motif finding was performed on ± 100 bp relative to the peak centre defined from ChIP-Seq. Peak sequences were compared to random genomic fragments of the same size and normalized G+C content to identify motifs enriched in the ChIP-Seq targeted sequence. To generate histograms for the average distribution of tag densities, position-corrected, normalized tags in

40 bp windows were tabulated within the indicated distance from specific sites in the genome (that is, Rev-Erb-binding sites). Clustering plots for normalized tag densities at each genomic region were generated using HOMER and then clustered using Cluster (<http://bonsai.hgc.jp/~mdehoon/software/cluster/>) and visualized using Java TreeView²⁶.

GRO-seq. GRO and library preparation for sequencing was described previously¹⁶. Four 10-cm plates of confluent BMDMs from wild-type control or Rev-Erb DKO were used as the starting material. Two biological samples were used per group. Approximately 10 million nuclei per sample were extracted and used for run-on and BrU incorporation. BrU-labelled nascent transcripts were immunoprecipitated with anti-BrdU agarose beads (Santa Cruz Biotech), washed, eluted and precipitated in ethanol.

BrU-precipitated RNA was subjected to first-strand cDNA synthesis. First, polyA tails were added using Poly(A)-polymerase (NEB). Reverse transcription was then performed using Scriptscript III Reverse Transcriptase (Invitrogen) with oNTI223 primer (5'-pGATCGTCGGACTGTAGAAGTCT; CAAGCAGAAGA CGGCATACGATTTTTTTTTTTTTTTTTTTVN-3') where the p indicates 5' phosphorylation, the semi-colon indicates the abasic dSpacer furan, and VN indicates degenerate nucleotides. Subsequently, excess oNTI223 primers were removed by Exonuclease I (Fermentas). First-strand cDNA products were fragmented with basic hydrolysis and size selected (105–400 nucleotides) in a 10% polyacrylamide TBE-urea gel (Invitrogen).

cDNA was subsequently circularized using CircLigase (Epicentre), and relinearized at the basic dSpacer furan with Apel (NEB). The single-stranded DNA (ssDNA) template was amplified to generate DNA for sequencing by Phusion Hig-Fidelity DNA Polymerase (Thermo Scientific) with primers oNTI200 (5'-CAAGCAGAAGACGGCATA-3') and oNTI201 (5'-AATG ATACGGCGACCA CGCAGAGTTCAGAGTTCTACAGTCCGACG-3'). PCR product was purified and size selected (140–225 bp) by gel electrophoresis on a non-denaturing 8% polyacrylamide TBE gel (Invitrogen). Purified DNA was then sequenced on Illumina Genome Analyzer II according to the manufacturer's instructions with the small RNA sequencing primer 5'-CGACAGGTTTCAGAGTTCTACAGTCC GACGATC-3'.

5'-GRO-seq. Reactions were stopped and RNA was extracted with 450 μ l Trizol LS reagent (Invitrogen), both according to the manufacturer's instructions. Following DNase treatment, the RNA was hydrolysed in 20 μ l total volume with 2 μ l RNA fragmentation buffer (Ambion) for 10 min, and divalent cations were removed by gel filtration. Fragmented RNA was then 3'-dephosphorylated with polynucleotide kinase (Enzymatics) for 2 h at 37 °C. The reaction was stopped with EDTA, and PNK was inactivated and RNA denatured by heating the reaction to 75 °C for 5 min, then cooled on ice for 2 min. BrU-containing RNA fragments were precipitated using anti-BrdU agarose beads. The resulting RNA was dephosphorylated with calf intestinal phosphatase (NEB) and 5'-de-capped with tobacco acid pyrophosphatase (Epicentre). The reaction was stopped and RNA was extracted with Trizol LS, and libraries were prepared by ligating Illumina TruSeq-compatible adapters to the RNA 3' and 5' ends with truncated mutant RNA ligase 2 (K227Q) and RNA ligase 1 (NEB), respectively, followed by reverse transcription, cDNA isolation and PCR amplification for 12 cycles. Final libraries were size selected on PAGE/TBE gels to 60–110 bp insert size. A detailed protocol is available on request.

Genome-wide gene expression analysis with GRO-seq. GRO-seq analysis of genome-wide gene expression was performed by HOMER followed by edgeR²⁷. Briefly, HOMER was used to generate a gene expression matrix by identifying uniquely mapped RNA tags to gene bodies based on RefSeq annotation for the mouse genome (mm9). Statistical analysis for differential expression was performed using edgeR²⁷ on raw sequencing reads from wild-type and Rev-Erb DKO macrophages with two biological replicates per group. Genes with $P < 0.005$ were considered as differentially expressed.

Enhancer-associated RNA analysis. To examine regulation of eRNA expression, putative enhancers sites were first defined based on ChIP-Seq enrichment of H3K4me1 and H3K4me3 flanking $\pm 1,000$ bp from the centre of the transcription factor of interest. Putative enhancers were defined by the following criteria: (1) regions were at least 2 kb away from annotated TSSs; (2) regions had at least 16 tags from H3K4me1 ChIP-Seq normalized to 10 million tags; and (3) normalized ChIP-Seq tag count for H3K4me1 was greater than H3K4me3. HOMER was used to quantify eRNA expression by tabulating normalized GRO-seq tags within ± 800 bp from the centre of Rev-Erb- or PU.1-bound intergenic enhancers. For 5'-GRO-seq experiments, tag counts within ± 250 bp of enhancers were tabulated. Histograms of RNA distribution at indicated enhancers were generated by tabulating average normalized RNA tag counts at a resolution of 40 bp within 2 kb from centres of specified genomic sites (for example, Rev-Erb enhancers). Only enhancers with > 4 tags from GRO-seq or 5'-GRO-seq within the specified window were included in the expression analysis.

Analysis of correlations between eRNAs and nearby protein-coding genes was performed by examining differential expression of eRNAs to that of the nearest expressing protein-coding genes. Briefly, Rev-Erb-bound enhancers were assigned to the nearest expressing annotated genes defined by having at least 20 sequencing tags normalized to the length of the gene body. Differential expression of eRNA was determined by GRO-seq from Rev-Erb DKO macrophages versus wild-type control, or by 5'-GRO-seq from Rev-Erb- α -overexpressing macrophages to control. Differential expression of annotated protein-coding genes was determined by GRO-seq in Rev-Erb DKO experiments. The data set was categorized as 'up', 'no change' and 'down' on the basis of the differential expression of the eRNA. For Rev-Erb DKO GRO-seq, eRNA with a >1.5-fold change in GRO-seq signal was considered to be differentially expressed; for the Rev-Erb- α overexpression experiment, a 2-fold cut-off in 5'-GRO-seq signal was used. Spearman rank correlation was used to test whether changes in eRNA and the corresponding protein-coding gene co-varied.

Construction of enhancer reporters. For construction of Rev-Erb enhancer reporter plasmids, 900–1,100 bp of sequence centred on Rev-Erb-bound sites flanked by demarcation of H3K4me1 were PCR amplified and cloned into pGL4-TATA-TK at the BamHI/SalI sites downstream of the luciferase reporter gene as previously described¹¹. The following primers were used to PCR-amplify enhancer sequences from mouse genomic DNA. *Arhgap25* 33 kb enhancer: 5'-GATCGTCGACTTTCCATGGGTCCAGAGATG-3'; 5'-GATCGGATCCAGCAGGCTGGGATATGAGT-3'. *Cx3cr1* 9.8 kb enhancer: 5'-GATCGGATCCCTACACCTGCACAAGCACACA-3'; 5'-GATCGTCGACAACCTGGGCGGAAATTTGAAA-3'. *Cx3cr1* 28 kb enhancer: 5'-GATCGGATCCGACCCTGGGTTGTCAGTAGG; 5'-GATCGTCGACACTTATGGGGGAGGATCTGG-3'. *Eif2c4* –20 kb enhancer: 5'-GATCGTCGACCCCTCAAAGCTAACCATCCA-3'; 5'-GATCGGATCCAAAGTCATCGGAGACCTGAAA-3'. *Mmp9* –5 kb enhancer: 5'-GATCGGATCCGTCGCTCAGCATCAGGAAAT-3'; 5'-GATCGTCGACACTTGGCAGGCAGAGTGAGT-3'. *P4ha2* 55 kb enhancer: 5'-GATCGGATCCGCCACAGCTCTGCTTTATGG-3'; 5'-GATCGTCGACGCTCACTGGCCTTGCTAACT-3'. *Slc7a8* 27 kb enhancer: 5'-GATCGTCGACCTGCATCCCGACTCATACCT-3'; 5'-GATCGGATCCCTCCAGCAAGCACTCTTTC-3'. As negative control, a genomic region devoid of Rev-Erb binding and other enhancer-like features was used (chr5:30,278,928–30,279,847: 5'-GATCGGATCCAGTTCATGTCCAGCGAA TC-3'; 5'-GATCGTCGACGGAGCAAGGAGGGAGAGAG-3').

For experiments testing the functional significance of the eRNA-coding sequences for *Mmp9* and *Cx3cr1*, various alterations of the enhancers were cloned into the BamHI/SalI site downstream of the luciferase gene in the pGL4 reporter driven by the *Mmp9* and *Cx3cr1* promoter, respectively. Inversion of the eRNA-coding sequence relative to the core element of *Mmp9* (388 bp) and *Cx3cr1* (210 bp) was achieved by Flip-PCR²⁸, a two-step overlap extension method modified from PCR site-specific mutagenesis. Briefly, the first amplification step consisted of two reactions using two pairs of flanking and internal primers to generate two fragments of the wild type sequence. The internal primers comprised the inversion site where the 3' end anneals to their respective targets and the 5' overhang is complementary to the opposing PCR fragment. The two internal primers are also complementary, allowing the two PCR fragments to anneal in an inverted fashion and to extend and amplify with flanking primers in the second step.

The following primers were used for constructing each enhancer variants. *Mmp9* –5 kb, 388 bp core enhancer: 5'-GATCGGATCCGGAAGCCGTTCC TTATCTCC-3', 5'-GATCGTCGACTACACCTGTCTACCAACAC-3'. Sense eRNA wild type: 5'-GATCGGATCCGATCGAGCTCAGGCTCTAG-3', 5'-GATCGTCGACACTTGGCAGGCAGAGTGAGT-3'. Antisense eRNA wild type: 5'-GATCGGATCCGTCGCTCAGCATCAGGAAAT-3', 5'-GATCGTCGACTACACCTGTCTACCAACAC-3'. Sense eRNA flipped: flanking primer 1, 5'-GATCGTCGACTGTGTGGGGTGGCAATGGA-3', internal primer 1, 5'-GTGTTGTGAGCAGGGTGTAACTTGGCAGGCAGAGTGAGT-3'; flanking primer 2, 5'-GATCGGATCCGACTCAGGACTCCAGGTCTAG-3', internal primer 2, 5'-AC TCACTCTGCCTGCCAAGTTACACCTGCTACCAACAC-3'. Antisense eRNA flipped: flanking primer 3, 5'-GATCGGATCCACTCACTGGCAGATACACAGC-3', internal primer 3, 5'-CTAGACCTGGAGTCTGAGTCGTGGCTCAGC ATCAGGAAAT-3', flanking primer 4, 5'-GATCGTCGACTACACCTGCTCA CCAACAC-3', internal primer 4, 5'-ATTTCTGATGCTGAGCCACGACTCA GGACTCAGGTCTAG-3'. *Cx3cr1* 28 kb, 210 bp core enhancer: 5'-TTCAGGG ATCCGCTGAGAGTTTCAGCATTCG-3', 5'-TATTTGTCGACCTTGCTTGT TTTCTAAGCTCC-3'; sense eRNA wild type: 5'-TTCAGGGATCCGCTGAG ATTTGACGATTGC-3', 5'-AGCATGTGACACTTATGGGGGAGGATCTG G-3'; antisense eRNA wild type: 5'-ATCGTGGATCCGACCCTGGGTTGTC AGTAGG-3', 5'-TATTTGTCGACCTTGCTTGTTCCTTAAGCTCC-3'; sense eRNA flipped: flanking primer 1, 5'-TTCAGGGATCCGCTGAGAGTTGTCAGC ATTGC-3', internal primer 1, 5'-ATCCTCCCCATAAGTCTTGCTGTTTCTT

AAGCTCC-3'; flanking primer 2, 5'-TAAGAAACAGCAAGACTTATGGGGG AGGATCTGG-3', internal primer 2, 5'-ATTATGTCGACGCTTAAAAATAAA CCTC-3'; antisense eRNA flipped: flanking primer 3, 5'-TATTTGTCGACCTTG CTTGTTTCTTAAGCTCC-3', internal primer 3, 5'-CTGACAACCCAGGGTC GCTGAGAGTTGCAGCA-3', flanking primer 4, 5'-TGCTGCAACTCTCAGCG ACCCTGGGTTGTCAG-3', internal primer 4, 5'-AAGATGGATCCAAACCAGC TGAAGATCAGCAG-3'. The promoters of *Mmp9* and *Cx3cr1* were each cloned into XhoI/BglII sites upstream of the luciferase gene in, respectively, pGL4-11- and pGL4-10-based vector with neomycin resistance gene. The following primers were used for promoter PCR amplification: *Mmp9*: 5'-GATCCTCGAGTGCCAAAGC TTTCCTGAGTG-3', 5'-GATCAGATCTGGTGAGGACCGCAGCTTCT-3'. *Cx3cr1*: 5'-ATCGGCTAGCTCTAGCCTCCCTGGGCACAT-3', 5'-TGCAAAGCTTCT CAAGTTACGACGCTGCAA-3'.

Enhancer reporter experiments. Enhancer reporters were transfected into RAW264.7 macrophages using SuperFect (Qiagen) as described previously¹¹, using 300 ng of enhancer reporter and 200 ng of β -actin-promoter-driven β -galactosidase. Plasmids were complexed with 5 μ l of SuperFect per 400 μ l of medium in a 24-well culture plate (Corning) seeded with 1×10^5 cells 24 h before transfection. Luciferase activity was measured 24 h after transfection using a Veritas microplate luminometer (Turner Biosystems) and normalized to β -galactosidase activity (Applied Biosystem) for transfection efficiency. Each experiment was performed at least three independent times, with each reaction done in triplicate. Data represent mean \pm s.d., and statistical significance was determined by one-way ANOVA followed by Tukey HSD test.

RNA isolation and RT-PCR. Total RNA from macrophages was harvested using RNeasy Kit (Qiagen) followed by DNase treatment using DNase (Qiagen) or TurboDNase (Ambion) according to the manufacturer's instruction. Total RNA (0.5–2 μ g) was used for cDNA synthesis using Superscript III Reverse Transcriptase (Invitrogen) with random hexamers. No template controls were prepared by excluding reverse transcriptase from first-strand cDNA synthesis. Quantitative transcript analysis was performed on an Applied Biosystems 7300 Real-time PCR system or Step One Plus using SYBR GreenER qPCR mastermix (Invitrogen). Values are normalized for *36B4* mRNA content. A modified $\Delta\Delta C_T$ method, which incorporates PCR efficiencies, was used to determine relative expression of RNA.

For the detection of RNA expression from the enhancer reporter, strand-specific primers were designed to anneal at a plasmid-specific sequence for first-strand cDNA synthesis. These primers anneal to 22 and 87 bp downstream of the SalI cloning site: pGL4_RT_en3 (CGAGTTGCATGATAAAGAAGA) and pGL4_RT_en3a (AGGAGCTGACTGGGTTGAAG). Total RNA harvested from RAW264.7 macrophages stably transfected with enhancer reporter (500 μ g ml⁻¹ G418) were isolated as described earlier. DNA was harvested, and primers annealing to the luciferase gene were used for qPCR to control for transfection efficiency.

Primers for quantitative PCR are as follows: *Mmp9* mRNA (CATTCCGCTGG ATAAGGAGT, GAAACTCACAGCCAGGAAGA); *Mmp9* sense eRNA 1 (AAG ATGGGGGAAATGGTAGG, ACTTGGCAGGCAGAGTGAGT); *Mmp9* sense eRNA 2 (CCCACTGCTTACCACTGTT, TCGACAACCTACCATTTC); *Mmp9* antisense eRNA (TGGAGTCCCACAAAATCCTC, TAGCTCAACTGTG GGGTGTG); *Mmp9* primary RNA transcript (AAGCGGACATTGTCATCCA, CAGGCATAAGAGCGGACAG); *Cx3cr1* mRNA (AGTTCCTTCCCATCTGCTC TC, AATGTCGCCCCAAATAACAGG); *Cx3cr1* 28 kb eRNA 1 (CTGCCTCAGG GAGAAACAAG, CTGCAACTCTCAGCAACCCAG); *Cx3cr1* 28 kb eRNA 2 (GCAC TACAATGTAATGACCTCTTTC, GATGCCCTCCGCCATTTC); *Ncoa5* (CCTGG CCCAGAGAGTCAA, ACAGGCCTCTCAGCATCAAA); *Csrnp1* (TCCTGTGGC CTCCAGGATTT, GGCACCGTGGGAAATAGTAG); *Rev-Erb α* DBD (AGAGA TGCTGTGCGTTTTGG, AGGCTGTCTAGTTGGTTGTT); *Rev-Erb β* C' (AGG CTCTCGTGACCTTTCTC, TCACTGTCTGTCTCTTACAG); *Rev-Erb β* (AGT GGCATGGTTCTACTGTGT, GCTCCTCCGAAAGAAACCCTTA); cyclopilin A (GGGTTCCTCTTTCACAGAA, GATGCCAGGACCTGTATGCT); *36B4* (AGG GCGACCTGGAAGTCC, CCCACAATGAAGCATTTTGGGA); luciferase (ACG TGCAAAAGAAGCTACCG, ATGGGAAGTCACGAAGGTGT).

siRNA transfection. Non-targeting control and siRNAs directed against *Mmp9* and *Cx3cr1* eRNA (Dharmacon) were transfected into ThioMac with DeliverX (Affymetrix) according to the manufacturer's protocol, or into BMDMs with Lipofectamine 2000 (Invitrogen) using 100 nM siRNA as described previously²¹. RNA was harvested from transfected macrophages 20–24 h after transfection.

The following siRNA oligonucleotides were used for *in vitro* studies. siGENOME non-targeting siRNA pool #2 (Thermo Science, D-001810): UAAGGCUAUGAA GAGAUAC, AUGUAUUGGCCUGUAUUAG, AUGAACGUGAAUUGCUCAA, UGGUUUACAUGUCGACUAA. Custom siRNA for *Mmp9* eRNA: GGUCACAC AAUGAGCUGAAUU, AGAAAGAACCAGCAGCAUUUU. Custom siRNA for *Cx3cr1* eRNA: CCUCUAAGAUGGCCAGUAAUU, UUACUGGCCAUCUUAG AGGUU.

ASO design. All ASOs used in this study contained a full phosphorothioate backbone and a 10-base 2'-deoxynucleoside gap flanked by 2'-modified nucleosides. These 2'-modified nucleosides were either 2'-O-(2-methoxyethyl) (MOE) or constrained 2'-O-ethyl (cET) modifications. The motif for the ASOs targeting the *Mmp9* eRNA tested was eek-10-kke, where e represents MOE, k represents cEt, and -10- represents the 10-base DNA gap. For the sense and antisense *Cx3cr1* eRNAs the motif used was kkk-10-kkk. ASOs were synthesized and purified as described previously^{29,30}. For each target strand, 78 test ASOs were screened for reduction of target RNA. A positive control targeting the coding sequence of *Mmp9*, Isis no. 535522 (GCACCTTTCCCTCGGATGGG, a 5-10-5 MOE gapmer), and a negative control matching no mouse transcripts, Isis no. 129700 (TAGTGGCGACCTACCCACGA, a 5-10-5 MOE gapmer), were included. Two ASOs that resulted in maximum reduction of *Mmp9* eRNA: Isis no. 566237 (*Mmp9* eRNA 1, 5'-ATTGTGTGACCCAGC) and Isis no. 566241 (*Mmp9* eRNA 2, 5'-CAAGCTTCAGCTCATT) were selected for further studies. In addition, ASOs targeting the *Cx3cr1* antisense-strand eRNA, Isis no. 586596 (*Cx3cr1* eRNA 1, 5'-TATGGCTGCCTCAGGG) and 586600 (*Cx3cr1* eRNA 2, 5'-TGAGGAGTTTCCCAT) were used. All oligonucleotides were designed to not contain G-strings with four Gs or two sets of three Gs in a row to prevent non-antisense-mediated effects²⁹.

ASO transfection. For the experiments with ASOs directed against the *Mmp9* sense-strand eRNA, oligonucleotides at a concentration of 100 nM were transfected into 1.5–2.5 million ThioMac using Cytofectin (Gene Therapy Systems) in Opti-MEM reduced serum medium (Invitrogen) at a concentration of 3.5 µg Cytofectin per ml. Experiments with the ASOs targeting the *Cx3cr1* antisense-strand eRNA (40 nM) were conducted in confluent wild-type BMDMs also using Cytofectin. Macrophages were incubated with ASO–Cytofectin complex for 4 h in 37 °C with 5% CO₂, then replaced with RPMI medium containing 10% FBS

(Hylcone), 100 U ml⁻¹ of penicillin and 100 mg ml⁻¹ of Streptomycin (Invitrogen). Macrophages were harvested for RNA analysis 16–24 h after transfection.

Thioglycollate-elicited sterile peritonitis and *in vivo* RNAi experiment. Experiments were performed as described previously²¹. Thioglycollate medium (2 ml) was delivered to each mouse by intraperitoneal injection on day 1. On day 2, 100 µg scrambled control siRNAs (Thermo Science, AUGUAUUGGCCUGU AUUAG, UGGUUUACAUGUCGACUAA) or *Mmp9* eRNA-specific siRNA (Thermo Science, GGUCACACAAUGAGCUGAAUU, AGAAAGAACCAGCA GCAAUUU) were complexed in Lipofectamine 2000 (Invitrogen) and serum-depleted medium for at least 5 min at room temperature with 1 ml final volume and delivered to mice by intraperitoneal injection using sterile 25-gauge needles and 1-cc syringes. Elicited macrophages in the peritoneal cavities were collected with 10 ml of PBS on day 3 and processed for RNA isolation and qRT-PCR analysis as described earlier.

25. Cho, H. *et al.* Regulation of circadian behaviour and metabolism by REV-ERB- α and REV-ERB- β . *Nature* **485**, 123–127 (2012).
26. Saldanha, A. J. Java Treeview—extensible visualization of microarray data. *Bioinformatics* **20**, 3246–3248 (2004).
27. Robinson, M. D., McCarthy, D. J. & Smyth, G. K. edgeR: a Bioconductor package for differential expression analysis of digital gene expression data. *Bioinformatics* **26**, 139–140 (2010).
28. Schanke, J. T. Sequence inversion by Flip-PCR. *Methods Mol. Biol.* **67**, 203–208 (1997).
29. Baker, B. F. *et al.* 2'-O-(2-Methoxy)ethyl-modified anti-intercellular adhesion molecule 1 (ICAM-1) oligonucleotides selectively increase the ICAM-1 mRNA level and inhibit formation of the ICAM-1 translation initiation complex in human umbilical vein endothelial cells. *J. Biol. Chem.* **272**, 11994–12000 (1997).
30. Seth, P. P. *et al.* Design, synthesis and evaluation of constrained methoxyethyl (cMOE) and constrained ethyl (cEt) nucleoside analogs. *Nucleic Acids Symp. Ser.* **52**, 553–554 (2008).

Functional roles of enhancer RNAs for oestrogen-dependent transcriptional activation

Wenbo Li^{1*}, Dimple Notani^{1*}, Qi Ma^{1,2}, Bogdan Tanasa^{1,3}, Esperanza Nunez¹, Aaron Yun Chen¹, Daria Merkurjev^{1,2}, Jie Zhang¹, Kenneth Ohgi¹, Xiaoyuan Song¹, Soohwan Oh^{1,4}, Hong-Sook Kim¹, Christopher K. Glass⁵ & Michael G. Rosenfeld¹

The functional importance of gene enhancers in regulated gene expression is well established^{1–3}. In addition to widespread transcription of long non-coding RNAs (lncRNAs) in mammalian cells^{4–6}, bidirectional ncRNAs are transcribed on enhancers, and are thus referred to as enhancer RNAs (eRNAs)^{7–9}. However, it has remained unclear whether these eRNAs are functional or merely a reflection of enhancer activation. Here we report that in human breast cancer cells 17 β -oestradiol (E2)-bound oestrogen receptor α (ER- α) causes a global increase in eRNA transcription on enhancers adjacent to E2-upregulated coding genes. These induced eRNAs, as functional transcripts, seem to exert important roles for the observed ligand-dependent induction of target coding genes, increasing the strength of specific enhancer–promoter looping initiated by ER- α binding. Cohesin, present on many ER- α -regulated enhancers even before ligand treatment, apparently contributes to E2-dependent gene activation, at least in part by stabilizing E2/ER- α /eRNA-induced enhancer–promoter looping. Our data indicate that eRNAs are likely to have important functions in many regulated programs of gene transcription.

We performed ER- α chromatin immunoprecipitation coupled with massively parallel DNA sequencing (ChIP-Seq) analysis using 1 h E2-treated (100 nM) MCF-7 human breast cancer cells and revealed 31,052 ER- α binding sites genome wide. This included only 902 on promoters (Supplementary Fig. 1a), in accordance with previously reported analyses^{10–12}, and 7,174 ER- α -bound potential enhancers based on the presence of H3K4me1 (refs 13, 14) and H3K27ac (ref. 15) (Supplementary Fig. 1b). Global run-on sequencing (GRO-seq) analysis of MCF-7 cells in similar conditions identified 1,309 E2-upregulated coding genes, of which 1,145 had an E2/ER- α -binding enhancer within 200 kilobases (kb) from their transcription start site (TSS) and were thus considered to be direct oestrogen-upregulated target genes (hereafter referred to as UP genes; Supplementary Fig. 1c). Of these, only 112 showed ER- α binding to their promoters (Supplementary Fig. 1c), consistent with suggestions^{10,11} that ER- α occupancy on enhancers is a key strategy underlying E2-induced gene expression. Most E2-regulated enhancers showed a rapid bidirectional activation of eRNAs, exemplified by the *FOXCI* locus (Supplementary Fig. 1e), which is about ~1.5 kb long as identified by GRO-seq, although ~10% exhibited an apparent unidirectional eRNA transcription⁸ (Fig. 1a and Supplementary Fig. 1f, g). These data suggest that eRNA induction in response to ER- α binding is a predictive mark of enhancer activity⁹. Binding of ER- α did not cause clear alterations in enhancer marks on ER- α -bound enhancers, such as H3K27ac (Supplementary Fig. 1h).

Approximately 83% of enhancers with detectable GRO-seq signals adjacent to UP genes exhibited E2-induced eRNA upregulation (Fig. 1a); for the remaining 17%, the tag count was not sufficient to assign upregulation bioinformatically. E2 induction of eRNA was not observed on non-ER- α -bound H3K27ac-marked enhancers

(Supplementary Fig. 1i). The median distance between enhancers exhibiting E2-induced eRNAs ($n = 1,248$; referred to as UP enhancers) and their closest UP genes was ~52 kb, compared with a median distance of ~270 kb between enhancers exhibiting no E2 induction of

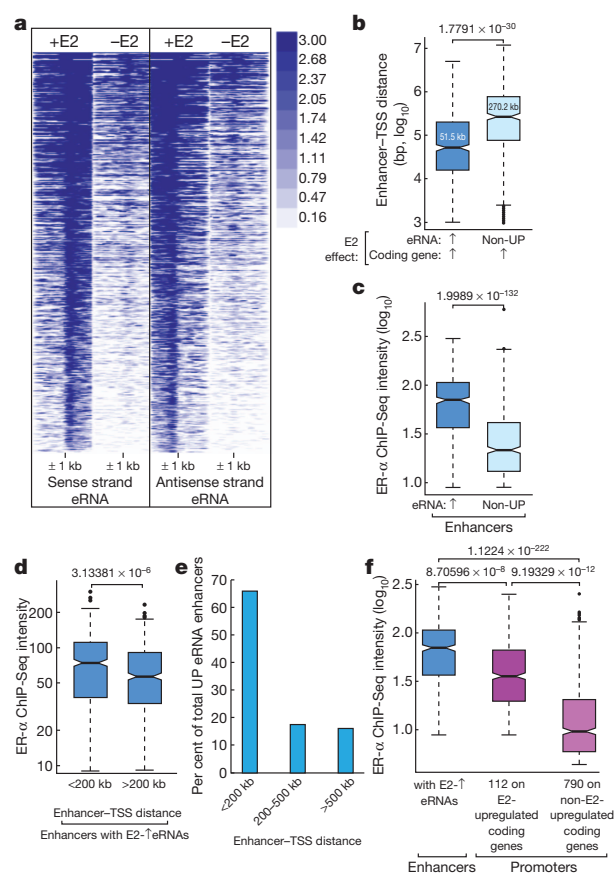


Figure 1 | E2 induction of eRNA in MCF-7 breast cancer cells. **a**, Heat map of GRO-seq showing bidirectional eRNA transcription at enhancers induced by E2. **b**, UP enhancers are closer to the UP genes (median ~52 kb) in comparison to enhancers with non-upregulated eRNAs (median ~270 kb). Up arrows indicate upregulation. **c**, ER- α binds more robustly to UP enhancers than to the enhancers with non-upregulated eRNA. **d**, Among the UP enhancers, the proximal ones within 200 kb from any E2-upregulated gene TSSs exhibit higher ER- α binding intensity than the distal cohort of UP enhancers located farther away. **e**, Most of the UP enhancers are in close proximity to E2-upregulated coding genes. **f**, ER- α binding intensity on UP enhancers is higher than on 112 promoters of E2-activated genes, which itself is higher than the 790 ER- α -bound promoters of genes did not show upregulation by E2. A log₁₀ scale is used for panels **b**, **c** and **f**. *P* values are given at the top of graphs, and were calculated using the Student's *t*-test.

¹Howard Hughes Medical Institute, Department of Medicine, School of Medicine, University of California, San Diego, La Jolla, California 92093, USA. ²Graduate Program in Bioinformatics, University of California, San Diego, La Jolla, California 92093, USA. ³Graduate Program, Kellogg School of Science and Technology, The Scripps Research Institute, 10550 North Torrey Pines Road, La Jolla, California 92037, USA. ⁴Graduate Program in Biological Sciences, University of California, San Diego, La Jolla, California 92093, USA. ⁵Cellular and Molecular Medicine, Department of Medicine, University of California, San Diego, La Jolla, California 92093, USA.

*These authors contributed equally to this work.

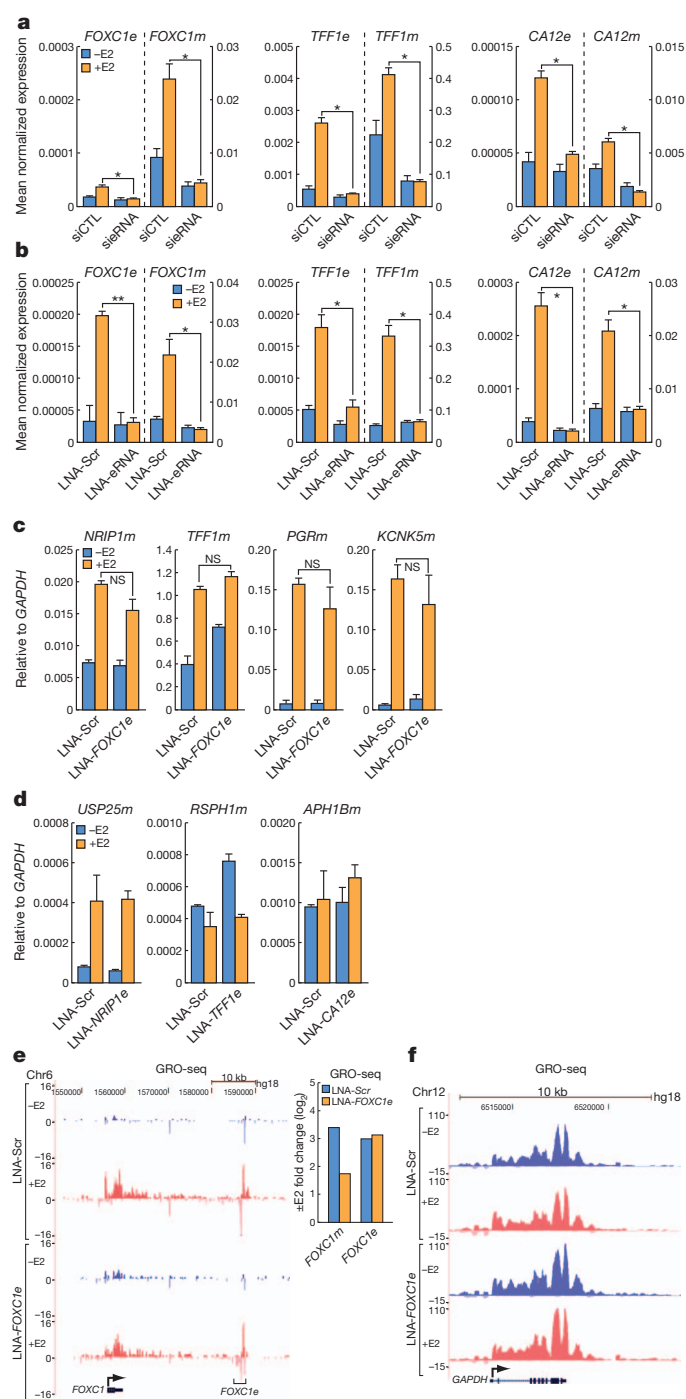


Figure 2 | Importance of eRNA for target gene activation. **a, b**, siRNA/LNA knockdown of eRNAs. Efficacy and effects on coding gene transcription were assessed by qPCR for the *TFF1*, *FOXCI* and *CA12* eRNAs and corresponding coding transcription units. Lower case 'e' and 'm' after gene names denote eRNA and gene mRNA, respectively. CTL, control; Scr, scramble. **c**, qPCR analysis showing no significant change of several E2 target coding genes when *FOXCI* eRNA was knocked down using LNA. NS, not significant. **d**, Lack of effect of *NR1P1*, *TFF1* or *CA12* eRNA knockdown on expression of other coding genes located distally, including *USP25* (520 kb from *NR1P1*), *RSPH1*, (120 kb from *TFF1*) and *APH1B* (110 kb from *CA12*). **e**, GRO-seq data from MCF-7 cells treated with LNA against *FOXCI* eRNA (*FOXCIe*) showing LNA's inhibitory effect on the transcription of the *FOXCI* coding locus, but not on the targeted enhancer region. The bar graph (right) shows that the LNA against *FOXCIe* knocked down E2 induction of *FOXCI* messenger RNA (tag counts over the whole gene length), but not transcription of the enhancer region. hg18, human genome 18. **f**, A similar GRO-seq snapshot as in **e**, showing the lack of effect from LNA against *FOXCIe* on *GAPDH* transcription. Data represent mean \pm standard error of the mean (s.e.m.) (**a, b**) and mean \pm standard deviation (s.d.) (**c, d**); ($n = 3$). * $P < 0.05$, ** $P < 0.01$.

question whether eRNAs are merely a by-product of enhancer activation or whether they might serve as key regulators of coding gene transcription^{7–9}. To investigate the potential roles of ligand-induced eRNAs on gene activation events, both specific short interfering RNAs (siRNAs)¹⁶ and locked nucleic acid antisense oligonucleotides (LNAs)¹⁷ directed against each eRNA transcript were designed on the basis of the peaks of eRNA exhibited by GRO-seq. To exclude off-target effects, experiments were performed with two different LNAs or siRNAs targeting each eRNA.

With a high efficiency of transfection (Supplementary Fig. 2a), both siRNA and LNA-mediated knockdown of the *TFF1*, *FOXCI* or *CA12* eRNAs revealed that, for each transcription unit, the induction of both the eRNA and of the adjacent coding gene, as assessed by quantitative polymerase chain reaction (qPCR) and GRO-seq, respectively, was significantly inhibited (Fig. 2a, b, e and Supplementary Fig. 2b, c). By contrast, these siRNAs/LNAs did not affect the housekeeping genes we tested (for example, *GAPDH*; Fig. 2f), or E2-regulated or non-E2-regulated transcription units more distal to the regulated enhancers (Fig. 2c, d). Ligand-induced increase of ER- α binding occurred even after eRNA knockdown (Supplementary Fig. 2d, e). Similar eRNA requirements for coding-gene induction by E2 were observed on the basis of knockdown of eRNAs adjacent to the *PGR*, *SLAH2*, *KCNK5*, *P2RY2*, *SMAD7*, *GREB1* and *NR1P1* genes using either siRNAs or LNAs (Fig. 3g, i and Supplementary Fig. 2b). GRO-seq data were consistent with the notion that LNA against eRNA reduces the levels of eRNA transcript post-transcriptionally, but not its nascent transcription (Fig. 2e, bar graph). Knockdown of an eRNA on an ER- α -bound distal enhancer (~222 kb from the *FOXCI* TSS) that did not exhibit E2-induced eRNA and with low ER- α -binding affinity did not affect neighbouring *FOXCI* gene induction (Supplementary Fig. 2f), further indicating that eRNA induction potentially marks E2-regulated functional enhancers. Although GRO-seq results (Fig. 2e) already indicate a lack of any LNA-mediated transgene silencing of the enhancer DNA, further assays—including methyl miner and enzyme digestion assays (Supplementary Fig. 3a–c)—confirmed unaltered enhancer methylation on the *FOXCI*, *P2RY2* or *NR1P1* enhancers. Additional supporting evidence was provided by using an LNA targeting the sense transcript from a regulatory region near the *GREB1* gene (*GREB1*-RR), which exhibits overlapping bidirectional transcription (Supplementary Fig. 3d, e); we observed no significant change in transcript level from the antisense strand by strand-specific qPCR. We also failed to observe any significant LNA effects on levels of total histone H3, H3K9me3 or H3K27me3 silencing marks on several targeted enhancers (Supplementary Fig. 3g). Together, these data suggest that siRNA/LNA-mediated knockdown of eRNAs does not elicit transgene silencing of the interrogated enhancers.

To validate independently that eRNAs *per se* are important for quantitative increases in target gene expression, we took advantage

eRNAs with UP genes (Fig. 1b). ChIP-Seq analysis revealed that UP enhancers showed significantly stronger binding of ER- α than enhancers not exhibiting eRNA upregulation (Fig. 1c). Proximal (<200 kb) UP enhancers constituted a majority of all UP enhancers and had a higher affinity for ER- α than did distal UP enhancers (Fig. 1d, e). The strength of ER- α binding was much higher on UP enhancers than on 112 ER- α -bound promoters of coding genes that showed E2 induction, whereas the remaining 790 ER- α -bound promoters of genes with no E2 upregulation exhibited the weakest ER- α binding (Fig. 1f).

On the basis of GRO-seq analyses, we selected ten highly upregulated transcription units for further experimentation, each associated with adjacent UP enhancers exhibiting ~2.5–5-fold E2 induction of eRNAs (Supplementary Fig. 1j). Despite increasing evidence for crucial nuclear functions of lncRNAs^{4–6}, it remains an unresolved

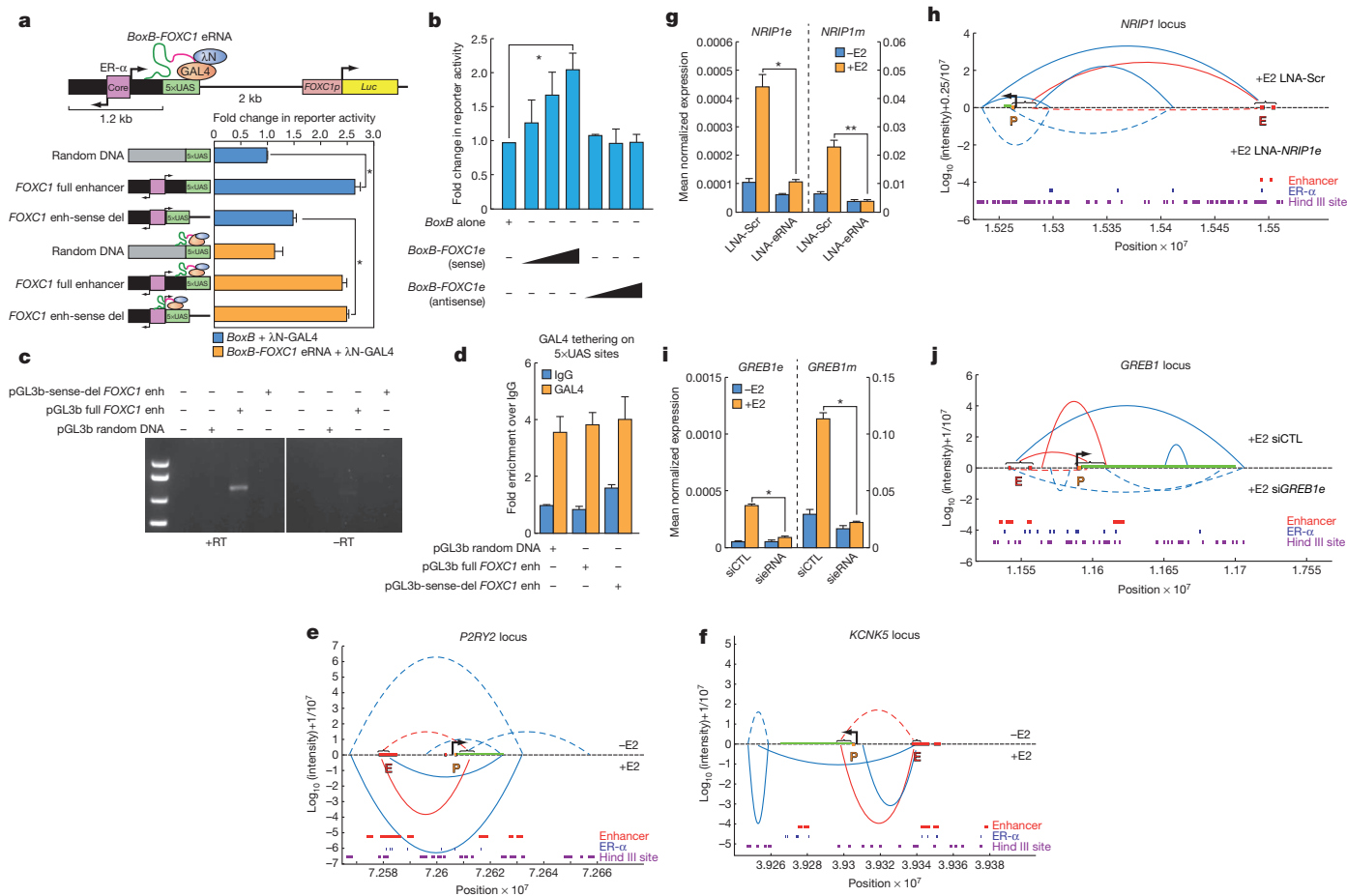


Figure 3 | Ligand-induced eRNA is functionally important. a, Schematic diagram of the *BoxB*- λ N tethering system on the *FOXCl* enhancer, which is upstream of a *FOXCl* native-promoter-linked luciferase (*Luc*). *FOXClp*, *FOXCl* promoter. 5 \times UAS sites are fused downstream to the *FOXCl* enhancer. GAL4- λ N fusion protein tethers *BoxB*-*FOXCl* eRNA to the 5 \times UAS sites. Bar graph shows the effects of the *FOXCl* eRNA on *FOXCl* promoter-driven *Luc* activity in the presence of E2 (24 h). Blue bars show how the activating function of the native full-length enhancer (bar 2) over random DNA (bar 1) is lost when the sense eRNA cassette is substituted with the 5 \times UAS site (bar 3). Orange bars show how this loss is largely rescued upon *FOXCl* eRNA tethering to the sense-eRNA-deleted enhancer cassette (enh-sense del; bar 6). b, eRNA function is sequence specific: *FOXCl*e sense eRNA but not antisense strand RNA could rescue the activity of sense-eRNA-deleted enhancer in the tethering assay. c, Gel picture showing plasmid-based eRNA expression from full-length enhancer (enh) but not from the sense-eRNA-deleted enhancer construct (pGL3b-sense-del *FOXCl* enh). RT, reverse transcriptase. d, Bar graph showing efficiency of GAL4 tethering on various pGL3b constructs. e, 3D-DSL data for the *P2RY2* locus, revealing

of a GAL4-*BoxB*-tethering-based reporter assay¹⁸. For this we engineered a chimaeric RNA by fusing *FOXC1* sense eRNA to *BoxB* viral RNA, permitting *BoxB-FOXC1* eRNA to be recruited by the RNA binding domain of λ N protein fused with the GAL4 DNA binding domain (λ N-GAL4). Thus eRNA can be artificially tethered to 5 \times UAS sites just downstream of the *FOXC1* enhancer in the reporter plasmid, in which luciferase (*Luc*) is under the control of the native *FOXC1* promoter (Supplementary Fig. 8). We observed that the presence of full-length *FOXC1* enhancer increased *Luc* expression to ~ 2.5 fold when compared to random DNA in place of the enhancer (Fig. 3a, blue bars). This effect was abolished when the sense eRNA sequence was deleted and substituted with 5 \times UAS sites, generating a non-functional ‘missense’ eRNA (Fig. 3a, blue bars, and Supplementary Fig. 8). Tethering of *BoxB-FOXC1* eRNA, but not *BoxB* alone, could fully rescue the activity loss of sense-eRNA-deleted enhancer (Fig. 3a, orange bars), whereas the antisense *FOXC1* eRNA could not (Fig. 3b). We confirmed the loss

strengthened promoter–enhancer interactions over basal conditions after 1 h E2 treatment. For all 3D-DSL data, the \log_{10} intensities of interaction counts plus 1 or 0.25 for presentation purposes are on the y-axis, and the x-axis depicts coordinates from the University of California, Santa Cruz (UCSC) genome browser. Interaction data are overlaid with positions of the enhancer, ER- α -binding sites and HindIII sites on the regions interrogated. The pertinent promoter–enhancer interaction is shown in red and other interactions are shown in blue. E, enhancer; P, promoter. **f**, 3D-DSL data for the *KCNK5* locus after 1 h E2 treatment. **g**, LNA knockdown of *NR1P1* eRNA effectively reduced the levels of both eRNA and associated coding gene transcripts. **h**, 3D-DSL data demonstrating significant reduction in promoter–enhancer interaction upon treatment of LNA against *NR1P1* eRNA. **i**, *GREB1*e siRNA knockdown diminished the levels of eRNA and associated coding gene transcript. CTL, control. **j**, 3D-DSL data for the *GREB1* locus showing significantly reduced enhancer–promoter looping as well as other genomic interactions after *GREB1*e-specific siRNA treatment. Dotted lines in panels **e** and **f** represent –E2 condition, but knockdown situation in panels **h** and **j**. Data show mean \pm s.d.; ($n = 3$). * $P < 0.05$, ** $P < 0.01$.

of plasmid-driven native *FOXC1* eRNA expression from the sense-eRNA-deleted reporter construct, and showed that GAL4 tethering was not altered (Fig. 3c, d). These data further support the suggestion that the sequence-specific eRNA transcript *per se*, rather than merely the process of enhancer transcription, is required for the actions of the eRNA on enhancer-dependent coding-gene activation events. This observation is consistent with recent studies of the role of ncRNAs in p53-dependent gene activation¹⁹ and in regulation of the *SNAIL* gene²⁰.

We next investigated whether enhancer–promoter looping is induced in the E2-activation events²¹, using a strategy analogous to chromosome conformation capture carbon copy (5C), which is named three-dimensional DNA selection and ligation (3D-DSL)²², to study the spatial organization of genomes^{23,24}. We first examined two E2-regulated transcription units: *P2RY2* and *KCNK5*. For *P2RY2*, E2 treatment significantly increased the specific promoter–enhancer interaction (Fig. 3e), and

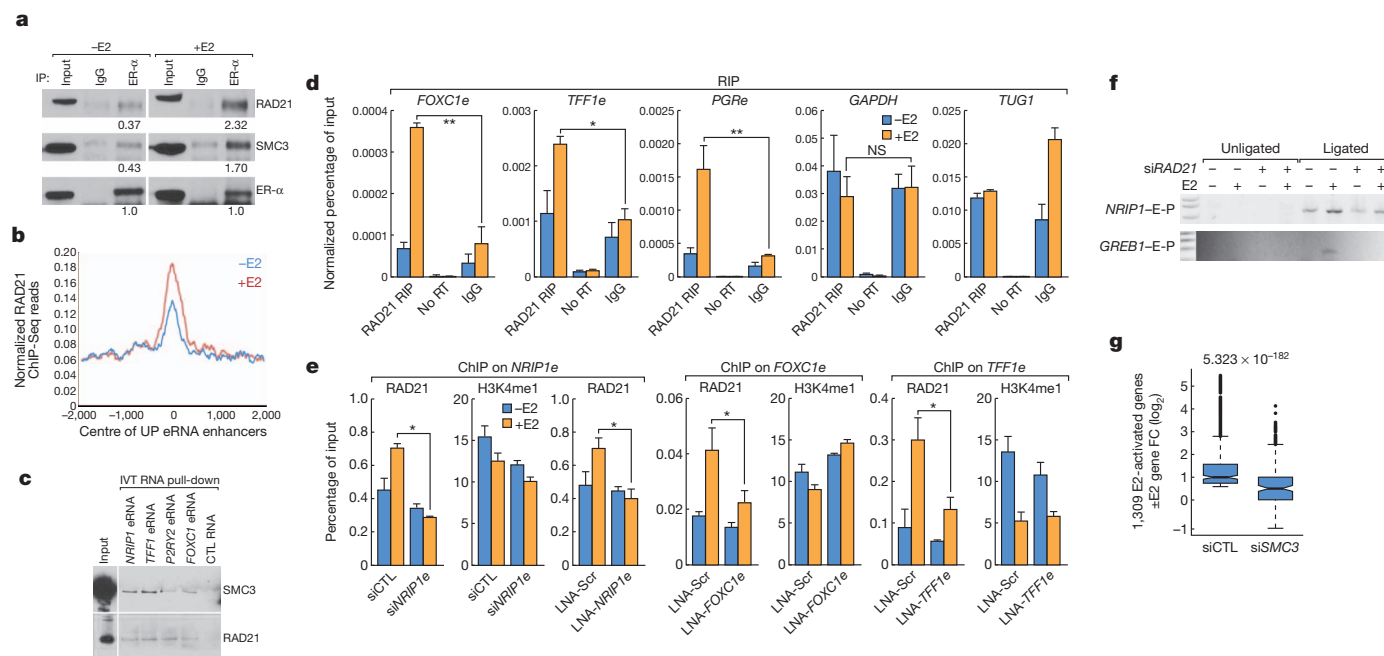


Figure 4 | Role of eRNA in cohesin-dependent gene activation. **a**, Co-immunoprecipitation (IP) of RAD21 and SMC3 with ER-α from E2 or ethanol-treated MCF-7 whole-cell extracts showing the physical interaction between ER-α and cohesin subunits, which is enhanced by E2 treatment. Numbers below blots indicate the band density (Image J, <http://rsbweb.nih.gov/ij/>) relative to that of the corresponding density of ER-α. **b**, RAD21 enrichment centred at UP enhancers as determined by ChIP-Seq, which shows moderate E2-induced increase. **c**, IVT RNA pull-down assay showing the interaction between cohesin subunits and eRNAs, but not a control RNA (RNA fragment of *Xenopus* elongation factor α; CTL). **d**, RIP-qPCR showing binding of RAD21

to selected regulated eRNAs but not to *GAPDH* or *TUG1*. RT, reverse transcriptase. **e**, ChIP-qPCR analyses represent the inhibitory effect from knockdown of *NRIP1e* (siRNA and LNA), *FOXC1e* or *TFF1e* on E2-induced RAD21 additional recruitment, but not on H3K4me1 binding. **f**, Effect of RAD21 depletion on the physical interaction between promoter–enhancer for the *GREB1* and *NRIP1* genes, assessed by 3C assay. E, enhancer; P, promoter. **g**, 1,309 E2-induced coding genes were defined by GRO-seq from the control siRNA (siCTL; ± E2) group, and then their fold changes (log₂ FC) in siCTL- versus siSMC3-transfected MCF-7 cells were plotted. Data show mean ± s.d.; (n = 3). *P < 0.05, **P < 0.01.

also induced a new E2-dependent interaction between the enhancer and the gene terminus region. Similarly, for the *KCNK5* locus, E2 treatment caused a clear increase in loops from enhancer to promoter, as well as to other regions near the terminator and promoter (Fig. 3f). These observations indicate that a major effect of ligand is to enhance specific promoter–enhancer interactions in parallel to induction of eRNA.

We next investigated whether E2-induced enhancer–promoter interactions are affected by eRNAs. The *NRIP1* locus exhibited specific enhancer–promoter and promoter–gene-terminus loops, whereas treatment with LNA against *NRIP1* eRNA caused a marked inhibition of these interactions (Fig. 3h) and E2 activation of the *NRIP1* gene (Fig. 3g). siRNA-mediated *GREB1* eRNA knockdown also coordinately inhibited *GREB1* gene induction and the two specific enhancer–promoter interactions induced by E2 and two additional non-enhancer loops (Fig. 3i, j). Together these experiments indicate that oestrogen causes quantitative, as well as some qualitative, alterations in the interactions between enhancers and coding-gene promoters, and that eRNAs are of functional importance, at least under the experimental conditions here, for enhancer–promoter interactions.

To address the possibility that eRNAs might also work *in trans*, we first estimated the absolute expression levels of the eRNAs, finding that most of the eRNAs we investigated were present at levels of <5–15 copies per cell, although several, including *TFF1* eRNA, were present at ~70–95 molecules per cell (Supplementary Fig. 4a, b), suggesting that these eRNAs were likely to function primarily *in cis*. Furthermore, we used chromatin isolation by RNA purification (ChIRP)²⁵ to identify potential sites where *FOXC1* eRNA localizes in the genome; despite robust detection of *FOXC1* eRNA from its transcribing site—establishing the efficacy of the biotin-labelled probes used (Supplementary Fig. 4c)—only 15 peaks could be confidently called, and for none was the nearest gene E2 regulated (Supplementary Fig. 4c). In addition,

qPCR analysis after knockdown of *FOXC1* eRNA revealed no significant effects on E2 activation of *NRIP1*, *TFF1*, *PGR* or *KCNK5* genes (Fig. 2c). GRO-seq after LNA transfection against *FOXC1* eRNA revealed that a large majority (>95%) of the E2-upregulated coding genes continued to exhibit clear E2-dependent upregulation. Therefore, any *trans* effects of eRNAs are likely to be relatively infrequent or quantitatively small. Of course, there are inevitably indirect effects observed after knockdown of any eRNA that downregulates a functional coding gene. However, at least for a few gene areas, there may be effects of enhancer-based long-range interactions. We identified at least one such example, between the *NRIP1* and *TFF1* loci, separated by ~27 Mb on chromosome 21, exhibiting an E2-induced increase of colocalization by fluorescence *in situ* hybridization (FISH; Supplementary Fig. 5a–c). Surprisingly, knockdown of *NRIP1e* eRNA by LNA caused a clear decrease in the interactions between these two genomic loci (Supplementary Fig. 5b, c), suggesting that such E2-induced colocalization was eRNA dependent.

Because several studies have implicated a role for cohesin in chromosomal interactions and enhancer–promoter looping events^{26–28}, we investigated whether cohesin was involved in the observed eRNA functions. First, co-immunoprecipitation showed that ER-α can interact with cohesin subunits (Fig. 4a). ChIP-Seq revealed that ~30–40% of RAD21 (a subunit of cohesin) binding sites overlap with putative H3K4me1/H3K27ac-marked enhancers in MCF-7 cells²⁸ (Supplementary Fig. 7h). After E2 treatment, both ChIP-Seq (Fig. 4b) and ChIP-qPCR data revealed a reproducible, but modest (50–200%), increased occupancy of RAD21 and SMC3 on the interrogated enhancers, as exemplified by *FOXC1e*, *NRIP1e* and *TFF1e* (Fig. 4e and Supplementary Fig. 6a). By *in vitro* transcribed (IVT) RNA pull-down, the investigated eRNAs could pull-down SMC3 and RAD21 from MCF-7 nuclear extracts (Fig. 4c and Supplementary Fig. 6b). RIP-qPCR confirmed the interaction between cohesin and several eRNAs,

but not with *GAPDH* or another nuclear RNA, *TUG1* (Fig. 4d). To test possible direct or indirect involvement of RNAs in cohesin recruitment to enhancers, we found that RNase treatment caused some decrease of the cohesin level in the chromatin-bound fraction of cells (Supplementary Fig. 6c). Knockdown of specific eRNAs by LNA or siRNA resulted in a decrease of cohesin recruitment (Fig. 4e) to enhancers in response to E2, with no significant alteration of the H3K4me1 mark (Fig. 4e), or ligand-dependent increase of ER- α recruitment (Supplementary Fig. 2d, e). Expression levels of cohesin subunits were not affected by knockdown of eRNAs (Supplementary Fig. 7a). siRNA-mediated depletion of RAD21 caused loss of enhancer–promoter interactions, both basal and E2 induced, when assessed by chromatin conformation capture (3C) assay for the *NR1P1* and *GREB1* loci (Fig. 4f). When we tested the role of cohesin in the oestrogen transcription program by GRO-seq, we noted that siSMC3 caused a broad inhibition of coding gene activation by E2 (Fig. 4g and Supplementary Fig. 7e, f), with only ~34% of E2-upregulated genes remaining induced (Supplementary Fig. 7g). Similarly, RAD21 knockdown inhibited E2 induction of genes, as revealed by the five targets evaluated (Supplementary Fig. 7d). We excluded alterations in levels of ER- α as the cause for these marked effects of cohesin depletion (Supplementary Fig. 7b, c). On the basis of these results, we speculate that many regulatory genomic regions, such as enhancers, harbour the cohesin complex, which ‘poises’ the enhancer for the stable eRNA-induced looping necessary for gene activation events. However, we cannot exclude the possibility that the role of cohesin could also reflect non-enhancer-based regulation.

Despite the discovery of enhancers more than 35 years ago^{1,2}, a full understanding of the mechanisms by which they regulate gene expression has been difficult to achieve. We have provided several lines of evidence that induced eRNA transcripts are functionally important for the actions of oestrogen-regulated gene enhancers, at least in part by contributing to the dynamic generation or stabilization of enhancer–promoter looping between the regulated coding transcription units and these ER- α -bound enhancers.

METHODS SUMMARY

MCF-7 cells were initially obtained from ATCC, maintained in culture and treated as described previously¹². They were hormone stripped for 3 days and treated or untreated with 100 nM oestradiol for 1 h to induce oestrogen target gene expression. Custom siRNAs were designed in-house and chemically synthesized by Bioneer and Sigma-Aldrich, whereas LNAs were designed and synthesized by Exiqon. Knockdown experiments with either siRNAs or LNAs were performed as transient transfections using Lipofectamine 2000, as per the manufacturer's instructions (Invitrogen). For siRNAs, hormone-stripped cells were subjected to two rounds of transfection and then treated with either vehicle or E2 for 1 h; for LNAs, cells were cultured for 24 or 48 h after transfection and exposed to the same treatment as described earlier. Real-time qPCR was carried out as previously described^{9,12}, normalized to either *ACTD* or *GAPDH*. FISH experiments were carried out as detailed previously²⁹, using commercially available bacterial artificial chromosome (BAC) probes obtained from Empire Genomics (Supplementary Table 1). The high-throughput sequencing libraries were prepared as per Illumina's HiSeq 2000 library reagent kit. Global run-on sequencing experiments (GRO-seq) were performed as previously reported³⁰. 3D-DSL used a conventional 3C step for ~200 kb surrounding each interrogated E2-regulated gene TSS, and was performed as previously described²², with all donor and acceptor probes designed using HindIII restriction sites. ChIP-Seq for ER- α , H3K4me1, H3K27ac and RAD21 were performed as described⁹. Detailed descriptions of bioinformatic analyses are provided in Methods.

Full Methods and any associated references are available in the online version of the paper.

Received 21 May 2012; accepted 22 April 2013.

Published online 2 June 2013.

- Newman, J. J. & Young, R. A. Connecting transcriptional control to chromosome structure and human disease. *Cold Spring Harb. Symp. Quant. Biol.* **75**, 227–235 (2010).
- Bulger, M. & Groudine, M. Functional and mechanistic diversity of distal transcription enhancers. *Cell* **144**, 327–339 (2011).

- Ong, C. T. & Corces, V. G. Enhancer function: new insights into the regulation of tissue-specific gene expression. *Nature Rev. Genet.* **12**, 283–293 (2011).
- Guttman, M. & Rinn, J. L. Modular regulatory principles of large non-coding RNAs. *Nature* **482**, 339–346 (2012).
- Wang, K. C. & Chang, H. Y. Molecular mechanisms of long noncoding RNAs. *Mol. Cell* **43**, 904–914 (2011).
- Mercer, T. R., Dinger, M. E. & Mattick, J. S. Long non-coding RNAs: insights into functions. *Nature Rev. Genet.* **10**, 155–159 (2009).
- Kim, T.-K. *et al.* Widespread transcription at neuronal activity-regulated enhancers. *Nature* **465**, 182–187 (2010).
- Hah, N. *et al.* A rapid, extensive, and transient transcriptional response to estrogen signaling in breast cancer cells. *Cell* **145**, 622–634 (2011).
- Wang, D. *et al.* Reprogramming transcription by distinct classes of enhancers functionally defined by eRNA. *Nature* **474**, 390–394 (2011).
- Welboren, W. J. *et al.* ChIP-Seq of ER α and RNA polymerase II defines genes differentially responding to ligands. *EMBO J.* **28**, 1418–1428 (2009).
- Carroll, J. S. *et al.* Genome-wide analysis of estrogen receptor binding sites. *Nature Genet.* **38**, 1289–1297 (2006).
- Kwon, Y. S. *et al.* Sensitive ChIP-DSL technology reveals an extensive estrogen receptor α -binding program on human gene promoters. *Proc. Natl Acad. Sci. USA* **104**, 4852–4857 (2007).
- Heintzman, N. D. & Ren, B. Finding distal regulatory elements in the human genome. *Curr. Opin. Genet. Dev.* **19**, 541–549 (2009).
- Heintzman, N. D. *et al.* Histone modifications at human enhancers reflect global cell-type-specific gene expression. *Nature* **459**, 108–112 (2009).
- Creyghton, M. P. *et al.* Histone H3K27ac separates active from poised enhancers and predicts developmental state. *Proc. Natl Acad. Sci. USA* **107**, 21931–21936 (2010).
- Ahlsenstiel, C. L. *et al.* Direct evidence of nuclear Argonaute distribution during transcriptional silencing links the actin cytoskeleton to nuclear RNAi machinery in human cells. *Nucleic Acids Res.* **40**, 1579–1595 (2012).
- Mayer, C., Schmitz, K. M., Li, J., Grummt, I. & Santoro, R. Intergenic transcripts regulate the epigenetic state of rRNA genes. *Mol. Cell* **5**, 351–361 (2006).
- Wang, K. C. *et al.* A long noncoding RNA maintains active chromatin to coordinate homeotic gene expression. *Nature* **472**, 120–124 (2011).
- Melo, C. A. *et al.* eRNAs are required for p53-dependent enhancer activity and gene transcription. *Mol. Cell* **49**, 524–535 (2013).
- Lai, F. *et al.* Activating RNAs associate with Mediator to enhance chromatin architecture and transcription. *Nature* **494**, 497–501 (2013).
- Fullwood, M. J. *et al.* An oestrogen-receptor- α -bound human chromatin interactome. *Nature* **462**, 58–64 (2009).
- Harismendy, O. *et al.* 9p21 DNA variants associated with coronary artery disease impair interferon- γ signalling response. *Nature* **470**, 264–268 (2011).
- Sanyal, A., Lajoie, B. R., Jain, G. & Dekker, J. The long-range interaction landscape of gene promoters. *Nature* **489**, 109–113 (2012).
- Lieberman-Aiden, E. *et al.* Comprehensive mapping of long-range interactions reveals folding principles of the human genome. *Science* **326**, 289–293 (2009).
- Chu, C., Qu, K., Zhong, F. L., Artandi, S. E. & Chang, H. Y. Genomic maps of long noncoding RNA occupancy reveal principles of RNA-chromatin interactions. *Mol. Cell* **44**, 667–678 (2011).
- Hadjir, S. *et al.* Cohesins form chromosomal *cis*-interactions at the developmentally regulated *IFNG* locus. *Nature* **460**, 410–413 (2009).
- Kagey, M. H. *et al.* Mediator and cohesin connect gene expression and chromatin architecture. *Nature* **467**, 430–435 (2010).
- Schmidt, D. *et al.* A CTCF-independent role for cohesin in tissue-specific transcription. *Genome Res.* **20**, 578–588 (2010).
- Cai, S. & Kohwi-Shigematsu, T. Intracellular relocation of matrix binding sites during T cell activation detected by amplified fluorescence *in situ* hybridization. *Methods* **19**, 394–402 (1999).
- Core, L. J., Waterfall, J. J. & Lis, J. T. Nascent RNA sequencing reveals widespread pausing and divergent initiation at human promoters. *Science* **322**, 1845–1848 (2008).

Supplementary Information is available in the online version of the paper.

Acknowledgements We thank K. Hutt for help with statistical analyses; M. Ghassemin from the University of California, San Diego (UCSD) Biomolecular/Proteomics Mass Spectrometry Facility for assistance with mass spectrometry; C. Nelson for cell culture assistance; J. Hightower for assistance with figure and manuscript preparation. We thank H. Chang for providing the *BoxB*, λ N–GAL4 constructs. We acknowledge the UCSD Cancer Center Specialized Support Grant P30 CA23100 for confocal microscopy. W.L. and D.N. are supported by Department of Defense (DoD) postdoctoral fellowships, BC110381 and BC103858, respectively. M.G.R. is an investigator with the Howard Hughes Medical Institute. This work was supported by grants DK 039949, DK018477, NS034934, HL065445, CA173903 to C.K.G., and from the DoD.

Author Contributions M.G.R., W.L., D.N., E.N. and C.K.G. conceived the project. W.L. and D.N. performed most of the experiments reported, with contributions from E.N. and A.Y.C. (FISH). Q.M., B.T. and D.M. performed bioinformatic analyses. Q.M., E.N. and B.T. made equivalent contributions to this study. Additional experiments/methods were contributed by X.S., S.O. and H.-S.K. J.Z. and K.O. assisted in deep-sequencing library preparations and sequencing. W.L., D.N. and M.G.R. wrote the final paper with input from C.K.G.

Author Information The sequencing data sets are deposited in the Gene Expression Omnibus database under accession GSE45822 Reprints and permissions information is available at www.nature.com/reprints. The authors declare no competing financial interests. Readers are welcome to comment on the online version of the paper. Correspondence and requests for materials should be addressed to M.G.R. (mrosenfeld@ucsd.edu).

METHODS

Antibodies. The antibodies used in this study were: anti-ER- α (HC-20, Santa Cruz); anti-H3K4me3 (07-473, Santa Cruz); anti-H3K4me1 (ab8899, Abcam); anti-H3K27ac (ab4729, Active Motif); anti-RAD21 (ab992, Abcam); anti-SMC3 (ab9263, Abcam); anti- α -tubulin (T5168, Sigma), anti-GAL4 (DNA-binding domain (DBD)) (06-262, Millipore); and anti-IgG (I5006, Sigma).

Cell culture. MCF-7 cells obtained from ATCC were cultured in DMEM media supplemented with 10% FBS in a 5% CO₂ humidified incubator. They were hormone stripped for 3 days in phenol-free media with charcoal-stripped FBS before receiving 100 nM E2 (Sigma) or ethanol treatment for 1 h for oestrogen signalling induction. MCF10A cells were a gift from B. H. Park and were essentially grown as described previously³¹. For E2 induction of MCF10A, the culture media was stripped of EGF.

siRNA and LNA transfections. LNAs were obtained from Exiqon; siRNAs were from Bioneer and Sigma-Aldrich (Supplementary Tables 2 and 3). For transfection of both siRNA and LNAs, cells were first hormone stripped for 1 day followed by siRNA/LNA (both at 40 nM) transfection using Lipofectamine 2000. After 2 days they were then treated with ethanol or E2 for 1 h. For some experiments, transfections were performed twice to achieve higher efficiency. Similarly, LNA transfections were performed 2 days after starvation in stripped media, and thus the LNA treatment lasted 24 h in some experiments.

RT-qPCR. RNA was isolated using Trizol (Invitrogen) or RNeasy column (Qiagen), and total RNA was reverse transcribed using SuperScript III Reverse Transcriptase (Invitrogen). Quantitative PCRs were performed mostly with StepOne Plus (Applied Biosystem). For normalization, ΔC_t values were calculated relative to the levels of *ACTB/GAPDH* transcripts. The experiments were repeated at least three times, and one representative plot is shown in figures; most *P* values were obtained using a two-tailed Student's *t*-test. Primers are listed in Supplementary Table 4.

ChIP-Seq. ChIP was performed as previously described⁹. Briefly, approximately 10⁷ cells were cross-linked with 1% formaldehyde at room temperature (~25 °C) for 10 min and neutralized with 0.125 M glycine. After sonication, ~75 μ g soluble chromatin was incubated with 1–5 μ g of antibody at 4 °C overnight. Immunoprecipitated complexes were collected using Dynabeads A/G (Invitrogen). Subsequently, immuno-complexes were washed, and DNA was extracted and purified by QIAquick Spin columns (Qiagen). For ChIP-Seq, the extracted DNA was ligated to specific adaptors followed by deep sequencing with the Illumina's HiSeq 2000 system according to the manufacturer's instructions. Usually, the first 48 bp for each sequence tag returned by the Illumina Pipeline was aligned to the hg18 assembly using BFAST or Bowtie2. Only uniquely mapped tags were selected for further analysis. The data was visualized by preparing custom tracks on the UCSC genome browser using HOMER³² (<http://biowhat.ucsd.edu/homer>). The total number of mappable reads was normalized to 10⁷ for each experiment presented in this study.

Identification of ChIP-Seq peaks. The ChIP-Seq peaks were identified by HOMER. Given different binding patterns of transcription factors and histones, parameters were optimized for the narrow tag distribution characteristic of transcription factors by searching for high read-enrichment regions within a 200-bp sliding window. Regions of maximal density exceeding a given threshold were called as peaks, and adjacent peaks were set to be >500 bp away to avoid redundant detection. The common artefacts from clonal amplification were circumvented by considering only one tag from each unique genomic position. The threshold was set at a false discovery rate (FDR) of 0.001 determined by peak finding using randomized tag positions in a genome with an effective size of 2×10^9 bp. For ChIP-Seq of histone marks, seed regions were initially found using a peak size of 500 bp (FDR <0.001) to identify enriched loci. Enriched regions separated by <1 kb were merged and considered as blocks of variable lengths. All called peaks were then associated with genes by cross-referencing with the RefSeq TSS database. Peaks from individual experiments were considered overlapping if their peak centres were located within 200 bp (for some analyses the distance between them could extend to 1 kb). The peaks within ± 1 kb apart from the RefSeq gene TSS site were considered to be promoter bound.

GRO-seq. GRO-seq experiments were performed as previously reported^{9,30,33}. Briefly, MCF-7 cells were swelled in swelling buffer (10 mM Tris-Cl pH 7.5, 2 mM MgCl₂, 3 mM CaCl₂) for 5 min on ice and then lysed in lysis buffer (swelling buffer with 0.5% IGEPAL and 10% glycerol) before being finally re-suspended in 100 μ l of freezing buffer (50 mM Tris-Cl pH 8.3, 40% glycerol, 5 mM MgCl₂, 0.1 mM EDTA). For the run-on assay, re-suspended nuclei were mixed with an equal volume of reaction buffer (10 mM Tris-Cl pH 8.0, 5 mM MgCl₂, 1 mM dithiothreitol (DTT), 300 mM KCl, 20 units of Superase-In, 1% sarkosyl, 500 μ M ATP, GTP, Br-UTP and 2 μ M CTP) and incubated for 5 min at 30 °C. The nuclear-run-on RNA (NRO-RNA) was then extracted with TRIzol LS reagent (Invitrogen) following the manufacturer's instructions. After base hydrolysis on ice

for 40 min and followed by treatment with DNase I and antarcctic phosphatase, the Br-UTP-labelled NRO-RNA was purified by anti-BrdU argarose beads (Santa Cruz Biotech) in binding buffer (0.5 \times SSPE, 1 mM EDTA, 0.05% Tween) for 3 h at 4 °C while rotating. Then T4 PNK (NEB) was used to repair the end of NRO-RNA. Subsequently, complementary DNA synthesis was performed as reported^{9,33} with few modifications. The RNA fragments were subjected to the poly-A-tailing reaction by poly-A polymerase (NEB) for 30 min at 37 °C. Reverse transcription was then performed using superscript III (Invitrogen) with oNT1223 primer (for sequence see Supplementary Table 5). The cDNA products were separated on a 10% polyacrylamide TBE-urea gel with the right product (~100–500 bp) being excised and recovered by gel extraction. After that, the first-strand cDNA was circularized by CircLigase (Epicentre) and re-linearized by ApeI (NEB). Re-linearized single-strand cDNA was separated by TBE gel and the products of the desired size were excised (~120–320 bp) for gel extraction. Finally, the cDNA template was amplified by PCR using the Phusion High-Fidelity enzyme (NEB) with primers oNT1200 and oNT1201 for deep sequencing (primers listed in Supplementary Table 5).

Computational analysis of GRO-seq. The sequencing reads were aligned to hg18 using Bowtie2. For analysing oestrogen effects on gene transcription, we counted the reads from the first 30 kb (assuming an RNA polymerase speed of ~0.5 kb min⁻¹ during 1 h E2 treatment) of the entire gene body, excluding the promoter-proximal region on the sense strand with respect to the gene orientation by using BED Tools or HOMER. EdgeR (<http://www.bioconductor.org/>) was used to compute the significance of the differential gene expression (FC ≥ 1.5 , FDR ≤ 0.01). Additionally, a read density threshold (that is, normalized GRO-seq read counts per kb) was used to exclude lowly expressed genes.

De novo identification of GRO-seq transcripts. GRO-seq read densities were analysed in a similar manner to ChIP-Seq. Provided that GRO-seq generated strand-specific data, separate tracks were uploaded onto the UCSC genome browser; tag-enriched sites were identified using a sliding window of 250 bp. Transcript initiation sites were identified as regions where the GRO-seq read density was increased threefold relative to the preceding 1 kb region. Transcript termination sites were defined by either a reduction in reads below 10% as compared to that of the TSS or when another transcript's start was identified on the same strand. Individual high-density peaks spanning a region less than 250 bp were considered artefacts and removed from the analysis. Transcripts were defined as putative eRNAs if their *de novo* called start sites was located distal to the RefSeq TSS (≥ 3 kb) and were associated with ER- α and H3K27ac co-bound regions.

Bioinformatics characterization of ER- α enhancers. The ER- α -H3K27ac co-bound regions are defined as those in which the distance from the centre of an ER- α peak to the H3K27ac peak-occupied region is ≤ 1 kb. Overall, two methods were used to assign the ER- α -bound enhancers to E2-upregulated genes: (1) identifying the E2-upregulated coding genes from GRO-seq first and then coupling each of them to their closest ER- α -H3K27ac co-bound enhancer within a certain distance (200 kb) (a 'gene-centric' view); and (2) characterizing the ER- α -H3K27ac co-bound enhancers first and then coupling each of them to their closest TSS that belongs to 1,309 E2-upregulated coding genes (an 'enhancer-centric' view). The comparison of ChIP-Seq tag intensity, GRO-seq transcription levels or distances between different categories (Figs 1 and 4 and Supplementary Fig. 1) are presented as boxplots by using either log or normal scales. The *P* values were determined by two-tailed Student's *t*-test.

ChIRP-Seq. The ChIRP experiment was performed essentially as per the original protocol²⁵, except for a few modifications. First, we designed antisense DNA probes targeting *FOXC1* eRNA ('odd' and 'even') (~40-base oligonucleotide) based on high oligonucleotide specificity (using BLAST and BLAT), moderate GC content (40–60%) and a *T_m* around 65 °C, with probes for *lacZ* RNA as control (all probes listed in Supplementary Table 8). All DNA probes were biotinylated and purified using the Label IT Nucleic Acid Labelling Kit (Mirus Bio). The sequencing reads were aligned to hg18 by Bowtie2 and the peaks were called by HOMER if they fulfilled three criteria: (1) they were consistently called in both the 'odd' and 'even' ChIRP-Seqs; (2) they did not intersect with the peaks in the ChIRP-Seq for *lacZ* RNA sample; and (3) they did not intersect with the satellite repeats or retrotransposon sequences. The remaining ChIRP peaks were divided into two categories: (1) highly confident peaks (peak score >8); and (2) weak-peaks (peak score ≤ 8). The peaks were extended with 1 kb for intersection analysis by using BedTools, and the peak annotation was carried out in HOMER.

RNA copy number quantification. To quantify each transcript, the PCR product using the qPCR primers for the transcript was purified and the concentration was measured. The absolute copy numbers of the PCR product were calculated as per the following. For example, for *GAPDH*, the number of single-stranded (ss)DNA molecules from 1 μ l of the 17 ng μ l⁻¹ PCR product of the *GAPDH* fragment (142 bp) with 87,788.56 Da molecular weight is about $2 \times (17 \times 10^{-9} \times 6.023 \times 10^{23})/87,788.56 = 2.32 \times 10^{11}$. The number of ssDNA molecules from 1 μ l of

the $16 \text{ ng } \mu\text{l}^{-1}$ PCR product of the *TFE1e* fragment (82 bp) with 50,696.92 Da molecular weight is about $2 \times (16 \times 10^{-9} \times 6.023 \times 10^{23}) / 50,696.92 = 3.8 \times 10^{11}$. Using these PCR products with known molecule copy numbers, standard curves can be generated by qPCR, which forms the basis of the quantification of the number of copies of eRNAs from cDNA samples. For cDNA samples, 3 μg of total RNA (which is, according to the QIAGEN manual, $\sim 2 \times 10^5$ cells) were converted into 20 μl cDNA. During multiple qPCR experiments using cells from different batches, the cycle number of target eRNA being amplified will vary within 2–3 cycles (~ 4 –8 fold). The copy number of *GAPDH* mRNA is largely consistent with previous reports³⁴. Considering that the efficiency of reverse transcriptase on *GAPDH* mRNA is estimated to be $\sim 50\%$ (ref. 35), which might be even lower for eRNAs, the real numbers of eRNA copies could be higher than the estimation.

Immunoprecipitation. Cells were collected with cold PBS and lysed with RIPA buffer (50 mM Tris pH 7.4, 150 mM NaCl, 1 mM EDTA, 0.1% SDS, 1% NP-40, 0.5% sodium deoxycholate, 0.5 mM DTT, protease inhibitor). The lysate was diluted 2–4 times with dilution buffer (50 mM Tris pH 7.4, 100 mM NaCl, 1 mM EDTA, 0.1% NP-40 and 10% glycerol, protease inhibitor). 2–5 μg of antibodies were added into the diluted cell lysate and incubated overnight at 4 °C. The next day, the protein complexes were collected by magnetic Dynabeads G for 2 h at 4 °C with rotation. The beads–antibody–protein complexes were then washed four times with wash buffer (50 mM Tris pH 7.4, 125 mM NaCl, 1 mM EDTA and 0.1% NP-40) and boiled for western blot analysis.

RIP and IVT RNA pull-down. The RIP experiment was done largely as per a previous protocol³⁶. Briefly, cells were cross-linked with 0.3% formaldehyde for 10 min at 37 °C. 2.5 M glycine was added (1/20 of the medium volume) to neutralize for 10 min at room temperature. The cell pellet was re-suspended in 0.6 ml of RIPA buffer (50 mM Tris pH 7.4, 150 mM NaCl, 1 mM EDTA, 0.1% SDS, 1% NP-40, 0.5% sodium deoxycholate, 0.5 mM DTT, protease inhibitor and Superscript-In 40 units per ml), sonicated once and incubated on ice with frequent vortex for 25 min. Subsequently, the supernatant was diluted with RIP dilution buffer (50 mM Tris pH 7.4, 150 mM NaCl, 1 mM MgCl₂, 0.05% NP40) and pre-cleared with $\sim 25 \mu\text{l}$ protein A sepharose slurry for 30 min at 4 °C. Antibodies were added and incubated overnight at 4 °C with rotation. The next day, the RNA–protein complex was collected using pre-washed $\sim 60 \mu\text{l}$ protein A sepharose beads for 1.5–2.5 h at 4 °C. After washing in RIPA buffer and RIPA-500 buffer (RIPA with higher salt: 500 mM NaCl), the beads were re-suspended in 150 μl of RIPA buffer with proteinase K at 45 °C for 45 min. RNA was extracted with TRIzol followed by DNaseI digestion. Reverse transcription was performed with SuperScript III RT kit (Invitrogen). For RIP-qPCRs, the amount of RNA in pull-down samples was calculated as the percentage of input *GAPDH* RNA of its respective group. The assay was repeated at least two times but was presented as a representative plot. *P* values were obtained using two-tailed Student's *t*-test.

For IVT RNA pull-down, first, plasmids carrying DNA sequences of the eRNA being investigated were linearized and *in vitro* transcribed using MEGATranscript kit (Ambion) with 25% of UTP being replaced by biotinylated UTP (Ambion). About 10 μg of biotinylated RNA was heated to 90 °C for 3 min, put on ice for 2 min and added into RNA structure buffer (10 mM Tris pH 7.2, 0.1 M KCl, 10 mM MgCl₂, 1 μl Superscript-In) for 20 min to form a structure. The biotinylated RNA was then mixed with pre-washed Streptavidin magnetic beads and incubated at room temperature for 30 min to conjugate the RNA with the beads, following the manufacturer's protocol. After that, $\sim 10 \text{ mg}$ nuclear extract in RIP buffer (20 mM Tris pH 7.4, 1 mM EDTA, 150 mM NaCl, 0.5 mM DTT, 0.1% NP-40, 5% glycerol, protease inhibitor and Superscript-In 40 units per ml) was then mixed with biotinylated RNA and incubated at 4 °C for 4 h. After being washed four times in high salt buffer (20 mM Tris pH 7.4, 500 mM NaCl, 0.05% Triton X-100, 10 units per ml Superscript-In), the beads were boiled for western blots.

DNA enzyme digestion methylation assay. The protocol largely follows a previous paper¹⁷. Briefly, genomic DNA was extracted from MCF-7 cells (AccuPrep, Bioneer) 24 h after transfection with LNA/siRNA against eRNAs, and was digested with HpaII (*NR1P1e*) or HhaI (*FOXCIe*), both from NEB, before qPCR amplification using primers (Supplementary Table 4) that spanned the enzyme digestion sites (Supplementary Fig. 3a). The relative resistance to restriction digestion was calculated by dividing the amount of DNA that remained after digestion by the amount before digestion.

Methyl miner assay. MCF-7 cells were transfected with LNA or siRNA for 24 h, after which they were subjected to DNA isolation using a QIAGEN DNA isolation column. 1 μg of each DNA was used for Biotin-tagged-MBD peptide pull-down as per the manufacturer's protocol (Invitrogen), after which unmethylated and methylated DNA fractions were collected, purified and subjected to qPCR analysis using the primers specified (Supplementary Table 4).

FISH and imaging. The cells were processed for DNA Immuno-FISH essentially as described previously²⁹, with BAC probes from Empire Genomics (Supplementary

Table 1). MCF-7 cells were treated with ethanol or E2, grown on acid-washed poly-lysine-coated coverslips, were washed with 1 \times PBS and immediately fixed with freshly made 4% paraformaldehyde/PBS for 10 min. Permeabilization was achieved by incubating in PBS containing 0.5% Triton X-100 for 15 min. FISH pre-hybridization treatments include incubating the coverslips in 0.1 N HCl for 5 min at room temperature, followed by digestion with 0.01 N HCl/0.002% pepsin for 5 min at 37 °C, stopped by 50 mM MgCl₂/PBS and equilibrated in 50% formamide/2 \times SSC 2 h before hybridization. 5 μl of probe/hybridization buffer mix was used per coverslip, with a hybridization programme of 76 °C for 3 min followed by overnight hybridization at 37 °C in a humidified dark chamber. The coverslips were then washed with pre-warmed WS1 (0.4 \times SSC/0.3% NP-40), WS2 (2 \times SSC/0.1% NP-40) and PBS, before being finally mounted with prolong gold-DAPI anti-fade mounting reagent (Invitrogen).

For FISH Image acquisition and data analysis³⁷, images were acquired using the Leica SP5 II confocal microscopy ($\times 63$ objective lens) with a resonance scanner. Z-stack data acquisition was set up across 3.2 μm thickness at 0.4 μm each step (9 steps for each three-dimensional image set). The three-dimensional images were then generated in Volocity (v.6.0.1). The FISH-positive gene loci were identified using the “Find Object Using % Intensity” (generally $>20\%$) function in combination with “Exclude Objects by Size” (generally $>0.1 \mu\text{m}^3$). The overlap between two FISH-positive gene loci was calculated by the function “Intersect” with size exclusion ($>0.03 \mu\text{m}^3$). The cells counted ($n > 100$ for each group; Supplementary Fig. 5) were from eight images/fields; the percentage of overlapping events from each one was calculated separately, which together generates the mean and s.d.

BoxB- λ N tethering assay. Similar to the previous method¹⁸, as described in Fig. 3a and Supplementary Fig. 8, the *BoxB* tethering system uses viral RNA–protein interactions, in which *BoxB* is a viral RNA that can be recognized and bound by viral anti-terminator protein λ N. Fusion of *FOXCI* eRNA with *BoxB* enables the fused *BoxB-FOXCIe* to be bound by λ N. Subsequently, λ N protein was fused to the DNA-binding domain (DBD) of GAL4, which then recognizes 5 \times UAS sites on the reporter plasmid DNA. Using this technique, *BoxB*-eRNA can be tethered to the 5 \times UAS sites on a reporter plasmid with the help of the λ N–GAL4 fusion protein¹⁸. Full-length *FOXCI* eRNA was cloned in pCDNA3.1 downstream to five copies of *BoxB*. This construct was co-transfected along with the reporter plasmids and λ N–GAL4 vector (Supplementary Fig. 8), which is also based on a pCDNA3.1 vector with CMV promoter.

FOXCI promoter was cloned in KpnI and BglII sites in pGL3-basic vector, 5 \times UAS sites were cloned at upstream SalI site in pGL3-basic vector, *FOXCI* full-length enhancer (1.2 kb) was placed just upstream to 5 \times UAS sites at the BamHI site. For deletion of the sense eRNA, the enhancer region was amplified including the full antisense transcript, the core region and 20 nucleotides from the sense eRNA of the *FOXCI* enhancer (thus called *FOXCI* enh-sense del enhancer, Fig. 3c) was also cloned at BamHI site upstream to 5 \times UAS site (Supplementary Fig. 8).

Luciferase reporter assay. Tethered plasmids alone or in combination were transfected along with Renilla-TK plasmid into MCF-7 cells that had been hormone stripped for 3 days. Six hours post-transfection, they were treated with 10 nM E2 for 24 h further, and then they were subjected to the luciferase assay using the Dual-Luciferase reporter assay kit (Promega); plates were read in Veritas Microplate Luminometer (Turner Biosystems).

3C. 3C was performed as previously described^{22–24}. Briefly 25×10^6 MCF-7 cells were fixed by adding 1% formaldehyde at room temperature for 10 min, and the reaction was stopped by glycine. Lysis buffer (500 μl 10 mM Tris-HCl pH 8.0, 10 mM NaCl, 0.2% Igepal CA630, protease inhibitors) was added and cells were incubated on ice. Next, cells were lysed with a Dounce homogenizer, and the suspension was spun down at 5,000 r.p.m. at 4 °C. The supernatant was discarded and the pellet was washed twice with 500 μl ice-cold 1 \times NEBuffer 2 (NEB). The pellet was then re-suspended in 1 \times NEBuffer 2 and split into five separate 50 μl aliquots. The extracted chromatin was then digested overnight with 400 units HindIII (NEB). Each digested chromatin mixture was ligated by T4 DNA Ligase (800 units) in 20 times the initial volume for 4 h at 16 °C. The ligation step was omitted in one chromatin aliquot from the five mentioned above as the unligated control. The chromatin was subsequently de-cross-linked overnight at 65 °C and purified twice with phenol and then with a mixture of phenol, chloroform and IAA (at a ratio of 25:24:1). DNA was precipitated and pellets were air-dried before re-suspending in 250 μl 1 \times TE buffer. To degrade any carryover RNA, 1 μl RNase A (1 mg ml^{−1}) was added to each tube and incubated at 37 °C for 15 min. DNA was further purified using phenol/chloroform/IAA and precipitated. The digestion and ligation efficiencies were checked and normalized before 3D-DSL.

Probe design for 3C. Donor and acceptor probes were designed on HindIII sites covering the enhancers and the gene body of the following genes: *GREB1*, *NR1P1*,

KCNK5 and P2RY2; by using custom Perl scripts (available upon request). The chosen regions for probe design covered the most prominent ER- α binding sites as well as enhancers. The uniqueness of the probe sequences was verified by Bowtie alignment to the human genome hg18 assembly. Universal adaptor sequences that are compatible with HiSeq 2000 flow cell design were added to the probe ends for bridge amplification of the ligation products and for direct sequencing. Acceptors were phosphorylated and both acceptors and donors were pooled individually in equimolar amounts for 3D-DSL (Supplementary Table 6).

3D-DSL. The DSL ligation products were prepared as described previously^{12,22}. 3D-DSL was performed as described previously²². Briefly, after 3C efficiency estimation, equal amount of 3C chromatin was biotinylated using the PhotoProbe Kit (Vector Lab). Donor and acceptor probe pools (20 fmol per probe) were annealed to the biotinylated 3C samples at 45 °C for 2 h followed by 10 min at 95 °C. The biotinylated DNA was immunoprecipitated with magnetic beads conjugated to streptavidin, and during this process unbound oligonucleotides were removed by stringent washes. The 5'-phosphate of acceptor probes and the 3'-OH of donor probes were ligated using Taq DNA ligase at 45 °C for 1 h. These ligated products were washed and eluted from beads and then amplified by PCR using primers A and B-AD (or primer B-BC1 and B-BC2 if bar coding was used) for deep sequencing on the Illumina HiSeq 2000, using primer A as the sequencing primer.

3D-DSL data analysis. After removing the adaptor sequences, the reads are aligned to a custom library that includes all the combinations of donors and acceptors. The alignment was performed with Novoalign, and the reads were counted for every possible interaction by using custom Perl scripts (available upon request). The reads that were generated by donor-acceptor ligations on the same restriction site were removed: the remaining number of reads included both intra- and inter-chromosomal interactions. We used the median value (~6 million) of all the samples from the same sequencing run for normalization; the reads accounting for ligation products in unligated controls were subtracted. In addition to standard tools, such as my5C³⁸ and HiTC³⁹, we used an intensity-based method to characterize the set of interactions. A related method was also used in 3C-seq procedures⁴⁰. A *P* value is assigned to an interaction based on the Poisson probability distribution function, $p(x) = e^{-\lambda} \times \lambda^x / x!$, where $p(x)$ is the probability of an interaction, x is the interaction intensity, and λ is the average interaction intensity considering all the potential interactions in the library; that is, the ratio (total number of usable reads)/(total number of all possible interactions given the set of acceptors and the set of donors). The *P* values were corrected for multiple testing

by using the Bonferroni correction method. In addition, for each interaction, we define supplementary parameters, such as (1) fold enrichment over Poisson's λ , and (2) a fold enrichment over background (where the background represents the average intensity of the ligations between the probes on the neighbouring restriction sites). We consider the interactions that meet the following criteria significant for downstream analyses: (1) a (corrected) *P* value < 0.01; and (2) a fold enrichment over background > 2 (although for display purposes in the figure plots we may also show the weak interactions).

To generate 3D-DSL plots Matlab was used; a 10-kb window was used to bundle the interactions, except for a 20-kb window for *NR1P1*. The interactions were plotted using a Bezier curve between the two positions with the third point in the middle of the positions with the *y*-axis corresponding to the \log_{10} intensity. For example, if the two *x*-axis positions are 1 and 2, and the intensity is 4, a Bezier curve is drawn between (1,0), (1.5,4), and (2,0). The peak locations were then added on the bottom of the plot as stated in the legend. Interactions at distances generally < 10 kb were not plotted for the *NR1P1* locus.

31. Abukhdeir, A. M. *et al.* Physiologic estrogen receptor α signaling in non-tumorigenic human mammary epithelial cells. *Breast Cancer Res. Treat.* **99**, 23–33 (2006).
32. Heinz, S. *et al.* Simple combinations of lineage-determining transcription factors prime *cis*-regulatory elements required for macrophage and B cell identities. *Mol. Cell* **38**, 576–589 (2010).
33. Ingolia, N. T. *et al.* Genome-wide analysis *in vivo* of translation with nucleotide resolution using ribosome profiling. *Science* **324**, 218–223 (2009).
34. White, A. K. *et al.* High-throughput microfluidic single-cell RT-qPCR. *Proc. Natl Acad. Sci. USA* **108**, 13999–14004 (2011).
35. Zhong, J. F. *et al.* A microfluidic processor for gene expression profiling of single human embryonic stem cells. *Lab Chip* **8**, 68–74 (2008).
36. Tsai, M. C. *et al.* Long non-coding RNA as modular scaffold of histone modification complexes. *Science* **329**, 689–693 (2010).
37. Rueden, C. T. *et al.* Visualization approaches for multidimensional biological image data. *Biotechniques* **43**, 31–36 (2007).
38. Lajoie, B. R. *et al.* My5C: web tools for chromosome conformation capture studies. *Nature Methods* **6**, 690–691 (2009).
39. Servant, N. *et al.* HiTC: exploration of high-throughput 'C' experiments. *Bioinformatics* **28**, 2843–2844 (2012).
40. Stadhouder, R. *et al.* Dynamic long-range chromatin interactions control *Myb* proto-oncogene transcription during erythroid development. *EMBO J.* **31**, 986–999 (2011).

Unusual architecture of the p7 channel from hepatitis C virus

Bo OuYang^{1,2,3}, Shiqi Xie⁴, Marcelo J. Berardi¹, Xinhao Zhao⁴, Jyoti Dev¹, Wenjing Yu⁴, Bing Sun^{4,5} & James J. Chou^{1,2,3}

The hepatitis C virus (HCV) has developed a small membrane protein, p7, which remarkably can self-assemble into a large channel complex that selectively conducts cations^{1–4}. We wanted to examine the structural solution that the viroporin adopts in order to achieve selective cation conduction, because p7 has no homology with any of the known prokaryotic or eukaryotic channel proteins. The activity of p7 can be inhibited by amantadine and rimantadine^{2,5}, which are potent blockers of the influenza M2 channel⁶ and licensed drugs against influenza infections⁷. The adamantane derivatives have been used in HCV clinical trials⁸, but large variation in drug efficacy among the various HCV genotypes has been difficult to explain without detailed molecular structures. Here we determine the structures of this HCV viroporin as well as its drug-binding site using the latest nuclear magnetic resonance (NMR) technologies. The structure exhibits an unusual mode of hexameric assembly, where the individual p7 monomers, *i*, not only interact with their immediate neighbours, but also reach farther to associate with the *i*+2 and *i*+3 monomers, forming a sophisticated, funnel-like architecture. The structure also points to a mechanism of cation selection: an asparagine/histidine ring that constricts the narrow end of the funnel serves as a broad cation selectivity filter, whereas an arginine/lysine ring that defines the wide end of the funnel may selectively allow cation diffusion into the channel. Our functional investigation using whole-cell channel recording shows that these residues are critical for channel activity. NMR measurements of the channel–drug complex revealed six equivalent hydrophobic pockets between the peripheral and pore-forming helices to which amantadine or rimantadine binds, and compound binding specifically to this position may allosterically inhibit cation conduction by preventing the channel from opening. Our data provide a molecular explanation for p7-mediated cation conductance and its inhibition by adamantane derivatives.

Many viruses have developed integral membrane proteins to transport ions and other molecules across the membrane barrier to aid various steps of viral entry and maturation^{9,10}. These membrane structures, known as viroporins, usually adopt minimalist architectures that are significantly different from those of bacterial or eukaryotic ion channels. Therefore, understanding the structural basis of how viroporins function broadens our knowledge of channels and transporters while generating new opportunities for therapeutic intervention.

The viroporin formed by the HCV p7 protein has been sought after as a potential anti-HCV drug target^{5,11}. p7 is a 63-residue membrane protein that oligomerizes to form ion channels with cation selectivity, for Ca²⁺ over K⁺ and Na⁺ (refs 2, 3, 12, 13), and a more recent study has also reported p7-mediated H⁺ intracellular conductance¹⁴. The p7 channel is required for viral replication¹⁵; it has been shown to facilitate efficient assembly and release of infectious virions^{16,17}, although the precise mechanism of these functions remains unclear. The channel activity can be inhibited by adamantane and long alkyl chain iminosugar

derivatives and hexamethylene amiloride *in vitro*, with varying reported efficacies^{2,3,12,13}. In addition to ion conduction, p7 has been shown to specifically interact with the non-structural HCV protein NS2, indicating that its channel activity could be regulated^{18,19}.

There is not yet a detailed structure of the p7 channel, although a number of NMR studies showed that the p7 monomer has three helical segments: two in the amino-terminal half of the sequence and one near the carboxy terminus^{12,20}. A single-particle electron microscopy (EM) study obtained a 16 Å resolution electron density map of the p7 oligomer using the random conical tilting approach⁴. The map shows that the p7 channel is a 42-kDa hexamer and adopts a flower-like shape that does not resemble any of the known ion channel structures in the database.

It is not known how the small p7 polypeptide assembles into what appears to be a complex channel structure, and whether the viroporin has adopted novel structural elements for cation selectivity and channel gating. Amantadine or rimantadine blocks the influenza M2 channel by binding to the small pore formed by four transmembrane helices^{21–23}, but the pore of the p7 hexamer is expected to be much bigger and it is thus unclear how these small molecules would fit. We sought to address these questions by determining detailed structures of the p7 hexamer and its drug-binding site.

We systematically tested p7 amino acid sequences from various HCV genotypes and found that the sequence from genotype 5a (EUH1480 strain) generated samples that were sufficiently soluble for structure determination (Supplementary Fig. 1). This p7 construct, designated here as p7(5a), could be efficiently reconstituted in dodecylphosphocholine (DPC) micelles at near physiological pH and generated high-quality NMR spectra (Supplementary Fig. 2). Negative-stain EM of the DPC-reconstituted p7(5a) in NMR buffer showed hexameric, flower-shaped particles that are similar to those in the electron micrographs of the p7 (JFH-1 strain, genotype 2a) hexamer in dihexanoyl-phosphatidyl-choline (DHPC) micelles used earlier for single-particle reconstruction⁴ (Supplementary Fig. 3). Moreover, isothermal titration calorimetry and NMR chemical shift perturbation analyses of p7(5a)–rimantadine interaction showed that the drug binds specifically to the reconstituted protein with a binding constant (*K*_d) from 50 to 100 μM at 3 mM detergent concentration (Supplementary Figs 4 and 5). The above results together indicate that the p7(5a) polypeptides reconstituted in DPC micelles form structurally relevant hexamers.

Structure determination of the p7(5a) hexamer by NMR used an approach taken earlier for oligomeric membrane proteins^{24–26}, which involves: (1) determination of local structures of the monomers; and (2) assembly of the oligomer with intermonomer distance restraints and orientation constraints. The NMR-derived restraints define an ensemble of structures with backbone root mean squared deviation (r.m.s.d.) of 0.74 Å (Fig. 1a). Each monomer consists of an N-terminal helix (H1) from residues 5–16, a middle helical segment (H2), with a

¹Department of Biological Chemistry and Molecular Pharmacology, Harvard Medical School, Boston, Massachusetts 02115, USA. ²State Key Laboratory of Molecular Biology, Shanghai Institute of Biochemistry and Cell Biology, Chinese Academy of Sciences, Shanghai 200031, China. ³National Center for Protein Science, Shanghai Institute of Biochemistry and Cell Biology, Chinese Academy of Sciences, Shanghai 200031, China. ⁴Molecular Virus Unit, Key Laboratory of Molecular Virology and Immunology, Institut Pasteur of Shanghai, Shanghai Institutes for Biological Sciences, Chinese Academy of Sciences, Shanghai 200025, China. ⁵State Key Laboratory of Cell Biology, Shanghai Institute of Biochemistry and Cell Biology, Chinese Academy of Sciences, Shanghai 200031, China.

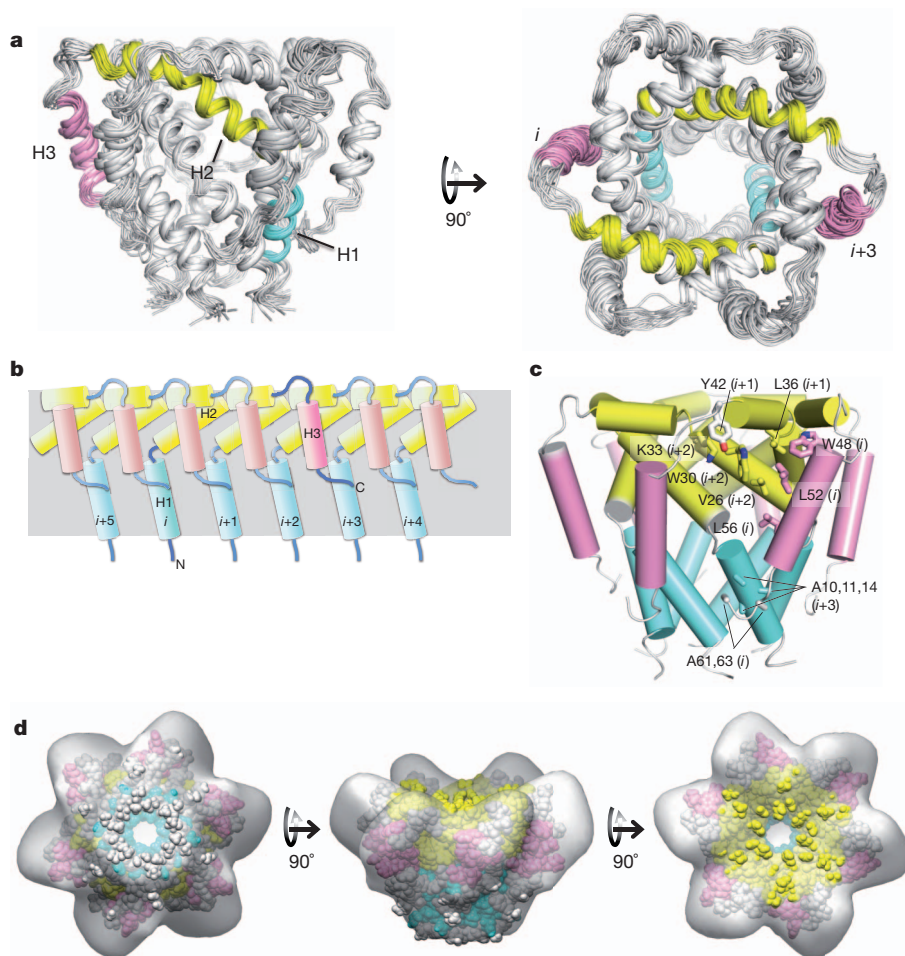


Figure 1 | NMR structure of the p7(5a) hexamer and its comparison to the EM map. **a**, Ensemble of 15 low-energy structures calculated using NMR restraints summarized in Supplementary Table 1. **b**, Two-dimensional drawing illustrating the intermonomer interactions among the H1 (blue), H2 (yellow) and H3 (pink) helical segments that are responsible for the hexameric assembly. **c**, Three-dimensional cartoon representation describing the global arrangement of helical segments and amino acids that seem to have a role in the packing of H3 against H1 and H2. **d**, Fitting the lowest-energy structure from the ensemble to the 16 Å EM map (EM database ID 1661)⁴. The fitting correlation is 0.94 as calculated with the program Chimera.

kink at Gly 34, from residues 20–41, and a C-terminal helix (H3) from residues 48–58. These secondary structures are consistent with earlier NMR studies of p7 monomers in DHPC detergent and organic solvent^{12,20}. There are no intramonomer contacts (Fig. 1a). The monomers are intertwined to form a tightly packed channel, where H1 and H2 form the channel interior and H3 is lipid-facing and packs against H2 of the *i*+2 and H1 of the *i*+3 monomer (Fig. 1a, b). The intermonomer association between H3 and H2 appears to be stabilized by interaction involving conserved residues such as Trp 30, Tyr 42 and Leu 52, and the contacts between H3 and H1 are mostly between the alanine-rich region of H1 (residues 10–15) and Ala 61 and Ala 63 of H3 (Fig. 1c). The overall structure of the p7(5a) hexamer has a flower-like shape that agrees with the EM map (EM database ID 1661), fitting to the map with a correlation coefficient of 0.94 (Fig. 1d).

The channel cavity has a funnel profile that resembles a champagne flute and is largely hydrophilic (Fig. 2a). The H2 helices form the wide cylindrical region (internal diameter (ID) ~12 Å) by packing with each other at large angles (angle between adjacent helices approximately -47°), and the H1 helices assemble at smaller packing angles (approximately -34°) to form the narrow conical region of the funnel (smallest ID at 6.8 Å). Residues 17–19 constitute the flexible joint between H1 and H2; their NMR resonances are significantly broader than other regions of the protein, indicating the presence of conformational exchange.

The channel architecture described above represents a novel topology and exemplifies how HCV has optimized the short p7 polypeptide to achieve a rather complex channel structure. We next addressed what elements are involved in cation conduction and gating. An in-depth examination of the channel interior found two strongly conserved polar residues with salient structural features (Fig. 2b). One is Asn 9,

which forms a ring of carboxamide that constricts the conical region of the channel (Fig. 2c). Residue 9 is asparagine in all strains except in genotype 2 viruses, where it is substituted with histidine. Both asparagines and histidines have affinity for monovalent and divalent cations. We propose that the Asn 9 ring serves as a broad selectivity filter that dehydrates cations, allowing them to pass the hydrophobic ring formed by Ile 6. The Ile 6 ring defines the narrowest point of the channel and probably serves as a hydrophobic gate. Another feature is the Arg 35 ring that defines the wider, C-terminal end of the channel (Fig. 2b). Placement of a positively charged ring on the other end of the pore was incomprehensible to us initially because it can repel cations. But the recent structure of an Orai Ca^{2+} channel also revealed a stretch of basic residues in the ion-conducting pore²⁷. We propose that one role of Arg 35 is to bind and obstruct anions at the pore entrance while allowing cations to diffuse into the pore. In this model, cation conduction is unidirectional from the C- to N-terminal end of the channel.

To test the above hypotheses, we established an assay that uses the two-electrode voltage-clamp technique to record p7-mediated current in *Xenopus* oocytes (see Methods). Owing to the poor stability of oocytes that overexpress p7(5a), p7 (JFH-1 strain, genotype 2a) was used instead for these experiments. As expected because of the proposed role of residue 9 in selectively dehydrating cations, replacing His 9 of p7(2a) with alanine caused a ~70% reduction in channel conductance at +80 mV (Fig. 2d). The proposed role of Arg 35 indicates that placing negatively charged residues at the channel entrance would bind cations and hinder their diffusion into the pore, and indeed the Arg35Asp mutation also reduced conductance by ~70% (Fig. 2d).

We next investigated the mechanism of amantadine binding to the p7 channel using proteins that are ^{15}N -labelled and deuterated so that nuclear Overhauser enhancement (NOE) between the protein backbone

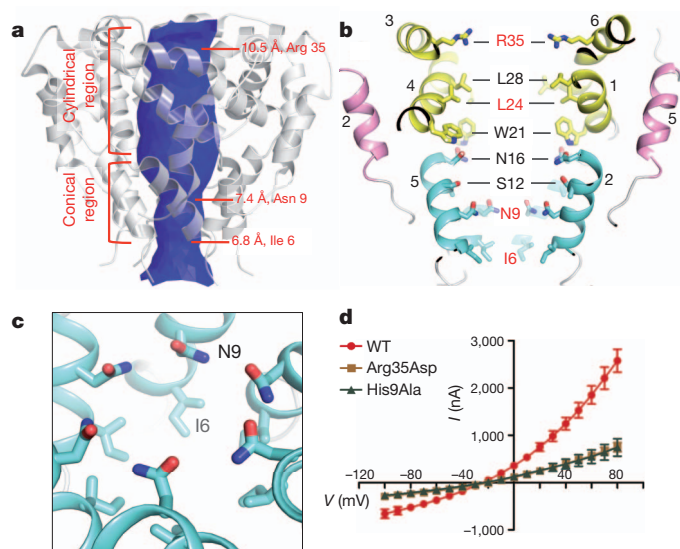


Figure 2 | The pore properties of the p7(5a) channel. **a**, The pore surface calculated using the program HOLE, showing the shape and constrictions of the pore. **b**, Sectional view of the channel showing the pore-lining residues with residues in red being strongly conserved. The numbers next to the helical segments represent the monomers to which the helices belong. Colour scheme as in Fig. 1. **c**, A close-up view of the rings formed by Asn 9 and Ile 6 that constrict the N-terminal end of the channel. **d**, The current-voltage relationships of wild-type (WT) p7(2a) and the His9Ala and Arg35Asp mutants. Each data point is the mean \pm s.e.m. (standard error of mean) calculated over measurements from six different oocytes ($n = 6$).

amide protons and drug protons could be measured unambiguously. At 10 mM amantadine (not corrected for drug partitioning to detergent micelles), the ^{15}N -edited nuclear Overhauser enhancement spectroscopy (NOESY) spectrum showed NOE crosspeaks between the adamantane protons and the amide protons of Val 26, Leu 55, Leu 56 and Arg 57 (Fig. 3a). We then identified contacts between the drug and protein side chains using protein that is ($^1\text{H}/^{13}\text{C}$)-labelled at the methyl

positions of alanines, valines and leucines but is otherwise deuterated. In this case, the ^{13}C -edited NOESY showed several methyl-drug NOEs (Fig. 3b).

These NOEs were used to dock amantadine into the structure determined in the absence of drug. In doing so, we emphasize that the relevance of the p7-amantadine complex is confined to only the drug-binding region because we do not know how and to what degree does drug binding alter the global conformation of the channel. The relatively poor stability of the protein-drug complex at the current stage of our study precludes full-scale structure determination. Nonetheless the available NMR data show that the drug adamantane binds to six equivalent hydrophobic pockets between the pore-forming and peripheral helices (Fig. 3c). The pocket consists of Leu 52, Val 53 and Leu 56 from H3, and Phe 20, Val 25 and Val 26 from H2. The amantadine amino group on average points to the channel lumen. The same NOESY spectrum as above recorded using a sample with 5 mM rimantadine indicates that rimantadine binds to the same pocket with the methyl and amino groups pointing to the lumen (Supplementary Fig. 6).

The binding site is overall consistent with a mutational study showing that mutations in residues 50–55 significantly reduce drug sensitivity of the channel²⁸. It is also consistent with a Leu20Phe mutation in genotype 1b virus originally identified in clinical trials that confers amantadine resistance^{8,29}. In the p7(5a) structure, residue 20 is an integral part of the drug pocket and is in direct contact with the drug adamantane. Therefore, replacing Leu 20 in p7(1b) with phenylalanine is expected to reduce hydrophobic interaction with the drug. Elucidation of previous functional data in the context of the structure suggests that the binding site shown in Fig. 3c is relevant to drug inhibition and that interactions between the drug adamantane and protein hydrophobic residues are critical for inhibition. Variations in the hydrophobicity of the binding pocket among the p7 variants (Supplementary Fig. 7) thus explain the large differences in drug efficacies observed between different HCV genotypes.

We have learnt from KcsA and other channels that a gated ion channel generally adopts two essential features: pore elements that provide ion selectivity, and a gating mechanism that can transiently

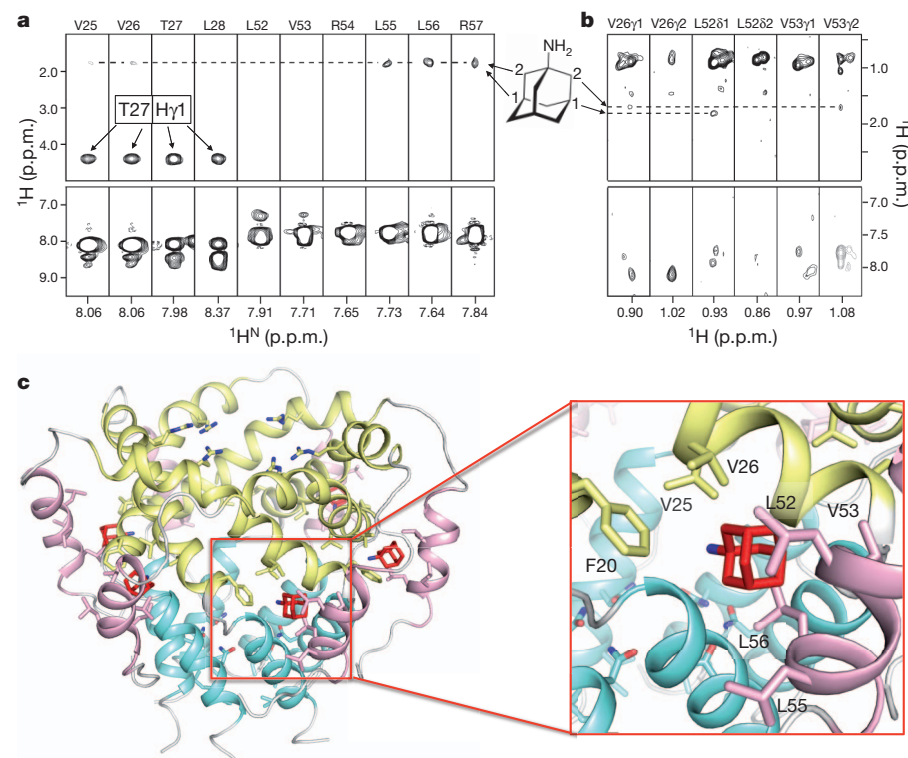


Figure 3 | NMR characterization of the amantadine binding site. **a**, Representative strips from the three-dimensional ^{15}N -edited NOESY-TROSY (transverse relaxation optimized spectroscopy) spectrum (300 ms NOE mixing time) recorded using a sample containing ^{15}N -, ^2H -labelled p7(5a) and 10 mM amantadine, showing amantadine NOEs to the backbone amide protons of Val 26, Leu 55, Leu 56 and Arg 57. **b**, Representative strips from the three-dimensional diagonal-suppressed ^{13}C -edited NOESY-HSQC spectrum recorded using a sample that is ^1H -, ^{13}C -labelled at the methyl positions of alanines, valines and leucines but is otherwise deuterated, showing drug NOEs to the side-chain methyl protons of Val 26, Leu 52 and Val 53. The spectra in **a** and **b** were recorded at ^1H frequency of 900 MHz. **c**, Amantadine docked into the p7(5a) hexamer using restraints from NOEs in **a** and **b** (left) and a close-up view of amantadine in the binding pocket (right). Colour scheme as in Fig. 1.

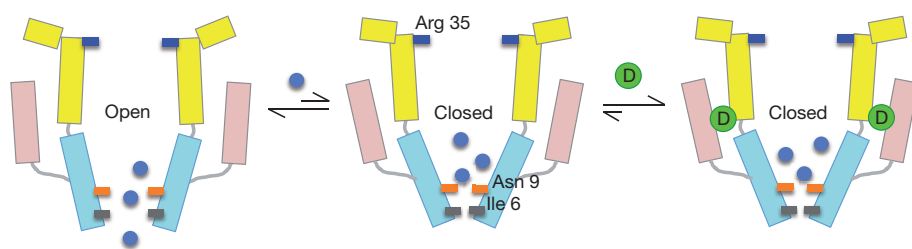


Figure 4 | A model for amantadine or rimantadine inhibition of the p7 channel. The two-dimensional cartoon drawing mimics the sectional view of the p7 channel in Fig. 2b. The channel undergoes conformational switching between the closed and the open states but favours the open state in the presence of cations (blue circles). Binding of amantadine or rimantadine (green circles, labelled with 'D' for drug) favours the closed state by restricting movements of the three helical segments that may be required for channel opening.

open the channel to allow ion permeation. By virtue of being a funnel, the p7 structure indicates that the tip of the funnel represented by the Ile 6 and Asn 9 rings is the key region for channel gating (Fig. 4). The role of the Asn 9 ring is to provide ion selectivity by recruiting and dehydrating cations near the funnel exit, whereas the Ile 6 ring is a hydrophobic constriction that would prevent water from freely passing through. Channel activation may involve reorientation of the H1 helices that widens the funnel tip, analogous to the dynamic C-terminal helix of KcsA³⁰, and such structural rearrangement can be afforded by the flexible hinge between H1 and H2, the intervening loop between H2 and H3, and the C-terminal tail that 'latches' onto H1. We thus propose that binding of adamantane derivatives inhibit channel activity by restricting the structural rearrangement. Our NMR titration data (Supplementary Fig. 5c) are consistent with this proposal, which shows that in the absence of rimantadine, the Ile 6 methyl resonance is split into an intense and weak peak, possibly corresponding to the open and closed state, respectively, and that increasing the drug concentration shifts the equilibrium that make the weak peak stronger. Although rigorous testing of the model is needed, the preliminary observation suggests the existence of multiple states of the p7 channel.

METHODS SUMMARY

The p7 sequence from HCV genotype 5a was mutated at five unconserved positions to improve protein stability and to facilitate NMR analyses (see details in Supplementary Fig. 1). The protein was expressed as a fusion to His 9–trpLE that formed inclusion bodies, and purified and reconstituted in DPC as previously described^{23,25}. A typical NMR sample contains 0.8 mM protein (monomer concentration), 200 mM DPC and 25 mM MES (pH 6.5).

For structure determination, the secondary structures of the p7(5a) monomers in the hexamer were first determined using standard NOE experiments. We then used a mixed sample in which 50% of the monomers are (¹⁵N/²H)-labelled and 50% ¹³C-labelled to measure exclusively NOEs between the ¹⁵N-attached protons of one subunit and the ¹³C-attached protons of the neighbouring subunits. This experiment provided key intermonomer NOEs between adjacent H1 and H2 helices for assembling the central cavity of the hexamer (Supplementary Fig. 8a). H3 was positioned based on orientation restraints from residual dipolar couplings (RDCs) and its intermonomer NOEs to H1 and H2 (Supplementary Fig. 8b, c). Structure calculation statistics are given in Supplementary Table 1. Protein–drug contacts were identified using (¹⁵N/²H)-labelled protein so that NOEs between protein backbone amide protons and drug protons could be identified unambiguously. Additionally, NOEs between the drug and protein side-chain methyl groups were measured with a diagonal-suppressed carbon NOESY using ALV labelled protein (see Methods).

Functional p7 mutants were analysed using the standard protocol for two-electrode voltage-clamp of *Xenopus* oocytes. After expressing the p7(2a) variants in oocytes, we recorded p7 currents across the oocyte plasma membrane at room temperature (~22 °C). For quantitative comparison of currents between the p7 variants, the protein expression levels in oocytes were examined using confocal microscopy.

Full Methods and any associated references are available in the online version of the paper.

Received 17 January; accepted 22 April 2013.

Published online 5 June 2013.

1. Moradpour, D., Penin, F. & Rice, C. M. Replication of hepatitis C virus. *Nature Rev. Microbiol.* **5**, 453–463 (2007).

2. Griffin, S. D. *et al.* The p7 protein of hepatitis C virus forms an ion channel that is blocked by the antiviral drug, amantadine. *FEBS Lett.* **535**, 34–38 (2003).
3. Pavlovic, D. *et al.* The hepatitis C virus p7 protein forms an ion channel that is inhibited by long-alkyl-chain iminosugar derivatives. *Proc. Natl Acad. Sci. USA* **100**, 6104–6108 (2003).
4. Luik, P. *et al.* The 3-dimensional structure of a hepatitis C virus p7 ion channel by electron microscopy. *Proc. Natl Acad. Sci. USA* **106**, 12712–12716 (2009).
5. Griffin, S. *et al.* Genotype-dependent sensitivity of hepatitis C virus to inhibitors of the p7 ion channel. *Hepatology* **48**, 1779–1790 (2008).
6. Wang, C., Takeuchi, K., Pinto, L. H. & Lamb, R. A. Ion channel activity of influenza A virus M2 protein: characterization of the amantadine block. *J. Virol.* **67**, 5585–5594 (1993).
7. Davies, W. L. *et al.* Antiviral activity of 1-sdamantanamine (amantadine). *Science* **144**, 862–863 (1964).
8. Mihm, U. *et al.* Amino acid variations in hepatitis C virus p7 and sensitivity to antiviral combination therapy with amantadine in chronic hepatitis C. *Antivir. Ther.* **11**, 507–519 (2006).
9. Fischer, W. B. & Sansom, M. S. Viral ion channels: structure and function. *Biochim. Biophys. Acta* **1561**, 27–45 (2002).
10. Nieva, J. L., Madan, V. & Carrasco, L. Viroporins: structure and biological functions. *Nature Rev. Microbiol.* **10**, 563–574 (2012).
11. Steinmann, E. *et al.* Antiviral effects of amantadine and iminosugar derivatives against hepatitis C virus. *Hepatology* **46**, 330–338 (2007).
12. Montserret, R. *et al.* NMR structure and ion channel activity of the p7 protein from hepatitis C virus. *J. Biol. Chem.* **285**, 31446–31461 (2010).
13. Premkumar, A., Wilson, L., Ewart, G. D. & Gage, P. W. Cation-selective ion channels formed by p7 of hepatitis C virus are blocked by hexamethylene amiloride. *FEBS Lett.* **557**, 99–103 (2004).
14. Wozniak, A. L. *et al.* Intracellular proton conductance of the hepatitis C virus p7 protein and its contribution to infectious virus production. *PLoS Pathog.* **6**, e1001087 (2010).
15. Sakai, A. *et al.* The p7 polypeptide of hepatitis C virus is critical for infectivity and contains functionally important genotype-specific sequences. *Proc. Natl Acad. Sci. USA* **100**, 11646–11651 (2003).
16. Jones, C. T., Murray, C. L., Eastman, D. K., Tassello, J. & Rice, C. M. Hepatitis C virus p7 and NS2 proteins are essential for production of infectious virus. *J. Virol.* **81**, 8374–8383 (2007).
17. Steinmann, E. *et al.* Hepatitis C virus p7 protein is crucial for assembly and release of infectious virions. *PLoS Pathog.* **3**, e103 (2007).
18. Popescu, C. I. *et al.* NS2 protein of hepatitis C virus interacts with structural and non-structural proteins towards virus assembly. *PLoS Pathog.* **7**, e1001278 (2011).
19. Vieyres, G. *et al.* Subcellular localization and function of an epitope-tagged p7 viroporin in hepatitis C virus-producing cells. *J. Virol.* **87**, 1664–1678 (2013).
20. Cook, G. A. & Opella, S. J. Secondary structure, dynamics, and architecture of the p7 membrane protein from hepatitis C virus by NMR spectroscopy. *Biochim. Biophys. Acta* **1808**, 1448–1453 (2011).
21. Stouffer, A. L. *et al.* Structural basis for the function and inhibition of an influenza virus proton channel. *Nature* **451**, 596–599 (2008).
22. Cady, S. D. *et al.* Structure of the amantadine binding site of influenza M2 proton channels in lipid bilayers. *Nature* **463**, 689–692 (2010).
23. Pielak, R. M., Oxenoid, K. & Chou, J. J. Structural investigation of rimantadine inhibition of the AM2-BM2 chimera channel of influenza viruses. *Structure* **19**, 1655–1663 (2011).
24. Oxenoid, K. & Chou, J. J. The structure of phospholamban pentamer reveals a channel-like architecture in membranes. *Proc. Natl Acad. Sci. USA* **102**, 10870–10875 (2005).
25. Schnell, J. R. & Chou, J. J. Structure and mechanism of the M2 proton channel of influenza A virus. *Nature* **451**, 591–595 (2008).
26. Van Horn, W. D. *et al.* Solution nuclear magnetic resonance structure of membrane-integral diacylglycerol kinase. *Science* **324**, 1726–1729 (2009).
27. Hou, X., Pedi, L., Diver, M. M. & Long, S. B. Crystal structure of the calcium release-activated calcium channel Orai. *Science* **338**, 1308–1313 (2012).
28. StGelais, C. *et al.* Determinants of hepatitis C virus p7 ion channel function and drug sensitivity identified *in vitro*. *J. Virol.* **83**, 7970–7981 (2009).
29. Foster, T. L. *et al.* Resistance mutations define specific antiviral effects for inhibitors of the hepatitis C virus p7 ion channel. *Hepatology* **54**, 79–90 (2011).
30. Cuello, L. G., Jogini, V., Cortes, D. M. & Perozo, E. Structural mechanism of C-type inactivation in K⁺ channels. *Nature* **466**, 203–208 (2010).

Supplementary Information is available in the online version of the paper.

Acknowledgements We thank R. Sounier for helping with making specific methyl-labelled protein, S. Brueschweiler for helping with ITC measurements, G. Bellot, J. Min and W. Shih for providing DNA nanotube liquid crystal, and K. Oxenoid for discussion. This work was supported by the National Key Project of 973 (2013CB530504) and National Science and Technology Major Project (2012ZX10002-007-003) (to B.S.) and NIH grant GM094608 (to J.J.C.).

Author Contributions B.O. and J.J.C. conceived the study; B.O. prepared samples; M.J.B. performed EM analysis; J.D. and B.O. performed NMR titration; B.O. and J.J.C.

collected and analysed NMR data and determined the structure; S.X., X.Z., W.Y. and B.S. designed and performed functional experiments; J.J.C. wrote the paper and all authors contributed to the editing of the manuscript.

Author Information The structure is deposited in the Protein Data Bank under the accession number 2M6X. Reprints and permissions information is available at www.nature.com/reprints. The authors declare no competing financial interests. Readers are welcome to comment on the online version of the paper. Correspondence and requests for materials should be addressed to J.J.C. (chou@cmcd.hms.harvard.edu) or B.S. (bsun@sibs.ac.cn).

METHODS

Sample preparation. The amino acid sequence of p7 from genotype 5a was slightly modified to allow for efficient reconstitution and protein sample stability. In this sequence, Thr1 is replaced with Gly, Ala12 is replaced with Ser, and the three cysteines at positions 2, 27 and 44 are replaced with Ala, Thr and Ser, respectively (Supplementary Fig. 1). The p7(5a) construct was cloned, expressed and purified as previously described^{23,25}. Briefly, the protein was expressed as a fusion to His9–trpLE that formed inclusion bodies. The peptide was released from the fusion protein by CNBr digestion and subsequently separated on a Proto-18C column by reverse-phase chromatography (more details given in Supplementary Methods). The lyophilized peptide was then dissolved in 6 M guanidine and DPC and refolded by dialysis against the NMR buffer. A typical NMR sample contains 0.8 mM protein (monomer concentration), 200 mM DPC and 25 mM MES (pH 6.5).

Assignment of NMR resonances. All NMR experiments were conducted at 30 °C on Bruker spectrometers equipped with cryogenic probes. Sequence-specific assignment of backbone chemical shifts was accomplished using three pairs of triple resonance experiments, recorded using a ¹⁵N/¹³C/²H-labelled sample. The triple resonance experiments were relaxation optimized (TROSY)³¹, including HNCA, HN(CO)CA, HNCACB, HN(CO)CACB, HN(CA)CO and HNCO³². Protein side-chain aliphatic and aromatic resonances were assigned using a combination of NOESYs including ¹⁵N-edited NOESY-TROSY (60 ms NOE mixing time, τ_{NOE}) and ¹³C-edited NOESY-HSQC (τ_{NOE} = 100 ms). Specific stereo assignment of the methyl groups of valines and leucines were obtained from a constant-time ¹H-¹³C HSQC spectrum recorded using a 15% ¹³C-labelled sample³³. **Assignment of local NOEs for determining the secondary structures.** The same ¹⁵N-edited NOESY-TROSY and ¹³C-edited NOESY-HSQC above with short τ_{NOE} were used to assign local NOEs. Combining the NOE restraints with chemical shifts, we could very precisely define the helical and loop regions of the individual monomers.

Measurement of residual dipolar coupling (RDC) constants. The backbone ¹H-¹⁵N RDCs were measured using a modified approach³⁴ of the strain-induced alignment in a gel method^{35,36}. In this experiment the p7(5a) channel in DPC micelles was soaked into a cylindrically shaped polyacrylamide gel (4.5%), initially of 6 mm diameter, which was subsequently radially compressed to fit within the 4.2-mm inner diameter of an open-ended NMR tube. The ¹H-¹⁵N RDCs were obtained from $^1J_{\text{NH}}/2$ and $(^1J_{\text{NH}} + ^1D_{\text{NH}})/2$, which were measured by interleaving a regular gradient-enhanced HSQC and a gradient-selected TROSY³⁷. The largest ¹H-¹⁵N RDC measured is 33.5 Hz.

Assignment of intermonomer NOEs. Intermonomer NOEs between protein backbone amide and side-chain methyl protons was assigned using a sample that was reconstituted with a 1:1 mixture of ¹⁵N-, ²H-labelled p7(5a) peptide and ¹³C-labelled peptide. Recording a ¹⁵N-edited NOESY-TROSY (τ_{NOE} = 300 ms) on a 900 MHz spectrometer with this sample allowed exclusive detection of NOE crosspeaks between the ¹⁵N-attached protons of one monomer and the ¹³C-attached protons of other monomers. The intermonomer NOEs between the neighbouring H1 helices and neighbouring H2 helices effectively defined the central cavity formed by these helices. The initial structural solution of the pore assembly then allowed us to assign complementary and self-consistent intermonomer NOEs between the aliphatic and aromatic protons in a pair of ¹⁵N-edited NOESY-TROSY and ¹³C-edited NOESY-HSQC recorded using a ¹⁵N-, ¹³C-labelled sample. These spectra were recorded with τ_{NOE} of 120 ms and 150 ms, respectively.

The packing of H1 and H2 helices between the adjacent monomers and RDC-derived orientation constraints together positioned the H3 helix of monomer *i* to be in contact with H2 of the *i* + 2 and H1 of the *i* + 3 monomers, and this conformation was confirmed by the unambiguous amide-methyl NOEs between H3 and H1/H2. The conformation as defined by the intermonomer NOEs was subjected to numerous rounds of self-consistency test with the NOE crosspeaks in the ¹³C-edited NOESY-HSQC spectrum to ensure that all NOEs are consistent with the structure. The overall distribution of intermonomer NOEs is illustrated in Supplementary Fig. 7.

Assignment of NOEs between protein and drug. We prepared a sample containing ¹⁵N-, ²H-labelled p7(5a), 10 mM amantadine (or 5 mM rimantadine), and perdeuterated DPC. The sample was used to record a ¹⁵N-edited NOESY-TROSY (τ_{NOE} = 300 ms) on a 900 MHz spectrometer. This experiment allowed exclusive detection of NOEs between the exchangeable amide protons and the drug protons. For assigning NOEs between the protein side-chain methyl protons and the drug protons, we prepared the ALV-labelled protein that is ¹H-, ¹³C-labelled at the methyl positions of alanines, valines and leucines but is otherwise deuterated.

The NOEs were measured using a ¹³C-edited NOESY with diagonal suppression, that is, interleaving two experiments: one with NOE mixing (300 ms) of the H₂ magnetization (NOE crosspeaks) and the other with mixing of the H₂C₂ magnetization (no NOE crosspeaks)³⁸. Subtracting the two spectra mostly cancelled the strong methyl diagonal peaks (~0.8 p.p.m.) and thereby unveiled the weak methyl-drug NOEs at ~1.7 p.p.m.

Structure calculation of the p7(5a) hexamer. Structures were calculated using the program XPLOR-NIH³⁹. The monomer structures (mainly the secondary structures) were first calculated using intramonomer NOE-derived distance restraints, backbone dihedral restraints derived from chemical shifts using the TALOS program⁴⁰, and RDC restraints. A total of 10 monomer structures were calculated using a standard simulated annealing (SA) protocol. Six copies of the lowest-energy monomer structure were used to construct an initial model of the hexamer using intermonomer NOE restraints collected from the mixed-labelled sample for the H1 and H2 helical segments. For each intermonomer restraint between two adjacent monomers, six identical distance restraints were assigned respectively to all pairs of neighbouring monomers to satisfy the condition of C6 rotational symmetry (as indicated by the EM data). The assembled hexamer was then subjected to refinement against RDCs to accurately orient the three helical segments. Finally, using the SA protocol, the hexamer was refined against the complete set of NOE restraints (including intramonomer and intermonomer distance restraints), dihedral restraints and RDC restraints. A total of 60 hexamer structures were calculated and 15 low-energy structures were selected as the structural ensemble. Ramachandran plot statistics for the structure ensemble, calculated using PROCHECK⁴¹, are as follows: most favoured (96.6%), additionally allowed (2.8%), generously allowed (0.6%) and disallowed (0.0%).

Whole-cell channel recording assay for p7. The cRNA of p7(2a) variants was synthesized and injected into *Xenopus laevis* oocytes at ~15 ng per oocyte. After about 16–30 h of expression, healthy oocytes were collected and subjected to channel recording using the two-electrode voltage-clamp technique⁴². The oocytes were first bathed in standard ORi solution (90 mM NaCl, 2 mM KCl, 2 mM CaCl₂ and 5 mM MOPS, pH 7.4) before being impaled with two microelectrodes. For recording p7-mediated current, we used a voltage-clamp protocol consisting of rectangular voltage steps from –100 to +80 mV in 10-mV increments, applied from a holding voltage of –60 mV. Expression levels of the p7 variants in oocytes were examined by confocal microscopy using haemagglutinin-tagged p7. More experimental details are described in Supplementary Methods.

- Pervushin, K., Riek, R., Wider, G. & Wuthrich, K. Attenuated T2 relaxation by mutual cancellation of dipole-dipole coupling and chemical shift anisotropy indicates an avenue to NMR structures of very large biological macromolecules in solution. *Proc. Natl Acad. Sci. USA* **94**, 12366–12371 (1997).
- Kay, L. E., Torchia, D. A. & Bax, A. Backbone dynamics of proteins as studied by 15N inverse detected heteronuclear NMR spectroscopy: application to staphylococcal nuclease. *Biochemistry* **28**, 8972–8979 (1989).
- Szyperski, T., Neri, D., Leiting, B., Otting, G. & Wuthrich, K. Support of 1H NMR assignments in proteins by biosynthetically directed fractional 13C-labeling. *J. Biomol. NMR* **2**, 323–334 (1992).
- Chou, J. J., Gaemers, S., Howder, B., Louis, J. M. & Bax, A. A simple apparatus for generating stretched polyacrylamide gels, yielding uniform alignment of proteins and detergent micelles. *J. Biomol. NMR* **21**, 377–382 (2001).
- Sass, H. J., Musco, G., Stahl, S. J., Wingfield, P. T. & Grzesiek, S. Solution NMR of proteins within polyacrylamide gels: Diffusional properties and residual alignment by mechanical stress or embedding of oriented purple membranes. *J. Biomol. NMR* **18**, 303–309 (2000).
- Tycko, R., Blanco, F. J. & Ishii, Y. Alignment of biopolymers in strained gels: A new way to create detectable dipole-dipole couplings in high-resolution biomolecular NMR. *J. Am. Chem. Soc.* **122**, 9340–9341 (2000).
- Weigelt, J. Single scan, sensitivity- and gradient-enhanced TROSY for multidimensional NMR experiments. *J. Am. Chem. Soc.* **120**, 10778–10779 (1998).
- Wu, J., Fan, J. S., Pascal, S. M. & Yang, D. General method for suppression of diagonal peaks in heteronuclear-edited NOESY spectroscopy. *J. Am. Chem. Soc.* **126**, 15018–15019 (2004).
- Schwieters, C. D., Kuszewski, J., Tjandra, N. & Clore, G. M. The Xplor-NIH NMR molecular structure determination package. *J. Magn. Reson.* **160**, 66–74 (2002).
- Cornilescu, G., Delaglio, F. & Bax, A. Protein backbone angle restraints from searching a database for chemical shift and sequence homology. *J. Biomol. NMR* **13**, 289–302 (1999).
- Laskowski, R. A., MacArthur, M. W., Moss, D. S. & Thornton, J. W. PROCHECK: a program to check the stereochemical quality of protein structures. *J. Appl. Cryst.* **26**, 283–291 (1993).
- Plugge, B. et al. A potassium channel protein encoded by chlorella virus PBCV-1. *Science* **287**, 1641–1644 (2000).

CORRIGENDUM

doi:10.1038/nature12182

Corrigendum: Functional organization of human sensorimotor cortex for speech articulation

Kristofer E. Bouchard, Nima Mesgarani, Keith Johnson & Edward F. Chang

Nature **495**, 327–332 (2013); doi:10.1038/nature11911

In this Article, the referral to the subcentral gyrus as ‘guenon’ was incorrect. As stated, the central sulcus does not terminate at the Sylvian fissure, but instead at the ventral-most U-shaped gyral area¹ (as shown in Fig. 1 of the original Article), which should be labelled ‘subcentral gyrus’. Guenon refers to the genus of Old World monkeys (*Cercopithecus*)², in which Brodmann initially characterized the cytoarchitecture of this cortical region³. The study results and findings are unchanged and not affected by this clarification of nomenclature. We thank N. Jenkinson and K. Watkins for bringing this to our attention.

1. Wagner, M., Jurcoane, A. & Hattingen, E. The U sign: tenth landmark to the central region on brain surface reformatted MR imaging. *AJNR Am. J. Neuroradiol.* **34**, 323–326 (2013).
2. Groves, C. P. in *Mammal Species of the World* 3rd edn (ed Wilson, D. E. & Reeder, D. M.) 154–158 (Johns Hopkins Univ. Press, 2005).
3. Brodmann, K. *Vergleichende Lokalisationslehre der Großhirnrinde* (Leipzig, 1909).

CORRIGENDUM

doi:10.1038/nature12197

Corrigendum: Human contribution to more-intense precipitation extremes

Seung-Ki Min, Xuebin Zhang, Francis W. Zwiers & Gabriele C. Hegerl

Nature **470**, 378–381 (2011); doi:10.1038/nature09763

Supplementary Figs 8, 9 and 11 of this Article each inadvertently included results for an extraneous empirical orthogonal function (EOF)—two extraneous EOFs in the case of the right-hand column of Supplementary Fig. 8. The time mean was removed prior to the detection analysis, so the rank of the covariance matrix (which determines the maximum number of EOFs required to describe the data fully) should be nine for the time series of Northern Hemisphere mean five-year means for 1951–1999 and eight for 1955–1999. Similarly, when combining two domains such as the Northern mid-latitudes and tropics (“Nmid+Ntro”), the rank of the covariance matrix is 18 for 1951–1999. Results for ten EOFs shown in the left panel of Supplementary Fig. 8 and the lower-right panel of Supplementary Fig. 9 reflect numerical artefacts and were incorrectly included in these plots, as were results for 19 and 20 EOFs in the right panel of Supplementary Fig. 8, and for nine EOFs in Supplementary Fig. 11. In addition, for the 1951–1999 single-domain analyses the 1955–1999 means were removed from the second set of control simulations prior to the detection analysis rather than the 1951–1999 means. This small error affected detection results using ten EOFs only in Supplementary Fig. 8. The corrected Supplementary Figs 8, 9 and 11 are provided as Supplementary Information to this Corrigendum. Our conclusions and results are unaffected.

Supplementary Information is available in the online version of this Corrigendum.

CAREERS

TURNING POINT Spacecraft designer's research takes off after move abroad **p.529**

UNITED STATES Shorter grant-eligibility period aims to speed independence **p.529**

NATUREJOBS For the latest career listings and advice www.naturejobs.com



FUNDING

Flirting with disaster

Draconian US federal budget cuts due to 'sequestration' are already having dramatic effects.

BY VIRGINIA GEWIN

For the past five years, Vern Schramm's lab has been working on a promising anticancer agent. The research has been successful — one of his grant-renewal proposals this year to the US National Cancer Institute (NCI) in Bethesda, Maryland, had a score in the top 10%. But a 1% drop in the US National Institutes of Health (NIH)'s payline (the percentage of applications funded), caused by US budget cuts known as sequestration, meant that Schramm didn't get his grant. It was his

second NCI grant renewal to go unfunded this year. The consequences have not been pleasant: Schramm has just had to let five postdocs go.

Sequestration, the across-the-board US federal budget cuts resulting from Congress failing to agree on deficit-reduction legislation, became official on 1 March and is exacerbating an already difficult research-funding situation (see *Nature* **494**, 158–159; 2013). Many US scientists dependent on government funding are likely to be affected, from those in long-running big projects that may have to close, to

established scientists who have not had grants renewed and must downsize their labs, to the young researchers who will lose their jobs or have difficulty securing funding as a result.

The NIH for example, faces a US\$1.5-billion budget cut over fiscal year (FY) 2012–13, which it says will result in the funding of some 700 fewer competitive research projects and the admission of 750 fewer new patients to the NIH Clinical Center in Bethesda. The US Department of Defense and the US National Science Foundation (NSF) each expects to offer 1,000 fewer grants, and the US Geological Survey has slashed its competitive-grants programme in water research to protect funding for key monitoring networks.

With the US economy improving, there is actually less pressure on politicians to compromise on a budget deal that would mitigate future sequestration-related cuts. Reinstatement of pre-sequestration funding levels seems unlikely in the current political climate. In principle, that means the cuts could continue for another nine years, with 8% decreases year over year, says Joseph Haywood, vice-president for science policy with the Federation of American Societies for Experimental Biology in Washington DC. As a result, "morale is very low" in the scientific community, he says.

"Funding lines were difficult before the sequester," says Schramm, who is chair of the biochemistry department at the Albert Einstein College of Medicine in New York City. "Now it is a research crisis."

STRUGGLING TO COPE

Although younger researchers are vulnerable to the cuts, they have some funding opportunities that established researchers do not. Young-investigator awards from private foundations, for example, often target those who have only recently received their PhDs. Young researchers also typically have an edge when it comes to NIH grants. At the NIH's National Heart, Lung and Blood Institute, for example, the payline for grants is 11% overall, but 21% for new investigators.

Worst hit will be assistant and associate professors doing fine, solid work that simply isn't in the top percentiles, says Laurie Glimcher, dean of Weill Cornell Medical College in New York City. To stave off the potential loss of a generation of scientists, her institute is trying to raise a bridge fund to provide relief to researchers who earned high scores but didn't get funded. "When you are funding fewer ►



PAUL RIVENBERG/M. P. McNALLY

Without additional long-term funding, the C-Mod lab, pictured here in 2012, will sustain major losses as a result of the sequester.

► than 10% of grant applications it's almost random — and the psychological impact of that is troubling," she says.

MEDICAL CENTRE MALAISE

Academic medical centres are doubly hit by the sequester. Not only is NIH funding down, but so too are fees that physicians receive under the government's Medicare insurance programme — by about 2%. President Barack Obama's programmes for affordable health care are also being reduced.

"The health-care industry is going through an enormous change, and the sequester on top of it makes an already tough situation now erratic," says Dean Li, vice-dean for research at the University of Utah School of Medicine in Salt Lake City. He says that his school will lose about \$19 million in research funding.

BIG LOSSES

The re-evaluation of long-term budgets has hit big physics projects as well. The sequester has meant major changes for the Plasma Science and Fusion Center (PSFC) at the Massachusetts Institute of Technology (MIT) in Cambridge, funded by the US Department of Energy. Money for the centre's cornerstone project, the Alcator C-Mod — a fusion experiment that uses a magnetic field to contain a plasma — was cut from \$25 million to \$14 million in FY2013, and was set to end in FY2014. Recent action from a congressional committee has extended C-Mod's life and may save some jobs, but the project is still in jeopardy.

If more permanent funds do not surface, C-Mod, which once supported 30 PhD students, will be left with many fewer; and as many as 70 postdocs, technicians and support staff could be laid off. "This was the largest student-training programme in any [fusion] experiment in the world," says

Miklos Porkolab, the PSFC's director, lamenting that no graduate students have entered the programme since March 2012. Negotiating budgets post-sequester has made staffing decisions increasingly difficult for administrators such as Porkolab, who is still trying to decipher the budget implications for C-Mod.

At the same time, transnational agreements mean that the United States has had to up its contribution to ITER, the world's largest nuclear-fusion reactor, which is under construction in the south of France. Support for ITER from the United States for FY2014 is \$225 million. "When we agreed to ITER over ten years ago, the community supported it but with additional funding, not through cuts to existing research programmes," Porkolab says. Even more disheartening, he adds, is that ITER probably will not be productive until 2025, and the United States won't have a trained pipeline of researchers ready, because its largest training facility will no longer exist.

Innovative national-security technology too will suffer under sequestration. The defence department intends to cancel or delay around 100 tests and demonstrations. "People were worried, initially, that sequestration would be like a jump off the Empire State Building," says Al Shaffer, acting assistant secretary of defence for research and engineering. "It's not going to be like that; it's going to be 1,000 cuts with a knife; slow and continual."

LOOKING FOR SOLUTIONS

The NSF has traditionally been the source of grants for research in biology other than biomedicine. But John Bruno, a marine ecologist at the University of North Carolina at Chapel Hill, has begun to wonder whether he should abandon the NSF altogether, rather than waste precious time writing grant applications that don't get funded.

His department is reconsidering whether NSF support should be a requirement for tenure. But the problem is that philanthropy cannot offer the same level of funding as government agencies once did, he says.

Some young researchers are playing it safe. Megan Williams, an assistant professor in neurobiology at the University of Utah in Salt Lake City, submitted her first grant application to the NIH on 5 June. Unsure about whether she will be funded, she is hoarding grant money received from private foundations and

has not hired a postdoc. Williams says that graduate students now ask about funding. They want to know which labs have money, to help them decide which to join.

David Cox, a neurobiologist at Harvard University in Cambridge, Massachusetts, has decided to take advantage of other countries' science investments. He is taking on foreign scientists who come with money from



"Funding lines were difficult before the sequester. Now it is a research crisis."

Vern Schramm

their home governments. One of his postdocs is paid for by the German government and another by a Taiwanese business conglomerate. "It may be overly dramatic," says Cox, "but I wonder if the last act of the US research establishment will be to serve as a training ground for other countries." ■

Virginia Gewin is a freelance writer in Portland, Oregon.

ALBERT EINSTEIN COLL. MED.

TURNING POINT

Riccardo Bevilacqua

In the middle of his PhD, Riccardo Bevilacqua left Italy for the United States to pursue his passion — designing spacecraft. He secured a three-year young-investigator grant this spring from the US Office of Naval Research (ONR) to design a low-Earth-orbit satellite to forecast space weather.

How did you first pursue your interest in spacecraft?

I completed a five-year *laurea*, essentially a master's programme, in aerospace engineering at the University of Rome in 2002. My thesis explored ways of controlling the orientation of spacecraft. I worked for a year in Spain developing software for satellites, and realized that I wanted to focus on research. I went back to Rome for a PhD, and my research adventure led me to the United States.

How did that happen?

Sometimes you have to be in the right place at the right time. I was at a conference where Marcello Romano from the US Naval Postgraduate School in Monterey, California, was demonstrating technology that could perform simulations I had worked on during my *laurea*. The Italian university system will sponsor a PhD student for up to 18 months abroad, and Romano was happy to host me. In his lab, I worked on optimizing the fuel use and timing of spacecraft operations — for example, docking a space shuttle at the International Space Station. I continued in his lab with a three-year postdoc.

Describe your job search.

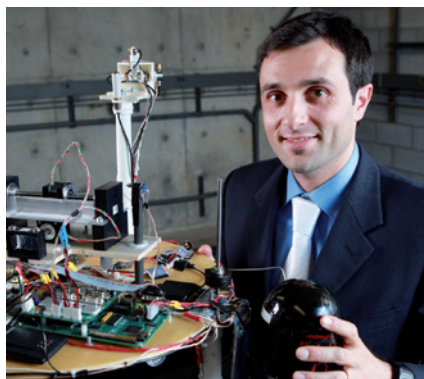
From the start of my postdoc I applied for at least 20 jobs, but I only got my first interview nine months before the end of the postdoc. All of a sudden, it was the right time in the job market. I had five interviews in a month.

You ended up at the Rensselaer Polytechnic Institute (RPI). How has that been?

After spending so much time in California, I didn't expect to end up in Troy, New York. But I also didn't expect the RPI to be so aggressive and supportive in terms of start-up funds, which was crucial for starting my lab, getting students and making important connections.

Do you have any plans to return to Italy?

The most difficult decision was to leave my country. I was receiving interview calls from Italian companies as I was accepting the postdoc position. That was a turning point — Italy has one of the worst research situations in



Europe and I realized I won't be back there for a long time. For me, it was the right decision to come to the United States — I grew up with the shuttle and all the amazing things this country has done in space. With support from funding agencies and the RPI, my research interests are better served here.

What does the award mean for your career?

The ONR award [US\$510,000] is funding my work building small spacecraft that can measure variables in low Earth orbits. Last year I received a \$334,000 young-investigator grant from the US Air Force Office of Scientific Research to support my work to prove that you could use the atmosphere to steer small spacecraft without propellant. That grant helped me to get the ONR award. The most important aspect of these grants is not their amount, it's the visibility. People know what you are doing and that leads to more projects that splinter off the original research.

Have the cuts to US federal spending affected your research goals?

I'm expecting cuts to existing grants but don't know by how much. I have four graduate students and would love to recruit more, but with the funding situation, I'm not sure how quickly I can grow my lab. Still, my research is attractive partly because we design small, cheap spacecraft that can do science at a reduced cost.

Where do you get your inspiration?

Inspiration can come from anywhere. One undergraduate showed me his origami designs and wondered how to apply them to my research. After thinking about it, I realized we could use those folding strategies to develop a sail to steer our spacecraft. ■

INTERVIEW BY VIRGINIA GEWIN

UNITED STATES

Jump start for postdocs

The US National Institutes of Health (NIH) in Bethesda, Maryland, has shortened the eligibility requirement for its popular Pathway to Independence award, a grant of up to US\$947,000 that helps postdoctoral researchers to establish their own labs. From February 2014, applicants must have a maximum of four years of postdoctoral training experience, rather than the current five. The change is intended to encourage postdocs to complete their training more quickly, says Sally Rockey, the agency's deputy director for extramural research. Lorraine Tracey, chair of the National Postdoctoral Association's board of directors in Washington DC, says that applicants should start planning their next career phase within their first postdoc year. The NIH hopes eventually to make awards to 30% of applicants, up from 23% at present.

EUROPE

University funding cuts

Public funding for universities in some European countries has dropped precipitously from 2008 to 2012 as a result of the global recession, leading to weakened research capacity and risking a 'brain drain', says a report by the European University Association (EUA), released on 10 June. Of 20 nations studied, 13 had less funding for universities in 2012 than in 2008, with the greatest cuts affecting Greece, Ireland, Lithuania and Hungary. "The prospects are dim," says Thomas Estermann, head of the EUA's governance, autonomy and funding unit. "If these trends continue, it will be much more difficult for researchers thinking about where they want to start their careers."

MEETINGS

Help with expenses

Early-career astronomers who need financial help with child or dependent care to attend the annual meeting of the Division of Planetary Sciences (DPS) of the American Astronomical Society, based in Washington DC, can apply for a US\$250 grant from the DPS. The division has set up the Susan Niebur Professional Development Fund to offer support to qualifying members, including graduate students and postdocs. The DPS has launched the fund with \$2,500 and is seeking contributions from its members and the astronomy community. This year's meeting is in October in Denver, Colorado.

PROBABILITY-1: TERMINATION

Minuscule moves in the struggle for funds.

BY EUAN NISBET

Through the days just before the inauguration of Lady Clinton as Viceroy, Washington buzzed with speculation and intrigue. In St Petersburg, the Tsar's spokesman denied that Preobrazhensky Guards were moving to the Alaska–Yukon border. Peking's Dowager Empress was silent, even though the Kaiser had despatched SMS *Bismark* to Tsingtao, overruling Chancellor Kohn's anguished pleading. In Foggy Bottom, the press clamoured for a statement from the Secretary. There'd been no fighting since 1918, when the Jerusalem Treaty ended the War of Turkish Succession. But despite a century of universal prosperity, clouds were dark.

Deep in the Smithsonian's corridors, two postdocs gloomily discussed events. "They can't fight, of course," Tom Garcia said. "There are only five battleships on the whole planet, and each empire is limited to 10,000 soldiers. But the League of Nations will impose huge sanctions."

Sara Chakrabarti, fellow in molecular palaeontology, was in misery. "We're breaking contract. It'll be a monster indemnity. Tens of billions. They'll take it out of the science budget, of course. We'll lose our funding."

Ever since the Turkish War, the League had diverted almost all the former military expenditure to science, reasoning that science is the principal beneficiary of war. Conversely, each time the League imposed sanctions, payment came from the science budget of the offending empire.

The birth of the Princess Heir Apparent had triggered the chaos. The Dowager of China loudly demanded betrothal to the three-year-old Emperor Hsüan-tung II, with Hong Kong as the dowry. Russia, supported by the Kaiser, justifiably claimed that the Princess was promised to the five-year-old Tsarevich, quoting an unwise commitment by a previous Prime Minister in London. Given the trade implications, British North America, India and Australasia all supported the Chinese proposal. Unhelpfully, from her winter palace in Nairobi, Queen Elizabeth, in council with former Viceroy Mandela and Archbishop-emeritus Tutu of Canterbury, proposed the extraordinary notion that the baby choose for herself when she came of age.

Reaching the bottom of the whisky bottle, Tom was scolded by Sara: "You're a quantum teleportationist! Can't you do something? Teleport us some gold bars out of Fort Knox, maybe?"



Tom sank his glass in misery. "Not a hope! Teleportation works in all space and all time. But it's incredibly selective. I can only wiggle single atoms, not kidnap gold bars. And I have to identify exactly a unique receptor at one specific moment in time, in all the long history of the entire Universe."

Sara yelled at him: "Useless!" She fell silent.

They sat in gloom for hours. Tom was washing in the depths of Russia's soul, Shostakovich's mighty 7th, *The Peace of Jerusalem*, when Sara suddenly muttered: "Maybe..."

"Maybe?" Tom asked.

"If you can rebuild just a molecule, then maybe," she said.

"All I can do is jiggle a few atoms. But I repeat: the target has to be specified. A single unique molecule, the only one in the Universe at that exact time."

Frantic days followed. Despite support from the outgoing American viceroy, the newly elevated Duke of Chicago, the Queen was overruled by Congress and India's Lok Sabha. Yukon and £250 billion placated Russia; Germany got Hanover but left Tsingtao; Constantinople's Sublime Porte signed the CO₂ Treaty for Turkish Arabia. Thus, Britain and China united, delighting American and Australian miners. India rested peacefully; Japan exhaled. All rejoiced, except the scientists. Sara and Tom expected layoff imminently.

Luckily Sara had privileged access to the Smithsonian collection. One night she crept into the exhibition commemorating the American Royal

Visit of King George the Wise, whose meeting with Field Marshal Washington led to the Great Democratic Reforms of 1783. A lock of George III's hair, given to the redoubtable Abigail Adams, was now in the museum.

As she delicately lifted a single strand of the king's hair, Sara noticed another royal lock nearby: a knot of Victoria's lovely cascades on loan from the Queen for the Inaugural celebrations. Sara quickly lifted that strand too, and scuttled back to her lab.

Two days later she had the DNA sequences of each monarch. All she needed now was their dates of conception, when their DNA molecules had been single, unique. That took guessing but they could spread the signal a bit.

Tom surfaced from the sublime bowels of the Sibelius 8th. "We can't do this! Changing history? Anything can happen!!"

Sara insisted. "Be patriotic! Stand up for the Union and Stripes! You're just jiggling a few atoms. George will have a chronic illness, so he'll be a less-effective bargainer in 1783. Remember how he out-negotiated Washington on American contributions to the Crown fiscus to pay the Royal Navy's budget? If King George hadn't won such a large share of military costs, the science budget here in America would be less at risk. Likewise if Victoria's Russian descendants have problems, we'll probably get away with a smaller fine and we might even keep the Yukon."

"Too dangerous!"

"Chicken!! The situation is terrible! Some soldier might even be hurt! Just tweak two little molecules! It's impossible to do long-term damage. All scholars agree history is inevitable, determined by mass movements. Tolstoy proved that. So did Sir Charles Marx."

She projected a 3D molecular hologram. "This is George the Wise's DNA. Target the day the sperm met the egg. Just switch these atoms," she pointed. "And here's Victoria's. Change her DNA this way."

"What will this do?" Tom asked as his finger hovered, ready to press the button.

"Nothing deadly — it'll just make George a little odd occasionally. It won't affect Victoria at all, or her son — only the female line marrying Russian royalty." Tom's finger pressed down as she added confidently: "For George, mild porphyria. For Victoria, haemophi..." ■

Euan Nisbet is in the Department of Earth Sciences, Royal Holloway, University of London, where, being Zimbabwean-Canadian, he studies ancient rocks and modern atmospheric methane.

ON NATURE.COM
Follow Futures:
@NatureFutures
go.nature.com/mtoodm

Diatom flickering prior to regime shift

ARISING FROM R. Wang *et al.* *Nature* **492**, 419–422 (2012)

Potential early warning signals for regime shifts are studied intensively in the field of ecology^{1–4}. Wang and colleagues¹ investigated changes in the sediment diatom composition of Lake Erhai, China, and concluded that a regime shift in diatom assemblages that occurred around 2001 was preceded by flickering behaviour for 10 to 30 years. We propose that their results may be more reflective of their data processing than of the diatom data. Although flickering behaviour before regime shifts may be observed in some palaeoenvironmental records, we question whether this behaviour applies to diatoms in Lake Erhai. There is a Reply to this Brief Communication Arising by Wang, R. *et al.* *Nature* **498**, <http://dx.doi.org/10.1038/nature12273> (2013).

Wang *et al.*¹ base their conclusions on changes in standard deviation, skewness and lag 1 autocorrelation of the diatom assemblage composition (detrended correspondence analysis; DCA) and its diversity (Hill's diversity index N2; HDI) in a sediment core. The statistics were calculated with a 59-year sliding window on the residuals from a linearly interpolated time series, detrended by subtracting a smooth exponential moving average.

We were intrigued by these results, and while investigating the underlying statistical analyses, we noticed three points. First, decreasing time resolution with depth implies that samples represent approximately 1 year in the upper part and approximately 4 years in the deeper part of the sediment profile (Supplementary Fig. 2 in ref. 1). Greater temporal aggregation in the deeper profile reduces the temporal variation in diatom composition, giving a reduced standard deviation for the oldest data. Second, linear interpolation to produce an annual time series alters the statistical properties of the time series by reducing the standard deviation, increasing autocorrelation and broadening the expected distribution of skewness⁵. Coarser resolution in the older sediment results in more interpolated values and thus lower standard deviation and higher autocorrelation. Third, their detrending does not subtract a smooth curve, but a phase-shifted version of the original data with a tendency to overshoot when the original curve changes direction. This results in large residuals when there are abrupt changes in the data. These are expected in the highest resolution part of the core, where there is least averaging and interpolation. The sensitivity tests applied¹ do not seem to address fully the fundamental problems of unevenly spaced temporal data⁵.

To assess the null expectation of their methods, we used a simulated time series with mean characteristics similar to those of the DCA¹ and added uncorrelated noise (Fig. 1a). Random variation of the underlying simulated time series is reduced unevenly by aggregation that mimics the sediment sampling from Lake Erhai and interpolation (Fig. 1b). Standard deviation is reduced by factors of approximately 6 in the older data and approximately 3 in the more recent data (Fig. 1c). The increase in standard deviation over time reported in the paper by Wang *et al.*¹ has a similar magnitude to that expected from a purely random process analysed with their methods. The skewness broadens when the sliding window spans data with varying standard deviations, and there is a slight shift towards negative values (Fig. 1d). The skewness reported also displays a shift towards negative values within the bounds of expected values. Data processing introduces strong autocorrelation in the older data that is reduced gradually with improved temporal resolution (Fig. 1e), consistent with the pattern that they described.

We reanalysed the data from the paper by Wang *et al.*¹ without interpolation, using a more robust detrending approach and accounting for differences in temporal aggregation by implicitly assuming

variance heterogeneity (Fig. 2a, b). There is a gradual increase of approximately 50% in the DCA standard deviation, much smaller than the increase they reported, and the HDI standard deviation does not change (Fig. 2c, d). Skewness in DCA and HDI displays quite different patterns to those reported in their paper, and remains within the approximate 95% confidence bounds (± 1.0) expected from a random normal process. Autocorrelation does not decrease over time and is generally low.

The trends in standard deviation, skewness and autocorrelation reported as potential early warning signals of a “regime shift in the trophic state of Lake Erhai” by Wang *et al.*¹ are consistent with the null expectation of their methods and are not reproduced with more robust methods. We therefore suggest that these may be an artefact of the numerical methods used and the inherent problems in time-series analysis of samples with uneven temporal spacing from sediment cores.

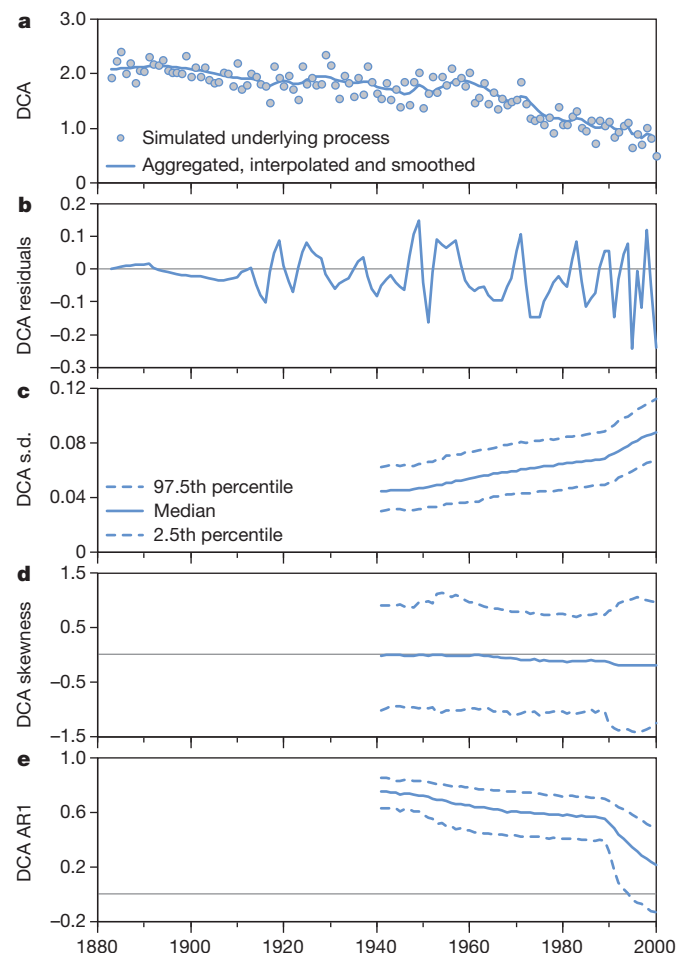


Figure 1 | Simulated data processing and early warning signals. **a**, One simulation of the underlying data-generating process and the time series resulting from temporal aggregation, interpolation and smoothing. **b**, Residuals from the simulated process in **a** and from the data processing in ref. 1. **c–e**, Distributions of standard deviation, skewness and lag 1 autocorrelation (AR1) from 1,000 simulations using a 59-year sliding window during the period between 1883 to 2000. This figure is for comparison with Fig. 3 of ref. 1. Grey horizontal lines mark 0 on the y axis.

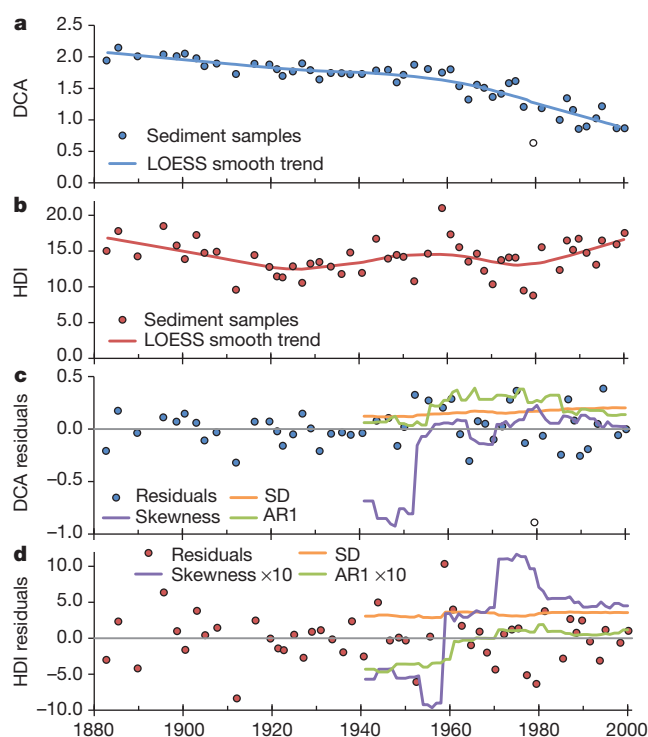


Figure 2 | Re-analysis of potential early warning signals compiled from the diatom community in Lake Erhai. **a, b,** Trends in diatom composition and diversity based on detrended correspondence analysis (DCA) of diatom composition (**a**) and Hill's diversity index N2 (HDI) (**b**) with LOESS smoothing functions used for detrending. **c, d,** Residuals from **a** and **b**, with s.d., skewness, and autocorrelation (AR1) calculated using a 59-year sliding window during the period between 1883 and 2000. Skewness and autocorrelation are scaled by factor 10 in **d**. One DCA observation deviated substantially from other observations (open symbol in **a** and **c**) and was not included in this re-analysis.

Methods

We simulated time series ($n = 1,000$) with an annual resolution of a process that resembles the characteristics of DCA¹: the mean decreases slowly before 1960 and faster thereafter, and the standard deviation of the uncorrelated noise is 0.25. The time series were aggregated to mimic the observed sample spacing. The remaining analysis follows ref. 1.

To repeat the analysis of early warning signals with more robust methods, we detrended the non-interpolated DCA and HDI values before 2001 (Fig. 1 in ref. 1) with a LOESS smoothing function. Residuals from detrending were standardized by the square root of the period that the values represent to account for differences in temporal aggregation. Autocorrelation is calculated from the data with missing values, calculation of early warning signals otherwise follow ref. 1.

Jacob Carstensen¹, Richard J. Telford² & H. John B. Birks²

¹Department of Bioscience, Aarhus University, Frederiksborgvej 399, DK-4000 Roskilde, Denmark.
email: jac@dmu.dk

²Department of Biology, University of Bergen, Thormøhlensgate 53 A, N-5006 Bergen, Norway.

Received 25 March 2013; accepted 2 May 2013.

1. Wang, R. *et al.* Flickering gives early warning signals of a critical transition to a eutrophic lake state. *Nature* **492**, 419–422 (2012).
2. Scheffer, M. *et al.* Early-warning signals for critical transitions. *Nature* **461**, 53–59 (2009).
3. Drake, J. M. & Griffen, B. D. Early warning signals of extinction in deteriorating environments. *Nature* **467**, 456–459 (2010).
4. Scheffer, M. *et al.* Anticipating critical transitions. *Science* **338**, 344–348 (2012).
5. Schulz, M. & Stettin, K. Spectrum: spectral analysis of unevenly spaced paleoclimatic time series. *Comput. Geosci.* **23**, 929–945 (1997).

Author Contributions J.C. instigated the writing of the Comment. J.C. and R.J.T. carried out statistical analyses. J.C., R.J.T. and H.J.B.B. discussed the results and contributed to writing the manuscript.

Competing Financial Interests Declared none.

doi:10.1038/nature12272

Wang *et al.* reply

REPLYING TO J. Carstensen, R. J. Telford & H. J. B. Birks *Nature* **498**, <http://dx.doi.org/nature12272> (2013)

Some issues have been raised with regard to our paper¹, by Carstensen *et al.*². In terms of our data processing, we were aware from the outset of the problems of unevenly spaced temporal data and sediment dating errors. We also wanted to duplicate, as far as possible, the methods published previously that had been used to identify early warning signals in palaeoenvironmental data (for example, ref. 3). Thus, we applied two standard smoothing functions (exponential and Gaussian kernel) to interpolated and non-interpolated (original) diatom data, expressed as three statistical indices (detrended correspondence analysis (DCA), Hill's diversity index N2 (HDI) and correspondence analysis), using different sliding-window sizes and the two-standard-deviation range of dates for each sample.

Despite their criticisms, the LOESS approach used by Carstensen *et al.*¹ also does not capture explicitly the unequal time increments in the sediment data and does not confront the dating error problem. However, the results described (Fig. 2 in ref. 1) still confirm increasing variance for DCA, albeit with reduced and possibly non-significant trends, and increased skewness if one 'outlier' is retained. We also

note that their results do not replicate the full range of our tests. They do not seem to address the issue of window size, the sensitivity to the full range of dating errors, or cover the full range of indices (there is no correspondence analysis). Their assumption that "Greater temporal aggregation in the deeper profile reduces the temporal variation in diatom composition" has to be countered by the observation that among the samples dating back to 1885 ($n = 49$), two of the seven larger temporal aggregations (≥ 3.4 years per sample compared to the mean of 2.4 ± 0.9 years per sample) are in fact recent samples, dated to 1986 and 1998 (Supplementary Fig. 2a in ref. 1).

The new simulation method proposed by Carstensen *et al.*¹ to test the null hypothesis is interesting, but again does not fully account for the temporal aggregation in the actual DCA data; instead, it 'resembles' our DCA data. The model does not use the real time periods in the sediment data derived from the dating model and it does not take into account the real errors in the dating model. Therefore, the simulation demonstrates a general principle for testing a null model but does not in itself overturn the findings from the analyses of our paper.

In conclusion, given the sensitivity of residuals to different smoothing functions and the choice of parameters (for example, window size and span value), the main implication of the work by Carstensen *et al.*¹ is that future studies of sediment data should evaluate the results from a wide range of smoothing-function options. In any case, we do not advocate the use of time-series analyses of sediment data alone to infer early warning signals. At Lake Erhai, China, our context included a wealth of real-time observations (for example, algal blooms) that amounted to *prima facie* evidence for increased ecosystem instability before a critical transition. In our view, the new results do not make a case for overturning the main findings of the paper.

Rong Wang^{1,2}, John A. Dearing¹, Peter G. Langdon¹, Enlou Zhang², Xiangdong Yang², Vasilis Dakos^{3,4} & Marten Scheffer³

¹Palaeoecological Laboratory, Geography and Environment, University of Southampton, Southampton SO17 1BJ, UK.

email: j.dearing@soton.ac.uk

²State Key Laboratory of Lake Science & Environment, Nanjing Institute of Geography & Limnology, Chinese Academy of Sciences, Nanjing 210008, China.

³Department of Aquatic Ecology & Water Quality Management, Wageningen University, PO Box 47, NL-6700 AA, Wageningen, The Netherlands.

⁴Integrative Ecology Group, Estación Biológica de Doñana, CSIC, C/Américo Vespucio S/N, E-41092 Seville, Spain.

1. Wang, R. *et al.* Flickering gives early warning signals of a critical transition to a eutrophic lake state. *Nature* **492**, 419–422 (2012).
2. Carstensen, J., Telford, R. J. & Birks, H. J. B. Diatom flickering prior to regime shift. *Nature* **498**, <http://dx.doi.org/10.1038/nature12272> (2013).
3. Dakos, V. *et al.* Slowing down as an early warning signal for abrupt climate change. *Proc. Natl Acad. Sci. USA* **105**, 14308–14312 (2008).

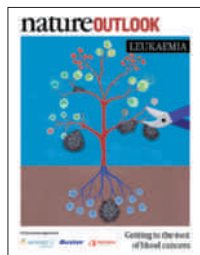
Author Contributions J.A.D., P.G.L. and V.D. wrote the reply following comments from R.W., E.Z., X.Y. and M.S.

doi:10.1038/nature12273

natureOUTLOOK

LEUKAEMIA

27 June 2013 / Vol 498 / Issue No 7455



Cover art: Nik Spencer

Editorial

Herb Brody, Apoorva Mandavilli, Michelle Grayson, Tony Scully, Nick Haines, Afsaneh Gray, Kevin Singer

Art & Design

Wes Fernandes, Nicola Hawes, Alisdair Macdonald, Andrea Duffy

Production

Donald McDonald, Susan Gray, Leonora Dawson-Bowling

Sponsorship

Will Piper, Greg Valero, Yvette Smith, Reya Silao

Marketing

Elena Woodstock, Hannah Phipps

Project Manager

Christian Manco

Art Director

Kelly Buckheit Krause

Publisher

Richard Hughes

Magazine Editor

Tim Appenzeller

Editor-in-Chief

Philip Campbell

Of all the cancers that can wage war on the body, leukaemia — the general term for cancers of the blood — has a reputation for being among the least malevolent.

Most solid cancers are riddled with dozens of mutations, making it impossible to know which mutation set a cell on the wrong path, or which one to target. Leukaemia seems simpler: one type of the disease, chronic myeloid leukaemia (CML), can be traced to a single gene fusion (page S4). Scientists were able to develop a drug, imatinib, that exploits the errant gene, increasing the five-year survival for CML to more than 95%. Most children with acute lymphoblastic leukaemia (ALL) also survive.

As we show in this Outlook, however, these headline statistics belie the reality for many patients.

As CML patients develop resistance to imatinib, doctors turn to one drug after another (S7). For many leukaemias, doctors still reach for the same toxic treatments they used in the 1970s (S8). Survivors of childhood leukaemia still suffer severe, even life-threatening, complications from the harsh treatments (S14).

Progress towards new therapies has been slow. Some scientists have been able to cure leukaemia by engineering immune cells to destroy cancer cells, but in fewer than a dozen people so far (S17). Bone-marrow transplants and cord-blood transplants are options, but both have limitations (S16). Other promising candidate drugs target chemical tags on DNA that alter gene expression without changing the genetic code (S10).

Cancer stem cells, a subset of cancerous cells able to regenerate and seed new tumours, are also best understood in leukaemia (S12). These and other lessons learned from the study of leukaemia may be broadly applicable to all cancer research.

We acknowledge the financial support of Novartis Oncology, Baxter International and Onconova Therapeutics in producing this Outlook. As always, *Nature* has full responsibility for all editorial content.

Apoorva Mandavilli

Guest editor

CONTENTS

S2 ONCOLOGY

Living with leukaemia

What is it, and how is it treated?

S4 GENETICS

Written in blood

Cracking leukaemia's genetic code

S7 PERSPECTIVE

Combined forces

Resistance is futile

S8 DRUG DEVELOPMENT

Target practice

Searching for the best treatment options

S10 EPIGENETICS

Reversible tags

The changing face of gene expression

S12 STEM CELLS

Bad seeds

An immortal foe

S14 DRUG SAFETY

Double jeopardy

A lifetime of side effects

S16 CELL BANKS

Life blood

Stored from the cord

S17 PERSPECTIVE

Assembly line immunotherapy

Mass production for T cells

COLLECTION

S18 **The rule of three in AML induction — is cladribine the answer?**

Frederick R. Appelbaum

S20 **SF3B1, a splicing factor is frequently mutated in refractory anemia with ring sideroblasts**

V. Visconte *et al.*

S24 **Clonal evolution in relapsed acute myeloid leukaemia revealed by whole-genome sequencing**

Li Ding *et al.*

S29 **Childhood leukaemia close to high-voltage power lines — the Geocap study, 2002–2007**

C. Sermage-Faure *et al.*

S37 **Role of the promyelocytic leukaemia protein in cell death regulation**

P. Salomoni, M. Dvorkina and D. Michod

Nature Outlooks are sponsored supplements that aim to stimulate interest and debate around a subject of interest to the sponsor, while satisfying the editorial values of *Nature* and our readers' expectations. The boundaries of sponsor involvement are clearly delineated in the *Nature Outlook* Editorial guidelines available at http://www.nature.com/advertising/resources/pdf/outlook_guidelines.pdf

CITING THE OUTLOOK

Cite as a supplement to *Nature*, for example, *Nature* Vol XXX, No. XXXX Suppl. Sxx–Sxx (2012). To cite previously published articles from the collection, please use the original citation, which can be found at the start of each article.

VISIT THE OUTLOOK ONLINE

The *Nature Outlook Leukaemia* supplement can be found at <http://www.nature.com/nature/outlook/leukaemia>

All featured articles will be freely available for 6 months.

SUBSCRIPTIONS AND CUSTOMER SERVICES

For UK/Europe (excluding Japan): Nature Publishing Group, Subscriptions, Brunel Road, Basingstoke, Hants, RG21 6XS, UK. Tel: +44 (0) 1256 329242. Subscriptions and customer services for Americas – including Canada, Latin America and the Caribbean: Nature Publishing Group, 75 Varick St, 9th floor, New York, NY 10013-1917, USA. Tel: +1 866 363 7860 (US/Canada) or +1 212 726 9223 (outside US/Canada). Japan/China/Korea: Nature Publishing Group — Asia-Pacific, Chiyoda Building 5-6th Floor, 2-37 Ichigaya Tamachi, Shinjuku-ku, Tokyo, 162-0843, Japan. Tel: +81 3 3267 8751.

CUSTOMER SERVICES

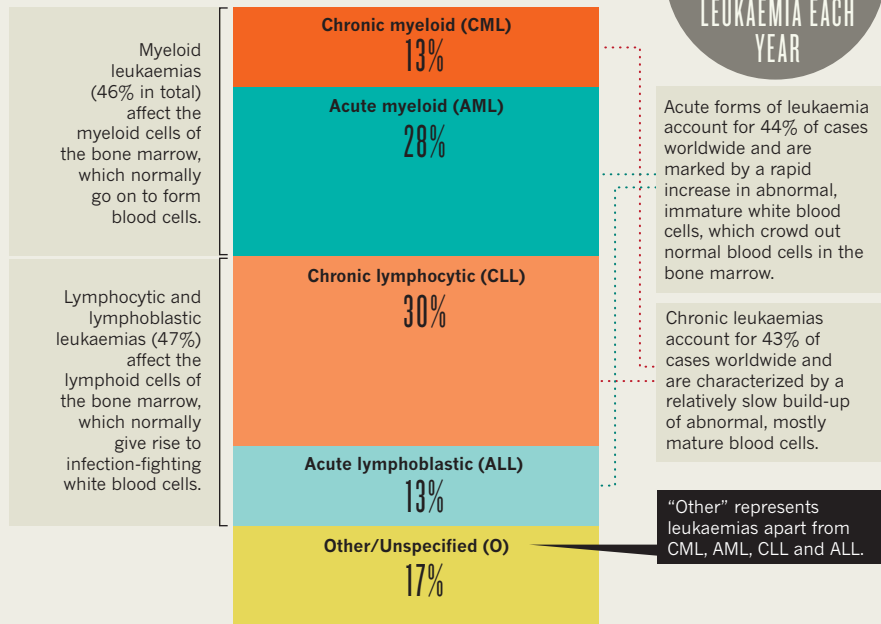
Feedback@nature.com
Copyright © 2012 Nature Publishing Group

LIVING WITH LEUKAEMIA

Leukaemias are cancers of the blood or bone marrow. But how do they form, and can they be treated? By Emily Elert.

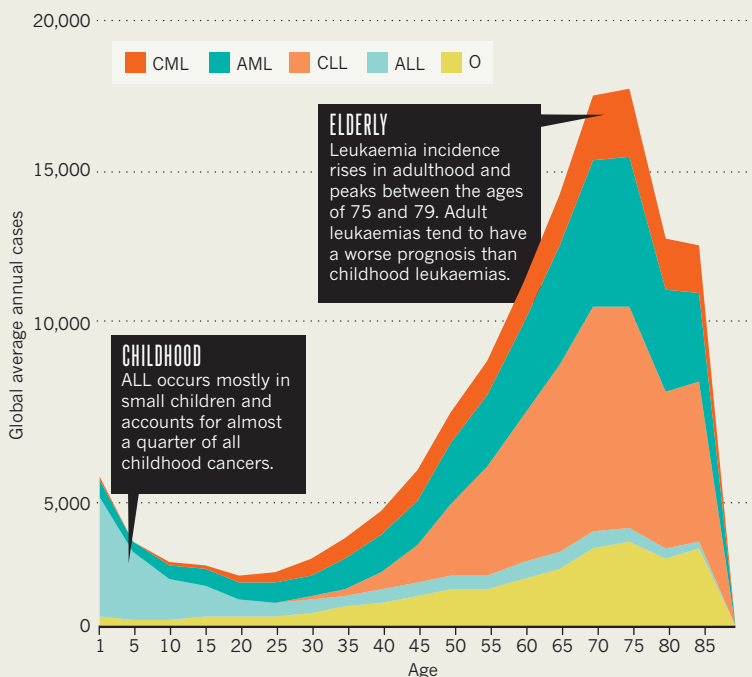
TYPES OF LEUKAEMIA

Most leukaemias are either myeloid or lymphocytic/lymphoblastic, depending on which cells they affect, and can be either chronic or acute.



AGE OF ONSET

Most leukaemia occurs in the elderly, but there is a separate, smaller peak in childhood.



TREATMENT TIMELINE

Important advances in the treatment of leukaemia.

1947

Aminopterin becomes the first known compound to inhibit the growth of cancer. It is shown to cause temporary remissions in acute lymphoblastic leukaemia in children.

1958

The US government shows that combination chemotherapy — the use of several chemical treatments at once — is much more effective at treating leukaemia (and cancer in general) than giving a single drug.

1975

The world's first successful bone-marrow transplant on a patient with lymphoma is conducted.

1940

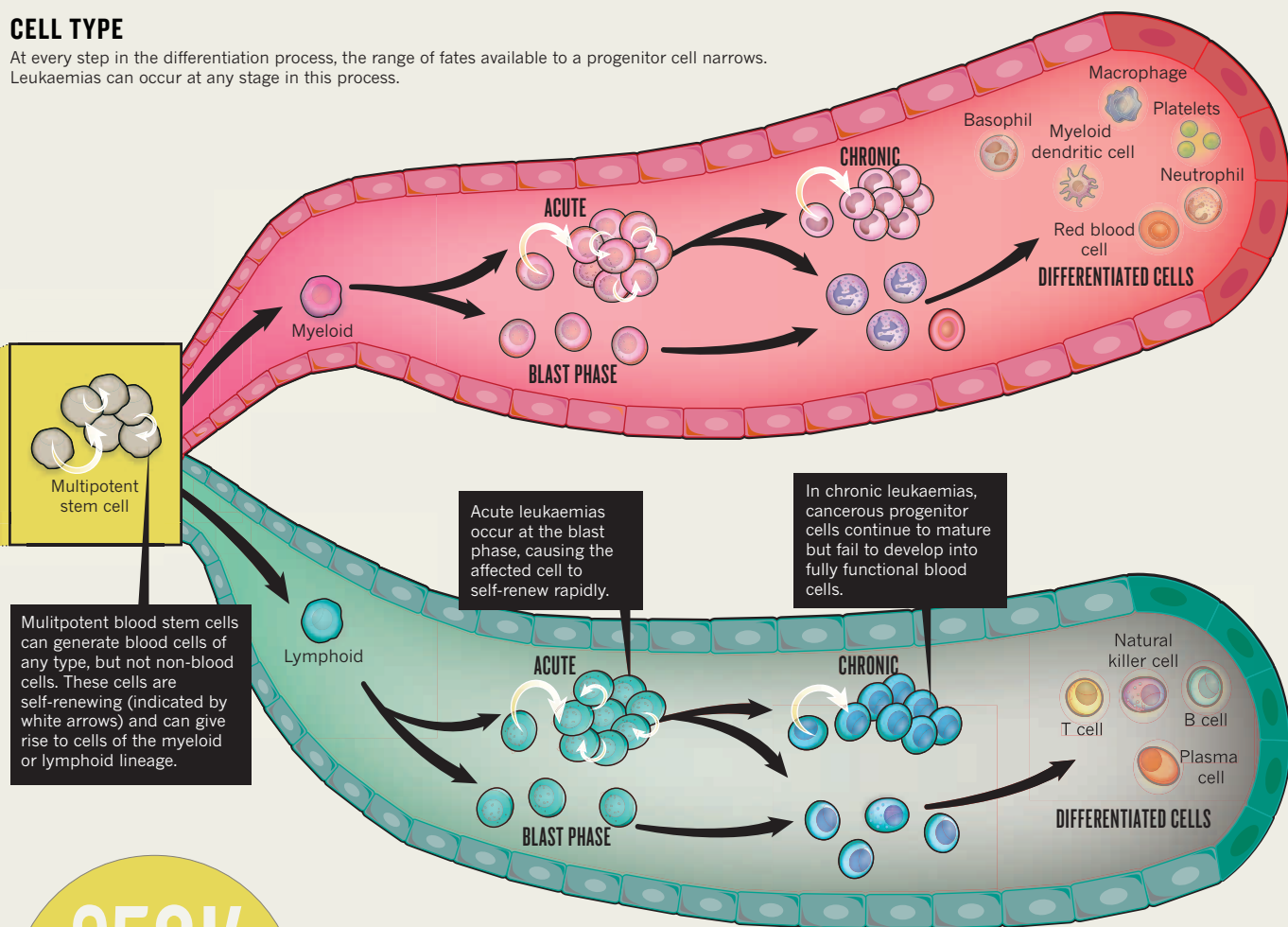
1950

1960

1970

CELL TYPE

At every step in the differentiation process, the range of fates available to a progenitor cell narrows. Leukaemias can occur at any stage in this process.

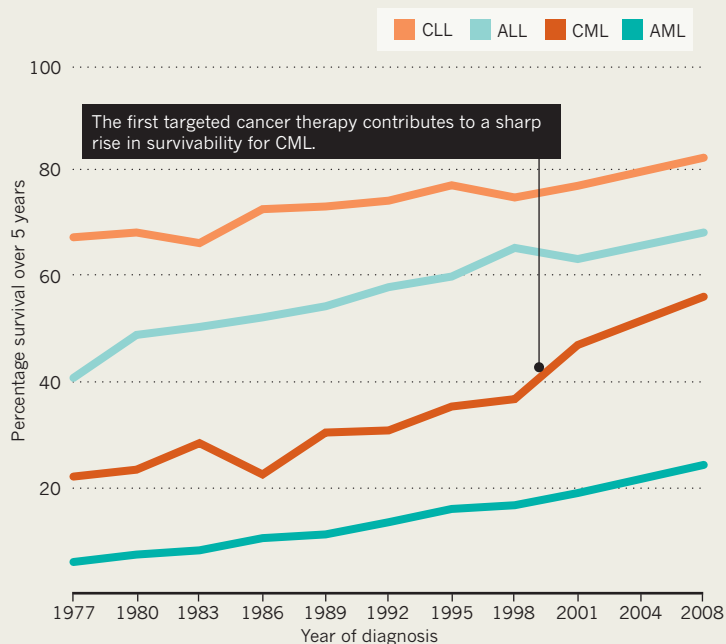


250K

DEATHS WORLDWIDE FROM
LEUKAEMIA EACH YEAR

5-YEAR SURVIVABILITY IN THE UNITED STATES

The likelihood of surviving with leukaemia for 5 years has been increasing steadily for more than 30 years as treatments have improved.



2008
Scientists sequence the genome of a patient with acute myeloid leukaemia, paving the way for better targeted therapies.

1995
Scientists discover the 'graft-versus-leukaemia' effect: giving leukaemia patients a dose of healthy white blood cells can help their cancer go back into remission.

1985
A bone-marrow transplant is used to cure leukaemia for the first time.

1986
The National Marrow Donor Program, a US bone-marrow transplant registry, is established.

2004
The first epigenetic drug is approved to prevent cancer in patients with myelodysplastic syndrome, which can lead to leukaemia.

1980

1990

2000

2010



Peter Nowell (left) and David Hungerford discovered the 'Philadelphia chromosome'.

GENETICS

Written in blood

Technologies that rapidly sequence DNA reveal deep genetic diversity both within and among individuals with leukaemia.

BY SARAH DEWEERDT

In 1959, David Hungerford of the Fox Chase Cancer Center and Peter Nowell from the University of Pennsylvania School of Medicine discovered that blood cells taken from two people with chronic myeloid leukaemia (CML) had a striking abnormality when viewed under the microscope: chromosome 22 in these cells had a big chunk missing.

That was the first glimpse of a genetic link to leukaemia — and, in fact, the first genetic abnormality associated with any form of cancer.

The stubby Philadelphia chromosome, named for the city of its discovery, is now known to be present in 95% of all people with CML.

The Philadelphia chromosome is formed when parts of chromosomes 9 and 22 swap places. This translocation brings together two genes, *BCR* and *ABL*, to create an abnormal entity, known as a fusion gene, which turns the cell malignant.

Despite the early identification of this fusion gene, knowledge of how single-gene changes contribute to leukaemia has been slow in coming. "We've known about these chromosome

changes for a long time, but not a lot else," says Mel Greaves, who studies childhood leukaemia at the Institute for Cancer Research in London.

This has begun to change in the past decade or so, as high-speed DNA sequencing technology has produced a flood of information about genes mutated in various forms of leukaemia. The identification of these genes should stimulate the development of new treatments for leukaemia and other cancers.

Studies are revealing that CML, with its straightforward link to a single genetic abnormality, is an anomaly. Most forms of leukaemia are caused by a combination of genetic mutations, with considerable variability both within and among individuals. Overall, a few hundred genes — including several dozen fusion genes — have been implicated in different kinds of leukaemia. But each individual case involves only a handful of the possible mutations.

This contrasts with solid cancers, such as breast or colon cancer, in which there are often dozens of mutations in a single individual. Solid tumours also show widespread genomic instability — with duplications, losses and the exchange of large chunks of DNA — which is rarely seen in leukaemia.

The relatively small number of genetic changes per tumour may help to explain why some forms of leukaemia are so susceptible to treatment. For example, about 95% of patients diagnosed with CML are still alive after five years, thanks to drugs that target the *BCR-ABL* fusion protein (see 'Target practice', page S8).

IN THE GENES

Leukaemia is classified as lymphoblastic or myeloid, according to the type of blood-cell precursors from which it arises, and as acute or chronic, depending on how aggressive it is (see 'Living with leukaemia', page S2). The list of contributing genes is distinct for each form of the disease, but there are substantial overlaps.

For example, the Philadelphia chromosome characteristic of CML is also found in about 5% of children with acute lymphoblastic leukaemia (ALL), the most common childhood cancer. About 25% of children with ALL carry a different chromosomal translocation, which results in the fusion of two genes called *ETV6* and *RUNX1*. *RUNX1* mutations are also common in acute myeloid leukaemia (AML), an aggressive form of the disease that primarily affects the elderly.

To find out which mutations cause disease, researchers look for ones that are 'recurrent', or present in multiple sufferers. In the largest leukaemia sequencing study undertaken so far, a team led by Timothy Ley, a cancer geneticist at Washington University in St Louis, Missouri, examined AML cells from 200 patients with the disease. Ley and colleagues decoded the cells' exomes — the protein-coding portions of genomes — from 150 of the patients, and whole-genome sequences from the other 50.

They found a treasure trove of information.

Among their key findings was that 99.5% of the AML patients studied had mutations in at least one of nine categories of genes, including tumour-suppressor genes, signalling genes and those that regulate the development of myeloid cells, from which the cancer arises. “We’ve been able to define the gene sets, or pathways, that are mutated in almost every patient,” says Ley.

Notably, they found that more than three-quarters of people who develop AML have mutations in genes involved in epigenetics — chemical modifications to DNA that affect its function without altering the genetic code (see ‘Reversible tags’, page S10).

The importance of epigenetic modifications in leukaemia has been one of the most surprising insights to emerge from sequencing studies, says Ross Levine, an oncologist at Memorial Sloan-Kettering Cancer Center in New York. “These are not genes that were on anyone’s radar three or five years ago, but they’re highly recurrent,” he says.

Another class of genes commonly mutated in leukaemia are those involved in the development and differentiation of various types of blood cells. In ALL, these genes vary depending on whether the cancer arises from precursors of B or T cells, two of the main classes of lymphocytes. It takes the B-cell route in 85–90% of cases in children and 75% in adults¹. It usually involves mutations in genes, such as *PAX5* or *IKZF1*, which control B-cell development. Cases triggered by T-cell mutations, on the other hand, usually involve genes in a signalling pathway called Notch, which is important in T-cell development.

GROWING BACK

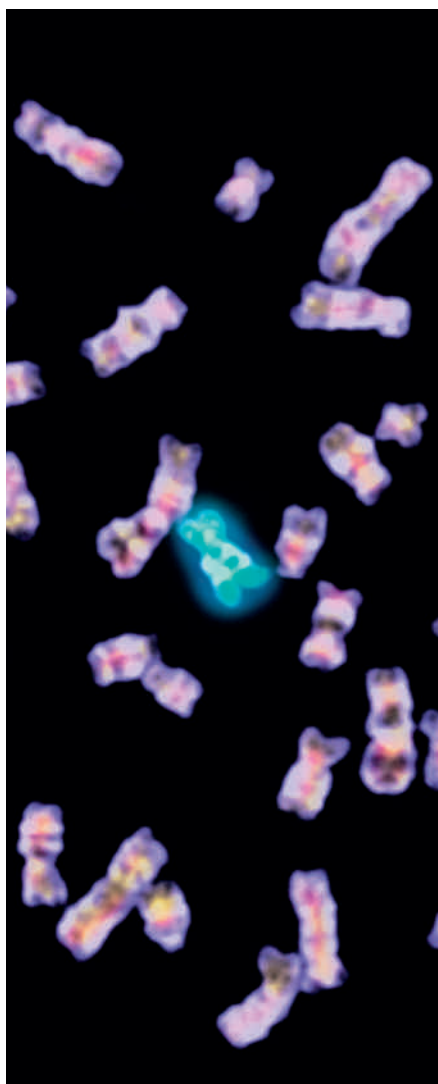
Of the four major leukaemia types, the one with the most diffuse genetics is chronic lymphocytic leukaemia (CLL). Sequencing studies suggest that a large number of genes can be involved, each mutated in a small proportion of cases. For example, mutations in a Notch pathway gene called *NOTCH1* are found in 12% of CLL cases², and mutations in the *POT1* gene appear in another 3.5% of cases³ (and 9% of those with the most aggressive form of this leukaemia).

The *POT1* gene binds to DNA at the telomere, the region at the tip of a chromosome, and protects it from damage. Telomeres have long been known to be involved in cancer, but this finding, reported in *Nature Genetics* in March 2013, is the first example of a telomere-protecting protein being implicated in cancer.

Assembling lists of genes that may be mutated in leukaemia is only the beginning of understanding its genetics. Even within a tumour there is enormous variability, with subsets of cells carrying different sets of mutations.

“Within each patient you’ve got this evolutionary tree of cancer,” says Greaves. “It’s not sufficient to list the mutations, because they segregate in different branches of the tree.”

One line of evidence for this evolutionary tree comes from studying leukaemia that



Parts of chromosomes 9 (blue) and 22 swap places to create the Philadelphia chromosome.

recurs after treatment, which is often genetically distinct from the original cancer. Greaves and his colleagues investigated this recurrent leukaemia, using fluorescent probes to analyse mutations in five people with ALL. They found that some of the tumour mutations in the initial sample had been replaced with others when they analysed the recurrent disease⁴. Ley’s group observed a similar pattern in AML, using whole-genome sequencing to compare DNA from leukaemia cells in eight people at diagnosis and at relapse⁵.

The implications of this slippery genetics for treatment are profound. Drugs targeting one set of mutations eradicate a portion of the leukaemia cells, but other subsets of cells then expand to take their place. “I think this explains a lot of treatment failures with targeted therapy,” Ley says.

Greaves compares the process to pruning a rosebush: chopping off one large branch will simply stimulate the growth of the other branches. “The challenge is to get rid of all the unwanted growth in a way that it doesn’t ever

come back,” he says. “So we need to chop it off at the base.”

In clinical terms, this means that therapies need to target not the tumour cells that are most prolific at the time of diagnosis, but rather the cells that carry the original mutations — because those mutations will be present in the entire tumour. But to do this, scientists must work out how to identify these original mutations.

Genetic variability also stems from the fact that leukaemia, like any cancer, involves two genomes: the host genome, representing the inherited set of genes, and the tumour genome, comprising the mutations acquired on the path to cancer. Most studies of genes involved in leukaemia have focused on the tumour genome.

In paediatric leukaemia, tumour genome mutations are acquired early — perhaps before birth. As lymphocyte precursors expand rapidly in the liver during fetal development, one of them may acquire a translocation or other mutation that sets it on the path to malignancy. The *ETV6-RUNX1* translocation linked to ALL, for example, has been found in newborns’ blood.

After birth, blood stem cells divide more slowly, about once a month on average, so it may take many decades for a cell to acquire the combination of mutations necessary to turn malignant. This explains why other forms of leukaemia, such as AML, primarily affect the elderly. “It really is just a disease of randomness and ageing,” Ley says.

INHERITED RISK

Despite the importance of these acquired mutations in triggering leukaemia, some researchers prefer to focus on inherited risk. “We’ve spent a lot of time looking at the mutations in the tumour genome, but we really haven’t spent much time looking at the host genome,” says Jun Yang, a pharmaceutical scientist at St Jude Children’s Research Hospital in Memphis, Tennessee.

Yang is among those who are trying to redress the balance. In the largest study of inherited risk genes so far, published in March 2013, his team scanned the genomes of 2,450 children with ALL and 10,977 controls⁶.

Three of the four risk genes they identified — *IKZF1*, *CEBPE* and *CDKN2A/2B* — were already known to have a role in leukaemia or blood-cell development. The fourth, *ARID5B*, had never been identified in studies of leukaemia tumour genomes, but preliminary evidence suggests that it may be involved in lymphocyte differentiation.

The gene variations identified in the study as being associated with ALL are common: some are carried by more than 20% of the population, most of whom do not develop the disease. Still, having even one high-risk variant almost doubles the risk of ALL; carrying six or more adds up to a ninefold higher risk.

Another approach to studying the role of the host genome involves families in which several members develop the same form of leukaemia.

These families are rare: familial AML accounts for only about 1% of all cases of this cancer, for example. But working out the genetics of familial leukaemia provides powerful evidence that a given gene is truly important in the development of cancer, says Marshall Horwitz, a geneticist at the University of Washington in Seattle. Horwitz was part of a team that linked mutations in a gene called *GATA2* to familial AML. Other researchers have identified AML families with mutations in *RUNX1* and *CEBPA*.

Together, those three genes — *GATA2*, *RUNX1* and *CEBPA* — account for about half of all familial AML. Other forms of familial leukaemia are also starting to give up their genetic secrets: Horwitz says that he and a group of collaborators have unpublished data pinpointing the first gene to be implicated in familial ALL.

MULTIPLE MUTATIONS

To understand the genetics of leukaemia, it is not enough to identify which individual mutations are possible, however. We also need to understand how multiple mutations collude to trigger a cancer (see 'Related disorders'). In mice, this process can be traced step by step.

George Vassiliou, a haematologist and cancer geneticist at the Wellcome Trust Sanger Institute in Hinxton, UK, and his colleagues generated mice with a defect in a gene called *NPM1*, which is mutated in 35% of patients with AML. About one-third of these mice develop AML late in life⁷. But when Vassiliou and his team induced additional mutations in blood-cell precursors, he says, "you get dramatic acceleration of leukaemia".

The same thing happens when the mutant mice are crossbred with mice bearing duplications of *FLT3*. These two genetic alterations are the ones most frequently seen together in AML. "Two mutations in isolation do a little bit but nothing dramatic," Vassiliou says. "Suddenly you put them together and the whole thing goes on fire, the mice get leukaemia very fast."

In humans, researchers have observed patterns in which genetic mutations are seen together in leukaemia. For example, the *ETV6-RUNX1* translocation and deletion of *PAX5* commonly occur together in B-cell ALL. These patterns affect a patient's prognosis and response to specific treatments, so researchers have begun to classify leukaemia on the basis of its genetic profile, rather than just the outward appearance of cells. "In the past ten years, we have gone from having 5 or 6 subtypes of childhood leukaemia to having 11 or 12, each of which has a different constellation of genetic changes," says Charles Mullighan, who studies the genomics of childhood leukaemia at St Jude Children's Research Hospital in Memphis.

By contrast, other mutations seem to be mutually exclusive. For example, *RUNX1* is commonly mutated in AML — but never in those AML cases involving a translocation called inversion 16. This is because inversion 16 results in a fusion gene called *CBFB-MYH1*,

RELATED DISORDERS

Looking for clues to leukaemia



Cells from a patient with myelodysplastic syndrome may help researchers understand leukaemia.

The genes involved in leukaemia overlap with those responsible for a group of other disorders in which the bone marrow is either unable to make healthy blood cells or makes too many of the wrong kind. Among the most important of these conditions is a non-aggressive form of cancer called myelodysplastic syndrome (MDS).

About one-third of people who have MDS go on to develop AML, and these patients have a particularly poor prognosis. A better understanding of MDS genetics might not only improve the diagnosis of MDS, but also help predict the progression from MDS to AML. More broadly, studying MDS genetics may shed light on how different combinations of mutations can make the difference between a cancer that is relatively quiescent and one that is aggressive.

Many mutations associated with AML have also been seen in people with MDS. Researchers have found that patients who have MDS and have mutations in AML-linked genes, such as *RUNX1* or *FLT3*, are more likely to progress to AML. Beyond that, however, little was known

about MDS genetics in its own right.

"Until recently, most of what we knew about the genetics of MDS was learned first in AML and other myeloid leukaemias, and then retrospectively applied to MDS," says Timothy Graubert, a haematologist at Washington University in St Louis, Missouri.

A handful of studies in the past few years has begun to identify mutations that are hallmarks of MDS. For example, more than half of those who have MDS carry a mutation in the spliceosome, a set of proteins involved in processing RNA. These mutations have also been found in other forms of leukaemia and in some solid tumours, but their link to MDS seems to be more robust. Researchers next plan to analyse how the spliceosome and other newly discovered mutations influence the prognosis of those who have MDS.

"This pathway will be important in cancer biology in general," Graubert says, "but it's the first example that we have of a genetic pathway that's disproportionately involved in MDS." — **S.D.**

which requires *RUNX1* to be functional to turn a cell malignant, says Pu Paul Liu, a molecular biologist at the National Human Genome Research Institute in Bethesda, Maryland, who first described this fusion gene in 1993. Liu is attempting to capitalize on this observation to develop a new treatment for this subtype of AML. He has identified a compound that disrupts the interaction between the fusion protein and *RUNX1*, and delays the development of leukaemia in a mouse model. He says he hopes to begin human trials of the drug soon.

Levine, whose lab is investigating clusters of mutations associated with poor prognosis, agrees that working out how leukaemia mutations combine is a promising approach. "Our

hope is that we're not studying a gene, we're studying a genotype," he says. "And that will lead to better models of leukaemia, and better insights into how leukaemia develops." ■

Sarah DeWeerd is a science writer based in Seattle, Washington.

1. Van Vlierberghe, P. & Ferrando, A. J. *Clin. Invest.* **122**, 3398–3406 (2012).
2. Puente, X. S. *et al. Nature* **475**, 101–105 (2011).
3. Ramsay, A. J. *et al. Nature Genet.* **45**, 526–530 (2013).
4. Anderson, K. *et al. Nature* **469**, 356–361 (2011).
5. Ding, L. *et al. Nature* **481**, 506–510 (2012).
6. Xu, H. *et al. J. Natl Cancer Inst.* **105**, 733–742 (2013).
7. Vassiliou, G. S. *et al. Nature Genet.* **43**, 470–475 (2011).

PERSPECTIVE



Combined forces

Beginning treatment with a combination of drugs should help to stop drug resistance developing, says **Charles L. Sawyers**.

The approval of imatinib in 2001 was a turning point in the treatment of chronic myeloid leukaemia (CML). Since then, imatinib — marketed by Novartis as Gleevec in the United States and Glivec elsewhere — and other, similar drugs have increased the lifespan of people diagnosed with CML from 5–6 years to 10–20 years.

This success is based on using imatinib as an opening salvo early in the course of the disease, and then deploying one of four next-generation drugs for those who develop resistance to it.

The current protocol is sequential: after failing to respond optimally to one drug, the patient is switched to another. But experimental evidence (and simple logic) shows that this approach increases the risk of multidrug resistance. There is, however, a better therapeutic approach that should delay or even prevent resistance: administering combinations of these drugs at the same time.

One can even envisage the possibility that combinations of these or other targeted therapies might do more than merely extend remissions of some with CML, and actually cure the disease. Considering that patients today are committed to decades of therapy with unknown long-term side effects and significant economic cost, it is time to re-examine the sequential-therapy model.

Imatinib, a tyrosine-kinase inhibitor (TKI), works by blocking the activity of an enzyme called ABL. There is no question that, used alone, imatinib gives durable responses for most newly diagnosed cases of CML. About 80% of those who take it will have complete cytogenetic remission (no evidence of cells in the bone marrow bearing the abnormal chromosome that defines CML) within five years.

The durability of response is impressive but not indefinite. Although 84% of patients in one large study were alive after 8 years, half were no longer receiving imatinib owing to treatment failure¹. The fact that most of these resistant patients respond to next-generation ABL inhibitors is one reason why survival remains high.

Resistance to imatinib most often results from a mutation of the driving oncogene in CML, known as *BCR-ABL*². More than 50 distinct *BCR-ABL* mutations have been reported. Amazingly, the current repertoire of TKIs covers all known resistance mutations; however, no single drug can prevent all forms of resistance. This means that sequential therapy can select for subpopulations of cells within the tumour that have multiple *BCR-ABL* mutations, conferring resistance to all TKIs³.

The next-generation drugs are more potent TKIs and produce more rapid declines in CML disease burden than imatinib. This translates into improved response rates and more durable remissions.

Dasatinib, marketed as Sprycel by Bristol-Myers Squibb, and nilotinib, marketed as Tasigna by Novartis, are already approved for frontline therapy of CML based on superior clinical outcomes in head-to-head comparisons against imatinib. Bosutinib, marketed by Pfizer as Bosulif, may follow suit based on similar clinical results. Ponatinib

is newer, so limited clinical data are available. This drug is particularly promising because it has the unique property of inhibiting a mutation called T315I that confers resistance to all the other CML drugs⁴.

The compelling clinical data argue that next-generation ABL inhibitors should replace imatinib. Caution is still in order, however, as these new agents have been studied for only 3–4 years compared with the 8–10 years of data that have amassed for imatinib.

Instead of focusing on which individual drug is best as a monotherapy, it is time for the CML community to consider whether combination therapy makes sense. Extrapolating from the experience with single- versus multi-agent therapy for tuberculosis and HIV/AIDS, a combination of two or three ABL inhibitors with non-overlapping *BCR-ABL* mutation resistance profiles would almost certainly prevent

the emergence of drug resistance. This is particularly true in the light of ponatinib's success against T315I.

An additional lesson from antiretroviral therapy is that combinations can greatly enhance the rapidity and depth of response. Indeed, investigators in France have already demonstrated that patients with the deepest responses (no *BCR-ABL* detectable for more than two years) may no longer need imatinib at all. They found that 40% of patients had not relapsed after 18 months, a result that raises the possibility that a cure may be in sight⁵.

The facts that next-generation ABL inhibitors have greater potency in clinical trials, and that two-drug combinations are superior to monotherapies in preclinical studies, suggest that more intensive upfront therapy, with the goal of eliminating all CML cells, deserves serious consideration.

Much has been said about the enormous cost of targeted cancer therapies, including a recent call by more than 100 CML experts to lower the price of all the tyrosine kinase inhibitors⁶. Multidrug therapy would lead to a further increase in the cost of CML therapy, but this additional expense would lead to substantial long-term savings if patients could be cured after just one or two years of treatment. ■

Charles L. Sawyers is chair of the Human Oncology and Pathogenesis Program at the Memorial Sloan-Kettering Cancer Center in New York and a Howard Hughes Medical Institute investigator. He is also a co-inventor of patents covering imatinib-resistant *BCR-ABL* mutations and serves on the board of directors of Novartis Pharmaceuticals. Novartis provided an unrestricted educational grant to support the production of this supplement. Novartis had no editorial input into the content of this article.

1. Marin, D. et al. *J. Clin. Oncol.* **30**, 232–238 (2012).
2. Shah, N. P. et al. *Cancer Cell* **2**, 117–125 (2002).
3. Shah, N. P. et al. *J. Clin. Invest.* **117**, 2562–2569 (2007).
4. Cortes, J. E. et al. *N. Engl. J. Med.* **367**, 2075–2088 (2012).
5. Mahon, F. X. et al. *Lancet Oncol.* **11**, 1029–1035 (2010).
6. Experts in chronic myeloid leukemia *Blood* **121**, 4439–4442 (2013).

EXPERIMENTAL EVIDENCE
SHOWS THAT A SEQUENTIAL
APPROACH INCREASES
THE RISK OF MULTIDRUG
RESISTANCE

Target practice

Better designs for clinical trials and the use of combination therapies may improve leukaemia treatment.

BY ALLA KATSNELSON

Thirty-five years ago, as a fellow at the MD Anderson Cancer Center in Houston, Texas, Elihu Estey read dozens of protocols for clinical trials of drugs for acute myeloid leukaemia (AML). He was particularly drawn to their 'rationale' sections, which explain why the therapy is expected to work.

"They all sounded very compelling," says Estey, now a haematologist at the University of Washington in Seattle. "But of course, very few of them worked."

Since then, researchers have made significant advances in treating many types of leukaemia. However, AML — an aggressive blood cancer that causes white-blood-cell precursors called myeloid cells to proliferate uncontrollably — has remained a tough nut to crack.

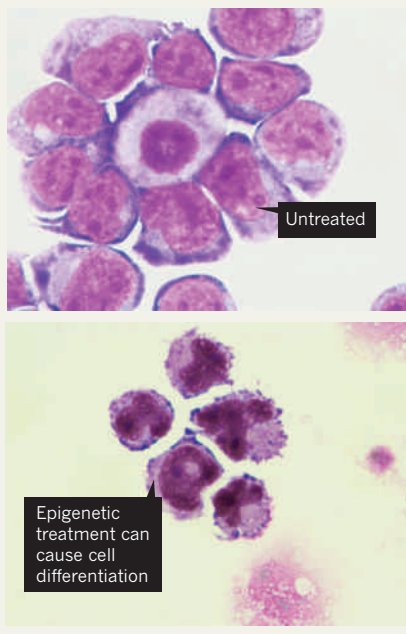
This is a big problem because AML accounts for about one-third of all leukaemia diagnoses. It is most common in people over 65 years of age, for whom the five-year survival rate is less than 10%; in younger adults the outcome is closer to 50%. And each person with AML — indeed, each cell in each person with AML — can carry a different combination of dozens of mutations (see 'Written in blood', page S4). This genetic diversity makes it difficult to design drugs, and to compare people in clinical trials.

The standard treatment for AML is a chemotherapy regimen developed in the 1970s. The least sick individuals might be eligible for blood-stem-cell transplantation. But that is a risky procedure with a mortality rate of 10–25% and long-lasting side effects. With the exception of an immune-based therapy currently in early-stage trials, no treatment on the horizon seems likely to alter this picture substantially. "There are no good drugs," says Estey.

The prognosis for other types of leukaemia is more promising. Acute lymphoblastic leukaemia (ALL), which accounts for 75% of cases of childhood leukaemia, has a 90% cure rate in children under 15, and some rare subtypes of adult leukaemias, such as hairy cell leukaemia and acute promyelocytic leukaemia, have a similarly positive outlook. Chronic lymphocytic leukaemia (CLL), which in most cases affects immune cells called B cells, responds to combinations of chemotherapy and treatment with monoclonal antibodies — immune molecules that bind to specific proteins — and has a survival rate of about 80% five years after diagnosis.

A CHANGE OF APPROACH

Epigenetic treatments are being developed for use in leukaemia cells.



Perhaps the most dramatic change in outcome has been in chronic myeloid leukaemia (CML), with the 2001 approval of imatinib, marketed by Switzerland-based Novartis as Gleevec in the United States and Glivec elsewhere. The drug's introduction caused the five-year survival rate for CML to shoot up from 30% to around 90%. Imatinib also provided an early proof of concept for therapies targeted to a particular genetic abnormality — an approach that holds promise for a variety of other diseases.

Imatinib blocks the activity of a tyrosine kinase called BCR-ABL — an enzyme that promotes cell signalling and growth, and often triggers cancer when mutated. The BCR-ABL gene is produced when segments of chromosomes 9 and 22 swap places, fusing the BCR and ABL genes, which are usually separated on the different chromosomes. About 95% of people with CML carry this chromosomal change.

The drug turned out to be far from perfect: about a third of people with CML do not fully respond to it or eventually develop resistance. Four other drugs that inhibit BCR-ABL have since been approved in an effort to fill in the gaps (see 'Combined forces', page S7). One of these drugs, ponatinib (Iclusig), approved in

December 2012, targets a particular mutation in BCR-ABL that makes cells resistant to imatinib and accounts for 20% of all BCR-ABL mutations.

The string of leukaemia drug approvals points to a growing awareness among scientists that no single drug is likely to be powerful enough to halt the disease on its own.

People with CML may need to switch from imatinib to other drug options as they develop resistance, says Hagop Kantarjian, an oncologist who chairs the leukaemia department at the MD Anderson Cancer Center. "Most patients can live their lives," he says, "provided they take their drugs and the drugs are changed up as needed."

Compared with CML, other types of leukaemia, such as AML and ALL, are genetically much more varied and, because they are acute, they mutate more rapidly over time. But targeted therapies such as imatinib can help when they are combined with other drugs, says oncologist Brian Druker, director of the Knight Cancer Institute at Oregon Health and Sciences University in Portland, Oregon, and one of three researchers responsible for developing imatinib. "By adding a targeted agent to standard chemotherapy, you can make a huge impact on the prognosis of an acute leukaemia."

BETTER TRIALS

Imatinib's dramatic success has helped to spur the development of drugs that inhibit other tyrosine kinase enzymes (see 'Recent leukaemia drugs'). One of the most promising targets is the enzyme FLT3, which is mutated in one-quarter of people with AML and increases the risk of relapse. A handful of FLT3 inhibitors are in trials. In a phase II clinical trial reported in December 2012, half of the people tested who carry a mutation in FLT3 responded to quizartinib, as did a third who lack the mutation.

Although promising, results from trials of FLT3 inhibitors show that simply identifying a mutation does not guarantee treatment success. Researchers still do not know which of the commonly seen mutations within AML cells are important, or what impact they might have, says Alan Burnett, a haematologist and AML specialist at the Cardiff University Experimental Cancer Medical Centre, UK.

Some combinations of mutations seem to be associated with more favourable disease outcomes, for example, but no one knows why. And pharmaceutical companies may be reluctant to develop drugs that would target a specific combination of mutations in a small number of affected individuals, says Burnett.

To address some of these problems, researchers are exploring new ways of structuring clinical trials. Usually, novel drugs are not compared against each other at an early stage of clinical testing, and results are hard to compare because trials

NATURE.COM
For some of the latest research on leukaemia drugs: go.nature.com/ublyhb

RECENT LEUKAEMIA DRUGS

Drugs approved since the start of 2012 and a sample of drugs in clinical trials.

Name	Marketed as	Manufacturer	Leukaemia type	Status	Mechanism of action
Ponatinib	Iclusig	Ariad Pharmaceuticals	CML, ALL	Approved in late 2012	Tyrosine kinase (BCR-ABL) inhibitor
Bosutinib	Bosulif	Pfizer	CML	Approved in late 2012	Tyrosine kinase (BCR-ABL, SRC) inhibitor
Midostaurin	(PKC412)	Novartis	AML	Phase III	Tyrosine kinase (multiple) inhibitor
Quizartinib	(AC220)	Ambit Bioscience	AML	Phase II	Tyrosine kinase (FLT3) inhibitor
EPZ5676	n/a	Epizyme	Acute leukaemia	Phase I	DOT1L inhibitor/epigenetics
Omacetaxine	Synribo	Teva	CML	Approved in late 2012	Protein translation inhibitor
Vosaroxin	n/a	Sunesis	AML	Phase III	DNA intercalator/topoisomerase II inhibitor
CART-19	n/a	University of Pennsylvania/Novartis	Diverse leukaemias	Phase I	Anti-CD19 chimaeric antigen receptor/immunotherapy
Actimab-A	n/a	MSKCC/Actinium Pharmaceuticals	AML	Phase I/II	Anti-CD33, armed with radioactive isotope actinium-225
Obinutuzumab	(Ga101)	Roche	CLL	Phase III	Anti-CD20 monoclonal antibody

can be designed in different ways. To combat this, Estey and his colleagues have pitted four test drugs against each other in the earliest phase of clinical trials¹, with the idea of taking only the best into further development.

The approach has not gained much traction in the United States but has taken off elsewhere, with about 10 drugs evaluated in the past six years in the United Kingdom, along with efforts in Denmark and New Zealand. The idea is to identify “more efficient ways of finding drugs that make a difference”, says Burnett, who leads the UK trials.

Druke, meanwhile, has helped to develop a screening system to test how well different people with leukaemia respond to a panel of 130 kinase inhibitors. The researchers use the data to predict which of the drugs might be most effective in each individual, and to help identify the driving molecular abnormality in the leukaemia². In early 2013, Druker launched a study comparing people treated with standard therapy with those receiving drugs hand-picked by his system. Experimental groups in a clinical trial generally receive the same treatment, but in this study their treatments differ, with individual molecular profiling used to select them.

ALTERED EXPRESSION

Other efforts to develop targeted drugs focus on epigenetic factors — enzymes that influence gene expression without altering the underlying genetic code (see ‘Reversible tags’, page S10). In the past few years, researchers have discovered that many epigenetic processes are dysregulated in leukaemia and other cancers. “With epigenetics you have a whole new class of enzymes that offer a different way to target cancer cells,” says Scott Armstrong, a paediatric oncologist at the Memorial Sloan-Kettering Cancer Center in New York. “That gets people pretty excited both in terms of clinical prospects and financial prospects.”

So far, however, the excitement has outpaced the achievement. Many epigenetics-based compounds work well in cultured leukaemia

cells and animal models (see ‘A change of approach’), but have been less successful in treating people. For example, the drugs 5-azacitidine (marketed as Vidaza) and decitabine (marketed as Dacogen) both interfere with DNA methylation — a brake system for gene expression. Both have gained widespread approval for the treatment of myelodysplastic syndrome, a non-aggressive cancer that progresses to AML in a third of patients.

But the benefit of these drugs is less clear in clinical trials for leukaemia. Unlike imatinib and other tyrosine kinase inhibitors, which target particular molecular markers, these epigenetic drugs may be less precise in their action, Armstrong says. The same problem afflicts another class of agents, known as histone deacetylase inhibitors, which modify DNA-associated proteins called histones, he says.

Armstrong’s team is focusing instead on a different epigenetic target: the DOT1L protein, which helps to regulate chromatin structure and gene expression. DOT1L seems to be required for cells carrying a mutation in a gene called *MLL* (also known as *KMT2A*) to become leukaemic³. That defect is present in about 5–10% of AML and ALL cases.

In September 2012, Armstrong and his colleagues, working with Epizyme, a biotech company based in Cambridge, Massachusetts, launched a clinical trial of a drug that blocks DOT1L in people with leukaemia carrying the mutant *MLL* gene. The drug, called EPZ-5676, “falls into the imatinib type of approach”, Armstrong says, in that it targets a specific genetic abnormality.

As efforts to develop these sorts of small-molecule drugs have continued, a powerful immunological approach, in the works for three decades, seems to be making impressive strides. Called chimaeric antigen receptor (CAR) therapy, the two-step approach involves

extracting T cells — immune cells that recognize pathogens and tumour tissue — from a person with leukaemia. The T cells are then armed with a receptor that allows them to kill the leukaemia and reintroduced.

This CAR therapy has brought about a complete or partial remission in 10 of 16 adults, and 6 of 8 children, who have received the treatment so far, says Carl June, an immunologist at the Perelman School of Medicine at the University of Pennsylvania in Philadelphia who led the team that developed the therapy⁴. In August 2012, Novartis announced that it would license June’s approach and fund his work to the tune of US\$20 million.

In March 2013, researchers led by Renier Brentjens and Michel Sadelain at the Memorial Sloan-Kettering Cancer Center reported remission in five people who received a similar treatment⁵. June and Brentjens have now launched a trial to compare the two techniques and determine which elements of each work best. Researchers at the MD Anderson Cancer Center and at the Baylor College of Medicine in Houston, Texas, are also developing CAR therapies.

“The principle that these drugs can work has been established,” says June. “Now it’s a question of optimizing and also of cell manufacturing” (see ‘Assembly line immunotherapy’, page S17).

Others are more circumspect. “At the risk of seeming too cynical, I have heard about many things that, like CAR, seemed very promising but did not pan out,” says Estey. “History would suggest that it alone will not be as successful as purported.” ■

Alla Katsnelson is a freelance science writer based in Astoria, New York.

1. Estey, E. H. & Thall, P. F. *Blood* **102**, 442–448 (2003).
2. Tyner, J. W. *et al. Cancer Res.* **73**, 285–296 (2013).
3. Deshpande, A. J. *et al. Blood* **121**, 2533–2541 (2013).
4. Kalos, M. *et al. Sci. Transl. Med.* **3**, 95ra73 (2011).
5. Brentjens, R. J. *et al. Sci. Transl. Med.* **5**, 177ra38 (2013).



JERRY NAUNHEIM JR.

Timothy Ley has found that 'epigenetic' changes that alter DNA expression offer a possible approach to tackling leukaemia.

EPIGENETICS

Reversible tags

Enzymes that modify gene expression without changing the DNA sequence are now viewed as central to the development of leukaemia — and may lead to new drugs.

BY JESSICA WRIGHT

Conversations about cancer often focus on genetics, with the blame placed on gene mutations that lead to rampant cell growth or stop tumour cells from dying.

But recent discoveries in leukaemia have shifted the focus away from genetics to epigenetics — small chemical changes to DNA or its associated proteins that alter the level of gene expression. Researchers have found that the sources of many leukaemias can be traced back to mutations in the enzymes that add or remove these chemical tags.

"A couple of years ago, if I had said that to somebody they would have laughed me out of the room," says Timothy Ley, a geneticist at Washington University in St Louis, Missouri. "There just was no clear notion that epigenetic modification would be so critically important for the pathogenesis of the disease."

Epigenetic tags regulate gene expression by acting as gatekeepers, blocking or allowing access to a gene's 'on' switch. These chemical tags (such as methyl or acetyl groups) are added directly to DNA or onto histones, the large spool-like proteins around which DNA is tightly wound. DNA methylation masks certain regions on the genome, whereas modifications to histones can loosen or tighten the DNA reel, altering which genes are exposed.

Epigenetic changes can either be inherited or accumulated throughout a lifetime. But importantly for cancer research, they are reversible. Researchers can tinker with the enzymes that add or remove the chemical tags, restoring the gene's normal role — an ability that makes these enzymes attractive targets for leukaemia drugs (see 'Target practice', page S8).

"It's easy to make inhibitors of enzymes," says Scott Armstrong, a paediatric oncologist at the Memorial Sloan-Kettering Cancer Center in New York. "Everyone sees this as a potential opportunity."

Among the more promising candidates are inhibitors of DOT1L, an enzyme that adds methyl groups to histones, and molecules that may block mutant forms of IDH1 and IDH2. These mutations lead to increased methylation of DNA. About ten drugs targeting epigenetic mechanisms are currently in development, but Armstrong predicts that the number may soon rival that of tyrosine kinase inhibitors, by far the most successful class of leukaemia drugs.

Epigenetics is likely to have a role in cancers beyond leukaemia too. "We're finding out that every other cancer's just like it, but I would argue that leukaemia has been one of the proving grounds," says Ross Levine, an oncologist at the Memorial Sloan-Kettering Cancer Center.

This is in part because it is easier to take a

specimen to study leukaemias — by taking blood or sampling bone marrow — than it is for solid tumours.

Leukaemia researchers have seen hints of the role of epigenetics in the disease for decades, with odd patterns of methylation being observed in people with leukaemia since the 1960s. Less clear were the specifics: which epigenetic pathways were disrupted, and through which enzymes? "This was the \$64,000 question," says Ley.

MANY MUTATIONS

As the cost of sequencing has fallen precipitously in the past five years, pieces of the puzzle have started to fall into place. Sequencing technology enables researchers to scan exomes — the protein-coding portions of genomes — or even entire genomes and reveal "the complete panoply of mutations present in these patients", Ley says. The data are making it clear that enzymes involved in epigenetics are prime players in leukaemia.

For example, in a study published in May 2013, Ley and his colleagues sequenced the whole genomes of 50 adults with acute myeloid leukaemia (AML) and the exomes of another 150. More than three-quarters of these individuals turned out to have a harmful mutation in an epigenetic enzyme¹. That is a significant correlation, even without knowing how

common the mutations are in people without AML, Ley says.

One of these enzymes, DNMT3A, adds methyl groups to DNA and was found to be mutated in 51 of the 200 patients. It had already caught Ley's attention. In a 2010 study, his team sequenced it in 281 individuals with AML and found that 62 of them — 22% — carried harmful mutations in it². These individuals were found to have a much shorter survival than AML patients without a DNMT3A mutation.

It is still unclear how these DNMT3A mutations contribute to leukaemia. On their own, they do not seem to change patterns of methylation or gene expression. However, they tend to co-occur with mutations in two other genes, *NPM1* and *FLT3*, and cells with mutations in all three genes have less methylation than controls do. This combination effect “is an important clue that we need to study in detail”, says Ley.

Ley's new study also found a strong link with leukaemia and two enzymes, *IDH1* and *IDH2*, which are essential to the Krebs cycle through which cells produce the energy they need to survive. Mutations in these enzymes ramp up DNA methylation, triggering gene expression changes that ultimately lead to cancer. Indeed, Ley and his team found mutations in *IDH1/2* in 39 of the 200 AML genomes they studied.

An *IDH1* cancer connection first surfaced back in 2008, when several research teams found mutations in *IDH1*, along with elevated methylation, in glioblastoma and astrocytoma brain tumours. The following year, Ley found an *IDH1* mutation in the genome of an individual with AML³.

The initial *IDH1* discoveries “made no sense” because *IDH1* was not known at the time to be involved in epigenetics, says Maria Figueroa, a pathologist at the University of Michigan in Ann Arbor, who helped reveal that role. “How would the Krebs cycle affect the epigenome?”

The answer would emerge only after Figueroa joined forces with others in the field.

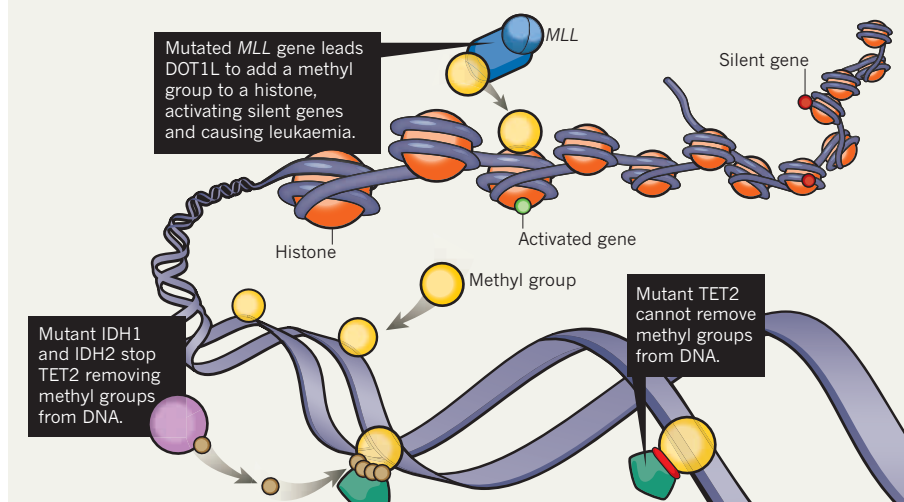
LOOKING FOR PATTERNS

Levine's group at the Memorial Sloan-Kettering Cancer Center was studying *TET2*, a leukaemia-linked gene that removes methyl tags from DNA. He noticed that people with leukaemia never seemed to have mutations in *IDH1* and *TET2* at the same time. The obvious explanation, he says, is that both mutations affect the same pathway, so a cell only ever needs one of them to become cancerous (see ‘An on-off switch for genes’).

Applying their skills in genetics, epigenetics and biochemistry, Levine's group and Figueroa worked together to show that mutant forms of the *IDH1* and *IDH2* enzymes stop *TET2* from removing methyl groups from DNA⁴. The mutations in the *IDH1* and *IDH2* genes that code for the enzymes cause a change in their function, rather than simply stopping them from being expressed. This makes them good drug targets, Figueroa says.

AN ON-OFF SWITCH FOR GENES

Mutations affecting enzymes that add or remove chemical tags to DNA or its associated proteins can change which genes are expressed, leading to leukaemia.



Mutations in *IDH1* and *IDH2* also seem to be involved in epigenetic modifications to histones. Histone modifications are another rich source of drug targets for leukaemia. Epizyme, a pharmaceutical company based in Cambridge, Massachusetts, has developed a small-molecule inhibitor of DOT1L, which adds methyl groups to histones.

The DOT1L connection to leukaemia can be traced back to 2005, when researchers found that mutations in this enzyme are associated with a fusion gene that is one of the oldest known risk factors for leukaemia⁵. The fusion gene forms when chromosome 11 swaps a large chunk of genetic material with any of a number of other chromosomes, as a portion of the *MLL* gene, located on chromosome 11, is joined to one of more than 60 possible partner genes.

Because this fusion is large enough to be visible under a microscope, researchers have been aware of its involvement in AML and acute lymphoblastic leukaemia since the 1990s. What was less clear, however, was how exactly it leads to the disorder.

In 2011, Armstrong and his team showed that many *MLL* fusions activate genes via DOT1L's histone-modifying activity⁶. Histones bind DNA throughout the genome, so tinkering with an enzyme that modifies them would be expected to have broad effects on gene expression. Surprisingly, however, removing the *DOT1L* gene from mice seems largely to affect those genes that the *MLL* fusion modifies, Armstrong found. And Epizyme's DOT1L inhibitor kills only those cells that have the *MLL* fusion gene. This sort of specificity, says Armstrong, is “central to the idea that epigenetics is likely to be a therapy”.

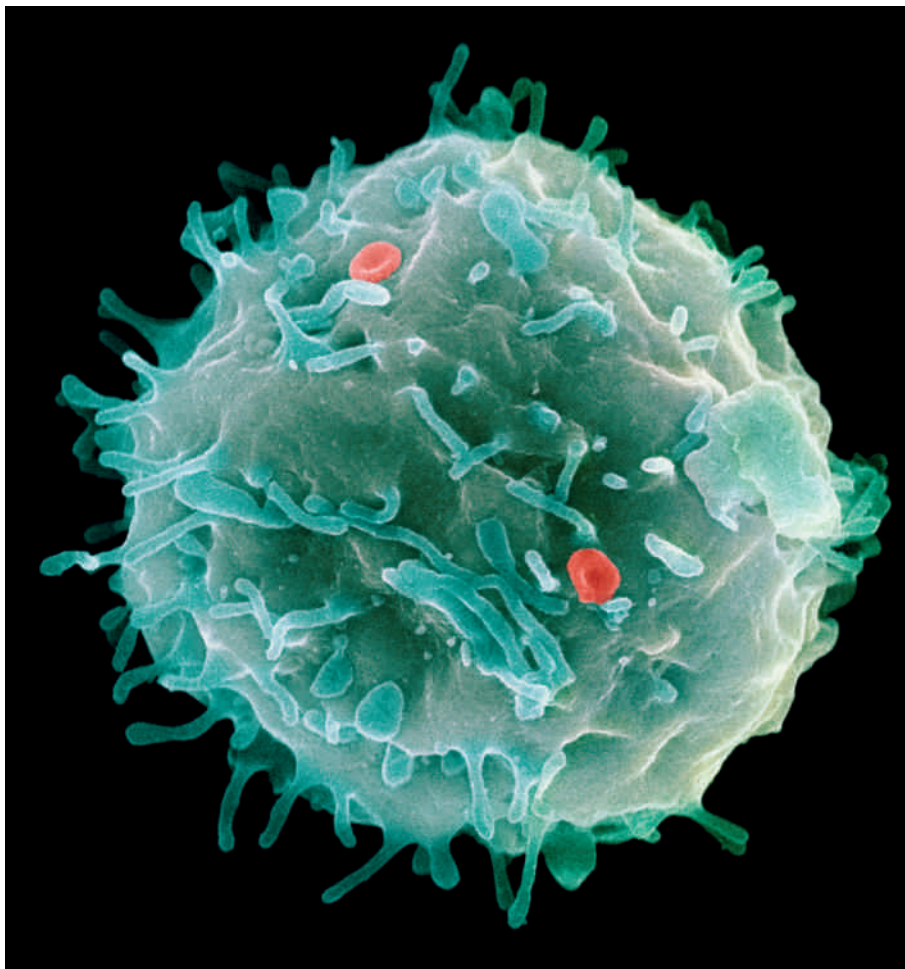
It may also make it possible to tailor epigenetic treatments for individuals based on their specific set of mutations. To that end, researchers are trying to pin down mutations and methylation patterns that delineate people into disease subgroups. In 2010, for example, Figueroa and her colleagues looked at how methyl tags are scattered across the genomes of 344 people with leukaemia⁷. They identified 16 distinct patterns of methylation and linked many of them to known leukaemia mutations. Individuals with *MLL* mutations, they found, have fewer methyl groups in a subset of genes than people in the other subgroups. People with *IDH* mutations, in contrast, have excessive methylation.

The technique researchers use to identify methylation patterns — screening the whole genome on a diagnostic microarray — is likely to be too complicated for clinics. But Figueroa's team is developing simpler methods to detect methylation status, which may help clinicians predict prognosis and decide on treatment options. “These are things we can do today, without waiting for novel therapies,” she says.

The ultimate goal is a designer drug for each subgroup of methylation patterns. In the meantime, “there is still a tremendous amount of work to be done,” says Armstrong. “We are just starting to understand who the players are, what the players do, and how they work together.” ■

Jessica Wright is a science writer based in New York City.

1. The Cancer Genome Atlas Research Network. *N. Engl. J. Med.* **368**, 2059–2074 (2013).
2. Ley, T. J. et al. *N. Engl. J. Med.* **363**, 2424–2433 (2010).
3. Mardis, E. R. et al. *N. Engl. J. Med.* **361**, 1058–1066 (2009).
4. Figueroa, M. E. et al. *Cancer Cell* **18**, 553–567 (2010).
5. Okada, Y. et al. *Cell* **121**, 167–178 (2005).
6. Bernth, K. M. et al. *Cancer Cell* **20**, 66–78 (2011).
7. Figueroa, M. E. et al. *Cancer Cell* **17**, 13–27 (2010).



Could mutations in haematopoietic stem cells, which give rise to blood cells, lead to leukaemia?

STEM CELLS

Bad seeds

Leukaemia treatments must eliminate the versatile cells that can bring the cancer back to life years later.

BY CASSANDRA WILLYARD

Deep within the spongy marrow that fills large bones lie cells that give rise to all the body's blood cells. These primitive cells, called haematopoietic stem cells, have the unique ability to divide indefinitely, making them essentially immortal.

Mounting evidence suggests that similarly immortal cells drive some types of leukaemia and other cancers. Just as haematopoietic stem cells can produce a vast array of blood cells, leukaemia stem cells generate the diversity of malignant cells seen in cancer.

John Dick, a cancer researcher at the University of Toronto in Canada, first isolated leukaemia stem cells in the 1990s. At the time, many cancer researchers believed that all cancer cells

are equally capable of seeding new cancers.

In contrast, the cancer-stem-cell model proposes that only a rare subset of cells has the ability to give rise to a new tumour (see 'Tumour hierarchy'). These cells can self-renew, are long-lived and can lie dormant for years.

"Those three things are properties that we generally don't target with our standard chemotherapeutic agents," says Catriona Jamieson, director of stem-cell research at the Moores Cancer Center at the University of California, San Diego. Conventional therapies may kill most cancer cells and induce remission, Jamieson says, but cancer stem cells persist, allowing the disease to come roaring back even in individuals who seem healthy.

Over the past decade, this model has sparked heated controversy. Some types of cancer, such

as acute myeloid leukaemia (AML), a disease that affects the cells that give rise to red blood cells, platelets and some immune cells, seem to follow the model. But in solid tumours and some other forms of leukaemia, the existence of cancer stem cells is uncertain.

Even for diseases that conform to the cancer-stem-cell model, researchers disagree over the cells' abundance, attributes and origin. One central question is whether cancer stem cells are normal stem cells that have turned malignant, or rather more mature cells that have regained some stem-cell-like properties.

"There is endless debate and confusion and contentiousness about their characteristics," says Mel Greaves, a cancer researcher at the Institute for Cancer Research in London. "They are slippery and diverse," he says. "That's why it's so tough to target them therapeutically."

SLIPPERY CELLS

Tough, perhaps, but not impossible. Researchers are developing drugs that can rouse leukaemia stem cells out of dormancy, making them more vulnerable to therapy, and target the pathways they need, such as those that promote self-renewal.

To isolate cancer stem cells for analysis, researchers use mice with compromised immune systems that allow human cancer cells to grow. They first sort cancer cells based on their surface markers — proteins found on the cell membrane that can be tagged with fluorescent molecules. For example, haematopoietic stem cells share an immune marker called CD34 and lack a marker called CD38.

The researchers then inject each group of cells into mice to see which ones cause disease. By taking the cancer cells from one mouse and transplanting them into another, they also examine the cells' ability to self-renew.

Dick, who developed the assay, first showed that it could be used to identify leukaemia stem cells in his landmark 1994 *Nature* paper¹. His team reported that a subset of leukaemia cells that both carry CD34 and lack CD38 — the same markers that characterize haematopoietic stem cells — can seed leukaemia in mice. Moreover, cells with the opposite characteristics — those that lack CD34 or have CD38 — do not trigger new cancers. The researchers interpreted these results as confirmation that those with CD34 and without CD38 are leukaemia stem cells.

Leukaemia researchers largely accepted Dick's findings. "It proved what had been predicted since the 1960s and '70s," Dick says.

But the cancer-stem-cell connection to leukaemia turns out to be more complicated than that. Over the past 15 years, researchers have tried to identify and characterize leukaemia stem cells. They have found that the cells are vastly more diverse than previously thought and, as a result, are more difficult to eradicate. "Our original thoughts about cancer stem cells were a gross oversimplification," says Brian

Huntly, a leukaemia researcher at the Cambridge Institute for Medical Research, UK, who was not involved in Dick's work.

In 2011, Dick and his colleagues took leukaemia cells from 16 people with AML, once again sorted those cells based on their surface markers, and injected them into mice with even more defective immune systems than those in the original study. This time, however, the researchers found that the leukaemia stem cells were not confined to a particular subset². In particular, the presence or absence of CD34 and CD38 did not dictate whether the cells could seed new tumours.

Another group, led by researchers from the University of Pennsylvania in Philadelphia, used a different mouse model but got similar results. The Pennsylvania team was likewise unable to isolate leukaemia stem cells using CD34 and CD38. What's more, they tried two other markers, CD45RA and lineage, which also showed no correlation to leukaemia cells.

Such results leave leukaemia researchers in a frustrating position. "Is there any marker or will there ever be a marker that is inextricably linked to the property of self-renewal?" asks Scott Armstrong, an oncologist at the Memorial Sloan-Kettering Cancer Center in New York. "I'd say we don't have such a marker."

Even so, scrutiny of leukaemia stem cells could lead to a better way to predict the course of the disease. In his 2011 study, Dick compared gene expression in leukaemia stem cells with other leukaemia cells. He identified 42 genes that were highly expressed only in the leukaemia stem cells. "Lo and behold," says Dick. "We came up with a signature." And this signature correlates with prognosis.

The researchers then divided 160 individuals with AML into two groups, based on their expression levels of the 42 genes. Those with high expression fared the worst: at any given time point, they were nearly two-and-a-half times more likely to die than members of the low-expression group.

Dick and his team now have data from 100 individuals that tie the signature even more closely to prognosis. "It tells us that not only are leukaemia stem cells real, but they must also be relevant," he says.

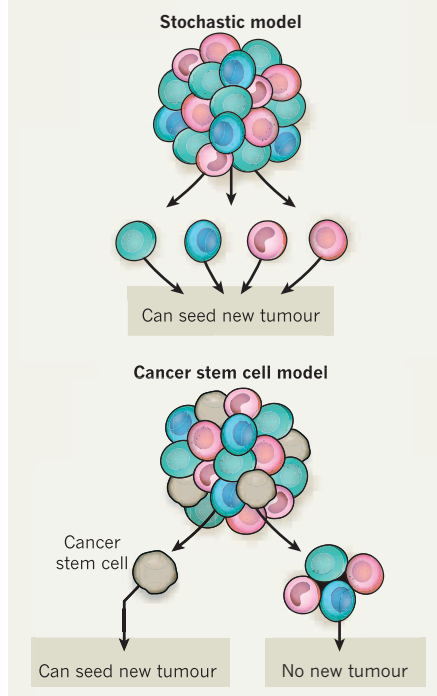
The fact that stem cells are difficult to pin down is not surprising. "Leukaemia is an evolutionary process," Greaves says. The disease originates with a single cell, but its descendants may acquire new mutations, making them genetically distinct. As a result, a drug that targets just one of these mutations may not eliminate all of the cancer cells, leaving some behind that can regenerate the tumour.

THINK LOCAL

One characteristic common to all leukaemia stem cells is that they require the particular microenvironment of the bone marrow, known as the stroma. Leukaemia cells grown in a flask divide rapidly. As a result, they are

TUMOUR HIERARCHY

In the stochastic model, all tumour cells have an equal ability to seed new tumours. In the cancer-stem-cell model, only a few 'stem cells' can self-renew and seed new tumours.



"exquisitely sensitive" to chemotherapy, which targets rapidly dividing cells, says oncologist John DiPersio at Washington University School of Medicine in St Louis, Missouri. But the stroma bathes the cells in growth factors and chemical signals that keep them in a dormant phase resistant to chemotherapy.

Part of what keeps these cells entrenched in the bone marrow is a chemical signal sent by the stroma called stromal cell-derived factor (SDF-1). This signal binds to a protein called CXCR4 on the stem cells' surfaces. "It tells the stem cells to stay put," says Washington University haematologist Daniel Link.

DiPersio and his colleagues speculated that if they could interrupt this signal, they might be able to make the cells more sensitive to chemotherapy. They tested the idea in 52 people with AML who were set to begin chemotherapy. Before starting treatment, each patient was administered a small-molecule drug called plerixafor, which the researchers believed would block the CXCR4 receptor³.

The results were encouraging. "Remission rates were close to 50%, which is about twice as high as historic controls for patients with relapsed AML," DiPersio says.

The group has launched a second study, this time combining plerixafor with granulocyte-colony stimulating factor (G-CSF), a growth hormone that dampens SDF-1 expression. They hope that the drugs — one affecting the signalling molecule, the other the receptor — will act synergistically and lead to an

even higher rate of remission. In a separate pilot study, Link is testing whether G-CSF can increase the effectiveness of chemotherapy in individuals with relapsed acute lymphoblastic leukaemia, a type of the disease in which immature white blood cells take over the bone marrow and spill out into the bloodstream.

Other researchers are looking for proteins present in leukaemia stem cells but not in normal haematopoietic stem cells. In 2010, a team of researchers from the RIKEN Center for Integrative Medical Sciences in Japan identified haematopoietic cell kinase (HCK), an enzyme involved in cell signalling, in dormant leukaemia stem cells taken from the bone marrow of people with AML.

In April 2013, the RIKEN researchers took the next step towards a therapy by identifying a compound that inhibits HCKs and seems to eliminate leukaemia stem cells. In mice, this compound abolished nearly all AML cells from blood and from the mice's bone marrow and spleen after three weeks of treatment⁴.

"The efficacy data in this paper are impressive, but it is way too early to get too excited," says Ravindra Majeti, a haematologist at Stanford University in Palo Alto, California. Majeti's research suggests that researchers may need to target not only leukaemia stem cells, but also seemingly normal haematopoietic stem cells.

Last year, Majeti and his team examined haematopoietic stem cells and leukaemia cells from six people with AML. In five of these individuals, haematopoietic stem cells in the bone marrow contained some of the same mutations present in the cancer cells⁵. They hypothesize that these cells could be precursors to fully fledged leukaemia. That's important, Majeti says, because it suggests that even if a drug eradicates the leukaemia, it may not provide a cure. "The preleukaemic stem cells could give rise to a related but distinct relapse through the acquisition of new mutations," Majeti says.

Researchers are also developing medications that target the key property of all stem cells — self-renewal. One signalling pathway that seems to play an important role in self-renewal hinges on two proteins: Wnt and beta-catenin. In April 2012, Armstrong reported that a small molecule that inhibits beta-catenin, given in combination with the targeted therapy imatinib (Gleevec, marketed in some countries as Glivec), eliminates leukaemia stem cells in a mouse model of chronic myeloid leukaemia.

Even cancers that do not seem to strictly adhere to the cancer-stem-cell model harbour cells that can self-renew. "They're bad actors," says Dick. "What we need is to begin to figure out what their Achilles heel is." ■

Cassandra Willyard is a science writer based in Brooklyn, New York.

1. Lapidot, T. *et al. Nature* **367**, 645–648 (1994).
2. Eppert, K. *et al. Nature Med.* **17**, 1086–1093 (2011).
3. Uy, G. L. *et al. Blood* **119**, 3917–3924 (2012).
4. Saito, Y. *et al. Sci. Transl. Med.* **5**, 181ra52 (2013).
5. Jan, M. *et al. Sci. Transl. Med.* **149**, 149ra118 (2012).



The identical twin on the right was given various treatments as a child for acute lymphoblastic leukaemia.

DRUG SAFETY

Double jeopardy

Leukaemia in children is highly curable, but many survivors suffer severe, even life-threatening, long-term effects. Scientists are seeking ways to deliver a safer cure.

BY MARY CARMICHAEL

One of Jolene Hanson's earliest memories is of eating birthday cake in a wheelchair at the University of Minnesota Medical Center in Fairview. It was 13 March 1976, her fourth birthday, and just 16 days after she was diagnosed with acute lymphoblastic leukaemia (ALL). In those days, ALL killed around two-thirds of the children it struck.

Hanson remembers little about her treatment except that her mother crushed one of her drugs and put it in her ice-cream. But her medical records show she was taking methotrexate, vincristine, doxorubicin, asparaginase, prednisone, cyclophosphamide and cytarabine, and had 12 rounds of radiation to her developing brain.

This intense therapy cured her. But it came with a curse: its long-term side effects have dogged her for 37 years. She is just 4 feet 8 inches tall — the radiation left her with growth hormone deficiency — and permanently bald. Her medical diary runs to nine pages of tra- vails: 15 October 1987, "Dr Ingvaldstat drained an ovarian cyst on my right side that was the size of an orange"; 20 July 1999, "I had a basal cell carcinoma spot removed from the posterior 3rd–4th lumbar vertebrae region"; and August 2004, "A few months of infertility drugs and seeing high risk doctors led to the conclusion of not being able to get pregnant."

She tries to stay upbeat despite all her medical problems. "Sometimes I just have to laugh about it," she says. "What else can I do?"

That question — what else can I do? — is also a pressing one for doctors seeking to treat

leukaemia without leaving behind sequelae that echo for decades, such as heart damage, cognitive deficits, secondary cancers and stroke.

LONG-TERM DAMAGE

These days, many cases of leukaemia are curable: more than 85% of children with ALL, the most common childhood leukaemia, survive. But more than a quarter of childhood cancer survivors report at least one severe, life-threatening or disabling health condition in the first 25 years after treatment.

The challenge for researchers is to find ways to lower the risk of these late effects without lowering the effectiveness of therapy. To minimize the risk, they introduce drugs that protect patients from some of the damage, replace harmful treatments, and seek biomarkers that indicate which patients are most vulnerable.

"There used to be this philosophy of 'Just be thankful you're alive and accept whatever problems come with treatment,'" says K. Scott Baker, a paediatric oncologist at the Fred Hutchinson Cancer Research Center in Seattle, Washington. "But that mindset has changed."

The doctors who treated paediatric leukaemia with radiation to the brain in the 1970s and '80s were less concerned with secondary effects than they were with the prospect of relapse. Most chemotherapy drugs leave the brain vulnerable to invading leukaemia cells because the drugs generally do not cross the blood–brain barrier.

"They weren't really thinking about what was going to happen to their patients in 20 or 30 years because they didn't know if they could cure anyone," says Lisa Diller, a paediatric oncologist who leads a survivors' programme at the Dana-Farber Cancer Institute in Boston, Massachusetts. Only when children began to survive in significant numbers did the risks of radiation to the developing brain become clear (see 'Late effects'): it caused brain tumours, growth hormone deficiency, hypothyroidism and problems with learning and memory.

REDUCING THE RISK

Today, many hospitals use radiation for children only where there is a high risk of relapse in the brain — if leukaemic cells have already taken hold there, for example, or if the disease is an unusually aggressive form that affects T cells.

They also administer less radiation these days — rarely more than 1,200 centigrays, half the cumulative dose Hanson received. Most children receive no radiation at all: doctors prefer to protect their young patients' brains from leukaemic invasion by injecting drugs such as methotrexate and cytarabine into their spinal fluid.

But these drugs can have long-term cognitive deficits and have other late effects of their own.

Methotrexate, for example, may impair balance and the ability to walk normally. The drug is linked to so many problems, says Les Robison, an

➔ **NATURE.COM**

To find out more about late effects in leukaemia:

go.nature.com/tkuqlc

epidemiologist and cancer researcher at St Jude Children's Research Hospital in Memphis, Tennessee, that it may some day be viewed in the same way we now regard brain radiation — as a treatment with so many long-term side effects that it should be avoided whenever possible.

Another class of drugs, anthracyclines, which includes the widely used doxorubicin, is linked to a different, life-threatening late effect: heart damage. Doctors have known for decades that doxorubicin and a similar drug, daunorubicin, can leave the left ventricular wall thin and weak, leading to congestive heart failure in some patients.

Doctors can avoid some of these late effects simply by lowering the dose. High doses of doxorubicin, for instance, cause congestive heart failure in 30% of adults, but halving the dose can dramatically shrink that percentage. Children are not so fortunate, however, as even low doses raise the risk of heart problems. And lowering the dose may reduce the effectiveness.

"If you take away some treatment to avoid toxicity, you're running the risk of taking away some efficacy," says Stephen Sallan, a paediatric oncologist at Dana-Farber. A better strategy may be to add a drug that can protect healthy cells against the damage caused by doxorubicin. But that is a tricky business, as research over the past three years makes clear.

No one really knows why doxorubicin is harmful to heart muscle. One possibility stems from the fact that the drug inhibits topoisomerase II, an enzyme that helps to relax DNA coils. Mice lacking this enzyme in their heart cells don't have cardiac injuries after doxorubicin treatment¹. But many researchers, including Sallan, say that doxorubicin's toxicity may result from the free radicals it generates — in which case giving patients antioxidants could help.

One class of drugs with antioxidant properties — angiotensin-converting enzyme (ACE) inhibitors — has yielded tantalizing results in rats, including the discovery that two ACE inhibitors could "almost totally prevent" several types of cardiac damage². There have also been some promising results in adult patients, but the drugs seem to be less effective in children. Sallan and his colleagues found that children who took ACE inhibitors after anthracycline therapy saw an initial strengthening of their left ventricular walls, but the effect did not last.

Sallan prefers to use a different cardioprotective drug, dexrazoxane, a free-radical scavenger used in women being treated for breast cancer. The drug seems to help, but the use of dexrazoxane is controversial. The European Medicines Agency barred doctors from prescribing it to children in 2011 after clinical trials showed that some children subsequently developed acute myeloid leukaemia and disorders that affect bone-marrow stem cells.

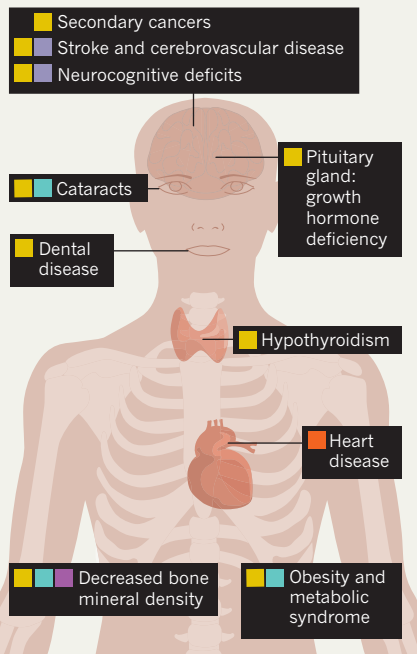
Sallan dismisses the agency's decision as "nuts" — and points out that those children were also receiving another drug linked to the same complications. But the US Food and Drug

LATE EFFECTS

Treatments for leukaemia can lead to long-term side effects in various parts of the body.

Treatments

- Cranial irradiation
- Doxorubicin
- Glucocorticoids
- Methotrexate
- Intrathecal chemotherapy



Administration took the European decision seriously enough to advise doctors of it, adding that dexrazoxane is not approved for use in children.

Another strategy for limiting the harm done by doxorubicin is to give it only to patients with the right genetics to handle it safely. For children with a particular genetic variant of *CBR3*, a gene that regulates doxorubicin metabolism, the cure may be worse than the disease. For these children, "there seems to be no safe dose" of doxorubicin, researchers say³.

LATER IN LIFE

Patients who dodge the late effects of radiation and chemotherapy are not necessarily out of danger. They may still face other risks if their treatment includes bone-marrow transplantation. "There is a whole set of issues that are unique, and some of them are quite long-term," says David Avigan, a haematologist and oncologist at Beth Israel Deaconess Medical Center in Boston, Massachusetts.

As with all transplants, bone-marrow transplants carry a risk that immune cells in the donor tissue will recognize the recipient as 'foreign' and attack the body. This can have serious consequences, including long-term damage to the liver, lungs, skin and gastrointestinal tract. A more surprising late effect in leukaemia survivors who have had bone-marrow transplants is the replacement of lean muscle mass with fat. This process is a natural part of ageing, but after

a bone-marrow transplant, it seems to be accelerated, says Baker. His team has shown that those who have bone-marrow transplants also develop insulin resistance, which is linked to diabetes, cardiovascular disease, and other problems that fall under the broad category known as 'metabolic syndrome' — a condition for which ALL survivors are already at increased risk.

Given how widespread late effects are, the problem has received surprisingly little study, especially in survivors of leukaemias other than paediatric ALL. The Childhood Cancer Survivors Study, led by Robison, tracked more than 20,000 children and has provided a wealth of data on them. But such studies require a huge investment of time and money, and the first long-term study⁴ of survivors of paediatric acute myeloid leukaemia was not published until 2008.

There are also few data on late effects in leukaemia survivors diagnosed as adults. "The paediatricians have been way ahead of us," says Ann Partridge, a medical oncologist at Dana-Farber who studies adult survivorship. "It's clear we need to do better for our adult survivors, now that we have adult survivors."

Those patients historically exposed to the harshest treatment — Jolene Hanson's generation — are now aged 40 or 50 and may develop a wave of late effects that mimic premature ageing. Diller has warned⁵, for example, that loss of bone density in paediatric ALL survivors may lead to increased risk of fractures in middle age.

Robert Hayashi, a paediatric haematologist and oncologist at St Louis Children's Hospital in Missouri, is concerned that intense steroid chemotherapy (such as the prednisone Hanson received) can put children at risk of premature arthritis. And Robison has discovered a group of survivors in their 30s and 40s who have surprisingly high blood pressure in the lungs for their age, resulting in breathing difficulties.

Sallan says that some children whose hearts are damaged by anthracyclines may avoid congestive heart failure for their first few decades, only to suffer it in later life. "There are late effects," he says, "and there are very late effects."

In Hanson's case, there certainly are. A few years ago, she says, she had a spell of good health, but in late 2012 she developed a brain tumour behind her right eye that required surgery. She might have preferred radiation to destroy the tumour — but radiation may have caused the tumour in the first place, and she has had too much already. Hanson says she's prepared for yet another round of late effects. "But I'm really hoping my body will leave me alone for a while." ■

Mary Carmichael is a science writer based in Malden, Massachusetts.

1. Zhang, S. *et al.* *Nature Med.* **18**, 1639–1642 (2012).
2. Sacco, G. *et al.* *Vasc. Pharmacol.* **50**, 166–170 (2009).
3. Blanco, J. G. *et al.* *J. Clin. Oncol.* **30**, 1415–1421 (2011).
4. Mulrooney, D. A. *et al.* *Cancer* **112**, 2071–2079 (2008).
5. Diller, L. N. *Engl. J. Med.* **365**, 1417–1424 (2011).

CELL BANKS

Life blood

Stem cells from the umbilical cord are among the latest weapons in the fight against leukaemia.

BY MELINDA WENNER MOYER

Breast or bottle? Cloth nappy or disposable? Circumcise or not? Expectant parents face many choices, and now there is another: whether and how to bank the blood from their baby's umbilical cord.

Cord blood, taken from the placenta and umbilical cord immediately after birth, is rich with stem cells that can be used to replace or replenish abnormal cells. In a child with leukaemia, these transplanted cells could replace the diseased blood-forming stem cells killed by radiation or chemotherapy.

Parents who choose to bank their child's cord blood have two options: private banks, which cost upwards of US\$3,600 for 20 years of storage¹, or free public banks that make it available to anyone who is a suitable match.

According to Bone Marrow Donors Worldwide in the Netherlands, more than 570,000 cord blood units are kept in public banks, and a 2008 survey found that 780,000 units are stored in 134 private banks². More than 25,000 cord-blood transplants have been performed globally to date.

In the past five years, the scientific consensus has favoured the public banking option, particularly for leukaemia, because people with the disease usually benefit more from others' stem cells than from their own.

"A child who develops leukaemia has evidence that his or her own immune system has already failed to prevent the leukaemia," says Hildy Dillon, senior vice-president of patient services at the Leukaemia & Lymphoma Society, a non-profit research and advocacy organization based in White Plains, New York. In fact, she says, stem cells from donors sometimes attack the cancer cells in what is known as a helpful 'graft-versus-leukaemia' effect.

UNRELATED BENEFITS

People with leukaemia benefit most from bone-marrow transplants, ideally from immune-matched relatives. But two-thirds of those who need transplants can't find a match, and the search for unrelated matched donors can take months, particularly for people of some ethnic backgrounds³.

Cord blood from unrelated donors can be an effective alternative. From 2003 to 2008, people with acute myeloid leukaemia who received cord-blood transplants from an unrelated donor had a 39% chance of surviving

three years later, compared with 45% after an unrelated bone-marrow transplant and 43% after an unrelated peripheral-blood transplant, according to the US Department of Health and Human Services.

One big advantage of cord blood is that it does not need to be perfectly matched by immune subtype to prevent graft-versus-host disease³, a condition in which the transplanted cells attack the recipient's tissues. This is because cord stem cells are immature and are enriched with regulatory T cells, a kind of immune cell that suppresses immune responses, says Eliane



Should parents bank their baby's cord blood?

Gluckman, a haematologist at the Hôpital St Louis in Paris, France, who in 1988 performed the first successful cord-blood transplant for a rare genetic disease⁴. And because cord stem cells are less likely than other stem cells to have been exposed to pathogens, they are less likely to transmit infectious diseases.

The main drawback of cord blood cells is that they take longer to engraft than do stem cells from more mature sources. This delay leaves recipients vulnerable to infection.

To limit the window of vulnerability, Marcel van den Brink, an oncologist at the Memorial Sloan-Kettering Cancer Center in New York, and his colleagues are testing a form of inter-

NATURE.COM
Watch an exclusive animation on how leukaemia develops:
go.nature.com/rpnw28

leukin-7, a growth factor secreted by cells in the bone marrow that speeds up T-cell recovery and engraftment⁵. And ProHema, a cell

therapy developed by California-based Fate Therapeutics, helps stem cells home to the bone marrow faster, shortening engraftment time.

But even if engraftment can be accelerated, cord-blood transplants will still face serious limitations. Doctors can extract only a limited number of cells from one umbilical cord — typically less than half the 20 million cells per kilogram of the recipient's body weight usually recommended for adult transplants.

"Cord blood works well, but the problem is the amount per sample that can be collected," says Mahendra Rao, director of the NIH Center for Regenerative Medicine in Bethesda, Maryland. "If we could expand it, pool it or in some other way augment the supply without losing its efficacy or introducing additional problems, there would be a sea change" in the prevalence of this approach, he says.

DOUBLING UP

To address this problem, researchers at the University of Minnesota began combining cord blood from two unrelated donors. Analysing 536 stem-cell transplants for leukaemia conducted between 2001 and 2008, they found that the 128 people with leukaemia who had received double cord-blood transplants were less likely to relapse or develop graft-versus-host disease than those who had received bone-marrow transplants. But the cord-blood recipients were also 2–3 times more likely to die from infection and haemorrhage. Combine these effects, and double cord-blood transplant recipients had a five-year cancer-free survival rate of 51%, similar to those who received bone-marrow or peripheral-blood transplants from relatives or immune-matched non-relatives⁶.

The researchers speculate that the unexpectedly low relapse rate may be because having two donors increases the chances of a beneficial graft-versus-leukaemia effect, with one or both sources of cells eliciting the response⁶.

Cord blood's future as a viable treatment is likely to depend on more than scientific problem solving. The American Medical Association, the International Federation of Gynecology and Obstetrics, and the UK Royal College of Obstetricians and Gynaecologists have all discouraged private cord-blood banking except in the case of known medical need, noting that public banking is generally more useful. The question is whether these recommendations will reach expectant parents — and whether the parents will heed them. ■

Melinda Wenner Moyer is a science writer based in Cold Spring, New York.

1. Kaimal, A. J. *et al. Obstet. Gynecol.* **114**, 848–855 (2009).
2. Ballen, K. K. *et al. Biol. Blood Marrow Transplant.* **14**, 356–363 (2008).
3. Smith, A. R. & Wagner, J. E. *Br. J. Haematol.* **147**, 246–261 (2009).
4. Gluckman, E. *et al. N. Engl. J. Med.* **321**, 1174–1178 (1989).
5. Perales, M. A. *et al. Blood* **120**, 4882–4891 (2012).
6. Brunstein, C. G. *et al. Blood* **116**, 4693–4699

PERSPECTIVE



Bruce L. Levine



Carl H. June

Assembly line immunotherapy

Bruce L. Levine and Carl H. June explore how to make engineered immune cells that can eradicate cancer widely available.

The myth of the chimaera, a beast that is part lion, part goat and part serpent, originated in ancient Lycia. Two millennia later and a few hundred kilometres to the south, scientists at the Weizmann Institute of Science in Rehovot, Israel, described a chimaeric receptor expressed in immune cells called T cells. This chimaera — part antibody and part T-cell receptor — can be designed to recognize and destroy any tumour.

T cells with these chimaeric antigen receptors (CARs) can eradicate kilograms of leukaemia in a few weeks in people whose cancers didn't succumb to the best available conventional therapies. But so far, this experimental therapy has been available only to small numbers of people in pilot trials at academic centres.

The central question now is whether this technique be scaled up to treat thousands of patients.

We think that by making use of equipment and facilities developed for blood banks and stem-cell laboratories, and by automating production, it will be possible to make these T-cell therapies widely available to the many people who need it. Indeed, thanks to this innovation, leukaemia treatment could be on the brink of an evolution similar to the one the automotive industry experienced in recent decades in its transition from manual assembly lines to robotic automation¹.

When the technique was first devised, it required manual selection of tumour-specific T cells before their numbers were increased in the lab by repeatedly stimulating them with specific tumour antigens. But this process requires expensive materials and takes weeks or months to generate billions of T cells.

In 1996, we reported an advance in culture technology that can efficiently produce large populations of T cells, approximating the mass of T cells in the human immune system². We attached two antibodies to cell-sized magnetic beads, and used these antibodies to deliver two signals needed for T-cell expansion. This process enabled us to generate sufficient quantities of T cells within ten days.

We and others have used this method to treat several hundred people enrolled in clinical trials for leukaemias and other cancers. In the past few years, this approach, combined with CARs, has produced remission in more than half the adults and children treated who have advanced acute and chronic lymphoid leukaemia^{3,4}.

Many scientists have raised legitimate concerns about the perceived complexity of this type of therapy and its broad applicability. Some have dismissed it as a fringe or boutique therapy that would be impossible to commercialize⁵. Also, regulations set up by the US Food and Drug Administration and the European Medicines Agency are largely intended for drugs prepared and tested far in advance of medical need, and for which a single production run serves thousands of

patients. Furthermore, the pharmaceutical industry's own quality control systems are geared towards generating large batches of drugs of consistent quality.

So, how can manufacturing be optimized, and how should consistency be judged when producing truly individualized medical therapies? The answer, we believe, lies in the creative use of existing facilities and a concerted effort to build the required infrastructure.

As a historical example, organ transplants, and bone-marrow and stem-cell transplants, were seen as exotic a few decades ago. Today, these therapies are accessible to tens of thousands of people. Conventional drugs are scaled up to large batches, but these personalized therapies were 'scaled out' to multiple medical centres with technically advanced operating theatres, laboratories and medical staff.

Equipment developed for blood banks and stem-cell laboratories is now routinely used in advanced T-cell therapy laboratories. In the short term, T-cell therapies will be produced in specialized cell-therapy production facilities located throughout the world at academic medical centres and biotechnology companies. Still, the current cell culture process requires extensive manipulation by highly skilled scientists and technicians. How will T-cell therapies achieve the mass production needed to treat large numbers of patients?

As CAR T-cell processing also becomes more automated, we will be able to efficiently produce individualized therapies for larger numbers of people. But technology alone cannot solve this problem.

Regulations and standards must evolve to reflect products that are personalized and sometimes administered in settings of urgent medical need.

Several pharmaceutical and biotechnology companies have entered this field in recent months with the aim of developing commercial-scale manufacturing of CAR T cells for worldwide application. We are optimistic that the resources and expertise of the pharmaceutical industry will create the infrastructure needed for the widespread availability of this disruptive technology. Developing engineered T-cell therapies in large numbers will be challenging, but it is justified given their power to treat cancer. ■

Bruce L. Levine is an associate professor in cancer gene therapy and **Carl H. June** is a professor of immunotherapy at the University of Pennsylvania's Perelman School of Medicine in Philadelphia.

1. Michalos, G. *et al.* *CIRP J. Manuf. Sci. Technol.* **2**, 81–91 (2010).
2. Levine, B. L. *et al.* *Science* **272**, 1939–1943 (1996).
3. Grupp, S. A. *et al.* *N. Engl. J. Med.* **368**, 1509–1518 (2013).
4. Porter, D. L. *et al.* *N. Engl. J. Med.* **365**, 725–733 (2011).
5. Baker, M. *Nature Med.* **17**, 519 (2011).

The authors declare a conflict of interest: go.nature.com/rpnw28

➔ **NATURE.COM**
For some of the latest research on T-cell therapies:
go.nature.com/zk2img

BY MAKING USE OF EXISTING EQUIPMENT AND FACILITIES, AND BY AUTOMATING PRODUCTION, IT WILL BE POSSIBLE TO MAKE THESE THERAPIES WIDELY AVAILABLE